

University of Zagreb
Faculty of Metallurgy
Sisak, Croatia



University of Ljubljana
Faculty of Natural Sciences and Engineering
Ljubljana, Slovenia



University North
Koprivnica, Croatia



Technical University of Košice
Faculty of Materials, Metallurgy and Recycling
Košice, Slovakia



ELKEM ASA
Oslo, Norway



PROCEEDINGS BOOK

18th INTERNATIONAL FOUNDRYMEN CONFERENCE

**Coexistence of material science and sustainable
technology in economic growth**



Sisak, May 15th – 17th, 2019

ORGANIZERS

University of Zagreb Faculty of Metallurgy, Sisak, Croatia

University of Ljubljana Faculty of Natural Sciences and Engineering, Ljubljana, Slovenia

University North, Koprivnica, Croatia

Technical University of Košice Faculty of Materials, Metallurgy and Recycling, Košice, Slovakia

ELKEM ASA, Oslo, Norway

PROCEEDINGS BOOK**18th INTERNATIONAL FOUNDRYMEN CONFERENCE**

Coexistence of material science and sustainable technology in economic growth

EDITORS

Natalija Dolić, Zdenka Zovko Brodarac, Anita Begić Hadžipašić

TECHNICAL EDITOR

Anita Begić Hadžipašić

PUBLISHER

University of Zagreb

Faculty of Metallurgy

Aleja narodnih heroja 3

44000 Sisak

Croatia

PRINT

InfOmArt Zagreb d.o.o.

Nikole Tesle 10

44000 Sisak

Croatia

ISSUE

200 copies

ISBN

978-953-7082-34-5

-A CIP record is available in computer catalogue of the National and University Library in Zagreb under the number 001029655.

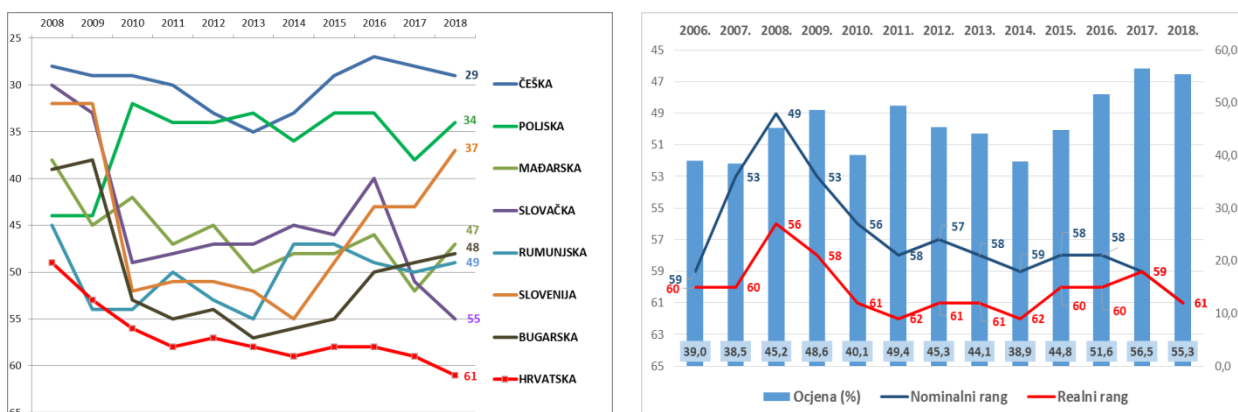
PREFACE

Foundry industry as a base branch represents an important factor contributing to the economic potential of each country. Current market development as well as technical and economic objective, the production of high-quality, low-cost and environmentally friendly casting, requires application of recent and advanced materials, as well as production technologies, followed and supported by understanding of production process.

Production imperative is pointed into the recent technologies and improved materials for everyday usage in our homes, workplaces, as well as materials with special requirements for specific applications such as those for the automotive or space industry. Industrial activities, which are defined as strategic activities in the Republic of Croatia are **Metal Casting** and **Production of Final Metal Products**, recognized as "*economic growth drivers*" because they are expected to realize higher rates of growth and employment.

According to the data of the Central Bureau of Statistics (DZS) and Financial Agency (FINA) and on the basis of analysis of the Sector for Financial Institutions, Business Information and Economic Analysis of the Croatian Chamber of Commerce and for the last analyzed 2017, the primary production of metals in the structure of Croatian industrial production is only 1.35% due to lack of economically viable primary raw materials and market fluctuations in their prices but also of the lack of modern production capacities. However, the valorization and export component of finished metal products stands out with a high share of almost 8.78%. Overall, this represents **10.13% of the industrial production of the Republic of Croatia**.

Croatia is also included yearly World Competitiveness Yearbook issued by Institute for Management Development (IMD) in Lausanne. "The World Year of Competitiveness" has been published every year since 1989 for the purpose of analysing and ranking the nation's ability to create and maintain an environment that maintains the company's competitiveness. In 2018 report, Croatia has ranked at 61th place from 63 world economy. The IMD methodology is based on an analysis of 4 factors of competitiveness, namely: economic results, public sector efficiency, business sector efficiency and infrastructure, and 5 indices for each area. Also, an overview of the status of the Republic of Croatia in the period from 2006 to 2018 is presented in the following graph.

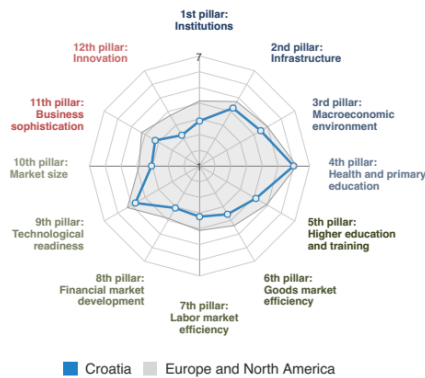


IMD World Competitiveness Yearbook 2018

An overview of the status changes suggests that the economic crisis with its negative effects since 2008 for many comparable countries ended in 2014, while the Republic of Croatia in 2018 shows no recovery. Economic results are based on high revenues from tourism but also on exports. Despite a skilled workforce, a high level of education and a reliable infrastructure, a bad business environment, a slow administration and the burden of parafiscal charges still dictate a relatively

low labor price. Progress can be expected through stronger collaboration between the academic community and the economy, with emphasis on investment in innovation, knowledge transfer and technology optimization, with the prerequisite for the management structure to recognize the importance of such cooperation. In addition, the "Competitiveness Report" for 2017-2018 goes to this year, according to which the Republic of Croatia shows a continuous decline and this year it has 74th position out of 137 world economies, as shown in the following graph.

Edition	2012-13	2013-14	2014-15	2015-16	2016-17	2017-18
Rank	81 / 144	75 / 148	77 / 144	77 / 140	74 / 138	74 / 137
Score	4.0	4.1	4.1	4.1	4.1	4.2



World Economic Forum, The Global Competitiveness Report 2017–2018

The problematic pillars of competitiveness are the continuity of business and innovation. The 5 most problematic factors for doing business in terms of efficiency valorization are identified: inefficient public administration, instability of legal regulation, tax regulations, and corruption and tax rates. These 5 factors can be regulated by public policy. Thereafter, there are four factors that the economy needs to recognize and impose as prerequisites for its competitiveness: inadequate capacity for innovation, availability of funding, limiting labor regulations, inadequately educated workforce. Identifying their own niche for competitiveness on the global market and following the stated public policy requirements for recognizing and incorporating them into development and funding strategies, as well as the education system in designing competent, creative and innovative workforce, can provide a synergy of positive moves towards increasing competitiveness.

Therefore, the importance of *coexistence of material science and sustainable technology in economic growth* reveals in collaboration between small and medium enterprises' (SMEs'), industry and higher education institutions (HEI). **International Foundrymen Conference** organized by University of Zagreb Faculty of Metallurgy, Sisak, Croatia in cooperation with University of Ljubljana Faculty of Natural Sciences and Engineering, Ljubljana, Slovenia, University North, Koprivnica, Croatia, Technical University of Košice Faculty of Materials, Metallurgy and Recycling, Košice, Slovakia, and ELKEM ASA, Norway found its significant position due to aforementioned reasons.

Coexistence of material science and sustainable technology in economic growth comprehends to recent technology and educated and skilled engineers. The Conference topics were designed as presentations of the current *"state of the art"* research in collaboration with industry, and production innovation with the aim to improve the competitiveness.

The scope of **18th International Foundrymen Conference (IFC)** covers scientific, technological and practical aspects concerning research, development and application of casting technology with the common perspective – increase of competitiveness. Special attention will be focused towards the

competitiveness ability of foundries, improvement of materials features and casting technologies, environmental protection as well as subjects connected to the application of castings.

During this Conference 35 paper will be presented. Book of Abstracts of the 18th International Foundrymen Conference includes summaries of the papers. The Proceedings book consists of papers *in extenso* published in electronic format (USB). Full length papers have undergone the international review procedure, done by eminent experts from corresponding fields, but have not undergone linguistic proof reading. Sequence of papers in Proceedings book has been done by category of papers in following order: plenary lectures, invited lectures, oral and poster presentation, and inside the category alphabetically by the first author's surname.

Within the Conference Student section is organized. This is an opportunity for industry to meet and recruit human resources as a main potential for business development. Coexistence of material science and sustainable technology in economic growth represent a knowledge transfer between small and medium enterprises' (SMEs'), industry and higher education institutions. Higher education at the Faculty of Metallurgy (HEI), conceived through the program and the learning outcomes, is based, inter alia, on promoting students' scientific and research work on applied topics, enabling ambitious and creative young people to become independent problem solvers, developing and supporting their curiosity, analytics and communication: **Graduates like the labour market need!**

This occasion represents an opportunity to discuss and increase the mutual collaboration between HEIs' and industry with the aim of information exchange related to advanced experience in foundry processes and technologies, gaining the new experience in presentation and / or teaching process within lifelong learning process.

The organizers of the Conference would like to thank all participants, reviewers, sponsors, auspices, media coverage and all those who have contributed to this Conference in any way.

President of Organizing Board



Assoc.Prof. Zdenka Zovko Brodarac, PhD



Monument to a Croatian poet Antun Gustav Matoš, Sisak, Croatia
[https://hr.wikipedia.org/wiki/Datoteka: Sisak Matos monument.JPG](https://hr.wikipedia.org/wiki/Datoteka:Sisak_Matos_monument.JPG)



Nikola III Zrinski on a silver thaler minted in Gvozdansko, Croatia
[https://en.wikipedia.org/wiki/Nikola III Zrinski](https://en.wikipedia.org/wiki/Nikola_III_Zrinski)

UNDER THE HIGH AUSPICES

President of Croatia
Kolinda Grabar – Kitarović

UNDER THE PATRONAGE

Ministry of Science and Education of the Republic of Croatia
Ministry of Economy, Entrepreneurship and Crafts of the Republic of Croatia
University of Zagreb
World Foundry Organization (WFO)
Mittel Europäische Giesserei Initiative (MEGI)
Chamber of Commerce of Republic of Croatia
Sisak – Moslavina County
City of Sisak

SPONSORED BY

SILVER SPONSOR

HEMOLAB Ltd, Beograd (RS)
LABTIM ADRIA Ltd, Sesvete (HR)

BRONZE SPONSOR

BENTOPRODUCT Ltd, Šipovo (BA)
BITUS Ltd, Zagreb (HR)
EBERT Ltd, Ljubljana (SI)
FERRO-PREIS Ltd, Čakovec (HR)
HAGI GmbH, Pyhra (AT)
HEINRICH WAGNER SINTO MASCHINENFABRIK GmbH, Bad Laasphe (DE)
LABEKO Ltd, Zagreb (HR)
MECAS ESI s.r.o., Plzen (CZ) & TC LIVARSTVO Ltd, Ljubljana (SI)
TROKUT TEST GROUP Ltd, Zagreb (HR)

MEDIA COVERAGE

IRT 3000
Foundry Lexicon
Foundry Planet

SUPPORTING ASSOCIATION AND COMPANIES

Croatian Foundry Association
Slovenian Foundry Association

ORGANIZING COMMITTEE

Zdenka Zovko Brodarac, president

Anita Begić Hadžipašić

Sandra Brajčinović

Damijan Cerinski

Natalija Dolić

Gordana Gojsević Marić

Martina Hrubovčáková

Franjo Kozina

Stjepan Kožuh

Ladislav Lazić

Jožef Medved

Marin Milković

Primož Mrvar

Tomislav Rupčić

Sanja Šolić

Iveta Vasková

PROGRAM COMMITTEE

Hasan Avdušinović (BA)

Branko Bauer (HR)

Anita Begić Hadžipašić (HR)

Jaka Burja (SI)

Lidija Čurković (HR)

Mile Djurdjević (AT)

Natalija Dolić (HR)

Peter Cvahte (SI)

Regina Fuchs-Godec (SI)

Dario Iljkić (HR)

Sebastjan Kastelic (SI)

Varužan Kervorkijan (SI)

Ivica Kladarić (HR)

Borut Kosec (SI)

Dražan Kozak (HR)

Stjepan Kožuh (HR)

Zoran Kožuh (HR)

Ladislav Lazić (HR)

Martina Lovrenić-Jugović (HR)

Srećko Manasijević (RS)

Dragan Manasijević (RS)

Jožef Medved (SI)

Daniel Novoselović (HR)

Mitja Petrič (SI)

Bojan Podgornik (SI)

Karlo T. Raić (RS)

Vera Rede (HR)

Zdravko Schauperl (HR)

Peter Schumacher (AT)

Ljerka Slokar Benić (HR)

Božo Smoljan (HR)

Tahir Sofilić (HR)

Davor Stanić (HR)

Sanja Šolić (HR)

Iveta Vaskova (SK)

Maja Vončina (SI)

Zdenka Zovko Brodarac (HR)

Irena Žmak (HR)

REVIEW COMMITTEE

Vesna Alar (HR)	Ladislav Lazić (HR)
Ljubiša Balanović (RS)	Martina Lovrenić-Jugović (HR)
Jakov Baleta (HR)	Dragan Manasijević (RS)
Marko Ban (HR)	Ivana Marković (RS)
Branko Bauer (HR)	Adrijana Milinović (HR)
Anita Begić Hadžipašić (HR)	Aleš Nagode (SI)
Mile Djurdjević (AT)	Daniel Novoselović (HR)
Natalija Dolić (HR)	Vesna Ocelić Bulatović (HR)
Nikša Čatipović (HR)	Mitja Petrič (SI)
Vladan Ćosović (RS)	Zora Pilić (HR)
Stanisław Gil (PL)	Grzegorz Piwowarski (PL)
Vesna Grekulović (RS)	Milena Premović (RS)
Tamara Holjevac Grgurić (HR)	Žarko Radović (ME)
Dario Iljkić (HR)	Ankica Rađenović (HR)
Ivan Ivec (HR)	Matija Sakoman (HR)
Miće Jakić (HR)	Božo Smoljan (HR)
Ivan Jandrlić (HR)	Ivan Stojanović (HR)
Sebastjan Kastelic (SI)	Sanja Šolić (HR)
Zvonimir Katančić (HR)	Iveta Vasková (SK)
Witold Kazimierz Krajewski (PL)	Tatjana Volkov Husović (RS)
Varužan Kevorkijan (SI)	Darja Volšak (SI)
Ana Kostov (RS)	Maja Vončina (SI)
Stjepan Kožuh (HR)	Domagoj Vulin (HR)
Jure Krolo (HR)	Zdenka Zovko Brodarac (HR)
Dajana Kučić Grgić (HR)	Irena Žmak (HR)

CONTENTS

Iulian Riposan, Mihai Chisamera, Stelian Stan, Mihail Firican GRAPHITE DEGENERATION IN THE SURFACE LAYER OF Mg-TREATED IRON CASTINGS – INFLUENCING FACTORS AND PRACTICAL SOLUTIONS	1
Hasan Avdušinović, Almaida Gigović-Gekić, Šehzudin Dervišić DECOMPOSITION OF AUSTENITE IN AUSTEMPERED DUCTILE IRON SAMPLES ON ELEVATED TEMPERATURES	2
Maroš Halama, Karol Koval, Andrej Petrik CORROSION MONITORING OF METAL RELEASE INTO ENVIRONMENT	9
Varužan Kevorkijan, Tomaž Šustar, Irena Lesjak, Marko Degiampietro, Janez Langus PROGRESS IN ON-LINE OPTICAL EMISSION SPECTROMETRY (OES) DATA- DRIVEN INSPECTION OF INCLUSIONS IN ALUMINIUM ALLOYS	10
Ivica Kladarić, Stjepan Golubić, Slavica Kladarić THE IMPACT OF APPLYING PVD COATINGS ON SURFACE ROUGHNESS OF QUENCHED AND TEMPERED STEELS	19
Dragan Manasijević, Duško Minić, Ljubiša Balanović, Milena Premović, Milan Gorgievski MICROSTRUCTURE AND SOLIDIFICATION BEHAVIOR OF THE Ga–Ge–Sb TERNARY ALLOYS	31
Jožef Medved, Stanislav Kores, Natalija Dolić, Maja Vončina INTERACTION BETWEEN MOLTEN ALUMINIUM AND HOT-WORKING TOOL STEEL	45
Primož Mrvar, Sebastjan Kastelic, Grega Gorše, Branko Bauer, Mitja Petrič POSSIBILITIES FOR PROVIDING OF UNIDIRECTIONAL SOLIDIFICATION OF COMPLEX CASTINGS IN THE TECHNOLOGY OF HIGH-PRESSURE DIE- CASTING	57
Sam Ramrattan NEW TESTS FOR CHEMICALLY BONDED FOUNDRY SANDS	58
Božo Smoljan, Dario Iljkić, Sunčana Smokvina Hanza PREDICTION OF WORKING STRESS OF QUENCHED AND TEMPERED STEEL AND CAST STEEL SPECIMEN	77

Zdenko Tonković, Karlo Seleš, Ante Jurčević, Jurica Sorić CRACK PROPAGATION PREDICTION IN HETEROGENEOUS MICROSTRUCTURE OF NODULAR CAST IRON	85
Tamara Aleksandrov Fabijanić, Mladen Franz, Stoja Rešković DETERMINATION OF MECHANICAL PROPERTIES OF NIOBIUM MICRO- ALLOYED STEEL USING INSTRUMENTED INDENTATION TEST	95
Jakov Baleta, Damijan Cerinski, Fengsheng Qi, Fang Wang, Jin Wang, Xuebin Wang THE INFLUENCE OF WATER MIST INJECTION ON THE FILM COOLING PROCESS OF CASTED TURBINE BLADES	106
Dipak Ghosh COMPARISON OF MOLDING SAND TECHNOLOGY BETWEEN ALPHASET (APNB) AND FURAN (FNB)	122
Ivan Jandrlić, Stoja Rešković, Ladislav Lazić, Tin Brlić, Dušan Ćurčija APPROPRIATE MATHEMATICAL MODEL FOR STRESS CALCULATION BASED ON THE MEASURED VALUES OF DEFORMATION AND TEMPERATURE CHANGES	145
Blaž Leskovar, Boštjan Markoli, Iztok Naglič COOLING RATE ASSESSMENT DURING NONEQUILIBRIUM SOLIDIFICATION OF COMPLEX Al–Mn-BASED ALLOYS	153
Milena Premović, Duško Minić, Dragan Manasijević, Aleksandar Djordjević THERMODYNAMIC DESCRIPTION OF THE TERNARY Ge–Sn–Ag, In, Zn	169
Ljerka Slokar Benić, Ivan Jandrlić, Stoja Rešković EFFECT OF SUBSEQUENT HEATING ON THE MICROSTRUCTURE AND MECHANICAL PROPERTIES OF Nb MICROALLOYED STEEL	180
Sandra Brajčinović, Anita Begić Hadžipašić, Jožef Medved, Stjepan Kožuh INFLUENCE OF MEDIUM ON CORROSION AND MICROSTRUCTURAL PROPERTIES OF HTCS-130 TOOL STEEL FOR HOT WORK	188
Natalija Dolić, Ivana Bunjan, Franjo Kozina CORRELATION OF MECHANICAL AND MICROSTRUCTURAL PROPERTIES IN AS-CAST CONDITION OF EN AW-5083 ALUMINIUM ALLOY USING STATISTICAL ANALYSIS	206
Stanisław Gil, Wojciech Bialik, Bolesław Machulec, Sławomir Kozłowski MODERNIZATION OF THE LADLE TO IMPROVE FERROALLOY REFINING CONDITIONS	220

Senka Gudić, Blanka Rakuljić, Ladislav Vrsalović, Milan Bizjak, Ivana Ivanić, Stjepan Kožuh, Mirko Gojić INFLUENCE OF Mn ON THE CORROSION BEHAVIOR OF CuAlMn ALLOY IN NaCl SOLUTION	227
Ivana Ivanić, Stjepan Kožuh, Nikolina Pavičić, Dijana Čubela, Omer Beganović, Borut Kosec, Mirko Gojić MICROSTRUCTURAL ANALYSIS OF COLD DRAWN CuAlMn SHAPE MEMORY ALLOY WIRE	237
Igor Jajčinović, Ivan Brnardić, Stjepan Kožuh, Kristina Tolić THE IMPACT OF MULTIWALL CARBON NANOTUBES ON THE PHOTOCATALYTIC PROPERTIES OF IMOBILIZED TiO ₂	247
Franjo Kozina, Zdenka Zovko Brodarac, Dalibor Drobnjak, Ivan Jukić INVESTIGATION OF IRON CONTAINING INTERMETALLICS IN AISi12 ALLOY WITH w (Mn/Fe) = 0.99	255
Stjepan Kožuh, Katarina Pavičić, Ivana Ivanić, Milan Bizjak, Mirko Gojić THE EFFECT OF ANNEALING TIME ON MICROSTRUCTURE AND IMPACT ENERGY OF STAINLESS STEEL AISI 316L	275
Ladislav Lukáč, Ján Kizek, Augustín Varga, Ladislav Lazić, Róbert Dzurňák SELECTED PARAMETERS THAT INFLUENCE EMISSION FORMATION DURING ALUMINUM MELTING	288
Ivana Manasijević, Ljubiša Balanović, Tamara Holjevac Grgurić, Emi Govorčin Bajsić INVESTIGATION OF THERMAL PROPERTIES OF THE Ga–In AND Ga–Sn EUTECTIC ALLOYS	295
Ivana Mihalic Pokopec, Ines Mance, Davor Cesarec, Branko Bauer PERMANENT MOULD CASTING OF ALUMINIUM ALLOY FORK	308
Vesna Ocelić Bulatović, Dajana Kučić, Antonio Ivančić, Lucija Kefurt EFFECT OF UV IRRADIATION ON THERMAL AND MECHANICAL PROPERTIES OF MATERIALS	322
Tahir Sofilić, Ivan Brnardić, Una Sofilić-Šimić, Laila Gumhalter-Malić WASTE OIL MANAGEMENT IN CROATIA FOR THE PERIOD 2007 – 2016	335
Paul Sponsel, Irena Žmak, Milan Vukšić THE CHARACTERISTICS AND ENVIRONMENTAL ASPECTS OF MAGNESIUM THIXOMOLDING VERSUS DIE CASTING PROCESS	349

- Uroš Stamenković, Svetlana Ivanov, Ivana Marković, Vesna Grekulović,
Jasmina Petrović, Milica Bošković** **363**
THE EFFECT OF THE AGING PROCESS ON THE DIFFERENT PROPERTIES OF
THE EN AW-6082 ALUMINUM ALLOY
- Sanja Šolić, Bojan Podgornik, Zdravko Schauperl, Matjaž Godec, Branko
Bauer, Vlado Tropša** **370**
INFLUENCE OF DEEP CRYOGENIC TREATMENT ON THE MECHANICAL
PROPERTIES OF ADI AUSTEMPERED AT THE LOWER AUSFERRITIC RANGE
- Ladislav Vrsalović, Ivana Ivanić, Stjepan Kožuh, Borut Kosec, Milan
Bizjak, Senka Gudić, Mirko Gojić** **378**
CORROSION BEHAVIOR OF CuAlMn AND CuAlMnNi ALLOY IN 0.9% NaCl
SOLUTION



18th INTERNATIONAL FOUNDRYMEN CONFERENCE
**Coexistence of material science and sustainable technology in
economic growth**

Sisak, May 15th-17th, 2019

<http://www.simet.hr/~foundry/>

**GRAPHITE DEGENERATION IN THE SURFACE LAYER OF Mg-TREATED IRON
CASTINGS – INFLUENCING FACTORS AND PRACTICAL SOLUTIONS**

Iulian Riposan^{*}, Mihai Chisamera, Stelian Stan, Mihail Firican

Politehnica University of Bucharest, Bucharest, Romania

Plenary lecture

Subject review

Abstract

Graphite degeneration, in terms of graphite becoming less compact, in the surface layer of Mg-treated cast irons is a common defect, which can occur with any moulding technique. This abnormal surface layer [0.1 to 3.0 mm thickness] may be present in any casting section thickness. However, it becomes most critical for thin wall castings, where it can easily be more than 10% of the total thickness, but also is a concern in heavy castings, due to the prolonged solidification time extending the metal-mould interaction time. The surface layer with degenerated graphite has a similar effect to a notch in the casting, reducing all the properties, especially as the fatigue limit and impact resistance.

The objective of the present work is to summarize the obtained results using selected data from some of the previous papers plus some unpublished data. It was considered residual Mg content [from compacted to nodular graphite formation], mould media chemistry [with/without S-content], with/without mould coatings [with/without S-content, with/without desulphurization agents (CaO, MgO, Talc, Mg_{met} or FeSiCaMg alloy)], with/without inoculation, at different inoculating variants.

Furan resin sand - PTSA mould, including sulphur, aggravated graphite degeneration, with the layer thickness increasing up to ten times compared to the Novolak resin coated sand moulds, without included sulphur, with higher surface layer thickness at lower Mg_{res}. Lower graphite nodularity, higher the size of the surface layer with degenerated graphite.

The application of a S-bearing mould coating strongly promoted graphite deterioration, or conversely, limited this process using desulphurization type coatings. MgO, (CaO + MgO + Talc) or Mg-FeSi bearing coating protected the graphite shape at the metal – mould interface, decreasing the average layer thickness. The Mg-FeSi coatings had an additional role to desulphurization providing supplementary Mg to raise the nodularising potential. The graphite characteristics within the section of the analyzed samples evolved in a clear relationship with the changes in the degenerate graphite surface layer, for the prevailing solidification conditions.

Inoculation increased graphite nodularity in the surface layer and decreased the surface layer thickness, at a strong relationship between these two parameters. The Inoculation Specific Factor, ISF [the ratio between increased nodularity/decreased surface layer thickness and total inoculant consumption for this effect] was used to evaluate the efficiency of inoculation variants.

Keywords: *nodular graphite, compacted graphite, graphite nodularity, casting skin, degenerated graphite layer, ferritic rim, inoculation, inoculation specific factor*

*Corresponding author (e-mail address): iulian.riposan@upb.ro

GRAPHITE DEGENERATION IN THE SURFACE LAYER OF Mg-TREATED IRON CASTINGS – INFLUENCING FACTORS AND SOLUTIONS

I. Riposan, M. Chisamera, S. Stan, M. Firican

The objective of the present work

is to summarize the obtained results

- using selected data from some of the previous published proprietary papers
- plus some unpublished data

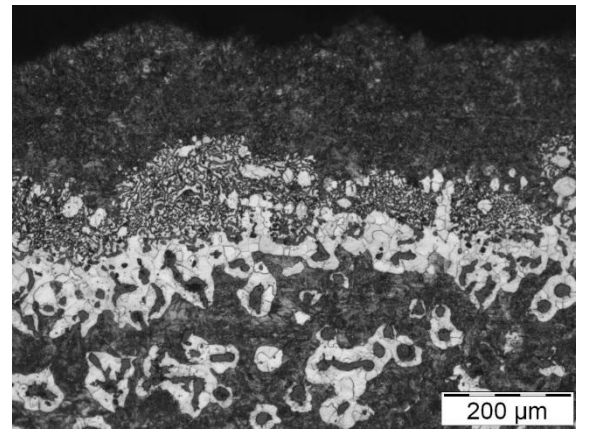
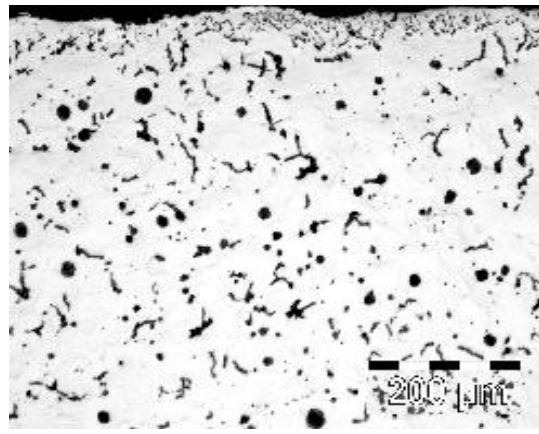
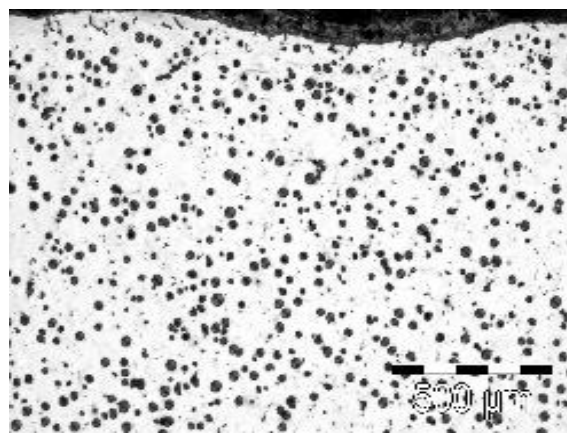
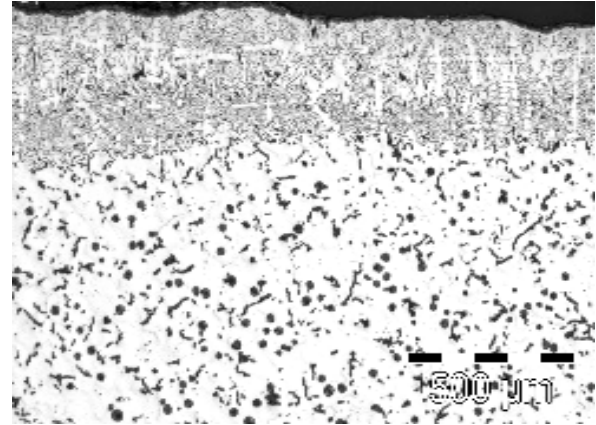
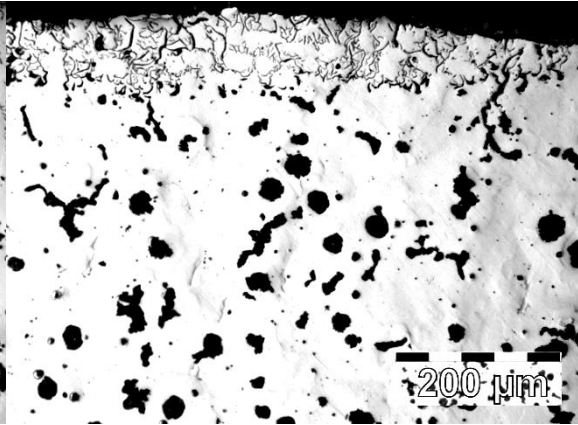
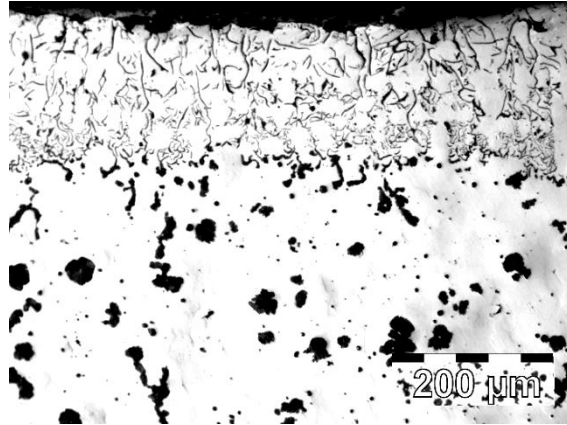
BACKGROUND

- residual Mg content [0.019 – 0.054%Mg_{res}, from CG to NG graphite formation],
- mould media chemistry [with & without **S** - content),
- with & without mould coatings:
 - coatings with & without **S**-content,
 - coatings with & without **desulphurizers** (CaO, MgO, Talc, Mg_{met}, FeSiCaMg),
[Int J Metalcast, 2012, 6(4), 61; Mat Sci Techn, 2012, 28(11), 1246; ISIJ Int, 2012, 52(10), 1848;
Int J Cast Met Res, 2013, 26(3), 138; AFS Trans, 2013, 121, 379; 71st WFC, 2014, Bilbao, Spain]

NEW EXPERIMENTS

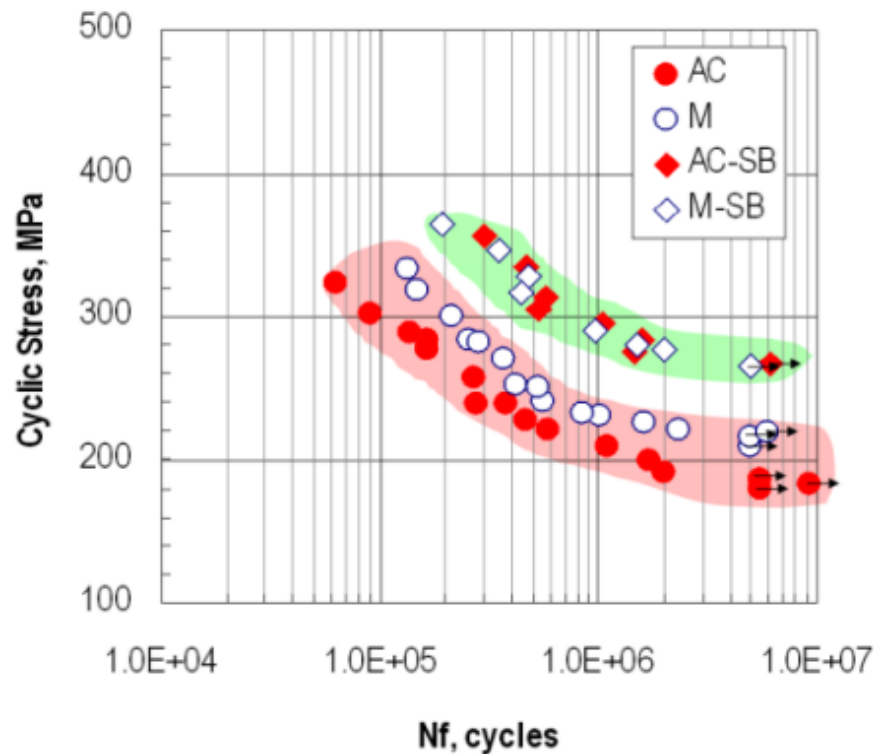
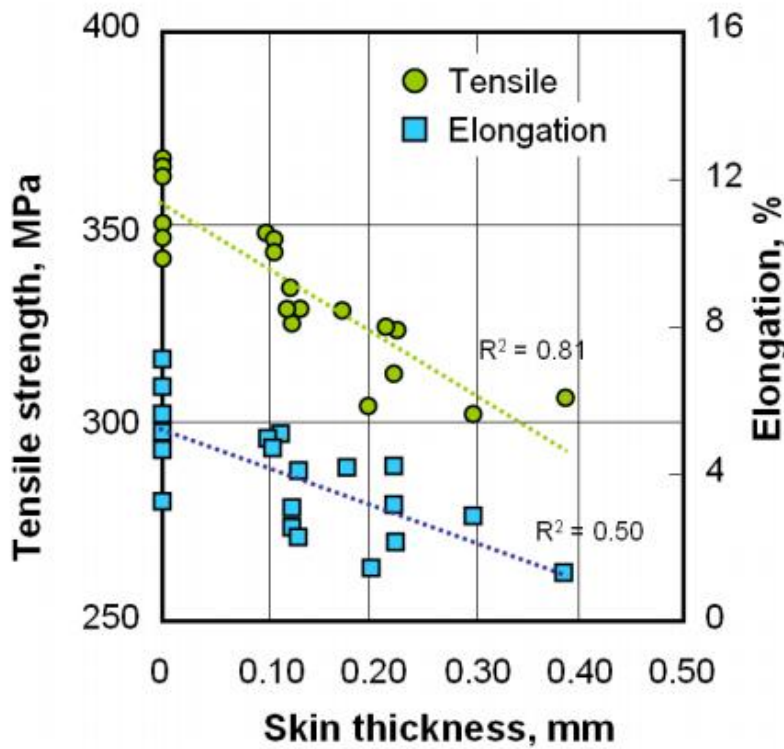
- with & without inoculation, at different inoculating variants:
 - conventional inoculants [Ca / Ca,Ba / Ca,RE / Ca,Ce,S,O - FeSi alloys]
 - conventional inoculants + inoculation enhancing [S,O,Al,Mg – CaSi alloy]

Mg - TREATED IRON CASTINGS SKIN



DETRIMENTAL EFFECTS OF CASTING SKIN - CGI

[**AC:** As Cast; **M:** Machined; **AC - SB:** As Cast + Shot Blasted; **M - SB:** Machined + Shot Blasted]



[S. Boonmee, D.M. Stefanescu, 10th Int. Symp. Science & Processing of Cast Iron, 2014, Mar del Plata, ARGENTINA]

I. LABORATORY EXPERIMENTS

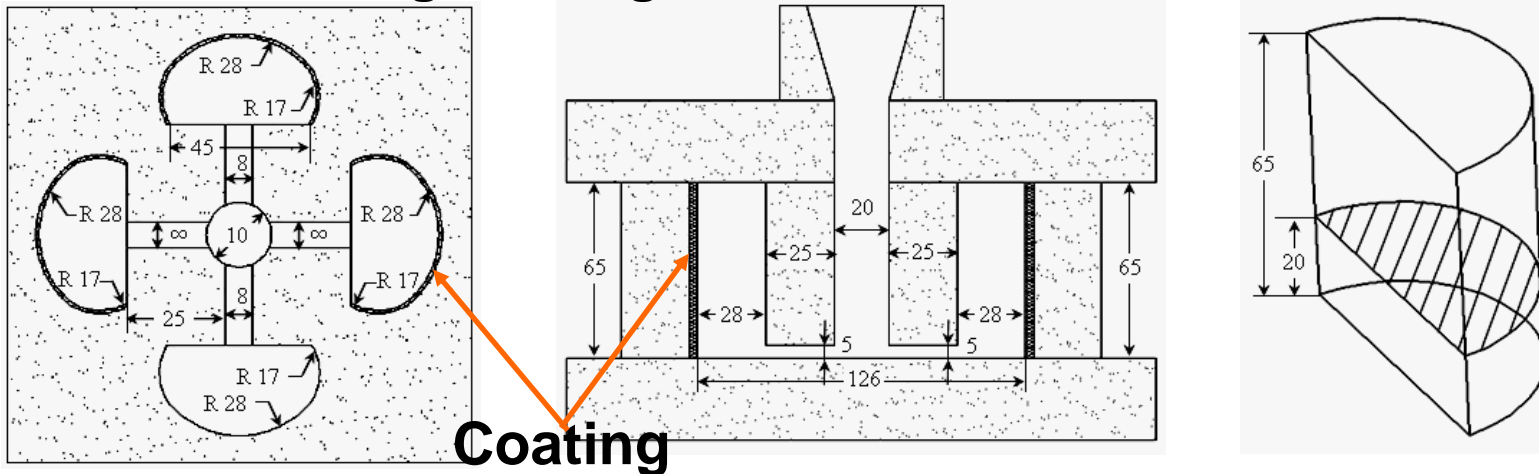
[Mg_{res} – Mould media – Mould Coating]

Samples: I. Furan resin (3.0wt.%) - P-Toluol Sulphonic Acid

FRS – PTSA Moulds [S – bearing mould]

Each mould includes 4 identical semi-cylindrical samples
with corners rounded to avoid end effect

0.56 kg, cooling modulus CM = 7.1 mm



II. NRS Moulds: Standard Quik-cup™ cups [No S mould]

Phenol- formaldehyde resin sand (Novolak) 0.35 kg, CM = 7.3mm

3 Coatings were applied to:

- concave surface of semi-cylindrical samples, *and*
- inner surface of the Quik-cups
- up to 0.01mm grain size materials in a 0.35 – 0.40 mm thick coating
- same coating binder, using expanded polystyrene - toluene solution

I. S - bearing coatings:

- **FRS-PTSA mould** (S in binder) + FeS₂ powder (49 – 52 %S), as added S
- **NRS mould** (no S) + FeS₂ powder *or* variable Elemental S addition (organic)

II. Desulfurizing type Coatings :

- MgO *or* (CaO + MgO + Talc) mixture / beneficial in heavy section DI castings

III. Desulfurizing Coating with supplementary Mg

- fine sized FeSiCaMgRE alloy *or* (Mg_{metal} + FeSi75) powder

*Structure Analysis

- FRS-PTSA mould semi-cylindrical samples

Surface layer thickness Structure in the Surface Layer and Center

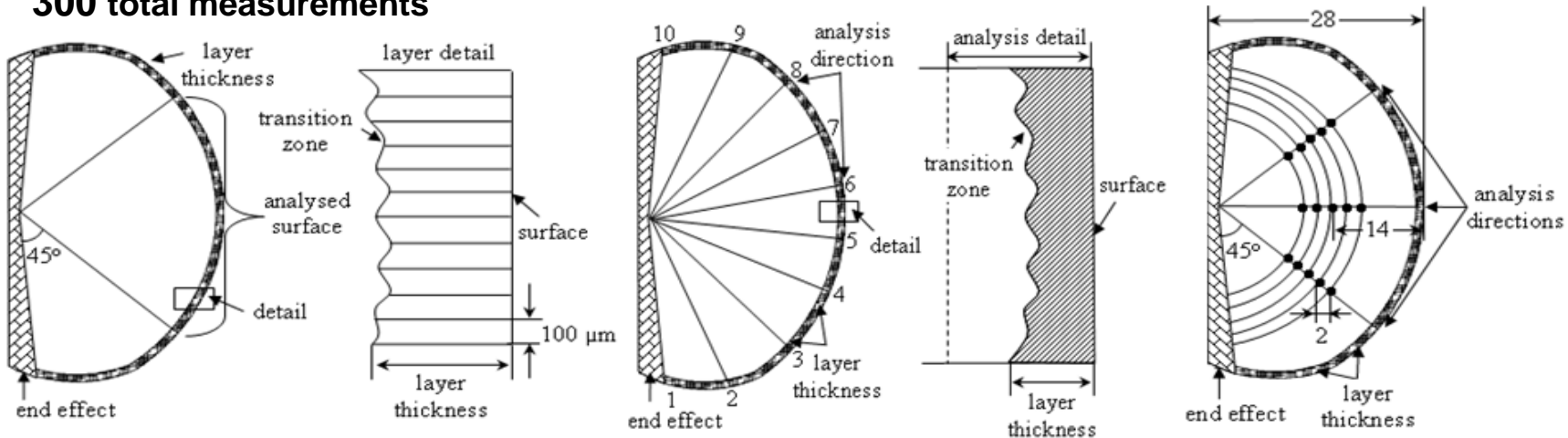
On 30mm total length 10 individual analysis directions 3 directions / 5 positions

100 μm between measurements

800 mm² total area analyzed

2mm apart

300 total measurements



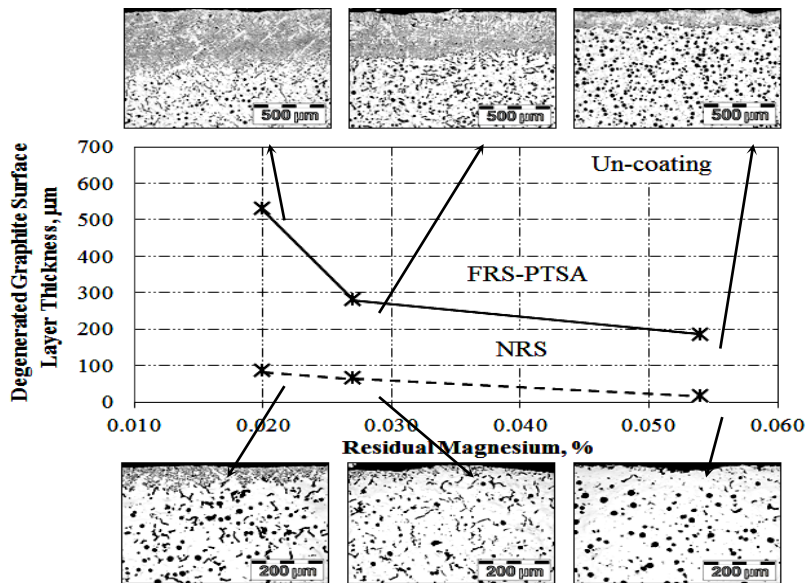
- NRS Moulds: Standard Quik-cup™ cups - Similar procedure

NOVOLAK Resin Sand Mould [No S]

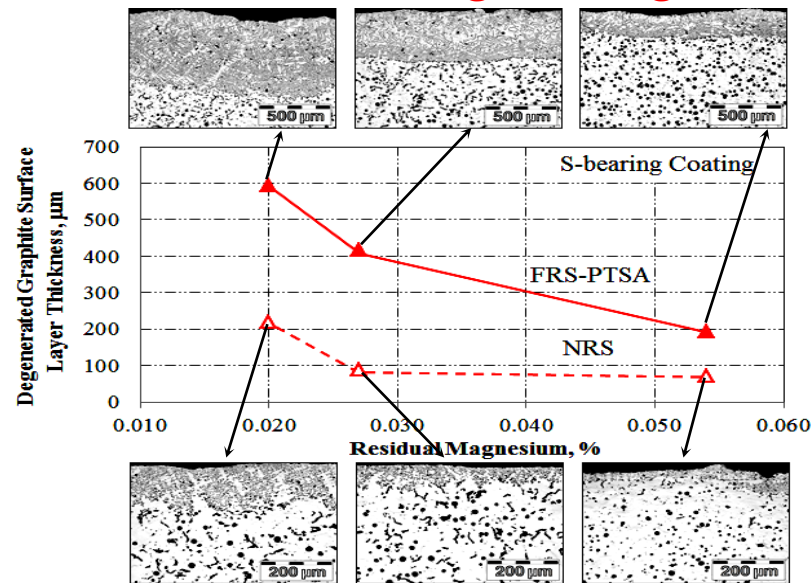
Furan Resin Sand Mould [S-including]

Mg_{res} [%]	Uncoated	Mould Coating		Mg_{res} [%]	Uncoated	Mould Coating	
		FeS_2	MgO			FeS_2	MgO
0.020				0.020			
0.027				0.027			
0.054				0.054			

Un-coating

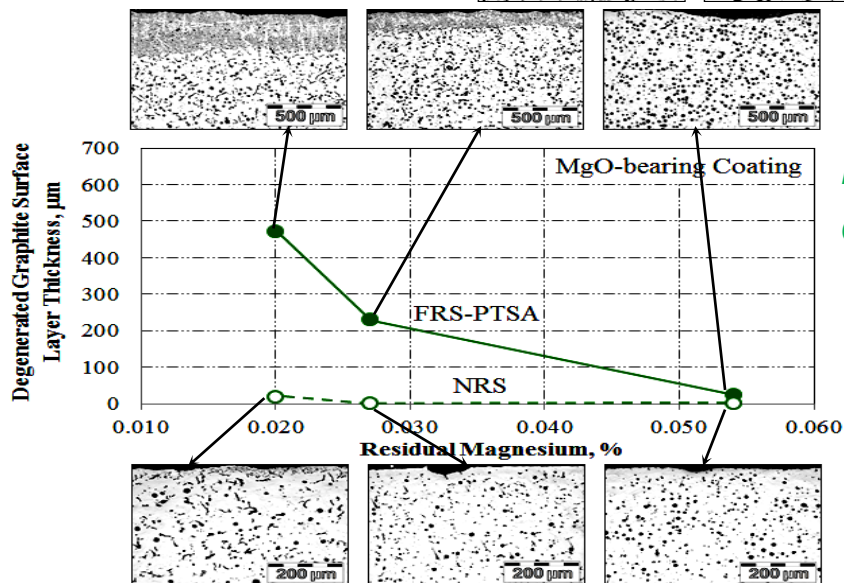


S - bearing coating



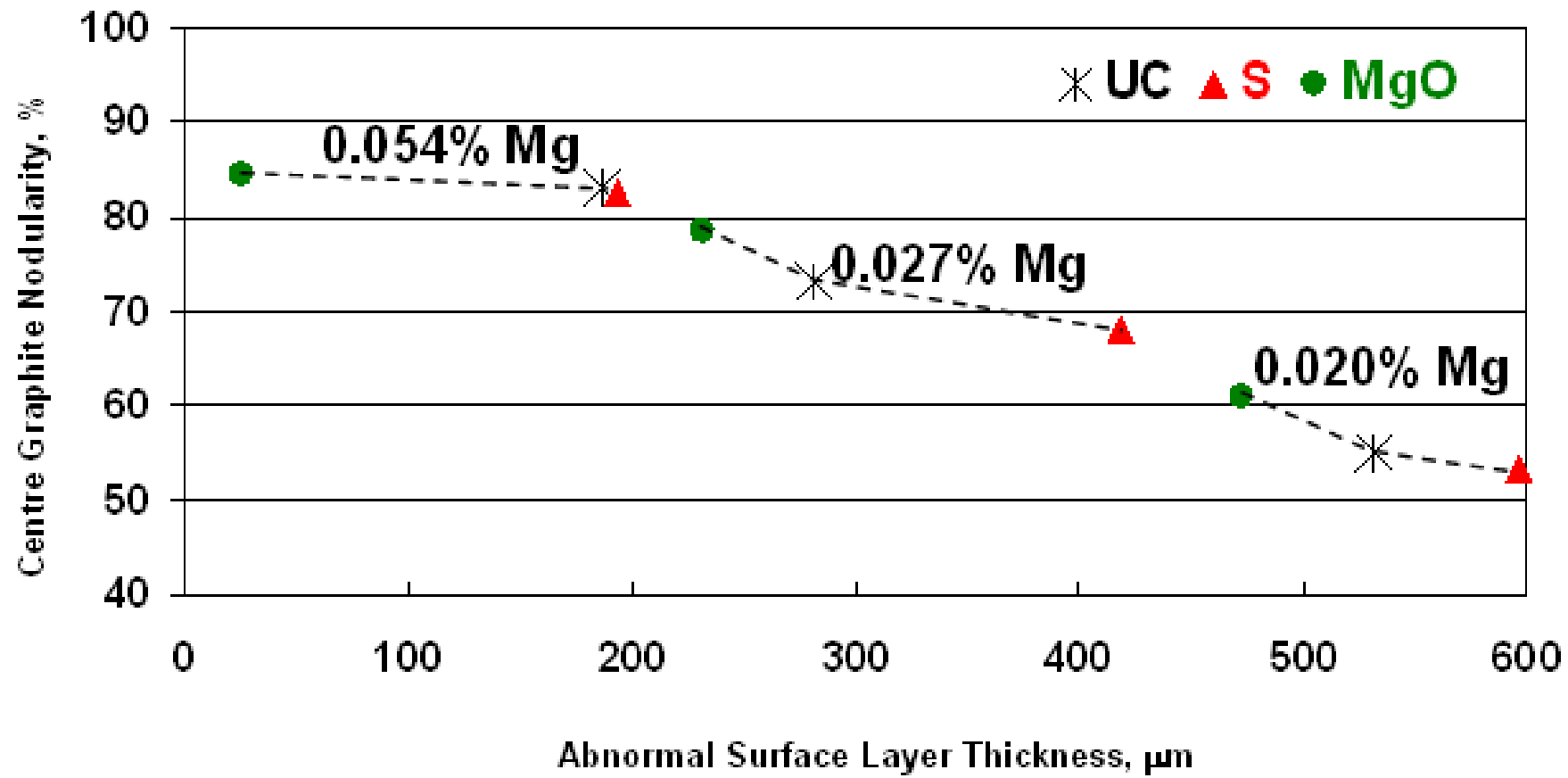
FRS-PTSA: Furan resin sand –
P-Toluol Sulphonic Acid
[S-bearing mould]

NRS: (Novolak) Phenol -
formaldehyde resin coated sand
(Croning process)
[No S-bearing mould]

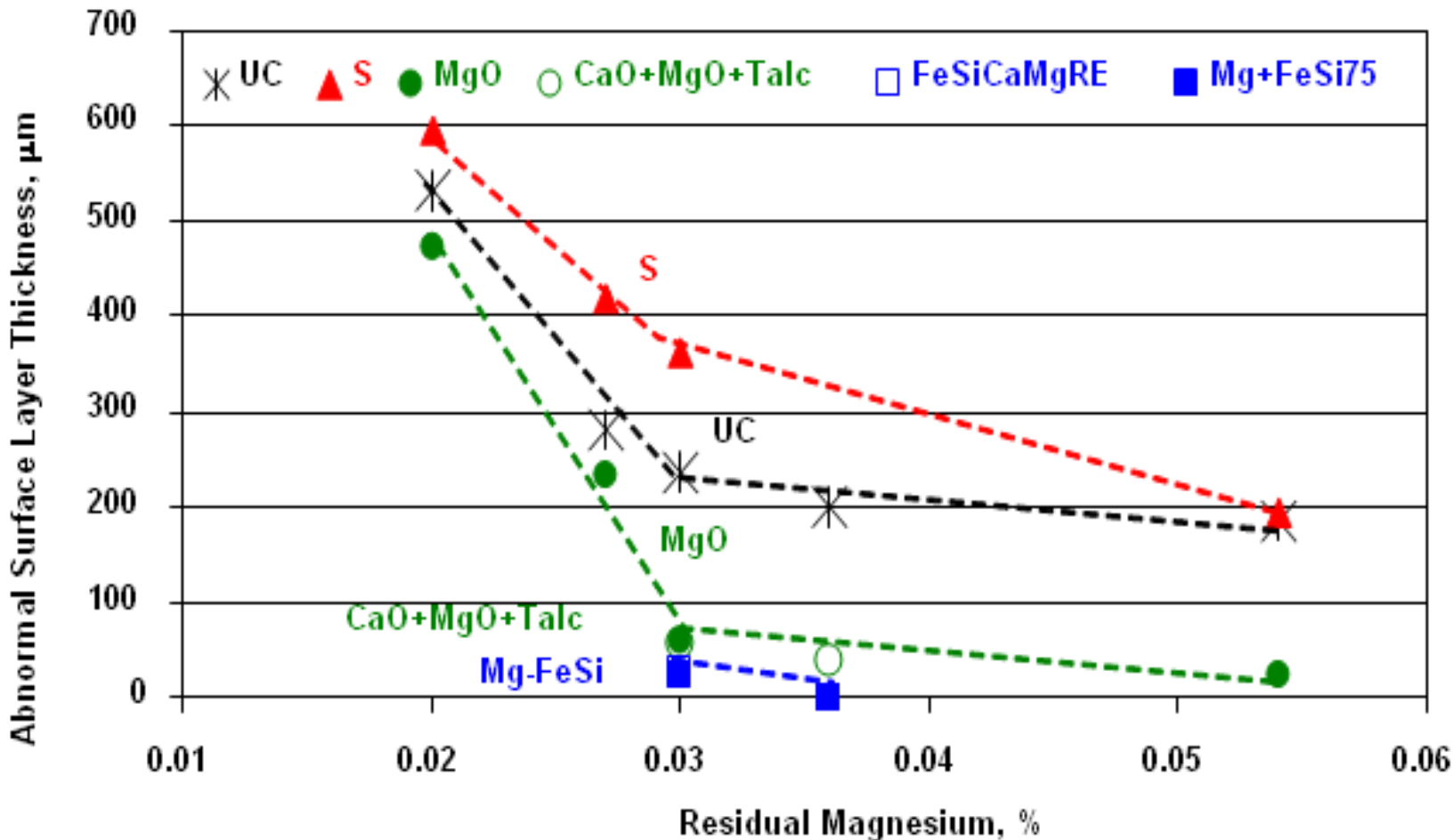


**MgO – bearing
coating**

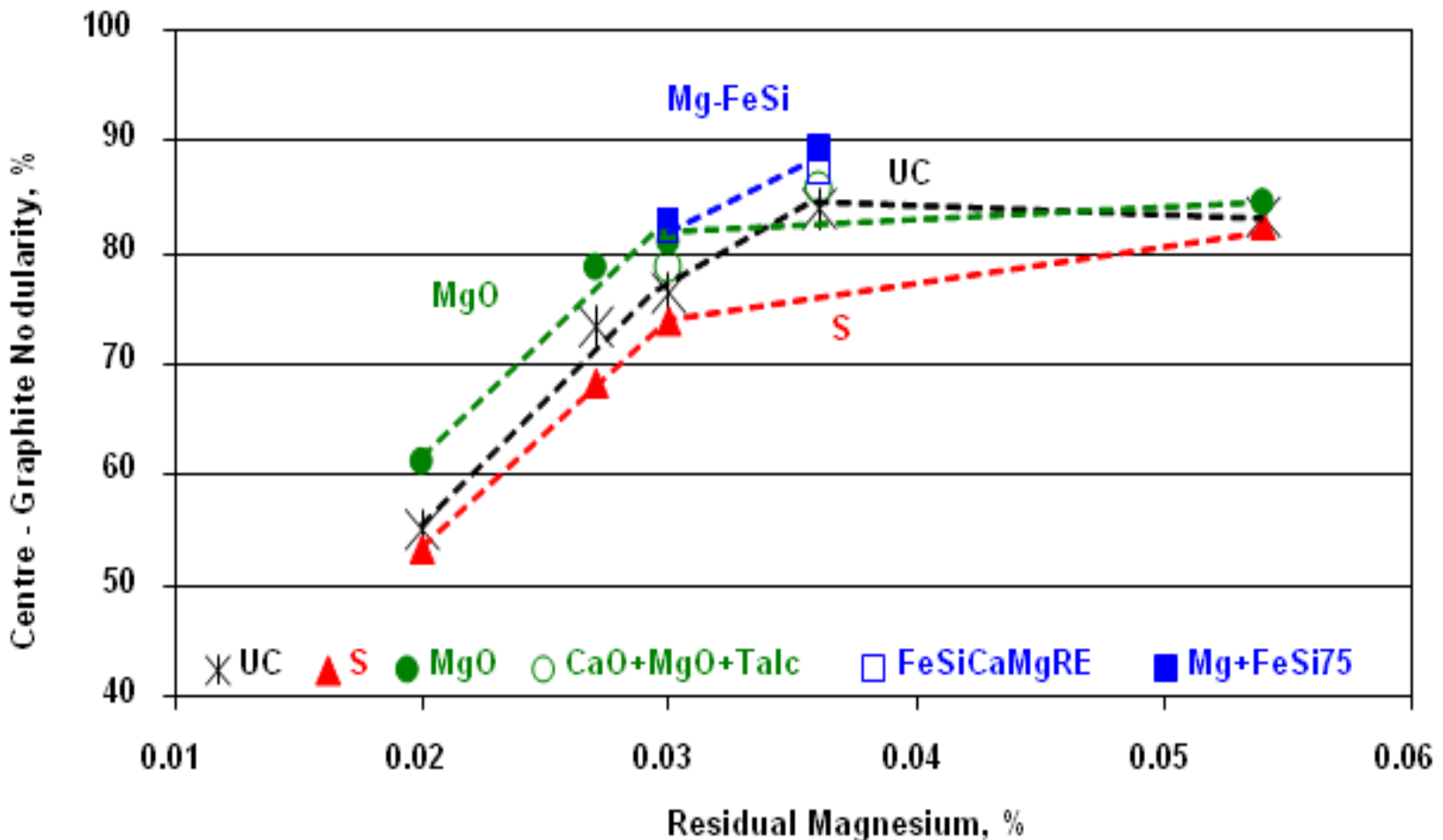
CENTRE GRAPHITE NODULARITY – SURFACE LAYER THICKNESS – NODULIZING POTENTIAL – MOULD COATING



GENERAL VIEW: FURAN RESIN (PTSA) MOULD – Mg_{res} VARIATION – MOULD COATING POTENTIAL



GENERAL VIEW: CENTRE GRAPHITE NODULARITY - Mg_{res} VARIATION - MOULD COATING POTENTIAL



- ❑ **It was re - confirmed that for the Furan Resin – PTSA moulds**
 - S delivered by the mould: graphite degeneration, skin of Mg-Iron Casting

- ❑ **It was found that the iron nodularising potential [Mg, Ce, La]**
 - **and Mould coatings**, with S content, or with Desulphurization capab., are important factors for graphite degeneration in the castings skin

- ❑ **Uncoated FRS - PTSA moulds, which have S in the binder**
 - skin thickness increasing as Mg_{res} decreased:
 - **CGI** is more sensitive compared to **NGI**, *and similarly*
 - **DI** with a marginal nodularising potential versus **normal DI**
 - for the specific solidification conditions

❑ **The application of a mould coating**

- strongly influenced graphite deterioration in the surface layer of castings
- either driving graphite degeneration further to less compact morphologies,
 - **when using S - bearing coatings**, *or conversely*,
- limiting the graphite degeneration to a narrower surface layer
 - **when desulphurization type coatings were employed**

❑ **If the coatings employed desulphurization materials,**

- such as MgO, *or* a mixture (CaO + MgO + Talc) *or* active Mg - bearing FeSi,
 - protected the graphite at the metal – mould interface
 - decreasing the average layer thickness in FRS - PTSA moulds *and*
 - increasing graphite nodularity over the casting section

❑ **It is presumed that the MgO *or* (MgO + CaO + Talc) coatings**

- acted locally to remove or capture any **S** released by the mould

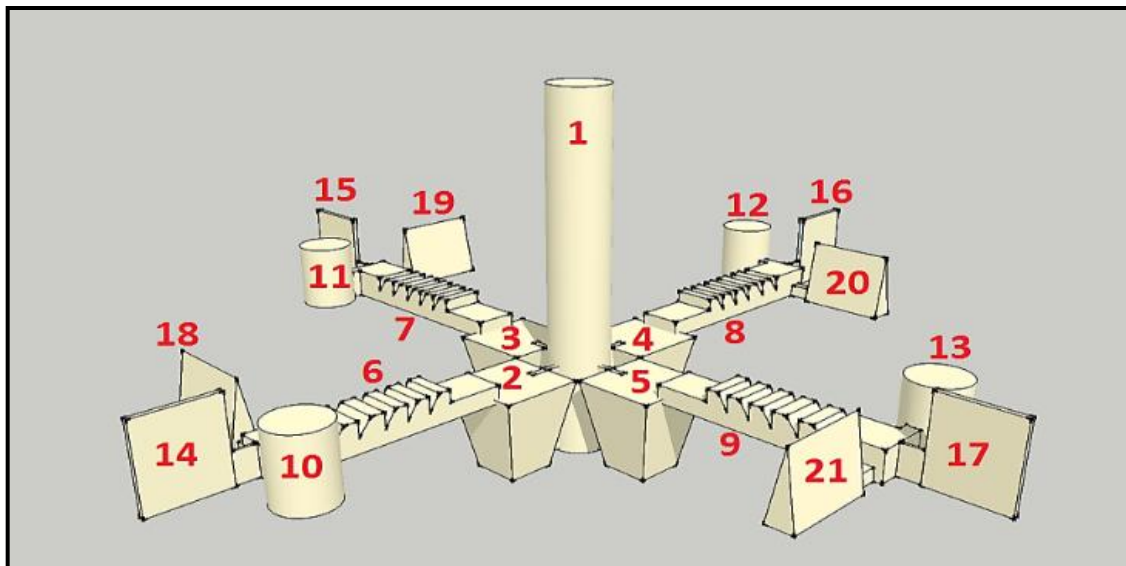
The coating mixes with Mg-FeSi, derived from nodulizers

- had an additional role to desulphurization, by providing supplementary active Mg,
 - to raise the nodularising potential prior to solidification

II. LABORATORY EXPERIMENTS

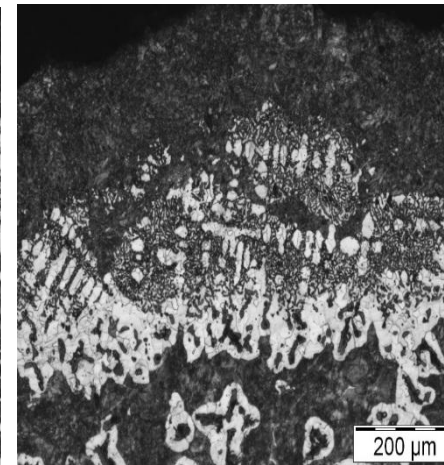
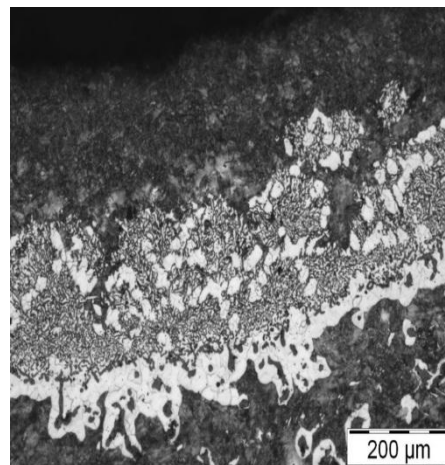
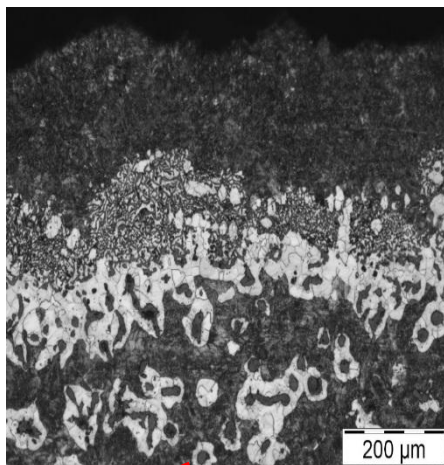
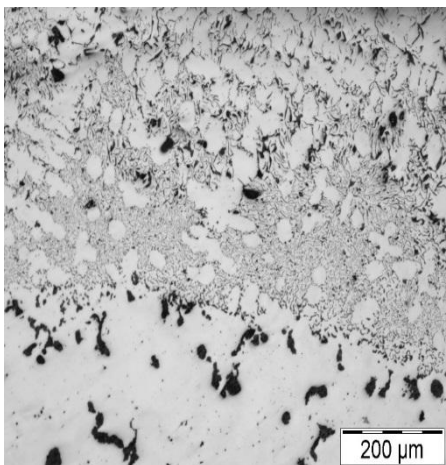
[Inoculation – High Nodularity Compacted Graphite Iron]

- **Ladle Mg-treated & In-mould inoculation [0.019 – 0.023%Mg_{res}, 4.3 – 4.4%CE]**
 - Ca-FeSi, Ca,Ba-FeSi & Ca,RE-FeSi alloys, 0.08-0.1wt.% consumption
 - S,O,Al,Mg-CaSi addition to Ca / Ca,Ba / Ca,RE alloys [1/3 ratio, 0.04wt%]
- **30 – 50% graphite nodularity and 60 – 70% Pearlite / 30 – 40% Ferrite ratio**
 - in 25mm diameter bars, in furan resin-bonded sand moulds

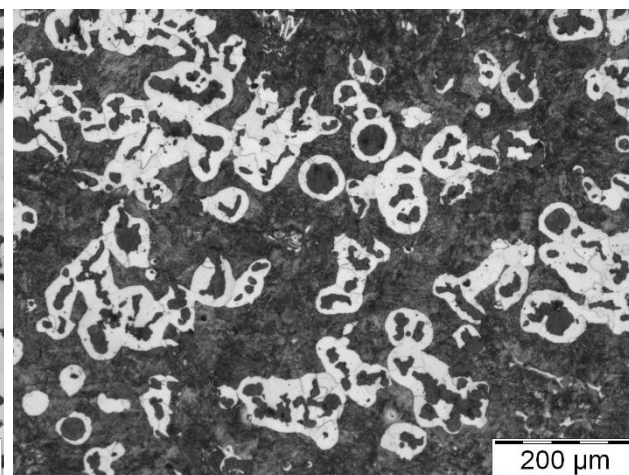
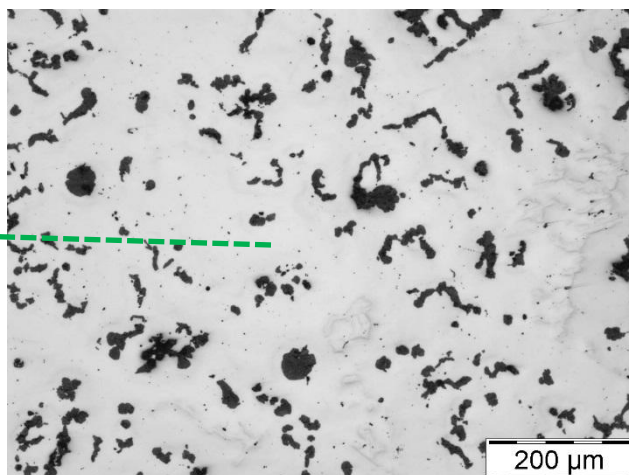
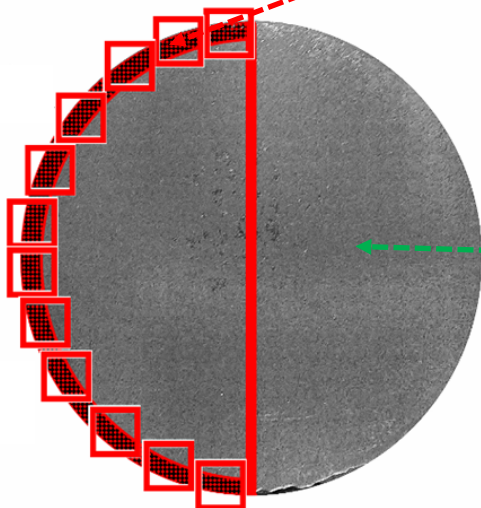


- 1 - Down sprue;
- 2, 3, 4, 5 - Reaction Chamber;
- 6, 7, 8, 9 - Runner;
- 10, 11, 12, 13 - Bar sample [25mm];
- 14, 15, 16, 17 - Plate sample [4mm];
- 18, 19, 20, 21 - W₃ Wedge sample [ASTM A 347]

CASTING SKIN

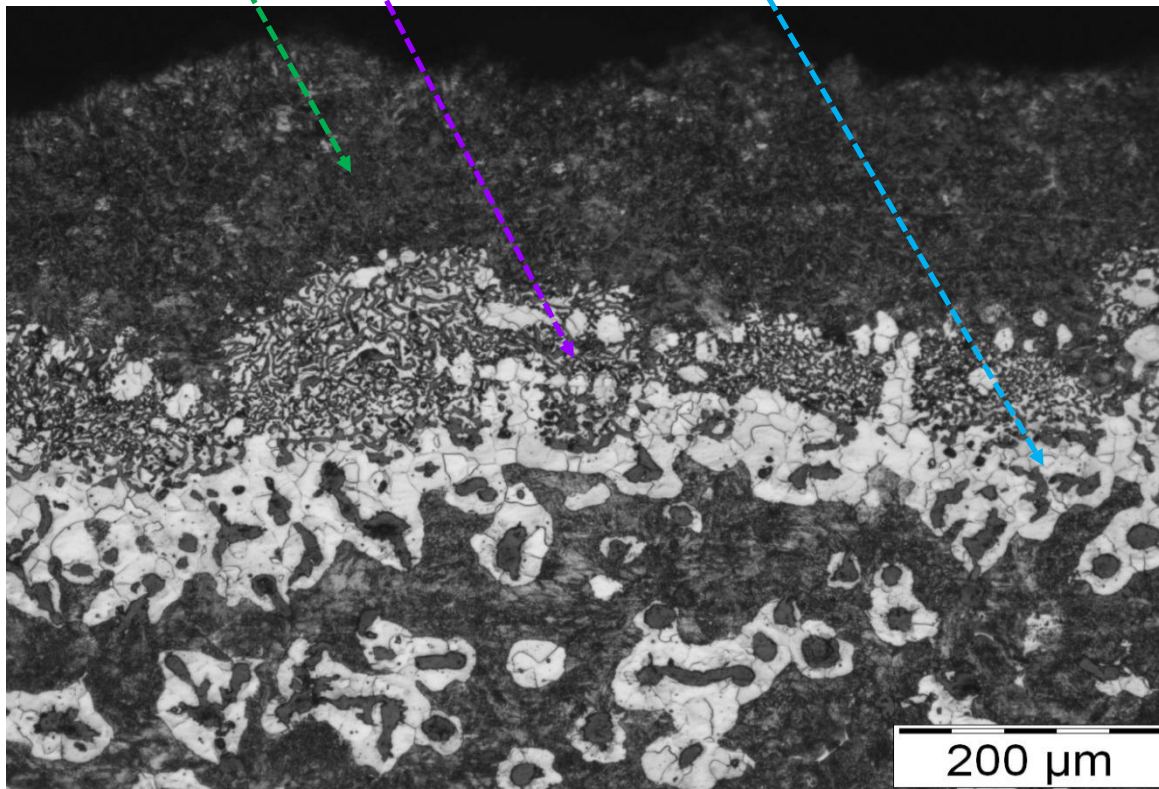


CASTING BODY

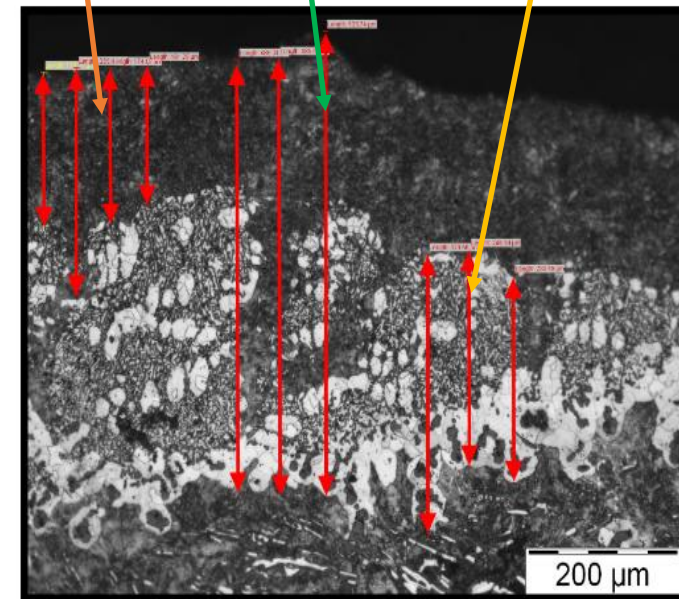


It was found in the done treatment and solidification conditions:

- **a complex surface layer**, including different sublayers as Graphite Morphology & Pearlite / Ferrite ratio formed for all of test castings;
- **a general lower graphite nodularity**, at 10 – 25% vs 30 – 50% in the casting body
- **an outer Pearlitic rim** associated with type A / E graphite *is followed by a*
 - **Ferritic rim** associated with **Fine type graphite** [like coral or type D], and
 - finally a **Ferritic rim** associated with **Compacted Graphite**,
- **before the body casting base structure**
 - 30 – 50% NG / 50 – 70% CG; 60-70% P / 30-40% F; more F amount in CG area

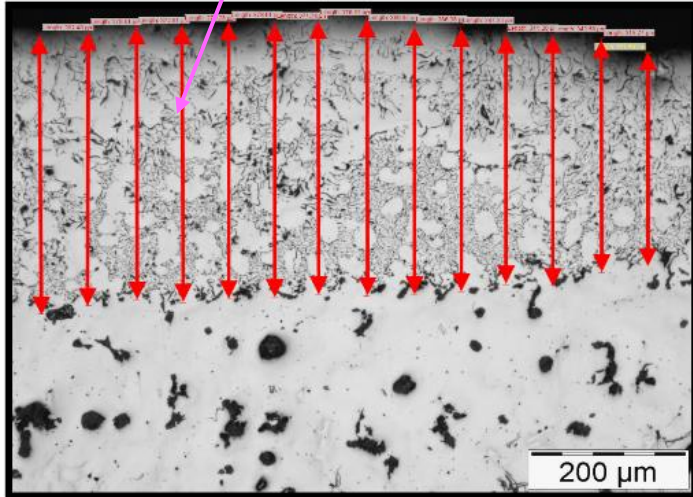


Pearlitic rim **Total rim** **Ferritic rim**

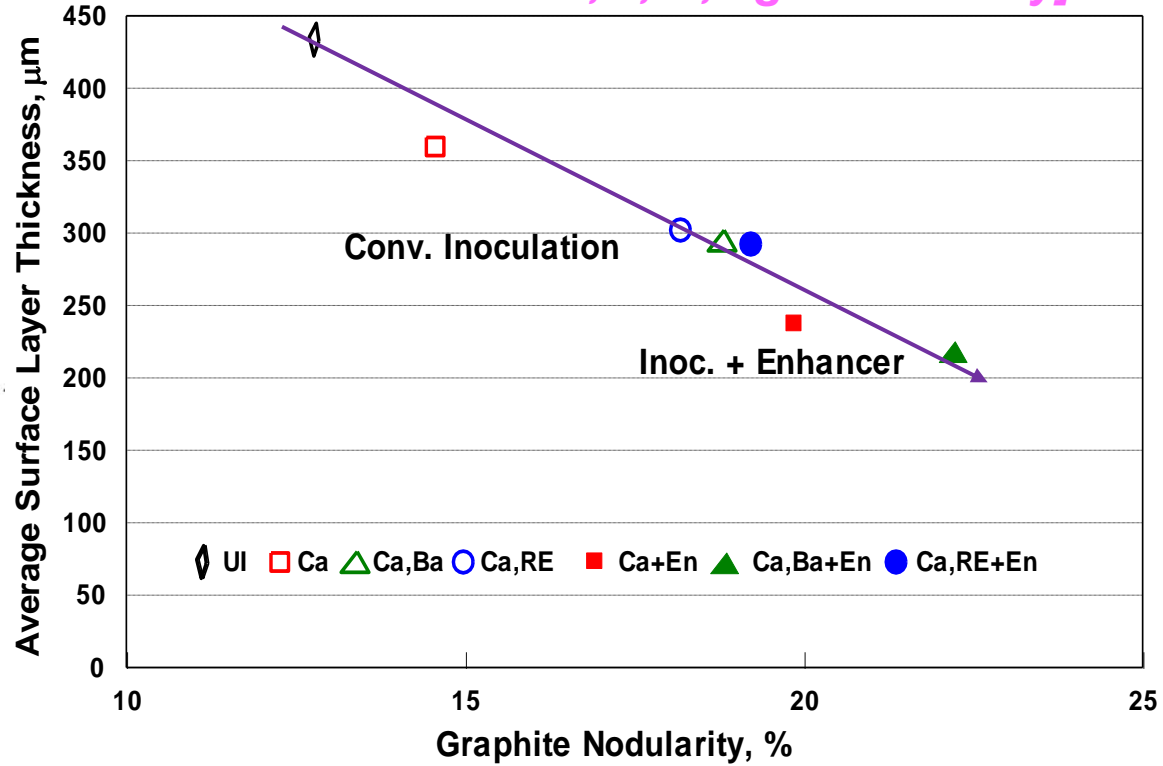


Average Surface Layer Thickness - Graphite Nodularity in the Surface Layer

[surface layer, un-etched samples]



[En - Inoculant Enhancer – S,O,Al,Mg - CaSi alloy]

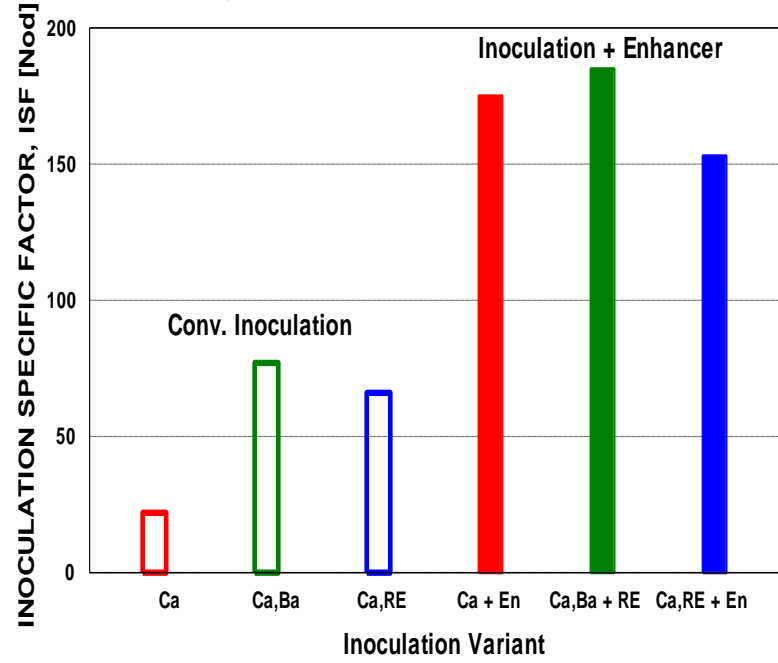
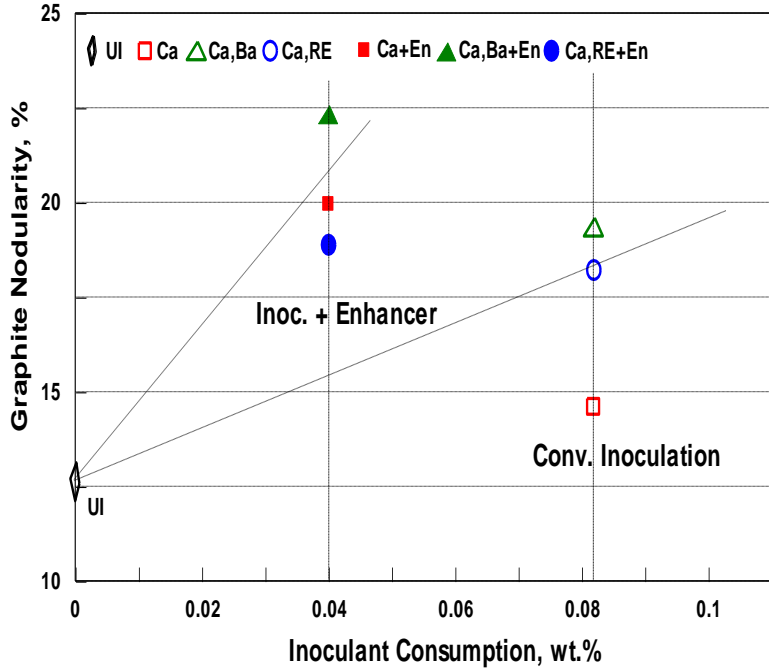


Influence of inoculant type in the surface layer of castings [un-etched samples]

Average graphite nodularity

Inoculation Specific Factor to increase nodularity

[En - Inoculant Enhancer – S,O,Al,Mg - CaSi alloy]



ISF – Inoculation Specific Factor, ISF =

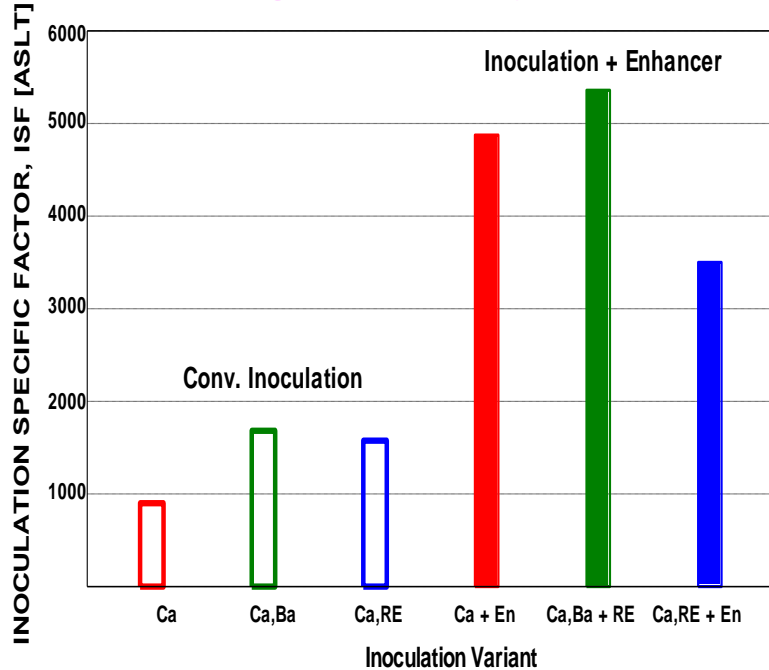
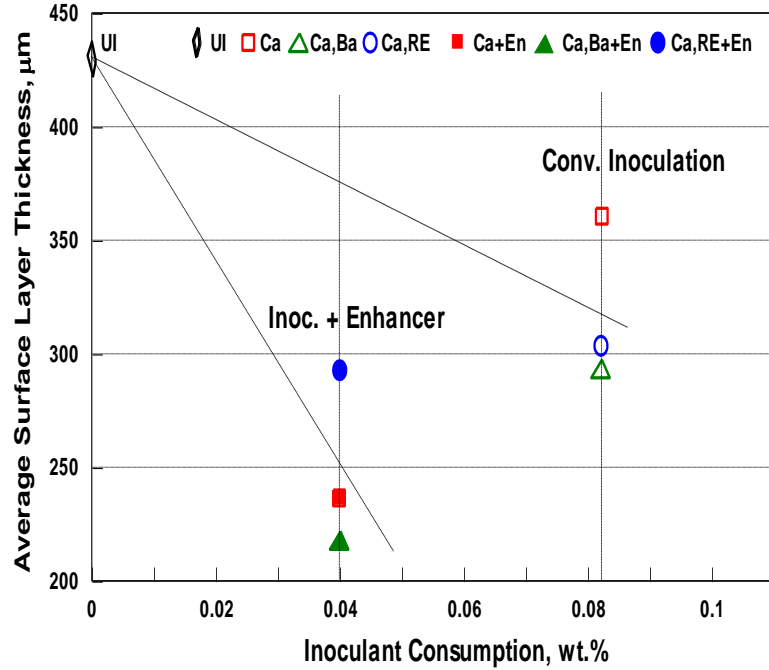
|Inoculation Effect (Nodularity Increasing)| / |Inoculant Consumption|

Influence of inoculant type in the surface layer of castings [un-etched samples]

Average skin thickness

Inoculation Specific Factor to decrease skin size

[En - Inoculant Enhancer – S,O,Al,Mg - CaSi alloy]



ISF – Inoculation Specific Factor, ISF =

|(Inoculation Effect (Skin decreasing)) | / |(Inoculant Consumption)|

Surface layer thickness & sublayers characteristics, from both graphite & metal matrix point of view:

- **Are different for un-inoculated & inoculated irons** and are depending on the inoculant variant;
- Generally, **inoculation** - **increased graphite nodularity** in the surface layer *and*
 - **decreased the surface layer thickness,**
 - at a strong relationship between these two parameters.
- **Pearlitic / Ferritic rim sublayers ratio** in the surface layer is also dependent on the inoculant type:
 - **thicker Pearlitic** rim in conventional inoculation *and*
 - **thicker Ferritic rim** in inoculation enhancing variants
- **As it was expected, in conventional inoculation variants,**
 - Ca,Ba-FeSi & Ca,RE-FeSi alloys performed Ca-FeSi alloy,
 - **but the best results were obtained for inoculation enhancing variants,**
 - **despite the reducing with 50% of consumption alloy.**

ISF [Inoculation Specific Factor] was used to evaluate inoculation efficiency to improve iron castings quality

- **ISF** refers to the capacity of inoculants to increase the graphite nodularity in the surface layer *and* to decrease its thickness
- **ISF** compares the ratio between increased nodularity / decreased surface layer thickness *and* total inoculant consumption for this effect
- **S,O,Al,Mg-CaSi alloy** improved the potency of all of the conventional inoculants, with Ca,Ba-FeSi alloy as performance
- The combination of inoculant & enhancer had the highest **ISF** level
- It appears that by this way is possible
 - to optimize the efficiency of simple conventional inoculants [Ca-FeSi]
 - or to obtain a higher performance of more potent inoculants [Ca,Ba-FeSi]
 - instead of use of Rare Earth bearing inoculants [Ca,RE-FeSi]

GENERAL CONCLUSIONS

- **Casting skin is present in all of Mg - treated iron castings:**
 - Higher in lower Mg_{res} content [CGI *versus* DI]
 - Higher in higher wall thickness level
- **Sulphur – the most detrimental influencing factor**
 - S - bearing mould / core media
 - S - bearing coating materials
- **Desulphurization action of the applied coatings**
 - Practical solution to limit / avoid casting skin
 - Mg - bearing coating the most effective
- **Efficient Inoculation to decrease skin sensitiveness**
 - More potent inoculants
 - Inoculation Enhancing

Make Good Iron Castings !!!

THANK YOU



18th INTERNATIONAL FOUNDRYMEN CONFERENCE
**Coexistence of material science and sustainable technology in
economic growth**

Sisak, May 15th-17th, 2019

<http://www.simet.hr/~foundry/>

**DECOMPOSITION OF AUSTENITE IN AUSTEMPERED DUCTILE IRON SAMPLES
ON ELEVATED TEMPERATURES**

Hasan Avdušinović^{1*}, Almaida Gigović-Gekić¹, Šehzudin Dervišić²

¹ University of Zenica Faculty of Metallurgy and Technology, Zenica, Bosnia and Herzegovina

² PhD student at University Džemal Bijedić Faculty of Mechanical Engineering, Mostar, Bosnia and Herzegovina

Invited lecture

Original scientific paper

Abstract

Mechanical properties of metallic materials strongly depend on microstructure. Microstructure changing of metallic parts on elevated temperatures highly limits possibilities of their application. The research in this paper is focused on microstructure changing of austempered ductile iron samples in case of reheating in temperature range between 250 °C and 700 °C. Decreasing of volume fraction of carbon enriched austenite was a measure of decomposition process.

Keywords: *austempered ductile iron, phase transformation, ausferrite, carbon enriched austenite*

*Corresponding author (e-mail address): hasan.avdusinovic@mtf.unze.ba

INTRODUCTION

Mechanical properties of the Austempered Ductile Iron (ADI) depend on the microstructure of the material after the heat treatment processes. Microstructure of metallic matrix strongly depends on the mechanism and kinetics of phase transformation developing successively during the austempering heat treatment [1,2]. Microstructure of the metallic matrix after the heat treatment, known as ausferrite, consists of the acicular ferrite and room-stable carbon enriched austenite. Austempering heat treatment consists of austenitizing and quenching followed by isothermal transformation. Important parameters for setting heat treatment are: temperature and holding time of the austenitizing and temperature and holding time of the isothermal transformation [3].

Scheme of the austempering heat treatment process is presented on Figure 1.



18th INTERNATIONAL FOUNDRYMEN CONFERENCE
**Coexistence of material science and sustainable technology in
 economic growth**

Sisak, May 15th-17th, 2019

<http://www.simet.hr/~foundry/>

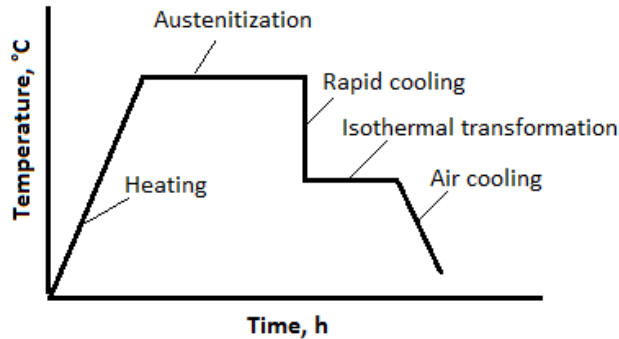


Figure 1. Scheme of the austempering heat treatment process

ADI is often used where high strength is needed and where excellent wear resistance and fatigue strength are required, such as gears and other similar products. The superior tribological properties of ADI will allow the gears to run temporarily without lubrication. Some applications of ADI include: timing gears, CV joints, steering knuckles sprockets, rollers, idlers, suspension housings and brackets, wear plates, wheel hubs, crankshafts, flanged shafts, etc.

All cases of application (mentioned earlier) require stability of the microstructure which depends of temperature range of application. Any type of microstructure decomposition leads to changing of mechanical properties. In a study performed by G. Nadkarni et al., volumetric changes associated to decomposition of the ausferritic microstructure were observed [4].

MATERIALS AND METHODS

The objective of this study was to determine the stability of the ausferrite during reheating at elevated temperature conditions. The main question was how ADI will change its microstructure after being exposed to elevated temperatures and on which temperature range the microstructure change is going to happen. Carbon enriched austenite decomposition during reheating at elevated temperature was a measure of ADI microstructure stability in this research task. Chemical composition of the base ductile iron is presented in Table 1.

Table 1. Chemical composition of the base ductile iron

Chemical element	C	Si	Mn	Cu	Ni
Wt. %	3.30	2.53	0.31	0.51	0.81

Base ductile iron was cast in standard “U” shape cast pieces. For characterization of the quality of the base ductile iron ten metallographic samples were cut and tested according to



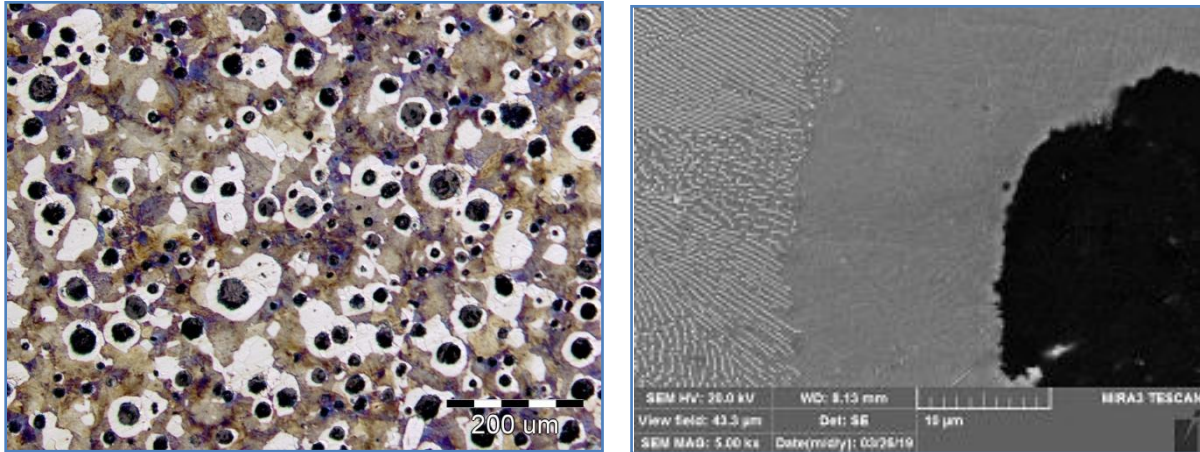
18th INTERNATIONAL FOUNDRYMEN CONFERENCE
**Coexistence of material science and sustainable technology in
economic growth**

Sisak, May 15th-17th, 2019

<http://www.simet.hr/~foundry/>

standard BAS ISO/TR 945-2 [5]. Optical microscopy “Olympus” equipped with software for image analysis was used for microstructure investigation. On each samples five different locations were observed. Form of the graphite was dominantly VI and graphite particle size was 3/4. Average value of the volume fraction of the graphite phase was 9.45.

Microstructure of the base ductile iron is shown in Figure 2a and b.

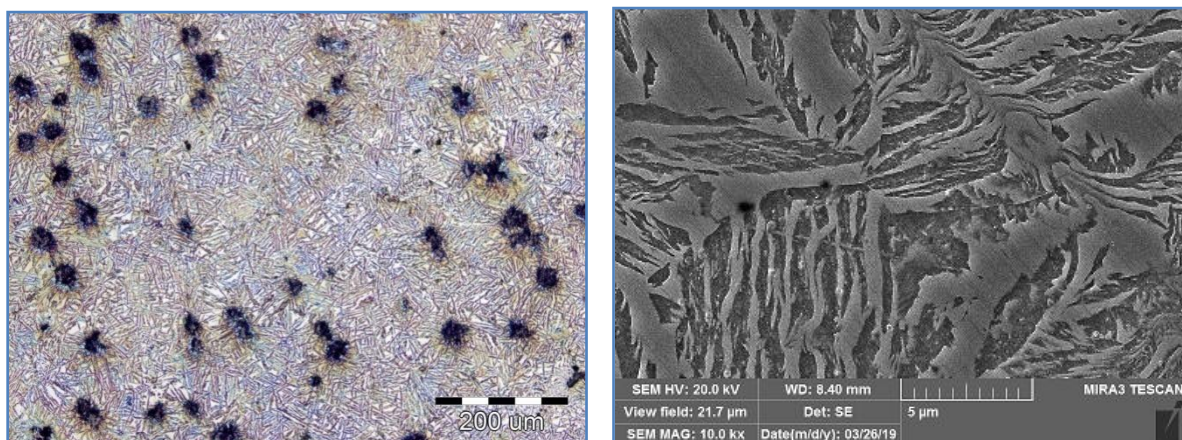


a) Optical Microscope, Mag: 100x, Nital etched,

b) SEM, Mag: 5000x, Nital etched

Figure 2. Microstructure of investigated ductile iron

Heat treatment of the base ductile iron was performed with following parameters: austenitization temperature – 870 °C, austenitization time – 90 min, isothermal transformation temperature – 350 °C, and isothermal transformation time – 90 min. Isothermal transformation was finished in salt bath (KNO_3) [6]. Samples of base ductile iron for heat treatment were prepared in prismatic shape (10x20x50 mm). Microstructure of the base material after heat treatment (ADI) is presented on Figure 3a and b.



a) Optical Microscope, Mag: 100x, Nital etched,

b) SEM, Mag: 10000x, Nital etched

Figure 3. Ausferrite microstructure of ADI samples



18th INTERNATIONAL FOUNDRYMEN CONFERENCE
**Coexistence of material science and sustainable technology in
economic growth**

Sisak, May 15th-17th, 2019

<http://www.simet.hr/~foundry/>

Microstructure decomposition of the ausferrite microstructure during reheating is characterized by linear changes. Dilatometric qualitative analysis of the ADI samples during reheating was performed on the dilatometer Netzsch 402/C/7. Heating and cooling rates for dilatometric investigation were 5 K/min.

RESULTS AND DISCUSSION

The thermal expansion curves of the tested ADI sample are presented in Figure 4.

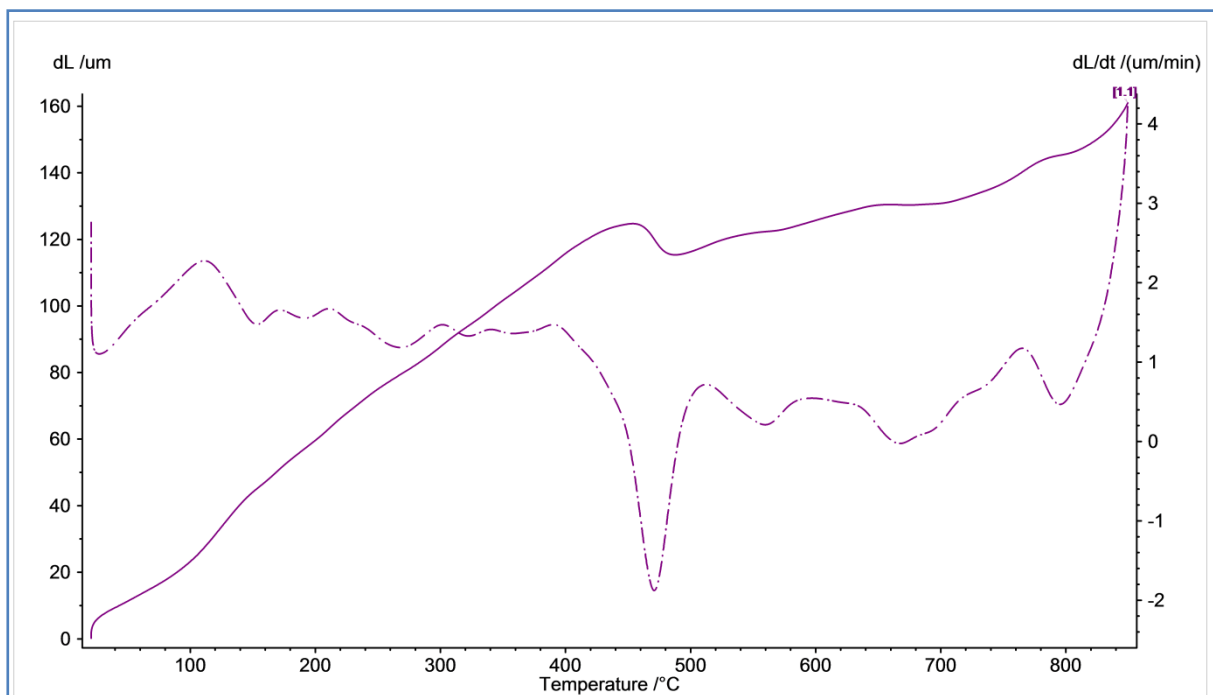


Figure 4. Dilatometric curve of ADI sample

(Solid line - thermal expansion curve; dashed line - first derivation of the thermal expansion curve)

Within the analysis of the first derivation curve of the ADI sample three different temperature ranges of the microstructure decomposition were observed. First temperature range between 200 °C and 400 °C, second between 400 °C and 500 °C and third temperature range above 500 °C. First temperature region is characterized by several effects (peaks) showing certain decomposition process within treated material. Second temperature region is characterized by most intensive effect (peak) indicating an intense process of transformation within the tested material. Third temperature region (similar to first temperature region) is characterized by several effects (peaks). To follow decomposition process of the ADI sample, six different reheating temperatures had been chosen to reveal carbon enriched austenite transformation: 250 °C, 350 °C, 450 °C, 500 °C, 600 °C, and 700 °C. In order to achieve that, simple experiment was performed. Six ADI samples were prepared



18th INTERNATIONAL FOUNDRYMEN CONFERENCE

Coexistence of material science and sustainable technology in
economic growth

Sisak, May 15th-17th, 2019

<http://www.simet.hr/~foundry/>

(heat treatment parameters explained in previous chapter) and reheated up to six chosen temperatures. Then, as soon as required decomposition effects had been achieved, the samples were rapidly removed from the furnace. After cooling in the air, the hardness measurements were carried out and volume fraction of the carbon enriched austenite was calculated using equation 1 [2].

$$V_a = 100 - (V_f + V_g) \quad (1)$$

where V_f is volume fraction of the ferromagnetic phase (ferrite) and V_g is volume fraction of the graphite phase (considered constant for examined alloy).

Volume fraction of the ferromagnetic phase is measured using FERITSCOPE FMP30. Brinell hardness of the tested samples was measured according BAS EN 6507-1/2007 [7]. Five measurements of the ferromagnetic phase fraction and hardness were carried out on each treated samples. Average values of the carbon enriched austenite volume fraction and hardness of the treated samples were presented in Table 2 and Figures 5 and 6.

Table 2. Average values of the volume fraction of the carbon enriched austenite and hardness of the treated samples

Sample No.	Reheating temperature [°C]	Volume fraction of the ferrite [%]	Volume fraction of the carbon enriched austenite [%]	Brinell Hardness [HB]
1	250	55.2	35.35	352
2	350	54.7	35.85	331
3	450	71.3	19.25	321
4	500	76.6	13.95	293
5	600	81.3	9.25	283
6	700	89.8	0.75	183



18th INTERNATIONAL FOUNDRYMEN CONFERENCE
**Coexistence of material science and sustainable technology in
economic growth**

Sisak, May 15th-17th, 2019

<http://www.simet.hr/~foundry/>

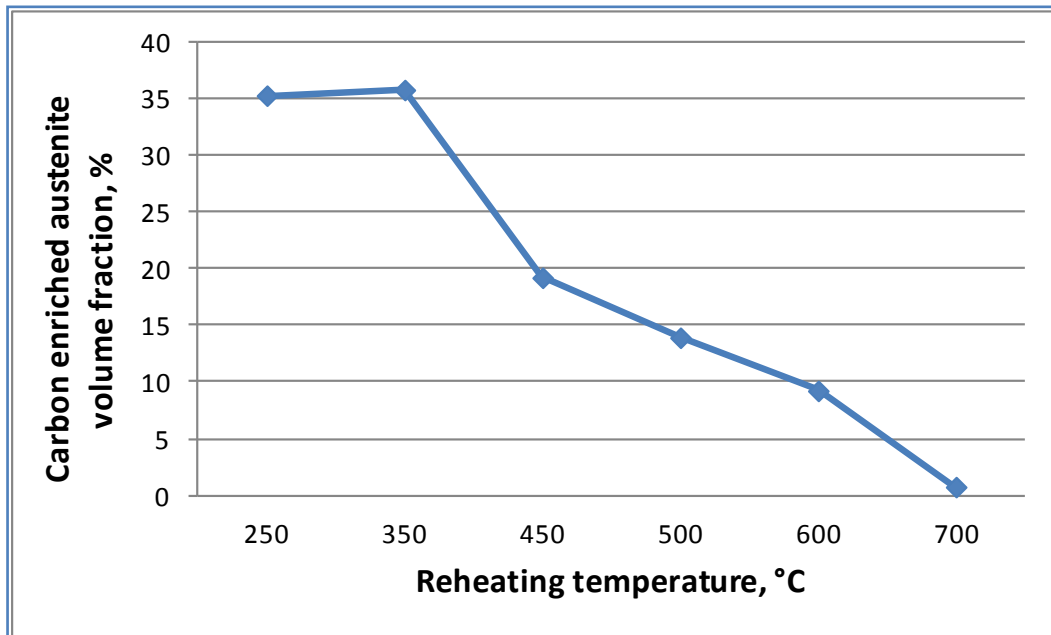


Figure 5. The effect of reheating temperature on the volume fraction of the carbon enriched austenite of the tested samples

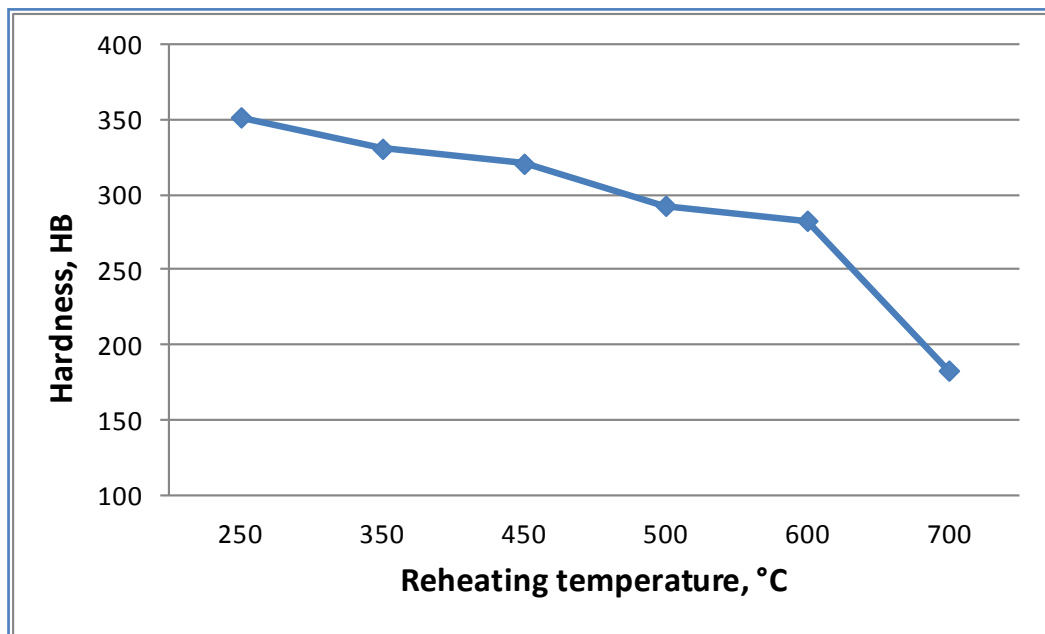


Figure 6. The effect of reheating temperature on the hardness of the tested samples

Decomposition process of carbon enriched austenite is accompanied with Fe carbide formation and increasing content of the ferrite in the microstructure. Although the decrease in carbon enriched austenite content in the microstructure is noticeable in the temperature



18th INTERNATIONAL FOUNDRYMEN CONFERENCE

Coexistence of material science and sustainable technology in economic growth

Sisak, May 15th-17th, 2019

<http://www.simet.hr/~foundry/>

range above 350 °C, hardness of the material does not follow this trend due to the presence of the carbides in microstructures. Noticeable drop of the hardness of the tested material is visible only above 600 °C. The effect corresponds to the graphitization of cementite below A_{c1} temperature.

CONCLUSIONS

The aim of this paper was to present the possibilities of determining the changes of the ausferrite microstructure at the elevated temperature by measuring volume fraction of carbon enriched austenite in the reheated samples. After analyzing of the experimental results the following can be concluded:

- Dilatometric curve (dashed line) for ADI sample shows three temperature ranges of ausferrite microstructure decomposition.
- The linear changes in the temperature range of 400 °C-500 °C indicate the most intense decomposition of the ausferrite microstructure.
- The amount of the carbon enriched austenite in reheated samples decreases with increasing the temperature.
- Noticeable drop of the hardness of the reheated samples is visible only above 600 °C.

Acknowledgements

This work was supported by the Ministry of Education and Science of Federation of Bosnia and Herzegovina.

REFERENCES

- [1] ASTM 897(M) Austempered Ductile Iron Specification, 1990.
- [2] A. Gazda, Analysis of decomposition processes of ausferrite in copper-nickel austempered ductile iron, Akademiai Kiado, Budapest, Hungary, 2010, DOI: 10.1007/s10973-010-0804-y.
- [3] J. R. Keough, K. L. Hayrynen, G. L. Pioszak, Designing with austempered ductile iron (ADI), AFS Proceedings, American Foundry Society, 2010, Schaumburg, IL, USA.
- [4] G. Nadkarni, S. Gokhale, J. D. Boyd, Elevated temperature microstructural stability of austempered ductile irons, AFS Transactions, 104(1996), pp. 985-994.
- [5] BAS ISO/TR 945-2.
- [6] S. Savićević, H. Avdušinović, A. Gigović-Gekić, Z. Jurković, M. Vukićević, M. Janjić, Influence of the austempering temperature on the tensile strength of the austempered ductile iron (ADI) samples, Metalurgija, 56(2017)1-2, pp. 149-152.
- [7] BAS EN 6507-1/2007.



18th INTERNATIONAL FOUNDRYMEN CONFERENCE

Coexistence of material science and sustainable technology in
economic growth

Sisak, May 15th-17th, 2019

<http://www.simet.hr/~foundry/>

CORROSION MONITORING OF METAL RELEASE INTO ENVIRONMENT

Maroš Halama^{1*}, Karol' Koval², Andrej Petrik¹

¹ Technical University of Košice Faculty of Materials, Metallurgy and Recycling, Košice, Slovakia

² Slovak Academy of Science Institute for Material Research, Košice, Slovakia

Invited lecture

Subject review

Abstract

Corrosion of metallic materials are known as strongly non-linear process due to the dependence on several factors concerning application environment such as temperature, humidity, amount of rainfall, pH, concentration of pollutants etc. Prediction of corrosion phenomena by classical statistical or mathematical methods often appears unsatisfying which is due to the complexity associated with the numerous physical-chemical processes. Nowadays, one of key enable technology such as artificial neural network can achieve promising approach to get more precise results.

The aim of corrosion monitoring is in development of corrosion sensor for prediction of atmospheric corrosion of basic structural metallic materials such as steel, zinc, copper using hyphenation of screening electrochemical technique with artificial neural network. The signal of sensor is caused by the corrosion reaction and corrosion reaction of structural metals depends on series of metereochemical variables (temperature, relative humidity, time of wetness, concentration of main pollutants, exposition time). Thus, based on robust database of values from field we could predict corrosion behavior from known variables under local atmospheric sites.

Keywords: *corrosion monitoring, prediction of life-time, run-off of metals, atmospheric aggressivity*

*Corresponding author (e-mail address): maros.halama@tuke.sk

CORROSION MONITORING OF METAL RELEASE INTO ENVIRONMENT



***Maroš HALAMA¹, Karol KOVAL' ², Katerina KREISLOVA³
Jeroen Van LESEBETENNS⁴***

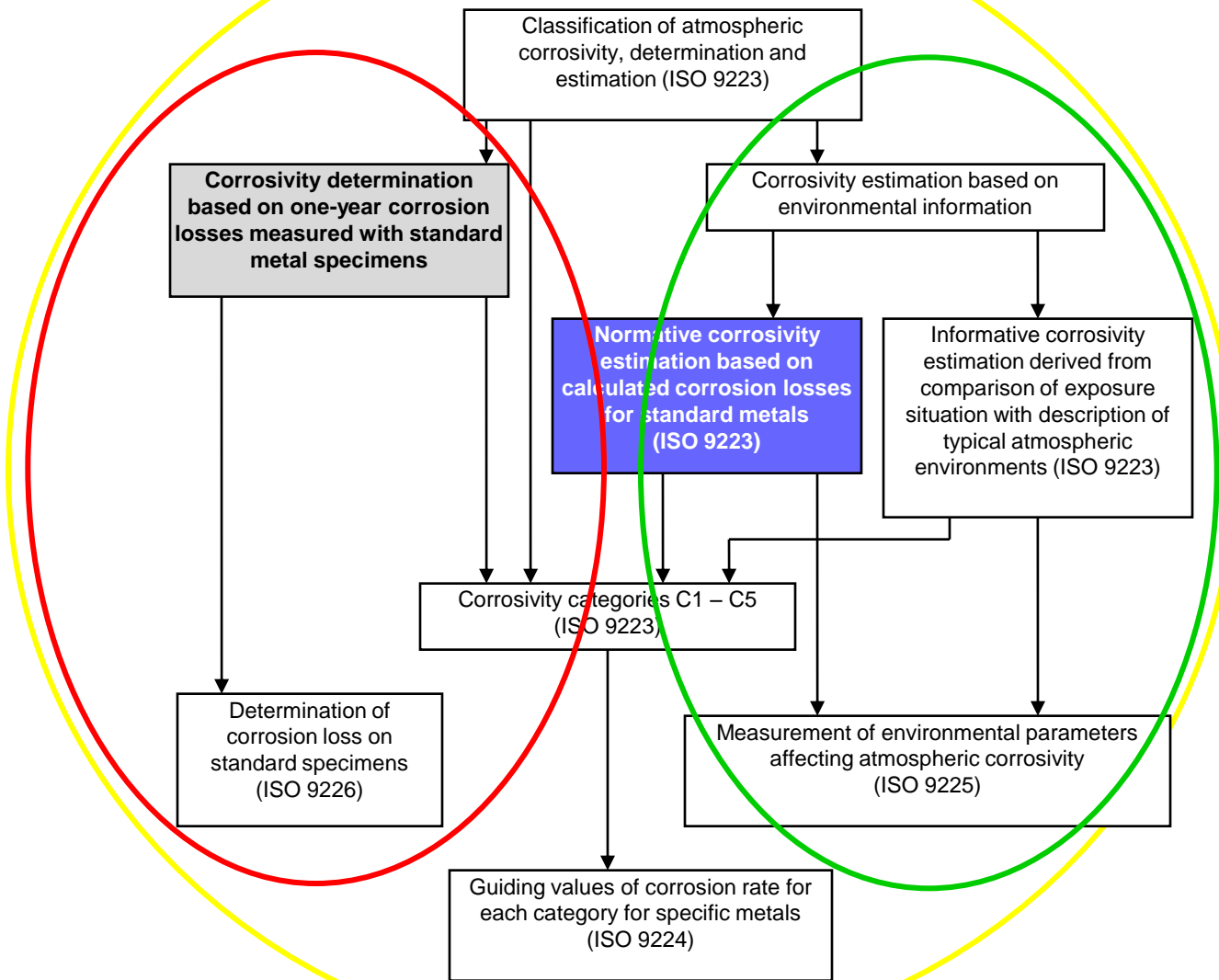
¹ Technical University of Košice, Faculty of Materials, Metallurgy and Recycling, Kosice, Slovakia

² Slovak Academy of Science, Institute of Materials Research, Kosice, Slovakia

³ SVUOM Ltd., Prague, Czech Republic

⁴ Gent University, FEE, Belgium

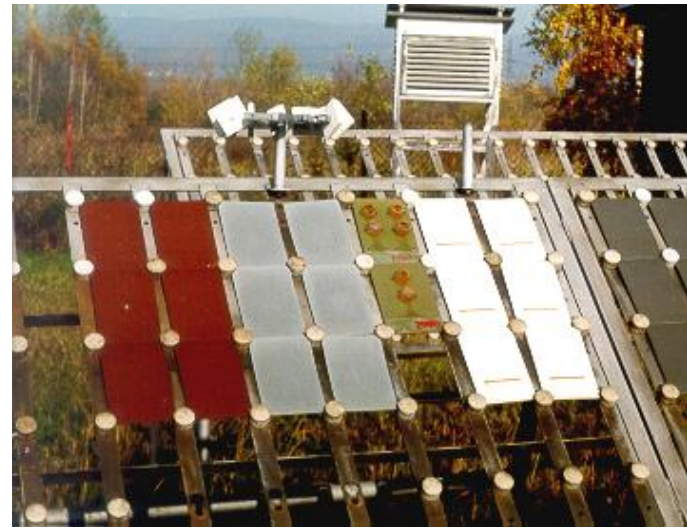
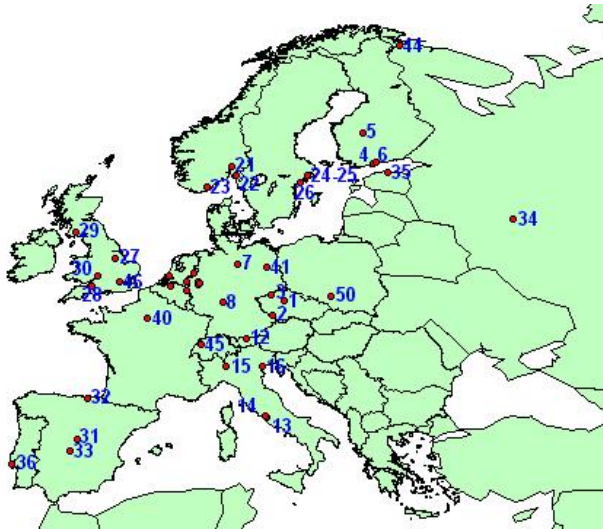
Estimation of atmospheric corrosion based on ISO 9223 and ISO 9224



environmental information + real corrosion = prediction

Measured parameters

- **environmental parameters** - temperature, relative humidity, concentration of gaseous pollutants (SO_2 , NO_x , O_3) and precipitation (amount, pH, conductivity, amount of SO_4^{2-} , NO_3^- , Cl^-)
- **corrosion mass loss** – carbon steel and other structural metals (zinc, aluminum, copper)



- ❖ new materials, selection of materials ↔ **corrosion research** (testing is necessary)
- ❖ rational application of metallic materials → known way of **degradation**
- **prolongation of lifetime**

Atmospheric corrosion – depends on series of factors:

atmospheric: temperature, relative humidity, time of wetness, wind velocity, pH of rainfall, concentration of main pollutants (SO₂, NO₂, NO_x), conductivity of surface electrolyte;

material: chemical composition, structure, microgeometry, compactness of corrosion layer, solubility, hygroscopic properties;

exposition: periodic wetness and drying, samples sheltered against rain, resp. unsheltered, intensity of radiance etc.

Motivation:

- research programmes of EU – programme UN ECE/EMEP dealing with atmospheric pollution, ICP, MULTI-ASSESS FP6 (database of variables influencing corrosion exist)
- mathematical and statistical methods – trendy (classical - more complicated)
- simulation of processes, modeling methods  **prediction**

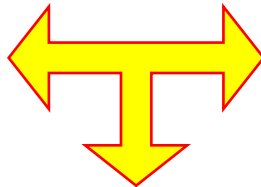
Different prediction techniques:

- **contemporary model** of atmospheric corrosion – D/R functions

$$K = K_{\text{dry}}(T, RH, SO_2, NO_2, O_3) + K_{\text{wet}}(\text{Rain}, H^+)$$

- **new model** for prediction of atmospheric corrosion – **huge environmental database** – D/R functions

$$K = K_{\text{dry}}(T, RH, SO_2, NO_2, O_3, HNO_3, PM10) + K_{\text{wet}}(\text{Rain}, H^+)$$



- application of **artificial neural network** (ANN)



University of Ljubljana

“Dose-response” functions :

- standard technique for modeling of atmospheric corrosion → classical mathematical function

$$D = f [C_i]$$

$$D_m = f (K, [H_2O], T, M) k_{i,m} [C_i]$$

D_m – rate of material degradation **m**;

K - coefficient of mass loss;

[H₂O] - invariable (covering relative humidity, rainfall,, time of wetness, etc.)
of available water on the material surface,

T - ambient temperature;

M - parameter covering surface morphology,

k_{i,m} – reaction rate between corrodant and material **m**

Example

$$\Delta h [\mu m] = 1,92 + 2,97SO_2TOW.t^{0,37} + 0,89SO_2TOW.v.t^{0,37} + 0,15O_3.t^{0,37}$$

where t [year]; SO₂ [μg.m⁻³]; O₃ [μg.m⁻³]; TOW (time of wetness/exposition time);
v (wind velocity) [m.s⁻¹]; R.h.[%].

❑ prediction by mathematical equations have still big „lacks“ (in MICAT errors ≈ 60%)

Why new approach ?

History

- measurements of corrosion processes - time depended,
- inadequately sensitive,
- required permanent presence of experimentator,
- manual evaluation,
- technical support in the form of programs absented ...

VS.

Present time

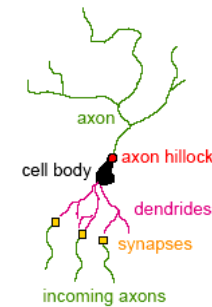
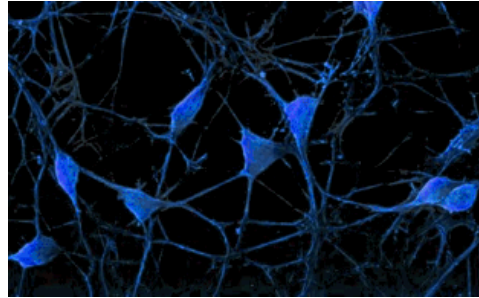
- huge amount of data,
- extract necessary information,
- programme support...

Partial solution in application of AI (ANN):

- extraction of important information
- prediction of time-depended events and their modeling

Artificial neural network:

➤ motivation from biological systems, similar to function of human brain (governing of information, storing, processing) => **adaptive network**



Advantages:

- ✓ absence of exact mathematical characterization of system,
- ✓ presence of strong non-linearities in atmosphere (complexity of physical-chemical processes in industry etc.),
- ✓ robust enough, able to generalize, elimination of errors (minimization),
- ✓ ability of learning on the basis of inputs from environment,
- ✓ ability to improve own performance

Choice of input parameters:

- ❖ for different metals could differ (strong or weak sensitivity on pollutants, etc.)
- ❖ theoretical and practical skills determine input variables:
T - temperature, TOW – time of wetness, R.h - relative humidity, rainfall, concentration of [Cl⁻], [SO₂] (weathering steel)
- ❖ **suitable software:** MATLAB – esp. toolbox NeuralSolution
Neural Tools by PALISADE

Choice of output parameters:

- corrosion process determined by :
mass loss Δm [g.year⁻¹], **thickness loss** Δh [μm .year⁻¹]
- experimental **database** of input and output values – part of training network
- ANN with selected architecture have **ability „to learn“**
minimization of errors in model

$$\text{min Error } (V, W) = \sum // O_{pi} - f_i //^2$$

Tab.1 Example of datasheet of environmental and corrosion values

exposure years	yearly average environmental data						corrosion losses [g.m ⁻²]			
	T	RH	SO ₂	NOx	rain	pH	steel	copper	zinc	aluminium
1	8,0	76,5	151,6		393,6		764,0	62,0	26,3	1,7
1	9,0	70,2	168,2		295,2		878,6	55,6	32,1	1,8
1	8,7	74,8	145,6		50,0		691,6	59,3	23,88	2,93
1	8,0	72,5	120,0		350,4		483,7	38,5	28,7	1,4
1	9,6	73,0	83,3	42,2	626,0	4,4	557,0	27,5	16,2	
1	7,5	77,8	36,4	32,2	500,4	4,1	292,7		7,8	
1	9,9	72,0	78,4	36,0	416,6	4,6			11,5	
1	8,9	71,0	49,0	35,6	431,6	4,2	350,0		11,6	
1	9,7	75,0	49,2	27,4	512,7	4,3	352,0		12,1	
1	8,7	72,9	29,5	35,6	424,7	4,5	293,0		8,8	
1	9,7	76,3	18,3	30,8	380,0	4,7	239,0			
1	9,2	80,0	17,9	24,8	510,0	4,4	223,6		4,6	
1	8,0	73,7	10,9	25,4	316,8	6,3	184,4			
1	8,3	76,0	18,1	25,2	442,2	5,9	183,1	12,45	8,8	
2	8,0	76,3	166,8		505,2		1118,6	89,0	48,4	2,8
2	8,8	74,1	165,0		409,2		1093,5	79,3	48,8	2,2
2	8,8	74,1	140,3		39,6		728,8	70,6	38,17	3,28
2	8,2	73,1	116,3		463,2		630,7	63,0	56,7	1,9
2	9,7	73,0	88,9	40,7	438,0	4,6		49,0	29,6	1,3
2	8,2	76,8	31,5	32,7	452,4	4,4			12,4	

Neural network architecture:

- 3 layer hierarchy: input, hidden and output
- joined with links, weight signaled about strength of connection

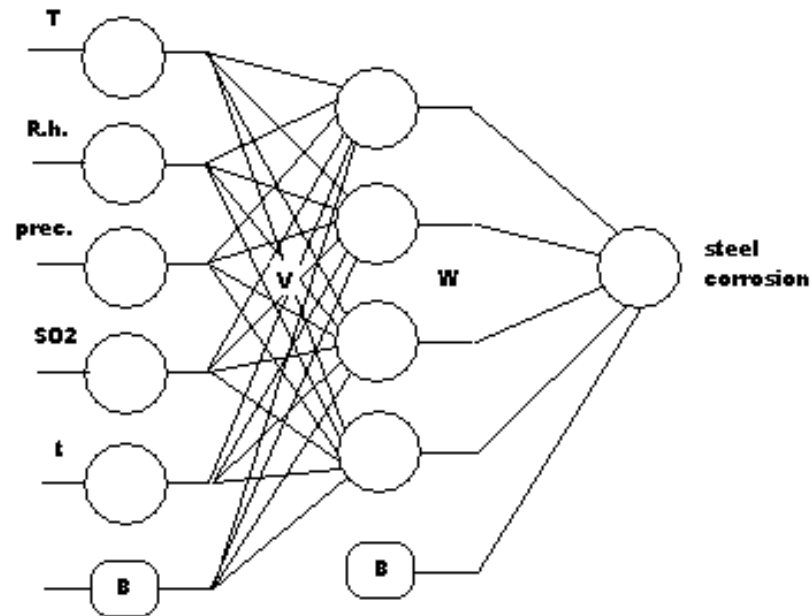


Fig. 1 Schematic illustration of experimental ANN model (multi-layer perceptron) [3]

- **learning process** → algorithm, gradient optimization procedure called BP
- **calculation of RMS errors** → checking recognition ability for prediction by new unknown inputs

The prototype of artificial neural model:

- historical data (**period 1969-2006**) from repeated **one-year** (6 series) and **short-term exposures** - maximum 5 years (5 series) of unalloyed carbon steel
- at 3 different atmospheric test sites in the Czech and Slovak Republic (Kopisty, Prague, Kasperske Hory, Košice) covering rural, industrial-urban and heavy industrial atmospheric environments (training data)
 - ❑ 5 UN ICP test sites (in Europe) in period 1997/98 (testing data)
 - ❑ 4 UN ICP test sites (in Europe) in period 2002/03 (testing data)

Tab.2 The range of environmental parameters for different exposure periods

environmental parameters	Czech test sites *	UN ICP Materials test sites **	
	1969 -2006	1997/98	2002/03
temperature (°C)	5,3 - 10,2	0,2 - 24,6	0,1 - 17,6
relative humidity (%)	70 - 80	61 - 87	30 - 82
amount of precipitation (mm)	284 - 1320	252 - 1744	196 - 1390
SO ₂ (µg.m ⁻³)	5,3 - 182,0	0,2 - 35,0	0,3 - 38,6
Cl ⁻ (mg/l)	0,5 - 7,6	0,1 - 13,3	0,1 - 13,1
pH of precipitation	4,1 - 6,4	4,3 - 6,7	4,3 - 6,6
PM ₁₀ (µg.m ⁻³)	-	-	6,6 - 61,3

* training data

** data for whole UN ICP Materials test sites network

 our prototype of interactive ANN model

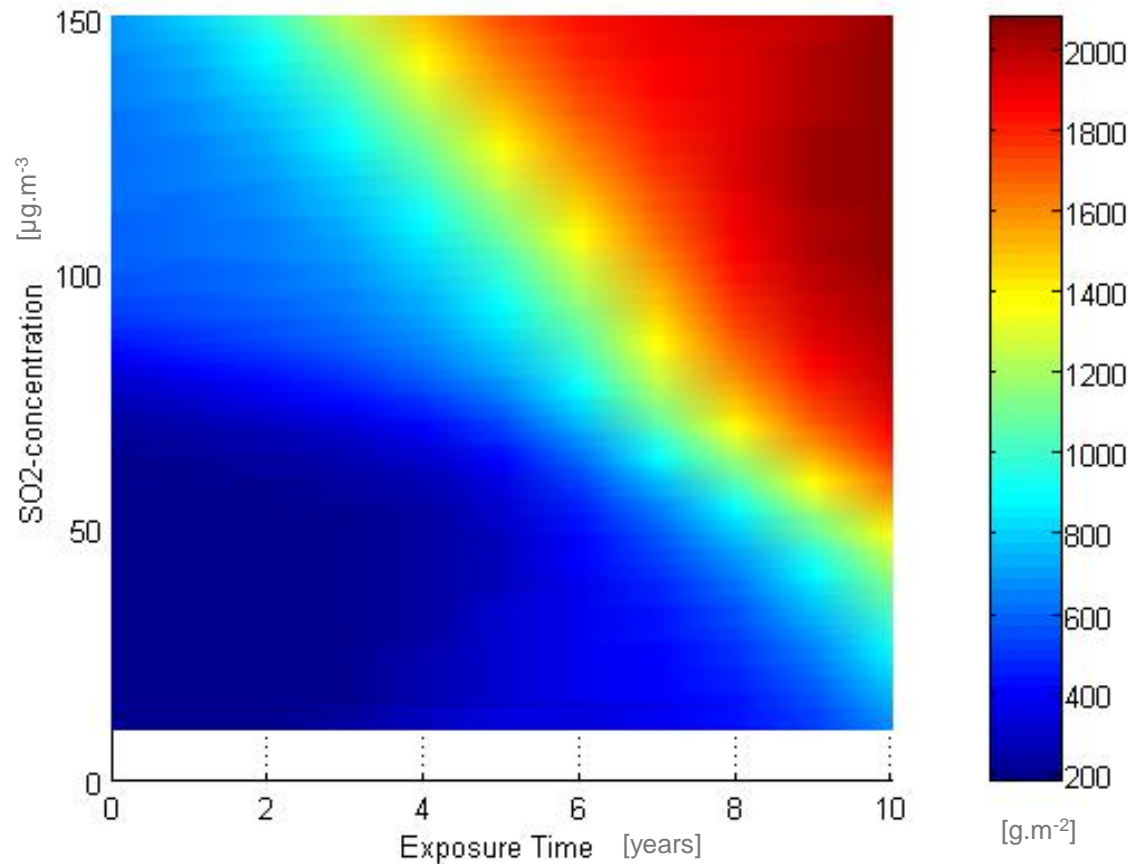


Fig. 2 Output of corrosion rate prediction in mass loss [g.m⁻²] of carbon steel exposed under long-term atmospheric conditions

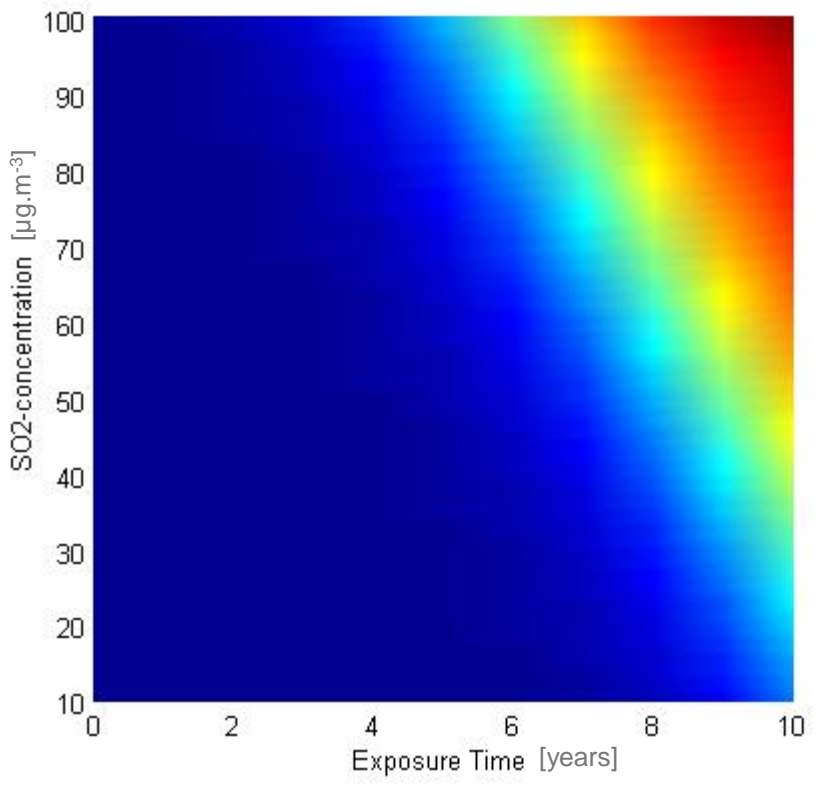
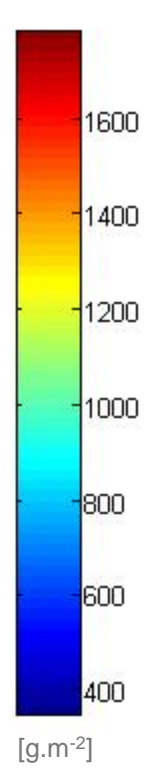


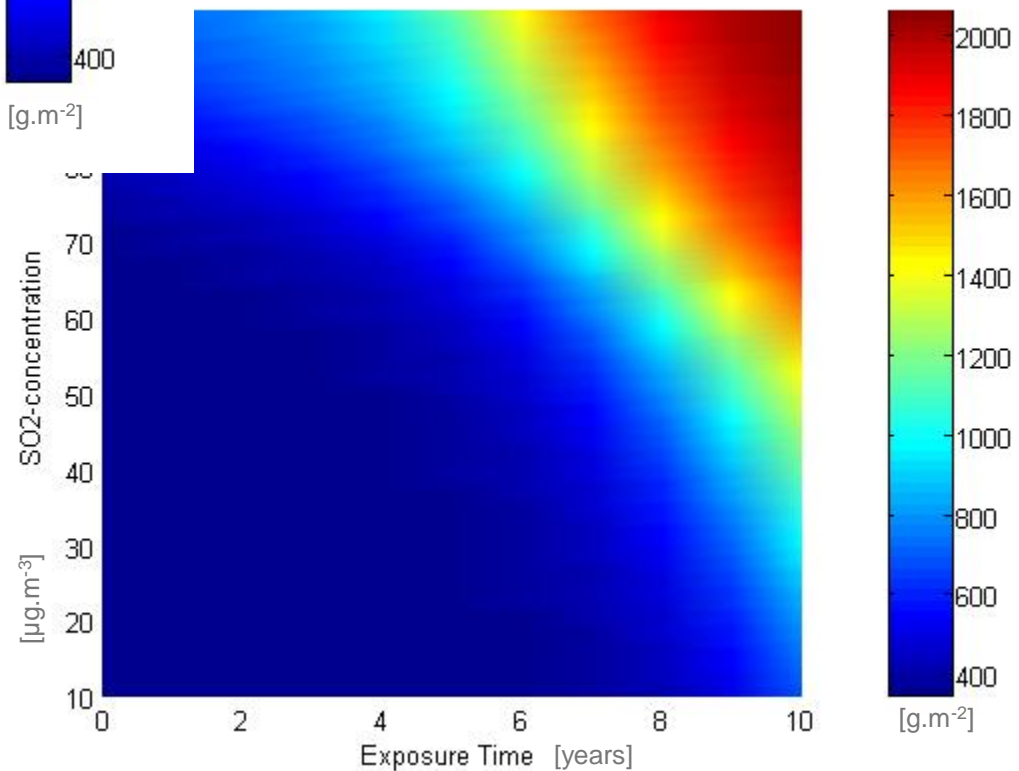
Fig.3 Paris, $T=13\text{ }^{\circ}\text{C}$, R.h.=70%, rain=650 mm

simulation of corrosion of Eiffel tower on site (1997-2017)



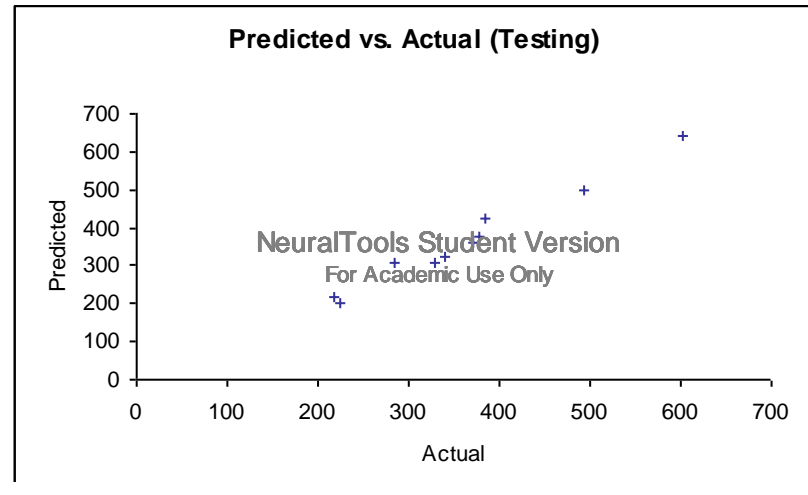
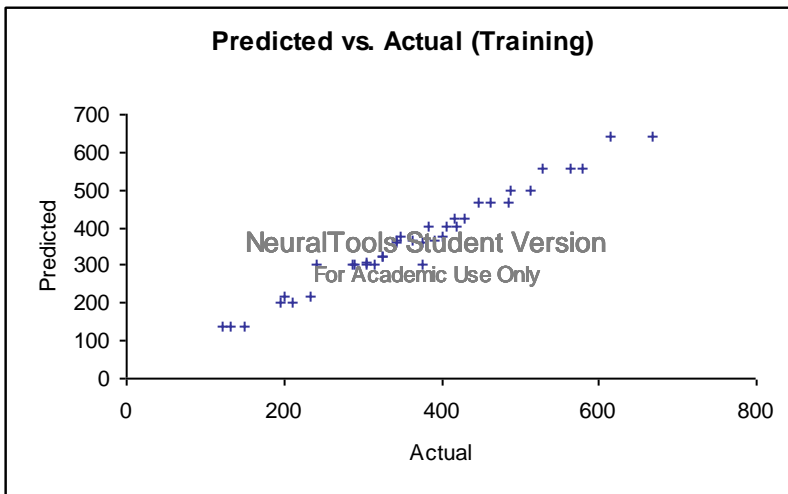
simulation of corrosion of Eiffel tower at hypothetical place (1997-2017)

Fig.4 Prague, $T=10\text{ }^{\circ}\text{C}$, R.h.= 75%, rain = 500 mm



Tab. 3 Results of predicted vs. real of corrosion losses of carbon steel [$\text{g}\cdot\text{m}^{-2}\cdot\text{a}^{-1}$] (yearly)

test site	real mass loss	D/R function 1	D/R function 2	ANN model
97/98				
Prague, CZ	182,0	262,2	163,5	181,2
Kopisty, CZ	241,4	287,4	176,1	239,4
Hurbanovo, SR	418,0	379,4	195,3	391,5
Kosice, SR	397,1	288,3	264,3	387,6
Waldhof, GE	144,0	100,4	60,9	128,2
Paris, FR	136,9	179,6	90,8	144,4
Tel Aviv, IS	323,5	217,8	173,7	331,0
02/03				
Prague, CZ	103,2	142,6	103,1	153,8
Kopisty, CZ	184,4	177,5	124,4	92,4
Waldhof, GE	84,8	79,9	91,6	220,1
Paris, FR	94,2	166,0	110,7	144,5



From database:

ratio 80%/20%
training/testing

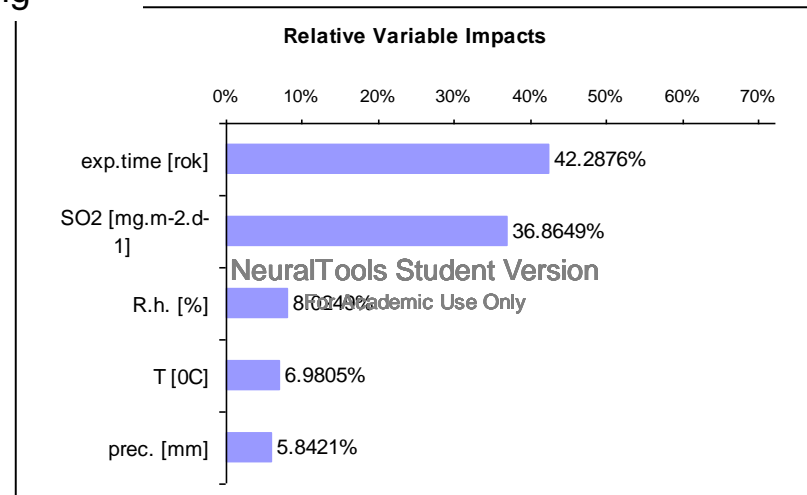
The best ANN models (carbon steel):

-3 neurons in hidden layer with 2058000 trials (**local database**)

-7 neurons in hidden layer with 1235236 trials (**larger database** - e.g. middle European)

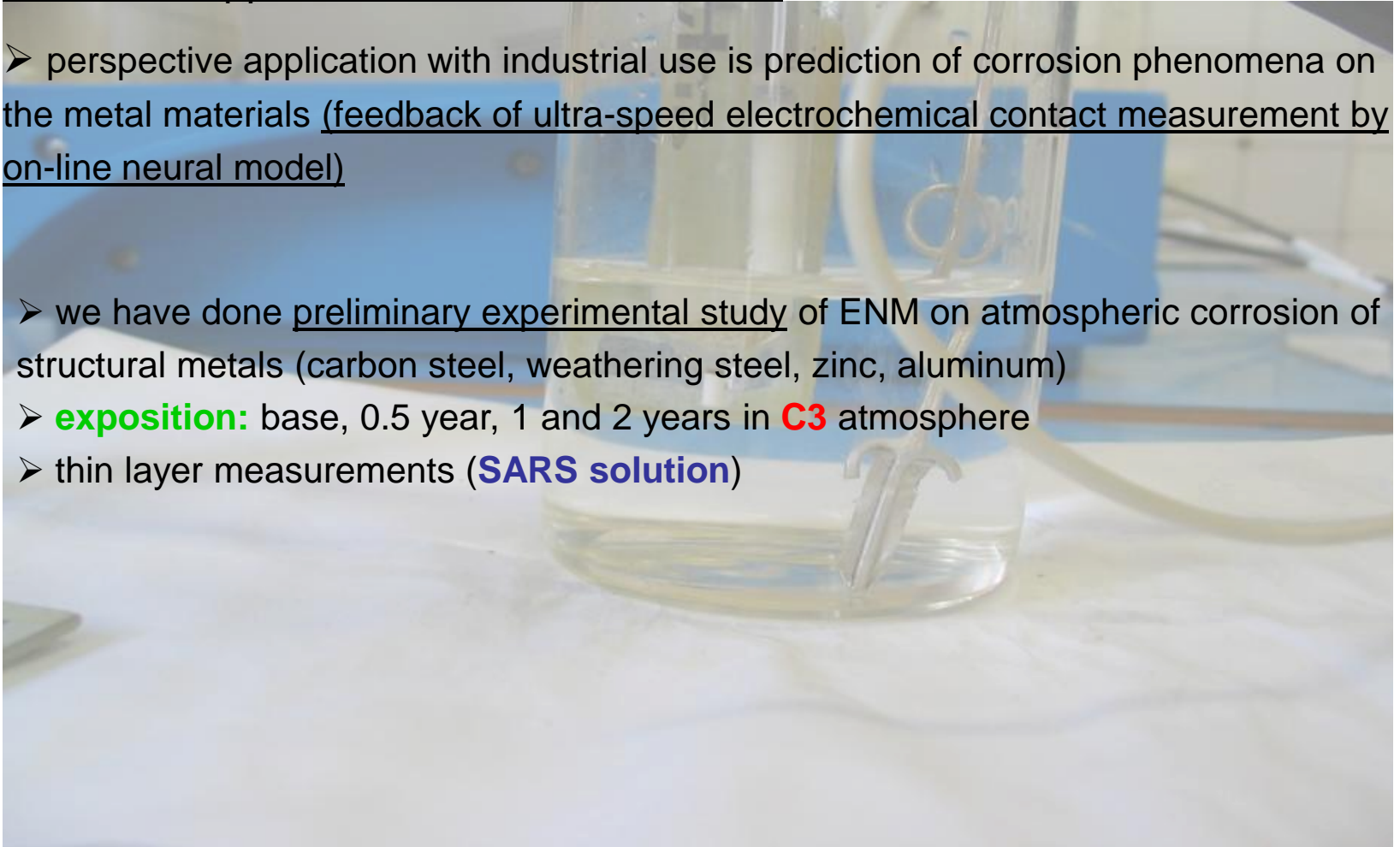
It means:

(1997-98): 0.44 – 10.97% errors in prediction on unknown values and 2-8% errors on trained values



Innovative approach via corrosion sensors:

- perspective application with industrial use is prediction of corrosion phenomena on the metal materials (feedback of ultra-speed electrochemical contact measurement by on-line neural model)
- we have done preliminary experimental study of ENM on atmospheric corrosion of structural metals (carbon steel, weathering steel, zinc, aluminum)
- **exposition:** base, 0.5 year, 1 and 2 years in **C3** atmosphere
- thin layer measurements (**SARS solution**)



Conclusions:

- the **D/R functions** have statistical deviations between 30 - 50%, they are applicable for mapping purposes. On the local scale the corrosion maps are overinterpreted depending on the density of grid of input data
- live prediction **ANN models** with output in the form of 2D maps allow prediction of the metal corrosion rate under various future climate scenarios with errors below 20% for carbon steel ▶ **higher efficiency**
- ANN models should determine majority of environmental and chemical variables and suggest about their potential synergic effects
- on a regional scale the corrosion rate prediction is fitting well. It gives high potential to create prediction model for larger area or climatic zone but the training set of data should be extended (**errors 32-61%**)
- using ANN method for prediction of atmospheric corrosion of metals need to be improved by expanding database of training values (**robustness = quality**)
- perspective application of **hyphenation of corrosion traditional methods with ANN** in construction industry (selection of the best metal material to local atmosphere, **corrosion sensors**)



TECHNICKÁ UNIVERZITA V KOŠICIACH
Fakulta materiálov, metalurgie
a recyklácie

2019 © by Halama

M.Sc. Maroš Halama PhD.
Vice-Dean for Research, Innovations & International Relations

Member, Steel Advisory Group, RFCS, EC
Vice-president, Slovak Association for Surface Treatment

Head of Corrosion Testing Lab at Promatech Centre

Technical University of Kosice
Faculty of Materials, Metallurgy and Recycling
Institute of Materials and Quality Engineering
Letna 9
042 00 Kosice
Slovakia

tel.: +421 55 602 2537

<https://fmmr.tuke.sk>

<http://www.promatech.sk>

<http://www.sspu.sk>

e-mail: maros.halama@tuke.sk



18th INTERNATIONAL FOUNDRYMEN CONFERENCE

Coexistence of material science and sustainable technology in
economic growth

Sisak, May 15th-17th, 2019

<http://www.simet.hr/~foundry/>

PROGRESS IN ON-LINE OPTICAL EMISSION SPECTROMETRY (OES) DATA- DRIVEN INSPECTION OF INCLUSIONS IN ALUMINIUM ALLOYS

Varužan Kevorkijan^{1*}, Tomaž Šustar², Irena Lesjak¹, Marko Degiampietro¹, Janez Langus²

¹ Impol Aluminium Industry, Slovenska Bistrica, Slovenia

² C3M Ltd, Ljubljana, Slovenia

Invited lecture

Original scientific paper

Abstract

Promising approach for fast inspection of inclusions in wrought aluminium alloys is the optical emission spectroscopy (OES). However, in order to separate the peaks corresponding to particular inclusions from the peaks obtained from various microstructural features in the matrix, an advanced filtering of the OES spectrum is necessary. The methodology developed in this work is based on big-data-driven predictions of whether the on-line analysing sample is good or bad. A sufficient amount of relevant data necessary for data-driven predictions was established by the systematic quality control of samples of AA6082 using optical and SEM microscopy and by analysing the same surface using OES. By following a machine-learning process, an algorithm was developed enabling the on-line division of the samples into good and bad, based on criteria received from the casting house. Although the obtained results are promising, the further improvements are necessary before this method could be validated.

Keywords: wrought aluminium, quality prediction, inclusions analysis, optical emission spectroscopy, big data, machine learning

*Corresponding author (e-mail address): varuzan.kevorkijan@impol.si

INTRODUCTION

Numerous research efforts have already been made to develop an **on-line**, industrial method of determining the non-metallic inclusions in wrought aluminium alloys [1-3]. A very promising approach is to use data obtained with optical emission spectroscopy (OES). The main concept is based on the difference in the concentrations of the observed element(s) in



18th INTERNATIONAL FOUNDRYMEN CONFERENCE

Coexistence of material science and sustainable technology in
economic growth

Sisak, May 15th-17th, 2019

<http://www.simet.hr/~foundry/>

the ablated sample and in the matrix, resulting in a different intensity between the baseline signal, obtained from the matrix, and the signal from the inclusion.

The suggested method is a software-based upgrading of the existing OES; however, it is only useful if the matrix is highly uniform, providing a sufficiently flat, noise-free, baseline signal for all the chemical elements appearing in the inclusions. Unfortunately, in the case of wrought aluminium alloys, the matrix is most often non-homogeneous, consisting of the primary dendrites, the eutectic intermetallic phases, the precipitates, as well as the crystal grains and crystallographic textures of different morphologies. In this case the baseline signal is not flat, but consists of several, or rather many, different peaks caused by the matrix non-uniformity. As result of that, determining the inclusions becomes difficult and more uncertain.

In order to obtain a reliable prediction model based on OES data, two steps had to be taken. First, a custom OES data-acquisition procedure was introduced in order to extract as much data as possible from each sample. After the OES data was analysed, it became clear that computer-assisted filtering of the OES spectrum of wrought aluminium alloys is necessary. Custom filtering of the OES data was developed and machine-learning methods used to construct a high-quality prediction model that achieves a high level of prediction accuracy on a large set of AA6082 samples.

METHOD

The research work can be divided into two complementary parts, both of which are crucial to obtain the optimal prediction of sample quality – OES data acquisition and OES data processing.

OES data acquisition

Samples of AA6082 were taken during the molten phase of wrought aluminium and prepared in the shape of discs with a diameter of 40 mm. The surface of the samples was first inspected using optical microscopy. The area and the number of inclusions on the inspected surface were determined using automatic image-recognition software and the quality of each sample was determined. Good samples have lower ratio between inclusion area and sample surface, than it is specified by casting house. Bad samples have higher value then specified.

After the optical inspection, the same surface of the samples was inspected using OES operated in the so-called Spark-DAT mode. In this mode the OES machine records the time evolution of the signal, as shown in Figure 1. The Spark-DAT signal can roughly be described by two values. The mean value of the signal is proportional to the average concentration of the corresponding chemical element in the aluminium alloy. The peaks in the signal, on the other hand, correspond to small parts of the inspected volume with an increased concentration of the corresponding chemical element.



18th INTERNATIONAL FOUNDRYMEN CONFERENCE
**Coexistence of material science and sustainable technology in
economic growth**

Sisak, May 15th-17th, 2019

<http://www.simet.hr/~foundry/>

The most prominent features of the Spark-DAT signal are peaks that correspond to volume parts with increased concentrations of the given chemical element (in this case Ti). For correlation we used signals from elements Ca, K, B, Fe, Ti, C, Al, N, Si, Mg, P and O. The number and magnitude of the peaks should be strongly correlated with the impurity of the sample, but our analysis showed that the correlation between the OES signal's purity and the sample quality determined on the basis of criteria from the casting house is much more demanding as stated in the literature.

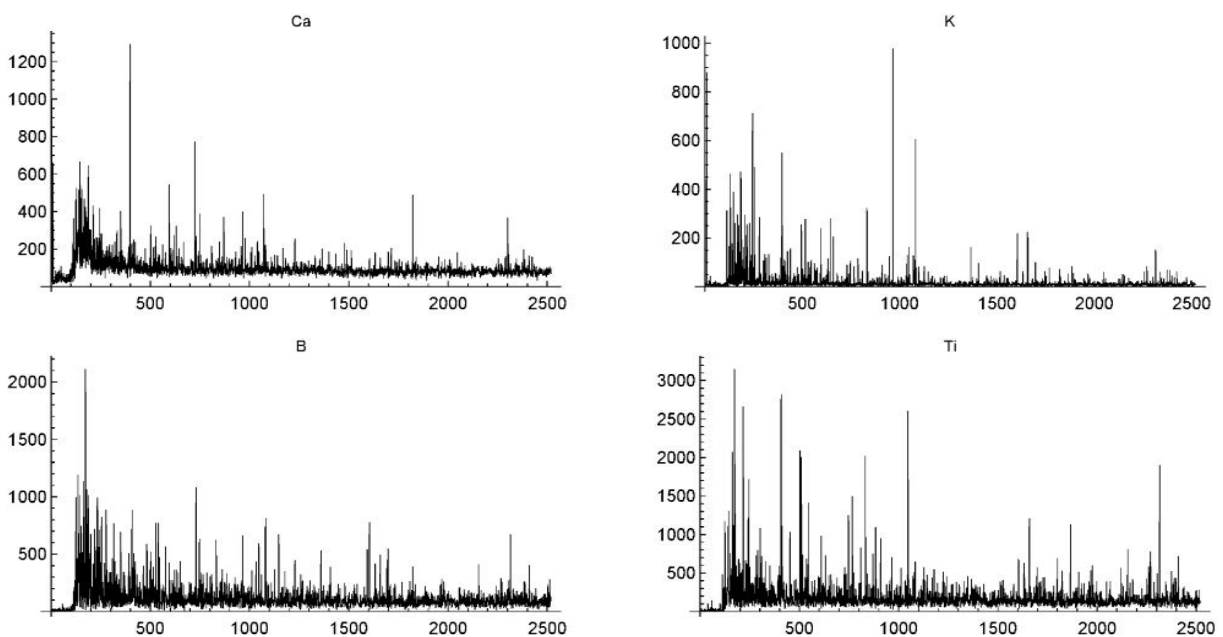


Figure 1. Example of OES Spark-DAT signal for chemical elements Ca, K, B and Ti

Traditional quality-control methods, like visual inspection, optical microscopy and metallography, rely on an inspection of the sample surface. In order to detect inclusions, they must, therefore, be present on the surface of the sample. The OES method, on the other hand, ablates a part of the sample and penetrates beneath the surface. The penetration depth and the area of one OES measurement in Spark-DAT mode was measured using a Zeiss Smartzoom 5 digital microscope (Figure 2).

In order to extract as much data as possible from one sample a special OES sampling procedure was performed on a large number of samples. Each sample was measured with 16 Spark-DAT measurements that were uniformly spaced over the whole area of the sample. The spacing pattern was selected so that the maximum amount of surface was inspected by the OES measurement and that there was minimal cross-contamination between neighbouring Spark-DAT measurements. Sampling was performed over a period of 18 months and included samples from regular production.



18th INTERNATIONAL FOUNDRYMEN CONFERENCE
**Coexistence of material science and sustainable technology in
economic growth**

Sisak, May 15th-17th, 2019

<http://www.simet.hr/~foundry/>

OES data processing

The prominent features of a Spark-DAT measurement are the peaks in the time evolution of the signals for the measured chemical elements (Ca, K, B, Fe, Ti, C, Al, N, Si, Mg, P and O). The mean value of the signal could be used to determine the average chemical composition of the measured sample, but our main focus was on the peaks in the signal. The literature states that there is a strong correlation between the number of peaks and the number of inclusions, and the peak magnitudes strongly correlate with the size of the inclusions in the wrought aluminium samples. The established quality control in IMPOL group uses optical microscopy images to determine the number and the area of inclusions in wrought aluminium and to determine the sample quality based on criteria set by the casting house. We would therefore expect that it should be a trivial task to find a correlation between the number/magnitude of the peaks in the OES signals and the sample quality, as determined by optical microscopy.

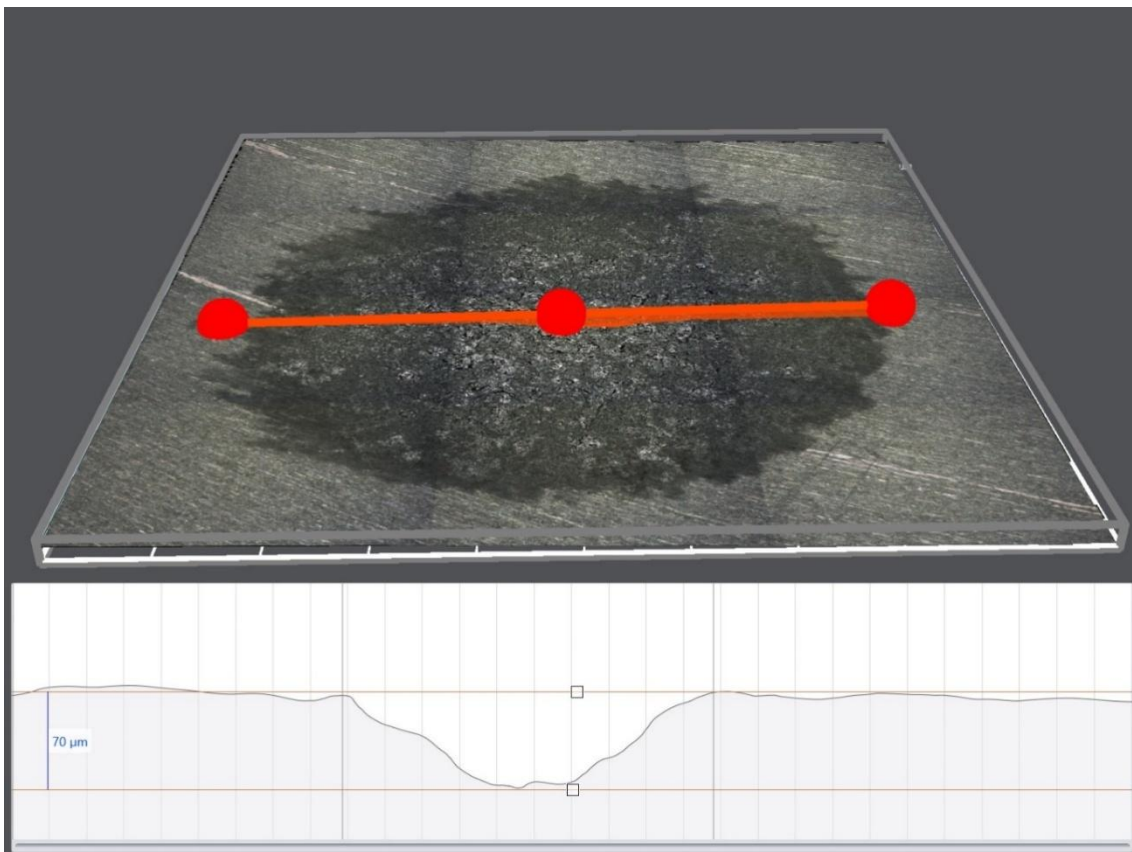


Figure 2. Detailed measurement of the volume that is evaporated during one OES measurement, measured with a Zeiss Smartzoom 5 digital microscope. One can see that although the sparking process covers a larger area (with an average diameter of 7.8 mm) the depth-penetrating ablation focuses on a smaller cone with a diameter of 1.2 mm and a depth of 70 μm



18th INTERNATIONAL FOUNDRYMEN CONFERENCE

Coexistence of material science and sustainable technology in
economic growth

Sisak, May 15th-17th, 2019

<http://www.simet.hr/~foundry/>

Once we started to compare the OES signals from samples that were characterised as good and signals from samples that were characterized as bad using optical microscopy, we were not able to find a clear correlation between the characteristics of the OES signals and the quality of the samples as determined by the optical microscopy. The problem is graphically represented in Figure 3, with a comparison of three different Spark-DAT signals. The first two signals seem to correspond to the expected correlations between the number/magnitude of the peaks and the sample quality, but the third signal negates the theoretically expected correlation. The signal that has the highest number and amplitude of peaks belongs to a sample that was qualified as good based on the optical microscopy.

In order to extract a correlation between the OES signals and the sample quality, as determined by optical microscopy (OM quality), a detailed analysis of the OES signals was performed. The signals were filtered and the measurements condensed into several different types of information, with each type used as the input for a machine-learning algorithm that constructed a neural-network-based model for predicting the sample quality. The quality of the prediction model was evaluated for each type of information and based on those results only four types of condensed information from the OES measurements were used in the construction of the composite neural-network-based quality-prediction model:

1. **Number of peaks** – According to the literature, the number of peaks in the OES signals should strongly correlate with the number of inclusions that contain the corresponding chemical element.
2. **Average peak amplitude** – A higher average peak amplitude should theoretically indicate larger inclusions.
3. **Sum of peak amplitudes** – This information combines both previous pieces of information and should theoretically indicate samples with both higher number and a larger size of inclusions.
4. **Peak correlations** – For a list of pairs of chemical elements (for instance B and Ti) the signals were correlated for peaks that were measured at the same time. The correlated peaks in the signals theoretically indicate inclusions that contain both elements of the correlated pair of chemical elements (for instance TiB₂).

For each type of information, a neural-network model was constructed using machine-learning methods. The learning set was constructed by randomly selecting 70% of the complete dataset, which means that 30% of the dataset was reserved for validation of the neural network. The combined quality-prediction model is a weighted combination of four individual neural-network prediction models.



18th INTERNATIONAL FOUNDRYMEN CONFERENCE
**Coexistence of material science and sustainable technology in
economic growth**

Sisak, May 15th-17th, 2019

<http://www.simet.hr/~foundry/>

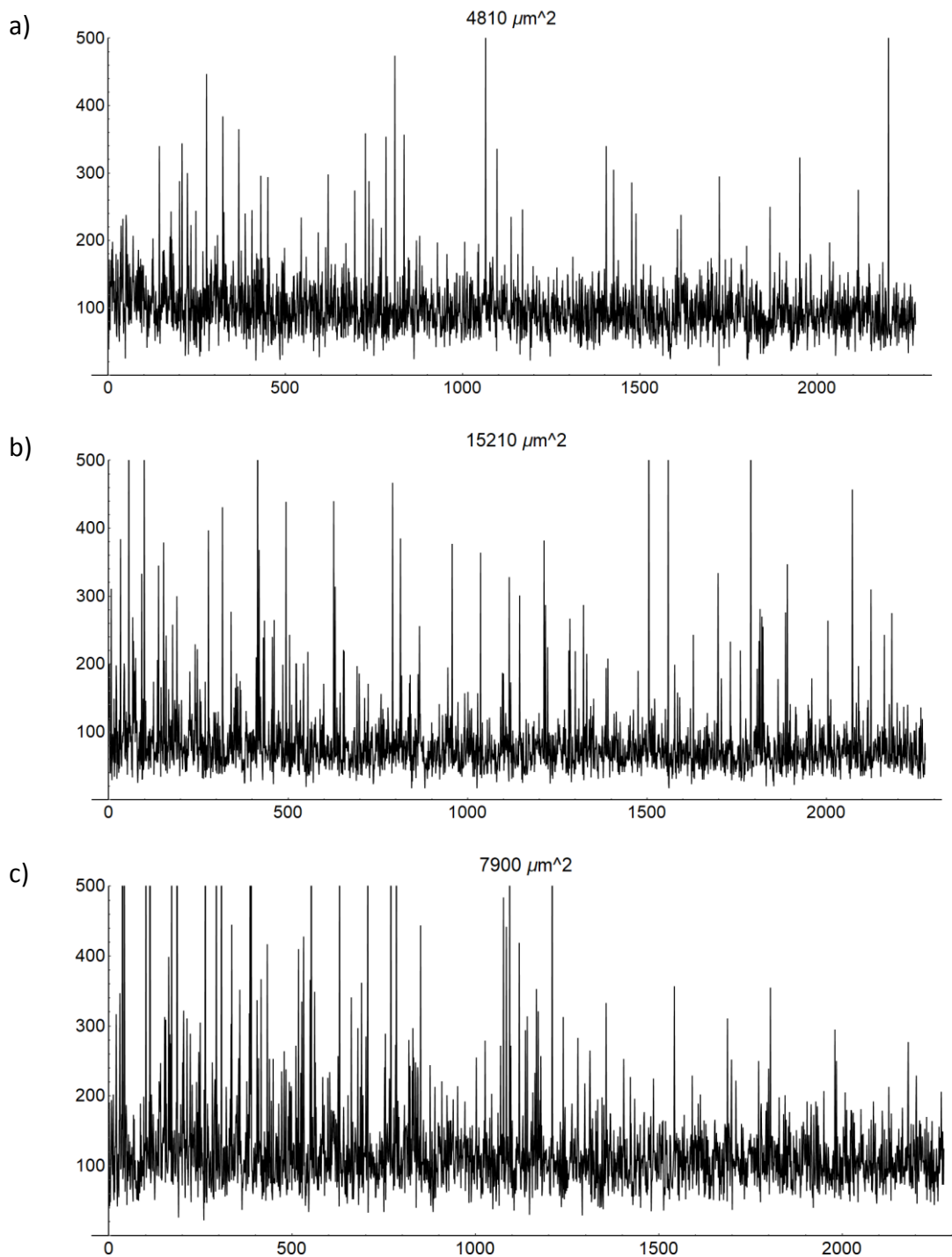


Figure 3. OES Spark-DAT signals for the element Ti from three different samples. The first sample (Fig. 3a) was qualified as an OM good sample. The second sample (Fig. 3b) was qualified as an OM bad sample. The third sample (Fig. 3c) that has the largest number of peaks with the highest amplitudes and should therefore have the largest number of inclusions was qualified as an OM good sample



18th INTERNATIONAL FOUNDRYMEN CONFERENCE
**Coexistence of material science and sustainable technology in
economic growth**

Sisak, May 15th-17th, 2019

<http://www.simet.hr/~foundry/>

RESULTS AND DISCUSSION

Optical microscopy quality control

A combination of meticulous OES data acquisition and specially developed OES data processing was applied to a large set of samples of AA6082 from regular production. The samples were first inspected using optical microscopy and the quality of the samples was determined based on criteria received from the casting house. This quality decision serves as a comparison for sample-quality prediction based on OES data processing. The results are presented in Table 1.

Table 1. Accuracy of the quality prediction in the case of optical microscopy quality control

Quality of samples predicted by OES	Quality of samples determined by optical microscopy		Overall prediction quality
	Good	Bad	
Good	92%	0%	93%
Bad	8%	100%	

As evident, the overall accuracy of the described quality-prediction model is 93% on all samples (70% learning set and 30% validation set). The prediction quality for the good samples is 92% and the prediction quality for the bad samples is 100%. This was achieved by slightly weighting the decision towards bad samples in order to avoid the case where the prediction model would classify a bad sample as a good one – a scenario that is feared by the casting house. We are aware that these accuracy numbers are only valid for the given set of samples and that the 100% prediction accuracy for bad samples will most likely drop with the inclusion of new samples.

Macroscopic quality control

The excellent agreement between the quality determined by the optical microscopy and the quality prediction based on the OES data is because the OES data comes from the same surface that was inspected using optical microscopy. Machine-learning methods were therefore able to construct a strongly correlated prediction model. What would happen if the OES measurements were performed on a different surface than the quality control? This question was answered by comparing the OES-based quality prediction with the results of the macroscopic quality control. The OES measurement is performed on a sample taken during the molten phase of wrought aluminium. Macroscopic quality control is performed on a solidified sample of wrought aluminium, which means that the data for the quality control and the OES quality prediction comes from a different part of the material batch. The results are compared in Table 2.



18th INTERNATIONAL FOUNDRYMEN CONFERENCE
**Coexistence of material science and sustainable technology in
economic growth**

Sisak, May 15th-17th, 2019

<http://www.simet.hr/~foundry/>

Table 2. Accuracy of the quality prediction in the case of macroscopic quality control

Quality of samples predicted by OES	Quality of samples determined by macroscopic control		Overall prediction quality
	Good	Bad	
Good	78%	21%	78%
Bad	22%	79%	

The overall accuracy of the prediction model drops to 78%. The prediction quality for good samples is 78 % and the prediction quality for bad samples to 79%, which indicates very balanced behaviour for the quality-prediction model.

CONCLUSIONS

The methodology developed in this work is based on big-data-driven predictions about whether the on-line analysed sample is good or bad. General customer requirements are that the total amount of inclusions (the percentage of the surface of the representative sample covered by the inclusions) should not exceed some critical value, and the maximum size of the individual inclusions should be smaller than prescribed. The big data with a sufficient amount of relevant data necessary for data-driven predictions was established by the systematic quality control of samples of AA6082 performed by optical and SEM microscopies, and by analysing the same surface using OES. The prediction methodology was based on the big-data filtering analytics of OES signals. By following a machine-learning process, an algorithm was developed that is capable of recognising sets of characteristic peaks in the OES spectrum, enabling the on-line dividing of samples into good and bad, depending upon the criterion received from the casting house.

The currently achieved quality of the predictions is about 90% when comparing the results of the quality prediction with a quality decision based on the results of optical microscopy. However, the recognition of good samples is much better than that of the bad ones and is close to 100%. This can be partly explained by the prevailing number of good samples in the data set – around 90% of samples were rated as good by the optical microscopy. The relatively good agreement between the prediction and the measurement results comes from the fact that both the optical microscopy and the OES measurement inspected the same sample surface.

The question remains as to whether the relatively small sample (disk with a diameter of 40 mm) is representative of the whole batch of the casting mass. This question was addressed by comparing the results of the OES quality-prediction model with the results of the macroscopic quality control that is performed on the surface of a solidified billet, which means that both methods inspected completely different parts of the material in question. The accuracy of the OES prediction model reached 78 %, which we believe can be further improved by increasing the number of samples in the learning set that is used to construct the neural network.



18th INTERNATIONAL FOUNDRYMEN CONFERENCE

Coexistence of material science and sustainable technology in
economic growth

Sisak, May 15th-17th, 2019

<http://www.simet.hr/~foundry/>

The currently developed OES data-acquisition method with 16 Spark-DAT measurements is a time-consuming process that limits the throughput of the OES-based quality-prediction method. We are currently investigating the effects of decreasing the number of Spark-DAT measurements, while keeping the level of the prediction quality above 80%. Initial findings show that it will indeed be possible to decrease the number of Spark-DAT measurements and thus speed up the OES quality-prediction method.

Further improvements (to the filtration procedure and the algorithm) along with the continued validation of the predicted quality with established quality-control procedures are necessary before this method can be validated to use in regular quality control.

REFERENCES

- [1] J. M. Böhlen, K. Li, L. J. Dorier, E. Halász, Advances in the ultra-fast inclusion analysis in steel by spark-OES, Proceedings of the 8th International Workshop on Progress in Analytical Chemistry and Materials Characterization in Steel and Metal Industries, (V. Tusset), 17-19 May 2011, Luxemburg, Belgium, pp. 101-108.
- [2] J. M. Böhlen, R. Yellepeddi, Combined quantitative analysis and ultra-fast analysis of nonmetallic inclusions by optical emission spectrometry, Millenium Steel (2009), pp. 167-171.
- [3] K. Li, E. Halász, J. M. Böhlen, Analysis of inclusions in steel and aluminum with the ARL iSpark Spark-DAT – Recent improvements, Metallurgical Analysis, CCATM 2010 Conference Proceedings, 30(2010), pp. 214-217.



18th INTERNATIONAL FOUNDRYMEN CONFERENCE

Coexistence of material science and sustainable technology in
economic growth

Sisak, May 15th-17th, 2019

<http://www.simet.hr/~foundry/>

THE IMPACT OF APPLYING PVD COATINGS ON SURFACE ROUGHNESS OF QUENCHED AND TEMPERED STEELS

UTJECAJ NANOŠENJA PVD PREVLAKA NA HRPAVOST POVRŠINE ČELIKA ZA POBOLJŠAVANJE

Ivica Kladarić^{1*}, Stjepan Golubić^{2*}, Slavica Kladarić³

¹ Josip Juraj Strossmayer University of Osijek Mechanical Engineering Faculty in Slavonski Brod,
Slavonski Brod, Croatia

² Bjelovar University of Applied Sciences, Bjelovar, Croatia

³ College of Slavonski Brod, Slavonski Brod, Croatia

Invited lecture

Original scientific paper

Abstract

PVD coatings of hard compounds reduce adhesion and abrasion wear, and some types of coatings also reduce the friction factor. The temperature of the PVD process is lower than the tempering temperature of quenched and tempered steels, there are no deformations of parts and no additional stresses. During the heat treatment, the PVD process is performed at the end because the PVD coating does not require subsequent heat treatment. In this paper, the impact of the application of PVD coatings (cVlC and nACVlC) on the surface roughness of three quenched and tempered structural steels (45S20, C45E and 42CrMo4) was investigated. All the steels were heat-treated by normalization, quenching and tempering and hardening before the coating process. Measurement results were statistically analysed. Based on the conducted experimental tests it was determined that change in the surface roughness of quenched and tempered steels after application of the PVD coating depends on the previous heat treatment of the steel, the type of coating and initial roughness, and less on the type of steel.

Keywords: PVD (Physical Vapour Deposition) coatings, quenched and tempered steels, surface roughness

*Corresponding author (e-mail address): ikladar@sfsb.hr



18th INTERNATIONAL FOUNDRYMEN CONFERENCE

Coexistence of material science and sustainable technology in
economic growth

Sisak, May 15th-17th, 2019

<http://www.simet.hr/~foundry/>

Sažetak

PVD prevlake tvrdih spojeva smanjuju adhezijsko i abrazijsko trošenje, a pojedine vrste prevlaka također smanjuju faktor trenja. Temperatura PVD postupka je niža od temperature popuštanja čelika za poboljšavanje, nema deformacija dijelova i unošenja novih naprezanja. Tijekom toplinske obrade, PVD postupak se izvodi na kraju jer PVD prevlaka ne zahtjeva naknadnu toplinsku obradu. U radu je ispitan utjecaj nanošenja PVD prevlaka (cVlC i nACVlC) na hrapavost površine tri konstrukcijska čelika za poboljšavanje (45S20, C45E i 42CrMo4). Svi čelici su prije postupka prevlačenja toplinski obrađeni normalizacijom, poboljšavanjem i kaljenjem. Rezultati mjerenja su obrađeni statistički. Na temelju provedenih eksperimentalnih ispitivanja utvrđeno je da promjena hrapavosti površine čelika za poboljšavanje nakon nanošenja PVD prevlaka ovisi o prethodnoj toplinskoj obradi čelika, vrsti prevlake i početnoj hrapavosti, a manje o vrsti čelika.

Ključne riječi: PVD (*Physical Vapour Deposition*) prevlake, čelici za poboljšavanje, površinska hrapavost

UVOD

Poboljšanje uporabnih svojstava strojnih dijelova i alata najčešće se ostvaruje izborom odgovarajućeg materijala. Danas se, uz izbor odgovarajućeg materijala, sve više pozornosti posvećuje razvoju i primjeni različitih postupaka toplinske obrade. Pojedini postupci provode se s ciljem promjene svojstava, posebno površinskih slojeva, kako bi se proširila upotreba u različitim uvjetima trošenja.

Postupcima površinske toplinske obrade bavi se inženjerstvo površina (eng. *Surface Engineering*). Suština primjene postupaka inženjerstva površina je u tome da se osnovni materijal (supstrat), prethodno odgovarajuće pripremljen, naknadno obradi jednom od površinskih tehnologija. Dobivena kombinacija svojstava površinskog sloja i osnovnog materijala ne može se postići upotrebom bilo kojeg jednorodnog materijala. Dvije osnovne grupe postupaka inženjerstva površina su modificiranje i prevlačenje. Kod modificiranja u površinskom sloju obratka dolazi do promjene strukture i svojstava, dok se kod prevlačenja prevlaka stvara na površini obrađivanog materijala [1].

Jedan od postupaka prevlačenja površina je fizikalno prevlačenje u parnoj fazi, odnosno PVD postupak (eng. *Physical Vapour Deposition*). Ovdje se radi o stvaranju površinskog sloja koji je različitog sastava od osnovnog materijala. PVD prevlake nastaju fizikalnim taloženjem u parnoj fazi. Stvaranje prevlake se izvodi transportom čestica (atoma, molekula i iona) u vakuumu koje se fizikalnim načinom prevode iz čvrste u parnu fazu. Pomoću PVD postupka moguće je postići tanke prevlake gotovo od svih kemijskih elemenata. Kemijski spojevi, kao što su metalni karbidi, nitridi ili oksidi, mogu se također izlučiti reaktivnim vođenjem procesa i danas su u tehničkoj primjeni od velikog značaja. PVD prevlake tvrdih spojeva smanjuju abrazijsko trošenje, a sniženje faktora trenja utječe na smanjenje adhezijskog trošenja [2,3]. PVD postupak načelno ima dobru prionjivost prevlake na osnovni materijal, daje glatke



18th INTERNATIONAL FOUNDRYMEN CONFERENCE

Coexistence of material science and sustainable technology in
economic growth

Sisak, May 15th-17th, 2019

<http://www.simet.hr/~foundry/>

površine i omogućuje postizanje tankih prevlaka. PVD postupak se izvodi kao završni postupak obrade jer PVD prevlaka ne zahtjeva naknadnu toplinsku obradu. Provodi se pri temperaturi ispod 500 °C, tako da su za njega prikladni i čelici kojima se popuštanje izvodi pri $\vartheta_p \geq 500$ °C (npr. brzorezni čelici, alatni čelici za topli rad, čelici za poboljšavanje) [4].

U ovisnosti o postupku nanošenja tvrde ili zaštitne PVD prevlake hrapavost površine se može povećati, smanjiti ili ostati nepromijenjena. Hrapavost površine nije jednaka u svim područjima zbog ogrebotina, dimenzionalnih prijelaza, uključaka, onečišćenja i sl. [5,6].

Primjena PVD prevlaka je višestruka: strojarska (alati, dijelovi strojeva), automobilska, vojna, tekstilna (vodilice, igle), prehrambena (pužne zavojnice), drvna (profilni alati), zlatarska (noževi, pile, kalupi), kemijska (zaštita od korozije), industrija papira (noževi, glodala, igle), prerada plastike (alati za brizganje), izrada satova (dekorativne prevlake), u medicini (kirurški alati, protetika), kao zaštitne i dekorativne prevlake na staklu, keramici itd. Zbog ekoloških razloga PVD prevlake uvode se i kao alternativa za galvansko nanošenje prevlaka kadmija, cinka, tvrdog kroma, nikla i sl. [1]. Primjeri primjene PVD postupaka prevlačenja metalnih dijelova prikazani su na slici 1.



Slika 1. Primjeri prevlačenja metalnih dijelova [7]

EKSPERIMENTALNI RAD

U okviru istraživanja primjenjivosti PVD prevlaka na konstrukcijskim čelicima provedena su mjerenja utjecaja nanošenja PVD prevlaka na hrapavost površine tri konstrukcijska čelika za poboljšavanje u normaliziranom, poboljšanom i zakaljenom stanju. Hrapavost površine uspoređivana je preko srednje visine neravnina Ra . Nakon toplinske obrade dvije skupine uzoraka prevučene su s dva tipa PVD prevlaka, a jedna skupina je ostala bez prevlake. Ovakav izbor čelika, toplinske obrade i prevlaka omogućuje postavljanje faktorskog plana pokusa 3^3 [6].

Izabrani su konstrukcijski čelici za poboljšavanje 45S20, C45E i 42CrMo4.

- Čelik 45S20 pripada skupini konstrukcijskih čelika za obradu na automatima. Kod obrade odvajanjem čestica daje kratke lomljene čestice. Primjenjuje se u normaliziranom ili u poboljšanom stanju.
- Čelik C45E je nelegirani čelik za poboljšavanje s povišenim sadržajem ugljika. Primjenjuje se u normaliziranom, poboljšanom ili kaljenom stanju (površinsko kaljenje) za izradu strojnih dijelova srednje čvrstoće.



18th INTERNATIONAL FOUNDRYMEN CONFERENCE

Coexistence of material science and sustainable technology in economic growth

Sisak, May 15th-17th, 2019

<http://www.simet.hr/~foundry/>

- Čelik 42CrMo4 je čelik za poboljšavanje legiran kromom i molibdenom. Primjenjuje se u normaliziranom, poboljšanom ili kaljenom stanju (površinsko kaljenje) za statički i dinamički opterećene dijelove vozila, motora i strojeva.

Parametri toplinske obrade izabrani su prema literaturnim podacima [8, 9] za toplinsku obradu konstrukcijskih čelika za poboljšavanje, tablica1.

Tablica 1. Izabrani parametri toplinske obrade

TO Čelik	Normalizacija		Poboljšavanje						Kaljenje		
	G_N °C	t h	G_a °C	t h	gašenje	G_p °C	t h	hlađenje	G_a °C	t h	gašenje
45S20	840	1	840	1	voda	560	2	zrak	840	1	voda
C45E	840	1	840	1	voda	560	2	zrak	840	1	voda
42CrMo4	840	1	840	1	ulje	560	2	zrak	840	1	ulje

Izabrane su dvije prevlake na osnovi zahtjeva koji se postavljaju za izbor čelika za izradu strojnih dijelova (tvrdoća površinskog sloja, niski faktor trenja itd.).

Izabrane PVD prevlake su cVlc i nACVlc.

- cVlc je dvostruka prevlaka s nanostrukturom koja nastaje kombinacijom TiCN + CBC prevlake. TiCN prevlaka je konvencionalna prevlaka, a CBC (*Carbon Based Coating*) je osnovna ugljična prevlaka. CBC komponenta koristi se kao suho mazivo s ciljem smanjenja faktora trenja.
- nACVlc je dvostruka prevlaka s nanostrukturom koja nastaje kombinacijom nACRo + CBC prevlake. nACRo (nAlCrN/a-Si₃N₄) je nanokompozitna prevlaka, a CBC komponenta koristi se kao suho mazivo s ciljem smanjenja faktora trenja. Kod nACVlc prevlake za poboljšanje veze s osnovnim materijalom nanosi se sloj titana.

Izabrane prevlake imaju visoku tvrdoću, nizak faktor trenja i tanke debljine slojeva, a temperatura primjene je u području uporabe konstrukcijskih čelika za poboljšavanje. Zbog male debljine slojeva nije potrebna korekcija tolerancija dimenzija na postojećim konstrukcijskim dijelovima. U tablici 2 prikazana su osnovna svojstva izabranih prevlaka.

Tablica 2. Svojstva izabranih PVD prevlaka [7]

Prevlaka	Boja	Nanotvrdoća GPa	Debljina μm	Faktor trenja (na čeliku)	Max. temp.uporabe °C
cVlc	siva	25	1 - 2	0,15	400
nACVlc	plavosiva	40-25	1 - 10	0,15	450

Izrada uzoraka

Za ispitivanja je izrađen 81 uzorak dimenzija 10×10×55 mm (slika 2). Uzdužne plohe (10×55 mm) obrađene su nakon toplinske obrade na različite površinske hrapavosti;



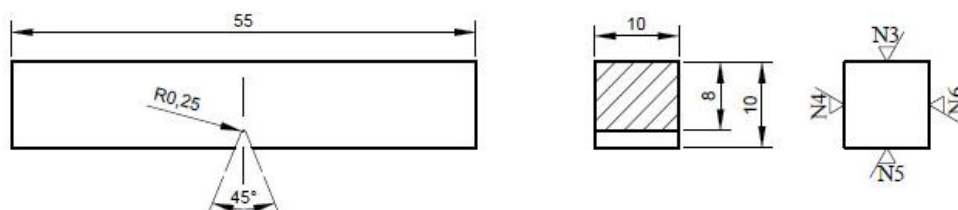
18th INTERNATIONAL FOUNDRYMEN CONFERENCE

Coexistence of material science and sustainable technology in economic growth

Sisak, May 15th-17th, 2019

<http://www.simet.hr/~foundry/>

N3 ($Ra \leq 0,1 \mu\text{m}$), N4 ($Ra \leq 0,2 \mu\text{m}$), N5 ($Ra \leq 0,4 \mu\text{m}$) i N6 ($Ra \leq 0,8 \mu\text{m}$). Klase hrapavosti označene su na čelu uzorka, a birane su prema hrapavostima koje se primjenjuju kod postupaka obrade metala odvajanjem čestica za izradu strojnih dijelova.



Slika 2. Uzorak za mjerenje hrapavosti površine

Prevlačenje uzoraka

Prevlačenje uzoraka PVD prevlakama provedeno je u tvrtki Gazela-Platit (Krško, Slovenija). Parametri prevlačenja izabrani su prema vrstama pojedinih prevlaka koje primjenjuje tvrtka Gazela-Platit. Za prevlaku cVlc temperatura postupka je iznosila 450 °C, a za prevlaku nACVlc temperatura postupka je iznosila 460 °C. Trajanje postupka za cVlc i za nACVlc prevlačenje bilo je jednako. Prva faza postupka je ugrijavanje predmeta na radnu temperaturu u trajanju od 1 h. U drugoj fazi provedeno je elektronsko čišćenje u trajanju od 15 min. Treća faza postupka je prevlačenje u trajanju od 3 h. Prevođenje iz čvrstog u plinovito stanje provedeno je pomoću električnog luka. Prije vađenja uzorci su hlađeni u peći 1 h do temperature od 100 °C. Također je provedeno mjerenje debljine prevlaka metodom kružnog izbruska, a izmjerene vrijednosti prikazane su u tablici 3.

Tablica 3. Izmjerene debljine prevlaka nakon prevlačenja [6]

Čelik	Debljina prevlake, μm					
	Normalizirano stanje		Poboljšano stanje		Kaljeno stanje	
	cVlc	nACVlc	cVlc	nACVlc	cVlc	nACVlc
45S20	1,79	2,64	1,68	2,84	2,10	2,68
C45E	2,09	2,59	1,65	2,52	1,70	2,75
42CrMo4	1,73	2,82	1,89	2,55	1,58	2,60

Mjerenje hrapavosti površina

Hrapavost je mjerena na uzorcima prije i nakon prevlačenja. Mjerenje je provedeno profilmetrom tvrtke Mitutoyo, tip SJ-201 P. Za umjeravanje je korišten etalon isporučen uz uređaj (etalon 178-601, serijski broj 431-708, $Ra = 3,05 \mu\text{m}$).

Hrapavost površine mjerena je na uzdužnim ploham (10×55 mm) svakog uzorka s početnom klasom hrapavosti N3, N4, N5 i N6, za svaki čelik, za svaku vrstu toplinske obrade i za svaku vrstu prevlake. Mjerenje je srednje aritmetičko odstupanje profila Ra kao jedan od najvažnijih



18th INTERNATIONAL FOUNDRYMEN CONFERENCE

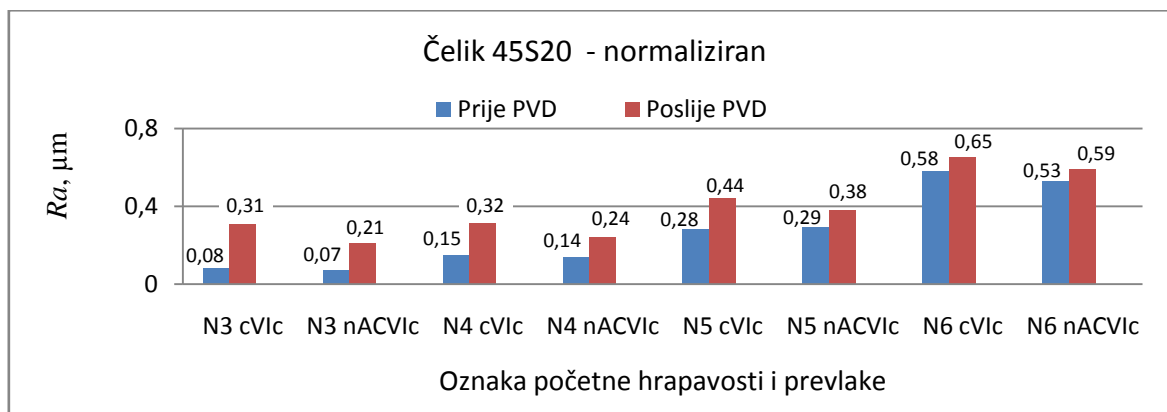
Coexistence of material science and sustainable technology in economic growth

Sisak, May 15th-17th, 2019

<http://www.simet.hr/~foundry/>

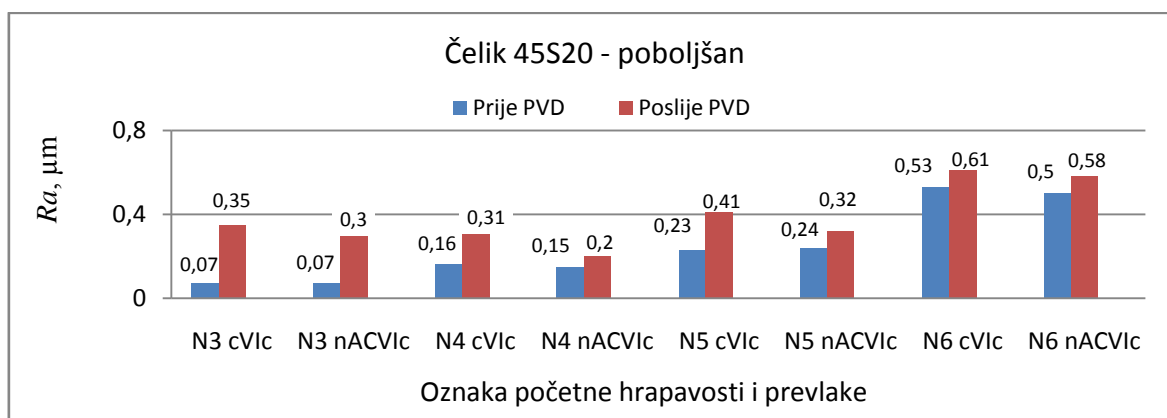
pokazatelja kada se uspoređuju hrapavosti površina obrađenih različitim postupcima strojne obrade.

Na slici 3 histogramski su prikazane izmjerene hrapavosti normaliziranog čelika 45S20 prije i nakon prevlačenja PVD prevlakama.



Slika 3. Hrapavosti normaliziranog čelika 45S20 prije i nakon prevlačenja PVD prevlakama

Na slici 4 histogramski su prikazane izmjerene hrapavosti poboljšanog čelika 45S20 prije i nakon prevlačenja PVD prevlakama.



Slika 4. Hrapavosti poboljšanog čelika 45S20 prije i nakon prevlačenja PVD prevlakama

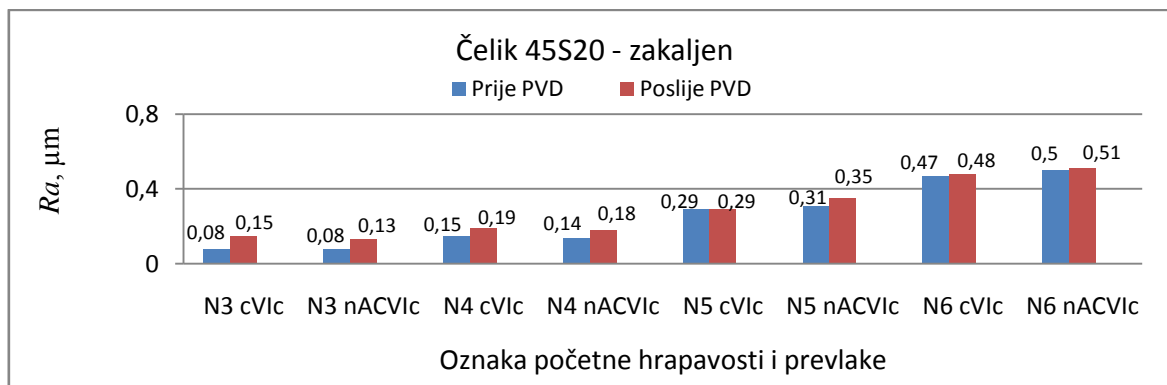
Na slici 5 histogramski su prikazane izmjerene hrapavosti zakaljenog čelika 45S20 prije i nakon prevlačenja PVD prevlakama.



18th INTERNATIONAL FOUNDRYMEN CONFERENCE
Coexistence of material science and sustainable technology in economic growth

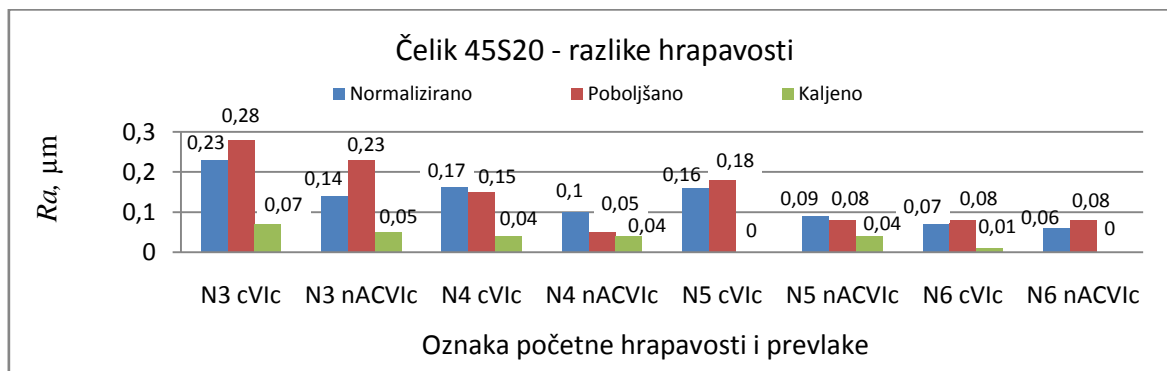
Sisak, May 15th-17th, 2019

<http://www.simet.hr/~foundry/>



Slika 5. Hrapavosti zakaljenog čelika 45S20 prije i nakon prevlačenja PVD prevlakama

Razlike hrapavosti toplinski obrađenog čelika 45S20 prije i nakon prevlačenja PVD prevlakama histogramski su prikazane na slici 6.



Slika 6. Razlike hrapavosti toplinski obrađenog čelika 45S20 prije i nakon prevlačenja PVD prevlakama

Kod svih stanja toplinski obrađenog čelika 45S20, utjecaj prevlačenja na hrapavost je bio manji što je klasa hrapavosti bila viša. Veće razlike hrapavosti uočene su nakon prevlačenja cVlc prevlakom u odnosu na nACVlc prevlaku. Razlike hrapavosti manje su za početno zakaljeno stanje u odnosu na početno normalizirano i poboljšano stanje.

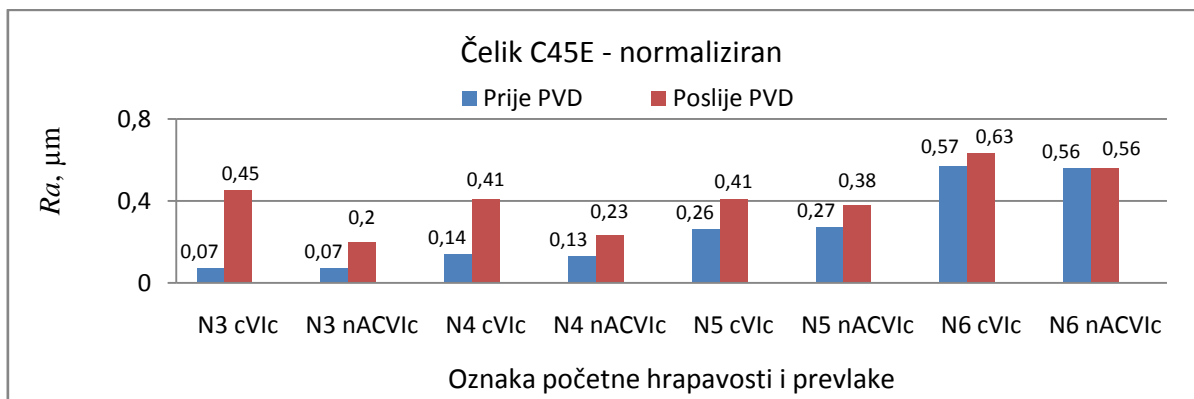
Na slici 7 histogramski su prikazane izmjerene hrapavosti normaliziranog čelika C45E prije i nakon prevlačenja PVD prevlakama.



18th INTERNATIONAL FOUNDRYMEN CONFERENCE
Coexistence of material science and sustainable technology in economic growth

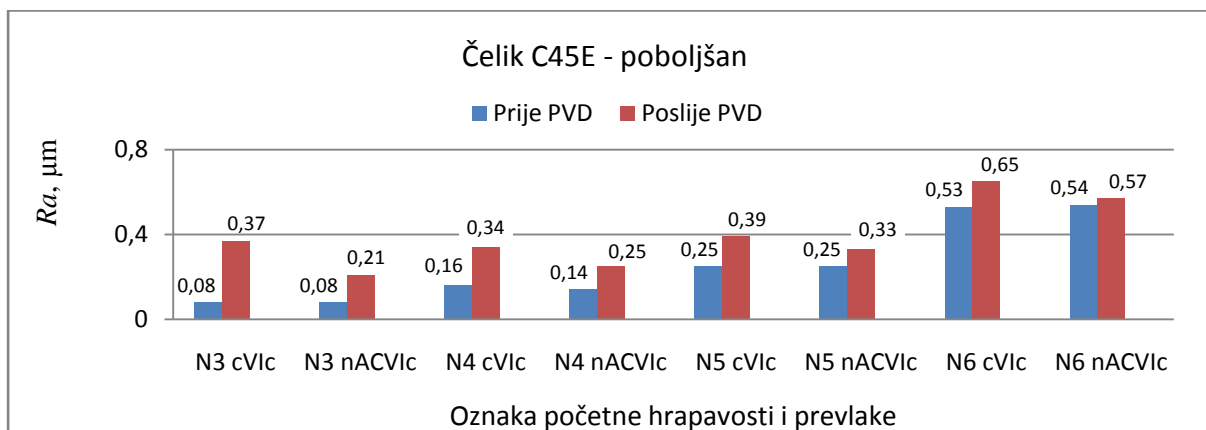
Sisak, May 15th-17th, 2019

<http://www.simet.hr/~foundry/>



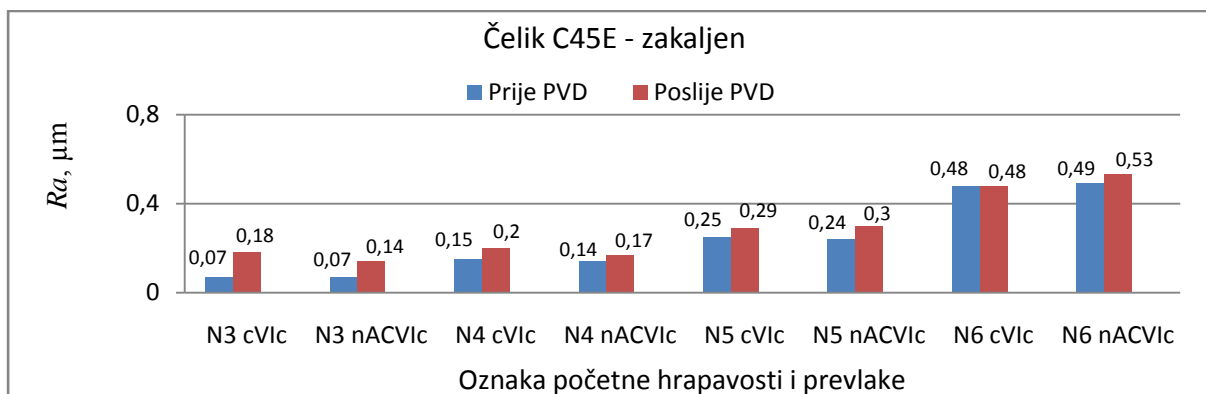
Slika 7. Hrapavosti normaliziranog čelika C45E prije i nakon prevlačenja PVD prevlakama

Na slici 8 histogramski su prikazane izmjerene hrapavosti poboljšanog čelika C45E prije i nakon prevlačenja PVD prevlakama.



Slika 8. Hrapavosti poboljšanog čelika C45E prije i nakon prevlačenja PVD prevlakama

Na slici 9 histogramski su prikazane izmjerene hrapavosti zakaljenog čelika C45E prije i nakon prevlačenja PVD prevlakama.



Slika 9. Hrapavosti zakaljenog čelika C45E prije i nakon prevlačenja PVD prevlakama

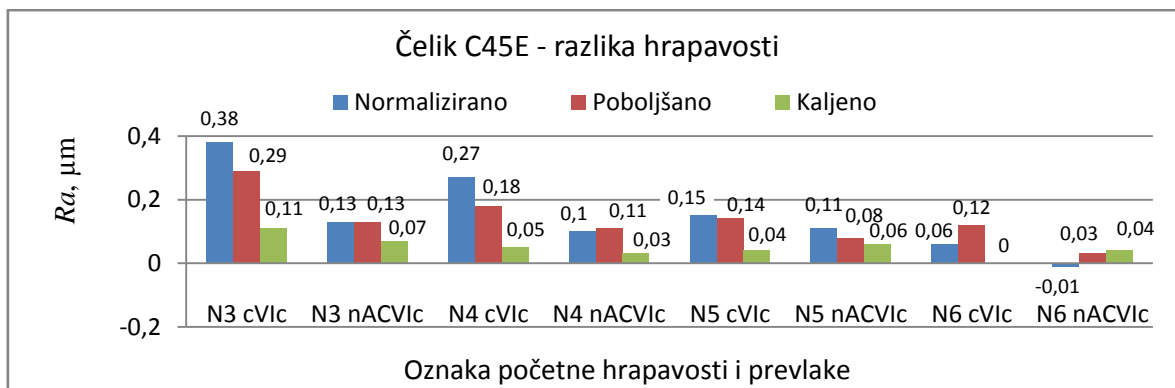


18th INTERNATIONAL FOUNDRYMEN CONFERENCE
Coexistence of material science and sustainable technology in economic growth

Sisak, May 15th-17th, 2019

<http://www.simet.hr/~foundry/>

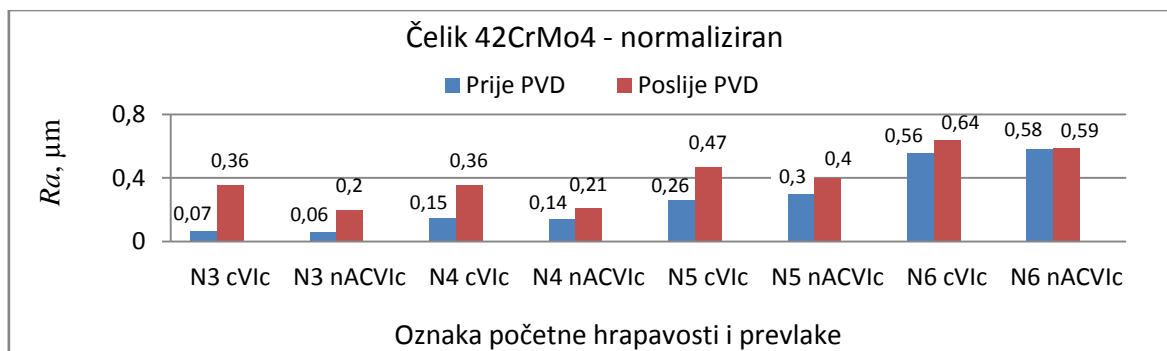
Razlike hrapavosti toplinski obrađenog čelika C45E prije i nakon prevlačenja PVD prevlakama histogramski su prikazane na slici 10.



Slika 10. Razlike hrapavosti toplinski obrađenog čelika C45E prije i nakon prevlačenja PVD prevlakama

Kod svih stanja toplinski obrađenog čelika C45E, utjecaj prevlačenja na hrapavost je bio manji što je klasa hrapavosti bila viša. Veće razlike hrapavosti uočene su nakon prevlačenja cVlc prevlakom u odnosu na nACVlc prevlaku.

Na slici 11 histogramski su prikazane izmjerene hrapavosti normaliziranog čelika 42CrMo4 prije i nakon prevlačenja PVD prevlakama.



Slika 11. Hrapavosti normaliziranog čelika 42CrMo4 prije i nakon prevlačenja PVD prevlakama

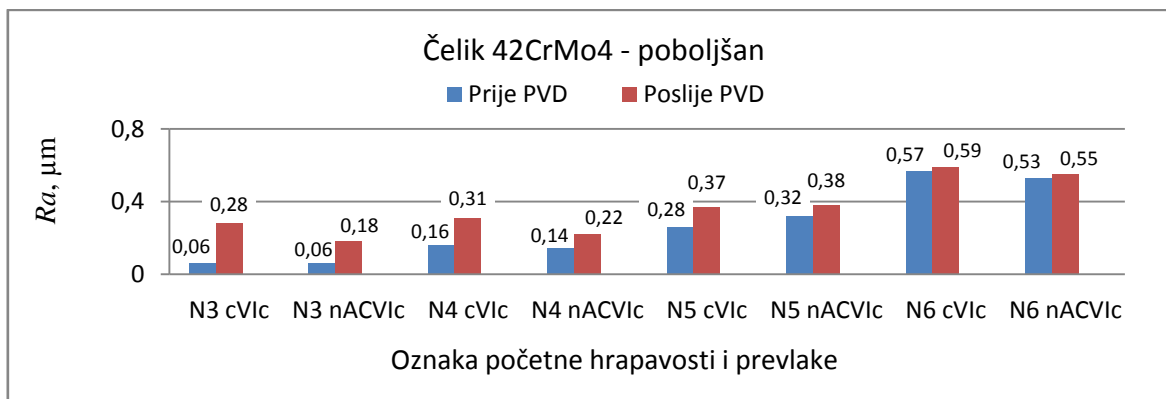
Na slici 12 histogramski su prikazane izmjerene hrapavosti poboljšanog čelika 42CrMo4 prije i nakon prevlačenja PVD prevlakama, dok su na slici 13 histogramski prikazane izmjerene hrapavosti zakaljenog čelika 42CrMo4 prije i nakon prevlačenja PVD prevlakama.



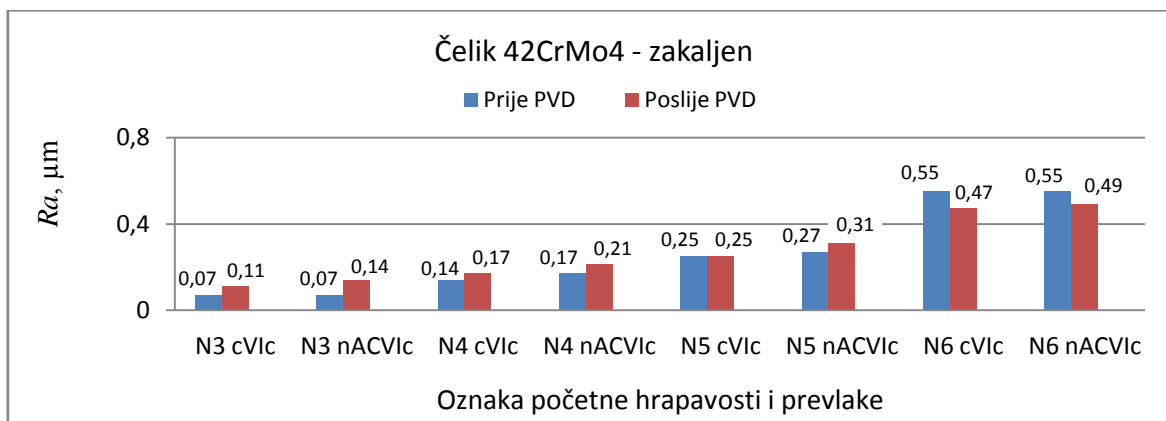
18th INTERNATIONAL FOUNDRYMEN CONFERENCE
Coexistence of material science and sustainable technology in economic growth

Sisak, May 15th-17th, 2019

<http://www.simet.hr/~foundry/>

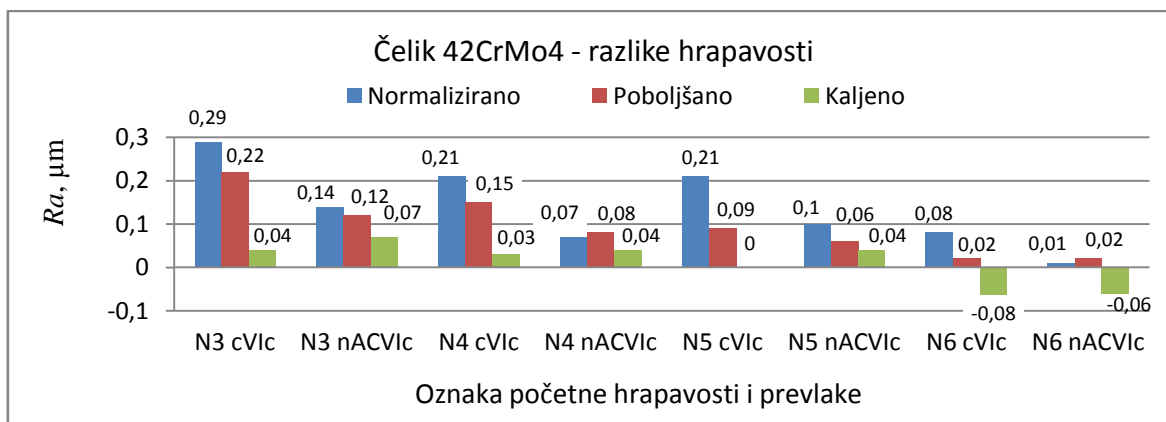


Slika 12. Hrapavosti poboljšanog čelika 42CrMo4 prije i nakon prevlačenja PVD prevlakama



Slika 13. Hrapavosti zakaljenog čelika 42CrMo4 prije i nakon prevlačenja PVD prevlakama

Razlike hrapavosti toplinski obrađenog čelika 42CrMo4 prije i nakon prevlačenja PVD prevlakama histogramski su prikazane na slici 14.



Slika 14. Razlike hrapavosti toplinski obrađenog čelika 42CrMo4 prije i nakon prevlačenja PVD prevlakama



18th INTERNATIONAL FOUNDRYMEN CONFERENCE

Coexistence of material science and sustainable technology in
economic growth

Sisak, May 15th-17th, 2019

<http://www.simet.hr/~foundry/>

Kod svih stanja toplinski obrađenog čelika 42CrMo4, utjecaj prevlačenja na hrapavost je bio manji što je klasa hrapavosti bila viša. Veće razlike hrapavosti uočene su nakon prevlačenja cVlc prevlakom u odnosu na nACVlc prevlaku.

RASPRAVA

U tablici 4 prikazani su rezultati statističke obrade razlika hrapavosti nakon prevlačenja u odnosu na hrapavosti prije prevlačenja.

Tablica 4. Rezultati statističke obrade razlika hrapavosti

Izvor varijacija	Analiza varijance za razliku hrapavosti			
	Suma kvadrata odstupanja SS	Stupnjevi slobode <i>df</i>	Srednje kvadratno odstupanje MS	$F_{rač.}$
Konstantni član	0,684450	1	0,684450	344,1216
Čelik	0,011025	2	0,005512	2,7715
Toplinska obrada	0,164558	2	0,082279	41,3676
Prevlaka	0,053356	1	0,053356	26,8256
Početna hrapavost	0,169706	3	0,056569	28,4410
Pogreška	0,125306	63	0,001989	

Prema statističkim tablicama za F-test, za 95 % vjerojatnosti i za stupnjeve slobode 1/63 granična vrijednost F varijable iznosi 3,99. Za stupnjeve slobode 2/63 granična vrijednost F varijable iznosi 3,14. Za stupnjeve slobode 3/63 granična vrijednost F varijable iznosi 2,75. Nakon obrade rezultata statističkim programom Statistica 12, za sve čelike, toplinske obrade i prevlake, uspoređujući izračunatu vrijednost F varijable s graničnim vrijednostima, utvrđeno je da na promjenu hrapavosti značajan utjecaj ima toplinska obrada ($F_{rač.} = 41,3676$), prevlaka ($F_{rač.} = 26,8256$) i početna hrapavost ($F_{rač.} = 28,4410$), dok vrsta čelika ($F_{rač.} = 2,7715$) statistički nema značajan utjecaj na promjenu hrapavosti. Kod svih čelika i svih stanja toplinske obrade, utjecaj prevlačenja na hrapavost je bio manji što je klasa hrapavosti bila viša. Razlike hrapavosti manje su za početno zakaljano stanje u odnosu na početno normalizirano i poboljšano stanje.

ZAKLJUČAK

Promjena hrapavosti površine nakon nanošenja PVD prevlaka ovisi o prethodnoj toplinskoj obradi čelika, vrsti prevlaka i početnoj hrapavosti, a manje o vrsti čelika.

Kod čelika u početnom normaliziranom i poboljšanom stanju utvrđeno je znatnije povećanje hrapavosti u odnosu na čelike u zakaljenom stanju. Razlog tome je što temperatura nanošenja PVD prevlaka utječe na zakaljenu strukturu kao naknadno popuštanje.



18th INTERNATIONAL FOUNDRYMEN CONFERENCE

Coexistence of material science and sustainable technology in
economic growth

Sisak, May 15th-17th, 2019

<http://www.simet.hr/~foundry/>

Popuštanjem martenzita dolazi do kontrakcije materijala pa dodatni utjecaj rasta volumena zbog prevlačenja naspram smanjenja volumena zbog popuštanja, u konačnici daje malu razliku hrapavosti.

Čelici prevučeni nACVlc prevlakom imaju manju hrapavost od čelika prevučениh cVlc prevlakom. Razlog tome može biti što je nACVlc dvostruka prevlaka koja nastaje kombinacijom nanokompozitne AlCrN/a-Si₃N₄ CBC prevlake, a cVlc dvostruka prevlaka nastala kombinacijom TiCN i CBC prevlake.

Na grublje pripremljenim površinama utvrđeno je manje povećanje hrapavosti nakon prevlačenja u odnosu na fino pripremljene površine. Razlog tome je što postupkom nanošenja PVD prevlaka dolazi do popunjavanja prethodnih neravnina pa dolazi do efekta zaglađivanja površine.

LITERATURA

- [1] M. Gojić, Površinska obradba materijala, Sveučilište u Zagrebu, Metalurški fakultet, Sisak, 2010.
- [2] T. Filetin, K. Grilec, Postupci modificiranja i prevlačenja površina, HDMT, Zagreb, 2004.
- [3] T. Burakowski, T. Wierzchoń, Surface engineering of metals principles, equipment, technologies, CRC Press, London (New York), 1999.
- [4] D. Krumes, Površinske toplinske obrade i inženjerstvo površina, Strojarski fakultet u Slavanskom Brodu, Slavonski Brod, 2004.
- [5] T. Krpan, Postupci prevlačenja površine metala iz parne faze, diplomski rad, Strojarski fakultet u Slavanskom Brodu, Slavonski Brod, 2017.
- [6] S. Golubić, Utjecaj nanošenja PVD prevlaka na svojstva konstrukcijskih čelika za poboljšavanje, doktorska disertacija, Strojarski fakultet u Slavanskom Brodu, 2018.
- [7] Gazela-Platit, katalog tvrdih prevlaka, interni katalog tvrtke Gazela d.o.o., Krško, Slovenija.
- [8] T. Filetin, F. Kovačićek, J. Indof, Svojstva i primjena materijala, Sveučilište u Zagrebu, Fakultet strojarstva i brodogradnje, Zagreb, 2007.
- [9] M. Novosel, D. Krumes, Željezni materijali II. dio: Konstrukcijski čelici, Strojarski fakultet u Slavanskom Brodu, Slavonski Brod, 1995.



18th INTERNATIONAL FOUNDRYMEN CONFERENCE

Coexistence of material science and sustainable technology in
economic growth

Sisak, May 15th-17th, 2019

<http://www.simet.hr/~foundry/>

MICROSTRUCTURE AND SOLIDIFICATION BEHAVIOR OF THE Ga–Ge–Sb TERNARY ALLOYS

Dragan Manasijević^{1*}, Duško Minić², Ljubiša Balanović¹, Milena Premović², Milan
Gorgievski¹

¹ University of Belgrade Technical Faculty in Bor, Bor, Serbia

² University of Priština Faculty of Technical Sciences, Kosovska Mitrovica, Serbia

Invited lecture

Original scientific paper

Abstract

Microstructure and solidification behavior of Ga–Ge–Sb ternary alloys were investigated experimentally, by using scanning electron microscopy with energy dispersive *spectroscopy* (SEM-EDS) and differential scanning calorimetry (DSC). Four ternary samples were prepared by melting of pure elements under an argon atmosphere. Phase transition temperatures of the investigated samples were determined by using DSC. The microstructure of the samples was analyzed and co-existing phases were identified. The results of microstructural and thermal analysis were compared with the results of thermodynamic calculation of phase equilibria and calculated equilibrium solidification paths. Good mutual agreement was observed. Two ternary eutectic reactions at 561.8 and 29.8 °C were predicted by thermodynamic calculations and confirmed by the results of thermal and microstructural analysis from the present work.

Keywords: Ga–Ge–Sb ternary system, microstructure, thermodynamic calculation

*Corresponding author (e-mail address): dmanasijevic@tfbor.bq.ac.rs

INTRODUCTION

The semiconducting metals and alloys are the subject of numerous investigations due to their important usage in various electronic and optoelectronic devices [1,2]. Investigations of phase relations, microstructure and solidification behavior in the semiconducting alloy systems are important for the development of new and the improvement of existing semiconductor materials [3]. The ternary Ga–Ge–Sb system, investigated in this study, includes the intermetallic semiconducting compound GaSb of the III-V family and Ge, which



18th INTERNATIONAL FOUNDRYMEN CONFERENCE

Coexistence of material science and sustainable technology in
economic growth

Sisak, May 15th-17th, 2019

<http://www.simet.hr/~foundry/>

also possess semiconducting properties. Thus, the knowledge of phase relations in the Ga–Ge–Sb system is both of technological and scientific significance.

In the present study the microstructure and the phase transition temperatures of the Ga–Ge–Sb ternary system were investigated using scanning electron microscopy with energy dispersive spectroscopy (SEM-EDS) and differential scanning calorimetry (DSC). The experimentally determined microstructure and phase transition temperatures were compared with the results of the thermodynamic predictions of phase equilibria, based on the optimized thermodynamic parameters for the binary boundary systems presented in the literature.

THERMODYNAMIC CALCULATION

A phase diagram of the Ga–Ge–Sb ternary system was calculated by the CALPHAD approach [4,5], using only optimized thermodynamic parameters for the constitutive binary systems. The CALPHAD method is based on constrained minimization of Gibbs energy for a given temperature, pressure and overall composition.

Phase diagram of the eutectic Ga–Ge binary system has been assessed by Ansara et al. [6]. The calculated phase diagram of the Ga–Ge binary system is shown in Figure 1.

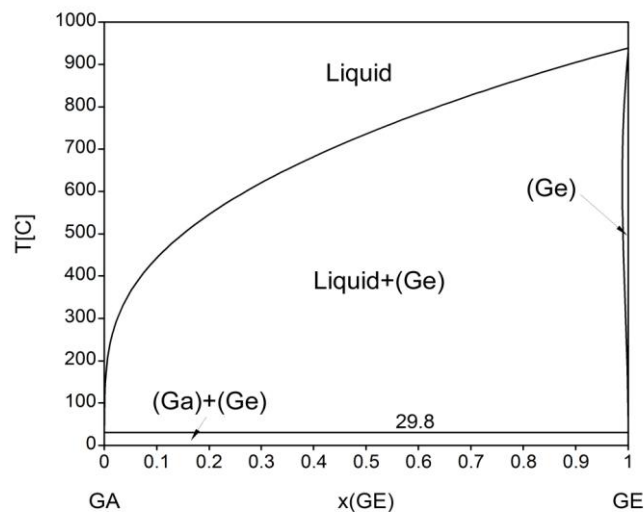


Figure 1. Calculated phase diagram of the Ga–Ge binary system using the thermodynamic parameters from Ref. [6]

The Ga–Sb system was assessed by Ansara et al. [7]. The calculated phase diagram, shown in Figure 2, includes the GaSb intermetallic compound and two eutectic reactions.



18th INTERNATIONAL FOUNDRYMEN CONFERENCE

Coexistence of material science and sustainable technology in economic growth

Sisak, May 15th-17th, 2019

<http://www.simet.hr/~foundry/>

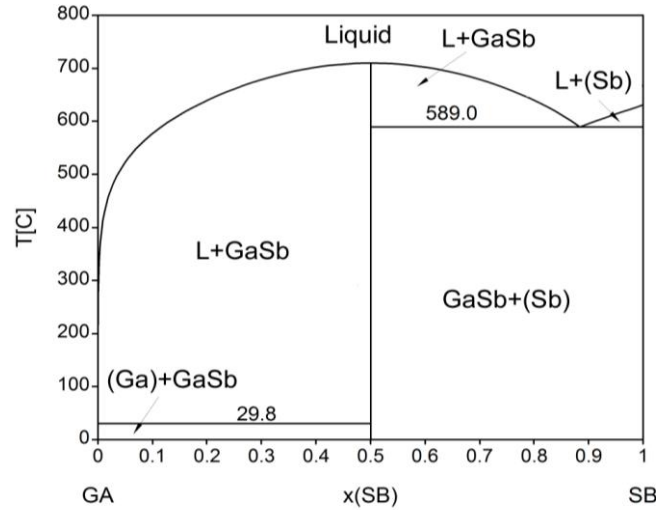


Figure 2. Calculated phase diagram of the Ga–Sb binary system using the thermodynamic parameters from Ref. [7]

The first thermodynamic optimization of the Ge–Sb system was performed by Chevalier [8] and later on by Wang et al. [9]. More recently, the Ge–Sb system was experimentally reinvestigated by Nasir et al. [10]. Based on the new experimental phase equilibria data by Nasir et al. [10] the Ge–Sb system has been re-optimized by Liu et al. [11]. The phase diagram of the Ge–Sb system is of a simple eutectic type (Figure 3) with complete mutual solubility of components in the liquid phase and small solubility of Ge in Sb.

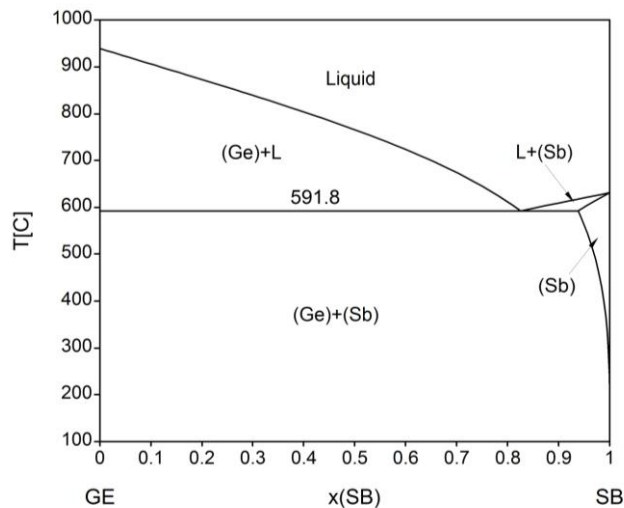


Figure 3. Calculated phase diagram of the Ge–Sb binary system using the thermodynamic parameters from Ref. [11]



18th INTERNATIONAL FOUNDRYMEN CONFERENCE
**Coexistence of material science and sustainable technology in
economic growth**

Sisak, May 15th-17th, 2019

<http://www.simet.hr/~foundry/>

The phases from constitutive binary subsystems considered for thermodynamic binary-based prediction of the Ga–Ge–Sb phase equilibria with their crystallographic data are given in Table 1.

Table 1. Considered phases, their database names and crystallographic data

Phase	Thermodynamic database name	Pearson symbol	Space group
Liquid	LIQUID		
(Ga)	ORTHORHOMBIC_GA	<i>oC8</i>	<i>Cmca</i>
GaSb	ZINCBLLENDE_B3	<i>cF8</i>	$\bar{F}43m$
(Sb)	RHOMBO_A7	<i>hR2</i>	$\bar{R}3m$
(Ge)	DIAMOND_A4	<i>cF8</i>	$Fd\bar{3}m$

Thermodynamic parameters for the Ga–Ge system were taken from Ref. [6], for the Ga–Sb system were published in Ref. [7], and thermodynamic data for the system Ge–Sb were taken from Ref. [11]. Phase (Ga) was thermodynamically treated as pure element using the lattice stabilities given by Dinsdale [12].

MATERIALS AND METHODS

Four ternary samples with compositions presented in Table 2 were prepared from pure elements (Ga 99.999%, Ge 99.999% and Sb 99.99%, Alfa Aesar). Weighed pieces of Ga, Ge and Sb were sealed in a quartz tube under Ar atmosphere, melted in a resistance furnace equipped with a digital controller and kept at 800 °C for a variable time from 30 to 60 minutes in order to get homogeneous liquid alloys which were cooled at a rate of 5 °C/min. One piece of around 0.2 g from each prepared alloy was cut for DSC analysis.

Table 2. Nominal and experimentally determined overall compositions of investigated samples

Sample	Sample target composition [at.%]	Sample experimental composition [at.%]
1	Ga ₂₀ Ge ₄₀ Sb ₄₀	Ga _{20.1} Ge _{39.3} Sb _{40.6}
2	Ga ₆₀ Ge ₂₀ Sb ₂₀	Ga _{59.8} Ge _{20.0} Sb _{20.2}
3	Ga ₄₀ Ge ₄₀ Sb ₂₀	Ga _{39.6} Ge _{40.4} Sb _{20.0}
4	Ga ₂₀ Ge ₂₀ Sb ₆₀	Ga _{19.6} Ge _{20.2} Sb _{60.2}



18th INTERNATIONAL FOUNDRYMEN CONFERENCE

Coexistence of material science and sustainable technology in
economic growth

Sisak, May 15th-17th, 2019

<http://www.simet.hr/~foundry/>

DSC measurements were carried out using a SDT Q600 (TA Instruments). Temperature calibration of DSC was performed by measuring the melting temperatures of pure elements (In, Zn and Ag) under the experimental conditions. Samples weighing about 50 mg were investigated at heating rate of 5 °C/min from room temperature up to 1000 °C. The reference material was empty alumina crucible. Three heating runs were conducted for each prepared alloy. The phase transition temperatures obtained during the second and third heating runs were mutually consistent and they were further analyzed.

TESCAN VEGA3 scanning electron microscope with energy dispersive spectroscopy (EDS) (Oxford Instruments X-act) was used for microstructural investigations and the measurements were carried out using an accelerating voltage of 20 kV. The overall compositions and compositions of coexisting phases were analyzed using EDS area and point analysis. For quantitative analysis of overall samples compositions EDS spectra were recorded at a small magnification (100x) over at least five different locations of the sample, and averaged experimentally determined overall compositions were in very good agreement with designed compositions (Table 2). The compositions of co-existing phases were determined correspondingly to the overall compositions; by examining EDS spectra over the surface of the same phase at a different parts of the sample (at least five different positions of the same phase were analyzed per phase). All SEM images of the microstructures were taken on the polished surfaces of the studied alloy samples in backscattered electron (BSE) mode.

RESULTS AND DISCUSSION

Phase relations in the Ga–Ge–Sb system

Based on thermodynamic parameter values the liquidus projection of the Ga–Ge–Sb ternary system is calculated and plotted in Fig. 5. Two ternary invariant eutectic reactions: $L \rightarrow (\text{Ge}) + \text{GaSb} + (\text{Sb})$ at 561.8 °C and $L \rightarrow (\text{Ge}) + \text{GaSb} + (\text{Ga})$ at 29.8 °C, and four primary crystallization regions ((Ge), GaSb, (Sb) and very narrow (Ga)) are predicted in this ternary system. Overall compositions of the investigated ternary samples 1-4 are labeled with symbols in Figure 4.



18th INTERNATIONAL FOUNDRYMEN CONFERENCE
Coexistence of material science and sustainable technology in
economic growth

Sisak, May 15th-17th, 2019

<http://www.simet.hr/~foundry/>

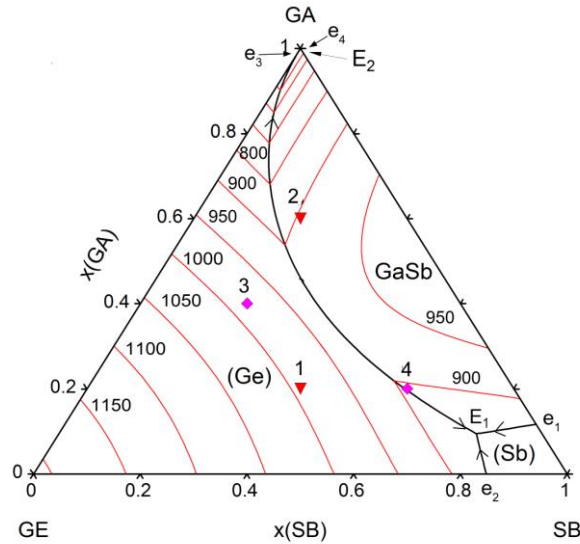


Figure 4. The calculated liquidus projection of the Ga–Ge–Sb ternary system with the marked compositions of the investigated ternary alloys. Temperatures of liquidus isotherms are given in Kelvins

The calculated temperatures of ternary eutectic reactions and the compositions of the related phases are listed in Table 3.

Table 3. Predicted invariant reactions in the Ga–Ge–Sb ternary system

T(°C) Reaction	Type	Phase	Composition	
			x(Ga)	x(Ge)
561.8 Liquid ↔ (Ge) + (Sb) + GaSb	E ₁	Liquid	0.097	0.139
		(Ge)	0.001	0.999
		(Sb)	0	0.050
		GaSb	0.5	0.0
29.8 Liquid ↔ (Ge) + (Ga) + GaSb	E ₂	Liquid	≈1	≈0
		(Ge)	≈0	≈1
		(Ga)	1	0
		GaSb	0.5	0.0



18th INTERNATIONAL FOUNDRYMEN CONFERENCE

Coexistence of material science and sustainable technology in
economic growth

Sisak, May 15th-17th, 2019

<http://www.simet.hr/~foundry/>

Thermal analysis

DSC measurements were performed using heating regime. Extrapolated onset temperature was established as a measure of invariant reaction temperature [13]. It is known that this parameter does not depend significantly on the experimental heating rate [13]. Peak maximum temperature was used for determination of other phase transitions and liquidus temperature.

The thermal analysis results together with the corresponding calculated phase transition temperatures are shown in Table 4 for comparison.

Table 4. Comparison between experimentally determined and calculated phase transition temperatures for the investigated alloys of the Ga–Ge–Sb ternary system

Sample	Sample target composition [at.%]	Sample experimental composition [at.%]	Phase transition temperature [°C]					
			First thermal effect (Solidus-Invariant)		Second thermal effect		Third thermal effect (Liquidus)	
			DSC	calculation	DSC	calculation	DSC	calculation
1	Ga ₂₀ Ge ₄₀ Sb ₄₀	Ga _{20.1} Ge _{39.3} Sb _{40.6}	559.6	561.8	641.9	636.7	734.0	727.5
2	Ga ₆₀ Ge ₂₀ Sb ₂₀	Ga _{59.8} Ge _{20.0} Sb _{20.2}	32.1	29.8	618.7	602.2	639.5	629.8
3	Ga ₄₀ Ge ₄₀ Sb ₂₀	Ga _{39.6} Ge _{40.4} Sb _{20.0}	31.3	29.8	651.2	637.6	718.5	714.2
4	Ga ₂₀ Ge ₂₀ Sb ₆₀	Ga _{19.6} Ge _{20.2} Sb _{60.2}	558.2	561.8	-	617.8	635.7	620.3

Examples of DSC curves for two investigated Ga–Ge–Sb samples with related calculated equilibrium solidification paths are presented in Figure 5 and 6.

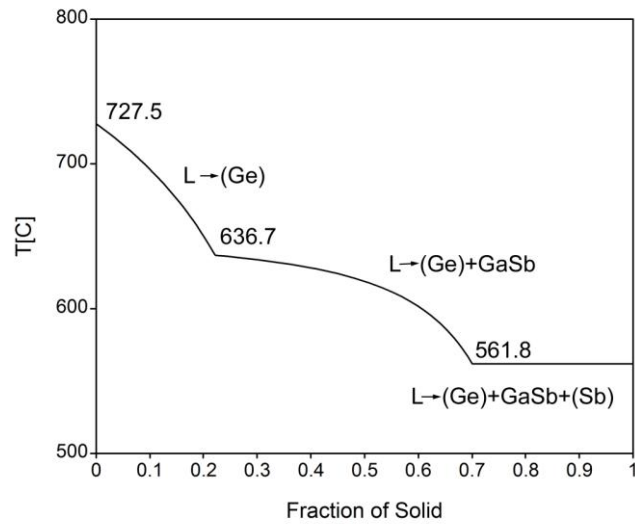
Calculated equilibrium solidification path for the sample 1 is given in Figure 5a. According to the results of calculation, solidification of sample 1 starts at 727.5 °C with the formation of primary (Ge) crystals from the melt. Simultaneous crystallization of (Ge) and GaSb crystals starts at 636.7 °C. At 561.8 °C the remaining part of the liquid phase isothermally converts into eutectic mixture of (Ge), GaSb and (Sb) phases according to the Liquid ↔ (Ge) + (Sb) + GaSb ternary eutectic reaction. Figure 5b shows DSC heating curve for the sample 1 with three identified endothermic effects. The onset temperature of the first detected endothermic peak at 559.6 °C is in good agreement with predicted temperature of Liquid ↔ (Ge) + (Sb) + GaSb ternary eutectic reaction at 561.8 °C. The peak temperature of the second detected endothermic effect, 641.9 °C, is related to the end of melting of GaSb phase. Third endothermic peak is connected to the end of the melting of primary (Ge) phase i.e. liquidus temperature. Measured liquidus temperature 734 °C is somewhat higher than the associated predicted liquidus temperature 727.5 °C (Table 4).



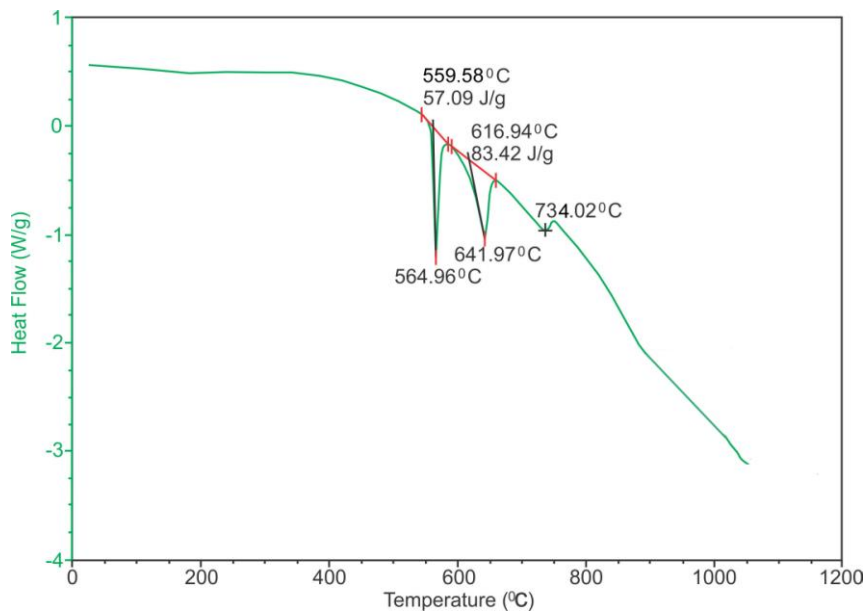
18th INTERNATIONAL FOUNDRYMEN CONFERENCE
**Coexistence of material science and sustainable technology in
economic growth**

Sisak, May 15th-17th, 2019

<http://www.simet.hr/~foundry/>



a)

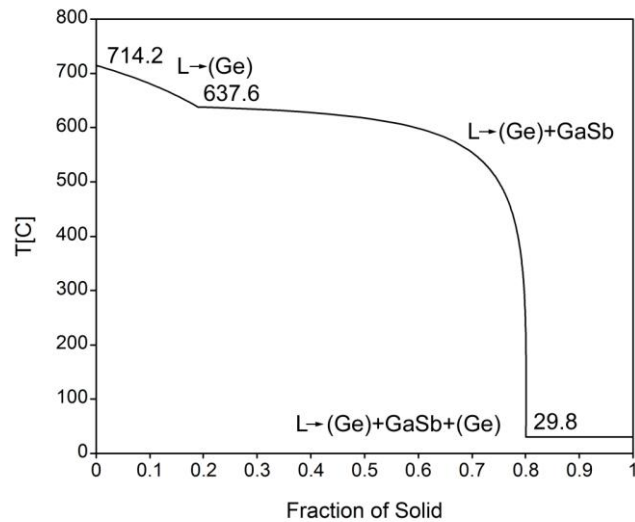


b)

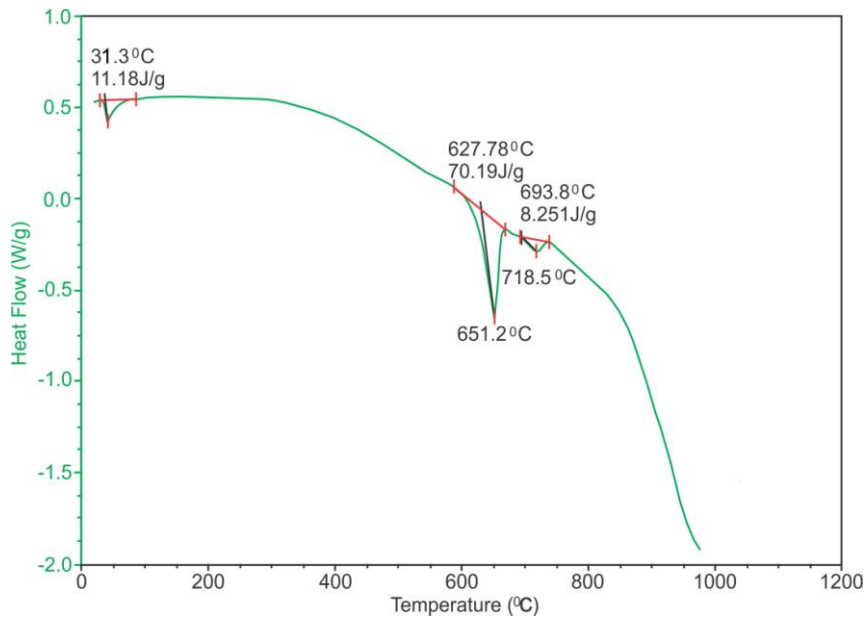
Figure 5. Sample 1: a) calculated equilibrium solidification path, b) DSC heating curve



18th INTERNATIONAL FOUNDRYMEN CONFERENCE
Coexistence of material science and sustainable technology in
economic growth
 Sisak, May 15th-17th, 2019
<http://www.simet.hr/~foundry/>



a)



b)

Figure 6. Sample 3: a) calculated equilibrium solidification path, b) DSC heating curve

According to the calculated solidification path for the sample 3 (Figure 6a), solidification of alloy starts at 714.2 °C with the formation of crystals of primary (Ge) phase. With further cooling the amount of (Ge) phase gradually increases and at 637.6 °C GaSb phase starts simultaneous crystallization with (Ge) phase. By reaching 29.8 °C the remaining part of the Ga-rich liquid phase isothermally solidifies according to the Liquid \leftrightarrow (Ga) + (Ge) + GaSb



18th INTERNATIONAL FOUNDRYMEN CONFERENCE

Coexistence of material science and sustainable technology in
economic growth

Sisak, May 15th-17th, 2019

<http://www.simet.hr/~foundry/>

ternary eutectic reaction. DSC heating curve for the sample 3 is presented in Figure 6b. It is characterized with the occurrence of endothermic peak close to the room temperature. Measured onset temperature is determined to be 31.3 °C and it is related to the melting of Ga-rich phase according to the predicted $(\text{Ge}) + (\text{Ga}) + \text{GaSb} \leftrightarrow \text{Liquid}$ eutectic reaction (Table 4, Figure 6a). The temperatures of the second and third detected peaks at 651.2 and 718.5 °C represent the end of the melting of GaSb and (Ge) phases, respectively.

Microstructure investigation

Microstructures of four samples from the different compositional regions of the Ga–Ge–Sb ternary system were studied using SEM-EDS. Average compositions of the co-existing phases obtained by EDS analysis are given in Table 5. Three-phase microstructure (Ge)+GaSb+(Sb) was identified within the samples 1 and 4 and three-phase microstructure (Ge)+GaSb+(Ga) was identified in the samples 2 and 3, which is in agreement with predicted phase equilibria and equilibrium solidifications paths (Figure 5 and 6).

Table 5. Summary of the phase compositions measured by SEM-EDS for the investigated Ga–Ge–Sb ternary alloys at room temperature

Sample	Sample EDS composition (at.%)	SEM-EDS composition of phase (at.%)			Phase identified
		Ga	Ge	Sb	
1.	$\text{Ga}_{20.1}\text{Ge}_{39.3}\text{Sb}_{40.6}$	6.2	88.2	5.6	(Ge)
		48.0	2.6	49.4	GaSb
		0	4.1	95.9	(Sb)
2.	$\text{Ga}_{59.8}\text{Ge}_{20.0}\text{Sb}_{20.2}$	5.7	90.9	3.4	(Ge)
		48.1	2.6	49.3	GaSb
		100	0	0	(Ga)
3.	$\text{Ga}_{39.6}\text{Ge}_{40.4}\text{Sb}_{20.0}$	6.7	88.2	5.1	(Ge)
		48.6	2.4	49.0	GaSb
		99.4	0	0.6	(Ga)
4.	$\text{Ga}_{19.6}\text{Ge}_{20.2}\text{Sb}_{60.2}$	4.3	94.2	1.5	(Ge)
		48.3	2.1	49.6	GaSb
		0	4.2	95.8	(Sb)

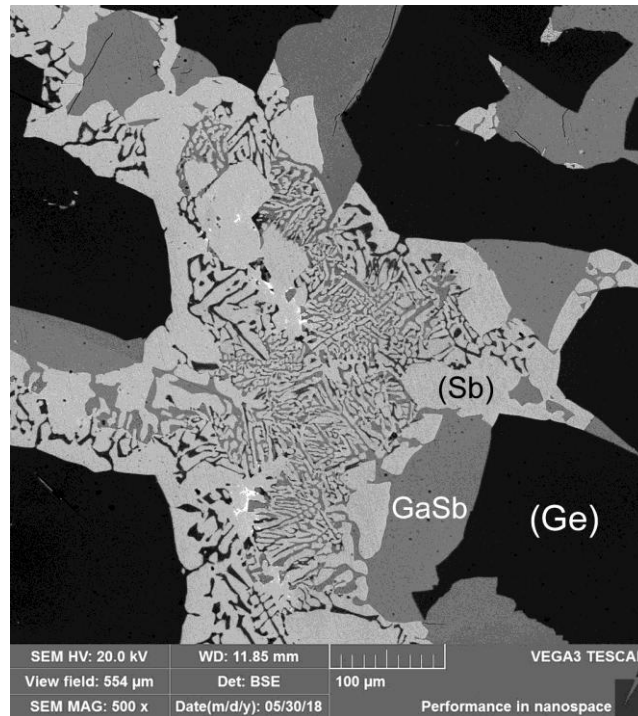
Examples of microstructures for the samples 1-4 are presented in Figure 7a-d.



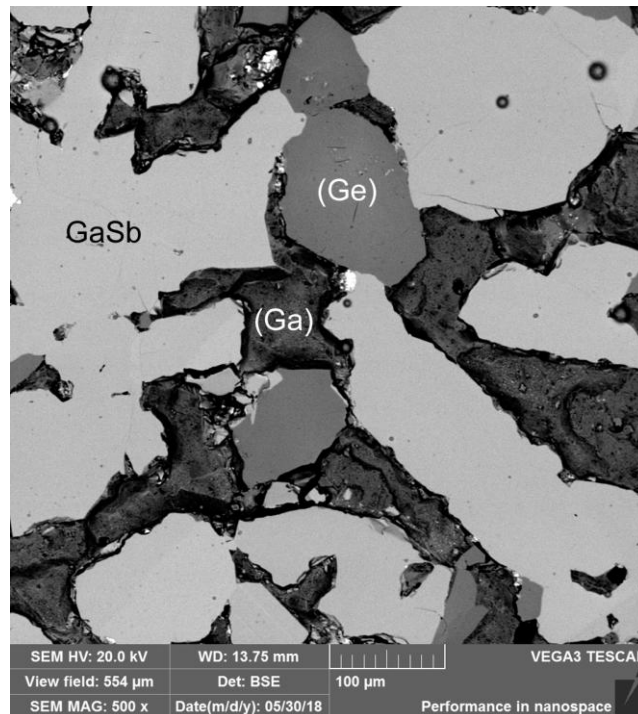
18th INTERNATIONAL FOUNDRYMEN CONFERENCE
**Coexistence of material science and sustainable technology in
economic growth**

Sisak, May 15th-17th, 2019

<http://www.simet.hr/~foundry/>



a)



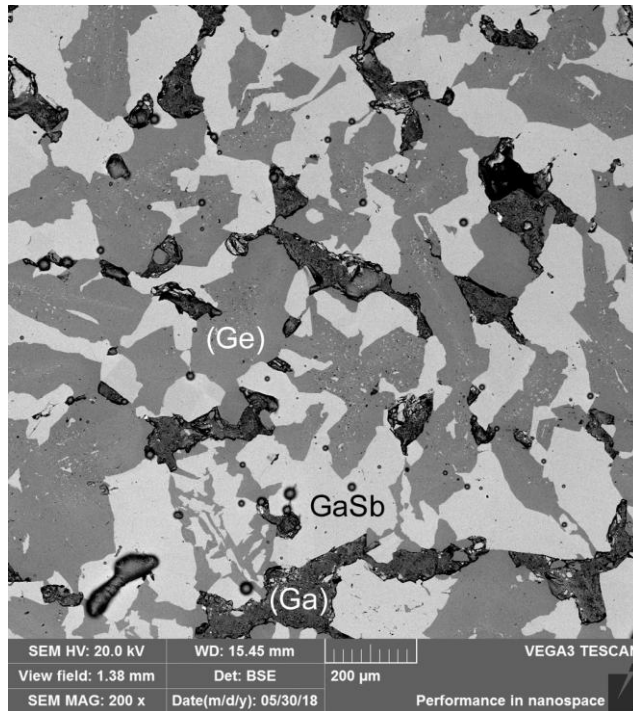
b)



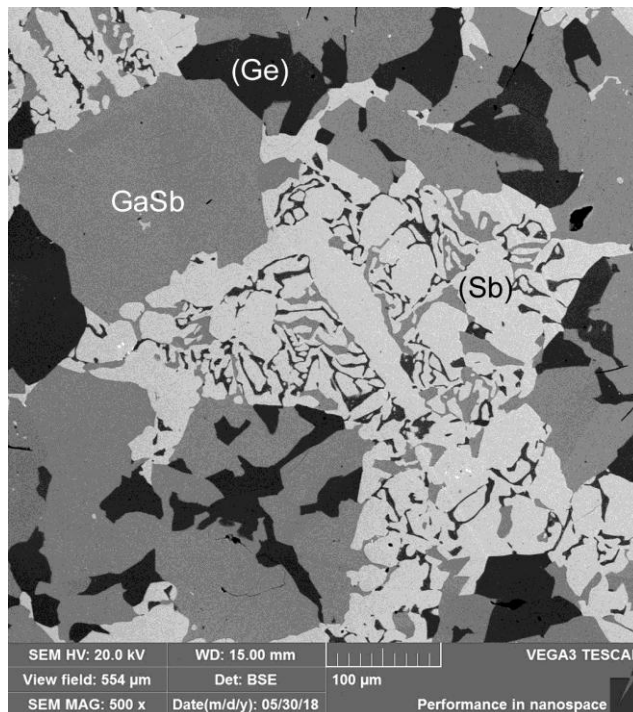
18th INTERNATIONAL FOUNDRYMEN CONFERENCE
**Coexistence of material science and sustainable technology in
economic growth**

Sisak, May 15th-17th, 2019

<http://www.simet.hr/~foundry/>



c)



d)

Figure 7. SEM images for the investigated alloys:
a) Sample 1, b) Sample 2, c) Sample 3, d) Sample 4



18th INTERNATIONAL FOUNDRYMEN CONFERENCE

Coexistence of material science and sustainable technology in
economic growth

Sisak, May 15th-17th, 2019

<http://www.simet.hr/~foundry/>

Microstructure of the sample 1 (Figure 7a) includes primary crystals of (Ge) phase (dark grains), grey grains of the GaSb intermetallic compound and bright grains of (Sb) phase. It can also be seen that the crystals of (Ge) and GaSb phases are surrounded by fine eutectic mixture formed by Liquid \leftrightarrow (Ge) + (Sb) + GaSb eutectic reaction.

SEM image of the Ga-rich sample 2 is shown in Figure 7b. Crystals of the primary GaSb phase appear as the bright phase. (Ge) phase appears as the grey phase and (Ga) phase as dark regions between crystals of the GaSb and (Ge) phases. The same three-phase (Ga)+(Ge)+GaSb microstructure was identified for the sample 3 (Figure 7c). Figure 7d shows SEM micrograph for the Sb-rich sample 4. Three phases can be recognized: (Ge) as the dark phase, GaSb as the grey phase and (Sb) as the bright phase.

CONCLUSIONS

Microstructure and phase transition temperatures of four Ga–Ge–Sb ternary alloys were investigated in this study using SEM-EDS and DSC methods. Phase equilibria of the ternary Ga–Ge–Sb system were calculated by the CALPHAD method, using optimized thermodynamic parameters for the boundary binary systems from literature. Results of thermodynamic calculation include liquidus projection of the Ga–Ge–Sb ternary system and equilibrium solidification paths for four investigated alloys. Two ternary eutectic reactions at 561.8 and 29.8 °C were predicted by thermodynamic calculations. Both invariant reactions were confirmed by the results of thermal and microstructural analysis from the present study. Calculated equilibrium solidification paths are in reasonable agreement with the results of thermal and microstructural analysis from the present study. Microstructure analysis of the investigated samples confirmed the co-existence of phases predicted by thermodynamic extrapolation of phase equilibria. It can be concluded that thermodynamic parameters for the constitutive binary systems can be successfully used for prediction of microstructure and solidification behavior of the ternary Ga–Ge–Sb alloys.

Acknowledgement

This work was supported by the Ministry of Education, Science and Technological Development of the Republic of Serbia (Project No. OI172037).

REFERENCES

- [1] S. Adachi, Properties of Semiconductor Alloys: Group-IV, III-V and II-VI Semiconductors, John Wiley & Sons, Ltd, 2009.
- [2] A. Rockett, The Materials Science of Semiconductors, Springer, 2008.
- [3] V. Tomashyk, Ternary Alloys Based on III-V Semiconductors, CRC Press, 2017. ISBN 9781498778381



18th INTERNATIONAL FOUNDRYMEN CONFERENCE

Coexistence of material science and sustainable technology in
economic growth

Sisak, May 15th-17th, 2019

<http://www.simet.hr/~foundry/>

- [4] N. Saunders, A. P. Miodownik, CALPHAD (A Comprehensive Guide), Elsevier, London, 1998.
- [5] H. L. Lukas, S. G. Fries, B. Sundman, Computational Thermodynamics: The Calphad Method, Cambridge University Press, Cambridge, UK, 2007.
- [6] I. Ansara, J. P. Bros, M. Gambino, Thermodynamic analysis of the germanium-based ternary systems Al-Ga-Ge, Al-Ge-Sn, Ga-Ge-Sn, Calphad, 3(1979), pp. 225-233.
- [7] I. Ansara, C. Chalillon, H. L. Lukas, T. Nishizawa, H. Ohtani, K. Ishida, M. Hillert, T. G. Chart, T. Anderson, A binary database for III-V compound semiconductor systems, Calphad, 18(1994)2, pp. 177-222.
- [8] P.-Y. Chevalier, A Thermodynamic Evaluation of the Ge-In, Ge-Pb, Ge-Sb, Ge-Tl and Ge-Zn systems, Thermochim. Acta, 155(1989), pp. 227-240.
- [9] J. Wang, C. Leinenbach, M. Roth, Thermodynamic description of the Au-Ge-Sb ternary system, J. Alloys Compd., 485(2009), pp. 577-582.
- [10] N. Nasir, A. Grytsiv, P. Rogl, A. Saccone, G. Giester, Phase equilibria in systems Ce-M-Sb (M= Si, Ge, Sn) and superstructure Ce₁₂Ge_{9-x}Sb_{23+x} (x = 3.8±0.1), J. Solid State Chem., 182(2009), pp. 645-656.
- [11] J. Liu, C. Guo, C. Li, Z. Du, Thermodynamic optimization of the Ge-Sb and Ge-Sb-Sn systems, Thermochimica Acta, 520(2011), pp. 38-47.
- [12] A. T. Dinsdale, SGTE data for pure elements, Calphad, 15(1991)4, pp. 317-425.
- [13] W. J. Boettinger, U. R. Kattner, K.-W. Moon, J. H. Perepezko, DTA and Heat-flux DSC Measurements of Alloy Melting and Freezing, NIST Special Publication 960-15, Washington, 2006.



18th INTERNATIONAL FOUNDRYMEN CONFERENCE

Coexistence of material science and sustainable technology in
economic growth

Sisak, May 15th-17th, 2019

<http://www.simet.hr/~foundry/>

INTERACTION BETWEEN MOLTEN ALUMINIUM AND HOT-WORKING TOOL STEEL

Jožef Medved^{1*}, Stanislav Kores², Natalija Dolić³, Maja Vončina¹

¹ University of Ljubljana Faculty of Natural Sciences and Engineering, Ljubljana, Slovenia

² Talum Tovarna aluminija Ltd Kidričevo, Kidričevo, Slovenia

³ University of Zagreb Faculty of Metallurgy, Sisak, Croatia

Invited lecture

Original scientific paper

Abstract

Hot-working tool steels are essential for production and processing of aluminium and aluminium alloys. The interaction between molten aluminium and hot-working tool steel is a result of chemical reaction at a phase boundary solid/liquid, causing the formation of intermetallic compounds. The consequence of molten aluminium flow along the tool surface is erosion or mechanical wear. In order to increase the lifetime of the tool it is necessary to examine and limit the interaction between tool steel and molten aluminium.

A laboratory device was designed to determine the interaction between tool steel and metallic melts. The experiments were carried out in melt of primary aluminium (purity of 99.7 mass %) and, for the comparison, in aluminium alloy AlSi12 at the temperature of 670 °C and 700 °C at 75 rpm and 150 rpm. The result of the interaction is the growth of a reaction layer, which is formed from intermetallic phases from system Al-Fe. It could be concluded that following parameters: temperature of the melt, the speed of rotating sample (rpm) and experiment duration time, have an impact on the wear of tool steel. Taking the results into consideration an interaction model between hot-working tool steel and molten aluminium was created.

Keywords: *interaction tool steel/molten aluminium, intermetallic phases from system Al-Fe*

*Corresponding author (e-mail address): jozef.medved@omm.ntf.uni-lj.si

INTRODUCTION

High pressure die casting is one of the leading casting processes in the modern industry. In the case of high pressure die casting, the melt is in contact with the tool, whereas the chemical interaction between the tool, made of hot-working tool steel and the melt occur. In

addition, mechanical and heat wear of the tools also occurs. For high productivity high resistance to these factors is required.

The chemical interaction occurs due to the solubility of iron in aluminium, which forms intermetallic phases in certain stoichiometric proportions, in accordance with the binary phase diagram Fe-Al. The most common phases are Al_5Fe_2 and $Al_{13}Fe_4$, which form so called reaction layer. In order to achieve the optimal mechanical and physical properties of the tools, it is necessary to limit or to prevent the emergence of these phases, whereas the mechanisms of origin have to be known.

The steel used in our study is UTOPMO1 and is most commonly used in the group of hot-working tool steels where the main alloying element is chromium. The steel UTOPMO1 has good hardenability from a relatively low austenitization temperature of about 1020 °C, good resistance to oxidation, tempering resistance, resistance to erosion with liquid aluminium, etc. [1,2]. Hardness after hardening is between 50 and 56 HRC, and after tempering with secondary hardening a similar hardness can be achieved.

For this purpose, the steel is alloyed with chromium, molybdenum and vanadium, which, by precipitating secondary carbides harden the matrix. After tempering, an optimal combination of hardness and ductility is achieved. This steel is used for hot forging tools, die casting tools, punching tools and for production of knives [2].

The wear resistance, that strongly affects the life of the tool steel in contact with liquid aluminium, depends on three factors:

1. Mechanical: due to the high speed and temperature of the melt during casting into permanent molds from tool steels, erosion of material from the surface of the tool occurs. Aluminium die-casting produces alternating mechanical stresses, which leads to a reduction in mechanical properties and leads to decay [3].
2. Chemical: due to the dissolution of iron atoms and other alloying elements from the tool steel in aluminium, the formation of intermetallic phases on the interphase surface between tool steel and liquid aluminium occurs. The resulting intermetallic phases have different physicochemical properties as the basis [4].
3. Heat: thermal fatigue occurs due to expanding and shrinking of steel during working cycles at aluminium die-casting. The tool is usually preheated to 400 °C, but the temperature can rise up to 700 °C. In this case, the surface layers of steel are expanded, which is in contrary to the interior of the steel, consequently on the surface the compression and at the core the tensile stresses appear. When the casting is removed from the tool, the tool is lubricated with a separating agent, which greatly cools the tool, causing tensile stresses on the surface and compression stresses inside the tool. These tensions are very high, close to the ultimate strength of the hot-working tool steel. Since cyclic use of the tool, this process repeats more than ten thousand times, cracks on the tool occur [1].

At the phase boundary tool steel/molten aluminium intermetallic phases as a result of the chemical reaction of the tool steel and aluminium melt are generated. The condition for the formation of phases is the optimal wetting and diffusion, resulting from the difference between the chemical potentials of the elements in liquid aluminium and solid tool steel. At the phase boundary between solid metal and intermetallic phases, atoms of aluminium and iron react and form new intermetallic phases, using solid metal atoms, causing the movement of phase boundary in the direction of solid metal [5].

In addition to the atoms of iron and aluminium, other alloy elements, in particular the alloying elements of the tool steel, such as silicon, manganese, chromium, molybdenum and vanadium, are also present in the boundary (reaction) layer. In general, these elements reduce the thickness of the intermetallic layer, whereas the greatest effect has silicon. The growth of the intermetallic phase Al_5Fe_2 takes place preferably in the direction [001] by diffusion through the vacancies, and therefore have a highly oriented morphology in the form of a tongue. Researches [6-8] showed that the proportion of vacancies in this direction for the phase Al_5Fe_2 is 30 %. It is assumed that silicon atoms occupy gaps in the intermetallic phase Al_5Fe_2 , causing the distortion of the crystal lattice and the reduction of activation energy. In order to reduce the vacancies content in Al_5Fe_2 , the diffusion coefficient of iron and aluminium in the phase Al_5Fe_2 and, consequently, the kinetics of the formation of intermetallic phases, is also reduced. As a consequence, the morphology of the Al_5Fe_2 phase changes, and inside this phase fine particles τ_1/τ_9 , characteristic for the ternary Al-Fe-Si system, are formed [9].

Selverian et al. [10] have discovered, that the addition of silicon to the melt of aluminium and zinc greatly reduces the exothermic nature of the reaction between aluminium and steel on which the lubricant is applied, since silicon forms a solid reaction layer acting as a barrier between steel and melt. The barrier greatly limits the diffusion of the atoms of aluminium and iron, so that the reaction kinetics is greatly reduced.

With this aim, the influence of the interaction between two different aluminium alloys and hot-working tool steel was studied. The wear of the sample from the UTOPMO1 tool steel and the reaction layer, which is established at the boundary between liquid aluminium and steel as a result of a chemical reaction was investigated. Experiments were performed on a specially designed device, whereas the samples were metallographically analyzed in order to determine the interaction.

MATERIALS AND METHODS

For the experiments samples from the UTOPMO1 tool steel were used, which chemical composition is shown in Table 1.

Table 1. Chemical composition of UTOPMO1 steel in mass % according to the internal standard SIJ Metal Ravne [2]

C	Si	Mn	Cr	Mo	V
0.37	1.0	0.38	5.15	1.30	0.40

The scheme of the used sample is shown in Figure 1a. The experiments were carried out on the laboratory device shown in Figure 1b. The device consists of an electric resistance melting furnace with a control system with which a constant temperature was maintained, the carrier on which the electric motor was placed and the ceramic crucible for the melt. The experimental sample is fixed to an electric motor via a steel or graphite rod, which rotates the sample with a constant revolutions per minute (rpm) in aluminium alloy melt.

Firstly, the Al-alloy was melted in an electric resistance furnace. The input parameters, which were used during the experiments, are shown in Table 2. When the temperature of the melt

reached 670 or 700 °C the sample was placed into the melt, the device for rotating the sample was turned on for 4 hours at 70 or 150 rpm. After the experiment was completed, the samples were taken from the furnace and left to cool in air.

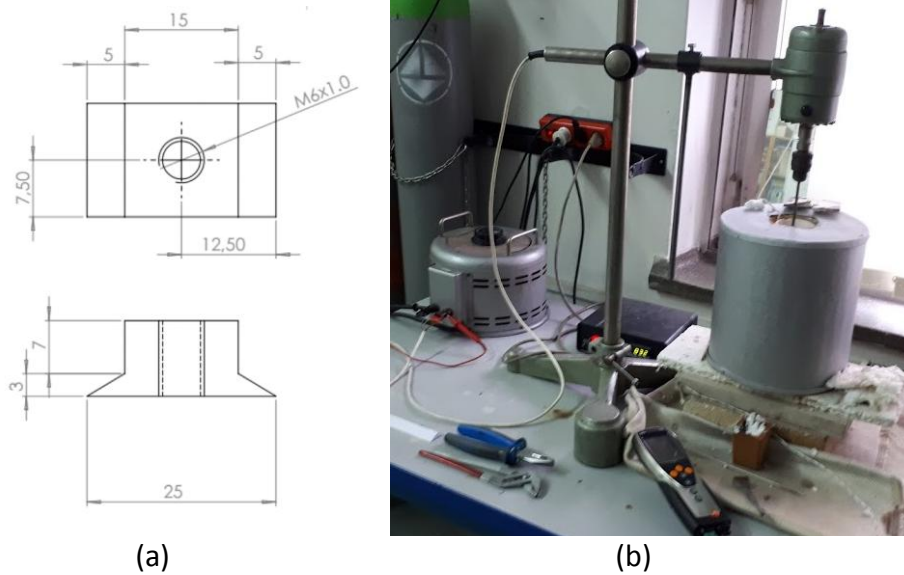


Figure 1. Schematic representation of the steel sample UTOPMO1 (a) and a device for determining the interaction between tool steel and liquid aluminium (b)

Table 2. Used materials and parameters to perform the experiments

Sample	Steel	Melt	Melt temperature [°C]	Rpm [min]	Time [h]
1	UTOP MO1	Al99.7	670	70	4
2		Al99.7	670	150	
3		Al99.7	700	70	
4		Al99.7	700	150	
5		AlSi12	670	70	

For the metallographic analysis of the reaction layer between the steel and the Al-alloy, the samples were cut in half. The samples were prepared by standard metallographic procedure. Light microscopy was performed on the Olympus BX 61 microscope. The identification of phases and interaction layers in the examined samples was carried out on the scanning electron microscope (SEM) JEOL JSM-5610 at the Faculty of Natural Sciences and Engineering. Some SEM analysis were also conducted at the Institute for Metals Materials and Technologies with a SEM JSM-6500F.

RESULTS AND DISCUSSION

The interaction between tool steel and molten aluminium was studied thermodynamically by modelling phase equilibria and phase diagrams. There are three phases in the Al-Fe system: $Al_{13}Fe_4$, Al_5Fe_2 and Al_2Fe (Figure 2a). In the Al-Fe-C-Cr-Mo system, besides the

mentioned binary phases, there are also carbides, whereas the aluminium carbide can also be formed. Aluminium with chromium forms the Al_7Cr phase, and with molybdenum Mo_3Al phase (Figure 2b).

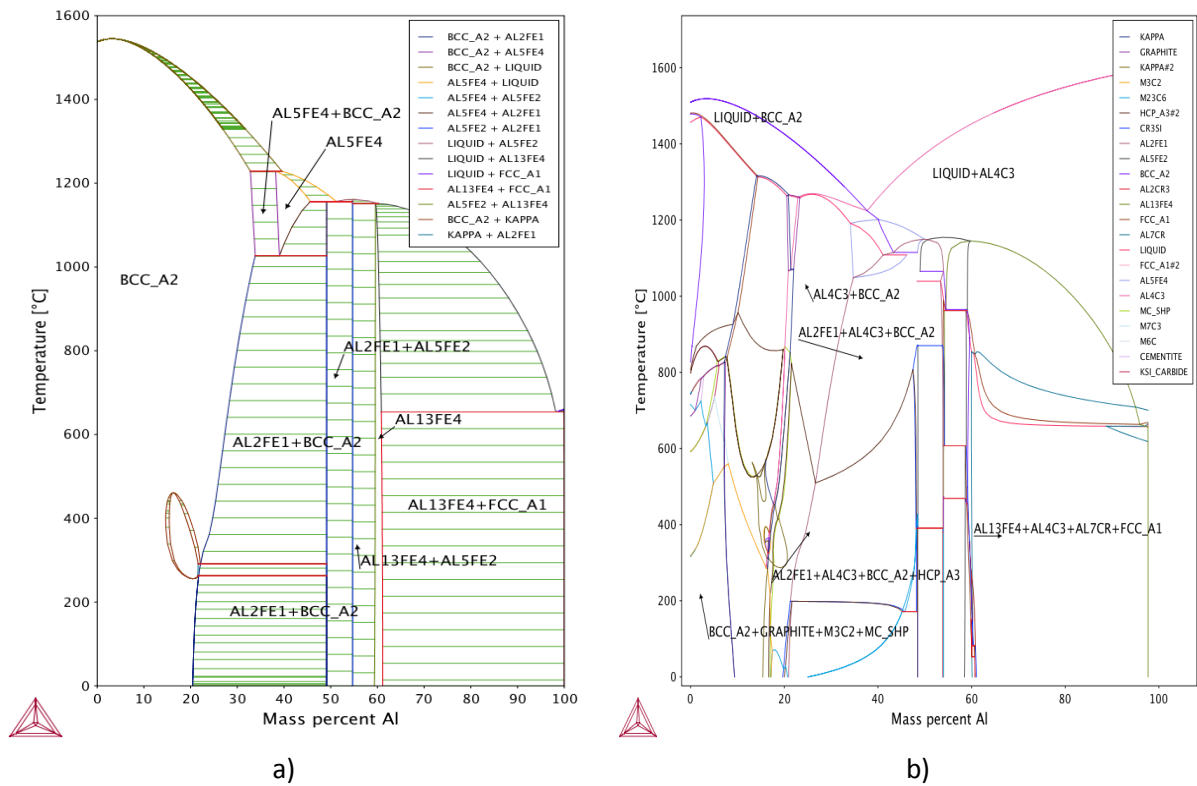


Figure 2. Phase equilibria in Al-Fe (a) and Al-Fe-C-Cr-Mo (b) systems

Figure 3 shows the microstructure of the sample 4 tested in alloy Al99.7 at a temperature of 700 °C and 150 rpm. The layer is composed of two sections. On the aluminium side most, likely it consists of Al-Fe and Al-phase. On the steel side there is a layer in the form of fingers that grow into steel. An increased proportion of iron phases (needles) is observed in aluminium. This example represents the highest values of the temperature of the melt and rpm, and in this case the wear of the sample is the highest. All samples were analyzed by the same procedure. Comparison of the images of the reaction layers taken in the same place (top and edge) of the samples is shown in Figure 4.

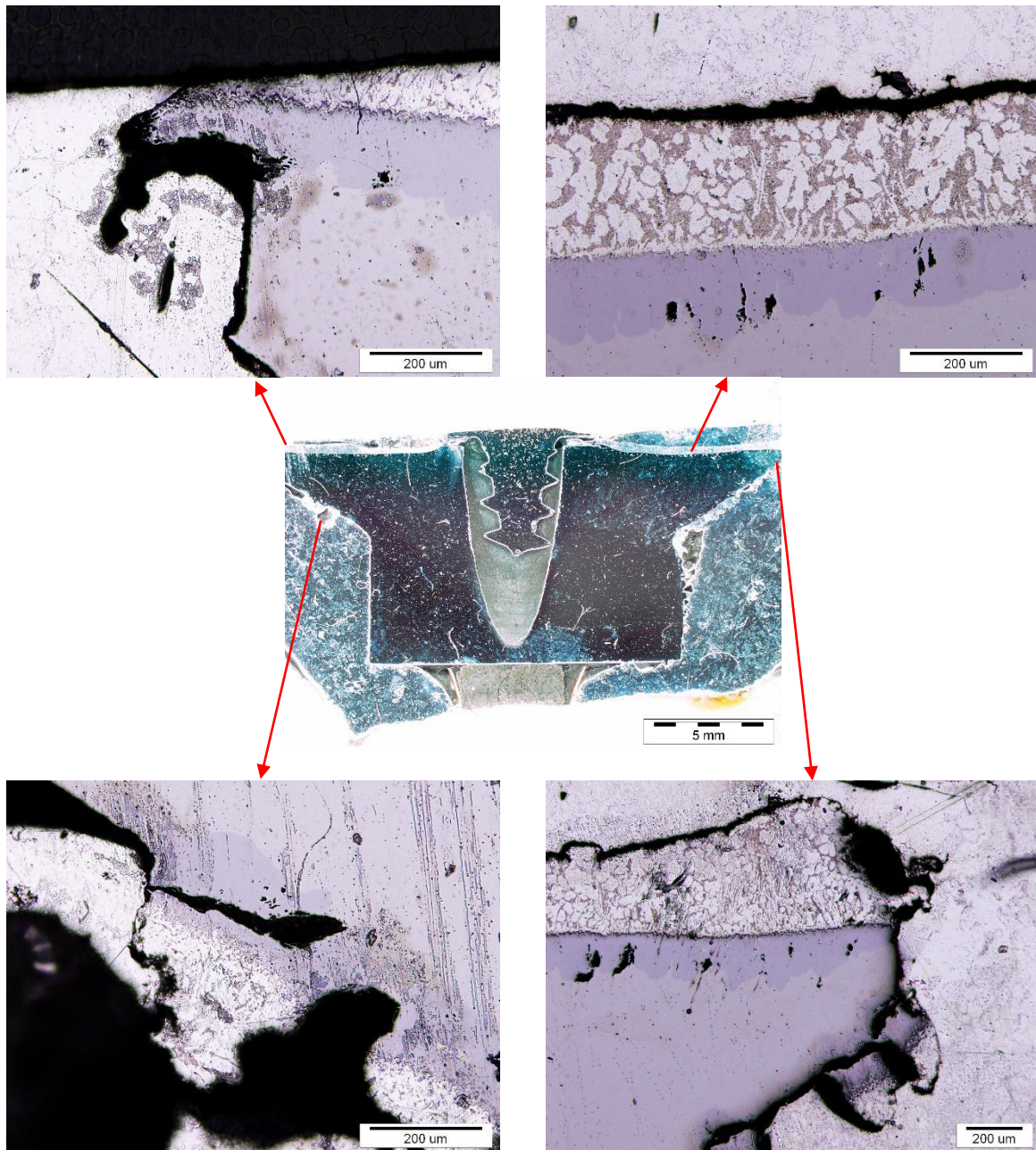


Figure 3. Macro image and microstructure of sample 4 in different places

Figure 4 shows the wear of all investigated samples. The comparison is made from the top of the sample at 50x magnification and at the side of the sample at 100x magnification. From the microstructure of the samples 1 and 2, the intermediate reaction layer is porous in sample tested at higher rpm. The wear of the sample 2 is greater due to the higher rpm. Samples 3 and 4 were tested at a higher temperature. From the microstructure in Fig. 4 it can be concluded that the reaction layer is thicker, with more porosity. In the aluminium, cracks appear immediately behind the layer with an increased iron-based needle phase. It is estimated that the proportion of iron in aluminium near the phase boundary is increased due to better diffusion of iron. Sample 4 was tested at higher temperatures and rpm. The wear of the sample 4 is very large and markedly stands out compared to the other samples. The reaction layer is cracked, and cracks are also visible in aluminium, where extensive areas

of eutectics (most dissolved iron) are observed. Following the cracks in the reaction layer, the reaction products break down and mix with liquid aluminium. Such phases need a lot of time to dissolve in aluminium.

For comparison, the wear resistance of UTOPMO1 in AlSi12 aluminium alloy at a temperature of 670 ° C and 70 rpm was tested. From the microstructure of sample 5 (Figure 4), a much thicker reaction layer is seen, which is composed at least from three different layers. This will be discussed and proved below. It was estimated that the proportion of iron in aluminium near the phase boundary is increased due to better diffusion of iron, whereas at least one layer contains also higher portion of silicon.

In the case of sample 1 in Figure 5, the growth of intermetallic Fe-phases in molten aluminium is observed in the form of a tongue. Two different layers, one is compact, slightly brighter and thicker (closer to steel), and the other in the form of needles or tongue can be distinguished. Analyses represent: 2 - dissolved Fe-phase in aluminium, 3 - steel composition, 4 - composition of the reaction layer closer to steel with a higher proportion of aluminium, silicon and chromium, 5 - composition of the reaction layer closer to aluminium, 6 - the composition of the reaction phase closer to steel with higher aluminium and lower silicon, and 7 - aluminium alloy. The concentration of aluminium is greater in the region of the layer closer to the aluminium alloy (spectrum 4), which could be Al_5Fe_2 phase and decreases when closer to the steel (spectrum 6), which could be $Al_{13}Fe_4$ phase, according to the literature. The layer closer to aluminium is fragmented, where iron dissolves in molten aluminium in the form of needles from Fe-phase (spectrum 5).

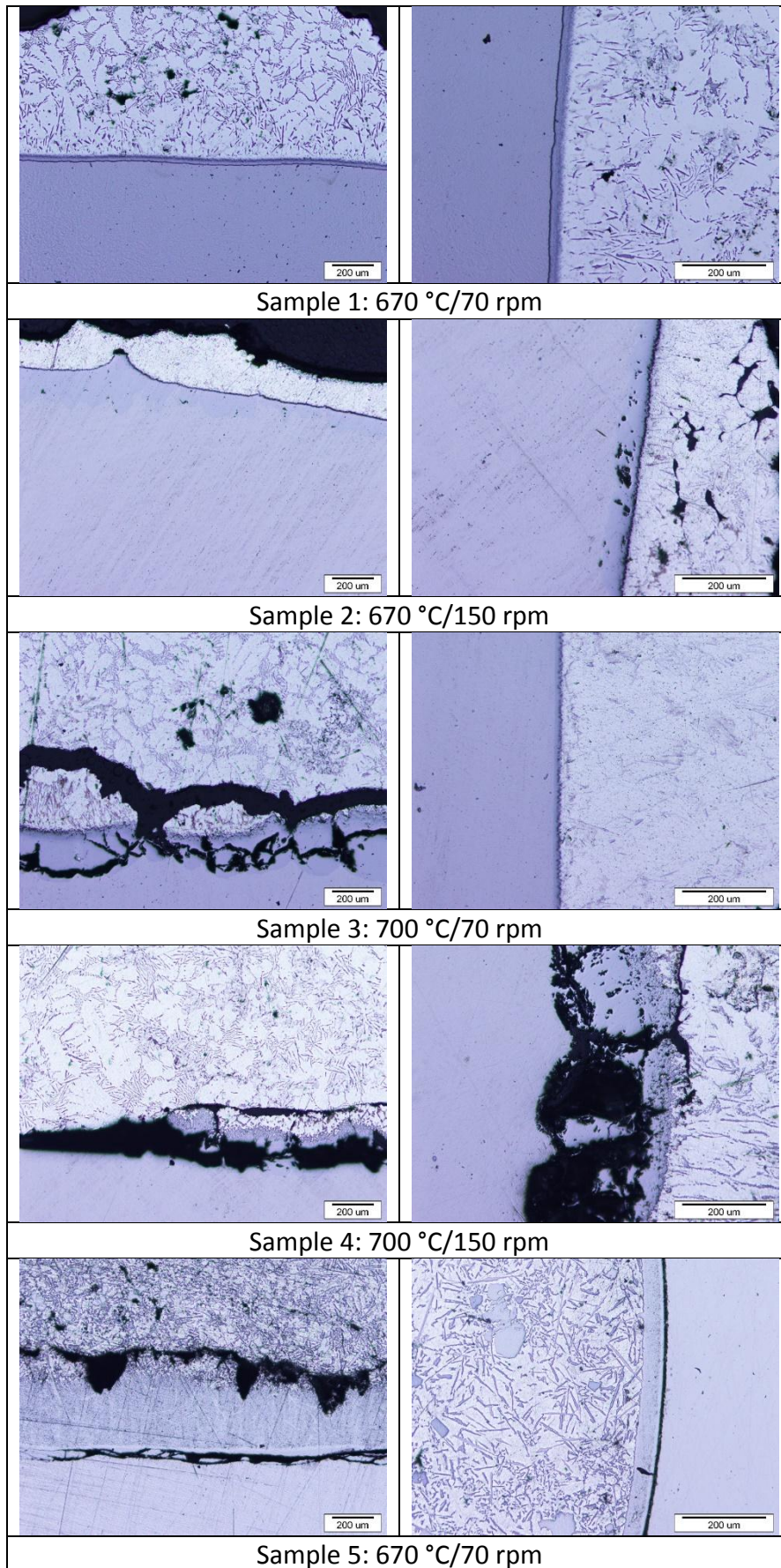
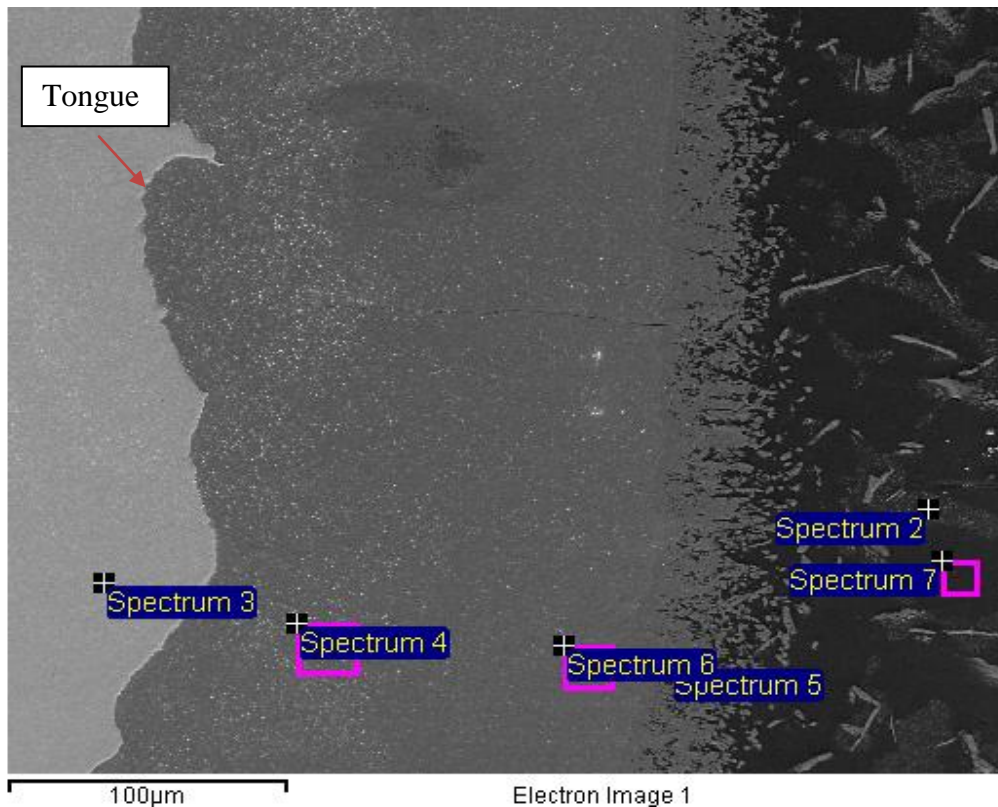


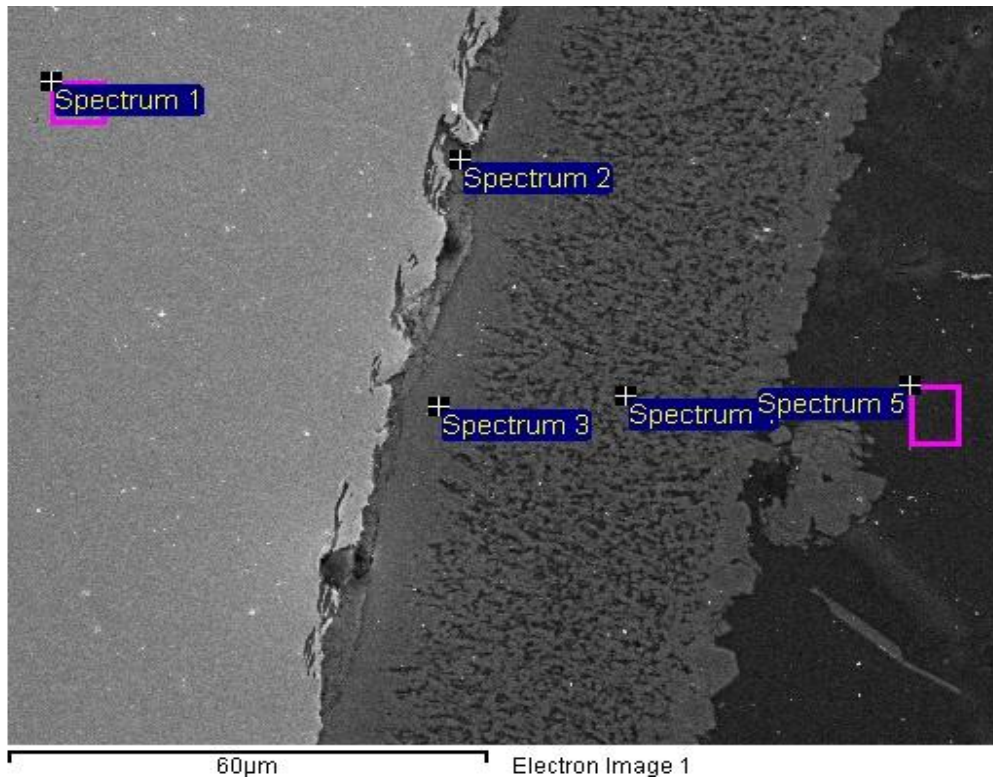
Figure 4. Micro-images of the reaction layers of the investigated samples



Spectrum	O	Al	Si	V	Cr	Mn	Fe	Mo	Total
Spectrum 2	1.3	97.7					1.0		100.0
Spectrum 3		1.0	1.1	0.4	5.6		90.9	1.0	100.0
Spectrum 4		53.9	0.8		2.5		42.8		100.0
Spectrum 5		60.2	0.3		1.4		38.1		100.0
Spectrum 6		55.9	0.6		2.3		41.2		100.0
Spectrum 7	0.8	99.2							100.0

Figure 5. Micrograph and EDS microanalysis of the interaction layer in the sample 1

Figure 6 represents the microanalysis of the sample 5 in mass %. Analyses in turn represent: 1 - steel composition, 2 - the composition of the reaction phase closer to steel with the presence of oxide and a high proportion of silicon (~ 12 mass %), 3 - the composition of the reaction phase closer to aluminium with a higher proportion of silicon, 4 - the aluminium composition closer to the boundary phase with a smaller proportion of silicon and 5 - the aluminium composition away from the interaction layer. It should also be noted that the reaction layer closer to the steel contains besides the silicon also higher concentration of iron. This layer is more compact, presumably due a diffusion of silicon into Al-Fe phase.



Spectrum	O	Mg	Al	Si	V	Cr	Mn	Fe	Cu	Total
Spectrum 1			0.68	1.12	0.31	5.36		92.53		100.00
Spectrum 2	4.68		50.66	11.95		1.76		30.94		100.00
Spectrum 3			54.83	12.88		1.84	2.02	27.57	0.86	100.00
Spectrum 4			70.34	7.40		2.10	3.30	15.41	1.45	100.00
Spectrum 5		0.34	91.84	6.45				0.77	0.60	100.00

Figure 6. Micrograph and EDS microanalysis of the interaction layer in the sample 5

CONCLUSIONS

It can be concluded that the stability of the hot-working tool steel, which is in contact with molten aluminium, depends on several parameters. A reaction takes course rapidly between the tool steel and the liquid aluminium, whereas the intermetallic reaction layer forms. Based on the results the following can be concluded:

- Metallographic investigations have demonstrated the formation of intermetallic Fe-phases, presumably Al_5Fe_2 and $Al_{13}Fe_4$. The reaction layer is double layer. Presumably, the phase Al_5Fe_2 appeared on the phase boundary with tool steel and is thicker, whereas the phase $Al_{13}Fe_4$ forms on the phase boundary with aluminium. Porosity and cracks are observed in the reaction layer. Cracks were also present in the aluminium region due to the concentration gradient of iron.
- The results showed increased wear on samples where the rpm was higher and/or the temperature was higher. The reaction layer is not completely uniform; in certain places it is departed and is thicker at a higher temperature.

- Iron from the tool steel diffuses through the reaction layer into liquid aluminium. At the saturation, iron phases are formed. It was also observed that during the wear of the tool steel, the layer departs, consequently, the smaller and larger particles of the iron intermetallic phase and the inclusion of the tool steel go into the aluminium melt (Figure 7).

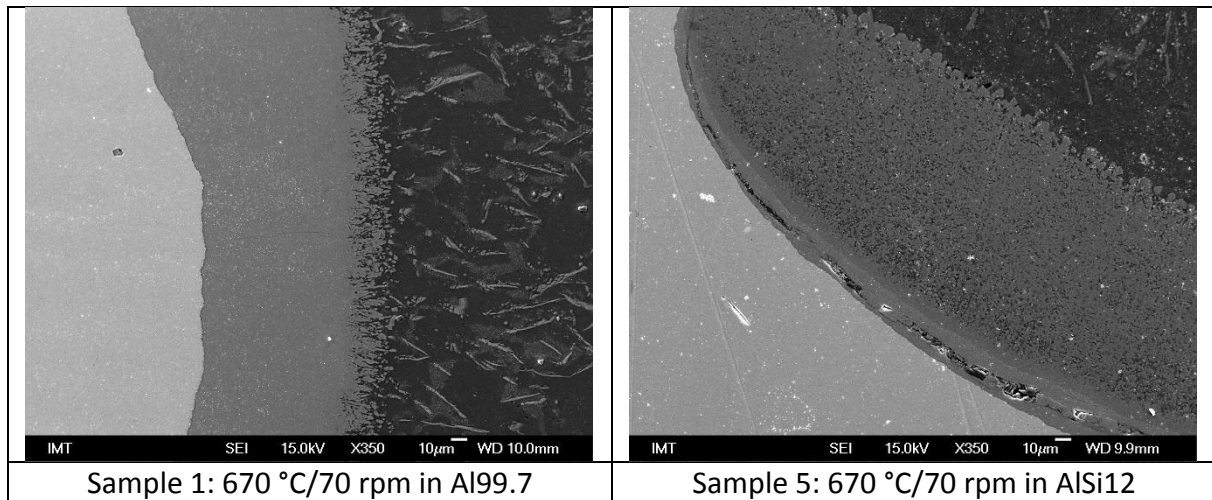


Figure 7. Micrograph of the interaction layer in the sample 1 and 5

Acknowledgements

This work was supported by A Republic of Slovenia, Ministry of Education, Science and Sport and by European Commission, European Regional Development. This work was made in a frame of program Materials and Technologies for New Applications (MARTINA, grant number: C3330-16-529008).

REFERENCES

- [1] R. A. Mesquita, Tool Steels: Properties and Performance, CRC Press, Taylor & Francis Group, 2017, pp. 258.
- [2] Steel selector: Steel SINOXX 4542, SIJ Metal Ravne, d.o.o., 2016, Accessible on Internet: <https://steelselector.sij.si/steels/PK346.html>, 15.1.2019
- [3] A. Persson, J. Bergstrom, Influence of surface engineering of the performance of tool steels for die casting, Proceedings of the 6th International Tooling Conference: the use of tool steels: experience and research, (J. Bergström, G. Fredriksson, M. Johansson, O. Kotik, F. Thuvander), Karlstad University, 10-13 September 2002, Karlstad, Sweden, pp. 1003.
- [4] K. N. Obiekea, S. Y. Aku, D. S. Yawas, Effect of pressure on mechanical properties and microstructure of die cast aluminium A380 alloy, Journal of minerals and materials characterization and engineering, 2(2014), pp. 248-258.

- [5] N. Tang, Experimental and theoretical research in interfacial reaction of solid Co with molten aluminium and its alloys, Transactions of nonferrous metals society of China, 25(2015)6, pp. 1715.
- [6] M. Yan, Z. Fan, Durability of materials in molten aluminium alloys, Journal of materials science, 36(2001), pp. 285-295.
- [7] F. Yin, M. Zhao, Y. Liu, Z. Li, Effect of Si on growth kinetics of intermetallic compounds during reaction between solid iron and molten aluminium, Transactions of nonferrous metals society of China, 23(2013)2, pp. 556-561.
- [8] S. Hwang, J. Song, Y. Kim, Effects of carbon content of carbon steel on its dissolution into a molten aluminium alloy, Materials science and engineering A, 390(2005)1-2, pp. 437-443.
- [9] Y. Erarslan, Wear performance of in-situ aluminium matrix composite after micro-arc oxidation, Transactions of nonferrous metals of China, 23(2013)2, pp. 347-352.
- [10] J. H. Selverian, A. R. Marder, M. R. Notis, The reaction between solid iron and liquid Al-Zn Baths, Metallurgical Transactions A, 19(1988), pp. 1193-1203.



18th INTERNATIONAL FOUNDRYMEN CONFERENCE
**Coexistence of material science and sustainable technology in
economic growth**

Sisak, May 15th-17th, 2019

<http://www.simet.hr/~foundry/>

**POSSIBILITIES FOR PROVIDING OF UNIDIRECTIONAL SOLIDIFICATION OF
COMPLEX CASTINGS IN THE TECHNOLOGY OF HIGH-PRESSURE DIE-CASTING**

Primož Mrvar^{1*}, Sebastjan Kastelic², Grega Gorše³, Branko Bauer⁴, Mitja Petrič¹

¹ University of Ljubljana Faculty of Natural Sciences and Engineering, Ljubljana, Slovenia

² TC Livarstvo, Ljubljana, Slovenia

³ LTH Castings, Ljubljana, Slovenia

⁴ University of Zagreb Faculty of Mechanical Engineering and Naval Architecture, Zagreb, Croatia

Invited lecture

Subject review

Abstract

In contemporary high pressure die casting (HPDC) foundries the mastery of each sequence in production cycle is the most important, where the strive to reliable master, as well as planning of composed molten metal, pouring and solidification process, ejection of castings, transport to the cooling place and cutting of gating system and overflows were done. For castings with a complex geometry and dimensional accuracy, the appropriate planning of pouring and feeding elements according to a heat economy of casting, rapid tooling and prototyping and then reliable manufacturing which includes the mastery of all the edge conditions in the process chain. In the paper the example of virtual analysis of casting from Al alloy will be presented with choosing of appropriate foundry technology HPDC, calculation of casting process which includes the filling process of cold chamber, model description of three phases at HPDC, flow of molten metal, solidification with considering the temporary air gap formation between the casting and tool, formation of stress and relaxation of it into deformations in each sequence, when the tool is opening, at ejection, cooling in water or on air and after cutting off the gating system. Since it is not always possible to produce the castings according to the principle of unidirectional solidification with a traditional approach, for the individual areas, which should be macroscopic dense (without porosity), the local squeezing process is performed in the sequence of the semi-solid state of the region. The location of the impression is marked by a local increase of pressure and a plastic deformation of the already solid part of the casting (solid shell). An example of a very detailed comprehensive treatment of these processes in the case of a real casting will be discussed. Further, the optimization of the processes of the local squeezing sequence and the overall solidification process will be presented. Comparisons will be made with calculations of volume defects, casting dimensions and deformations with experimentally obtained castings produced from LTH Castings' industrial technology practice. Proven complete master of high-pressure die-casting have the result of an important financial effect and decreasing of required time to start of serial production of castings.

Keywords: *high pressure die casting, unidirectional solidification, local squeezing, pressure analyses, shrinkage porosity*

*Corresponding author (e-mail address): primoz.mrvar@omm.ntf.uni-lj.si

POSSIBILITIES FOR PROVIDING OF UNIDIRECTIONAL SOLIDIFICATION OF COMPLEX CASTINGS IN THE TECHNOLOGY OF HIGH PRESSURE DIE-CASTING

Primož Mrvar¹, Sebastjan Kastelic², Grega Gorše³, Branko Bauer⁴, Mitja Petrič¹

¹ *University of Ljubljana, Faculty of Natural Sciences and Engineering, Aškerčeva 12, Ljubljana, Slovenia,*

² *TC livarstvo, Teslova 30, Ljubljana, Slovenia*

³ *LTH Castings, Litostrojska cesta 46, Ljubljana, Slovenia*

⁴ *University of Zagreb, Faculty of Mechanical Engineering and Naval Architecture, Ivana Lučića 5, Zagreb, Croatia,*



University of Ljubljana
Faculty of Natural Sciences and Engineering
Department of Materials and Metallurgy

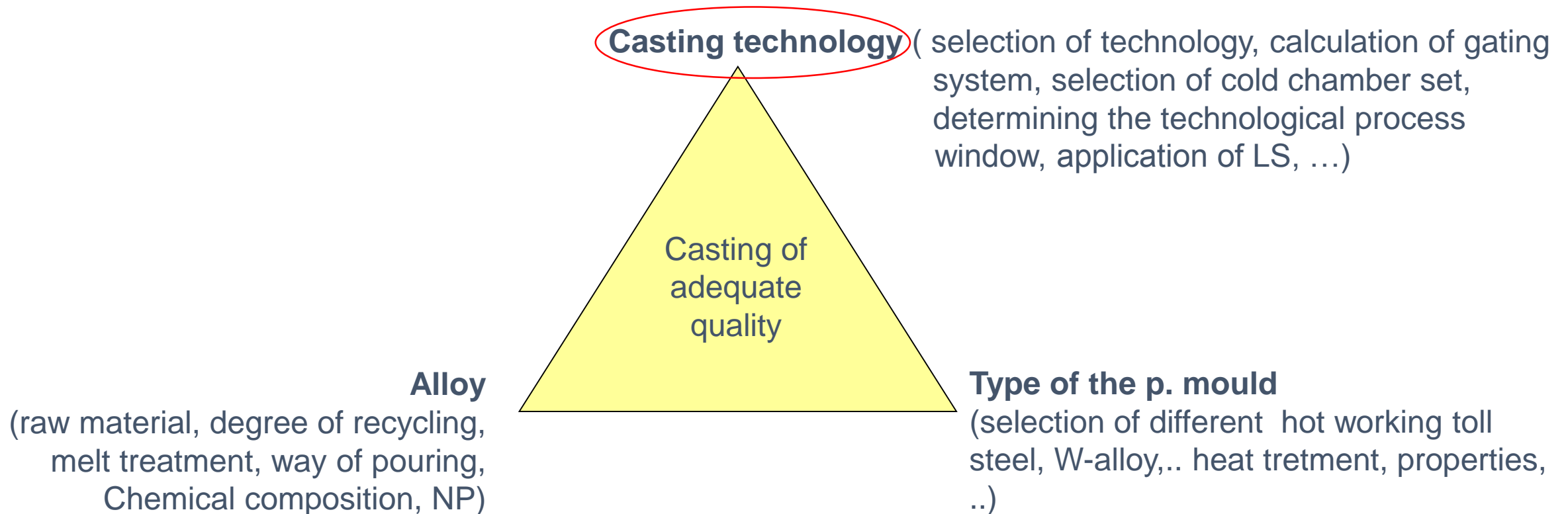


LTH Castings

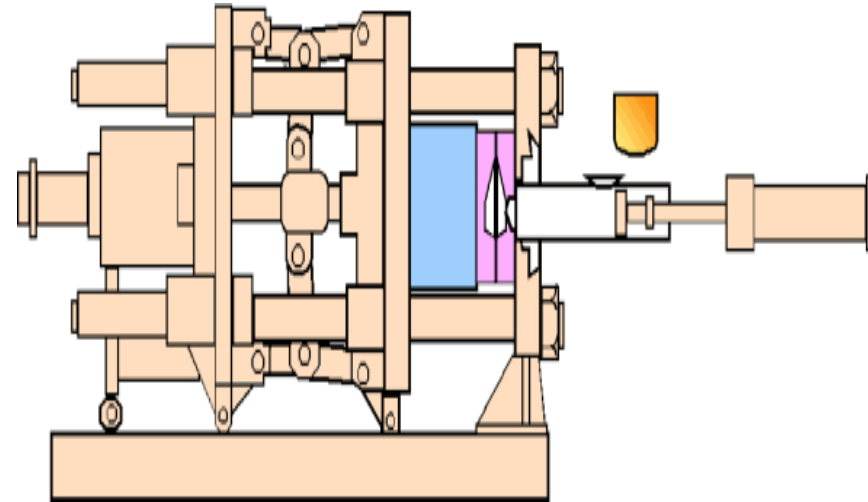
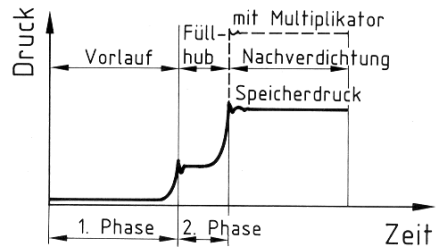
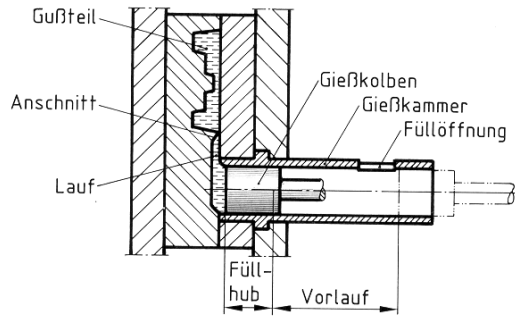


Casting, technology

- Permanent mold (GDC, GDTC, HPDC; LPDC;)
- Sand or ceramic mould (GSC, INV,)
 - Gravity (G, T)
 - **Pressure (HPDC, LPDC)** ←
 - Centrifugal (H, V)
 - Vacuum
 - Continues,...



HPDC



1

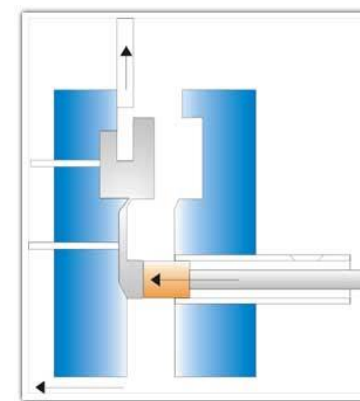
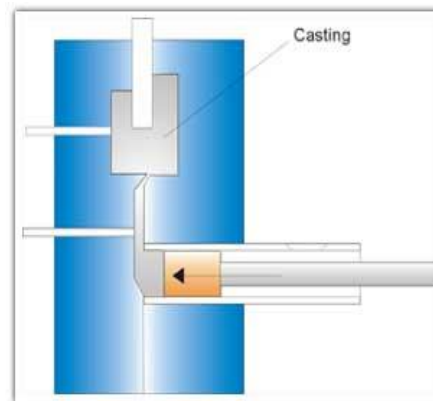
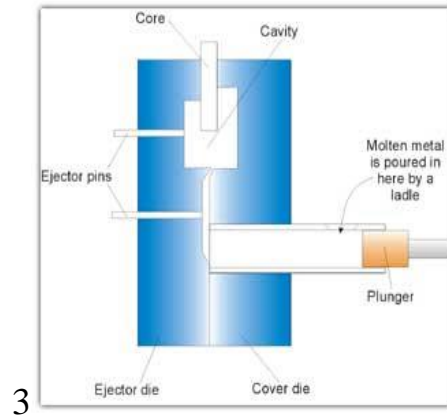
Piston motion

2

Die cavity filling

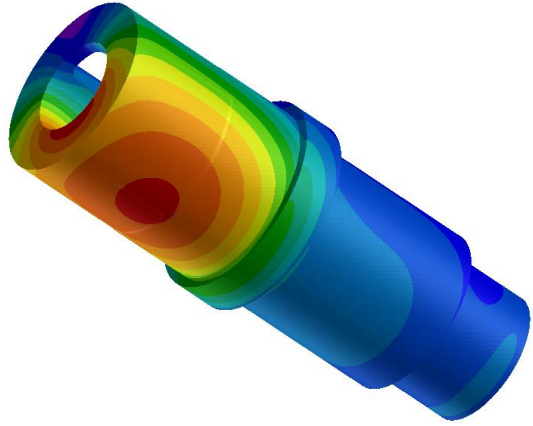
3rd

phase effect



3

HPDC- Cold chamber

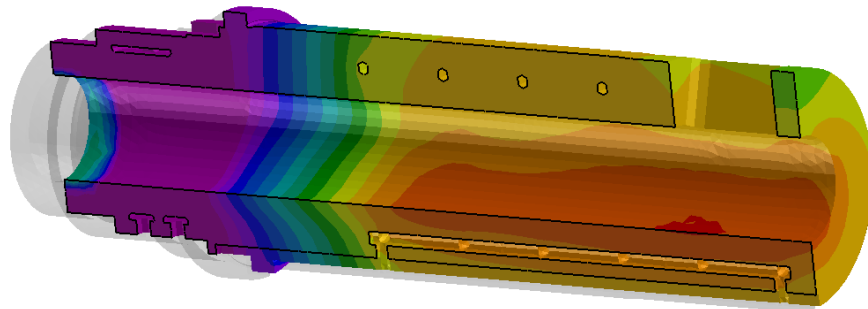


1. - What is the main problem to pour the molten Al alloy?

- Solubility of iron in Al alloys
- Cycle time

2. - How to increase the efficiency of working the c. chamber?

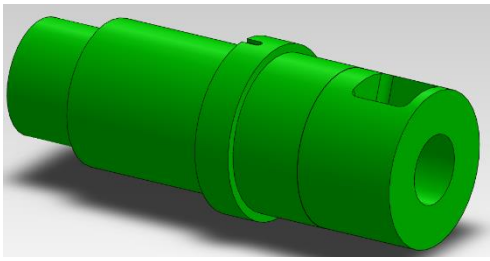
- Decreasing the solidification of molten alloy in chamber (t for stage I and II have to be short, T of chamber high).....development of hot chamber machine for Al ?
- This cause the new situation which is connect with time for shot (II. Stage)
- Increasing the life time of sleeve and piston
- Increasing of yield of molten metal



HPDC- Cold chamber

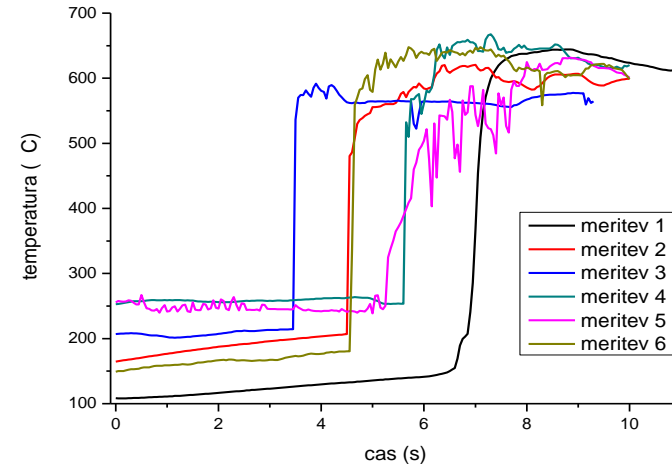
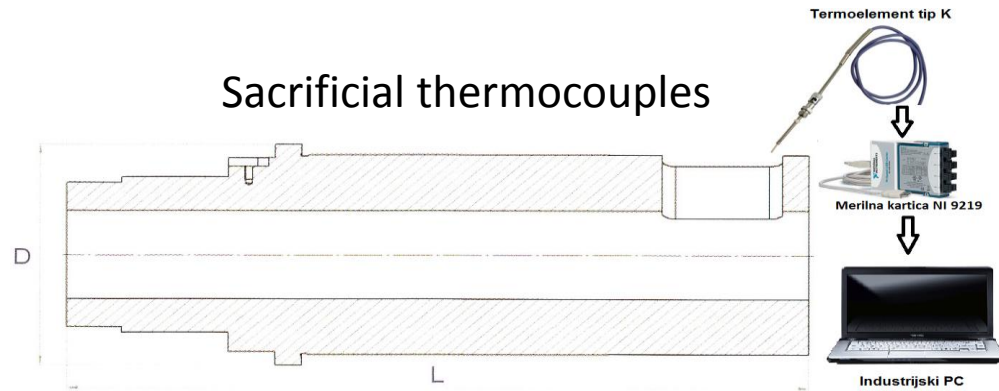
3. - What is the main problem to prepare the accurate calculation of casting process for HPDC?

- It is necessary to choose and/or calculate or measure the real materials data
 - T_l , T_s , $f_s-f(T)$, $\rho-f(T)$, $\eta_f(T)$, E , ..
- The calculation should start in the stage 0
- The description of stage I to III is required for accuracy
- The boundary conditions have to be set properly (T , HTC , $t..$)
- The geometry should be describe with fine mash
- Technological process window should reflect the real (experimental) data input



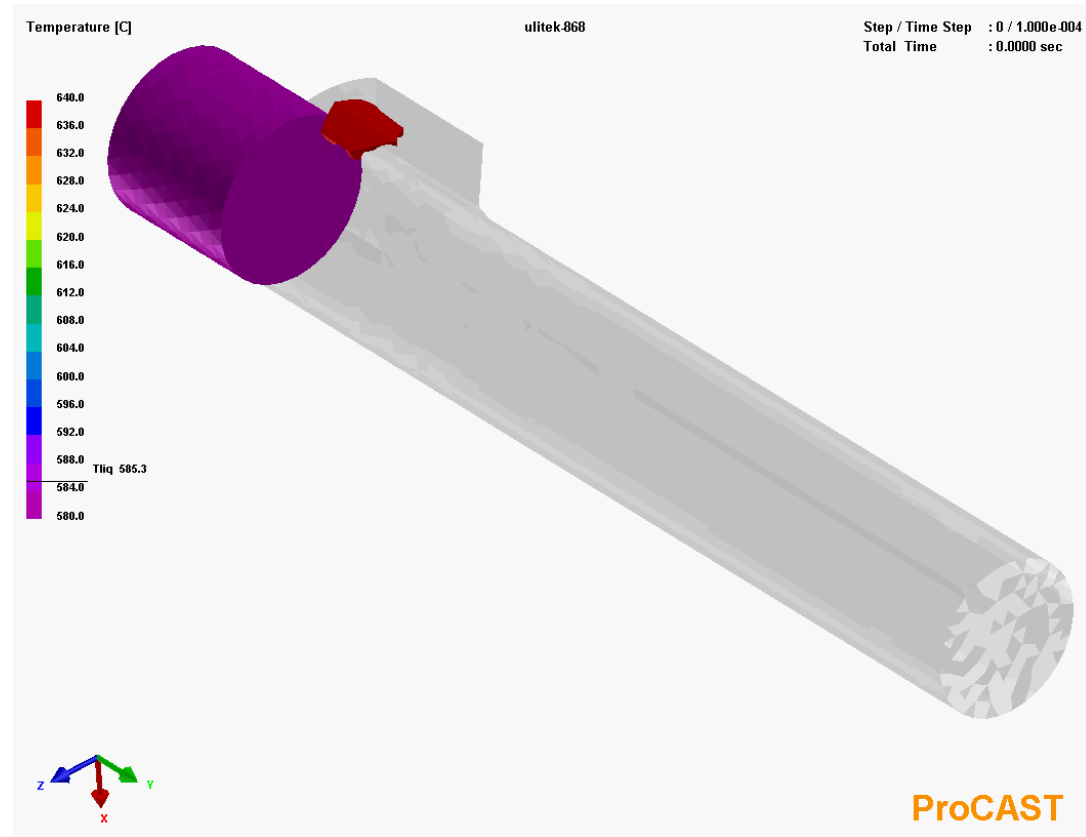
Calculation of melt flow and melt temperature drop from furnace to casting chamber

- Measurements of melt temperature in the casting chamber before the first stage starts

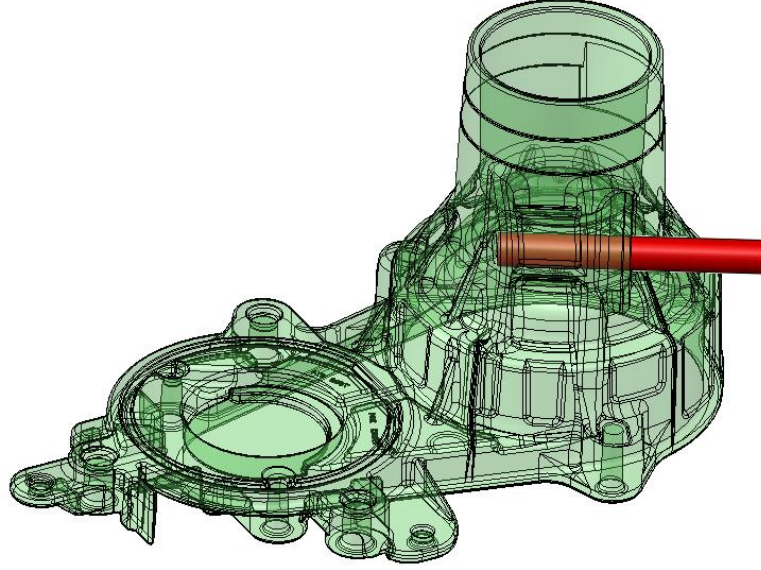


- **Simulation of melt flow and melt temperature drop from furnace to casting chamber**

- Filing of casting chamber calculation compered with experimentaly determined temperatures.
- Temperature in the chamber before the shot at 650 °C, temperature of the melt in the casting furnace 677 °C ⇒ temperature drop 20 - 30°C.



Example 1: Investigated geometry of casting and their gating system



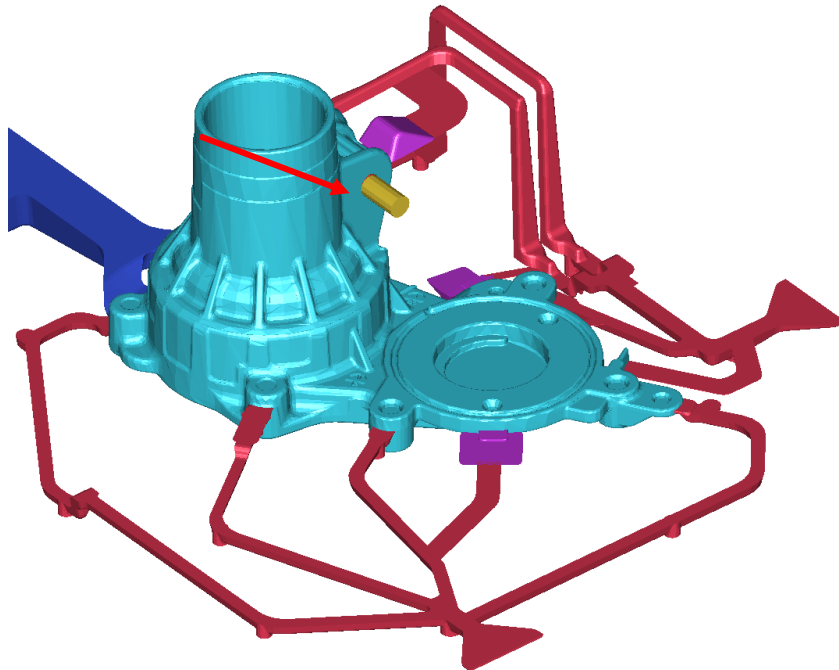
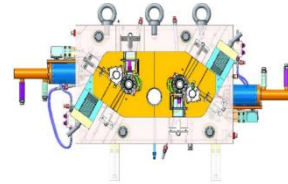
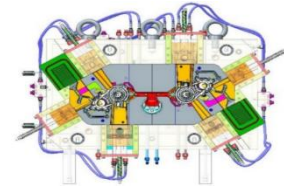
- Material

- Alloy: AlSi9Cu3

- $T_{\text{liquidus}} = 588^{\circ}\text{C}$

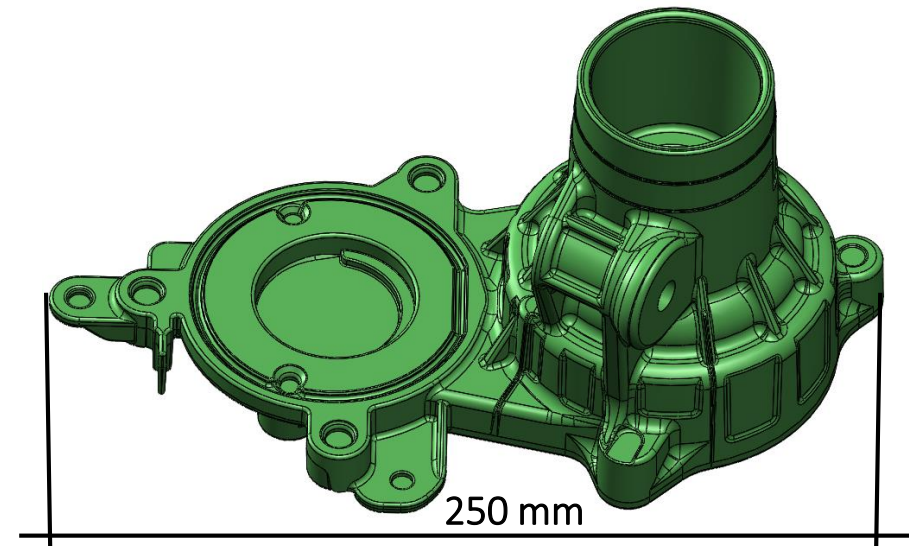
- $T_{\text{Solidus}} = 508^{\circ}\text{C}$

- Pouring temperature 660°C

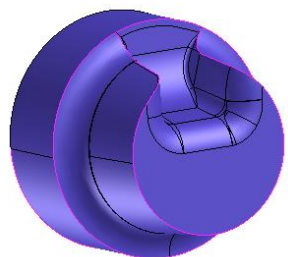
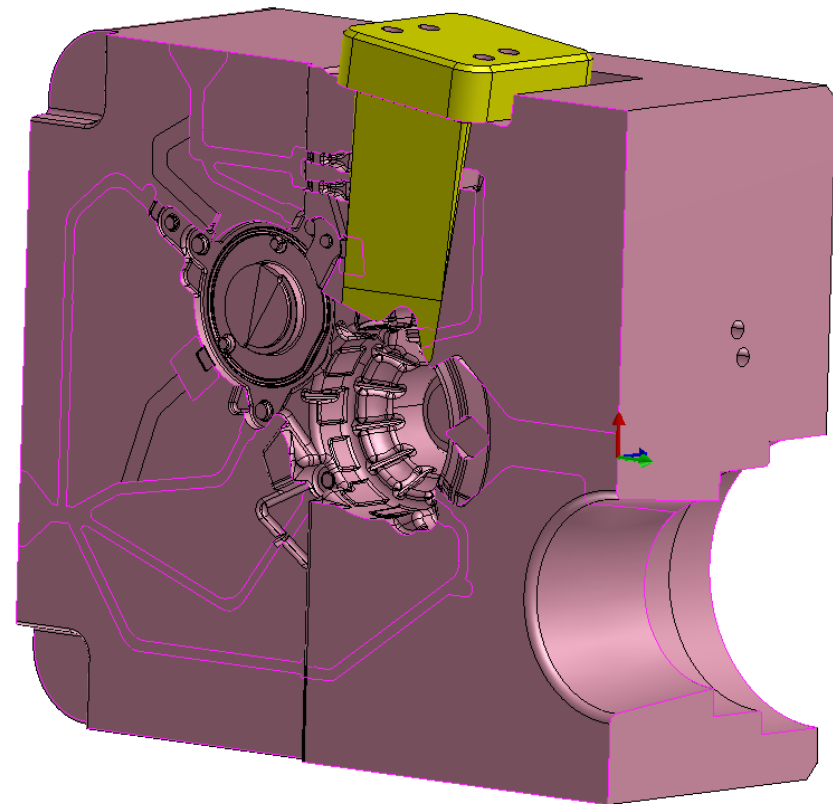
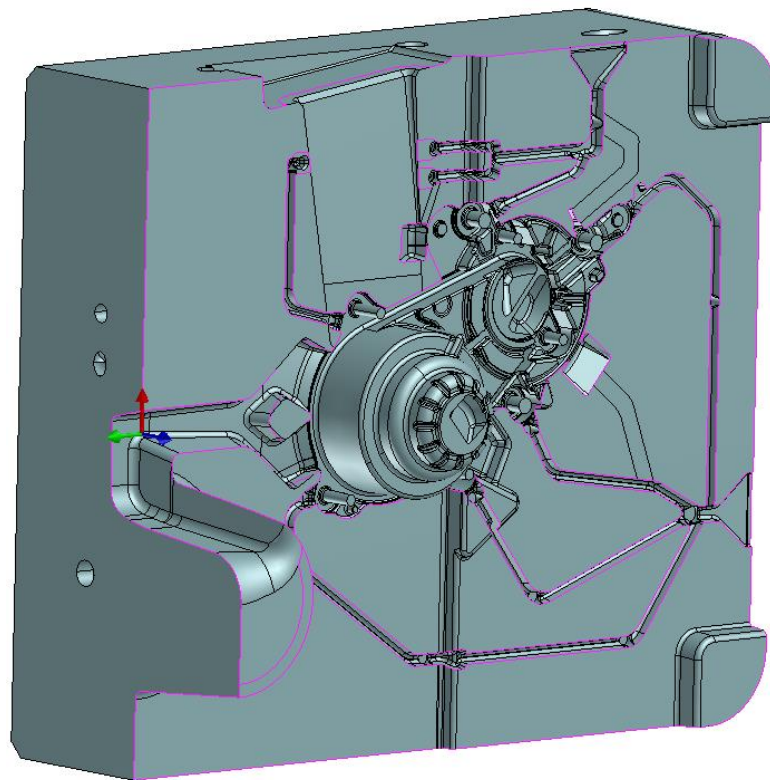
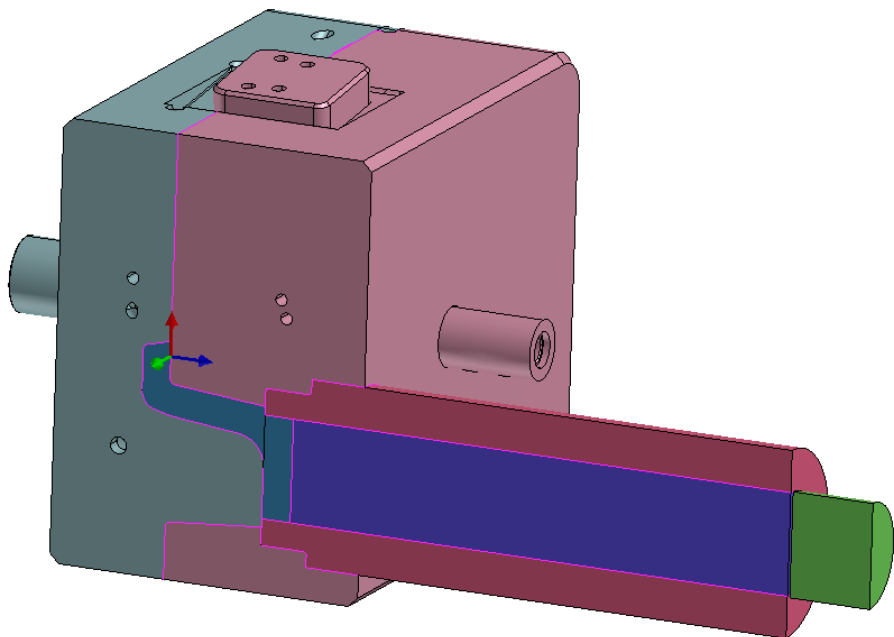


- Brut weight of shot (2 castings): 3,1 kg

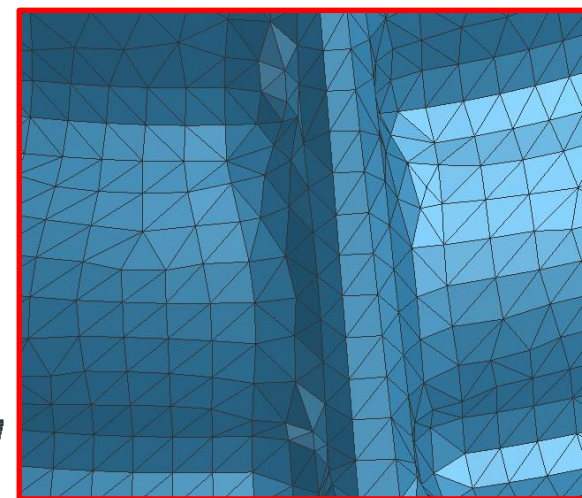
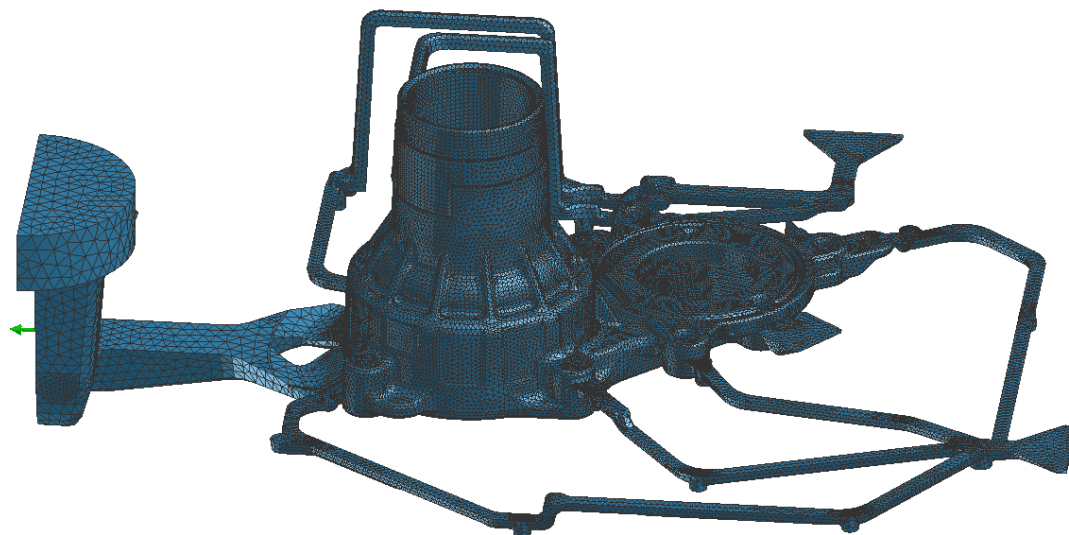
- Net weight of casting: 0,8 kg



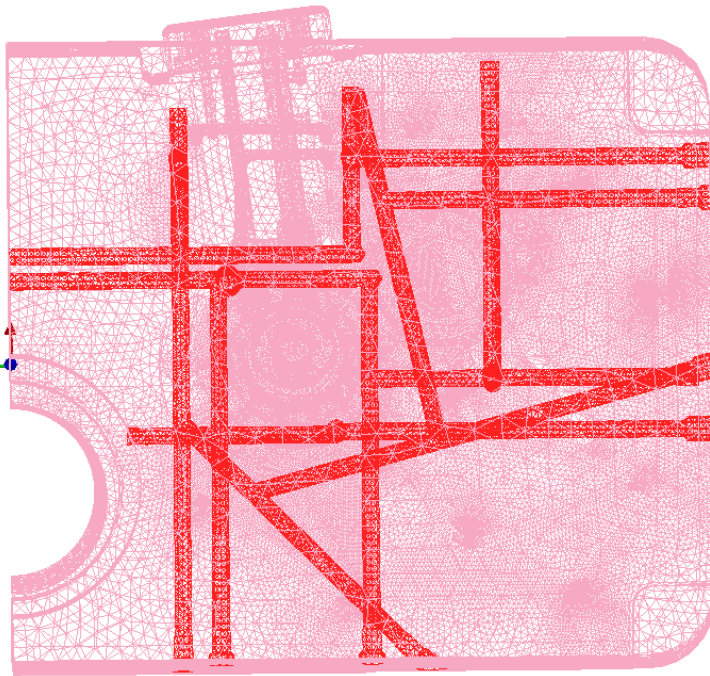
Geometry of tool assembled with cold chamber set



Casting distributor

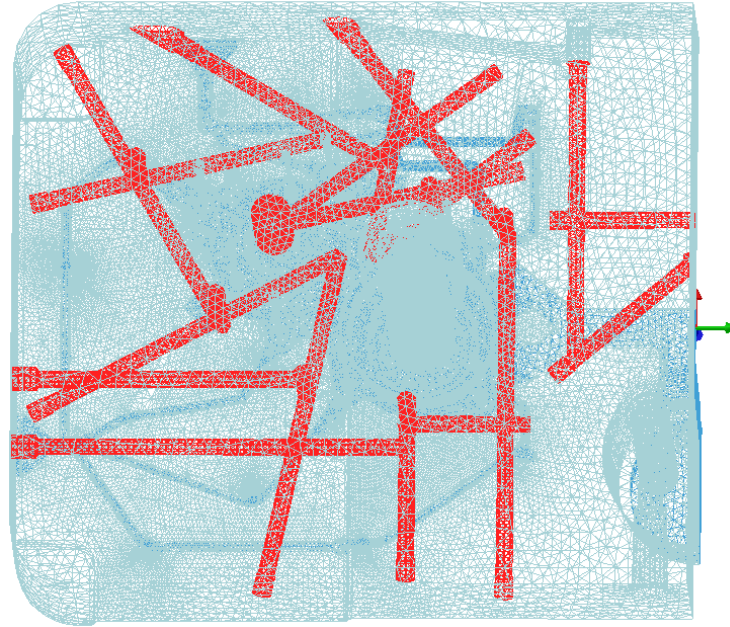


- The origin layout of Cooling and heating channels



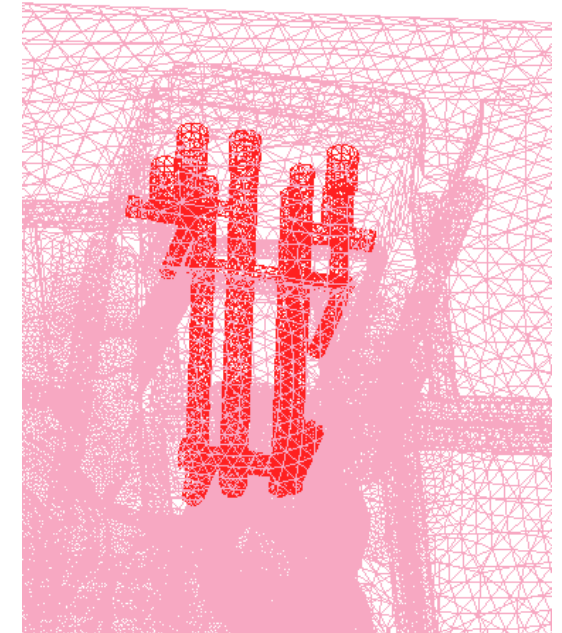
Property	Type	Value	Temp	Time
Film Coeff	V...	2.0000e+003 W/m^2k	C	sec
Emissivity	V...		C	sec
Ambient Te...	V...	1.8000e+002 C		sec
Heat Flux	V...	W/m^2		sec
View Factor		OFF		

Fixed side of die; T-oil 180°C



Property	Type	Value	Temp	Time
Film Coeff	V...	2.0000e+003 W/m^2k	C	sec
Emissivity	V...		C	sec
Ambient Te...	V...	1.6000e+002 C		sec
Heat Flux	V...	W/m^2		sec
View Factor		OFF		

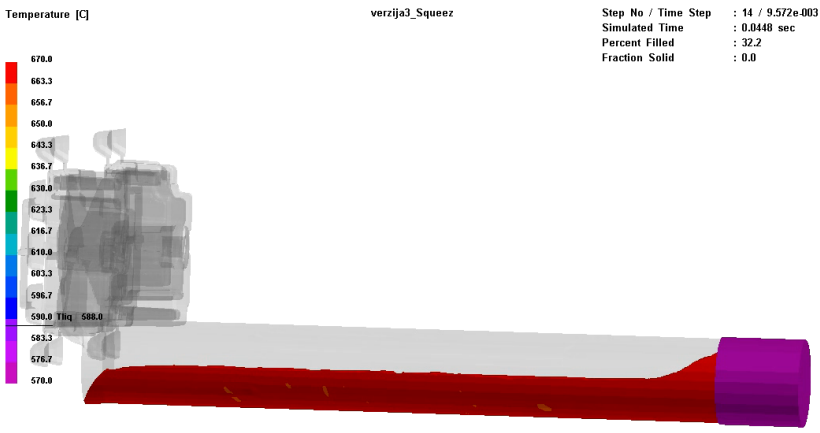
Moveable side of die; T-oil 160°C



Property	Type	Value	Temp	Time
Film Coeff	V...	2.0000e+003 W/m^2k	C	sec
Emissivity	V...		C	sec
Ambient Te...	V...	1.6000e+002 C		sec
Heat Flux	V...	W/m^2		sec
View Factor		OFF		

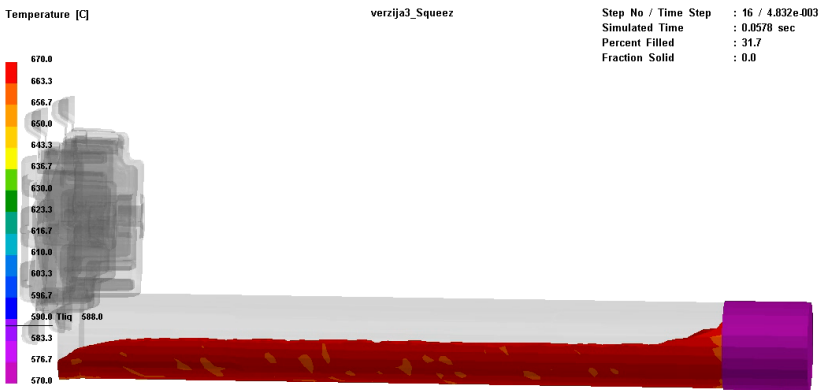
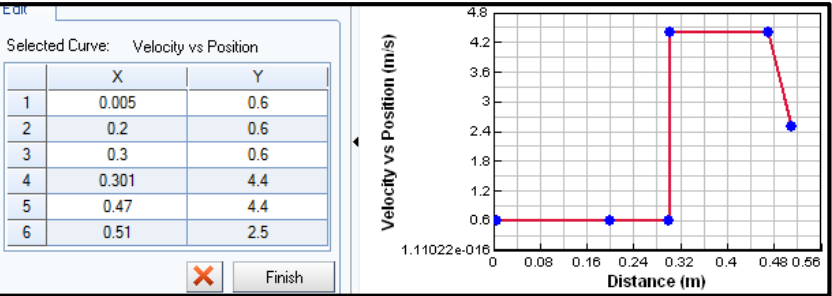
Side core of die; T-oil 160°C

• Example of optimization the sequence I ; Cooling of molten metal in the cold chamber in the first stage



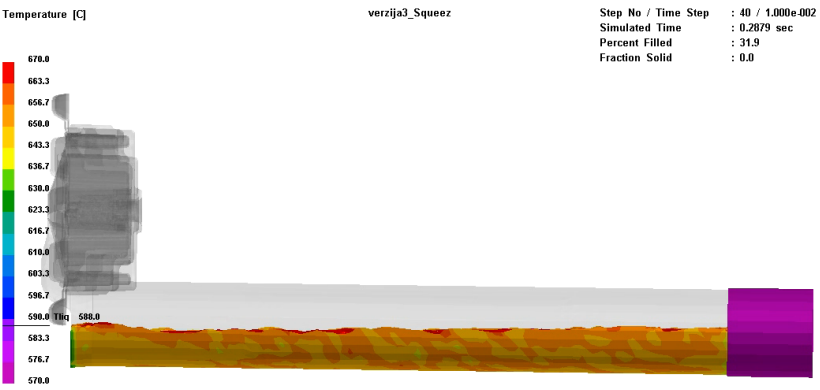
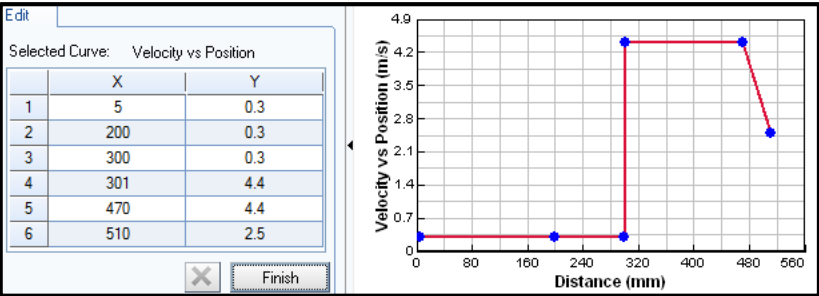
ProCAST

V₁ = 0,6 m/s



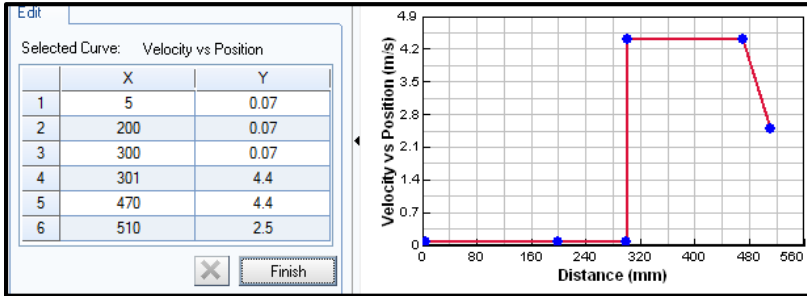
ProCAST

V₁ = 0,3 m/s



ProCAST

V₁ = 0,07 m/s

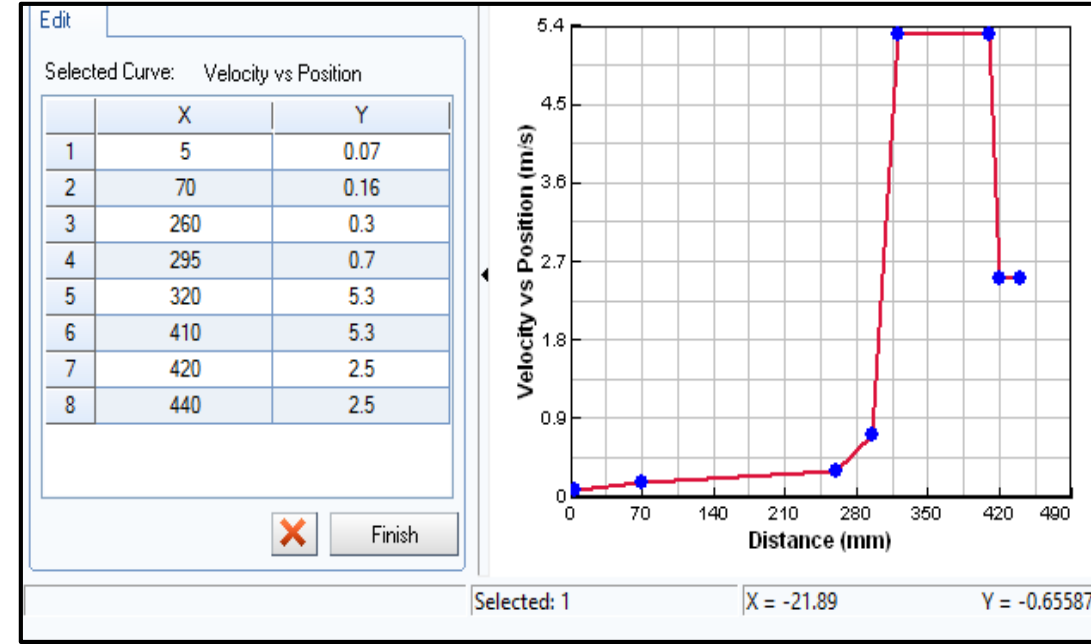
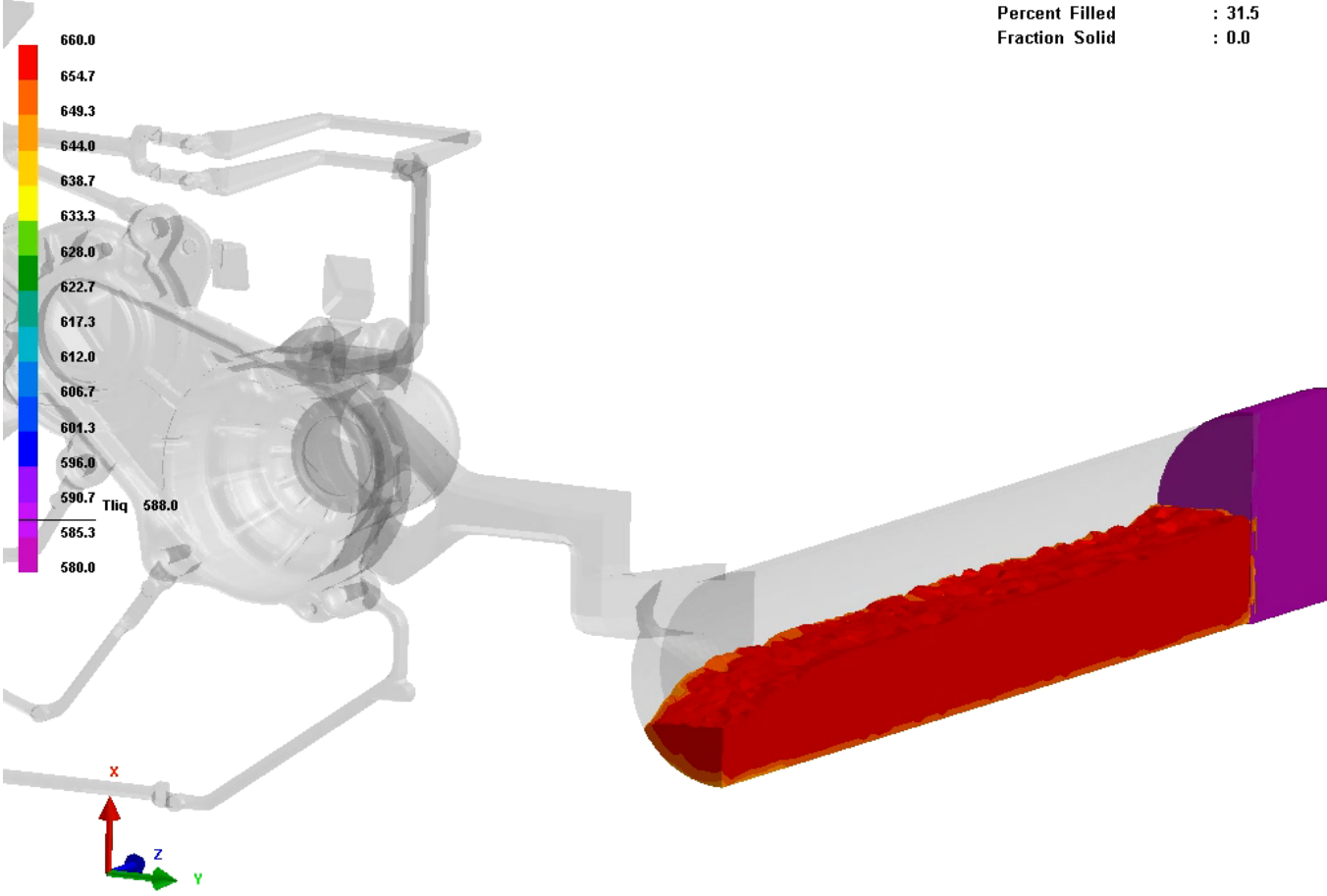


Temperature [C]

squeeze_LTH

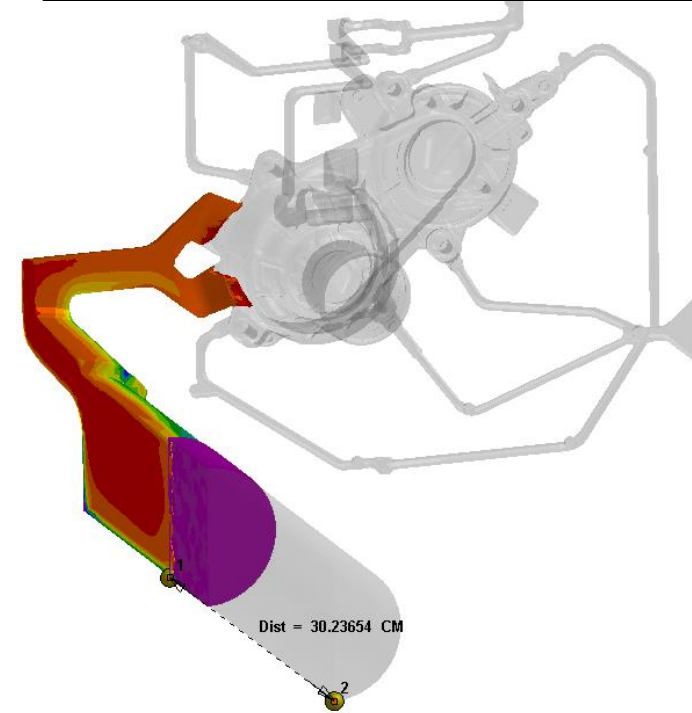
Step No / Time Step : 20 / 5.236e-003
Simulated Time : 0.0881 sec
Percent Filled : 31.5
Fraction Solid : 0.0

Sequence of piston movement



Path - Velocity

ProCAST

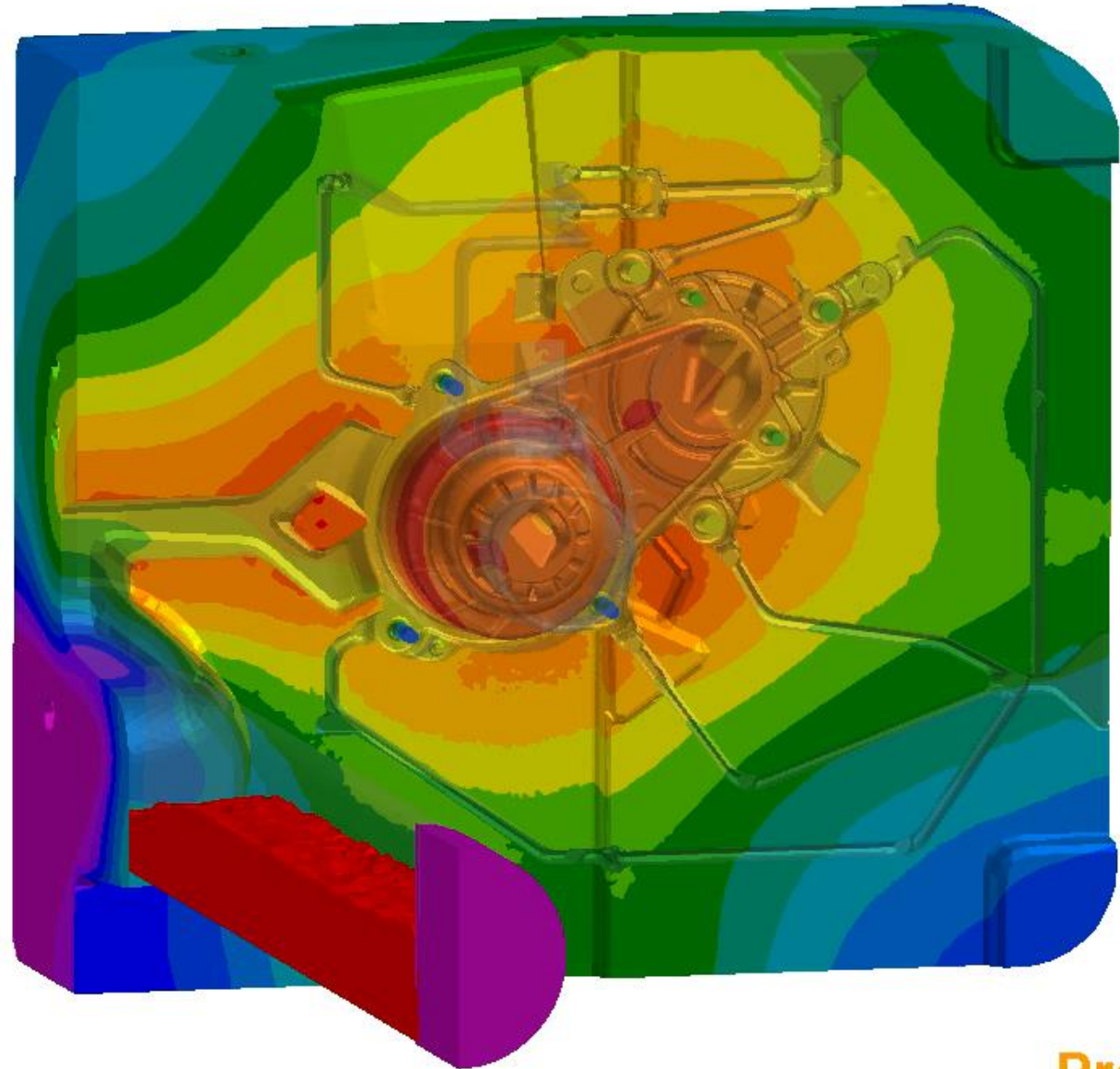
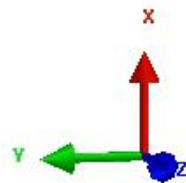
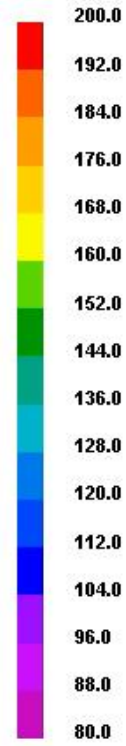


- Calculation of filling

Temperature [C]

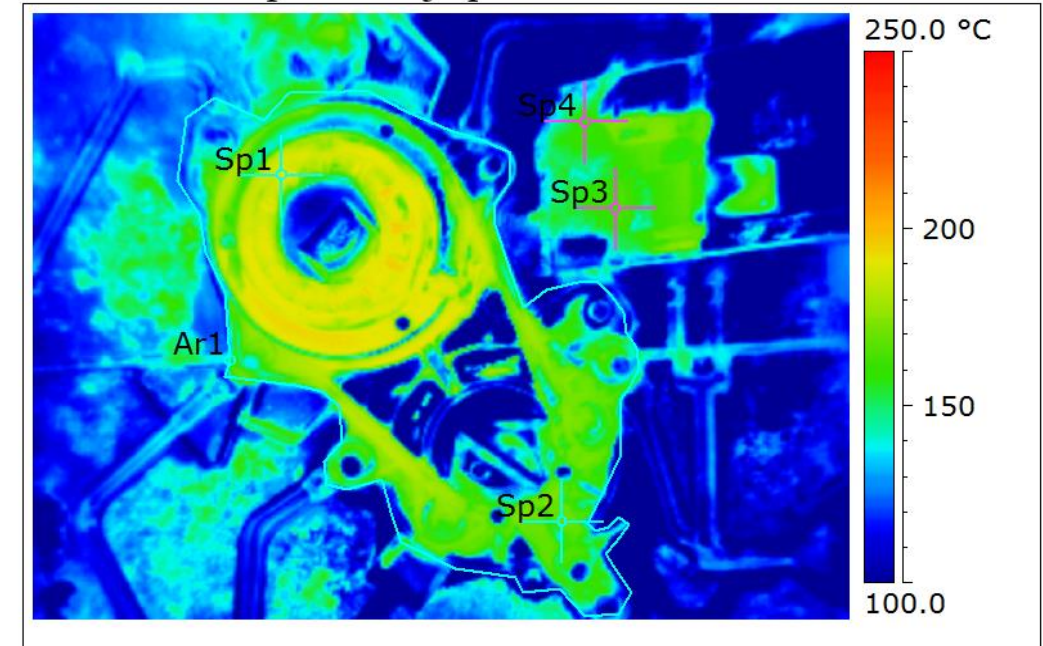
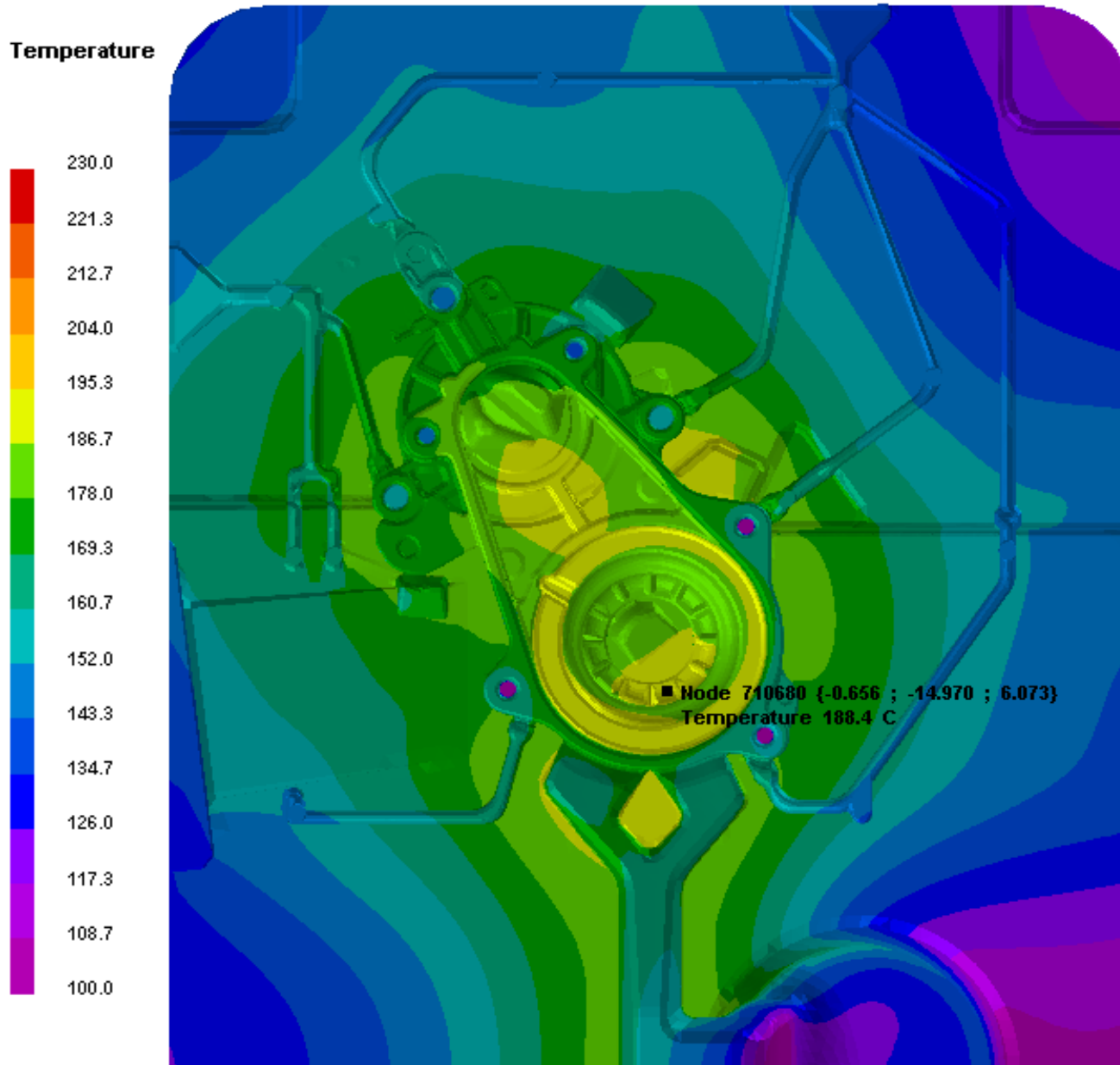
squeez_LTH

Step No / Time Step : 20 / 5.236e-003
Simulated Time : 0.0881 sec
Percent Filled : 31.5
Fraction Solid : 0.0



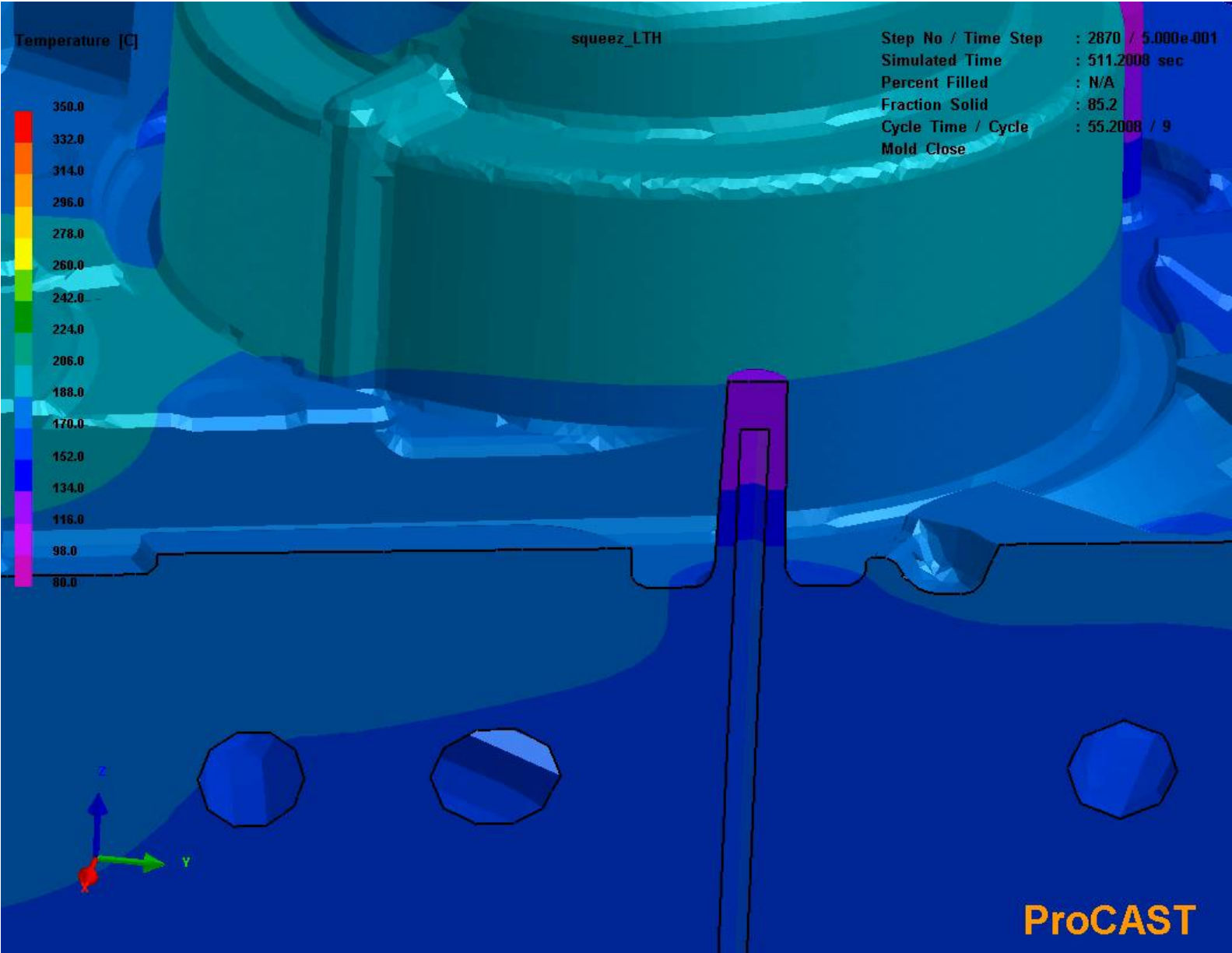
Comparison between calculated temperature field and experimentally determined; movable side of die

Pomična stran po mazanju pri robotu

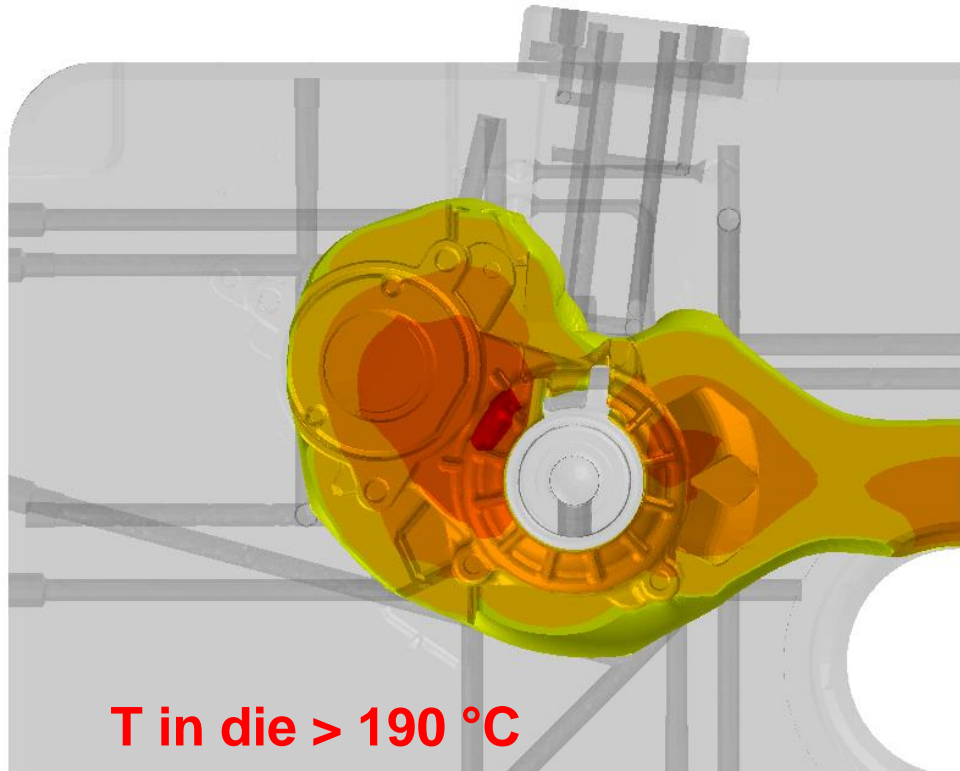
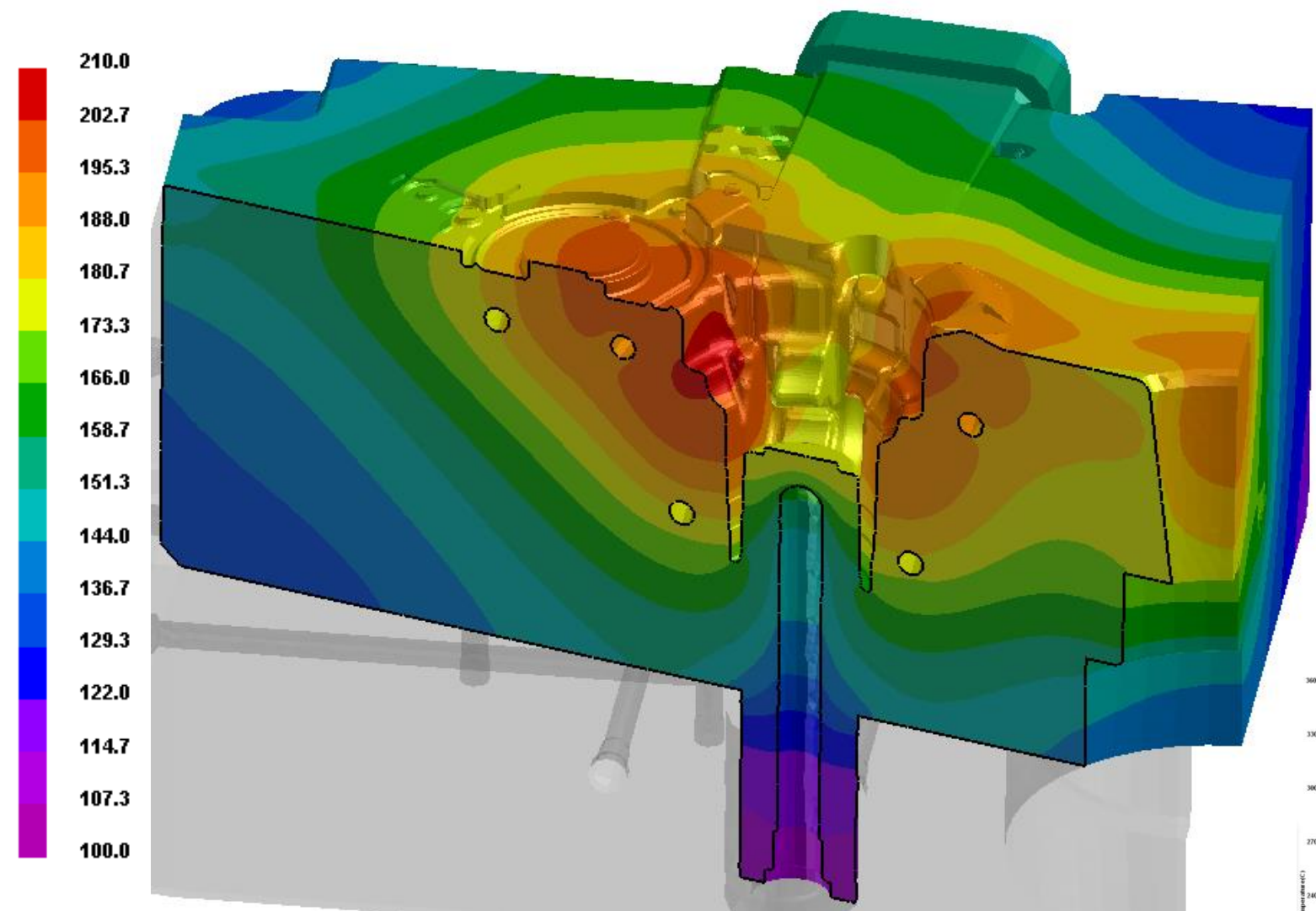


Date	11.04.2016
<u>Filename</u>	IR_14818.jpg
Image Time	12:27:22
Sp1 Temperature	187.6 °C
Sp2 Temperature	166.9 °C
Sp3 Temperature	160.5 °C
Sp4 Temperature	160.0 °C
Ar1 Min. Temperature	78.2 °C
Ar1 Max. Temperature	195.7 °C
Ar1 Average Temperature	150.0 °C
Sp1 <u>Emissivity</u>	0.80
Sp2 <u>Emissivity</u>	0.80
Sp3 <u>Emissivity</u>	0.80
Sp4 <u>Emissivity</u>	0.80

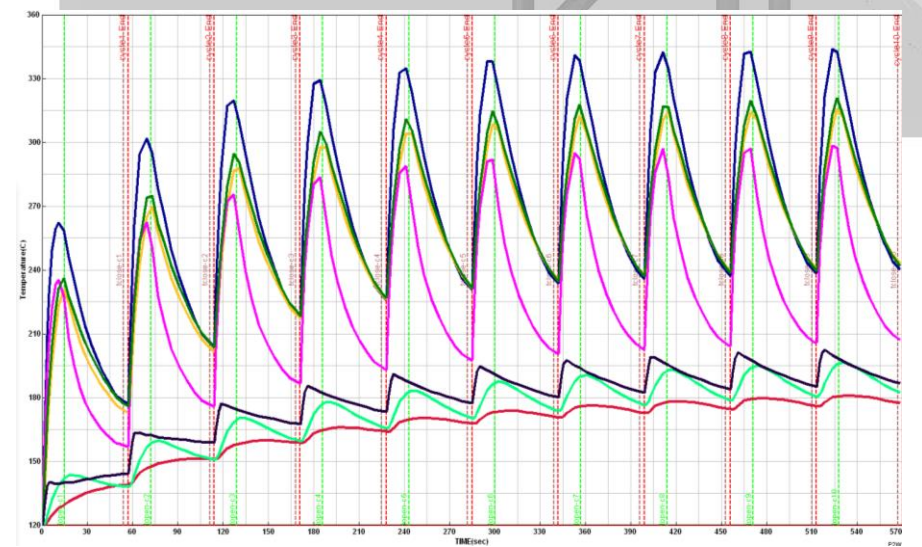
Movable side of die: Cycling calculation on die which is cooled by Jet Cooling system



Temperature [C] Fixed side of die; The temperature field was stabilized after 10 cycles



T in die > 190 °C

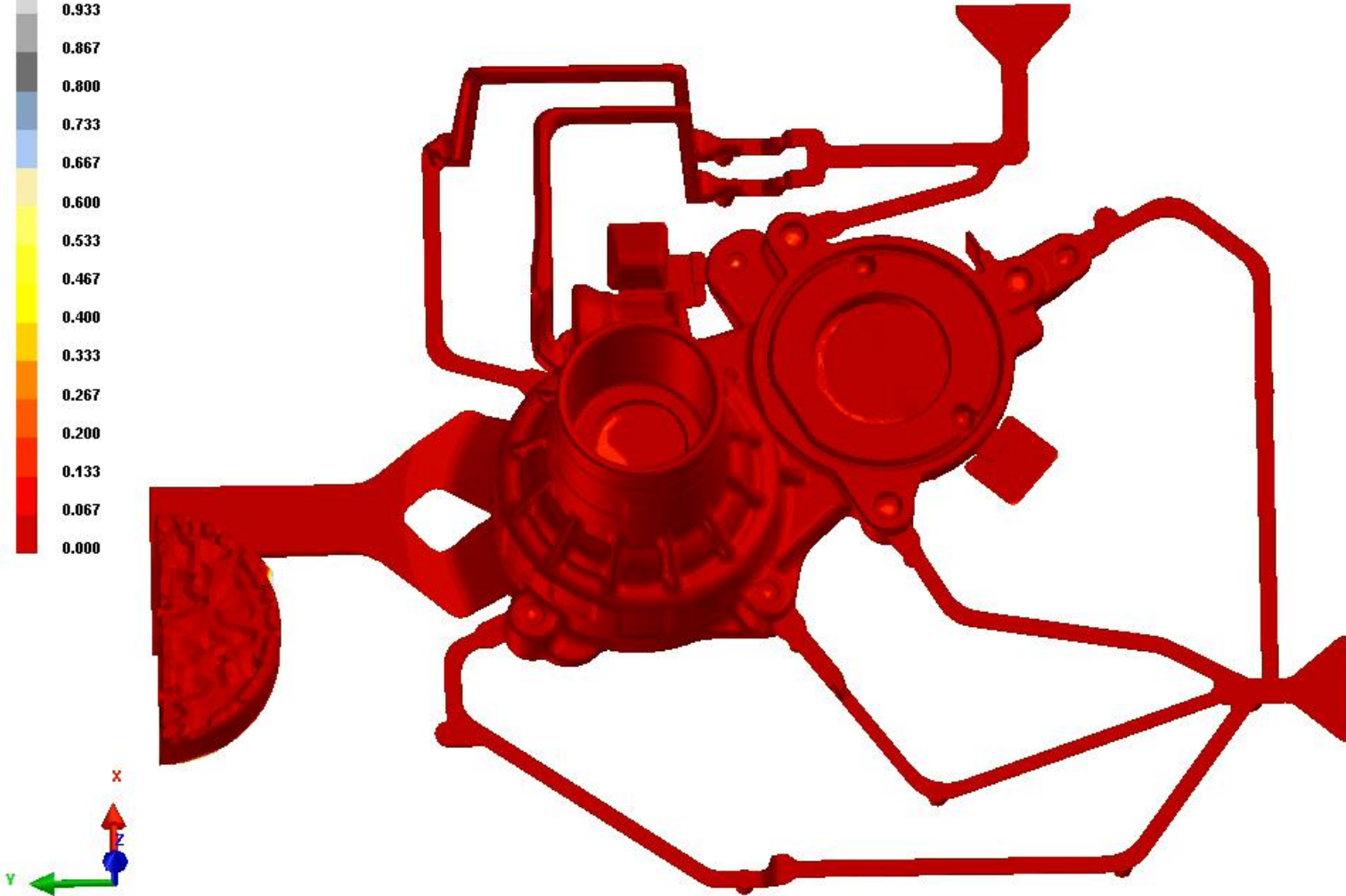
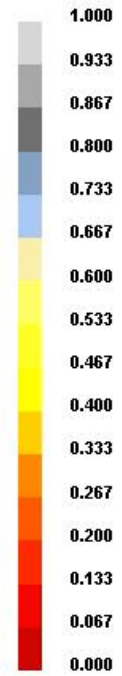


- **Calculation of solidification sequence**

Fraction Solid

squeez_LTH

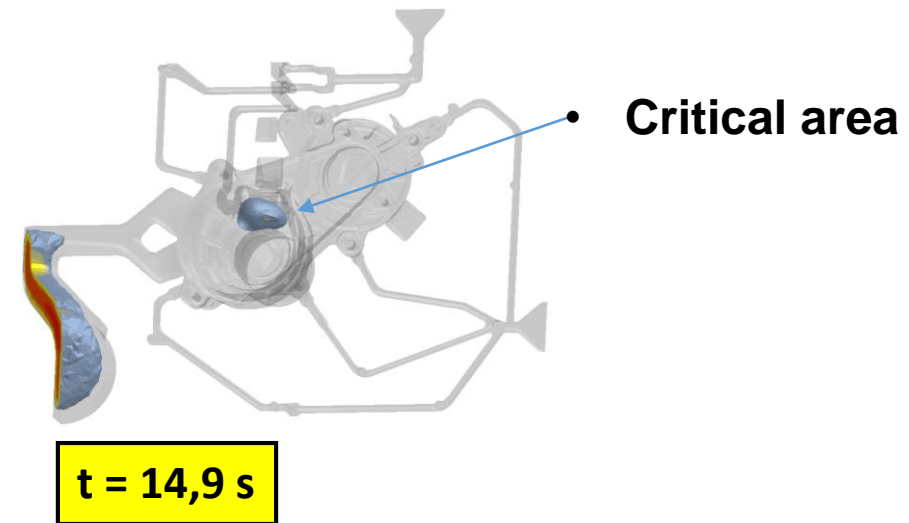
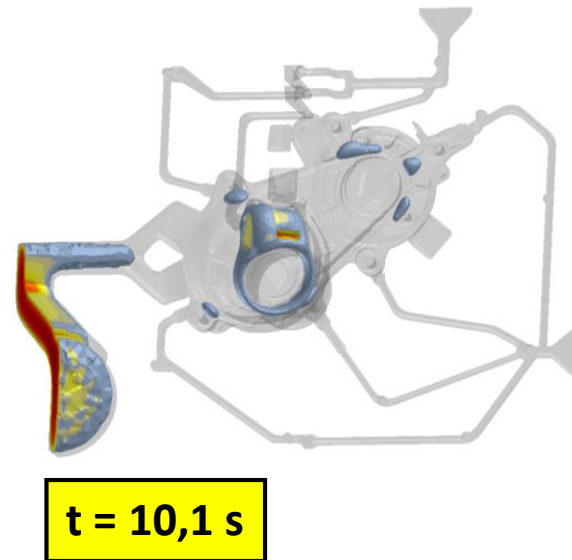
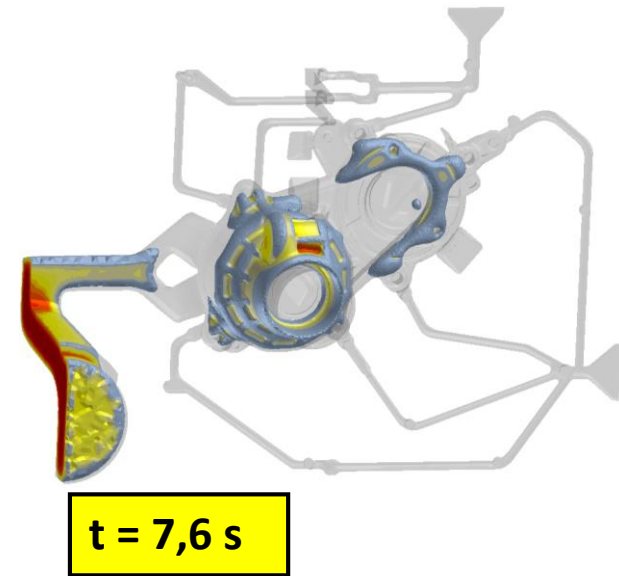
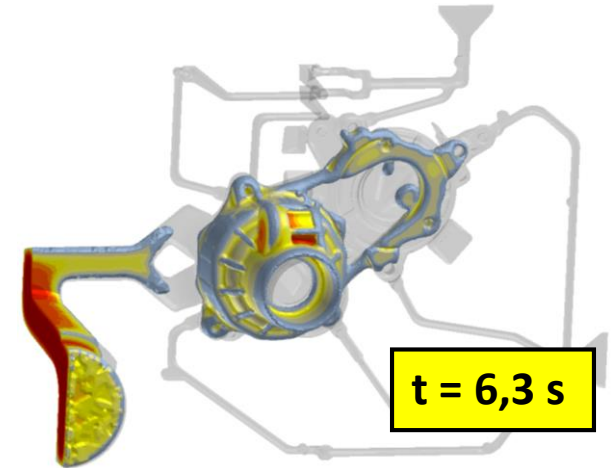
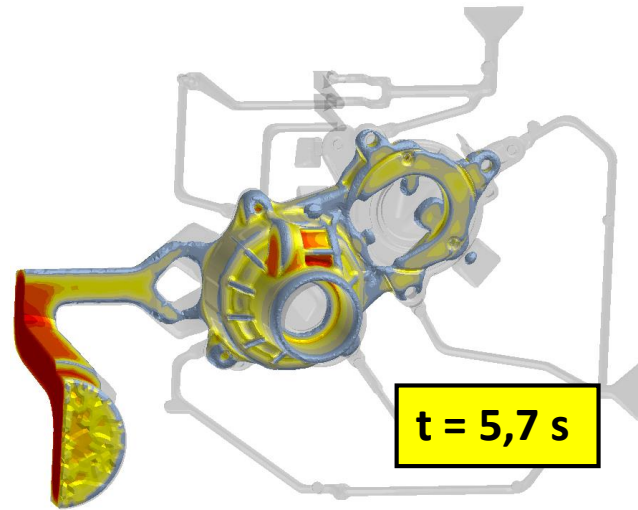
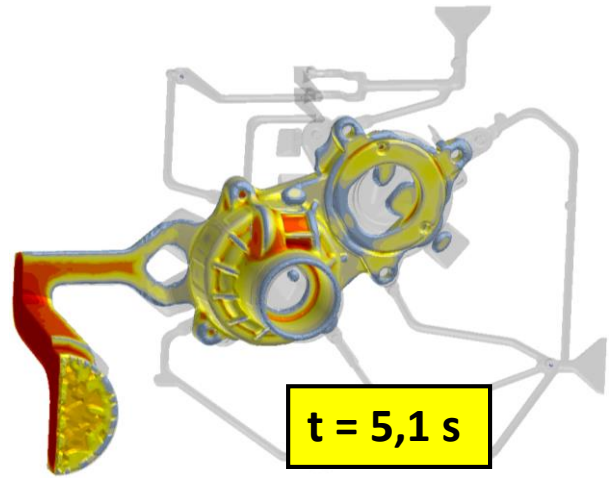
Step No / Time Step : 2096 / 2.258e-002
Simulated Time : 1.5648 sec
Percent Filled : 100.0
Fraction Solid : 0.0



- **Unidirectional solidification is not possible**

ProCAST

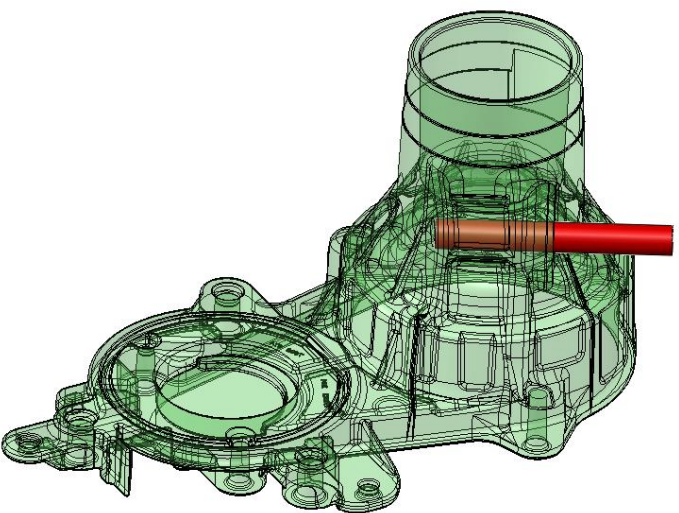
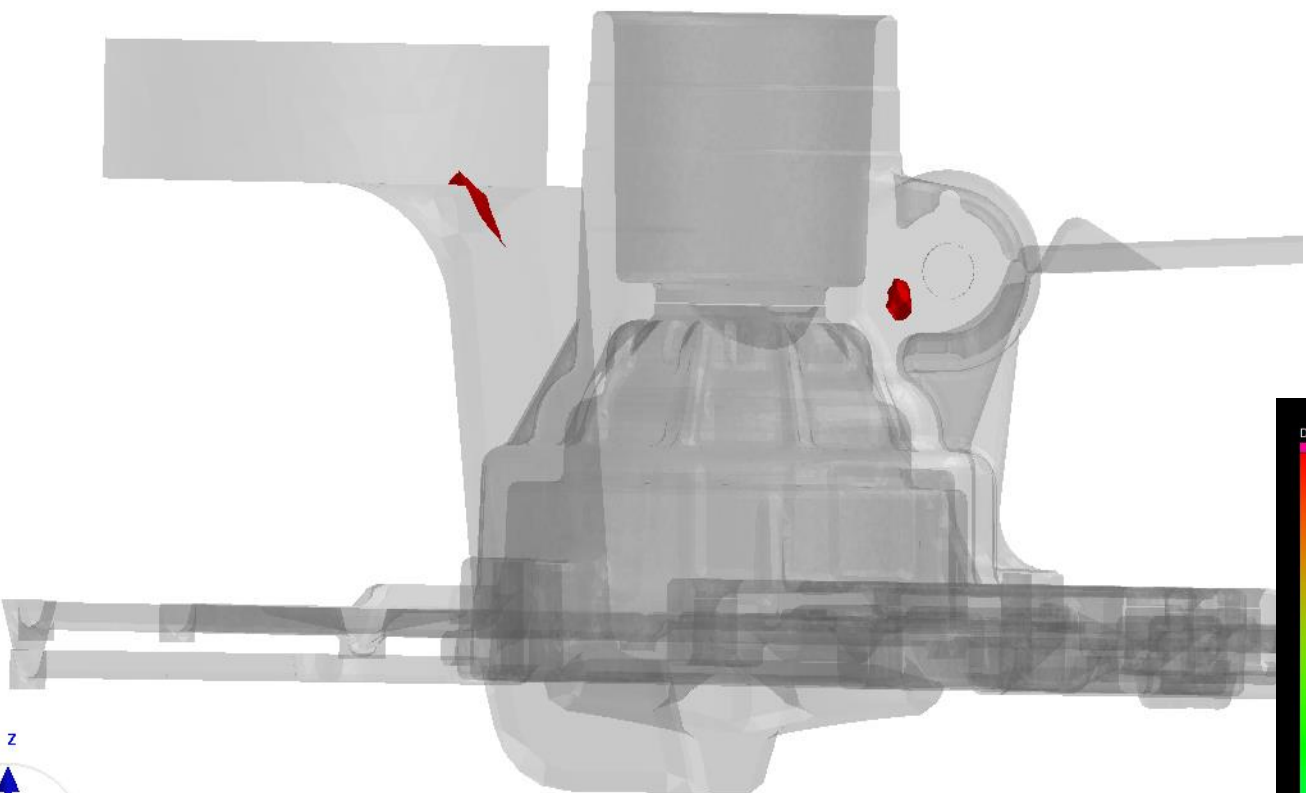
***Calculation of solidification sequence versus time / Last solidified areas in the casting**



Calculation of porosity with out of LS / hole in the as cast state

squeez_LTH

Total Shrinkage Porosity [%]



*Presented shrinkage porosity areas are not allowed, with help of the local squeezing can be eliminate

Parameters of loc. squeezing

The screenshot displays a CAD software interface with a 3D mesh model of a mechanical part. A red circular region is highlighted on the model, with a dimension line indicating a diameter of 11 mm. The interface includes a menu bar, a toolbar, and a file explorer on the left. Two windows are open:

- Process Condition Manager:** A table listing process conditions.
- Process Condition Database:** A window showing the details of a selected process condition, including a table of properties and values.

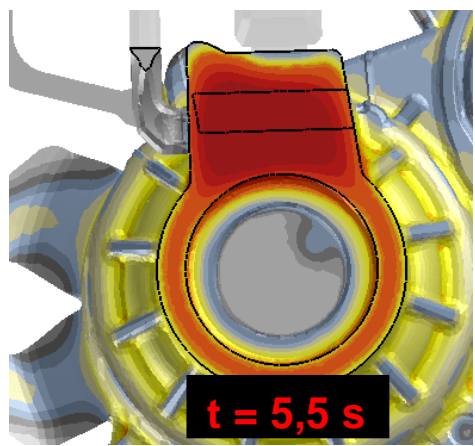
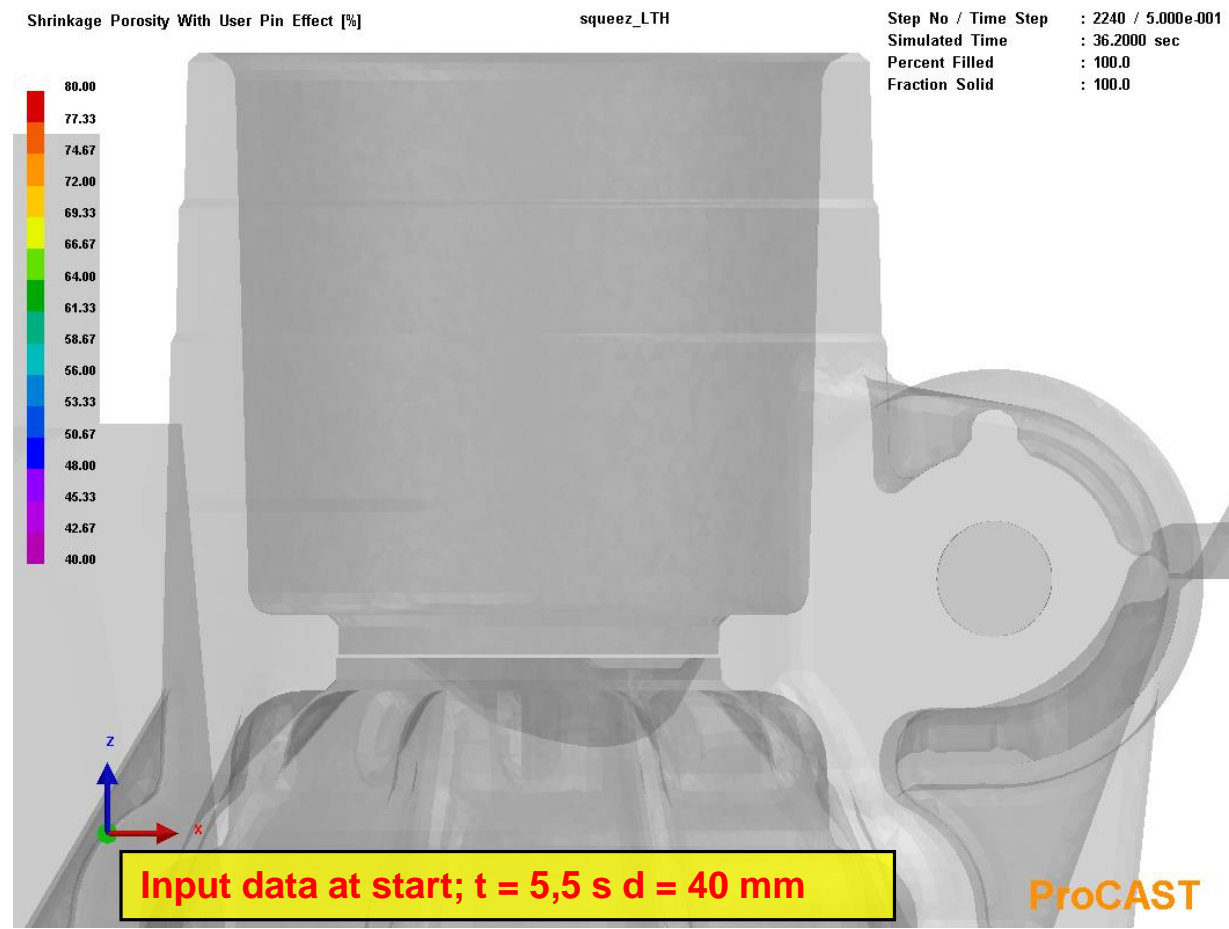
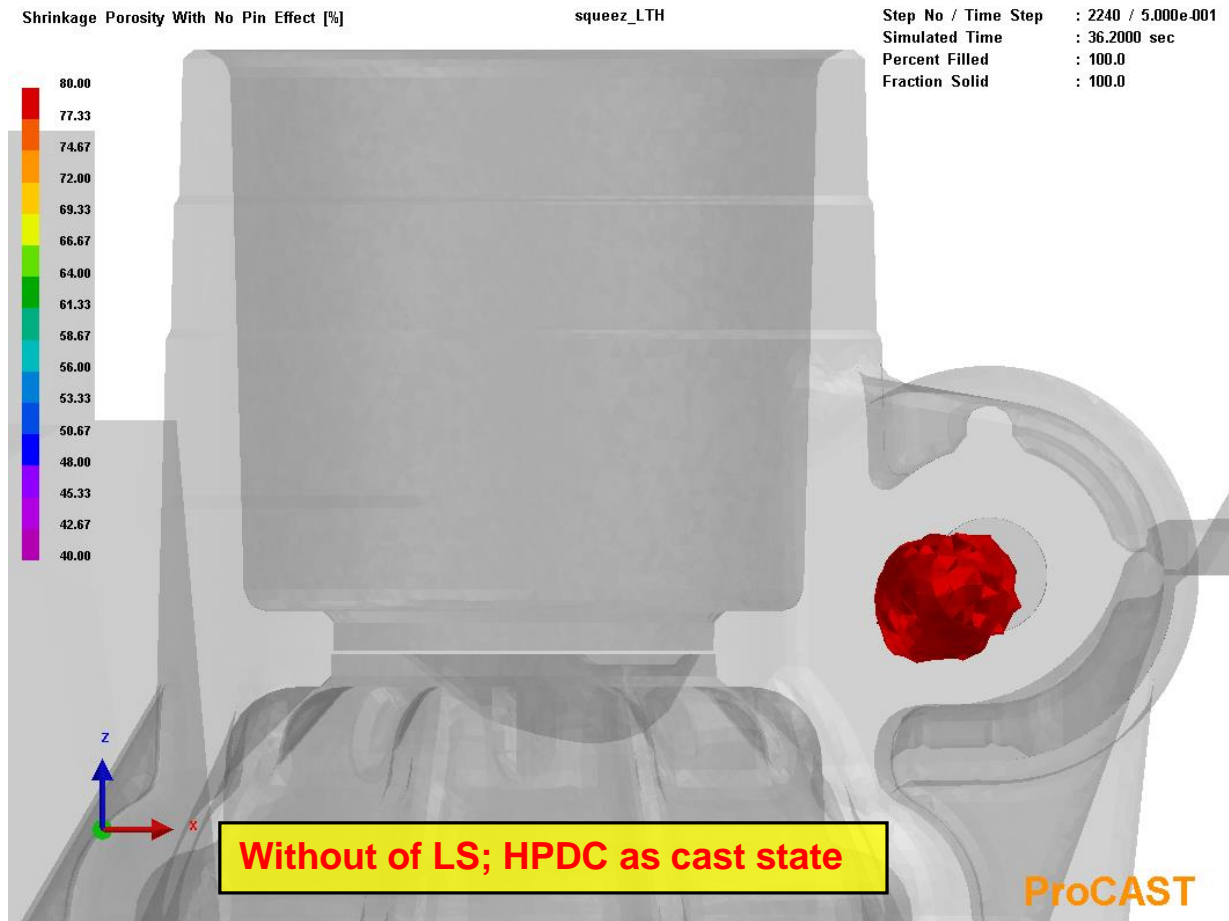
Process Condition Manager Table:

SL	Name	Type	Entity	Boundary Cond.	Area(Sq. m.)
7	Heat_6	Heat	USER_kanalai_stabilna	kanal_180_stopinj	114221.51...
8	Heat_7	Heat	USER_kanalai_stransko...	kanal_160_stopinj	25096.1575
9	Heat_8	Heat	USER_fontana	kanal_120_stopinj	11406.8902
10	Heat_9	Heat	USER_obroc_komora	voda_obroc	4256.7085
11	Translate v(x)_1	Translate v(x)	bat	LTH_gorse_mag_V1	
12	Pin Squeeze	Pin Squeeze	USER_Pin Squeeze	Squeeze_t-5_5-d...	78.4271

Process Condition Database Table:

Property	Value	Unit
Activation Time	5.5000e+000	sec
Withdrawal Time	1.7000e+001	sec
Push-in Distance	3.0000e-002	m

Calculation of s. porosity

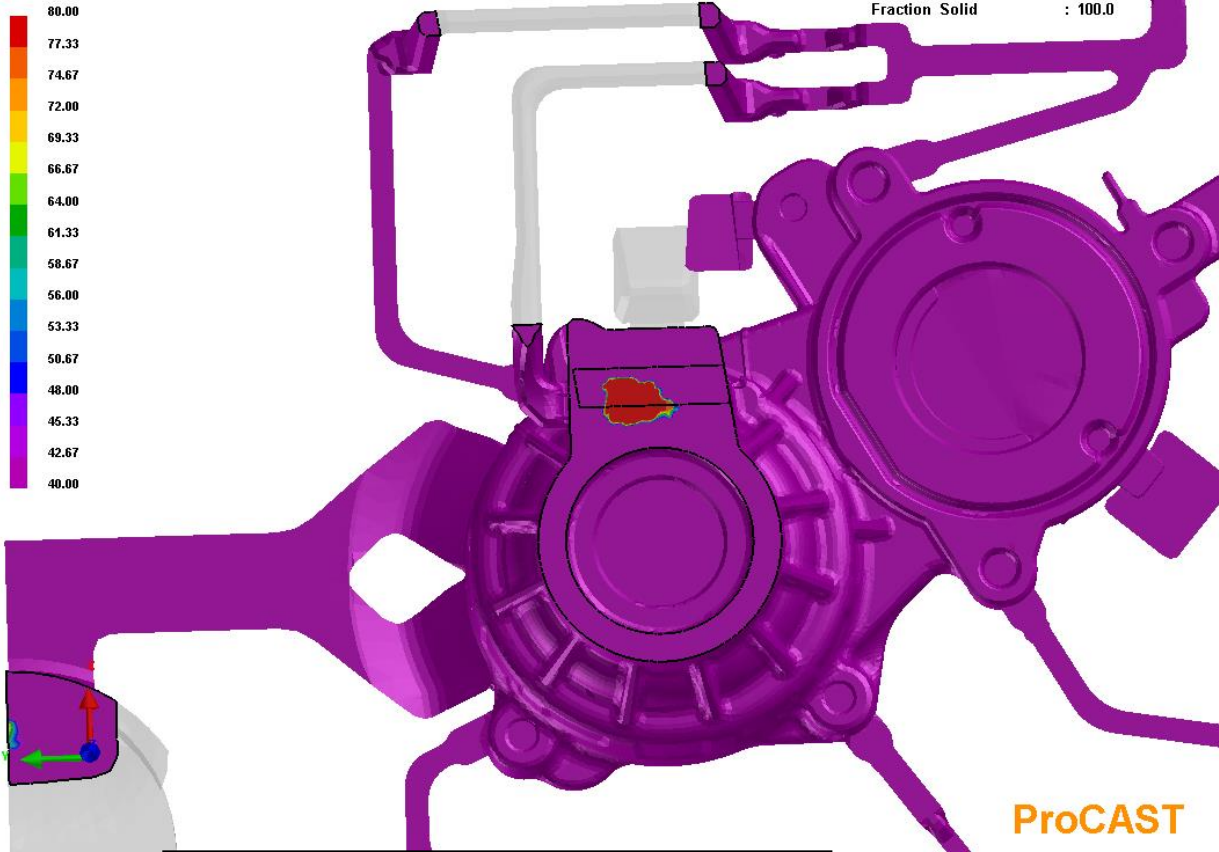


Calculation of porosity

Shrinkage Porosity With No Pin Effect [%]

squeeze_LTH

Step No / Time Step : 2240 / 5.000e-001
Simulated Time : 36.2000 sec
Percent Filled : 100.0
Fraction Solid : 100.0

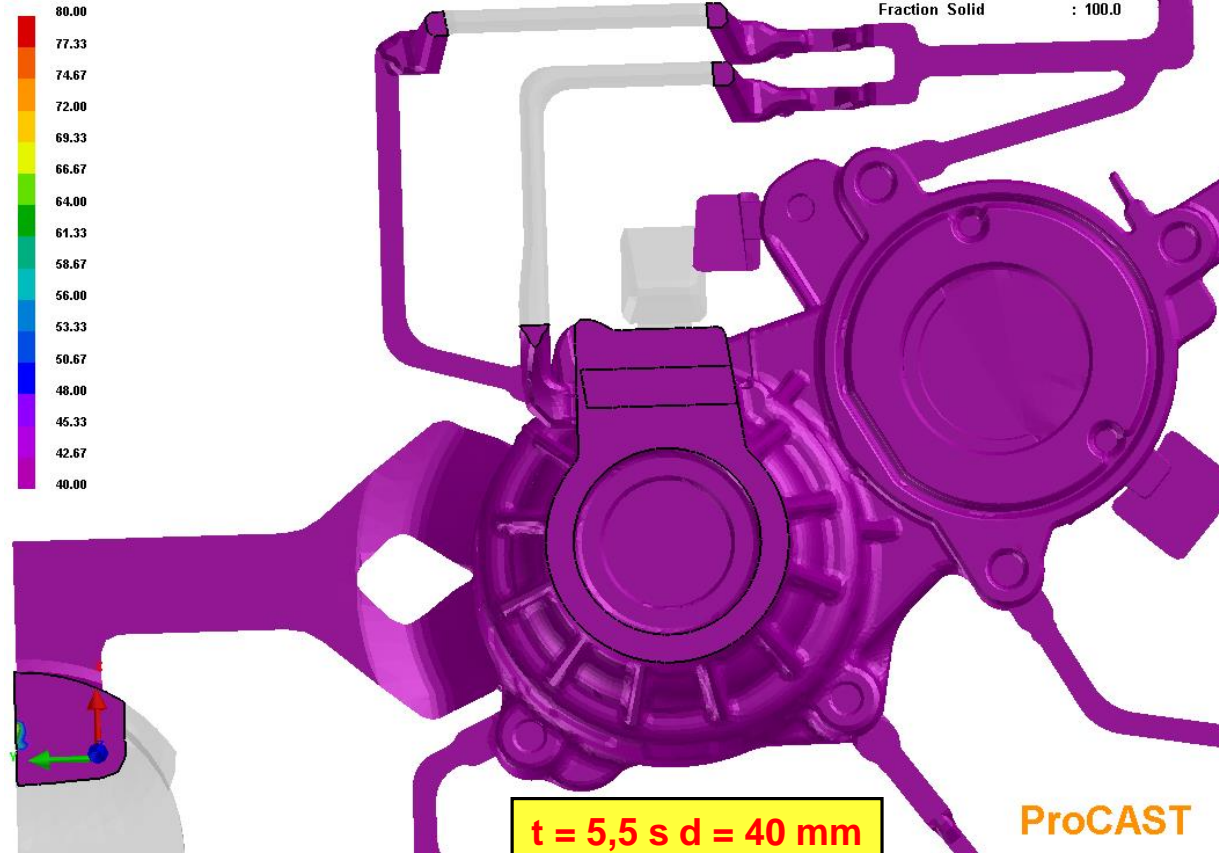


Without of LS; HPDC as cast state

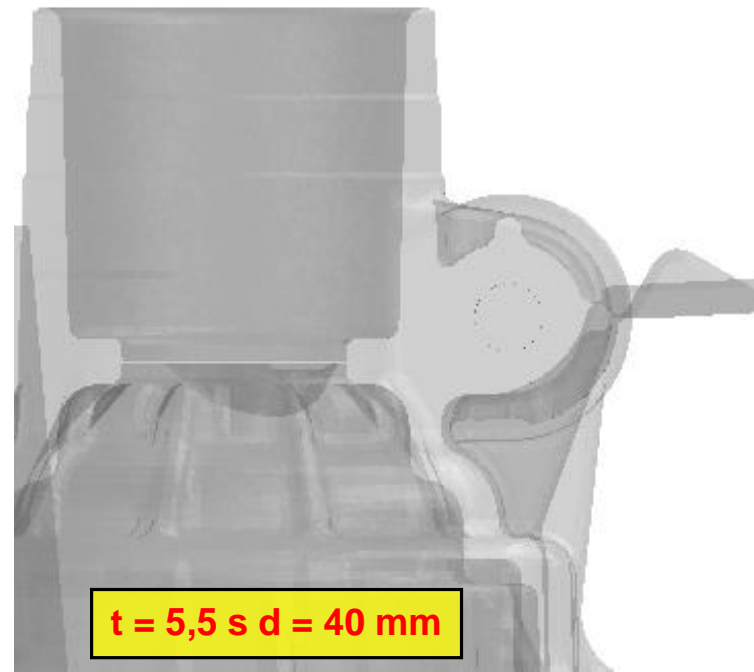
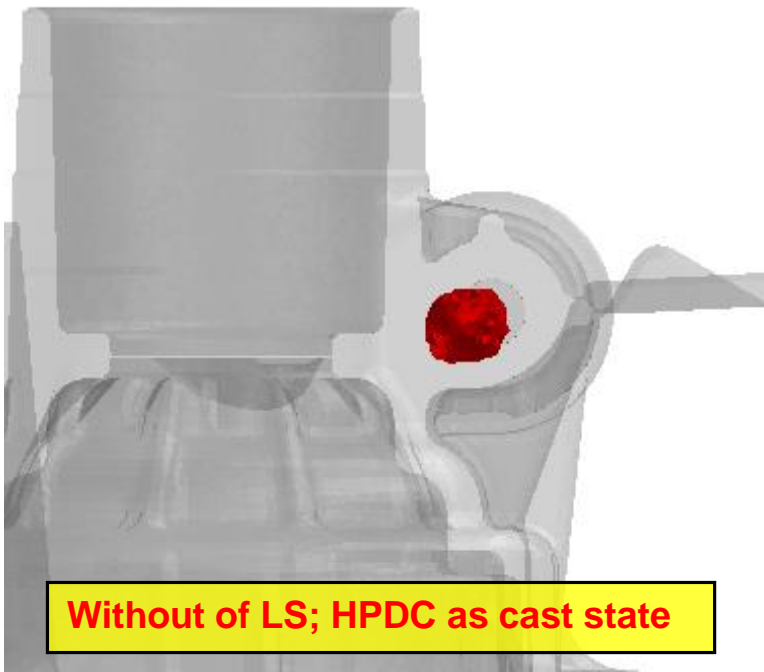
Shrinkage Porosity With User Pin Effect [%]

squeeze_LTH

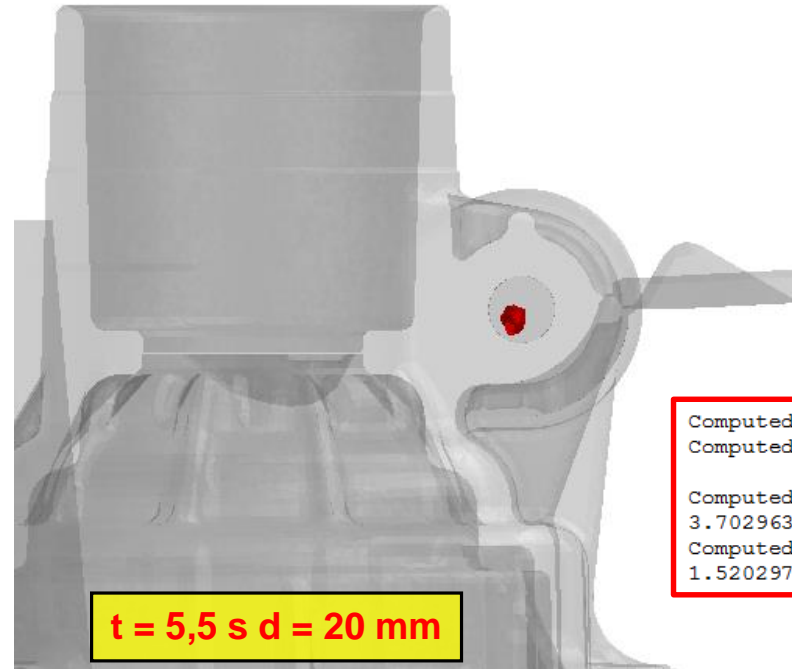
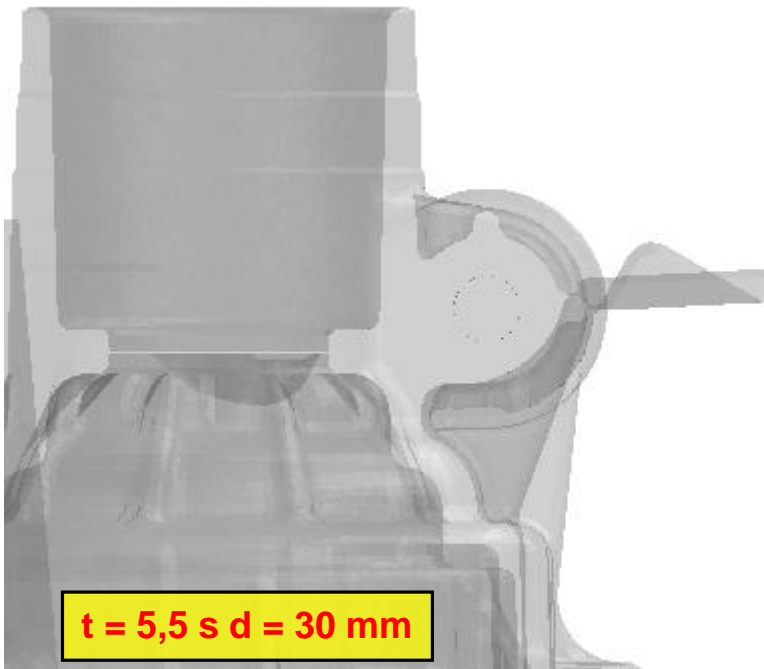
Step No / Time Step : 2240 / 5.000e-001
Simulated Time : 36.2000 sec
Percent Filled : 100.0
Fraction Solid : 100.0



t = 5,5 s d = 40 mm



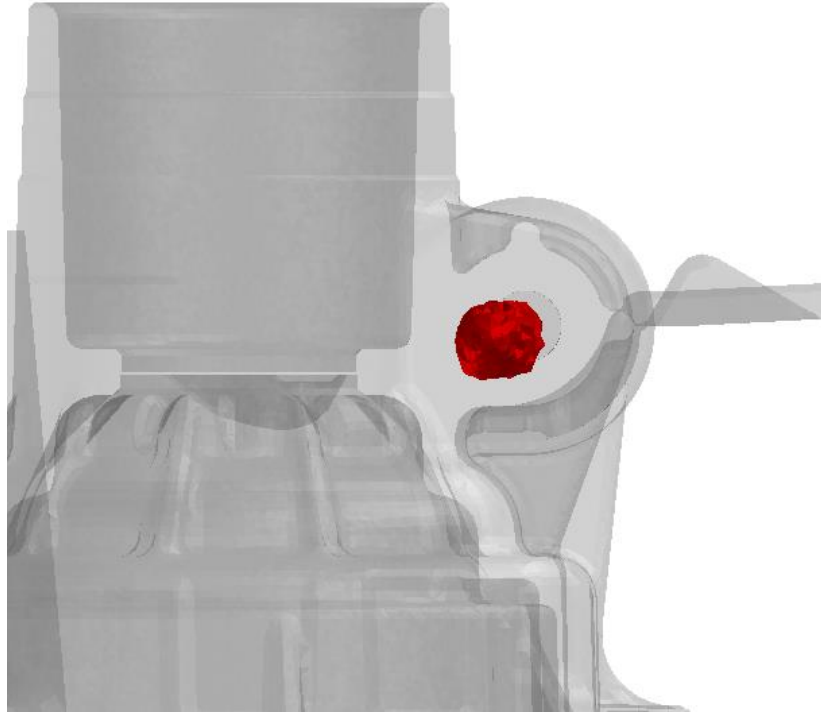
- Calculation of s. porosity; $t = \text{const.}$, path distance is changing



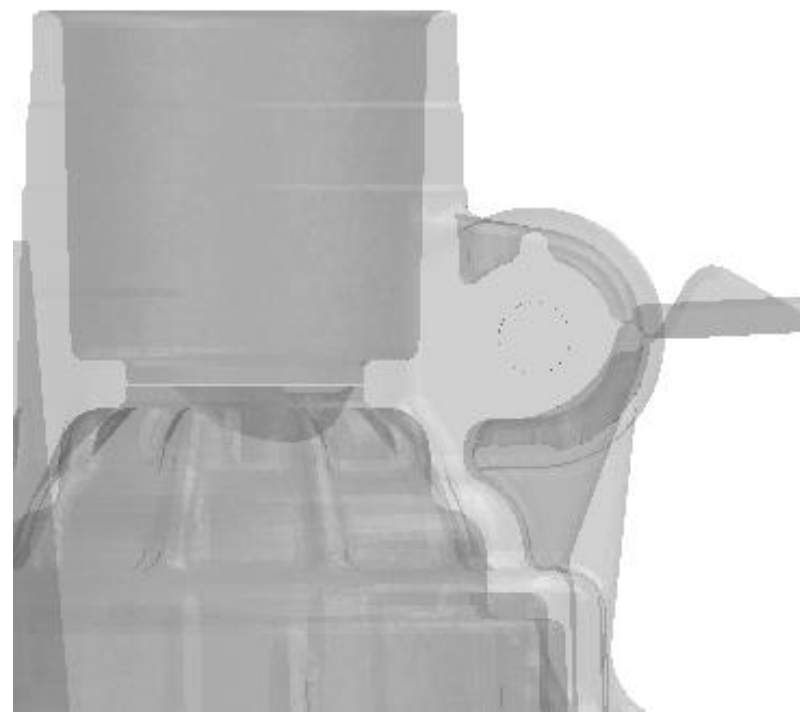
Optimal parameters

```
Computed squeeze pin activation time = 5.199998e+00 seconds  
Computed squeeze pin withdraw time   = 1.670001e+01 seconds  
  
Computed squeeze pin activation time (after filling) =  
3.702963e+00 seconds  
Computed squeeze pin withdraw time   (after filling) =  
1.520297e+01 seconds
```

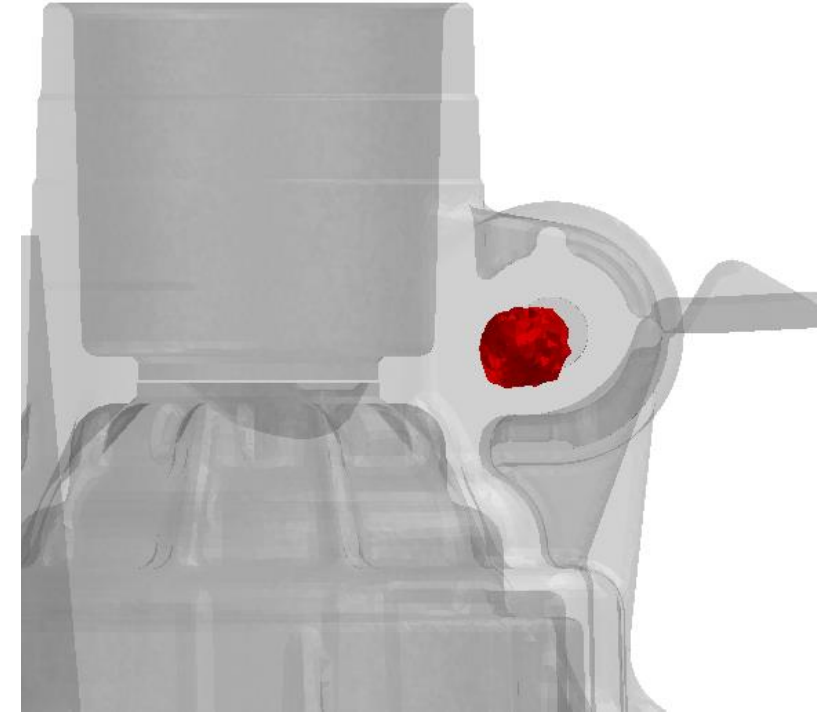
- Calculation of porosity; - path distance = const., - time is changing



t = 3,0 s d = 40 mm

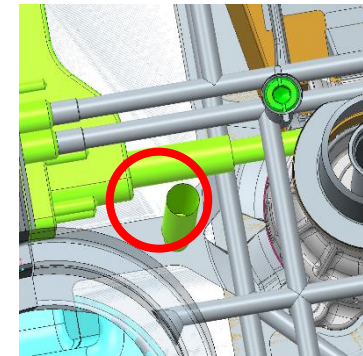
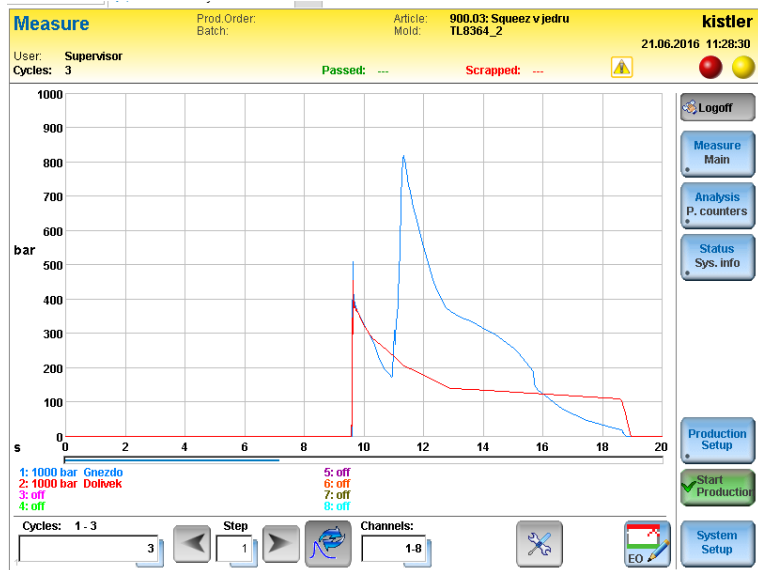
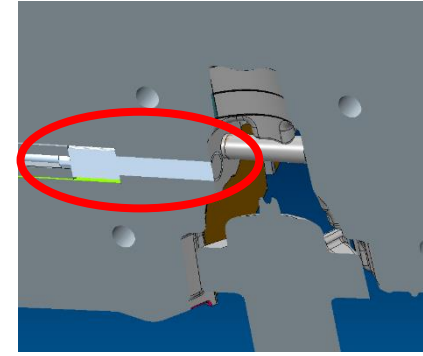
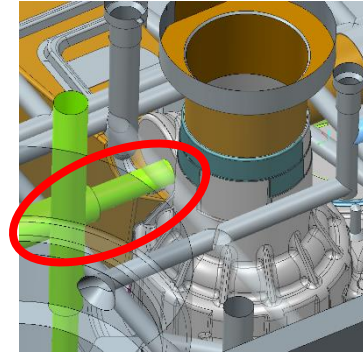
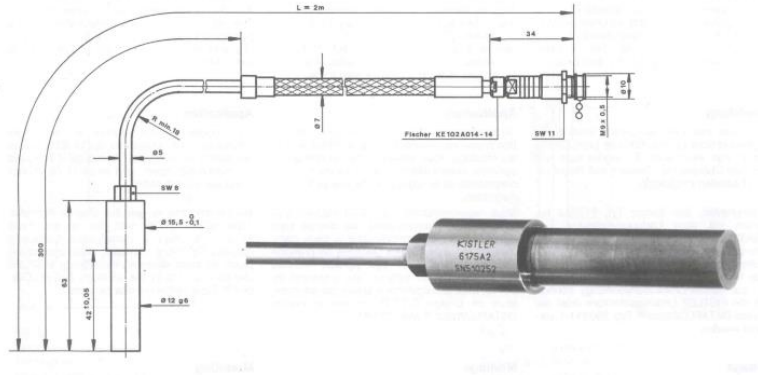


t = 5,5 s d = 40 mm



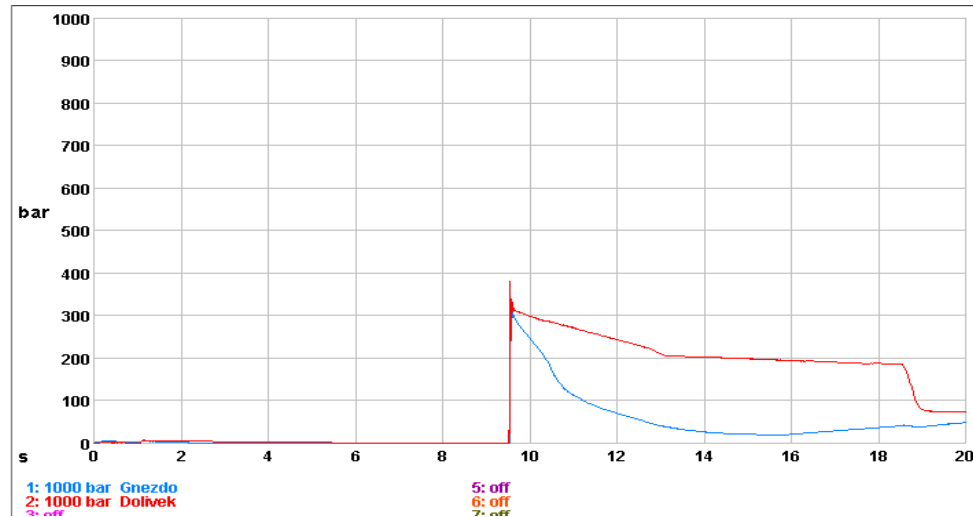
t = 9,0 s d = 40 mm

- Measurements of pressure at LS process

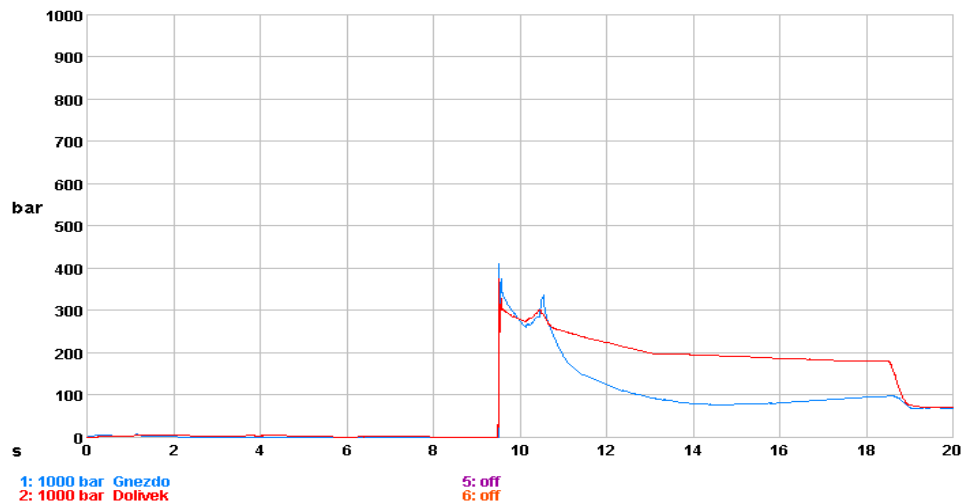


2 Pressure sensors was implemented on gating system and on local squeezing area

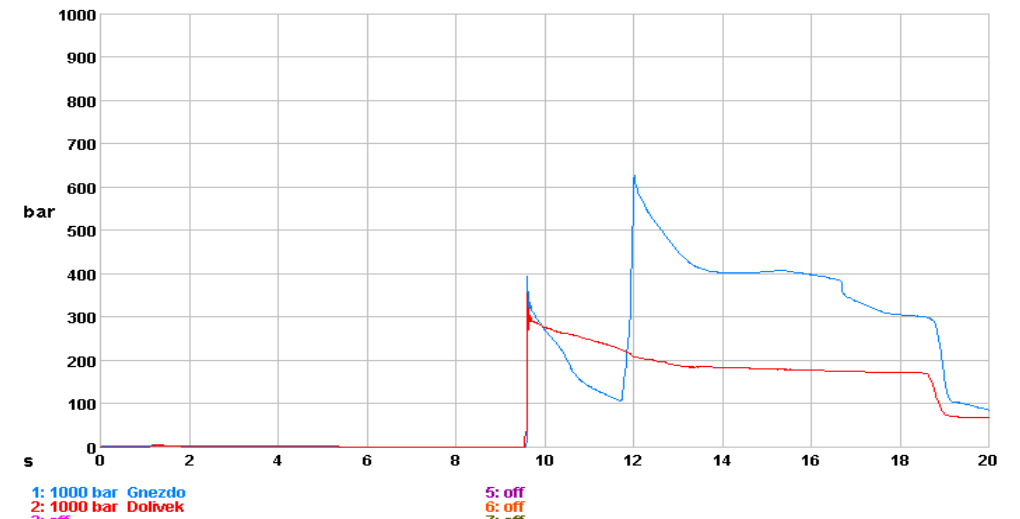
- without squeeze pin (as cast state)



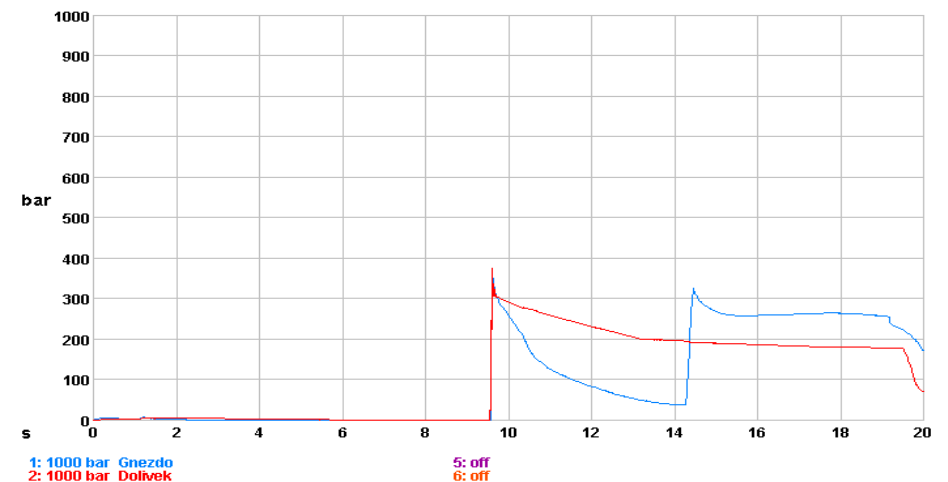
- 0,5 s squeeze pin start delay after change from II to III sequence



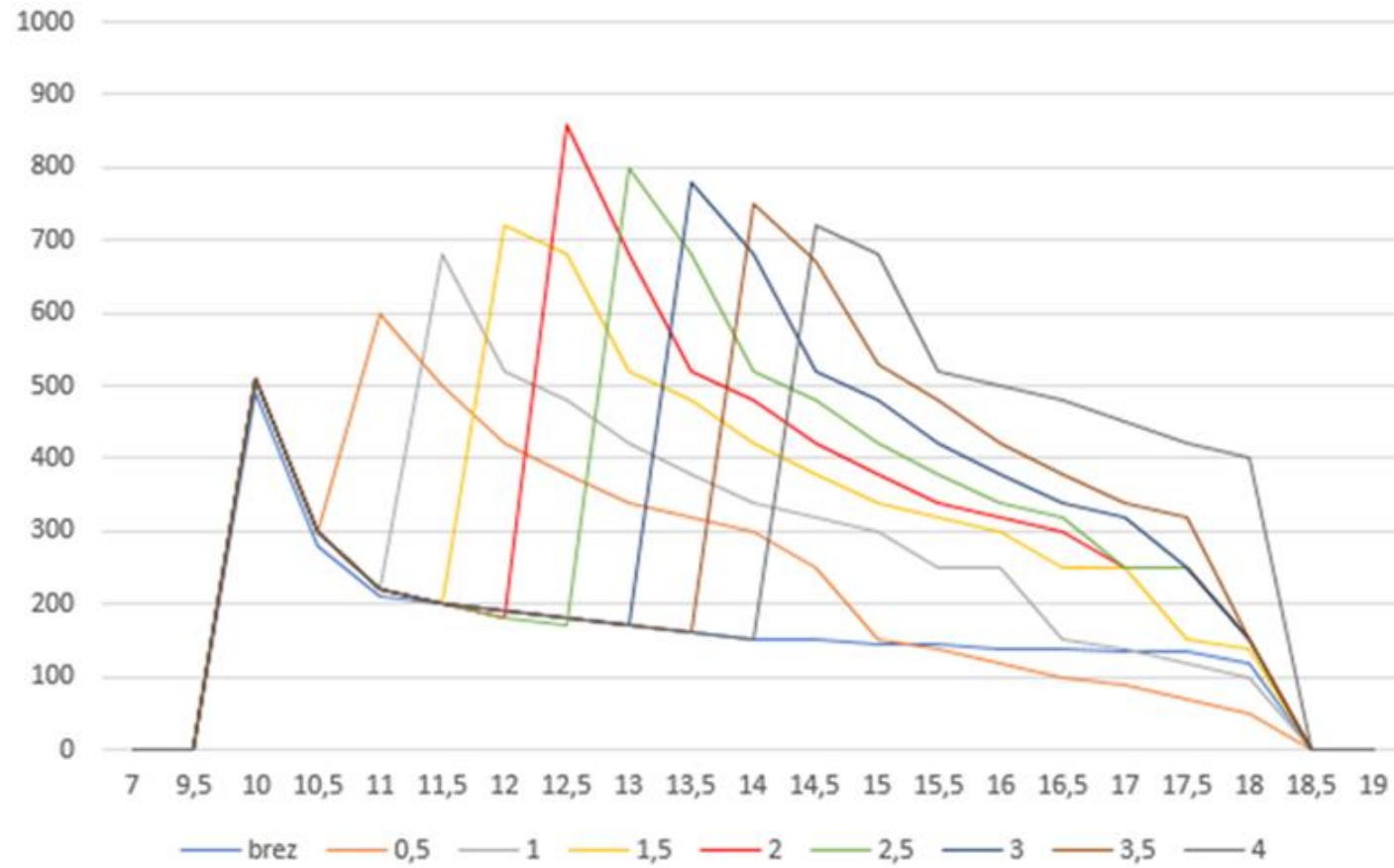
- 2s squeeze pin start delay after change from II to III sequence



- 4,5s squeeze pin start delay after change from II to III sequence

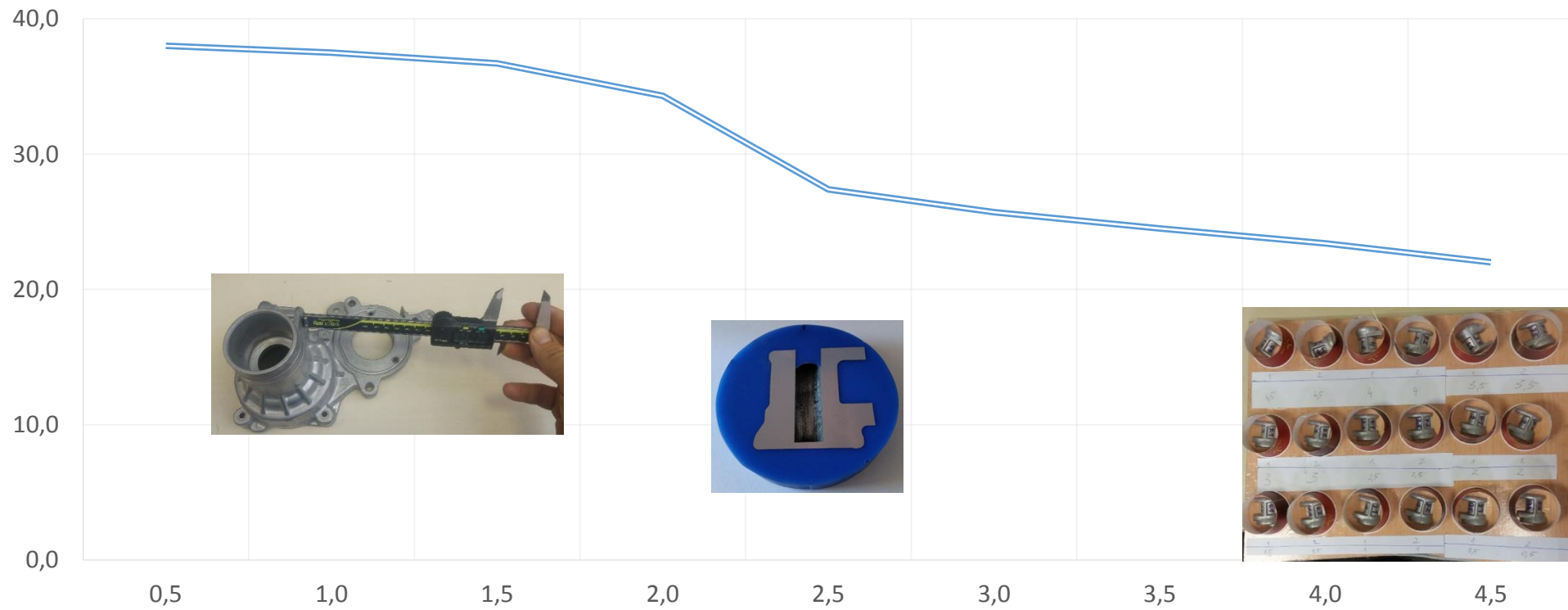


Time of squeeze pin start delay after change from II to III sequence

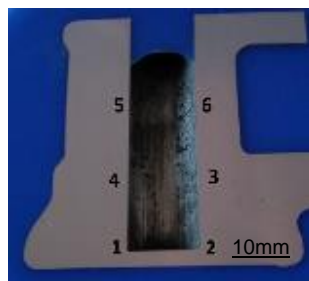


- Depth of squeeze pin implementation (path of LS pin)

Number of experiment	1	2	3	4	5	6	7	8	9	10
Time of delay after end of II. seq. [s]	0,5	1,0	1,5	2,0	2,5	3,0	3,5	4,0	4,5	6,0

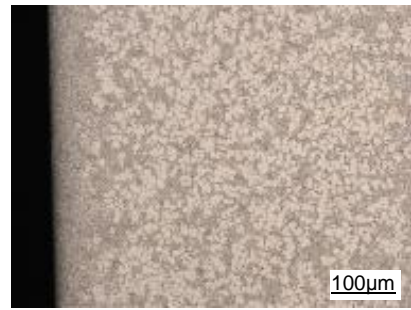
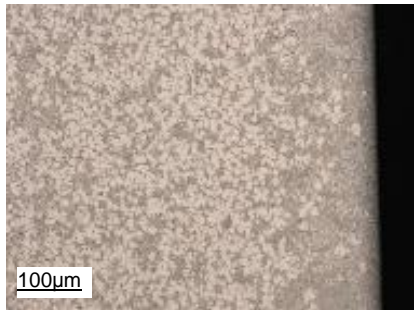


$t_{LSP} = 0,5 \text{ s}$



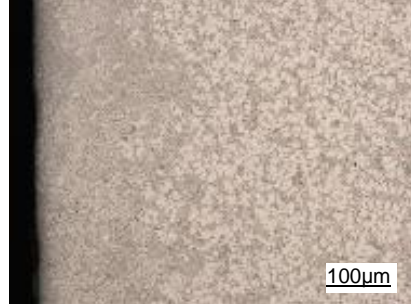
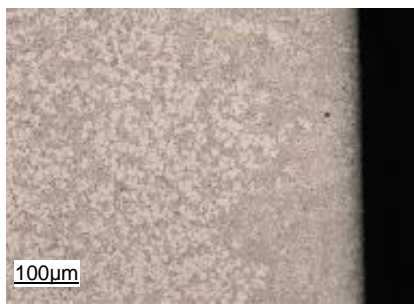
Mesto 5

Mesto 6



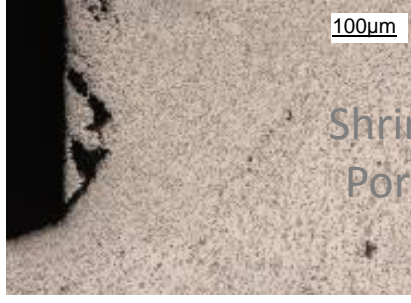
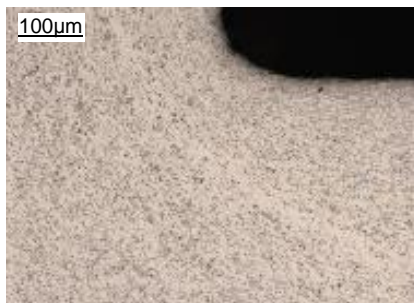
Mesto 4

Mesto 3

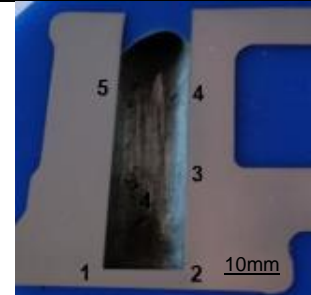


Mesto 1

Mesto 2

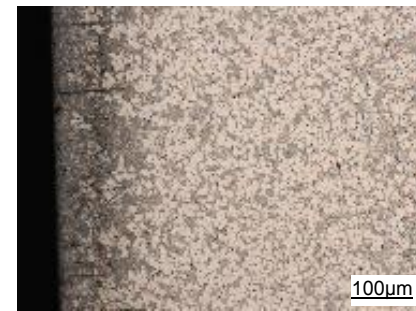
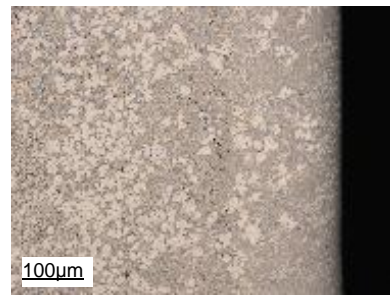


$t_{LSP} = 1 \text{ s}$

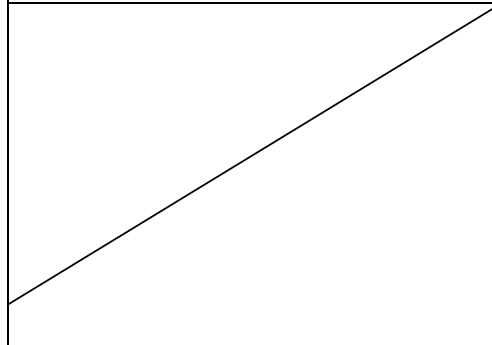


Mesto 5

Mesto 4

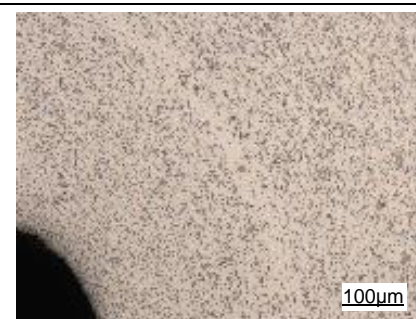


Mesto 3

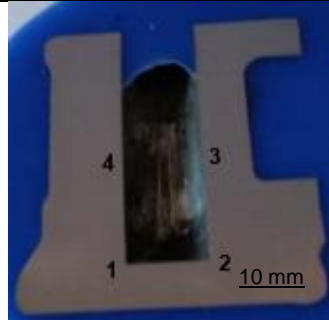


Mesto 1

Mesto 2

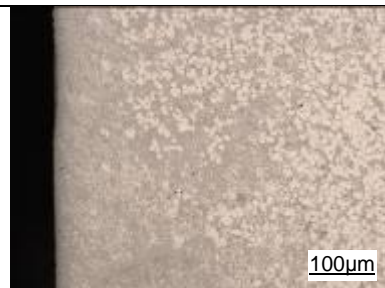
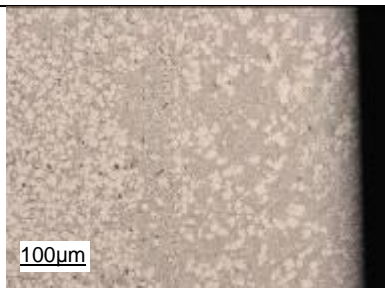


tLSP = 2 s



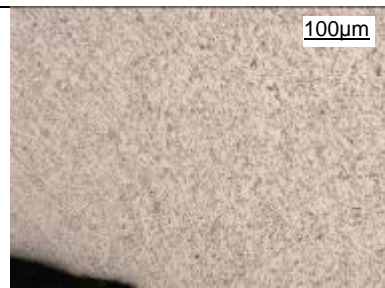
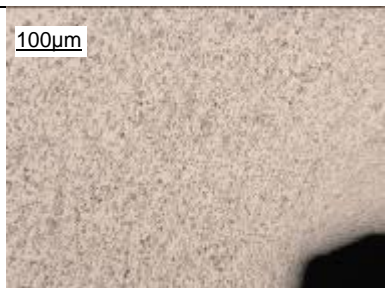
Mesto 4

Mesto 3

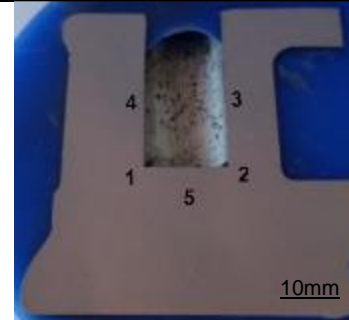


Mesto 1

Mesto 2

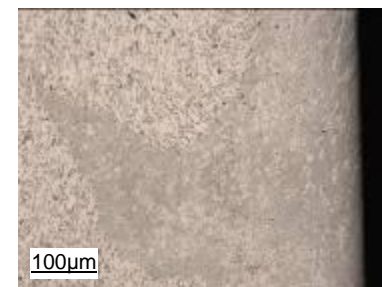
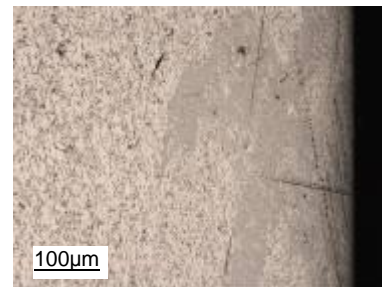


tLSP = 4,5 s



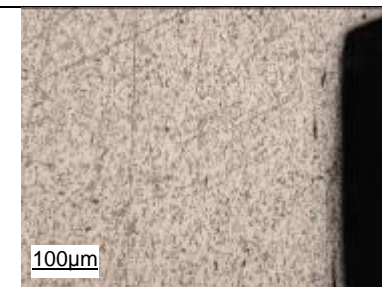
Mesto 4

Mesto 3

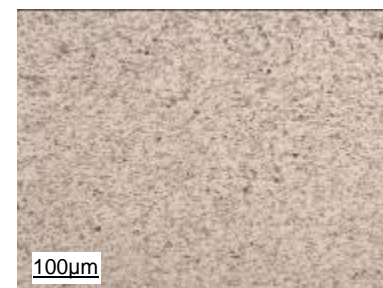


Mesto 1

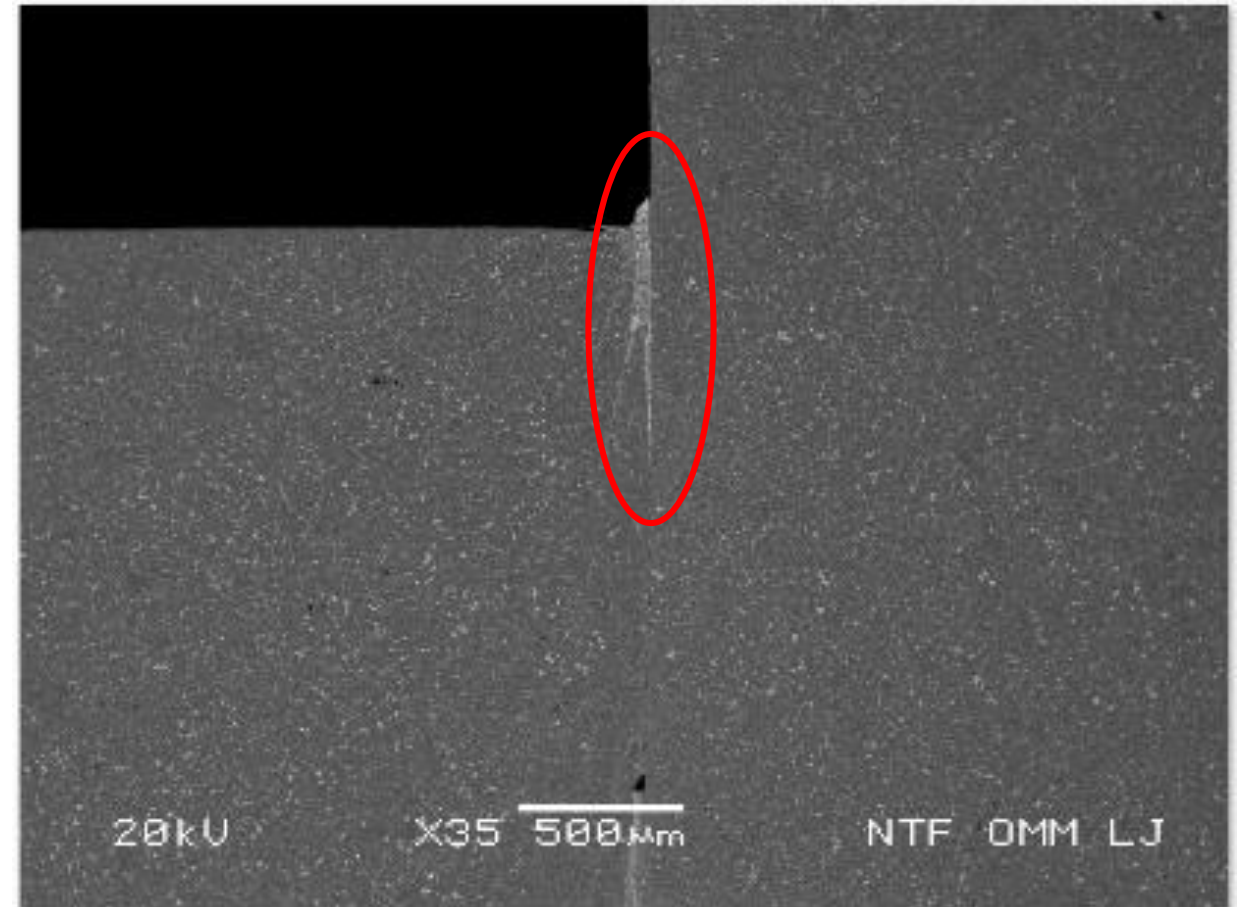
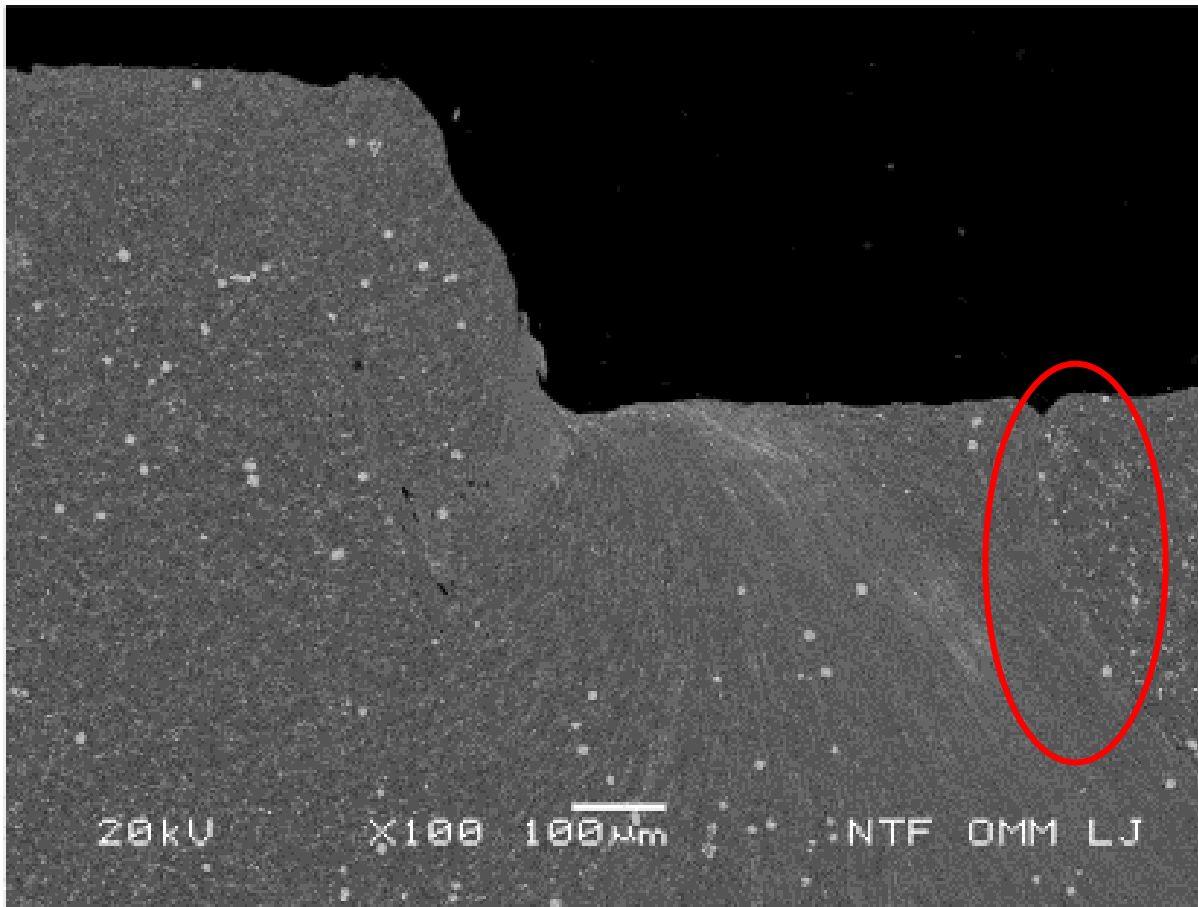
Mesto 2



Mesto 5

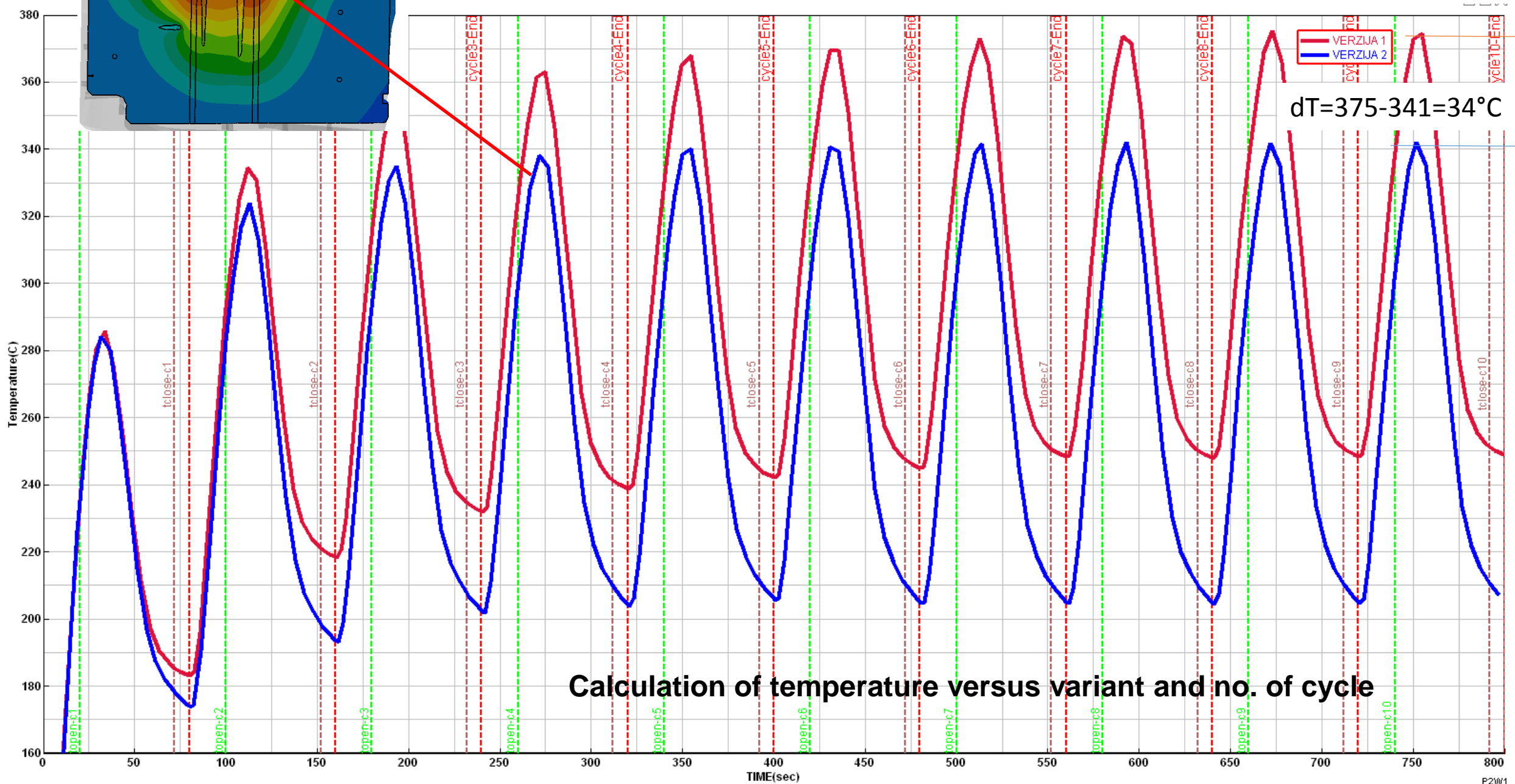


- Microstructure of casting on area where LS occurred; 226

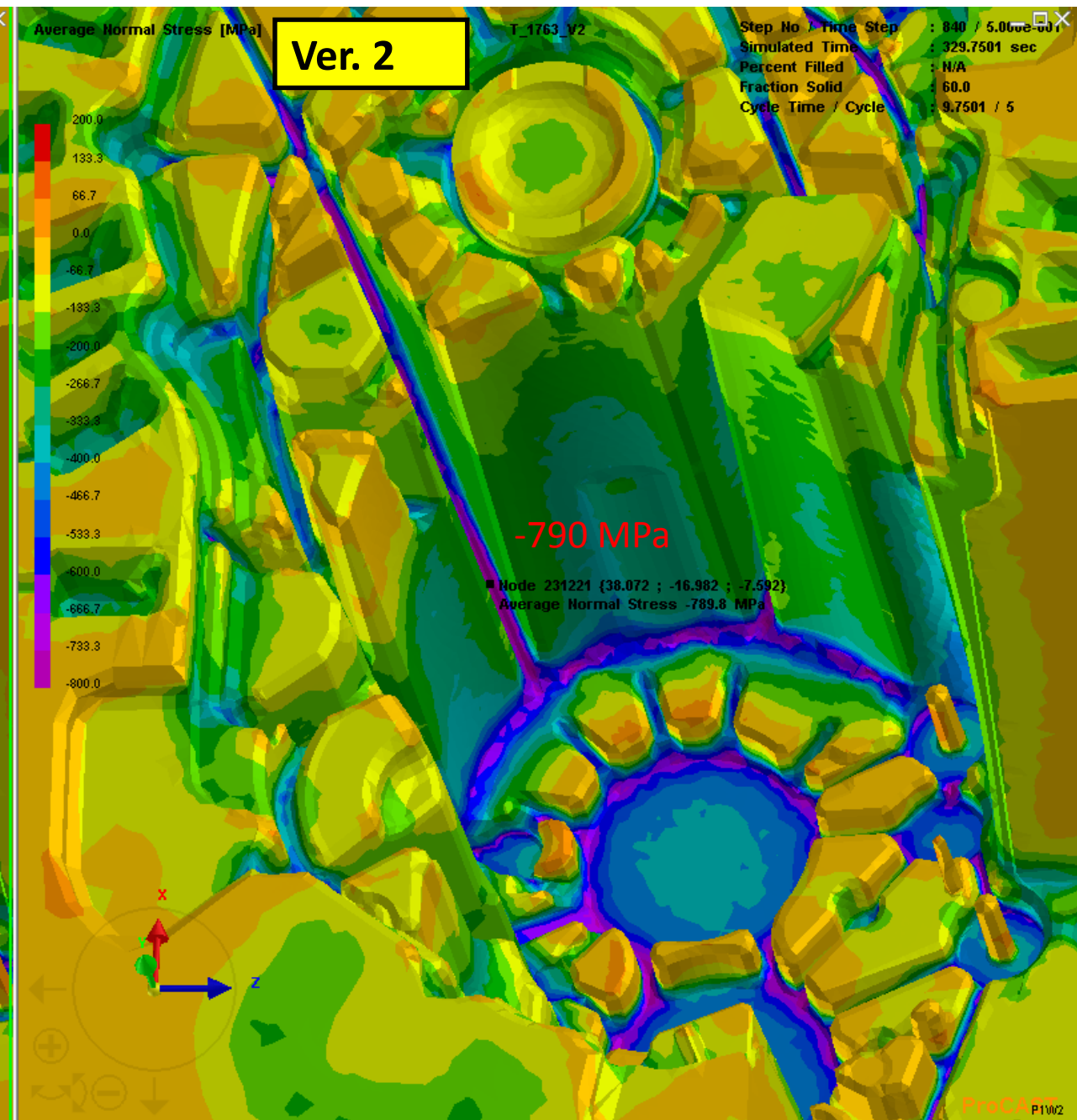
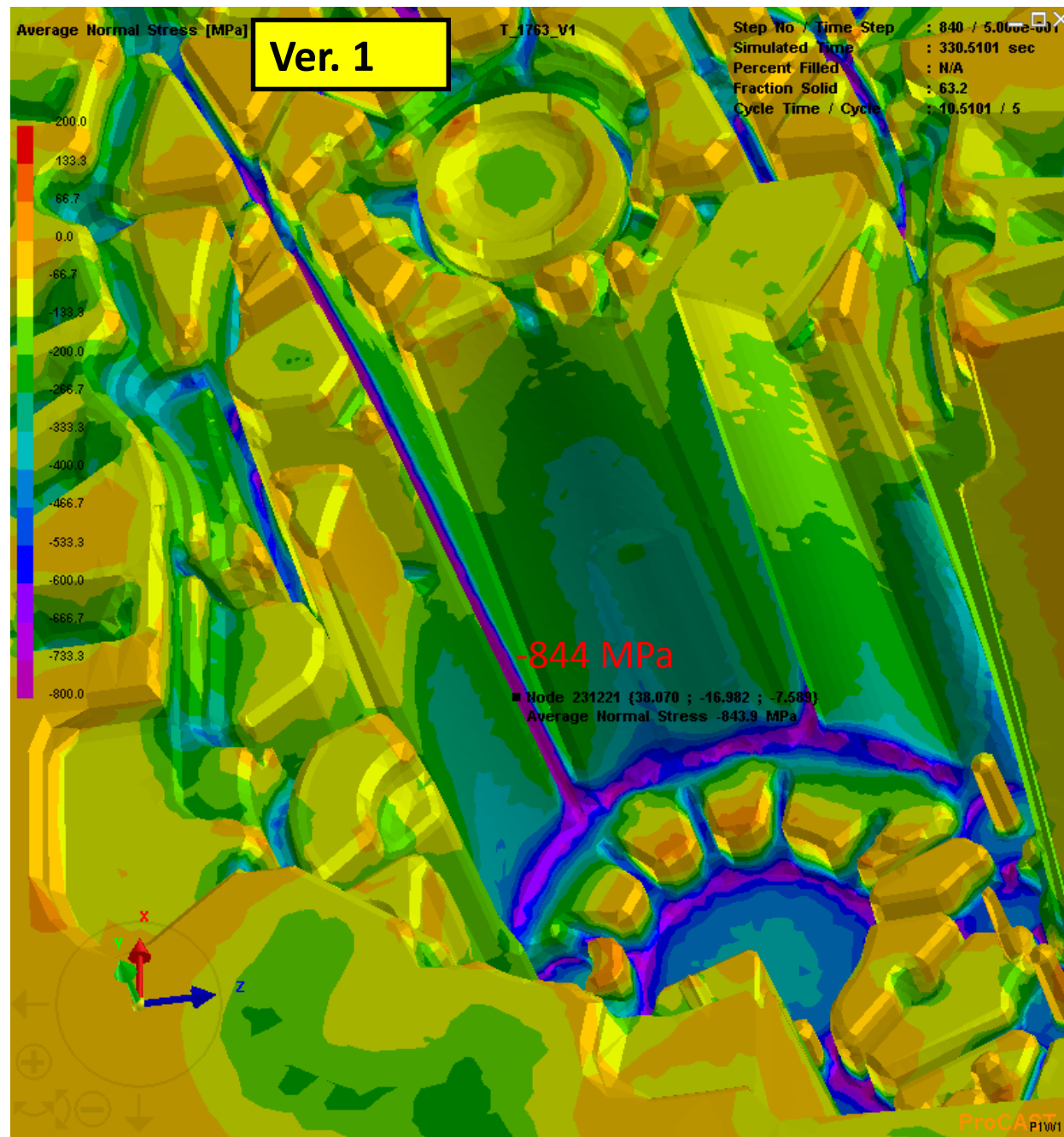


- Cold laps,
- Flow lines

- Effective cooling

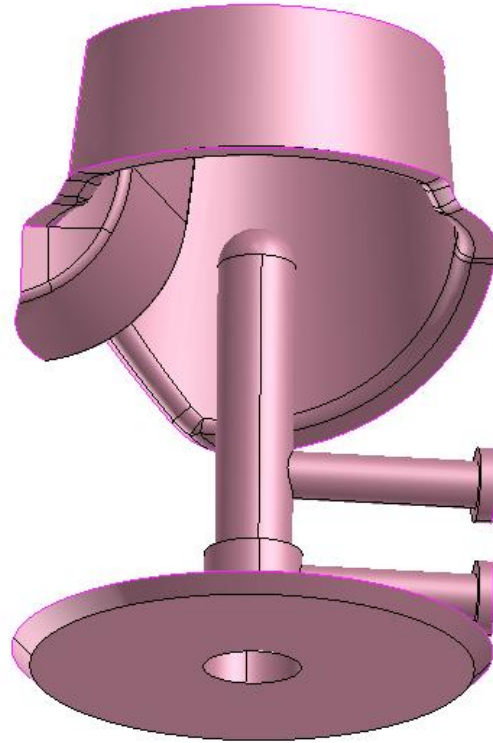
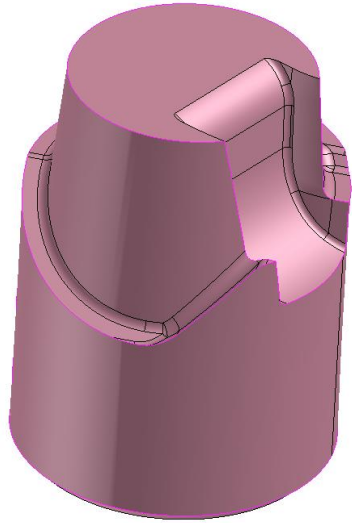


The calculation of normal stresses in the tool

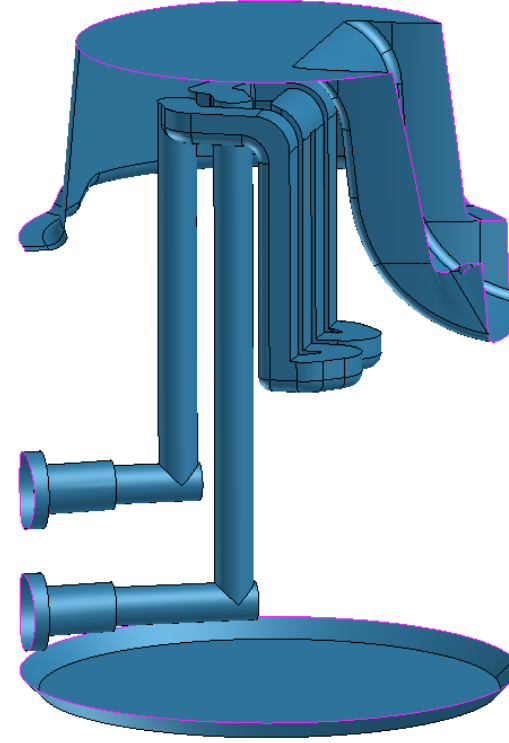




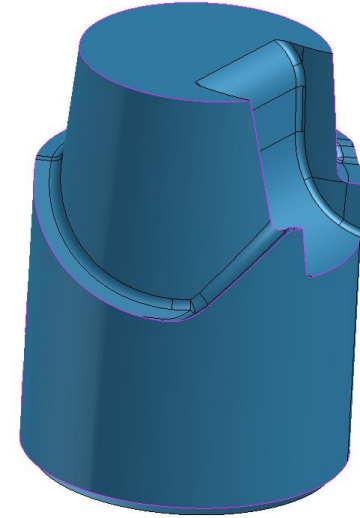
Example 2: Technology optimization - distributor



ver. 1



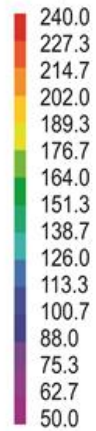
ver. 2





Technology optimization - distributor

Temperatura (°C)



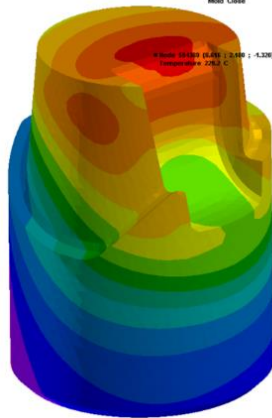
Temperature in critical area was in ver. 1- 235,3 °C, with new cooling system the temperature was 94,7 °C

Temperature drop with new cooling system was 60 %.
Stresses with new cooling system were lower for 47 %.

Distributor with version 1 cooling system made 65.080 cycles, new distributor made 79.129 cycles. Life time prolonged for 21 %.



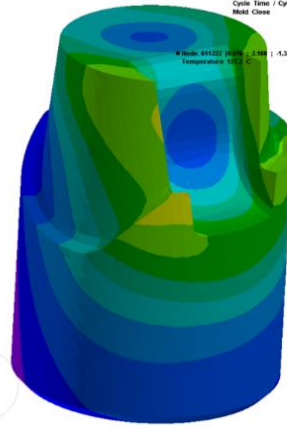
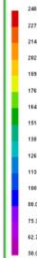
Temperature [C]



T-1595_V1

Step No / Time Step : 2389 / 5.816e+05
Simulated Time : 648.6563 sec
Percent Elapsed : 98.8
Fraction Solid : 98.2
Cycle Time / Cycle : 64.6563 / 18
Mold Close

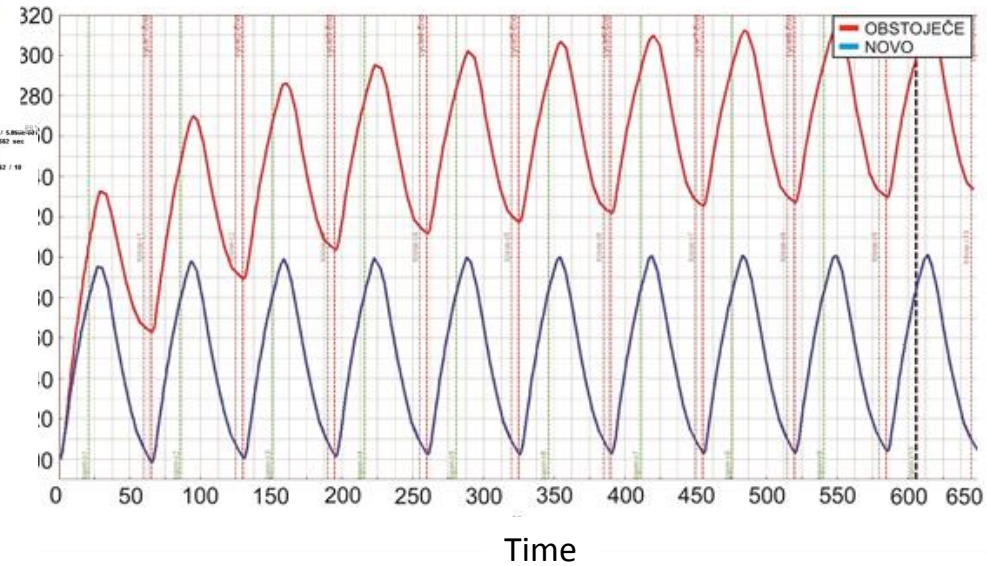
Temperature [C]



T-1595_V2

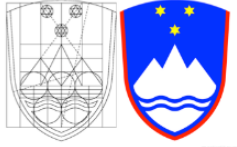
Step No / Time Step : 3488 / 5.816e+05
Simulated Time : 648.7562 sec
Percent Elapsed : 98.8
Fraction Solid : 98.2
Cycle Time / Cycle : 64.7562 / 18
Mold Close

ProCAST



Short conclusions

- Including advanced numerical simulations in early technology development phase can reduce costs:
 - optimal casting technology can be defined before real testing
 - casting defects under acceptable limits
 - finding critical areas during design phase
- With adequate process and technology optimization it is possible to:
 - prolong the dies lifetime
 - shorten production cycle of casting
- With displacement of internal cooling and heating channels near the casting cavity surface the temperature field and also stresses are decreased
- Experimentally determined d_l values vs. T can be usefully applied for prediction of total contraction in HPDC part
- With help of calculation of casting process it is possible to realize the technology and technological process window before the tool is manufactured
- When the unidirectional solidification is not possible the use of LS can be accepted.
- Time of delay have to be calculate for each geometry and depended from local fracture solid. Calculated and experimentally obtained values are practical the same value.
- Microstructure analyses show that according to technological process window no critical areas was found.
- Pressure of III. sequence can be generally decrease what cause lover residual stress.



SREČNO!
ЗВЕСНО!

Good luck!
GOOD LUCK!



18th INTERNATIONAL FOUNDRYMEN CONFERENCE

Coexistence of material science and sustainable technology in
economic growth

Sisak, May 15th-17th, 2019

<http://www.simet.hr/~foundry/>

NEW TESTS FOR CHEMICALLY BONDED FOUNDRY SANDS

Sam Ramrattan*

Western Michigan University, Kalamazoo, Michigan, USA

Invited lecture

Subject review

Abstract

Chemically bonded sand cores and molds are more commonly referred to as precision sand systems in the high production automotive powertrain sector. Their behavior in contact with molten metal can lead to casting defects. Consequently, the interaction is of great interest and an important part of metal casting technology. The American Foundry Society (AFS) sand testing is based on physical, mechanical, thermal and chemical properties of the sand system. Foundry engineers have long known that certain AFS sand tests provide limited information regarding control of molding and casting quality. The inadequacy is due to the fact that sand casting processes are inherently thermo-mechanical, thermo-chemical and thermo-physical.

New AFS standardized testing has proven useful for laboratory measurement of these characteristics in foundry sand using a disc-shaped specimen. Similarly, the equivalent disc-shaped specimens are used for casting trials. In order to accomplish near-net-shape casting with minimal defects, it is necessary to understand both the properties of the sand system, as well as the interface of molten metal when different binders, additives and/or refractory coatings are used. The methodology for the following chemically bonded sand tests is described:

- Disc Transverse
- Impact
- Modified Permeability
- Abrasion
- Thermal Distortion
- Quick Loss on Ignition

The analysis and interpretation of data related to the new standard sand tests are discussed.

Keywords: *chemically bonded sand, permeability test, thermal distortion test, loss on ignition*

*Corresponding author (e-mail address): ramrattan@wmich.edu



18th INTERNATIONAL FOUNDRYMEN CONFERENCE

Coexistence of material science and sustainable technology in economic growth

Sisak, May 15th-17th, 2019

<http://www.simet.hr/~foundry/>

INTRODUCTION

The most popular medium for the production of cast powertrain metal parts is sand. Sand has many pluses, but it is far from perfect. Problems with chemically bonded sand systems arise from variation in materials and processes. This can come from many sources such as grain size, grain shape, chemical composition, binder level, additives, work-time, strip time, pouring temperature, metallostatic pressure, etc. [1]. Thus, chemically bonded sand has many potential sources of variation; but it is still subject to the pressures of delivering near-net shaped castings. Understanding those variations is a key issue for achieving good process control, and there have been several studies toward that end.

Sand's versatility and ease of use foster rapid innovation in an industry where the ability to change quickly can mean survival. This is especially true with the development of chemically bonded sand systems. Unfortunately, the binder system is also a significant source of variation. The concentration of binder in the sand, and the mix of the binder constituents can all have significant effects on the final castings. Additionally, new binders are constantly being developed in response to various environmental and product quality concerns, thus creating new potential sources of variation.

Chemically bonded sands used with cores and molds are conventionally processed by techniques such as hot-box, no-bake, and cold box [1]. When sand composites (mold and core media) come in contact with elevated temperature, the heat transferred causes thermo-mechanical movement and thermo-chemical reactions that result in dimensional changes at the mold-metal interface. At any given temperature these dimensional changes or thermal distortions are attributable to simultaneous changes in both the sand and the binder. Depending on the type of binder used and the temperature at any point in the sand plane, thermally induced reactions occur simultaneously along with sand expansion leading to significant distortions in the composite shape [2].

A disc-shaped specimen has been used as a supplementary mechanical test specimen for chemically bonded sands in the foundry industry. With the support of the American Foundry Society (AFS), Western Michigan University (WMU) has developed new standardized thermo-mechanical and physical tests for chemically bonded sands employing the same simple geometry for a specimen.

The aim is to ascertain new standard foundry sand testing using chemically bonded disc-shaped specimens for:

- Disc Transverse
- Impact
- Modified Permeability
- Abrasion
- Thermal Distortion
- Quick Loss on Ignition



18th INTERNATIONAL FOUNDRYMEN CONFERENCE
**Coexistence of material science and sustainable technology in
economic growth**

Sisak, May 15th-17th, 2019

<http://www.simet.hr/~foundry/>

MATERIALS AND METHODS

The methodology consisted of two major steps; preparation of chemically bonded disc-shaped specimens and testing of disc-shaped specimens. To ensure that the study was executed methodically, an experimental design of two binder levels at elevated temperature with 15 specimens per cell was employed.

Note: All specimens were prepared and tested in laboratory conditions. Ambient conditions were controlled: temperature at $20 \pm 1^\circ\text{C}$ and relative humidity at $50 \pm 2\%$.

Preparation of PUCB Specimens

Polyurethane cold box (PUCB) specimens were prepared using washed and dried round grain silica sand (Table 1).

Table 1. Properties of PUCB Sand

Source	AFS/gfn	Shape	% PUCB Resin	Roundness/Sphericity (Krumbein)	pH	Acid demand (pH-7)
Illinois, USA	59-65	Round	0.9 or 1.4	0.8/0.8	7.1	0.8

The PUCB disc-specimens (50 mm dia., 8 mm thick) were prepared by blowing the specimens with a laboratory core blower into a four-cavity disc core box (Figure 1). Each cavity had its own gate opening and a vent opposite the gate.



Figure 1. Four-cavity disc core box

Materials: Silica sand (Table 1), PUCB binder system Part 1 and Part 2 (mixture ratio 55 Part 1: 45 Part 2)

Equipment: DeLonghi mixer, core box, core blower.



18th INTERNATIONAL FOUNDRYMEN CONFERENCE
**Coexistence of material science and sustainable technology in
economic growth**

Sisak, May 15th-17th, 2019

<http://www.simet.hr/~foundry/>

Procedure:

1. Add weighed sample of sand to DeLonghi Mixer.
2. Make two pockets in the sand.
3. Add Part I component into one pocket and Part II to the other pocket.
4. Mix for 1 minute.
5. "Flip" mixture and mix for 1 additional minute.
6. Using laboratory core blower set at 0.379 MPa (55 psi) for 0.5 second blow the mixed sand into the three cavities of the core box (Figure 1).
7. Cure by gassing with TEA using a Luber gas generator. Gassing parameters: 1 sec gassing with TEA, followed by an air purge for 6 seconds (gas pressure was 0.172 MPa (25 psi) and air purge pressure was 0.103 MPa (15 psi)).

Specimen Weight

The disc-shaped specimens were weighed prior to conducting any tests using a four place digital balance and the weights recorded. The purpose of this measurement check is to identify specimen-to-specimen variability.

Disc Transverse Test (DTS)

Disc transverse strength tests (DTS) were used to measure the strength of the sand specimens prior to the thermal distortion test (TDT), and after TDT. Strengths before TDT relate to handling of the core/mold material after core/mold production, prior to pouring. The strengths after TDT relate to shakeout/collapsibility characteristics.

Equipment: A sand strength machine (Dietert Model 490-A) equipped with a disc transverse accessory (Figure 2).

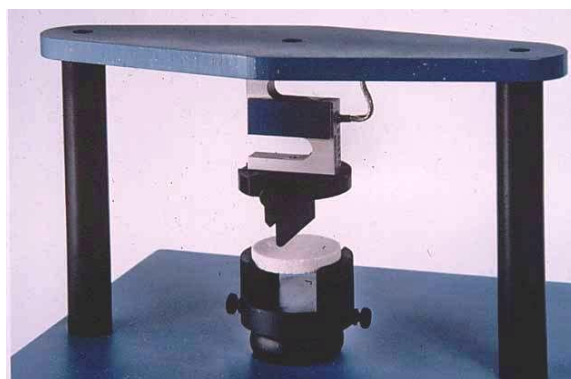


Figure 2. Disc transverse strength (DTS) tester

Procedure: The disc-shaped specimen was fitted into specimen holder on the testing machine and was supported on its ends. It was then subjected to a transverse force by applying the load with a 2.00 mm thick rounded edge blade across its diameter. Loading was performed at a constant linear load rate. A load-cell electronically sensed the specimen



18th INTERNATIONAL FOUNDRYMEN CONFERENCE
**Coexistence of material science and sustainable technology in
economic growth**

Sisak, May 15th-17th, 2019

<http://www.simet.hr/~foundry/>

failure, digitally displaying the results. The maximum load to failure was recorded. The complete test procedure is detailed in the AFS Mold and Core Test Handbook [3].

Impact Testing

An impact testing machine (Tinius Olsen) equipped with a disc specimen holder was used to measure the toughness of the sand specimens prior to and after the TDT. Impact strengths before TDT relate to handling of the core/mold material after core/mold production and prior to pouring. The impact strengths after TDT testing relate to shakeout/collapsibility characteristics.

The disc-shaped specimen was supported on its edge on a specimen holder on the impact testing machine (Figure 3). It was then subjected to impact energy by dropping a uniform load with a 2.00 mm thick rounded edge blade across its diameter. A load-cell electronically sensed the specimen failure, digitally recording the results. The maximum energy to failure (Joules) was recorded.



Figure 3. Disc-shaped specimen on holder at impact

Modified Permeability

Permeability and MQI tests were performed to provide a measure of the specimen's venting characteristics.

Equipment: A Gerosa Simpson permeability tester (Figure 4), Disa George Fisher Mold Quality Indicator (MQI) (Figure 5). A specimen holder designed and fabricated at WMU (Figure 6).

Permeability is a measure of gas flow through a porous media, such as a sand mold or core. It was calculated for each specimen by use of equation 1.

$$P = (V \times H) / (P \times S \times T) \quad (1)$$

Where:

P: Permeability,



18th INTERNATIONAL FOUNDRYMEN CONFERENCE

Coexistence of material science and sustainable technology in
economic growth

Sisak, May 15th-17th, 2019

<http://www.simet.hr/~foundry/>

V: Percolated volume (ml),
H: Height of test sample (cm),
P: Air pressure (g/cm²),
S: Area of sample (cm²),
T: Time in minutes.

The permeability of a sand mold or core is affected by several factors including the size, shape, distribution, and method of compaction of the sand in the mold or core box. Furthermore, permeability is directly affected by the quantity of resin in the sand. Permeability testing is very common in the foundry industry and is part of the sand control tests performed on a regular basis at most foundries. A Gerosa Simpson permeability tester (Figure 4) was used to perform the permeability tests conducted in this experiment. The specimen holder was designed and fabricated at WMU. A special rubber gasket was used between the specimen and the holder to provide a seal. Additionally, a plug was used to restrict the airflow in order for the Gerosa Simpson machine to detect the permeability of each specimen.

The Mold Quality Indicator (MQI) test, which is inversely related to permeability, was also studied. The MQI number is a measurement of the resulting backpressure developed from the resistance of airflow through a mold or core. The MQI unit (Figure 5) was equipped with an air pump, air tubing, and a rubber/foam contact head connected to the end of the tubing. An MQI unit is typically deployed somewhere along the molding line to perform real time measurements on the molds waiting to receive the molten metal. With some modifications to the original rubber contact head, this instrument was utilized with the WMU specimen holder.

Procedure: The specimen was secured into a holder (Figure 7), which was then fixed to the permeability tester. The test was then started and the permeability measured. The holder with the specimen was then removed and attached to the MQI unit for measurement.



Figure 4. Permeability tester with accessory attached



18th INTERNATIONAL FOUNDRYMEN CONFERENCE
**Coexistence of material science and sustainable technology in
economic growth**

Sisak, May 15th-17th, 2019

<http://www.simet.hr/~foundry/>



Figure 5. MQI with accessory attached



Figure 6. Specimen in gasket within holder accessory

Abrasion Test

Abrasion resistance defines the property of a material surface to resist wear while in contact with another material. The determination of the abrasion/wear resistance of a cured surface layer plays a vital role in the estimation of effect on sand mold surface due to handling procedures. This test method encompasses ability to compare strength for different sand specimens against scratch or wear caused by handling.

Equipment: Teledyne Standard Abrasion Tester Model 503 equipped with a custom sample holder for disc specimens (Figure 7).



18th INTERNATIONAL FOUNDRYMEN CONFERENCE
**Coexistence of material science and sustainable technology in
economic growth**

Sisak, May 15th-17th, 2019

<http://www.simet.hr/~foundry/>

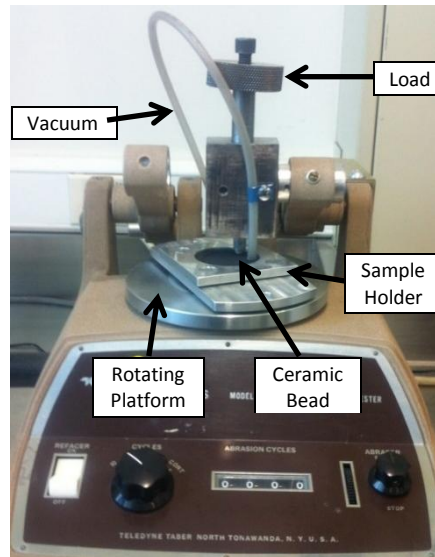


Figure 7. Abrasion Tester

Procedure: The 50 mm dia. x 8 mm thick disc-shaped specimens were weighed and secured onto the sample holder using four screws, one at each corner. The sample holder was mounted onto the abrasion tester with a ceramic bead pressing against the specimen surface perpendicularly as shown in Figure 7. A desired load was applied onto the ceramic bead by mounting corresponding circular weights on top of the abrading assembly. The specimen was then rotated in clockwise direction maintaining a constant rotational speed for a desired number of cycles/rotations. To ensure the proper contact between the ceramic bead and sand specimen surface, a vacuum was applied continuously to pull any loose sand particles during the test run. Reweighing the specimen and calculating the weight loss or percent weight loss then determined the abrasion/wear resistance of the specimen surface.

$$c = a - b \quad (2)$$

$$\%c = (c/a) 100 \quad (3)$$

Where:

a: Initial weight (g) of specimen,

b: Final weight(g) of specimen after test,

c: Total weight loss(g),

%c: % Weight loss.

The sand specimens were tested for 10 cycles/rotations with a load of 250 g on the ceramic bead and thereafter calculating weight loss and percent weight loss as defined in equations 2 and 3.



18th INTERNATIONAL FOUNDRYMEN CONFERENCE
**Coexistence of material science and sustainable technology in
economic growth**

Sisak, May 15th-17th, 2019

<http://www.simet.hr/~foundry/>

Thermal Distortion Testing (TDT)

TDT has the capability to represent the heat and pressures that sand binder systems, will experience from molten metal filling and solidifying in a mold. The word “represent” must be emphasized since molten metal has never been used with the TDT, and there is no exact simulation of casting condition during the test.

Operating conditions of the TDT device are like those where a mass of molten metal is pressing against the mold wall in a pseudo-static state. The load (metallostatic head pressure) on the specimen is held constant, and the specimen can only move into or out of the face of the hot surface depending on whether the specimen is expanding or plastically deforming (**Error! Reference source not found.**). Holding the temperature of the hot surface constant during testing simulates the mass of molten metal.

All of the functionality of the device is accomplished through the use of several instruments, controllers, mechanical devices, and a computer that is used to record data. The description of these features follows below.

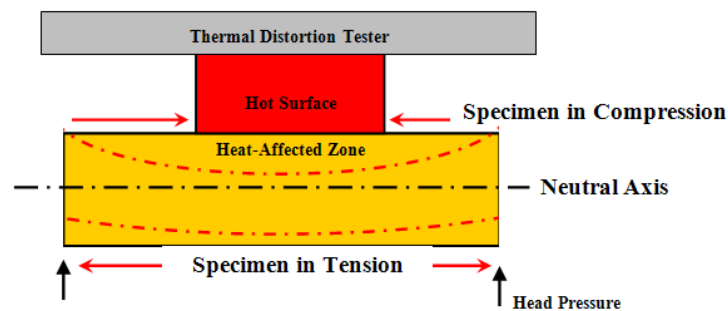


Figure 8. TDT stresses on specimen

Load Calculations: A disc-shaped specimen receives a load about the circumference of one side as the other side is pressed onto a heated metal surface. Dividing this total load by the area of the heated surface approximates pressure. Thus, varying the load emulates a metallostatic pressure while controlling the metal surface temperature [4].

Loading Mechanism: The loading mechanism allows for the approximation of metallostatic pressures during the mold filling and solidification of a casting. For better control and quantification of the resulting distortion, a uniaxial pressure load needs to be applied. This is accomplished by a free floating linear bearing slide that is coupled with an electronic actuator to provide the movement. The slide ensures that center axis of the specimen comes into contact with the center axis of the heated surface. The specimen is loaded into a ceramic tray. The tray locates the specimen against two pins. In addition, the tray is recessed so that any thermal-mechanical movement that takes places will not be restricted.



18th INTERNATIONAL FOUNDRYMEN CONFERENCE
**Coexistence of material science and sustainable technology in
economic growth**

Sisak, May 15th-17th, 2019

<http://www.simet.hr/~foundry/>

To prevent any shear forces from acting on the specimen surface in contact with the heater, a two-axis gimbal was used. The gimbal used three separate rings, one ring was fixed to the linear slider while the remaining two rings were allowed to rotate on two axes, each of which was 90 degrees from each other and oriented 90 degrees to the heated surface axis (Figure 9).

The axes for this gimbal system are centered at the face of the specimen. This prevents scuffing might occur when the specimen experienced uneven distortion since a static fluid would not create a shear load on a mold wall.

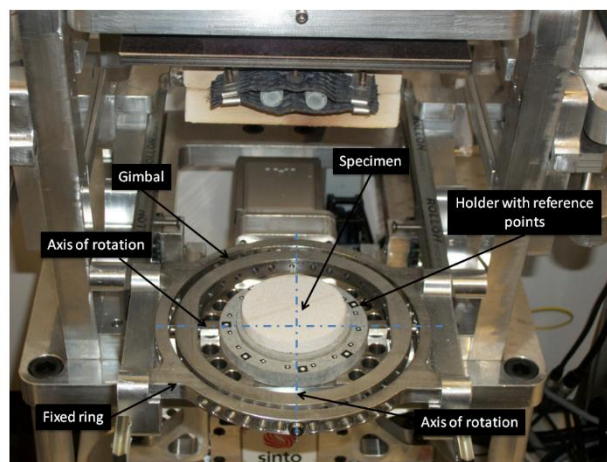


Figure 9. Gimbal Assembly

Heat Source: To provide temperatures that simulate molten metal, a direct current power supply was wired in series with resistive heating elements. These elements pass through the heater mass/tip made out of MAR 247 (a super alloy). The utilization of a large heated mass has the purpose of assuring that the 90 second test is conducted with as constant of a temperature as possible. The heater is enclosed in insulation to direct the heat to the specimen. To account for thermal expansion of MAR 247, the insulated enclosure is allowed to move freely in the longitudinal and radial direction.

Instrumentation: This version of the TDT uses a variety of devices to collect data and control the heating process. The data that is acquired during each test is radial and longitudinal deflection, temperature at the hot surface and backside of specimen, and time. Longitudinal deflection in the specimen is tracked using a real time feedback loop within a commercial controller. The controller software uses the load as a reference and maintains the set value by changing the position of the actuator. To track radial movement, the TDT uses a green light camera system. This system uses the green light to create a shadow of the specimen so that the read-head can measure specimen diameter. The temperature of the hot surface is sensed by a K-type thermocouple. To measure the temperature on the backside of the specimen, a non-contact infrared device was used. Time is recorded based on the sampling



18th INTERNATIONAL FOUNDRYMEN CONFERENCE
**Coexistence of material science and sustainable technology in
economic growth**

Sisak, May 15th-17th, 2019

<http://www.simet.hr/~foundry/>

rate of the data acquisition system. All the temperature and movement signals are fed back to a data acquisition system that is attached to a personal computer (PC). Data is analyzed, stored, and displayed for each test.

Procedure: To operate the TDT (Figure 10) the temperature control was adjusted to 1000°C (1832°F) to represent the cast iron-sand mold interface.

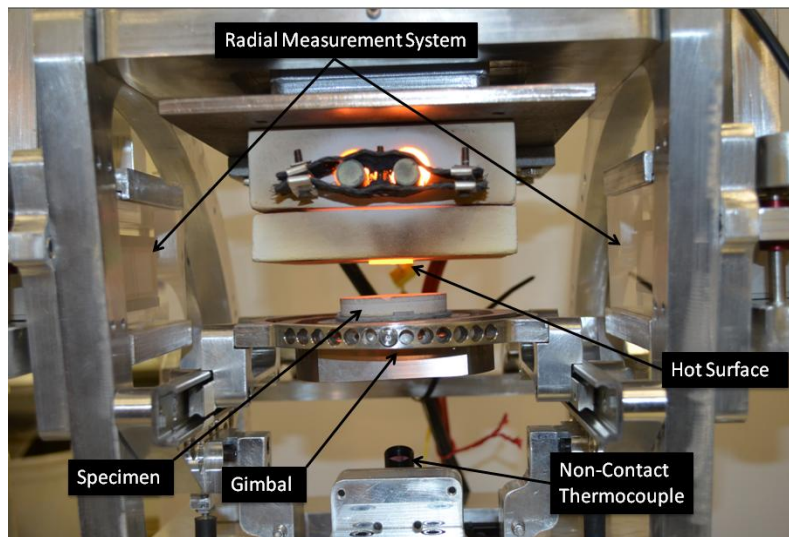


Figure 10. Thermal Distortion Tester (TDT)

To simulate the force of molten metal to a 15.24 cm (6 in) head height for cast iron with a density of 6.92 g/cm³ (0.25 lb/in³) providing a head pressure of 0.01 MPa (1.50 psi) (Head Height * Metal Density), actuator on the TDT was adjusted to a predetermined load of 331 g. The predetermined load was chosen for the test on the basis of the weight calculated to represent a 15.248 cm (6 in) cast iron head height (Contact Area of TDT Hot Surface * Head Pressure), representing a head pressure typical of a medium sized iron casting.

The temperature at the hot surface was controlled using a K-type thermocouple and controlling, monitoring and plotting graphs of temperature/time versus distortion being performed by using an integrated computer peripheral and data acquisition system. The disc shaped specimen was mounted onto a pivoting holder (Figures 9 and 10) and the specimen was automatically raised to achieve a symmetrical contact with the 2.00 cm (0.787 in.) dia. hot surface. A linear voltage displacement transducer (LVDT) was engaged at this point, which simultaneously engaged a laser to measure the distortion in longitudinal and radial directions. The distortions versus time/temperature curves were generated using the integrated data acquisition system. The thermal distortion tests were performed over a 90 second interval, being based upon the recommendations from a committee of foundry experts.



18th INTERNATIONAL FOUNDRYMEN CONFERENCE

Coexistence of material science and sustainable technology in
economic growth

Sisak, May 15th-17th, 2019

<http://www.simet.hr/~foundry/>

For the longitudinal distortion it is possible to differentiate between expansion (D_E) and plastic distortion (D_p) separately from the thermal distortion curve (TDC). In this investigation, the authors chose to record the total distortion (TD) and simply state:

$$TD = \sum D_E + \sum D_p \quad (4)$$

Further, the distortion radial (D_R) indicating expansion was monitored using a high speed laser micrometer scanning sensor (resolution of 0.05 μm). Detailed procedure for the TDT has been defined in AFS transactions [2,4].

Prior to TDT, each specimen was weighed. Following TDT the surface of the specimen was blown with 0.14 MPa (20 psi) air pressure to remove any loose sand grains. The specimens were then again weighed, and the percent change in mass was recorded. Following weighing, the specimens were visually examined looking for signs of thermally induced cracking of the surface, loss of sand where contact was made with the hot surface, and any other discolorations or visual changes. If the core/mold media breaks down, this may be indicative of the tendency to produce cuts and washes, erosion/inclusion type defects. In interpreting this data, it is critical to identify the components causing the change in mass. The percent change in mass was calculated based upon the weight before and after as a percent of the weight before.

Change in mass: Prior to TDT each specimen was weighed. Following TDT the surface of the specimen was blown with 0.014 MPa (2 psi) air pressure to remove any loose sand grains. The specimens were reweighed, and the percent change in mass was recorded. Then the specimens were visually examined for signs of thermally induced cracking (veining) of the surface, loss of sand where contact was made with the hot surface, and any other discolorations or visual observations. If the core/mold media breaks down, this may be indicative of the tendency to produce cuts and washes, erosion/inclusion type defects. In interpreting this data, it is critical to identify the components causing the change in mass. The percent change in mass was calculated based upon the weight before and after as a percent of the weight before.

Quick Loss on Ignition

The loss-on-ignition (LOI) is the difference in weight before and after ignition of the sand sample. LOI is performed at an AFS-defined temperature or at metalcasting temperature, (e.g. cast iron requires 1427 °C (2600 °F)) [3,5]. The main method for determining LOI involves heating samples to a temperature at which organic materials volatilize and decompose. The resulting loss in weight from the sample is the LOI measurement. LOI measurement indicates the amount of combustibles in raw sand. In chemically bonded sand, they absorb binder and reduce its effectiveness. Thus, LOI measurements can provide essential information about the overall quality of a foundry's sand system.



18th INTERNATIONAL FOUNDRYMEN CONFERENCE
**Coexistence of material science and sustainable technology in
economic growth**

Sisak, May 15th-17th, 2019

<http://www.simet.hr/~foundry/>

Foundries depend on a test of combustibles (LOI) to help manage their new sands, green sand systems, chemically bonded cores and molds, sand additives, and reclaimed sands. Each application has an established control range. The testing procedures defined by the AFS (Mold & Core Test Handbook) calls for use of either a muffle or microwave furnace [3]. Unfortunately those tests are considerably slow. The time lag between testing and results can allow certain sand related defects if high levels of organic materials are present in foundry sand systems. A fast LOI test will allow foundries to identify the organic materials in sand in real time [5].

Procedure: (Figure 11)

1. Turn on the computer data acquisition and induction LOI tester.
2. Weigh 3.00 g sample (sand dried at 93 °C (200 °F)) into crucible using an analytical balance.
3. Place crucible with sample on ceramic support of the induction LOI tester.
4. Position crucible with sample into the induction coil.
5. Test (heating up to 1093 °C (2,000 °F)) and data acquisition starts, logs data, and stops automatically after five minutes or no further mass change.
6. Remove sample and cool.
7. Interpret the LOI curve for results.

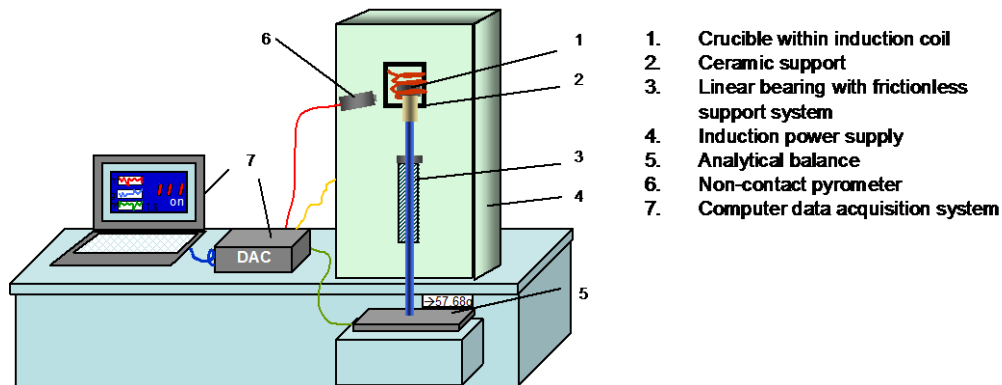


Figure 11. Schematic of induction LOI testing system

RESULTS AND DISCUSSION

Chemically bonded sand test results are shown in Table 2. Though there was on significant differences in specimen weight there were differences in properties. The LOI results indicated the chemically bonded disc-shaped specimens were produced to target. The 1.4 % PUCB samples were stronger and tougher in ambient conditions.



18th INTERNATIONAL FOUNDRYMEN CONFERENCE
Coexistence of material science and sustainable technology in
economic growth

Sisak, May 15th-17th, 2019

<http://www.simet.hr/~foundry/>

TDT results are shown in Table 3. All specimens were tested at 1000 °C (1832 °F). TDT and percent change in mass results are presented according to percent PUCB binder in each sample (Table 3). In addition, TDC, temperature versus time plots and picture information related to the systems are presented in Figures 12 and 13 and Tables 3, 4 and 5.

Table 2. Summary of test results of PUCB samples

Test	0.9 % PUCB		1.4 % PUCB	
	Mean	σ	Mean	σ
Specimen Weight (g)	24.35	0.26	24.87	0.34
DTS (#)	30.57	1.67	35.38	2.23
Impact Strength (J)	0.39	0.08	0.44	0.07
Permeability (#)	179	2.32	171	2.56
MQI (#)	114	1.76	120	2.40
Abrasion (% loss)	4.67	0.66	2.13	0.71
LOI (%)	0.86	0.12	1.35	0.25

Table 3. Thermo-mechanical properties of PUCB samples

PUCB Sample	Results of Thermal Dist. Testing @ 3.25 N for 90 seconds				Observation During Elevated Temp. Testing		
	% Binder	DE Longitudinal (mm)	DP Longitudinal (mm)	TD Total Longitudinal Dist. (mm)	DR Radial Dist. (mm)	% Change in Mass	Cracks and Fractures
0.9		0.069	0.113	0.182	0.220	8.7	faint
1.4		0.051	0.107	0.158	0.234	1.6	large

TDT

The TDCs for all systems tested showed undulations that indicate thermo-mechanical and thermo-chemical changes in the binder system at elevated temperature [2,4]. The longitudinal distortion curves all showed an initial expansion (upward movement of a TDC) before plastic deformation (downward movement of a TDC) (Figure 12). The radial distortion (D_R) clearly indicated an expansion trend (Figure 12).

For specimens tested at 1000°C (1832°F), there was expansion for ~ 15 seconds followed by plastic deformation for the duration of the test. All specimens had similar TDCs and the two binder levels (0.9 % and 1.4 %) were not significantly different (Figure 12) (Table 3). This finding is supported by the temperature versus time data (Figure 13).



18th INTERNATIONAL FOUNDRYMEN CONFERENCE
Coexistence of material science and sustainable technology in
economic growth

Sisak, May 15th-17th, 2019

<http://www.simet.hr/~foundry/>

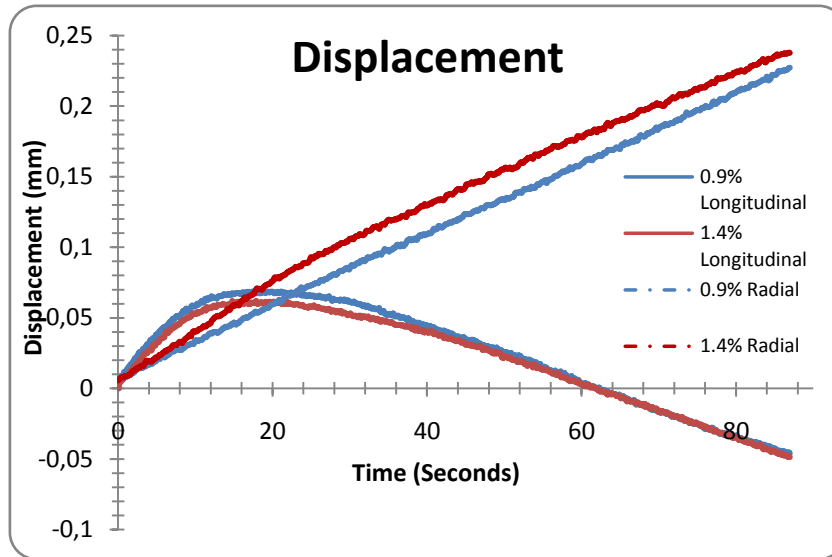


Figure 12. Longitudinal and Radial TDC for 0.9 % and 1.4 % PUCB specimens

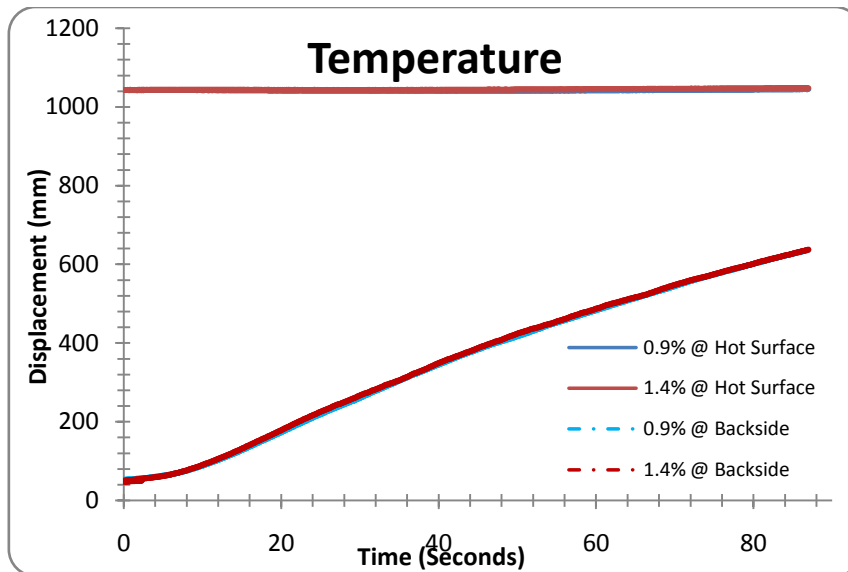


Figure 13. Temperature versus time plots between the hot surface and the back of specimens

Mass Change

There are considerable heat induced thermo-chemical reactions occurring in both PUCB samples as is evident from the surface cracks found on tested specimens and percent change in mass values (Tables 3 and 4). Expansion cracks were macroscopically evident on certain specimens. The crack propagation was more pronounced in 1.4 % PUCB specimens (Tables 3 and 4). As was observed with the original TDT craters were evident at the hot



18th INTERNATIONAL FOUNDRYMEN CONFERENCE
**Coexistence of material science and sustainable technology in
 economic growth**

Sisak, May 15th-17th, 2019

<http://www.simet.hr/~foundry/>

surface/specimen interface where binder bridges pyrolyzed and sand grains broke loose [2,4]. The percent change in mass for all systems tested is shown in Tables 3 and 4. The 0.9 % PUCB specimens had more mass losses when compared to the 1.4 % PUCB specimens (Tables 3 and 4).

Observations from the heat-affected zone of specimens tested are shown in Table 4. The hot surface/specimen interface showed a crater with black discoloration due to binder degradation, the discoloration was present on the opposite side of the specimen. This indicated that there was significant heat transfer across and through the specimen (Figure 13). In addition, sand binder losses were evident at the hot surface/specimen interface where binder bridges pyrolyzed and sand grains broke loose. The loose sand at the hot surface/specimen interface was white. Expansion cracks were macroscopically evident on the specimens.

Table 4. PUCB specimens before and after TDT

	0.9 % PUCB disc	1.4 % PUCB disc
Before TDT		
After TDT		
After TDT (0.07 MPa air)		

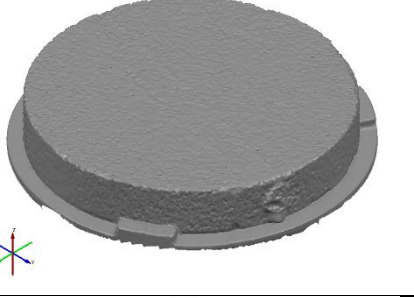
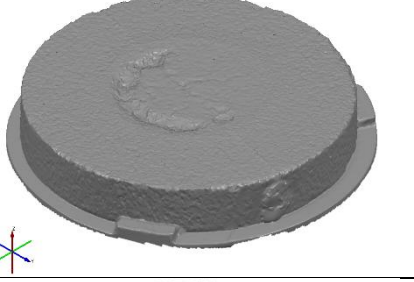
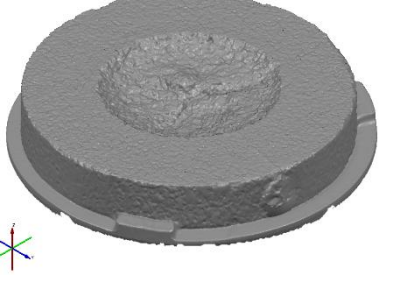
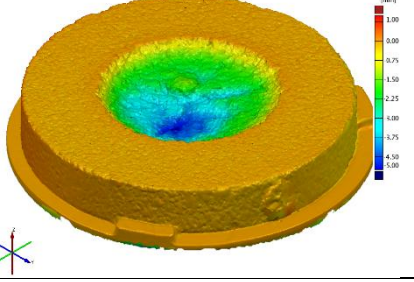


18th INTERNATIONAL FOUNDRYMEN CONFERENCE
Coexistence of material science and sustainable technology in
economic growth

Sisak, May 15th-17th, 2019

<http://www.simet.hr/~foundry/>

Table 5. Digital images of a PUCB specimen before and after TDT

Description	Scanned Images
Before TDT	
After TDT	
After TDT - and 0.07 MPa air blow	
Deviation plot After TDT	
Deviation plot After TDT - and 0.07 MPa air blow	



18th INTERNATIONAL FOUNDRYMEN CONFERENCE
**Coexistence of material science and sustainable technology in
economic growth**

Sisak, May 15th-17th, 2019

<http://www.simet.hr/~foundry/>

Total Surface Deviation

Observations were made macroscopically and supported with photographs and images from an ATOS II white light scanner [6]. Comparing surface deviation is achieved by alignment of the disc-shaped specimens before and after TDT. The specimen holder incorporates a set of reference points (Figure 14). As long as the sample is not moved in the holder, the surface deviation can be tracked at each stage of testing.

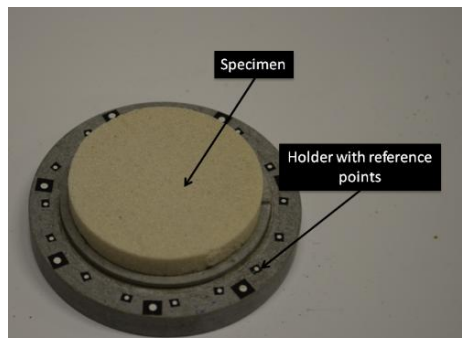


Figure 14. Gimbal assembly with reference points incorporated into holder

Table 5 shows images from an ATOS II white light digital scanner [6]. The first three gray images show a specimen's surface as it sat in the holder before TDT, immediately after TDT, and after the loose material was blown away. Scans were taken at each step. The three images were used to develop deviation plots. The specimen surface before TDT was set as reference and the other two surfaces were analyzed for deviations from the reference. The color plots show these deviations. The same deviation scale was used for both color plots. The holder at the base of the specimen shows no deviation and most of the specimen's surface shows little deviation with the exception of the region which was in contact with the hot surface.

CONCLUSIONS

The DTS, impact, permeability, MQI, abrasion, LOI and thermal distortion tests results indicate that there is relatively lower test-to-test variability with the disc-shaped specimens. The new AFS standard tests were able to discriminate between the chemically bonded PUCB sand specimens.

It is important to recognize that because the disc-shape specimen is simple in geometry it can be easily incorporated at the core box/tool parting-line and vented to produce disc-shaped specimens in core/mold production. This would not be easily achieved using the traditional dog bone tensile or transverse tensile specimens. Supplementary, the disc-shape specimen offers the opportunity for much more than mechanical testing. Disc-shape



18th INTERNATIONAL FOUNDRYMEN CONFERENCE

Coexistence of material science and sustainable technology in
economic growth

Sisak, May 15th-17th, 2019

<http://www.simet.hr/~foundry/>

specimens are also used in testing physical and thermal properties of chemically bonded sands and casting trials have been developed for this specimen type [4].

Further studies should be conducted on various other sand and binder systems as well as on different specimen thicknesses. The thermo-mechanical changes brought forth are in the forms of TDC, mass loss, and cracks on the surface of the test specimens. There was no difference in distortion (longitudinal and radial) between the 0.9% and 1.4% PUCB specimens at 1000°C (1832°F) with a 3.25N (0.73 lbf) load representing 15cm (6 inch) cast iron metallostatic head pressure.

The elevated temperature and pressure did promote distortion on the PUCB specimens. The TDT was able to capture and record both longitudinal and radial distortion curves. Further, time versus temperature data across the specimen was acquired. Heat transfer and thermal gradient information is important input data for solidification simulation programs.

Acknowledgements

This paper would not be possible without support and input from American Foundry Society (AFS) 4F Research Committee. Instrumentation support was provided by Sintokogio, Ltd. The author gratefully acknowledges G. Hall and P. Thannhauser from Western Michigan University, for their technical support.

REFERENCES

- [1] Metals Handbook, American Society for Metals ASM, vol. 15: Casting, ASM International, 2008, ISBN: 978-0-87170-711-6.
- [2] R. Iyer, S. Ramrattan, J. Lannutti, W. Li, Thermo-mechanical properties of chemically bonded sands, AFS Transactions, 109(2001), pp. 1-9.
- [3] American Foundry Society Test Procedures, Mold and Core Test Handbook, 3rd. ed., Schaumburg, IL USA, 2006.
- [4] A. J. Oman, S. N. Ramrattan, M. J. Keil, Next generation thermal distortion tester, AFS Transactions, 13(2013), pp. 1454.
- [5] S. N. Ramrattan, P. G. Ikononov, Five Minute LOI Test, AFS Transactions, paper 06-124 (2006), pp. 1-6.
- [6] ATOS User Manual ATOS Software, v9.01, GOM mbH, Braunschweig, Germany, 2014.



18th INTERNATIONAL FOUNDRYMEN CONFERENCE

Coexistence of material science and sustainable technology in
economic growth

Sisak, May 15th-17th, 2019

<http://www.simet.hr/~foundry/>

PREDICTION OF WORKING STRESS OF QUENCHED AND TEMPERED STEEL AND CAST STEEL SPECIMEN

Božo Smoljan¹, Dario Iljkić^{2*}, Sunčana Smokvina Hanza²

¹ University North, Department of Packaging, Koprivnica, Croatia

¹ Polytechnic of Pula College of Applied Sciences, Pula, Croatia

² University of Rijeka Faculty of Engineering, Rijeka, Croatia

Invited lecture

Original scientific paper

Abstract

In this paper, the prediction of working stress of quenched and tempered steel and cast steel shaft has been done. The method of simulation of working stress was applied in workpiece of complex form. The working stress was characterized by yield strength and toughness. Proposed method was successfully applied in optimization of the manufacturing of quenched and tempered engineering steel components.

Starting point in studying of the mechanical properties of steel castings can be the fact that the mechanical properties of steel castings are derived from the mechanical properties of ordinary steel metal matrix reduced by the influence of the typical as-cast structure, i.e. casting defects on those properties. Hardness and yield strength will be unaffected by most defects. Coarse as-cast microstructure of cast steel lowers ductility and toughness, i.e. impact energy and fracture toughness.

Estimation of hardness distribution can be based on time, relevant for structure transformation, i.e., time of cooling from 800 to 500 °C ($t_{8/5}$). Hardness of quenched and tempered steel can be expressed as function of maximal hardness of actual steel, hardness of steel with 50 % of martensite in microstructure, according to the time and temperature of tempering. The algorithm of estimation of yield strength and toughness was based on hardness, HV.

Keywords: *steel, cast steel, heat treatment, mathematical modelling, mechanical properties*

*Corresponding author (e-mail address): darioi@riteh.hr



18th INTERNATIONAL FOUNDRYMEN CONFERENCE

Coexistence of material science and sustainable technology in
economic growth

Sisak, May 15th-17th, 2019

<http://www.simet.hr/~foundry/>

INTRODUCTION

Basic manufacture processes in steel production are melting and pouring, hot forming, and adequate heat treatment processes. Variation in microstructure and mechanical properties of quenched and tempered steel and cast steel arises from different processing histories.

Quenched and tempered steel has relatively good ratio between yield strength and toughness due to fine dispersion of ferrite-cementite mixture. Yield strength and toughness of quenched and tempered steel are higher if the grain size of previous austenite is finer. Refinement of previous austenite grain size may reduce the hardenability of steel. Due to reduced hardenability of steel, bainite or fine pearlite can be formed instead of martensite after the quenching [1]. Mechanical properties of quenched and tempered steel are better if as-quenched microstructure is consisting of homogenous martensite.

Mechanical properties of steel, i.e., hardness, yield strength and toughness are in relation with each other. All mechanical properties of quenched steel directly depend on the degree of quenched steel hardening [2]. Hardness distribution in quenched steel specimen could be predicted by computer simulation, and after that yield strength and toughness can be predicted based on hardness distribution. The numerical simulation of hardness distribution in quenched steel specimen is one of the highest priorities in simulation of phenomena of steel quenching and in prediction of mechanical properties of quenched steel specimen [3,4].

Two main problems should be solved in simulation of steel quenching: prediction of temperature field change, and prediction of microstructure composition. Mathematical model of microstructure composition in quenched steel can be based on characteristic time of cooling from 800 to 500 °C ($t_{8/5}$) during the quenching. The hardness at specimen points can be estimated by the conversion of cooling time results to hardness by using both, the relation between cooling time and distance from the quenched end of Jominy specimen and the Jominy hardenability curve. The time of cooling at specimen point can be predicted by numerical simulation of cooling using the finite volume method [5,6].

MATHEMATICAL MODELLING OF HEAT TRANSFER

The temperature field change in an isotropic rigid body with coefficient of heat conductivity, $\lambda/\text{Wm}^{-1}\text{K}^{-1}$, density, ρ/kgm^{-3} and specific heat capacity, $c/\text{Jkg}^{-1}\text{K}^{-1}$ can be described by Fourier's law of heat conduction:

$$\frac{\delta(c\rho T)}{\delta t} = \text{div} \lambda \text{ grad} T + q' \quad (1)$$

Characteristic boundary condition is:



18th INTERNATIONAL FOUNDRYMEN CONFERENCE
**Coexistence of material science and sustainable technology in
economic growth**

Sisak, May 15th-17th, 2019

<http://www.simet.hr/~foundry/>

$$-\lambda \frac{\delta T}{\delta n}_s = \alpha(T_s - T_f) \quad (2)$$

where T/K is the temperature, t/s is the time, T_s/K is surface temperature, T_f/K is quenchant temperature, $\alpha/Wm^{-2}K^{-1}$ is heat transfer coefficient.

Solution of Equation (1) can be found out using the finite volume method [5]. If the total volume is divided in N number of control volumes, discretization system has N linear algebraic equations, with N unknown temperatures of control volumes. Time of cooling from T_a to specific temperature in particular point of a specimen is determined as sum of time steps, and in this way, the diagram of cooling curve in every grid-point of a specimen is possible to find out.

MATHEMATICAL MODELLING OF HARDNESS AND MICROSTRUCTURE COMPOSITION

Hardness and microstructure properties of steel or cast steel specimen after quenching can be estimated based on isothermal transformation (IT) diagrams, continuous cooling transformation (CCT) diagrams and characteristic cooling times from 800 to 500 °C.

When using isothermal transformation (IT) diagrams, in accordance to the Scheil's additivity rule, characteristic microstructure transformation of steel or cast steel specimen after quenching is completed when transformed part of microstructure, X is equal to one [7,8]. After calculation of microstructure composition at different location of a specimen, hardness can be estimated by:

$$HRC = X_p HRC_p + X_f HRC_f + X_b HRC_b + X_m HRC_m \quad (3)$$

where X_p , X_f , X_b , X_m are contents of pearlite, ferrite, bainite, martensite respectively, and HRC_p , HRC_f , HRC_b , HRC_m are HRC hardness of pearlite, ferrite, bainite, martensite respectively.

When using continuous cooling transformation (CCT) diagrams, hardness and microstructure composition at different location of steel or cast steel specimen after quenching can be estimated by drawing the cooling curves in the CCT diagram [7]. This is a very simple method which is often used.

Also, hardness at different location of steel or cast steel specimen after quenching can be estimated by the conversion of the calculated characteristic cooling times from 800 to 500 °C, $t_{8/5}$ to the hardness by using both, the relation between cooling times, $t_{8/5}$ and Jominy distance and the Jominy hardenability curve [9]. Cooling times, $t_{8/5}$ of characteristic microstructure composition can be calculated based on cooling times in characteristic points in Jominy specimen with 95 % of martensite, 50 % of martensite, 100 % of pearlite and 50 % of pearlite in microstructure. The microstructure composition in characteristic Jominy points



18th INTERNATIONAL FOUNDRYMEN CONFERENCE

Coexistence of material science and sustainable technology in
economic growth

Sisak, May 15th-17th, 2019

<http://www.simet.hr/~foundry/>

can be calculated based on characteristic hardness. Hardness, microstructure composition of characteristic steel microstructure and characteristic temperature of austenite decomposition were calculated based on Jominy test results [10].

The referent hardness at steel or cast steel specimen points in the quenched and tempered state can be estimated from the as-quenched hardness, HRC_{quenched} , by [11-14]:

$$HRC_{\text{tempered}} = \frac{HRC_{\text{quenched}} - HRC_{\text{min}}}{K} + HRC_{\text{min}} \quad (4)$$

where HRC_{min} is the materials constant. K is the factor between as-quenched and tempered hardness. Factor K can be expressed by:

$$K = C_1 \cdot t^{n_1} \exp \left[A \left(\frac{a}{T_{\text{temp}}} \right)^{n_2} - B \right] \quad (5)$$

where T_{temp}/K is the tempering temperature, t/h is the time of tempering, while A , B , C_1 , a , n_1 and n_2 are the material constants, that are established by regression analysis of hardness of quenched and tempered steel. The algorithm for prediction of hardness of tempered and quenched steel given by Equation (4) and Equation (5) was established by regression analysis.

MATHEMATICAL MODELLING OF MECHANICAL PROPERTIES

Mechanical properties of steel or cast steel after quenching or quenching and tempering directly depends on degree of quenched steel hardening [2]. Relation between hardness HV, and ultimate tensile stress, R_m/Nmm^{-2} is equal:

$$R_m = 3.3HV \quad (6)$$

Relation between hardness HV, and yield strength, $R_{p0.2}/\text{Nmm}^{-2}$ of steel or cast steel after quenching or quenching and tempering is equal to [13]:

$$R_e = R_{p0.2} = (2.64 + 0.33C)HV + 170C - 200 \quad (7)$$

Coefficient C which is ratio between the actual hardness HRC and martensite hardness HRC, should be taken in account since as-quenched and quenched and tempered properties of steel or cast steel depends on degree of quenched steel hardening [2].



18th INTERNATIONAL FOUNDRYMEN CONFERENCE

Coexistence of material science and sustainable technology in
economic growth

Sisak, May 15th-17th, 2019

<http://www.simet.hr/~foundry/>

Maximal Charpy-V notch toughness of quenched and tempered steel is achieved in steel produced by manufacturing process with optimal process parameters, and can be estimated by [11,13]:

$$KV = 264.26 - (1.129 - 0.554S)HV; KV \leq 80 J \quad (8)$$

$$KV = 442.84 - (2.201 - 1.082S)HV; KV > 80 J \quad (9)$$

Starting point in studying of the mechanical properties of steel castings can be the fact that the mechanical properties of steel castings are derived from the mechanical properties of ordinary steel metal matrix reduced by the influence of the typical as-cast structure, i.e. casting defects on those properties. Hardness and yield strength will be unaffected by most defects. The only effect on yield strength will be that due to the reduction in area. Since most defects occupy at most only a few per cent of the area of the casting, this effect is usually hardly detectable. Coarse as-cast microstructure of cast steel lowers ductility and toughness. Impact toughness of quenched and tempered cast steel was predicted based on pouring temperature, temperature of mould during the pouring and fact that steel castings are not subjected to different metallurgical and mechanical processes of microstructure improvement in so far as wrought steels.

Relation between impact energy of cast steel, KV_{sc}/J after quenching or quenching and tempering, and impact energy of steel, KV/J after quenching or quenching and tempering is equal to [13]:

$$KV_{sc} = KV(a - b\Delta q_1 - c q_k) \quad (10)$$

where KV_{sc}/J is impact energy of cast steel, KV/J is impact energy of steel produced by optimal manufacturing process parameters, $\Delta q_1/^\circ C$ is difference from optimal temperature of pouring, $q_k/^\circ C$ is temperature of mould during the pouring, a , b , and c are constants, that are established by regression analysis of impact energy of quenched and tempered cast steel. The expression for prediction of impact energy of quenched and tempered cast steel given by Equation (10) was established by regression analysis.

Fracture toughness, $K_{Ic}/Nmm^{-3/2}$ of steel or cast steel after quenching or quenching and tempering can be estimated from yield strength, $R_{p0.2}/Nmm^{-2}$ and impact energy, KV/J . The Rolfe-Novak correlation can be successfully used for that purpose [15]:

$$K_{Ic} = \sqrt{6.4R_{p0.2}(100KV - R_{p0.2})} \quad (11)$$

APPLICATION EXAMPLE

The established method for prediction of working stress is applied in design of manufacturing process of the shaft made of steel 42CrMo4. Geometry of steel shaft is shown in Figure 1. The chemical composition of investigated shaft is: 0.38 %C, 0.23 %Si, 0.64 %Mn, 0.019 %P, 0.013 %S, 0.99 %Cr, 0.16 %Mo. Jominy test results of the investigated steel, 42CrMo4 are shown in Table 1.



18th INTERNATIONAL FOUNDRYMEN CONFERENCE

Coexistence of material science and sustainable technology in economic growth

Sisak, May 15th-17th, 2019

<http://www.simet.hr/~foundry/>

Table 1. Jominy test results of steel 42CrMo4

Jominy distance/mm	1.5	3	5	7	9	11	13	15	20	25	30
Hardness HV	610	605	590	576	555	524	487	446	379	344	324
Jominy distance/mm	35	40	45	50	55	60	65	70	75	80	-
Hardness HV	311	303	297	293	292	291	289	288	288	288	-

Two different manufacture processes of the shaft were designed. In the first process, the shaft is made of steel. It is assumed that steel is produced by optimal manufacturing process parameters. In the second process, the shaft is made of cast steel. The pouring temperature was 1514 °C and the temperature of mould during the pouring was 105 °C. In both processes, the shaft is quenched from 850 °C for 45 min/oil with H-value equal to 0.2 and tempered at 560 °C for 60 min/air.

Distribution of hardness of steel and cast steel in as-quenched state is shown in Figure 2. Distribution of hardness of steel and cast steel in quenched and tempered state is shown in Figure 3. Critical location for crack growth are locations 1, 2, 3, 4 and 5 (Figure 1). Microstructure composition and mechanical properties in critical locations of steel and cast steel shaft in quenched and tempered state are shown in Table 2.

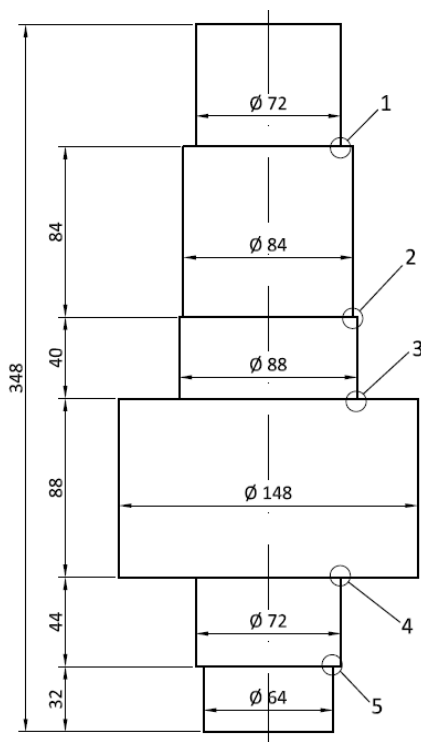


Figure 1. Geometry of steel shaft

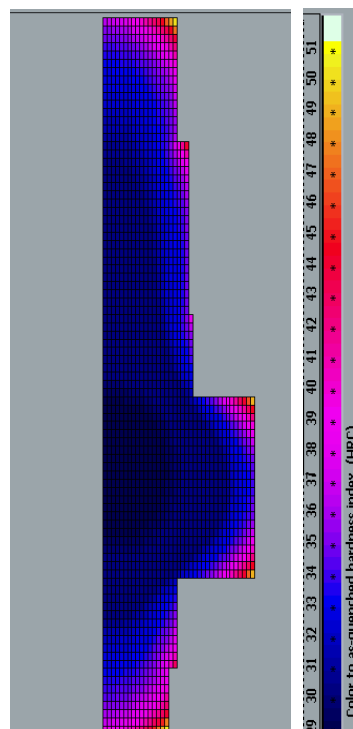


Figure 2. As-quenched steel and cast steel hardness distribution

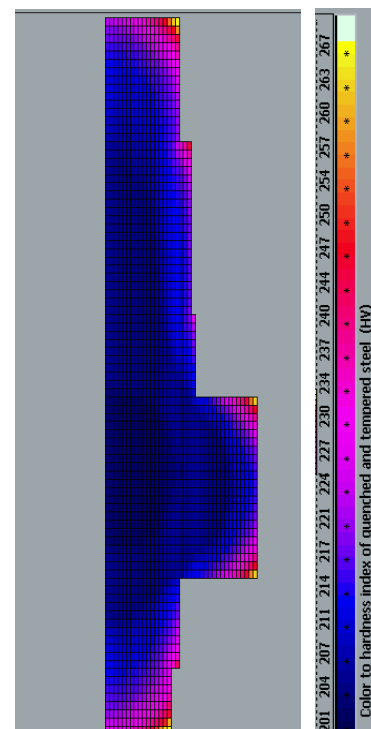


Figure 3. Quenched and tempered steel and cast steel hardness distribution



18th INTERNATIONAL FOUNDRYMEN CONFERENCE

Coexistence of material science and sustainable technology in economic growth

Sisak, May 15th-17th, 2019

<http://www.simet.hr/~foundry/>

Table 2. Microstructure composition and mechanical properties in critical locations of quenched and tempered steel and cast steel shaft

Properties		Critical location (Figure 1)									
		1		2		3		4		5	
		Steel	Cast steel	Steel	Cast steel	Steel	Cast steel	Steel	Cast steel	Steel	Cast steel
Phase fractions/%	F+P	5.2		5.6		7.1		7.1		4.7	
	B	66.6		69.8		83.2		83.2		61.3	
	M	28.2		24.6		9.7		9.7		34.0	
Hardness HV		218		216		206		206		224	
Yield strength R_e/Nmm^{-2}		541		531		483		483		570	
Impact energy KV/J		124	58	124	58	121	57	121	57	124	58
Fracture toughness $K_{Ic}/MPam^{1/2}$		202	135	200	133	189	126	189	126	208	138

CONCLUSIONS

A mathematical model for prediction of mechanical properties of quenched and tempered steel and cast steel was developed. The model is based on finite volume method. The mathematical model has been applied in optimization of the manufacturing of a quenched and tempered shaft. The hardness distribution in the quenched workpiece is estimated based on time of cooling from 800 to 500 °C, $t_{8/5}$, and on results of the Jominy test. Hardness of quenched and tempered steel and cast steel can be expressed as function of maximal hardness of actual steel, hardness of steel with 50 % of martensite in microstructure, according to the time and temperature of tempering. The prediction of yield strength and toughness is based on steel hardness.

It can be concluded that working stress of quenched and tempered shaft can be successfully predicted by the proposed method. Proposed method was successfully applied in optimization of the manufacturing of quenched and tempered engineering steel components. The further experimental investigations are needed for final verification of established model. For efficient estimation of steel toughness from hardness, additional data about microstructure are needed.

REFERENCES

- [1] S. Mahajan et al., Grain refinement of steel cyclic rapid heating, *Metallography*, 6(1973), pp. 337-345.



18th INTERNATIONAL FOUNDRYMEN CONFERENCE

**Coexistence of material science and sustainable technology in
economic growth**

Sisak, May 15th-17th, 2019

<http://www.simet.hr/~foundry/>

- [2] B. Smoljan, Prediction of mechanical properties and microstructure distribution of quenched and tempered steel shaft, *Journal of Materials Processing Technology*, 175(2006)1, pp. 393-397.
- [3] L. A. Dobrzański, W. Sitek, The modelling of hardenability using neural networks, *Journal of Materials Processing Technology*, 92-93(1999), pp. 8-14.
- [4] J. Trzaska, L. A. Dobrzański, A. Jagiełło, Computer programme for prediction steel parameters after heat treatment, *Journal of Achievements in Materials and Manufacturing Engineering*, 24(2007)2, pp. 171-174.
- [5] S. Patankar, *Numerical heat transfer and fluid flow*, McGraw Hill Book Company, New York, 1980, ISBN 0-07-048740-5.
- [6] B. Smoljan, Numerical simulation of as-quenched hardness in a steel specimen of complex form, *Communications in Numerical Methods in Engineering*, 14(1998)1, pp. 277-285.
- [7] ASM Handbook, *Heat Treating*, Vol. 4, ASM International, 1991.
- [8] S. Smokvina Hanza, *Mathematical modeling and computer simulation of microstructure transformations and mechanical properties during steel quenching*, doctoral thesis, University of Rijeka, Faculty of Engineering, Rijeka, 2011. (in Croatian)
- [9] A. Rose, F. Wever, *Atlas zur Wärmebehandlung der Stähle I*, Verlag Stahleisen, Düsseldorf, 1954.
- [10] B. Smoljan, D. Iljkić, Computer modeling of mechanical properties and microstructure of quenched steel specimen, *Proceedings of the 5th International Conference on Thermal Process Modeling and Computer Simulation*, 16-18 June 2014, Orlando, FL USA.
- [11] E. Just, *Verguten—Werkstoffbeeinflussung durch Harten und Anlassen*, VDI, Bericht, 256(1976), pp. 124-140.
- [12] T. Reti, I. Felde, M. Guerrero, S. Sarmiento, Using generalized time-temperature parameters for predicting the hardness change occurring during tempering, *Proc. of the International Conference on New Challenges in Heat Treatment and Surface Engineering (Conference in honour of Prof. Božidar Liščić)*, Dubrovnik-Cavtat, Croatia, 2009.
- [13] D. Iljkić, *A Contribution to the development of the mechanical properties prediction of quenched and tempered steel and cast steel*, doctoral thesis, Department of Materials Science and Engineering, Faculty of Engineering, University of Rijeka, (2010) (in Croatian).
- [14] B. Smoljan, D. Iljkić, G. E. Totten, Mathematical modeling and simulation of hardness of quenched and tempered steel, *Metallurgical and Materials Transactions B*, 46(2015)6, pp. 2666-2673.
- [15] *Impact Toughness Testing*. In section: *Impact Toughness Testing and Fracture Mechanics*. ASM Handbook-Volume 8: *Mechanical Testing and Evaluation*, Material Park, OH, ASM International, 2000.



18th INTERNATIONAL FOUNDRYMEN CONFERENCE

Coexistence of material science and sustainable technology in
economic growth

Sisak, May 15th-17th, 2019

<http://www.simet.hr/~foundry/>

CRACK PROPAGATION PREDICTION IN HETEROGENEOUS MICROSTRUCTURE OF NODULAR CAST IRON

Zdenko Tonković*, Karlo Seleš, Ante Jurčević, Jurica Sorić

University of Zagreb Faculty of Mechanical Engineering and Naval Architecture, Zagreb, Croatia

Invited lecture
Original scientific paper

Abstract

The crack propagation prediction occurring on the microstructural level of heterogeneous materials, such as nodular cast iron, is a very challenging problem. According to the results of recent investigations, the emerging phase-field approach to fracture has a strong potential in modelling the complex crack behaviour in a simple manner. In this study, recently developed phase-field staggered solution scheme with the residual norm stopping criterion has been employed for the fracture analysis of heterogeneous microstructure exhibiting complex crack phenomena. The microstructural geometries based on the metallographic images of the nodular cast iron and the material properties of an academic brittle material have been used in numerical simulations where the graphite nodules have been considered as porosities. The proposed algorithm efficiently recovers the complicated crack path driven by the complex microstructural topology.

Keywords: *phase-field fracture modelling, staggered algorithm, Abaqus, nodular cast iron, crack initiation and propagation*

*Corresponding author (e-mail address): zdenko.tonkovic@fsb.hr

INTRODUCTION

The nodular cast iron, as a heterogeneous material, is widely used for many structural components in engineering practice. The realistic description of its deformation responses demands an accurate modelling at both macroscopic and microscopic scales. The nodular cast iron consists of graphite spheroids or nodules, positioned in an either ferritic or pearlitic matrix, providing high fatigue strength. As presented in [1], the size, shape, spatial distribution, volume fraction and the properties of the constituents making up the microstructure have a significant impact on the behaviour of material properties observed at



18th INTERNATIONAL FOUNDRYMEN CONFERENCE

Coexistence of material science and sustainable technology in
economic growth

Sisak, May 15th-17th, 2019

<http://www.simet.hr/~foundry/>

the macroscale. The results of experimental studies on the mechanical behaviour of the ductile nodular cast iron EN-GJS-400-18-LT, depending on its material microstructure, are well elaborated in the previous publications of the authors' research team [2,3]. Figure 1 shows the cracked specimen with exposed nodular cast iron microstructure. As can be seen, the crack is directed towards the graphite nodule which then acts as a barrier for further crack propagation.



Figure 1. Microstructural crack exposure [3]

The numerical modelling of fracture processes in such highly heterogeneous microstructure is an important and challenging problem, comprised of complex crack initiation, propagation, branching and merging mechanisms. Over the years, different numerical approaches and methods have been proposed for material fracture modelling. These numerical methods can be generally classified as discrete and diffuse crack interface methods. Commonly used discrete crack interface numerical methods for material fracture within the finite element framework introduce the crack as a geometric discontinuity. Its mesh-density and direction dependence problem as a result of crack propagation occurring along the element edges has been successfully alleviated via automatic remeshing [4] or enriching the standard finite element shape functions through a partition of unity method (XFEM) [5]. While these methods show great success in solving the crack propagation problems, they often lack computational efficiency or provide spurious damage growth and incorrect solutions when dealing with complex fracture phenomena, especially on three-dimensional problems.

In contrast, diffuse crack interface methods regularize the sharp crack discontinuity within some volume which is often controlled by some length-scale parameter. The phase-field approach to fracture is classified as diffuse method as it approximates the sharp crack discontinuity by introducing the damage parameter that continuously varies over the domain between the fully broken and intact material phases. Therefore, the need to numerically track the discontinuities of the displacement field is avoided. It has been demonstrated that it handles the complex fracture processes well even in three dimensional settings. However, it can also be computationally very expensive due to the aforementioned length-scale parameter often requiring very fine mesh. For the brittle material behaviour assumption, the phase-field approach is mostly based on the Griffith's theory where crack propagation is determined by the energy of the surface tension. The fracture processes occurring at microlevel of heterogeneous materials have been the subject of current research activities in scientific community [6], still with many unresolved issues at hand.

Due to the non-convexity of the phase-field free energy functional with respect to the phase-field and displacement field [7], robust staggered algorithms are commonly used in the numerical implementations. The staggered algorithms uncouple the system of equations to solve it in an incremental-iterative manner [8].



18th INTERNATIONAL FOUNDRYMEN CONFERENCE
**Coexistence of material science and sustainable technology in
economic growth**

Sisak, May 15th-17th, 2019

<http://www.simet.hr/~foundry/>

In this paper, the staggered algorithm with residual norm based stopping criterion developed in the authors' former work [9] is presented. The performance of the implementation is demonstrated on the heterogeneous microstructure fracture analysis.

PHASE-FIELD FRACTURE FORMULATION

The basic equations of the phase-field fracture approach for linear elasticity are compiled in Table 1. Herein Ψ^b is the body's stored elastic deformation energy of an elastic n -dimensional body Ω with crack surface $\Gamma(t)$ and Ψ^s is the fracture induced dissipated energy. $\boldsymbol{\varepsilon}$ is the small strain tensor, G_c represents the fracture toughness, l is the length scale parameter that regulates the width of the crack band approximation, while \mathbf{u} denotes the displacement field. In the presented regularized framework, the crack geometry is approximated by a smeared representation defined by a scalar phase-field parameter $\phi \in [0,1]$, which takes value of 1 for the fully broken material state and the value of 0 for the bulk material. Furthermore, a degradation function $(1 - \phi)^2$ is introduced to account for the subsequent loss of stiffness in the region representing the diffusive crack (i.e. $\phi \rightarrow 1$). In addition, the history field $H(t) := \max_{\tau \in [0,t]} \psi_e(\tau)$ [8] is employed instead of ψ_e to prevent the crack "healing". More details on the phase-field fracture formulation can be found in [10].

Table 1. The basic equations of the phase-field fracture approach for linear elasticity

Phase-field free energy functional:

$$\Psi = \Psi^b + \Psi^s = \int_{\Omega/\Gamma} \psi_e(\boldsymbol{\varepsilon}) d\Omega + \int_{\Gamma} G_c d\Gamma. \quad (1)$$

Elastic deformation energy density:

$$\psi_e = \frac{1}{2} \lambda \text{tr}^2(\boldsymbol{\varepsilon}) + \mu \text{tr}(\boldsymbol{\varepsilon}^2). \quad (2)$$

Regularized free energy functional:

$$\Psi(\mathbf{u}, \phi) = \int_{\Omega} (1 - \phi)^2 \psi_e(\boldsymbol{\varepsilon}) d\Omega + \int_{\Omega} \frac{G_c}{2} \left[l (\nabla \phi)^2 + \frac{1}{l} \phi^2 \right] d\Omega. \quad (3)$$

Governing equations obtained using the principle of virtual work:

$$\int_{\Omega} (1 - \phi)^2 \frac{\partial \psi_e(\boldsymbol{\varepsilon})}{\partial \boldsymbol{\varepsilon}} d\Omega = \mathbf{F}^{\text{ext}}, \quad (4a)$$

$$\int_{\Omega} \left\{ G_c l \Delta \phi + \frac{G_c}{l} \phi \right\} d\Omega = \int_{\Omega} 2(1 - \phi) H d\Omega. \quad (4b)$$



NUMERICAL IMPLEMENTATION

The phase-field formulation is implemented into the finite element framework by means of the four-node plane strain element with the standard displacement degrees of freedom and the phase-field parameter ϕ as an additional degree of freedom at each node. The same shape functions are applied to interpolate both fields, ϕ and \mathbf{u} . Finally, in accordance with the staggered solution scheme, the decoupled system of equations is obtained as follows

$$\begin{aligned} \mathbf{K}^{\phi\phi}\phi &= \mathbf{R}^{\phi}(\mathbf{u}, \phi), \\ \mathbf{K}^{uu}\mathbf{u} &= \mathbf{R}^u(\mathbf{u}, \phi), \end{aligned} \quad (5)$$

where \mathbf{K}^{uu} and $\mathbf{K}^{\phi\phi}$ are stiffness matrices, while \mathbf{R}^u and \mathbf{R}^{ϕ} are residual force vectors corresponding to the degrees of freedom \mathbf{u} and ϕ , expressed as

$$\begin{aligned} \mathbf{R}_i^u &= \int_{\Omega} \mathbf{B}_i^{uT} \boldsymbol{\sigma} d\Omega - \int_{\Omega} \mathbf{N}_i^{uT} \bar{\mathbf{b}} d\Omega - \int_{\partial\Omega} \mathbf{N}_i^{uT} \bar{\mathbf{t}} d\partial\Omega, \\ \mathbf{R}_i^{\phi} &= \int_{\Omega} \left\{ G_c / \mathbf{B}_i^{\phi T} \nabla \phi + \left[\frac{G_c}{l} + 2H \right] \mathbf{N}_i^{\phi} \phi - 2\mathbf{N}_i^{\phi} H \right\} d\Omega, \end{aligned} \quad (6)$$

and

$$\begin{aligned} \frac{\partial \mathbf{R}_i^u}{\partial \mathbf{u}_j} &= \mathbf{K}_{ij}^{uu} = \int_{\Omega} \mathbf{B}_i^{uT} \frac{\partial \boldsymbol{\sigma}}{\partial \boldsymbol{\epsilon}} \mathbf{B}_j^u d\Omega, \\ \frac{\partial \mathbf{R}_i^{\phi}}{\partial \phi_j} &= \mathbf{K}_{ij}^{\phi\phi} = \int_{\Omega} \left\{ G_c / \mathbf{B}_i^{\phi T} \mathbf{B}_j^{\phi} + \left[\frac{G_c}{l} + 2H \right] \mathbf{N}_i^{\phi} \mathbf{N}_j^{\phi} \right\} d\Omega. \end{aligned} \quad (7)$$

In the above equations, \mathbf{B} denotes the displacement differentiation matrix, \mathbf{N} stands for the shape function matrix, while \mathbf{C} is the elasticity matrix. Figure 2 shows the flowchart of the staggered solution scheme implemented in the FE software Abaqus [11] via layered manner of user elements generated with UEL and UMAT subroutines. The flowchart corresponds to the updated version of the algorithm [12] which is openly accessible on Mendeley repository. For more information on the updated version, see [12].

Here, the solution estimates ϕ_n^k and \mathbf{u}_n^k are obtained by the Newton-Raphson procedure after the non-converging iteration as follows

$$\begin{aligned} \phi_n^k &= \phi_n^{k-1} + \Delta \phi_n^k = \phi_n^{k-1} + \mathbf{K}^{\phi\phi} \left(\mathbf{u}_n^{k-2}, \phi_n^{k-1} \right)^{-1} \cdot \mathbf{R}^{\phi} \left(\mathbf{u}_n^{k-2}, \phi_n^{k-1} \right), \\ \mathbf{u}_n^k &= \mathbf{u}_n^{k-1} + \Delta \mathbf{u}_n^k = \mathbf{u}_n^{k-1} + \mathbf{K}^{uu} \left(\mathbf{u}_n^{k-1}, \phi_n^{k-1} \right)^{-1} \cdot \mathbf{R}^u \left(\mathbf{u}_n^{k-1}, \phi_n^{k-1} \right). \end{aligned} \quad (8)$$

For more details on the numerical implementation, see [9,13]. The presented phase-field approach has been evaluated and verified on standard benchmark examples in [9] and on the problems of real microstructural geometries in [13], in comparison to the common single



iteration staggered algorithm [8]. Here, its capability has been demonstrated through the simulation of the fracture phenomena occurring on the microstructural geometry of the nodular cast iron by the numerical example elaborated in the next section.

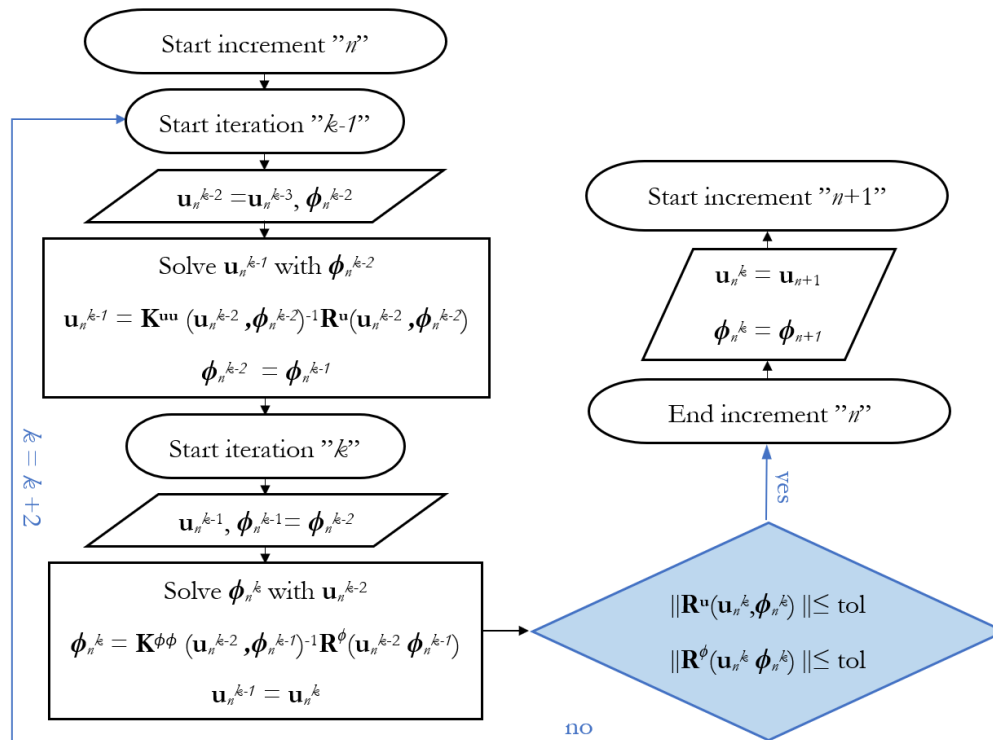


Figure 2. RCTRL staggered algorithm flowchart

NUMERICAL EXAMPLE

Figure 3 shows the heterogeneous microstructure of the nodular cast iron grade EN-GJS-400-18-LT produced by the in-mould casting process which has been carried out by the metallography in the authors' research team previous work [2,3]. This ductile nodular cast iron consists of graphite nodules surrounded by a ferritic matrix. For the considered material the volume fraction of graphite nodules is about 7% with circularity of 0.7 (a value of 1.0 indicates a perfect circle). Since the presented numerical algorithm predicts the brittle fracture nucleation and propagation at this moment, academic brittle material properties are used instead of the ones corresponding to the ductile nodular cast iron. As a numerical idealization, the graphite nodules are intended to be substituted with spheres. In the considered 2D case, the spheres are projected as circles. Since the academic brittle material properties are already assumed, it seems justified to idealize the nodules as spheres, i.e., circles, to speed up the numerical simulations.

Fourteen different samples or Microstructural Volume Elements (MVEs) are randomly selected from the metallographic image while still satisfying the average graphite nodules



18th INTERNATIONAL FOUNDRYMEN CONFERENCE
**Coexistence of material science and sustainable technology in
economic growth**

Sisak, May 15th-17th, 2019

<http://www.simet.hr/~foundry/>

content of ~7%, as schematically shown in Figure 3 and Table 2. The size of the samples is 161.7 x 161.7 μm. The MVEs are uniformly discretized with ~30 000 finite elements with an average characteristic element length of $h=0.001$ mm. The material properties are selected as Young's modulus $E = 200$ GPa, Poisson's ratio $\nu = 0.3$ and fracture toughness $G_c = 1 \times 10^3$ N/m. The regularizing parameter is set to $l=0.0025$ mm. The displacement boundary conditions imposed on the MVE are presented in Figure 4.

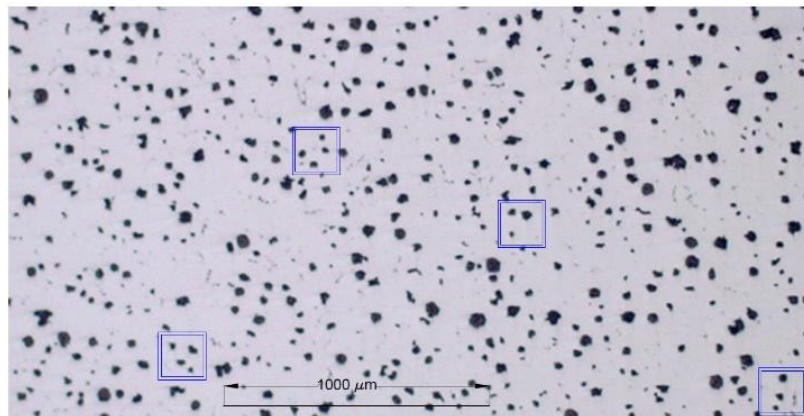


Figure 3. Metallographic image of EN-GJS-400-18-LT microstructure [3] with the selection of samples satisfying the global average graphite nodules content

Table 2. Critical force for different samples under tensile loading

Serial number of MVE	Pore share, %	Critical force, N	Critical force deviation from average, %
1	6.19	282.9	3.80
2	6.53	250.5	8.67
3	5.94	290.0	6.13
4	6.30	282.3	3.58
5	6.74	261.3	4.17
6	6.11	254.4	7.00
7	6.51	302.5	10.00
8	6.39	281.7	3.36
9	6.21	285.9	4.80
10	6.50	249.5	9.12
11	6.24	263.9	3.16
12	6.01	276.1	1.38
13	6.30	277.6	1.93
14	6.11	252.5	7.80
	Average pore share, %	Average critical force, N	
	6.29	272.2	



18th INTERNATIONAL FOUNDRYMEN CONFERENCE
**Coexistence of material science and sustainable technology in
economic growth**

Sisak, May 15th-17th, 2019

<http://www.simet.hr/~foundry/>

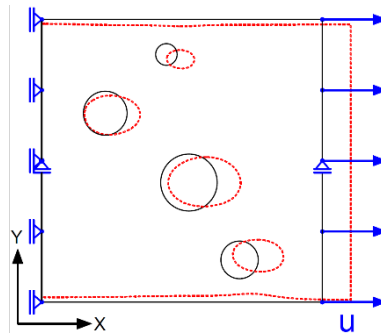


Figure 4. Displacement boundary conditions imposed on the MVE

The problem is solved with the proposed algorithm in the displacement-controlled regime. Figure 5 presents crack paths in the simplified geometry of a nodular cast iron microstructure. As evident, the proposed phase-field formulation can successfully calculate the complicated crack paths on an arbitrary microstructural geometry. The reaction force of the right edge of MVE versus the displacement diagrams for all considered MVEs are shown in Figure 6. It is obvious that there is no significant difference in the post-peak behaviour of the specimens. In that area the force-displacement curves demonstrate a rapid drop in stiffness after reaching a critical force value as a consequence of an abrupt crack propagation between the microstructural inclusions. Such crack propagation is typical for a class of brittle materials, which is in accordance with the assumptions established in this work. Furthermore, the maximum force and displacement are shown in Table 2.



18th INTERNATIONAL FOUNDRYMEN CONFERENCE
Coexistence of material science and sustainable technology in
economic growth

Sisak, May 15th-17th, 2019

<http://www.simet.hr/~foundry/>

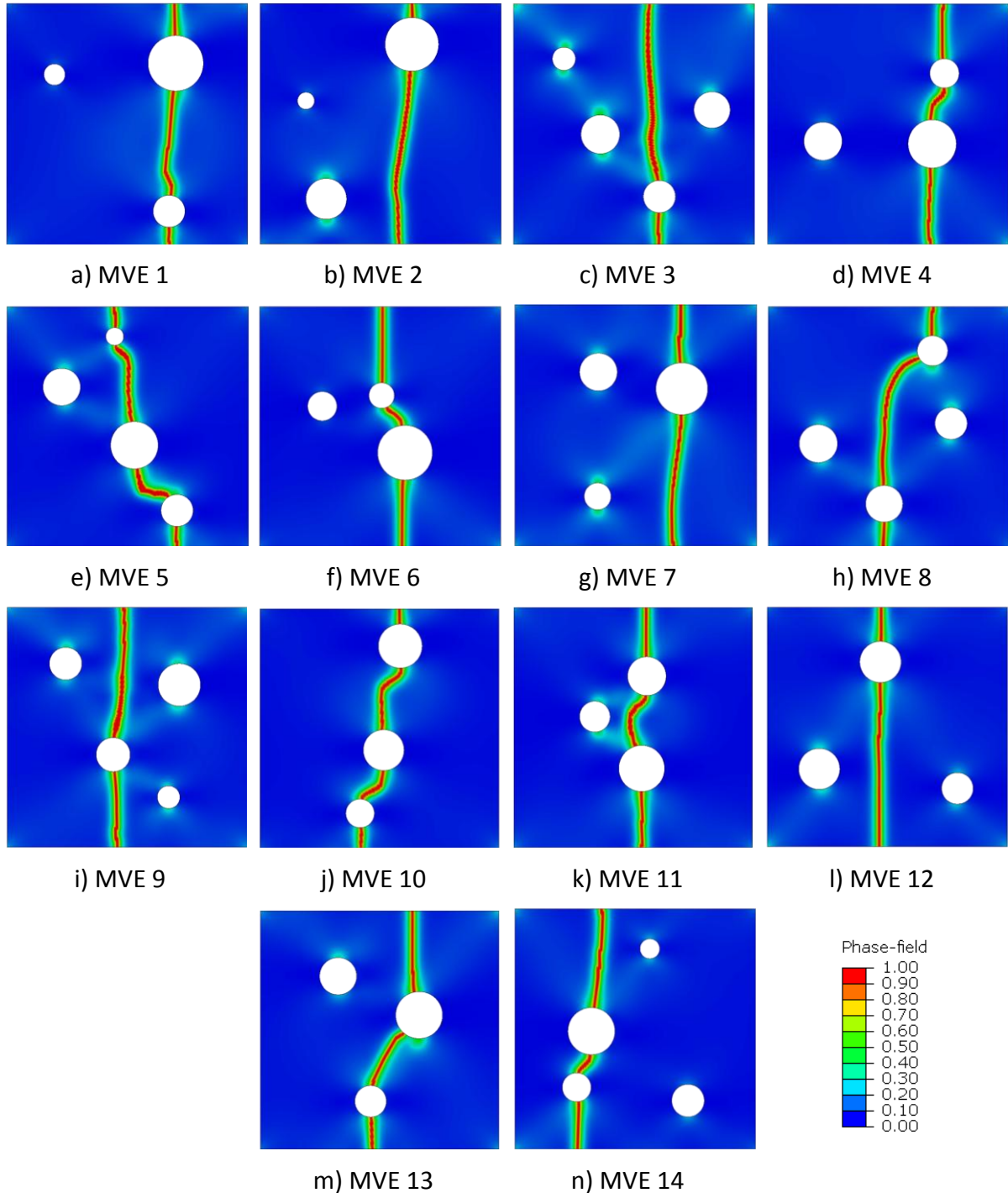


Figure 5. Crack paths in the simplified geometry of a nodular cast iron microstructure



18th INTERNATIONAL FOUNDRYMEN CONFERENCE
**Coexistence of material science and sustainable technology in
economic growth**

Sisak, May 15th-17th, 2019

<http://www.simet.hr/~foundry/>

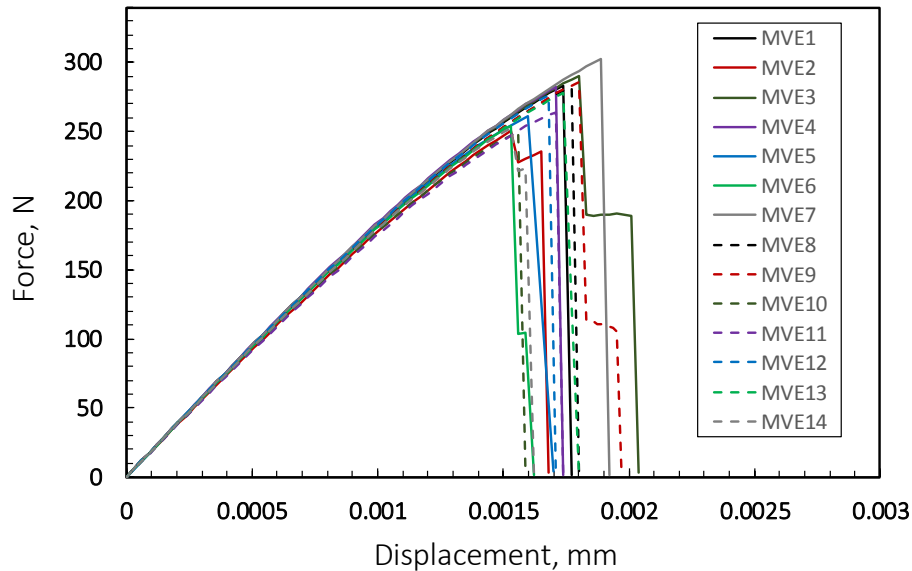


Figure 6. Force-displacement response for all considered MVEs

CONCLUSIONS

The fracture analysis of the heterogeneous microstructural geometry based on the microstructural imaging of nodular cast iron has been performed in this paper. The phase-field staggered algorithm with residual norm based stopping criterion, recently developed as a part of author's previous study, has been utilized. The algorithm was implemented into the finite element program Abaqus by means of the custom linear quadrilateral finite elements with the phase-field parameter as an additional degree of freedom. The concise implementation details are presented together with the demonstration of the model capabilities on the heterogeneous nodular cast iron microstructure represented by the series of MVEs. The obtained results display the ability of the model to capture the brittle crack initiation and propagation, resulting in complex crack paths on heterogeneous microstructural geometries. Although an academic brittle material was employed together with simplifications to geometry, it can still be observed that the maximal deviation of the critical force is not obtained on the MVEs with greatest deviation from average pore share, which shows how the microstructural geometry arrangement also plays a significant role together with the porosity ratio. However, it has to be emphasized that the obtained results serve as a demonstration of the algorithms capabilities on complex heterogeneous microstructural geometries and, due to these simplifications, do not represent a realistic material behaviour.



18th INTERNATIONAL FOUNDRYMEN CONFERENCE
**Coexistence of material science and sustainable technology in
economic growth**

Sisak, May 15th-17th, 2019

<http://www.simet.hr/~foundry/>

REFERENCES

- [1] G. Hütter, L. Zybell, M. Kuna, Micromechanisms of fracture in nodular cast iron: From experimental findings towards modeling strategies – A review, *Eng. Fract. Mech.*, 144 (2015), pp. 118-41.
- [2] P. Čanžar, Z. Tonković, J. Kodvanj, Microstructure influence on fatigue behaviour of nodular cast iron, *Mater. Sci. Eng. A*, 556(2012), pp. 88-99.
- [3] P. Čanžar, Experimental and Numerical Modelling of Fatigue Behaviour of Nodular Cast Iron, Faculty of Mechanical Engineering and Naval Architecture, University of Zagreb, PhD Thesis, 2012 (in Croatian).
- [4] A. R. Ingraffea, V. Saouma, Numerical modeling of discrete crack propagation in reinforced and plain concrete, (G. C. Sih, A. DiTommaso (eds)), *Fracture mechanics of concrete: Structural application and numerical calculation, Engineering Application of Fracture Mechanics*, vol 4., Springer, 1985, Dordrecht, pp. 171-225. DOI: 10.1007/978-94-009-6152-44.
- [5] N. Moës, J. Dolbow, T. Belytschko, A finite element method for crack growth without remeshing, *Int. J. Numer. Methods Eng.*, 46(1999)1, pp. 131-150.
- [6] T. T. Nguyen, J. Yvonnet, Q. Z. Zhu, M. Bornert, C. Chateau, A phase field method to simulate crack nucleation and propagation in strongly heterogeneous materials from direct imaging of their microstructure, *Engineering Fracture Mechanics*, 139(2015), pp. 18-39.
- [7] B. Bourdin, G. A. Francfort, J. J. Marigo, Numerical experiments in revisited brittle fracture, *Journal of the Mechanics and Physics of Solids*, 48(2000)4, pp. 797-826.
- [8] C. Miehe, M. Hofacker, F. Welschinger, A phase field model for rate-independent crack propagation: Robust algorithmic implementation based on operator splits, *Computer Methods in Applied Mechanics and Engineering*, 199 (2010)45-48, pp. 2765-2778.
- [9] K. Seleš, T. Lesičar, Z. Tonković, J. Sorić, A residual control staggered solution scheme for the phase-field modeling of brittle fracture, *Engineering Fracture Mechanics*, 205 (2018), pp. 370-386.
- [10] C. Miehe, F. Welschinger, M. Hofacker, Thermodynamically consistent phase-field models of fracture: Variational principles and multi-field FE implementations, *International Journal for Numerical Methods in Engineering*, 83(10) (2010) pp. 1273-1311.
- [11] Abaqus 6.14-1, Dassault Systemes Simulia Corp., Providence, RI, USA, 2014.
- [12] K. Seleš, Abaqus Code for a Residual Control Staggered Solution Scheme for the Phase-Field Modeling of Brittle Fracture, <https://data.mendeley.com/datasets/p77tsyrbx2/3>, Mendeley data 2018.
- [13] K. Seleš, A. Jurčević, Z. Tonković, J. Sorić, Crack Propagation Prediction in Heterogeneous Microstructure using an Efficient Phase-Field Algorithm, *Theoretical and Applied Fracture Mechanics*, 100(2019), pp. 289-297.



18th INTERNATIONAL FOUNDRYMEN CONFERENCE

Coexistence of material science and sustainable technology in
economic growth

Sisak, May 15th-17th, 2019

<http://www.simet.hr/~foundry/>

DETERMINATION OF MECHANICAL PROPERTIES OF NIOBIUM MICRO- ALLOYED STEEL USING INSTRUMENTED INDENTATION TEST

Tamara Aleksandrov Fabijanić^{1*}, Mladen Franz¹, Stoja Rešković²

¹ University of Zagreb Faculty of Mechanical Engineering and Naval Architecture, Zagreb, Croatia

² University of Zagreb Faculty of Metallurgy, Zagreb, Croatia

Oral presentation

Original scientific paper

Abstract

Niobium Nb micro-alloyed steels belong to a group of structural steels. They are alloyed with a small content of Nb (0.02-0.1 wt.%) which has a significant influence on many properties. Nb exhibits a strong affinity for nitrogen N and carbon C and causes the formation of niobium carbide NbC, niobium nitride NbN and niobium carbonitride Nb(C, N) in a structure which prevents grain growth and slows the recrystallization process and thus contributes to precipitation hardening. The mechanical properties of Nb micro-alloyed steel with Nb content of 0.035 wt.% were researched using instrumented indentation test. The indentation was carried out using different loads to determine the effect of the applied load on the measured properties and to research the applicability of the method for this group of materials. Based on the slope of the force-penetration depth curve during the loading and unloading, the Martens hardness, indentation hardness, indentation modulus, Vickers hardness, elastic/plastic work and creep characteristic were determined.

Keywords: Nb micro-alloyed steel, instrumented indentation test, mechanical properties

*Corresponding author (e-mail address): tamara.aleksandrov@fsb.hr

INTRODUCTION

Niobium Nb micro-alloyed low carbon steel contains small amounts of Nb as an alloying element (0.02-0.1 wt%), which has a significant impact on many material properties [1]. Niobium shows a strong affinity for nitrogen and carbon and causes the formation of niobium carbide and niobium nitride within the structure of the steel which improve the grain refining, retardation of recrystallization, and precipitation hardening [1-6]. Those precipitates are dispersed in the form of small Nb (CN) precipitates, which are arranged in



18th INTERNATIONAL FOUNDRYMEN CONFERENCE

Coexistence of material science and sustainable technology in
economic growth

Sisak, May 15th-17th, 2019

<http://www.simet.hr/~foundry/>

fine lines [1,2,4]. Grain refinement is the only mechanism that simultaneously increases strength, toughness and ductility and makes Nb one of the most effective microalloying element, even if added in very small content [7]. Consequently, the toughness, hardness, yield point, ultimate tensile strength, formability, and weldability of the micro-alloyed steel is increased with a small decrease in elongation [1-6].

Today, there is a wide range of tests for the determination of the material's mechanical properties. Besides conventional tests such as tensile test, macro hardness measurement and Charpy impact test, instrumented indentation technique is widely used for the characterization. Instrumented indentation technique is relatively new technology developed in recent years which directly measures the mechanical properties from indentation load /displacement measurements [8]. It can measure accurately not only the hardness but also Young's modulus of each phase, accordingly, provides reliable data for the microstructure and performance design of material [8]. No visual observation of the indentation is required; eliminating the subjectivity of diagonal length measurements [9].

To research the applicability of instrumented indentation technique for this group of materials the research described in the paper is performed.

MATERIALS AND METHODS

The mechanical properties of Nb micro-alloyed low carbon steel using instrumented indentation test were researched in the paper. The chemical composition of low carbon Nb micro-alloyed steel is shown in Table 1.

Table 1. Chemical composition of the researched Nb micro alloyed steel, wt%

C	Mn	Si	P	S	Al	Nb	N
0.09	0.75	0.05	0.018	0.014	0.020	0.035	0.0081

Dynamic ultra-microhardness tester, type: DUH-211, manufactured by Shimatzu, Japan, was used for the instrumented indentation test. Triangular indenter with 115 ° tip angle (Berkovich indenter) was used. Measurements were performed using different forces; 5 measurements with the maximum forces F_{max} of 100 mN, 200 mN and 1961 mN were performed. The load of 1961 mN corresponds to measuring method HV0.2. Different forces were applied to investigate the influence of the test force on the measured properties and to investigate the applicability of the methods for this kind of materials.

Based on carried measurement, different mechanical properties were determined as follows [10]:

Martens hardness HM is determined from the values given by the force/indentation depth curve during the increasing of the test force (applied force), preferably after reaching the specified test force according to [10]:



18th INTERNATIONAL FOUNDRYMEN CONFERENCE
Coexistence of material science and sustainable technology in
economic growth

Sisak, May 15th-17th, 2019

<http://www.simet.hr/~foundry/>

$$HM = \frac{F}{26.43 \times h^2} \quad (1)$$

where is:

h – indentation depth, F – applied force.

Martens hardness (HMs) is determined from the slope of the increasing force/indentation depth curve according to equation [10]:

$$HM_s = \frac{1}{26.43 \times m^2} \quad (2)$$

where is:

m – slope of the curve, determined by the linear regression of the increasing force / indentation depth curve

Indentation hardness H_{it} is defined as a measure of resistance to permanent deformation and was calculated according to [10]:

$$H_{it} = \frac{F_{max}}{A_p} \quad (3)$$

Where is:

A_p – projected area of contact between the indenter and the test piece determined, for triangular indenter with 115 ° tip angle (Berkovich indenter) $A_p = 23.96 \cdot h_c^2$;

h_c - the depth of the contact between the indenter and the sample determined, $h_c = h_{max} - \frac{3}{4}(h_{max} - h_r)$;

h_r . derived from the force-displacement curve and is the intercept of the tangent to the unloading cycle at F_{max} with the displacement axis as presented in Figure 1.

Indentation modulus E_{it} is calculated from the slope of the tangent for the calculation of indentation hardness H_{it} according to equation [10]:

$$\frac{1}{E_r} = \frac{1-V^2}{E_{it}} + \frac{1-V_i^2}{E_i} \quad (4)$$

$$S = \frac{dP}{dh} = \frac{2 \times E_r \times A_p^{0.5}}{\pi^2} \quad (5)$$

Where is:

E_r – reduced modulus of elasticity, E_i - modulus of indenter ($1.14 \cdot 10^6$ N/mm²), V_i - Poisson ration of indenter (0.07), V - Poisson ration of the sample, S – inclination when unloading.



18th INTERNATIONAL FOUNDRYMEN CONFERENCE
**Coexistence of material science and sustainable technology in
economic growth**

Sisak, May 15th-17th, 2019

<http://www.simet.hr/~foundry/>

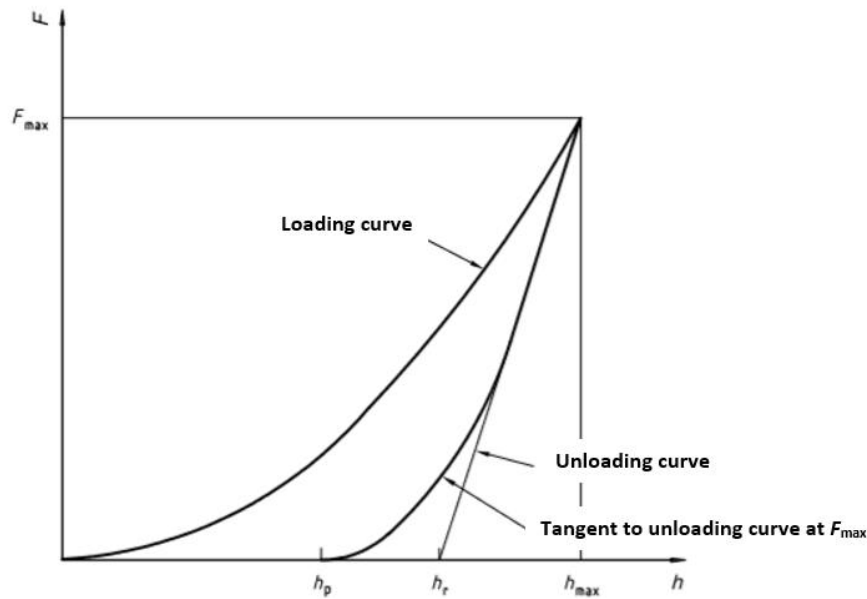


Figure 1. Force / indentation depth diagram [11]

Indentation creep C_{it} is defined as a relative change of indentation depth with respect to time of force application and is calculated according to [10]:

$$C_{it} = \frac{h_2 - h_1}{h_1}, (\%) \quad (6)$$

Where is:

h_1 – indentation depth at the time of maximum force, h_2 – indentation depth at the time of holding time.

Plastic and elastic parts of indentation work η_{it} is defined as a ratio of elastic work and total mechanical work W during application of the force and is calculated according to [10]:

$$\eta_{it} = \frac{W_{elast}}{W_{total}}, (\%) \quad (7)$$

$$W_{total} = W_{elast} + W_{plast} \quad (8)$$

Based on the performed measurement, HV hardness is calculated from the equation [10]:

$$HV = 0.0924 \times H_{it} \quad (9)$$



18th INTERNATIONAL FOUNDRYMEN CONFERENCE
Coexistence of material science and sustainable technology in
economic growth

Sisak, May 15th-17th, 2019

<http://www.simet.hr/~foundry/>

RESULTS AND DISCUSSION

The results of measurements are presented in Tables 2 to 4 while the force-indentation depth graphs are presented in Figures 2 to 4.

Table 2. Measurement results for the maximum force F_{max} of 100 mN

	F_{max} [mN]	h_{max} [μ m]	h_p [μ m]	h_r [μ m]	HM_s [N/mm ²]	H_{it} [N/mm ²]	E_{it} [N/mm ²]	C_{it} [%]	η_{it} [%]	HV*
1	101.52	1.4567	1.297	1.3775	2135.313	2170.154	1.76E+05	1.810	9.001	200.5
2	101.4	1.3285	1.193	1.2518	1547.631	2619.763	2.00E+05	1.243	8.517	242.1
3	101.43	1.2197	1.0531	1.1371	1888.213	3158.442	2.08E+05	2.601	9.122	291.8
4	101.4	1.4215	1.2736	1.3383	1967.441	2290.985	1.71E+05	1.710	9.581	211.7
5	101.45	1.267	1.0902	1.1867	1933.469	2907.497	2.05E+05	2.244	9.622	268.7
Aritm. mean	101.44	1.3387	1.1814	1.2583	1894.413	2629.368	1.92E+05	1.921	9.169	243.0
Std. Dev.	0.049	0.1	0.108	0.101	215.167	413.143	17109.432	0.521	0.455	38.174

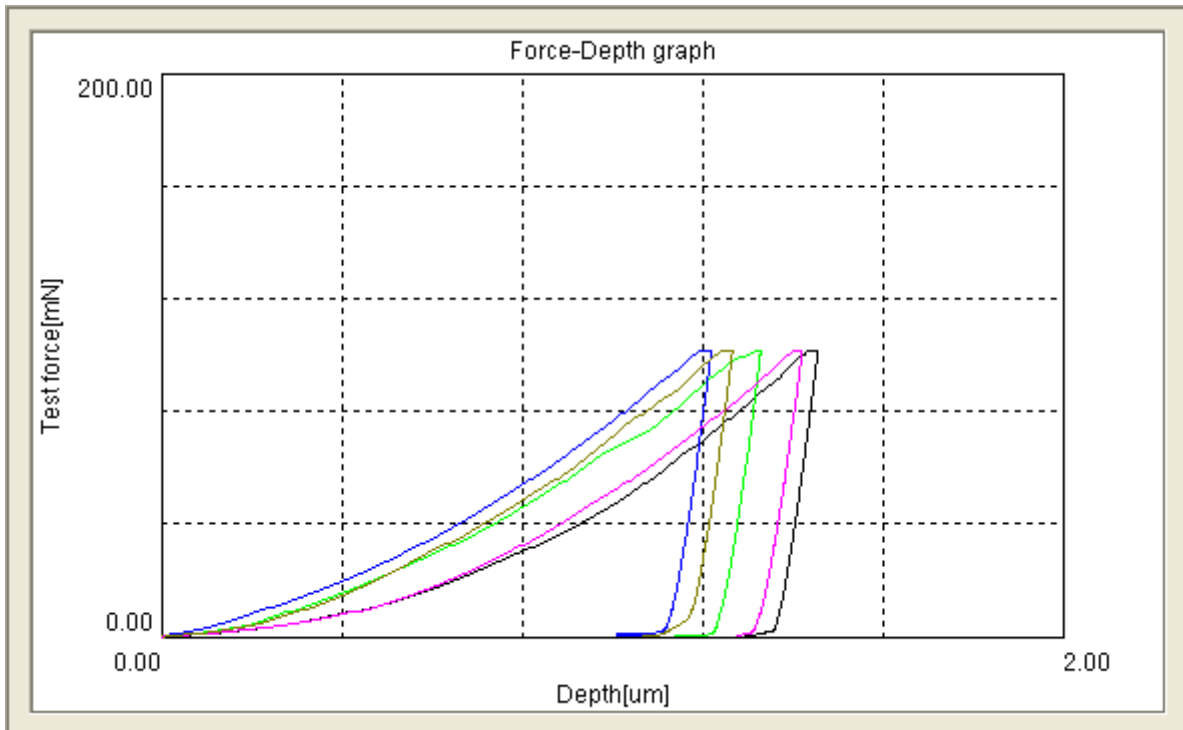


Figure 2. Force – indentation depth graphs for the maximum force F_{max} of 100 mN



18th INTERNATIONAL FOUNDRYMEN CONFERENCE

Coexistence of material science and sustainable technology in
economic growth

Sisak, May 15th-17th, 2019

<http://www.simet.hr/~foundry/>

Significant variations of measured hardness values and indentation modulus were obtained for the measurements with the maximum force F_{max} of 100 mN, as presented in Table 2 and Fig. 2. The lowest calculated Vickers hardness amounts to 200.5 HV while the highest Vickers hardness amounts to 291.8 HV. The standard deviation with the value of 17109.4 N/mm² was determined for the measured indentation modulus E_{it} , the lowest E_{it} amounts to 171000 N/mm² while the highest E_{it} amounts to 208000 N/mm². Indentation modulus is comparable to Young modulus of elasticity of steel. The reason for variations of measured properties may be attributed to microstructural characteristics. The microstructure of the researched sample consists of ferrite and perlite with Nb precipitates in the interaction with dislocations. The size of precipitates was measured to be in the range of 4–10 nm [1-2] and cannot be observed by an optical microscope. Since the indentations are quite small they were most probably positioned in one phase regions, only ferritic or perlitic.

Indentation creep C_{it} amounts to 1.9 % with the standard deviation of 0.5 % meaning that no significant relative change of indentation depth with respect to time of force application occurred.

Elastic part of indentation work amounts to approximately 9 % with the standard deviation of 0.45 % meaning that mostly plastic deformation occurred as a consequence of the applied load.

Table 3. Measurement results for the maximum force F_{max} of 200 mN

	F_{max} [mN]	h_{max} [μ m]	hp [μ m]	h_r [μ m]	HM_s [N/mm ²]	H_{it} [N/mm ²]	E_{it} [N/mm ²]	C_{it} [%]	η_{it} [%]	HV*
1	208.47	2.0399	1.8808	1.9117	1696.448	2302.891	1.583e+005	3.377	8.999	212.8
2	211.15	2.1396	1.9705	2.0110	1405.255	2111.089	1.512e+005	4.077	8.464	195.6
3	211.16	1.9922	1.8312	1.8618	1877.274	2455.803	1.618e+005	3.631	9.422	226.9
4	210.55	1.8688	1.6965	1.7371	1477.437	2804.792	1.724e+005	4.092	9.157	259.2
5	211.15	2.1450	1.9649	2.0128	1657.001	2105.589	1.455e+005	4.496	9.714	194.6
Aritm. mean	210.50	2.0371	1.8688	1.9069	1622.683	2356.033	1.579e+005	3.935	9.151	217.7
Std. Dev.	1.165	0.115	0.113	0.115	186.954	290.208	10290.551	0.437	0.471	26.81

The differences of measured hardness values and indentation modulus were noted for the measurements performed with the maximum force F_{max} of 200 mN as for 100 mN applied force. Still, standard deviations are smaller compared to standard deviations determined for the results obtained by 100 mN applied force. The lowest calculated Vickers hardness amounts to 194.6 HV while the highest Vickers hardness amounts to 259.2 HV. The standard deviation with the value of 10290.5 N/mm² was determined for the measured indentation modulus E_{it} , the lowest E_{it} amounts to 145500 N/mm² while the highest E_{it} amounts to 172400 N/mm². The hardness and indentation modulus are lower compared to hardness



18th INTERNATIONAL FOUNDRYMEN CONFERENCE
**Coexistence of material science and sustainable technology in
economic growth**

Sisak, May 15th-17th, 2019

<http://www.simet.hr/~foundry/>

and indentation modulus determined by 100 mN test force indicating that the measured values are dependent of the applied load.

Indentation creep C_{it} amounts to 3.9 % with the standard deviation of 0.4 % which is higher compared to 100 mN results while the elastic part of indentation work amounts to approximately 9 % with the standard deviation of 0.45 % and corresponds to the elastic part of indentation work of 100 mN results.

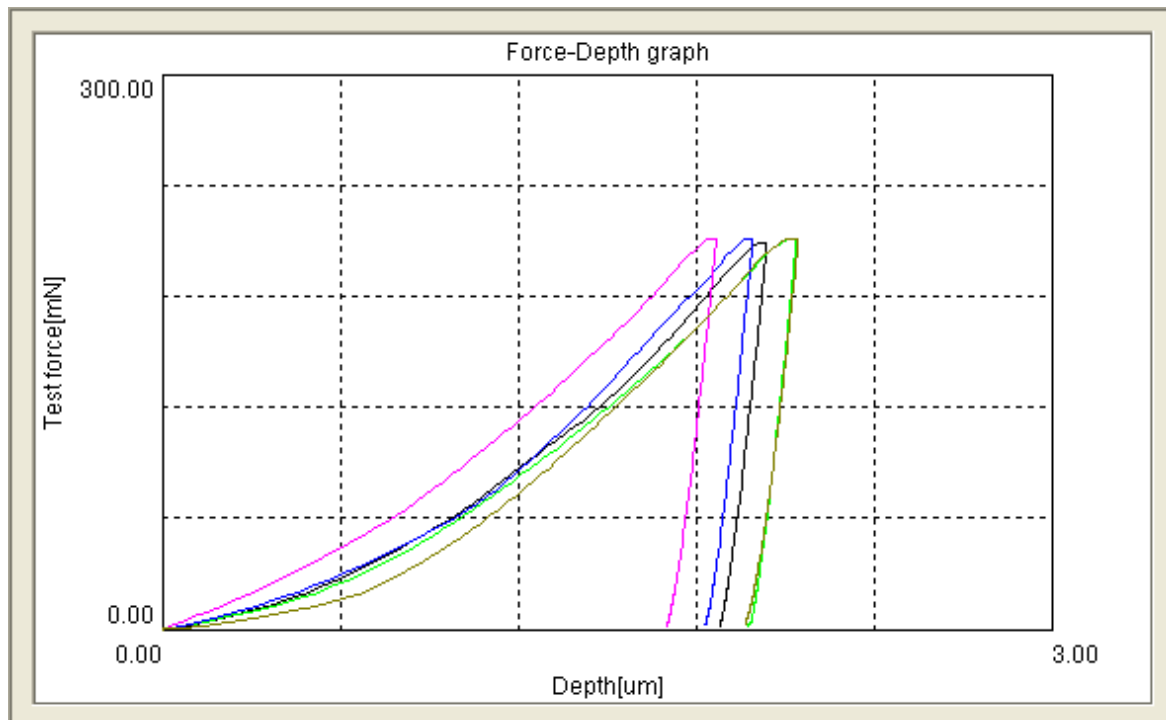


Figure 3. Force – indentation depth graphs for the maximum force F_{max} of 200 mN

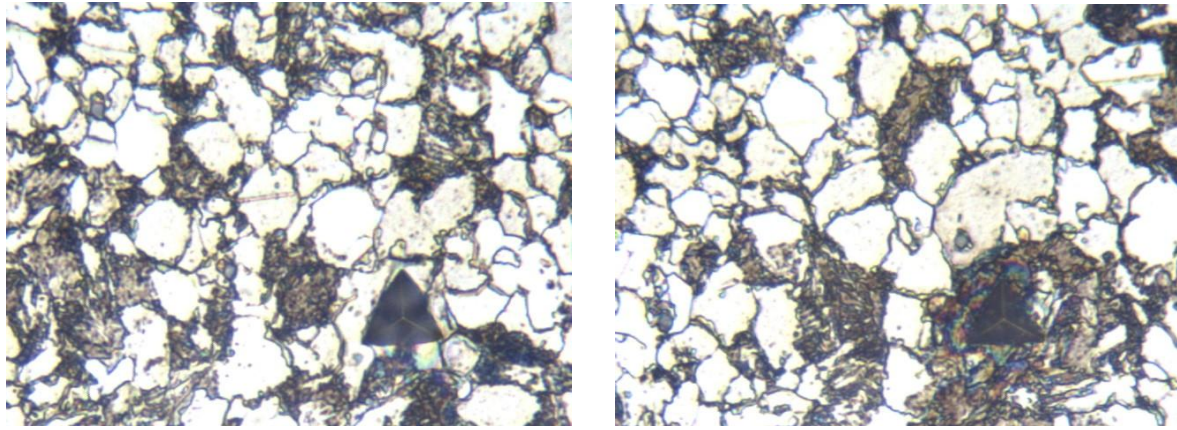
As already stated in the text, the variations of measured hardness and indentation modulus may be attributed to microstructural characteristics. The indentations on the etched samples surface were analysed on optical measurement system which is integral part of the machine. The microstructure with indentation is presented in Figure 4.



18th INTERNATIONAL FOUNDRYMEN CONFERENCE
**Coexistence of material science and sustainable technology in
 economic growth**

Sisak, May 15th-17th, 2019

<http://www.simet.hr/~foundry/>



a)

b)

Figure 4. Indentations applied by 200 mN force

a) ferrite region; b) perlite region

The microstructure of the researched sample consists of a ferrite and perlite with Nb precipitates.

Indentation presented in Figure 4. a) placed in the ferrite region is smaller compared to indentation placed in the perlite region (Figure 4. b) which explains the differences in measured hardness and other properties. Differences are not desirable when determining the mechanical properties of the material in general, but it is desirable when the mechanical properties of the individual phases need to be determined, which is also one of the advantages of the instrumented indentation technique. For determination of sample's mechanical properties in general, the force of 1969 mN was applied which corresponds to measuring method HV0.2 (Table 4 and Figure 5).

Table 4. Measurement results for the maximum force F_{max} of 1969 mN

	F_{max} [mN]	h_{max} [μ m]	hp [μ m]	h_r [μ m]	HM_s [N/mm ²]	H_{it} [N/mm ²]	E_{it} [N/mm ²]	C_{it} [%]	η_{it} [%]	HV*
1	1969.53	6.2181	5.3752	5.6733	1861.861	2435.563	1.13E+05	1.077	13.231	225.1
2	1968.69	6.3136	5.471	5.7678	1729.125	2357.0	1.10E+05	1.094	13.115	217.8
3	1968.5	6.1885	5.4082	5.6349	1682.922	2464.885	1.12E+05	1.09	13.254	227.8
4	1968.28	6.2727	5.3419	5.7291	1844.821	2388.136	1.12E+05	1.136	13.005	220.7
5	1968.27	6.5354	5.6419	6.0000	1560.165	2183.37	1.08E+05	1.065	12.339	201.7
Aritm. mean	1968.65	6.3057	5.4477	5.761	1735.779	2365.791	1.11E+05	1.092	12.989	218.6
Std. Dev.	0.52	0.137	0.119	0.143	123.961	110.161	1818.187	0.027	0.377	10.179



18th INTERNATIONAL FOUNDRYMEN CONFERENCE
**Coexistence of material science and sustainable technology in
economic growth**

Sisak, May 15th-17th, 2019

<http://www.simet.hr/~foundry/>

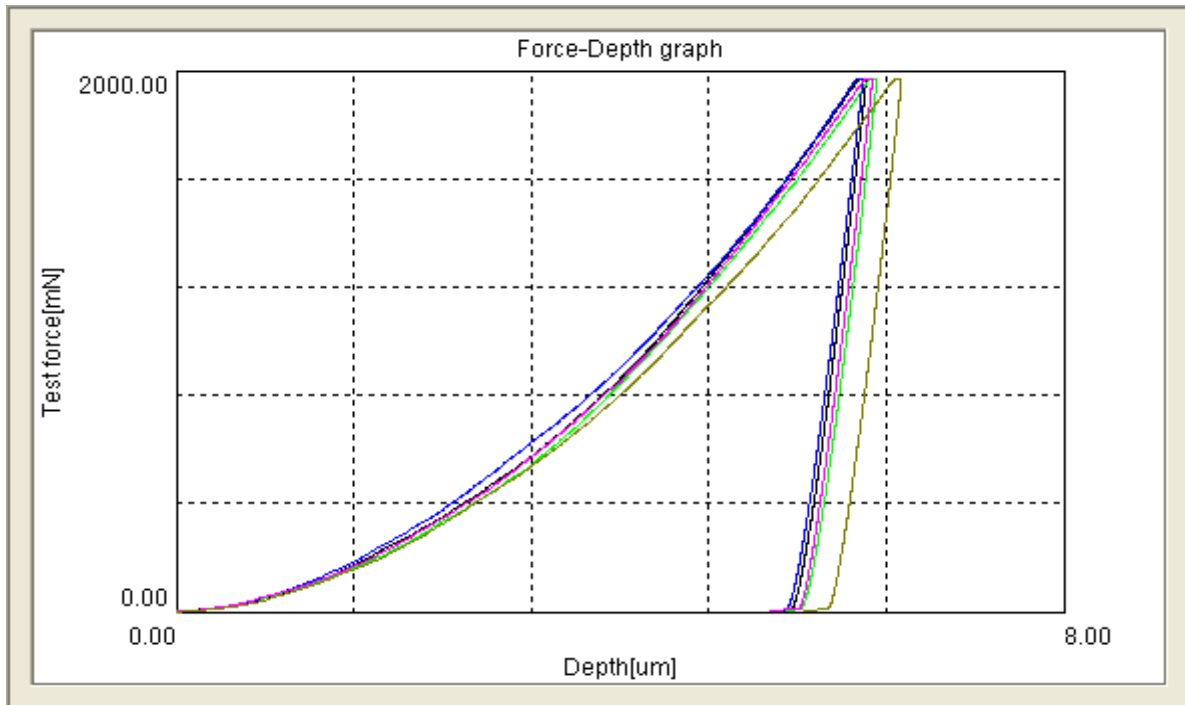


Figure 5. Force – indentation depth graphs for the maximum force F_{max} of 1969 mN

The variations of measured hardness values and indentation modulus are not significant since both ferrite and perlite grains are covered by indentions as presented in Figure 6. Accordingly, standard deviations are significantly smaller compared to standard deviations determined by lower forces (100 mN and 200 mN). The lowest calculated Vickers hardness amounts to 201.7 HV while the highest Vickers hardness amounts to 225.1 HV. The standard deviation with the value of 1818.2 N/mm^2 was determined for the measured indentation modulus E_{it} whose arithmetical mean amounts to 111000 N/mm^2 . The indentation modulus is much lower compared to indentation modulus determined by smaller loads and compared to Young modulus of elasticity which will be the topic of future research.



18th INTERNATIONAL FOUNDRYMEN CONFERENCE
**Coexistence of material science and sustainable technology in
economic growth**

Sisak, May 15th-17th, 2019

<http://www.simet.hr/~foundry/>

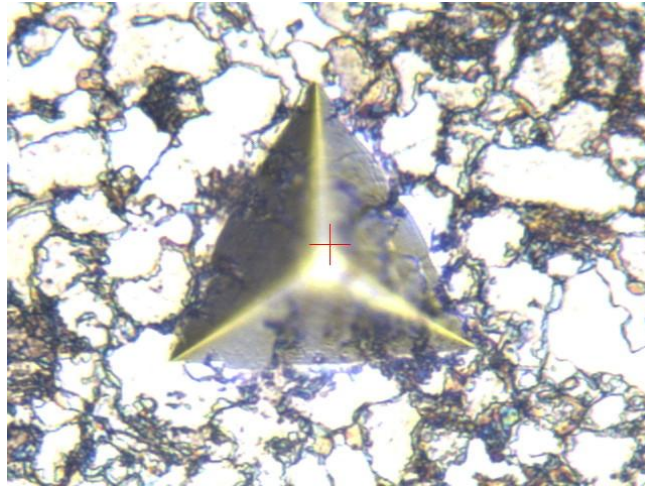


Figure 6. Indentation applied by 1969 mN force in two phase regions

CONCLUSIONS

From the conducted research can be concluded as follows:

- The maximum applied force F_{max} significantly influenced the measured mechanical properties of low carbon Nb micro-alloyed steel; higher values of hardness and indentation modulus and bigger standard deviations of measuring results were obtained for smaller forces. Smaller forces are not recommended for determination of sample's mechanical properties in general.
- Deviation of the measured properties may be attributed to microstructural characteristics since the low carbon Nb micro-alloyed steel consists of ferrite and perlite phases with Nb precipitates. The load of 100 mN and lower could be applied for the determination of mechanical properties of the individual phases.
- The maximum applied force didn't significantly affect the indentation creep values and the ratio of elastic and overall work.

Acknowledgements

This work has been fully supported by the Croatian Science Foundation under the Project Number IP-2016-06-1270.



18th INTERNATIONAL FOUNDRYMEN CONFERENCE

Coexistence of material science and sustainable technology in economic growth

Sisak, May 15th-17th, 2019

<http://www.simet.hr/~foundry/>

REFERENCES

- [1] T. Brlić, T. Aleksandrov Fabijanić, I. Jandrić, M. Franz, Ž. Alar, S. Rešković, The influence of Nb content on the mechanical properties of micro alloyed low carbon steels, Proceedings of 19th World Congress on Materials Science and Engineering, Conference Series Ilc LTD, 11-13.6.2018., Barcelona, Spain, pp. 151-152.
- [2] I. Jandrić, S. Rešković, T. Brlić, Distribution of stress in deformation zone of niobium microalloyed steel, Metals and Materials International, 24(2018)4, pp. 746-751.
- [3] S. Shanmugama, N. K. Ramiseti, R. D. K. Misra, T. Mannering, D. Panda, S. Jansto, Effect of cooling rate on the microstructure and mechanical properties of Nb-microalloyed steels, Materials Science and Engineering A, 460-461(2007), pp. 335-343.
- [4] D. Bhattacharya, Microalloyed steels for the automotive industry, Technol. Metal. Mater. Miner., 11(2014)4, pp. 371-383.
- [5] M. I. Equbal, P. Talukdar, V. Kumar, R. K. Ohdar, Deformation behavior of micro-alloyed steel by using thermo mechanical simulator and finite element method, Proc. Mater. Sci., 6(2014), pp. 674-681.
- [6] W. B. Morrison, Overview of microalloying in steel, The Proceedings of the Vanitec Symposium, The Vanadium International Technical Committee, Vanitec Limited, Westerham Kent, England, 2000, Guilin, China, pp. 25-35.
- [7] C. Klinkenberg, S. G. Jansto, Niobium microalloyed steels for long products, Proceedings Book of International Conference New Developments in Long and Forged Products: Metallurgy and Applications, AIST, Warrendale, PA, 2006, pp.135.
- [8] X. Wang, X. Yang, Z. Guo, Y. Zhou, H. Song, Nanoindentation Characterization of Mechanical Properties of Ferrite and Austenite in Duplex Stainless Steel, Advanced Materials Research, 26-28(2007), pp. 1165-1170.
- [9] D. Li, VICKERS HARDNESS VS. MACRO INSTRUMENTED INDENTATION A COMPARATIVE STUDY, Accessible on Internet <http://nanovea.com/App-Notes/vickers-hardness.pdf>, 15.3.2019.
- [10] Shimadzu Dynamic Ultra-micro hardness Testing DUH-211/DUH-211S, Instructional Manual, c347-05351F, September 2009.
- [11] ISO 14577-1:2015: Metallic materials - Instrumented indentation test for hardness and materials parameters - Part 1: Test method



18th INTERNATIONAL FOUNDRYMEN CONFERENCE

Coexistence of material science and sustainable technology in
economic growth

Sisak, May 15th-17th, 2019

<http://www.simet.hr/~foundry/>

THE INFLUENCE OF WATER MIST INJECTION ON THE FILM COOLING PROCESS OF CASTED TURBINE BLADES

Jakov Baleta¹, Damijan Cerinski^{1*}, Fengsheng Qi², Fang Wang², Jin Wang³, Xuebin Wang⁴

¹ University of Zagreb Faculty of Metallurgy, Sisak, Croatia

² Northeastern University School of Metallurgy, Shenyang, People's Republic of China

³ Hebei University of Technology School of Energy and Environmental Engineering, Tianjin, People's
Republic of China

⁴ Xi'an Jiaotong University School of Energy and Power Engineering, Xi'an, People's Republic of China

Oral presentation

Original scientific paper

Abstract

Casted turbine blades are usually made of Ni-based super alloys, which are capable to withstand higher temperatures than other technical metal materials and have good corrosion resistance properties. The combustion efficiency highly depends on the temperature, but currently used turbine blades materials are not capable to withstand such conditions, therefore utilising the film cooling process is necessary. The influence of water mist injection on the film cooling process of casted turbine blades was numerically investigated. CFD simulations were performed to describe the interaction between the hot stream gas from the combustion chamber and the coolant jet from a cooling hole along with the water mist injection. The validation case with the cylindrical hole was compared to the experimental results and results from Large Eddy Simulation (LES) available in the literature. Temperature distributions were analysed and compared to the case with a laidback hole and console configuration to investigate the influence of injecting the water mist on cooling performance. The results showed the possibility of improving the film cooling performance by implementing the water mist injection system which allows the increase of the temperature in the combustion chamber, and consequently overall gas turbine efficiency.

Keywords: *CFD, casted turbine blades, film cooling, water mist injection*

*Corresponding author (e-mail address): dcerinski@simet.hr



18th INTERNATIONAL FOUNDRYMEN CONFERENCE

Coexistence of material science and sustainable technology in
economic growth

Sisak, May 15th-17th, 2019

<http://www.simet.hr/~foundry/>

INTRODUCTION

According to thermodynamics laws, gas turbine efficiency highly depends on the condition of gas flow from the combustion chamber. Higher gas temperature at the turbine section inlet initiates higher overall efficiency due to the more energy accumulated in the combustion products [1]. Albeit, turbine blades materials recorded significant development in recent years, especially by implementing superalloys, highest gas temperatures are still limited with its properties [2]. One reliable way to cope with this issue is to implement film cooling of the turbine blades with an aim to prevent highest temperatures reaching the blade surface [3]. The importance of the film cooling process is very well elaborated in the research by Mishra et al. [4]. They performed metallurgical analysis of an un-cooled fractured blade on the aircraft engine, which was exposed to the higher temperature because of the failure in the engine control system. Their analysis showed that fatigue caused the failure on the turbine blade, and cracks were initiated at the leading edge and propagated to the trailing edge due to the blade surface oxidation. Film cooling process is based on the additional cold flow through small channels which passes through the turbine blade. The geometry of cooling channels represents a parameter which influences on the film cooling efficiency. In order to improve film cooling performance, the optimal geometry of the cooling channel needs to be determined [5].

Numerical modelling, specifically Computational Fluid Dynamics (CFD) models were recognized by many researchers as a valuable tool for optimizing the film cooling process over the turbine blades [6]. Hence, Zhu et al. [7] combined numerical and experimental analysis of turbine blades film cooling with cylindrical and fanshaped holes by varying mainstream pressure gradients. Their main findings were summed as a high impact of pressure gradients on cylindrical holes cooling performance, while much lower effect was noticed with fanshaped holes. Also, Yu et al. [8] numerically analysed the converging slot-hole with a different mainstream Reynolds number and at different blowing ratios. Results showed the small reduction of enthalpy loss coefficient by increasing the Reynolds number and blowing ratio, although the cooling effectiveness was highly enhanced. A similar group of authors also numerically investigated different configuration of round-to-slot multi-row cooling holes performance under real engine conditions [9]. In the conclusion they suggested equivalent-area configuration of round-to-slot holes as an optimal cooling solution considering the enthalpy loss coefficient, coolant feeding ratio and overall film cooling efficiency. The effect of pin-fin shaped cooling holes was numerically and experimentally researched by Tan et al. [10]. Two hole shapes were modelled, first was elliptical, while the other one was drop-shaped and the results were compared to the cylindrical hole configuration. Main findings of this research were manifested in better cooling efficiency of pin-fin shaped holes, especially the configuration with elliptical holes. The influence of hole geometry on film cooling performance within the blade leading edge was investigated by Fan et al. [11]. In this research, the vortex chamber was introduced before the cooling channel and diameter ratio (DR), defined as a diameter of cooling hole divided by vortex chamber diameter, was varied and optimal solution of DR=0.1 was determined. The parameter which can also influence on the cooling performance is the



18th INTERNATIONAL FOUNDRYMEN CONFERENCE

Coexistence of material science and sustainable technology in
economic growth

Sisak, May 15th-17th, 2019

<http://www.simet.hr/~foundry/>

orientation of cooling holes. Guided by that, Liu et al. [12] experimentally and numerically investigated two different cooling holes orientation angle where they remarked few phenomena which occur under different hole orientation angle, and suggested more research by varying the hole orientation angle to determine the optimal solution. The enhancement possibility of horn-shaped and cylindrical hole film cooling process by adding the secondary hole injection was numerically investigated in research by Zhu et al. [13]. Authors varied secondary hole inclination angle and noticed that the efficiency of higher inclination angle was in a correlation with blowing ratio. In other words, for optimal cooling efficiency inclination angle needs to be increased if the blowing ratio is higher. The influence of backward injection holes was discussed in research by Park et al. [14]. The results showed that by adding cooling holes with opposite stream direction than the hot flow, the cooling efficiency could be improved. Another way to improve the film cooling effectiveness is by implementing the hole blockage configuration. Tian et al. [15] performed numerical simulations and presented small cooling improvement by adding the tetrahedral hole blockage configuration.

An additional method for improving the film cooling performance is the injection of water mist droplets together with coolant flow. In research by Baleta et al. [16] the implemented water mist injection model for spray cooling process within the CFD code was demonstrated. In that way, Wang et al. [17] numerically simulated the injection of water mist droplets in order to enhance the film cooling effectiveness, and they achieved three times better cooling coverage compared to the simulation without water mist. Also, analysis of surface blades film cooling with and without water mist was performed by Tian et al. [18]. In this research initial droplets diameter was varied and results of three cases ($1\ \mu\text{m}$, $5\ \mu\text{m}$ and $10\ \mu\text{m}$) were analysed. Results indicate that with smaller droplets, higher evaporation rate was achieved, and consequently the overall cooling efficiency increases. The influence of water mist injection on a cooling channel configuration with a deposition was analysed by Wang et al. [19]. They showed that the injection of water mist improved the cooling performance, especially downstream the deposition due to the droplets intention to fly downstream to the wall. It is also possible to implement some other numerical approach for modelling the film cooling process. In this manner, Dávalos et al. [20] developed Artificial Neural Network (ANN) model where input and output data was gathered from previously validated CFD simulations. The ANN and CFD results were in good agreement and authors showed that the model could be used for the optimization process. Considering the literature review above, there is a possibility to improve the film cooling process by varying the cooling hole geometry and implementing the water mist injection. Thus, in this study, three different shaped cooling holes were modelled and the influence of water mist injection was numerically analysed using the CFD software AVL FIRE®.

This research is structured as follow: first, a short description of mathematical model is shown, then the simulation setup is described. The validation of research model is provided next, while at the end, the results and final conclusion with suggestions for future work are given.



18th INTERNATIONAL FOUNDRYMEN CONFERENCE

Coexistence of material science and sustainable technology in
economic growth

Sisak, May 15th-17th, 2019

<http://www.simet.hr/~foundry/>

MATERIAL AND METHODS

Within this section the used mathematical model is described, geometry is analysed and at the end simulation setup is provided.

Mathematical model

The motion of fluid is described with transport equations which solve the continuum based on conservation laws of mass (Equation of Continuity), momentum (Newton's second law) and energy (The First Law of Thermodynamics). They are obtained by using the finite volume approach where the observed domain is divided into a number of control volumes and a mathematical description is developed for the finite control volume. The general transport equation of some extensive properties φ can be written as:

$$\int_V \frac{\partial}{\partial t} (\rho\varphi) dV + \int_S (\rho\varphi) u_i n_i dS = \int_S \left(\Gamma_\varphi \frac{\partial \varphi}{\partial x_i} \right) n_i dS + \int_V S_\varphi dV \quad (1)$$

The first term on the left-hand side of the equation represents the rate of change of the properties φ within the finite control volume, while the second term is the net convective flux of this property across the surface of the control volume. The first term on the right-hand side is the net diffusive flux across the control volume boundaries, and the second term is the source or sink of the property φ . Substituting the term φ with some physical properties, each conservation law is prescribed. Substituting φ with following properties: density (ρ), momentum (ρu_i) and energy density (ρe), conservation laws of mass, momentum and energy are obtained. In order to solve a turbulent behaviour of the flow, a well-known $k - \varepsilon$ turbulence model was applied [21].

Geometry description

The geometry consists of a hot flow channel and a cooling hole (Figure 1). The geometry represents a small part of a volume above the turbine blade where the inlet is faced to the leading edge, while the outlet is faced to the trailing edge. In order to investigate the influence of hole geometry on the film cooling efficiency, four different cooling hole configurations were modelled.

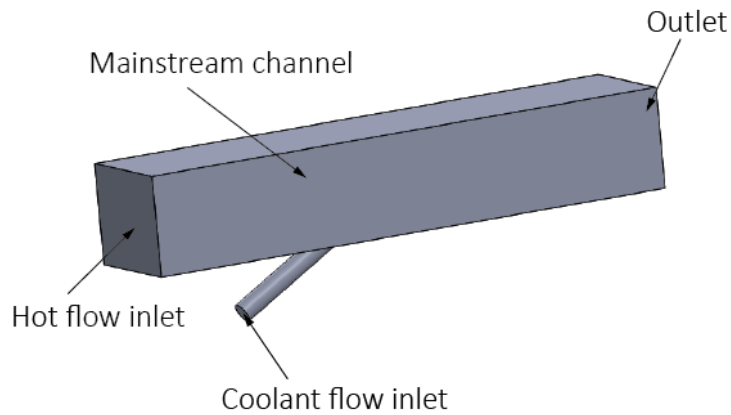


Figure 1. Geometry for simulations

In Figure 2 dimensions of the geometry are shown with a round hole cooling configuration. The diameter in all four geometries was set to 10 mm and all outer dimensions, together with a coolant channel angle, remained unchanged.

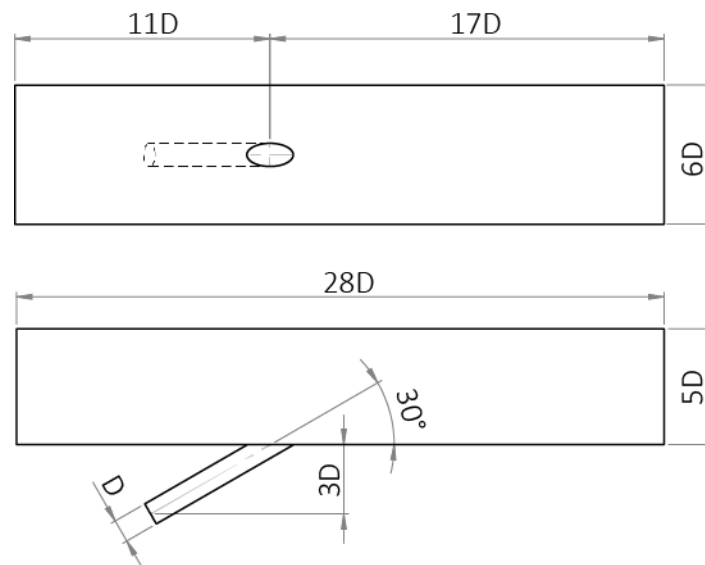


Figure 2. Geometry dimensions of the round hole cooling configuration

In Figure 3 other three coolant hole configurations are shown. For easier further correspond on each case, geometries are named in the following order: round hole, laidback hole, fanshaped hole and console. All geometries were modelled in CAD software SolidWorks and further imported into the CFD software AVL FIRE® for meshing procedure.



18th INTERNATIONAL FOUNDRYMEN CONFERENCE
**Coexistence of material science and sustainable technology in
economic growth**

Sisak, May 15th-17th, 2019

<http://www.simet.hr/~foundry/>

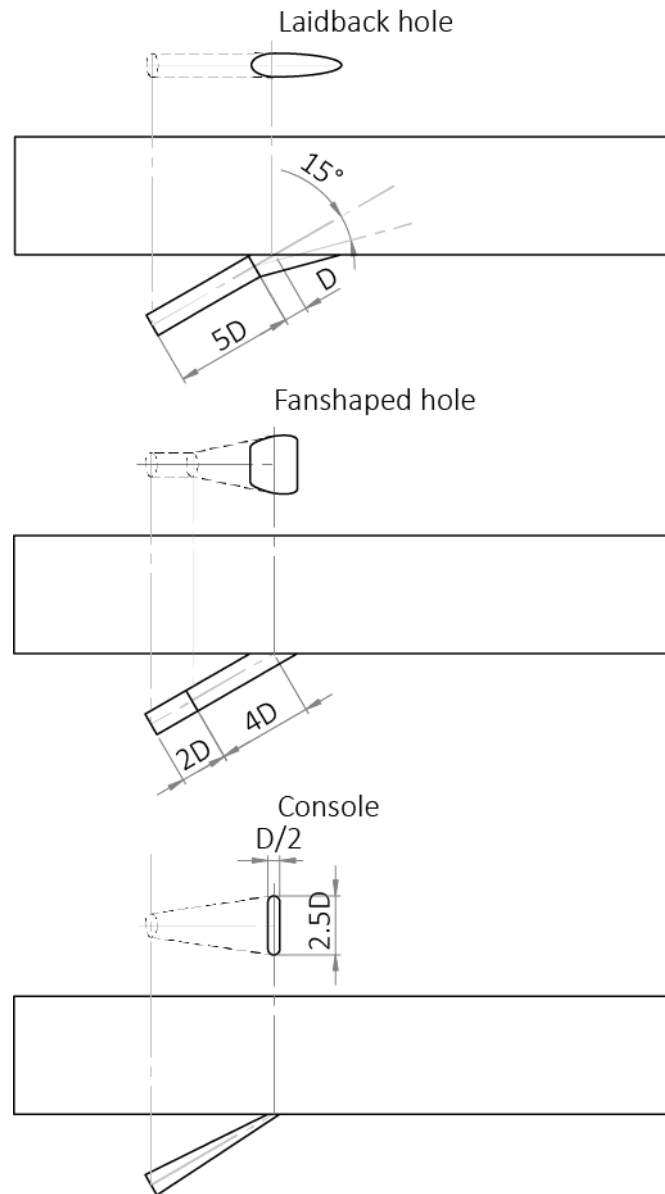


Figure 3. Cooling hole geometry variation

Simulation setup

In this section simulation setup is shown. The section is divided into three subsections. First, mesh dependency setup is shown, further the boundary and initial conditions are described, and at the end, other numerical setup is obtained.

Mesh dependency setup

The mesh dependency test needs to be performed to choose the discretisation level which provides the optimal choice between solution accuracy and computational time. In this research mesh dependency test was performed on a round hole coolant configuration



18th INTERNATIONAL FOUNDRYMEN CONFERENCE
**Coexistence of material science and sustainable technology in
economic growth**

Sisak, May 15th-17th, 2019

<http://www.simet.hr/~foundry/>

without the water mist injection. Three meshes with a different number of control volumes (CV) were generated with resolutions shown in Table 1.

Table 1. Different mesh resolution

Mesh	Total number of CV
Rough	264122
Medium	569245
Fine	726613

Boundary and initial conditions

Selections for boundary conditions are shown in Figure 4 while in Table 2 boundary conditions are prescribed.

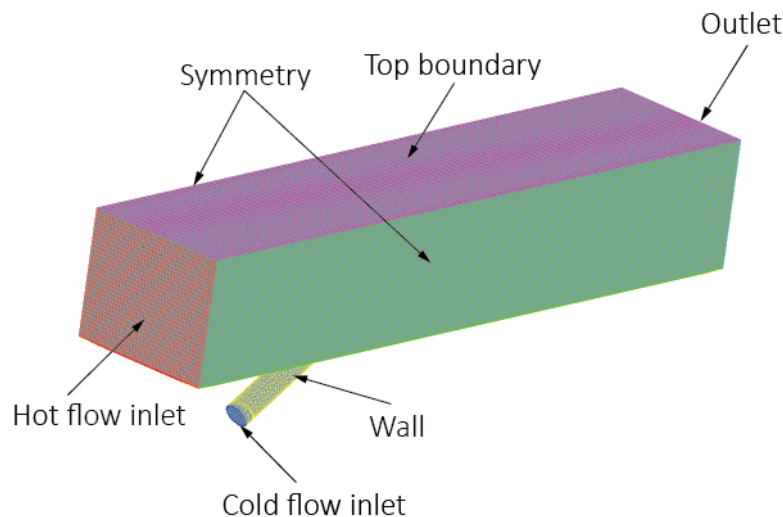


Figure 4. Selections for boundary conditions

Conditions of cold flow were determined by a blowing ratio, M which can be expressed as:

$$M = \frac{u_c \rho_c}{u_h \rho_h} \quad (2)$$

where the density ratio of cold and hot flow was set to 1.75. Turbulence intensity and turbulent length scale were set as same values for both cold and hot flow. At the cold flow inlet selection, the injection of water mist was prescribed, where the mass flow was calculated as 33% of cold mass flow.



18th INTERNATIONAL FOUNDRYMEN CONFERENCE
**Coexistence of material science and sustainable technology in
economic growth**

Sisak, May 15th-17th, 2019

<http://www.simet.hr/~foundry/>

Table 2. Boundary conditions

Hot flow inlet temperature	540 K
Hot flow inlet velocity	130 m/s (40 m/s for simulations with water mist)
Cold flow inlet temperature	310 K
Blowing ratio	$M = 0.5$
Water mist mass flow	33% of cold mass flow
Wall	Adiabatic boundary condition
Symmetry	Symmetry
Top boundary	grad = 0
Outlet	$p = 1 \text{ bar}$
Turbulence intensity	5.2%
Turbulent length scale	5 μm

Numerical setup

A steady state numerical simulations were performed for cases without water mist, while the transient mode was applied when the water mist was considered. For turbulence and energy transport equations the first order Upwind Differencing Scheme (UDS) was applied, whilst for the continuity equation, the Central Differencing Scheme (CDS) was employed. For the momentum equation, a combination of CDS and UDS was proposed by introducing a blending factor of 0.5. The convergence of the solution was achieved when the normalised momentum, energy and pressure residuals reached a value below than 10^{-4} . The pressure-velocity coupling was performed by using the SIMPLE algorithm.

MODEL VALIDATION

The model was validated with results from experimental analysis and LES simulations with a case without the water mist. The experimental results were obtained from research by Saumweber and Schulz [22], while the results of LES simulations were taken from the research by Wang et al. [23]. The comparison of the cooling efficiency for a cylindrical cooling hole configuration is shown in Figure 5. The cooling efficiency is described with the following expression:

$$\eta = \frac{T_{hf} - T_{wall}}{T_{hf} - T_{cf}} \quad (3)$$

In the equation above the term T_{hf} represents the hot flow inlet temperature, term T_{cf} is the cold flow inlet temperature, while T_{wall} is the radial averaged wall temperature along



18th INTERNATIONAL FOUNDRYMEN CONFERENCE

Coexistence of material science and sustainable technology in
economic growth

Sisak, May 15th-17th, 2019

<http://www.simet.hr/~foundry/>

the axial distance through the mainstream channel starting from the centre of the cooling hole. Observing the Figure 5, it can be noticed that in the vicinity of the cooling hole, research model gives a slightly higher cooling efficiency than the experiment and LES simulation, while this difference is decreased through the mainstream channel. It can be concluded that the research model provides satisfying results and it can be used for analysing other hole geometries.

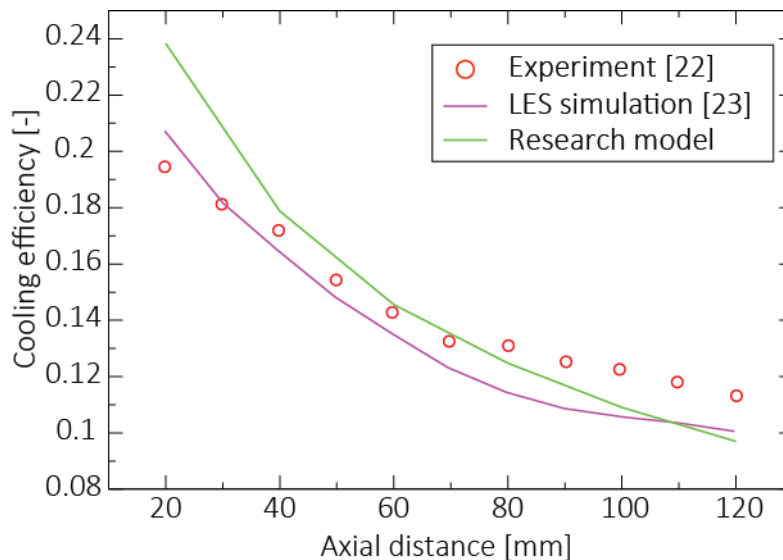


Figure 5. Model validation – cooling efficiency

RESULTS AND DISCUSSION

In this section, the mesh dependency test will be analysed, and furthermore the influence of the cooling hole geometry together with water mist injection will be investigated.

Mesh dependency test

First, the mesh dependency test will be performed in order to determine the optimal computational mesh. In Figure 6 radial wall temperature profiles, distant 40 mm from the cooling hole centre, for three different computational meshes are shown. It is visible that the medium and fine mesh provides same temperature profiles, while with the rough mesh there is some deviation in the middle of the geometry.



18th INTERNATIONAL FOUNDRYMEN CONFERENCE
**Coexistence of material science and sustainable technology in
economic growth**

Sisak, May 15th-17th, 2019

<http://www.simet.hr/~foundry/>

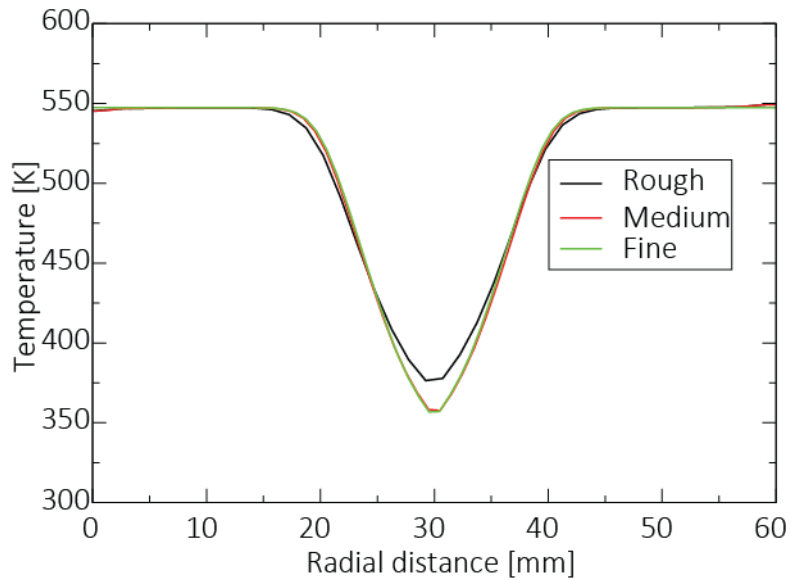


Figure 6. Radial wall temperature for different meshes

Velocity radial profiles for different meshes are shown in Figure 7. It is visible that the rough mesh significantly deviates from finer meshes, while the medium mesh has a small deviation in comparison to the fine mesh.

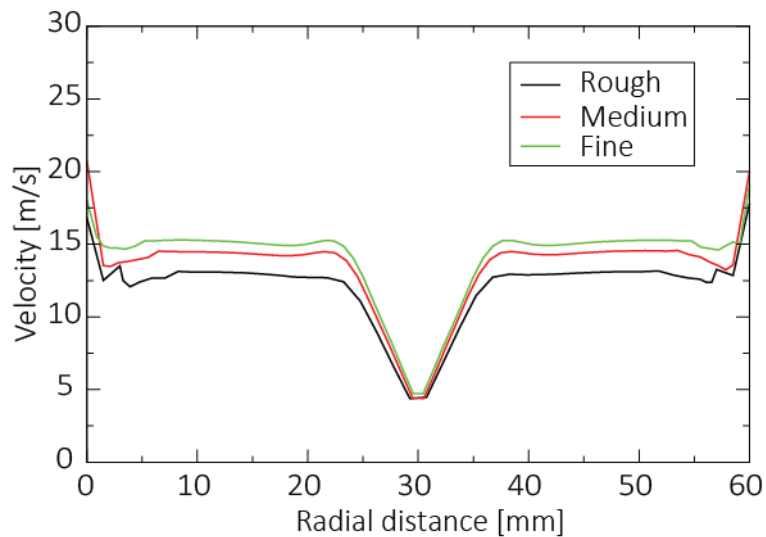


Figure 7. Velocity radial profiles for different meshes

Mesh dependency test shows that the medium mesh provides satisfactory accuracy for this research, and in all other simulations, medium mesh configuration was used.



18th INTERNATIONAL FOUNDRYMEN CONFERENCE
**Coexistence of material science and sustainable technology in
economic growth**

Sisak, May 15th-17th, 2019

<http://www.simet.hr/~foundry/>

The influence of cooling geometry hole

As it was already stated before, four different cooling hole configurations were observed: cylindrical, laidback, fanshaped and console configuration. In Figure 8 temperature distributions from a side view through the computational domain are shown. It is visible that simulations with round and laidback holes create a thicker film cooling layer than other configurations, while the coolant flow is more axially penetrated through the mainstream channel.

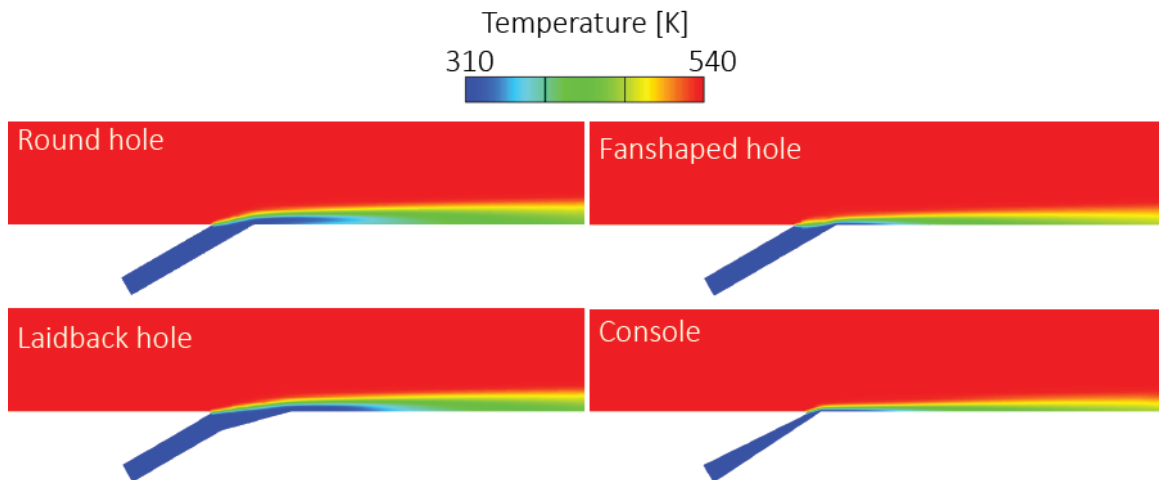


Figure 8. Temperature distribution comparison

The top view of the mainstream channel is analysed in Figure 9. It is visible that with wider cooling hole outlet, the wider cooling trace is achieved. Also, it can be noticed that the laidback hole configuration achieves the best coolant propagation in the axial direction, while the console configuration achieves widest cooling area together with second best propagation in the axial direction.

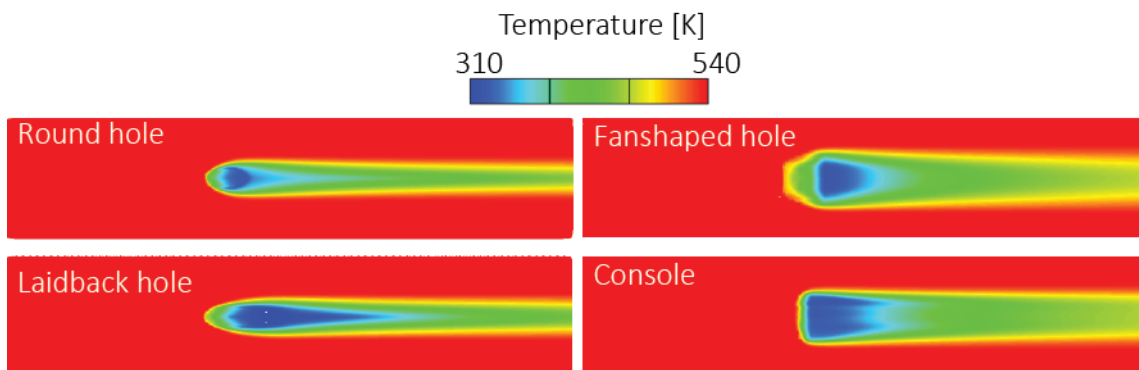


Figure 9. Temperature distribution comparison from top view



18th INTERNATIONAL FOUNDRYMEN CONFERENCE
**Coexistence of material science and sustainable technology in
economic growth**

Sisak, May 15th-17th, 2019

<http://www.simet.hr/~foundry/>

Quantitative comparison of different hole configurations is presented in Figure 10 and 11. Radial temperature profile located 40 mm downstream from the centre of the cooling hole shows that temperature drop depends also on the width of the cooling trace. This is expected because narrow cooling trace means that all cooling capacity is concentrated over a smaller area and will thus absorb more heat. On the other hand, a wider cooling trace will cause smaller temperature drop over a wider area. Thus, laidback hole has the biggest temperature drop and console configuration has the most uniform cooling over the blade width.

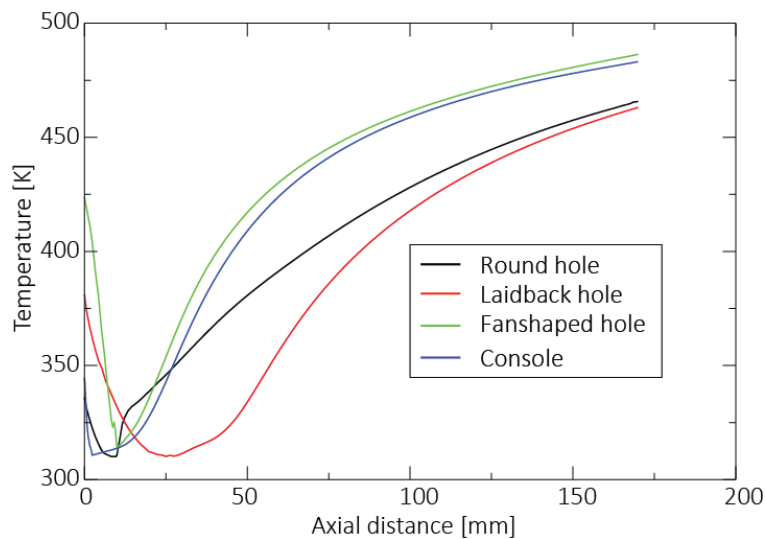


Figure 10. Axial temperature profile along the mainstream channel

Although the area around cooling hole bears the most heat load, effective cooling system also takes into account blade area downstream. Figure 11 depicts the temperature profile for studied hole configurations. Round hole and laidback hole show better axial cooling compared to the fanshaped hole and console configuration, due to the fact that narrow cooling trace retains more cooling capability further downstream. It should be also noted that better axial cooling doesn't necessarily mean good coverage over the blade width. Due to this reason laidback hole has been employed for further investigation as a candidate with the best axial cooling results and console has been employed as a candidate with the best cooling distribution over the blade width.

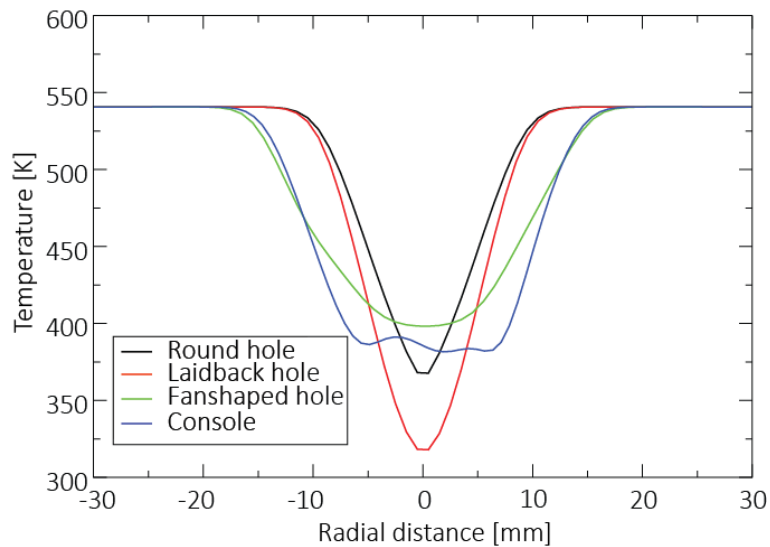


Figure 11. Radial temperature profile distant 40 mm from the cooling hole

The influence of water mist injection

Water mist injection is simple technic which improves film cooling efficiency by utilizing latent heat of the water droplets. In Figure 12 effect of water mist injection on axial cooling is presented. The injection of water mist enhances the axial cooling only slightly in the case of console configuration, but more pronounced in the laidback hole case. Once again, the reason behind this behaviour can be traced back to the cooling pattern of the hole. More uniform temperature distribution over the blade width in the console case means that there is less chance for droplets to evaporate, whereas narrow cooling stripe of laidback hole will leave more hot areas that can transfer heat to water droplets.

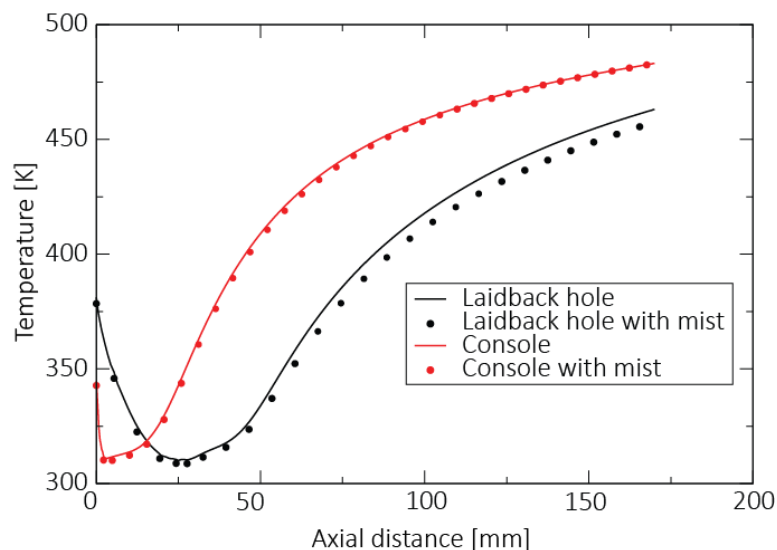


Figure 12. The influence of water mist injection on axial temperature profile



18th INTERNATIONAL FOUNDRYMEN CONFERENCE
**Coexistence of material science and sustainable technology in
economic growth**

Sisak, May 15th-17th, 2019

<http://www.simet.hr/~foundry/>

As has been mentioned previously, better axial cooling doesn't necessarily mean better integral cooling performance. Cooling efficiency, as defined by equation 3, takes into account average temperature over the blade width and, when it is calculated along the blade, gives good assessment of overall cooling performance. In Figure 13 it can be seen that console configuration has around 30% higher cooling efficiency at the beginning and retains it over the whole blade length. Even in the base case without mist injection, its efficiency overcomes the laidback hole with mist injection, finally proving the console case as possessing superior cooling performance. Further investigation should include the influence of hole geometry on deposit formation, so final design decisions could be made.

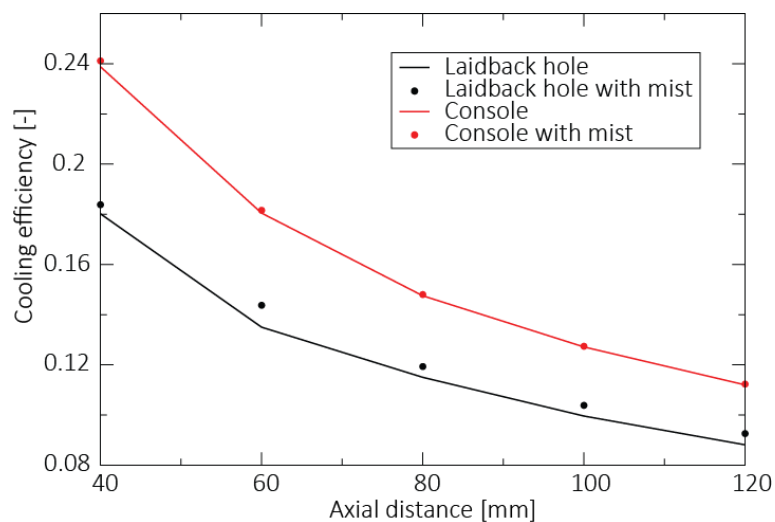


Figure 13. Cooling efficiency comparison

CONCLUSIONS

In this research the analysis of different shaped holes for the turbine fan film cooling process was performed. First, a mesh dependency test was analysed to choose the optimal computational mesh. Then the model was validated with experimental results and results from LES simulations. The influence of cooling hole geometry was analysed by modelling three different geometries, namely: laidback, fanshaped and console and the results were compared to the case with the cylindrical hole configuration. The results showed that the laidback hole configuration obtained the best penetration of cold flow in axial direction of mainstream, while the second one was the console configuration. The console cooling another advantage was manifested as the widest cooled area of mainstream channel. The influence of water mist was investigated on two cooling hole configuration: laidback hole and console. The results showed higher influence of water mist injection for laidback hole configuration due to the cooling pattern of the hole. In the end, a comparison of cooling efficiency was shown, where additionally the console configuration was recognized as



18th INTERNATIONAL FOUNDRYMEN CONFERENCE

Coexistence of material science and sustainable technology in economic growth

Sisak, May 15th-17th, 2019

<http://www.simet.hr/~foundry/>

possessing superior cooling performance. Further investigations should include the influence on deposit formation, so the final design decisions could be made.

Acknowledgements

Authors thank the group at AVL-AST, Graz, Austria, for their support in providing the software AVL FIRE®.

REFERENCES

- [1] G. Xie, X. Liu, H. Yan, Film cooling performance and flow characteristics of internal cooling channels with continuous/truncated ribs, *Int. J. Heat Mass Transf.*, 105(2017), pp. 67-75. DOI:10.1016/J.IJHEATMASSTRANSFER.2016.09.065.
- [2] J. Wang, Q. Li, B. Sundén, J. Baleta, M. Vujanović, Two-phase flow simulation of mist film cooling with deposition for various boundary conditions, *Numer. Heat Transf. Part A Appl.*, 71(2017), pp. 895-909. DOI:10.1080/10407782.2017.1326790.
- [3] J. Wang, M. Vujanovic, B. Sundén, A review of multiphase flow and deposition effects in film-cooled gas turbines, *Therm. Sci.*, 22(2018), pp. 1905-1921. DOI:10.2298/TSCI180108258W.
- [4] R. K. Mishra, J. Thomas, K. Srinivasan, V. Nandi, R. Raghavendra Bhatt, Failure analysis of an un-cooled turbine blade in an aero gas turbine engine, *Eng. Fail. Anal.*, 79(2017), pp. 836-844. DOI:10.1016/J.ENGFAILANAL.2017.05.042.
- [5] M. G. Ghorab, Film cooling effectiveness and heat transfer analysis of a hybrid scheme with different outlet configurations, *Appl. Therm. Eng.*, 63(2014), pp. 200-217. DOI:10.1016/J.APPLTHERMALENG.2013.10.005.
- [6] L. Andrei, L. Innocenti, A. Andreini, B. Facchini, L. Winchler, Film Cooling Modeling for Gas Turbine Nozzles and Blades: Validation and Application, *J. Turbomach.*, 139(2016), pp. 011004. DOI:10.1115/1.4034233.
- [7] H.-R. Zhu, Z.-G. Liu, C.-L. Liu, Investigation on the Influence of Various Mainstream Pressure Gradients on the Film Cooling Performances of Cylindrical Hole and Expansion Shaped Holes, *Int. J. Turbo Jet-Engines.*, 31(2014), pp. 1-12. DOI:10.1515/tjj-2013-0029.
- [8] Y. Yao, J. Zhang, X. Tan, Numerical study of film cooling from converging slot-hole on a gas turbine blade suction side, *Int. Commun. Heat Mass Transf.*, 52 (2014), pp. 61-72. DOI:10.1016/J.ICHEATMASSTRANSFER.2014.01.008.
- [9] X. Zhu, J. Zhang, X. Tan, Numerical assessment of round-to-slot film cooling performances on a turbine blade under engine representative conditions, *Int. Commun. Heat Mass Transf.*, 100(2019), pp. 98-110. DOI:10.1016/J.ICHEATMASSTRANSFER.2018.12.008.
- [10] X.-M. Tan, J.-Z. Zhang, Q.-Z. Cai, Effects of Pin-Fin Shapes on Mesh-Fed Slot Film Cooling for a Flat-Plate Model, *J. Therm. Sci. Eng. Appl.*, 11(2019), pp. 031002. DOI:10.1115/1.4041882.



18th INTERNATIONAL FOUNDRYMEN CONFERENCE

Coexistence of material science and sustainable technology in
economic growth

Sisak, May 15th-17th, 2019

<http://www.simet.hr/~foundry/>

- [11] X. Fan, C. Du, L. Li, S. Li, Numerical simulation on effects of film hole geometry and mass flow on vortex cooling behavior for gas turbine blade leading edge, *Appl. Therm. Eng.*, 112(2017), pp. 472-483. DOI:10.1016/J.APPLTHERMALENG.2016.10.059.
- [12] C. Liu, L. Ye, H. Zhu, J. Luo, Investigation on the effects of rib orientation angle on the film cooling with ribbed cross-flow coolant channel, *Int. J. Heat Mass Transf.*, 115(2017), pp. 379-394. DOI:10.1016/J.IJHEATMASSTRANSFER.2017.08.063.
- [13] R. Zhu, T.W. Simon, G. Xie, Influence of secondary hole injection angle on enhancement of film cooling effectiveness with horn-shaped or cylindrical primary holes, *Numer. Heat Transf. Part A Appl.*, 74(2018), pp. 1207-1227. DOI:10.1080/10407782.2018.1490088.
- [14] S. Park, E. Y. Jung, S. H. Kim, H.-S. Sohn, H. H. Cho, Enhancement of film cooling effectiveness using backward injection holes, *Int. J. Therm. Sci.*, 110(2016), pp. 314-324. DOI:10.1016/J.IJTHERMALSCI.2016.08.001.
- [15] K. Tian, J. Wang, Z. Chen, L. Yang, G. Ahmed, B. Sundén, Effect of Hole Blockage Configurations on Film Cooling in Gas Turbine Components, *Chem. Eng. Trans.*, 61(2017), pp. 229-234. DOI:10.3303/CET1761036.
- [16] J. Baleta, F. Qi, M. Zivic, M. Lovrenic-Jugovic, Numerical investigation of the transient spray cooling process for quenching applications, *Therm. Sci.*, 22(2018), pp. 1943-1953. DOI:10.2298/TSCI180120261B.
- [17] J. Wang, P. Cui, J. Baleta, Z. Guzović, Effects of surface deposition and droplet injection on film cooling, *Energy Convers. Manag.*, 125(2016), pp. 51-58. DOI:10.1016/J.ENCONMAN.2016.03.038.
- [18] K. Tian, J. Wang, C. Liu, L. Yang, B. Sundén, Effect of blockage configuration on film cooling with and without mist injection, *Energy*, 153(2018), pp. 661-670. DOI:10.1016/J.ENERGY.2018.04.050.
- [19] J. Wang, P. Cui, B. Sundén, R. Yang, Effects of deposition locations on film cooling with and without a mist injection, *Numer. Heat Transf. Part A Appl.*, 70(2016), pp. 1072-1086. DOI:10.1080/10407782.2016.1230395.
- [20] J. O. Dávalos, J. C. García, G. Urquiza, A. Huicochea, O. De Santiago, Prediction of Film Cooling Effectiveness on a Gas Turbine Blade Leading Edge Using ANN and CFD, *Int. J. Turbo Jet-Engines.*, 35(2018), pp. 101-111. DOI:10.1515/tjj-2016-0034.
- [21] B. E. Launder, D. B. Spalding, The numerical computation of turbulent flows, *Comput. Methods Appl. Mech. Eng.*, 3(1974), pp. 269-289. DOI:10.1016/0045-7825(74)90029-2.
- [22] C. Saumweber, A. Schulz, Effect of Geometry Variations on the Cooling Performance of Fan-Shaped Cooling Holes, *J. Turbomach.*, 134(2012), pp. 061008. DOI:10.1115/1.4006290.
- [23] C. Wang, J. Zhang, H. Feng, Y. Huang, Large eddy simulation of film cooling flow from a fanshaped hole, *Appl. Therm. Eng.*, 129(2018), pp. 855-870. DOI:10.1016/J.APPLTHERMALENG.2017.10.088.



18th INTERNATIONAL FOUNDRYMEN CONFERENCE

Coexistence of material science and sustainable technology in economic growth

Sisak, May 15th-17th, 2019

<http://www.simet.hr/~foundry/>

COMPARISON OF MOLDING SAND TECHNOLOGY BETWEEN ALPHASET (APNB) AND FURAN (FNB)

Dipak Ghosh*

Forace Polymers Pvt. Ltd, Haridwar, India

Oral presentation

Original scientific paper

Abstract

The paper focuses on investigation of properties of two most widely used self-set sand binder systems across the Globe, APNB and FNB for making molds and cores in foundries to produce castings of different sizes involving wide range of metals and alloys, ferrous and nonferrous. This includes study of compression strength values of samples made out of molding sand at different binder addition level using new, mechanically reclaimed and thermally reclaimed sand. Strength values studied include dry strength (at room temperature) simulating different stages of mold handling, namely stripping and pre heating, followed by degraded strength after wash application in warm condition and then recovered strength after cooling of wash applied samples. Attempts have also been made to study hot and residual strength of samples at elevated temperature. Volume of gases generated for both binders in laboratory at 850°C have also been measured. Nature of gases including harmful BTEX and PAH generated on pyrolysis of FNB and APNB bonded sands are already documented in a publication [1]. This exercise has once again been repeated with latest binder formulations in use in two foundries in India and results are included in this paper.

Key words: *Alphaset, Furan, foundries, sand, hot strength, residual strength, gases, environment*

*Corresponding author (e-mail address): dghosh@foracepolymers.in

INTRODUCTION

In 2015, worldwide casting production reached 104.1 millions metric tons (MT) with contribution from first two producers, China and India are approximately 47.2 million MT and 11.35 MT respectively [2]. Large number of foundries with huge manpower is engaged in manufacturing castings for various sectors like Transportation, Agriculture, Defense, Valves,



18th INTERNATIONAL FOUNDRYMEN CONFERENCE

Coexistence of material science and sustainable technology in economic growth

Sisak, May 15th-17th, 2019

<http://www.simet.hr/~foundry/>

Pump, Textile, Power etc. India is a country with 5000 foundries engaging 500,000 direct and 150,00,00 indirect persons [3].

Foundry industries can be classified into two broad sectors, green sand foundries and no bake foundries. In green sand foundries molds are made out of green sand (sand, bentonite, dextrin, carbon additive and water) and cores out of resin bonded sand, no bakes (self-sets and gas cured) or baking type. Automotive foundries are classic examples of green sand foundries. In no bake foundries both molds and cores are made out of resin bonded sand. Self-set binders in foundry terminology are those where hardening of molds and cores made out of resin bonded sand take place in absence of heat or gas. One of the major applications of self-sets are to make small and medium size repeating molds in FLL where stripping takes place on roll over and molds produced are flaskless. Classic examples are foundries producing valve body castings and components of pumps. Other big area is to produce big castings in boxed molds in floor. Examples are castings for wind mill, turbine and big valve body.

Two most common self-sets in use in modern foundries are so called Alphaset (APNB) and Furan (FNB). Incidentally foundry industry is one of the most polluting industries in manufacturing sector. Apart from enhanced quality requirements and faster productivity, modern foundries demand improved workplace environment matching other manufacturing sectors. Whereas, inorganic binders are most environment friendly, formulations available so far can't replace organic self-sets right away. One publication [4] confirms that modified sodium silicate using liquid (esters) hardeners can work as a complete self-set matching properties of organic self-sets including mold collapsibility. Reclaimability (thermo-mechanical process) of used sand is as high as 95%. Workplace environment is obviously of high level.

Alphaset (APNB) process

This is two part system, binders and hardeners. Binders are phenol-formaldehyde resole type of resins in aqueous alkaline (NaOH, KOH) media and hardeners are single or blend of esters of ethylene glycol, glycerol, dibasic acids and also alkene carbonates and lactones. Hardening (curing) of APNB sand takes place in two stages [1]. In first stage, partial polymerization of resole chains (chain lengthening and partial crosslinking) take place when metal ions (Na^+ , K^+) separating small chains are withdrawn by esters during hydrolysis. Strength developed at this stage in molds and cores are sufficient for stripping, handling and closing. A secondary reaction is thought to occur when the partially polymerized resin contacts heat during the pouring operation, yielding an extremely rigid structure to molds. Major variables in resin formulations are phenol: formaldehyde mole ratio, total alkalinity, ratio of Na^+ , K^+ , non-volatile content, viscosity (extent of reaction) and moisture content. Resins advance on storage as evidenced by rise in viscosity. Advancement is associated with reduction in bench life and drop in strength of mixed sand. Rate of advancement varies directly with storage temperature. Whereas there is no data available in literature relating expiry of binder with change in physical parameters, author feels, individual foundries can correlate expiry with viscosity at a particular temperature say 30°C. In his experience, the



18th INTERNATIONAL FOUNDRYMEN CONFERENCE

Coexistence of material science and sustainable technology in economic growth

Sisak, May 15th-17th, 2019

<http://www.simet.hr/~foundry/>

value in Indian formulations is 40 secs by Ford cup no 4 (100 cps) at 30°C and it happens in close to 90 days when storage temperature is between 25-30°C.

In foundries, a lot is talked about difference in role of NaOH and KOH in Alphasets formulations. Many believe, KOH is superior to NaOH in terms of lower binder demand to get equivalent strength. Author feels, recipe and process parameters, rather than nature of alkali, dictates binder demand for achieving required dry strength at various stages. Formulating right binder compositions to meet requirements of individual foundries is an art. However, according to a publication [5] sodium based formulations offer better reclaimability by mechanical process and in case of thermal reclamation, it is opposite. NaOH based formulations offer more viscosity than KOH based in formulations with equal non volatile content. Most of the formulations contain both in judicious proportions to adjust viscosity of final solution, rate of binder advancement, ease of reclaimability of used sand and of course unit price.

Hardeners used as curatives differ in rate of hydrolysis to release acids thus controlling bench life of mixed sand and in turn strip time. Blend of hardeners with varying hydrolysis constant behave almost arithmetically calculated way, influencing reactivity. Resin hardener reactivity can be tested by noting down time for gelation on constant stirring of 100 gm resin with 20 gm hardener at a particular temperature. Use of slower hardeners increase bench life of mixed sand but at cost of reduction of bench life: strip time ratio, but without much effect on final strength. Storage life of hardeners are well over one year.

Binder demand for Alphasets system varies from 1.2-1.8 % by weight of sand to meet strength requirements at stripping (manual and roll over), handling and closing in case of boxed as well as flaskless molds. It is estimated that compression strength required at strip vary from 2.0 to 7.5 kg/cm² and final dry compression of 18 to 25 kg/cm² to handle all molds, post strip till closing. Hardener demand is between 18-22% by weight of binder. Variation of hardener addition beyond this range don't influence bench life and strength of mixed sand, contrary to other organic binders.

Reclamation of used sand is done mechanically (attrition, MR), thermally (TR) or both. In mechanical process, reclaimability is not more than 70%. Mechanical, followed by thermal increases reclaimability up to 95%. However, in case of thermal reclamation, an additive (0.6-1% by weight of sand) in form of suspension in water is required to be atomized in thermal reclamation chamber (650°C) where reaction of inorganic components of mechanically reclaimed sand and additive bring down its melting temperature and eventually removes with fines [6]. The additive formulation is however very specific and has got huge effect on quality of thermally reclaimed sand. Most important effect is drop in strength of TR sand on storage as reported by some foundries. Alternately, secondary reclamation of mechanically reclaimed Alphasets bonded sand gives reuse level of as high as 85% and quality of reclaimed sand produced is excellent with loss on ignition of <1%.

Being free from N, S and P, this system is suitable for pouring all types of metals including SG iron and steel. Further, it is well documented [7] that when liquid metal is poured in APNB bonded molds, bonds relax momentarily (thermoplastic deformation) before picking up further strength. This unique behavior compensates for (reversible) expansion of silica sand



18th INTERNATIONAL FOUNDRYMEN CONFERENCE

Coexistence of material science and sustainable technology in economic growth

Sisak, May 15th-17th, 2019

<http://www.simet.hr/~foundry/>

at 573°C avoiding crack in molds and in turn producing castings free from veining. Post relaxation, strength pick up by molds are good enough to produce near neat shape castings.

A research paper [6] says that molding sands produced using APNB technology are characterized by significantly lower harmfulness than FNB molding sands. However, Alphaset resins, although contain very low level of free formaldehyde, evolve formaldehyde, a potential eye irritant during curing with esters. This is also documented in a patent [8]. GC (Figure 1) of liquid portion of gelled mass after curing with esters conclusively prove generation of formaldehyde during gelation. Rate of emission varies with ambient temperature and type of ester. Higher ambient temperature and faster hardeners aggravate emission rate. Smell of formaldehyde are traceable in pouring area also. Heat curing of resin is associated without emission of smell of formaldehyde, substantiating fact that evolved formaldehyde during curing with esters is not in free form in resins.

Furan (FNB) process

Like Alphaset, this is another popular process for making molds and cores by self-set process. Binders are series of resin formulations based on furfuryl alcohol (FA) and formaldehyde (in form of aqueous solution or paraformaldehyde, a solid) in presence of phenol, urea or both. Catalysts are single or blend of organo - inorganic & or inorganic acids.

Hardening of furan bonded sand takes place by reduction in PH with addition of acids. Bench life of mixed sand and strip time of molds are controlled by % catalyst addition with respect to resin and also by changing acids of different potency.

Major variables in FNB formulations are contents of FA, Urea and Phenol. Besides % variation of reactive monomers, variation in process parameters and PH at different stages of reaction offer possibility of synthesizing innumerable formulations having wide range of properties. Stability of Furan resins are better than Alphaset and can vary from 3 months to 12 months depending on formulations, when stored between 25-30°C. Here again, advancement is evidenced by increase in viscosity, drop in water tolerance, reduction in bench life and drop in strength of mixed sand.

Original furan formulations used to be based on polymers of Urea, FA and formaldehyde (UF/FA) containing substantial portion of free FA (up to 70%) with total FA being as high as 90%. With increase in FA price and EU regulation (EC no 1272/2008) [9] of restricting upper limit of free FA to 25% in furan formulations, phenol was introduced as third reactant with formaldehyde providing flexibility in range of formulations. Incidentally hybrid formulations involving three reactants with formaldehyde could offer resins as good as high FA based resins yet keeping free FA in regulated range.

Catalysts for furan formulations are based on aqueous solution of organo - inorganic acids like PTSA monohydrate, XSA and inorganic acids like Phosphoric acid. Unlike APNB, in case of FNB, speed of cure can be varied by varying level of catalyst addition which usually ranges from 30-60% by weight of resin. In addition, various catalysts with various dilution ratio increase probability of manipulation of cure speed further. Special care is taken to avoid freezing of concentrated catalysts at low temperature. Storage stability of catalysts are practically unlimited.



18th INTERNATIONAL FOUNDRYMEN CONFERENCE

Coexistence of material science and sustainable technology in economic growth

Sisak, May 15th-17th, 2019

<http://www.simet.hr/~foundry/>

Binder demand in FNB formulations are lowest among all other systems. In mechanically reclaimed or blended sand it works very well at addition level as low as 0.8% by weight of sand. In new or thermally reclaimed sand, usually used in mold facing and cores, addition goes up to 1.2% by weight of sand.

Reclaimability of furan bonded sand is best among all. In mechanical reclamation, it's as high as 90%. Foundries opting for more, reclaim partial quantity of mechanically reclaimed sand by thermal process. Quality of thermally reclaimed FNB sand is as good as or better than new sand.

Furan formulations usually contain 0-10% N and 5-15% water. The lower the N and water content, the higher is the grade of furan binder [10]. In furan, N comes from urea which is easily dissociated at metal pouring temperature to liberate nascent or atomic N which is more soluble in liquid iron than in solid. Absorption of nitrogen and/or hydrogen by the molten iron, either individually or jointly, may result in subsurface porosity defects [11]. In general, limit of allowed N contents in resins for steel and SG iron of heavy section thickness is 0-2%, that of CI and SG of low section thickness is 2-5% and that of non-ferrous is without limit. However, N content in molding sand rather than in binder is guiding factor for selectivity of metal to be poured. Recommended upper limit for N in molding sand while pouring CI and SG iron of low section thickness is 0.15% which is 0.10% in case of steel and heavy SG iron castings. In non-ferrous castings increase in N content in resin improves de-coring property. Upper limit being the level till Urea separation in resin.

Sulphur bearing catalysts used as curatives for furan resins decompose through following reactions [12]:



During metal pouring, SO₂ shifts to casting surface and react with Mg used to produce SG iron castings as SO₂+Mg→MgS+O₂, reducing its concentration and eventually flake graphite formation at surface. Depending upon wall thickness and cooling rate, surface degeneration can occur between 0.2 to 1 mm. Bauer [13] suggests limiting value for S in molding sand below 0.15% in case of castings up to 25 mm thick and 0.07% up to 75 mm thick. Use of low Sulphur content catalysts, Cao, Mgo and talc based dressings is preventive measures for S degeneration in SG iron castings.

Furan systems contain Sulphur which on pyrolysis release SO₂, a potential air pollutant. Aryl Sulphonic acids used for curing may release BTX during and after pouring of liquid metal. FNB with extremely low level of free formaldehyde (not traceable by analytical method) and catalyst compositions with less than 1% free Sulphuric acid when used at addition level as low as 0.8:30 can work as cleaner system compared to APNB. A publication [14] says "the Furfuryl alcohol based binder (furan type) was identified to offer the greatest potential for improvement in productivity, casting, quality and environmental acceptability". The other two binders in the publication compared are phenolic urethane and ester cured phenolics.



18th INTERNATIONAL FOUNDRYMEN CONFERENCE

Coexistence of material science and sustainable technology in economic growth

Sisak, May 15th-17th, 2019

<http://www.simet.hr/~foundry/>

EXPERIMENTAL PART: INSTRUMENTAL

GC:

Liquid portion of mass released on gelation of with hardener for APNB (100 gm resin + 20 gm hardener)

TGA:

Measurement parameters:

- Char residue
- 1% degradation temperature

Test conditions:

- Ramp temperature- 10°C /mt.
- Nitrogen flow rate- 60 ml/mt.
- Heating range- room temperature to 750°C

Py/GC/MS method: of cured mass of FNB & APNB

The analysis was carried out in a platinum coil pyroprobe (Pyroprobe 5000, CDS, Analytical Inc.). Approximately 1 mg of the solid sample was centered in a quartz tube and heated to final temperature means: 900 (only in case of APNB)) and 1100°C (both in case of APNB and FNB) using a heating ramp of 10°C/ms. The hold time at the final temperature was 5s. The pyrolysis products were separated on a 30m × 0.25mm × 0.25 μm (film thickness) capillary column (Rxi-5MS, Restek). The inlet was set to a split flow of 30mL/min. The flow rate of the carrier gas (He, 99.9999%) was 1mL/min. A Single Quadrupole (ISQ, Thermo Scientific) MS was used to detect the pyrolytic degradation products. The MS was used in the full scan mode from 30 to 600 atomic mass units (a.m.u.). The transfer line temperature and ion source temperature was 250°C, the electron energy (EI) was equal to 70 eV and emission current was 50 μA. The gas products were identified based on the mass spectral library NIST MS Search 2.0 Libera (Chem. SW, Version 2.0, Fairfield, CA, USA).



RESULTS AND DISCUSSION

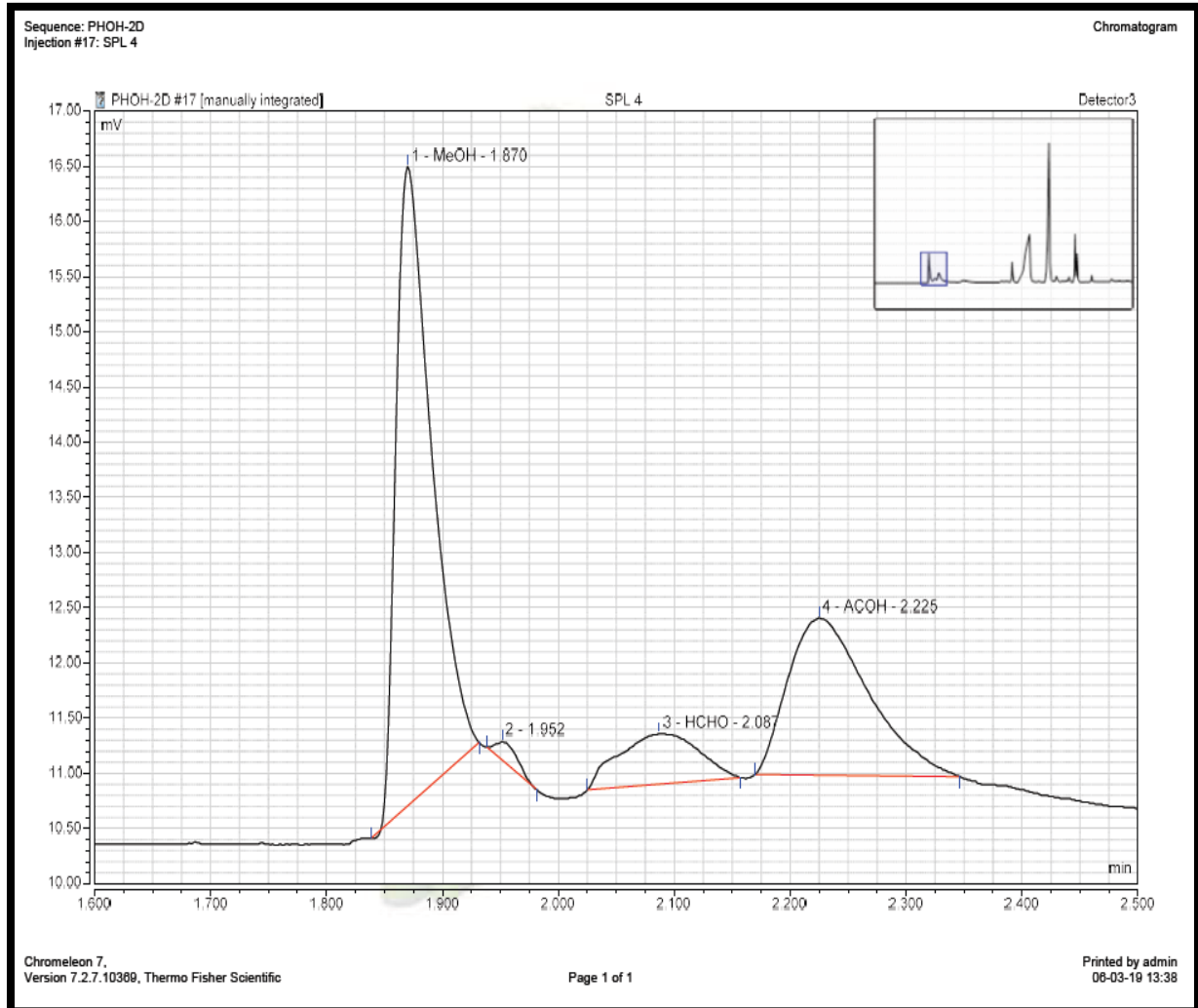


Figure 1. GC of liquid portion of mass released on gelation of Resin and Hardener 100:20 (W/W)

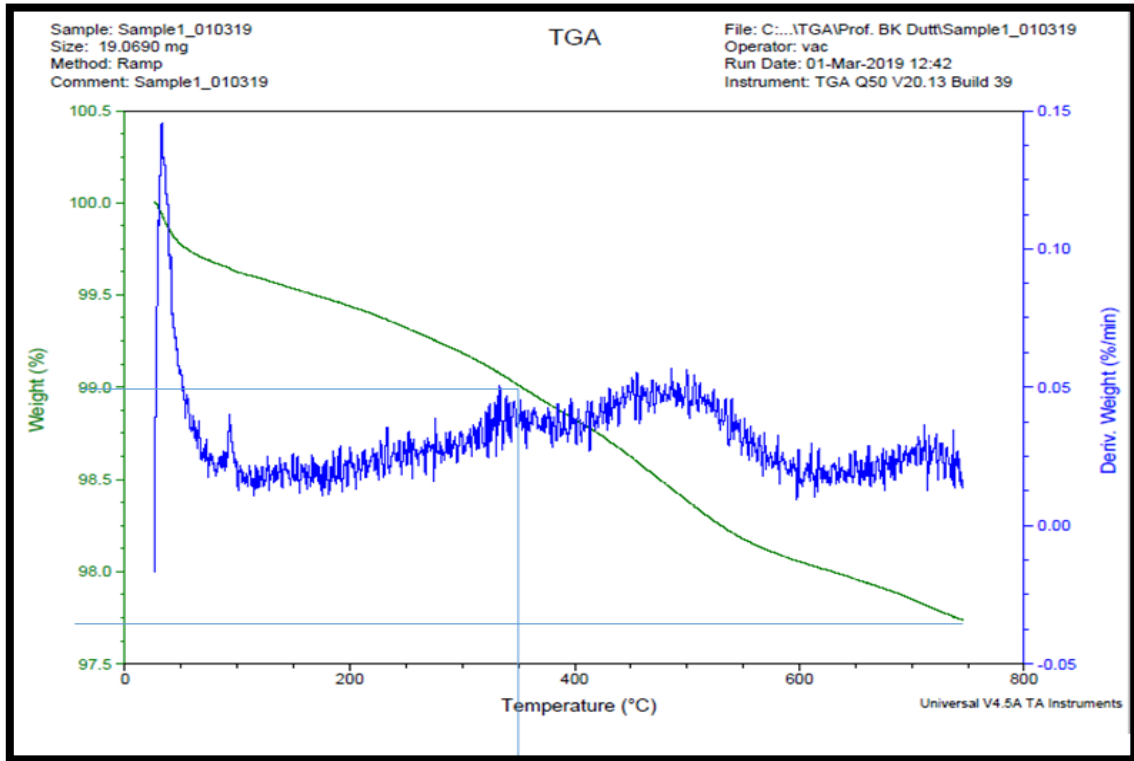


Figure 2. TGA of Alphaset bonded mechanically reclaimed (1.8:20) sand

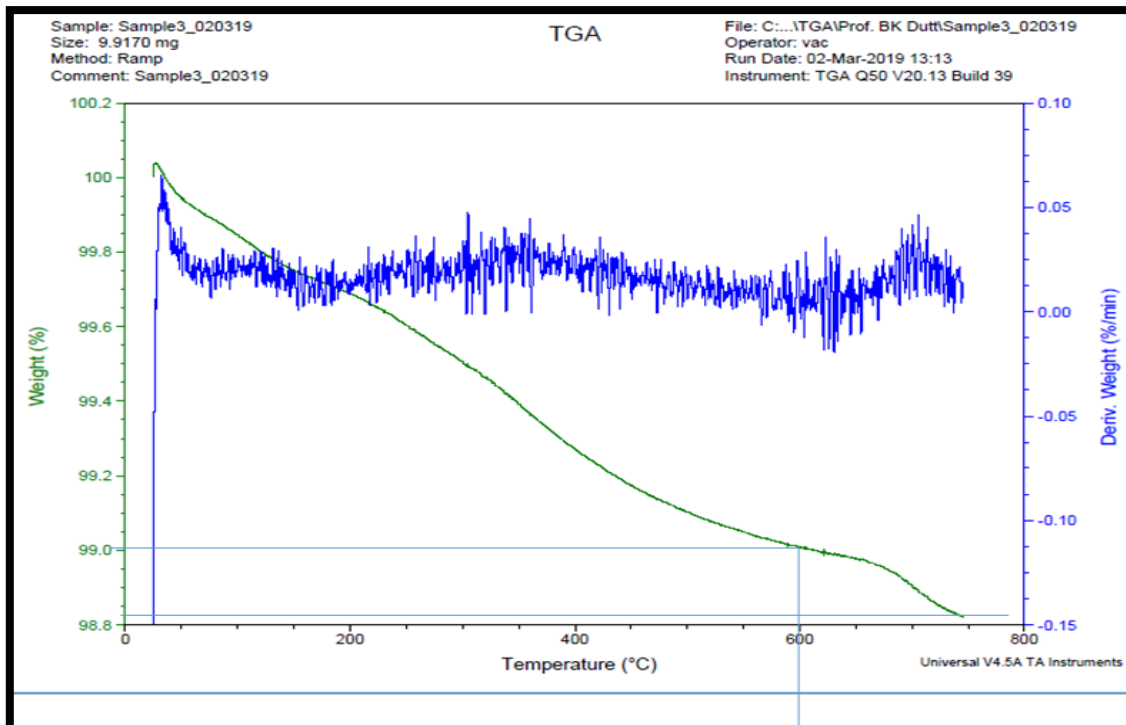


Figure 3. TGA of Alphaset bonded new (1.8:20) sand



18th INTERNATIONAL FOUNDRYMEN CONFERENCE
Coexistence of material science and sustainable technology in economic growth
Sisak, May 15th-17th, 2019
<http://www.simet.hr/~foundry/>

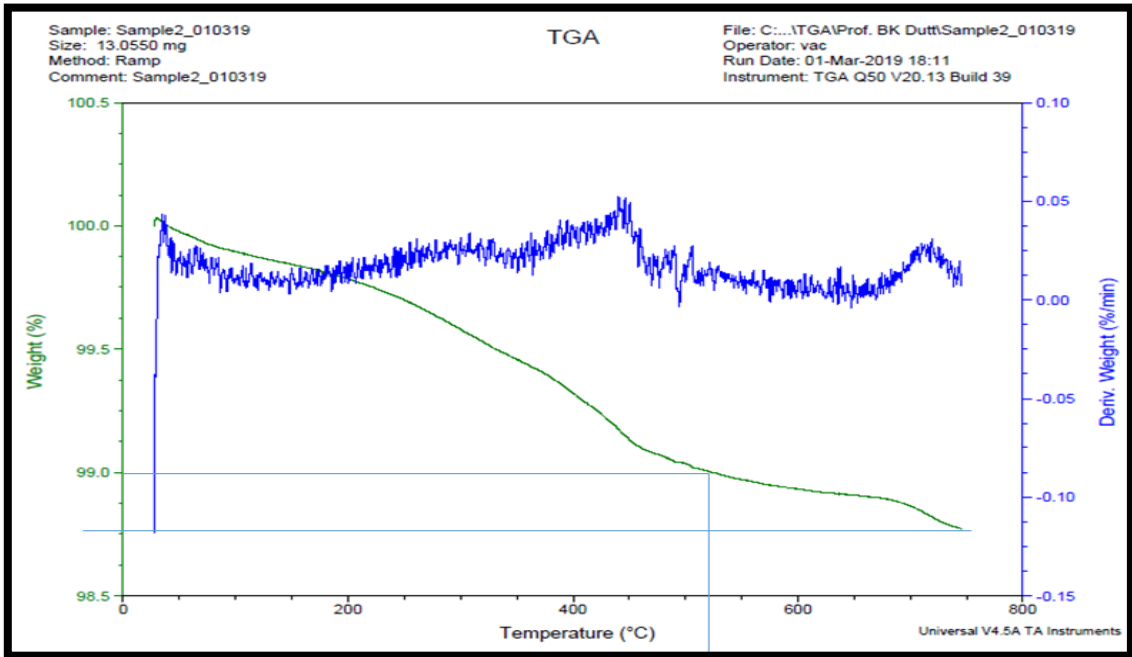


Figure 4. TGA of Furan-bonded (New) 1:50 sand

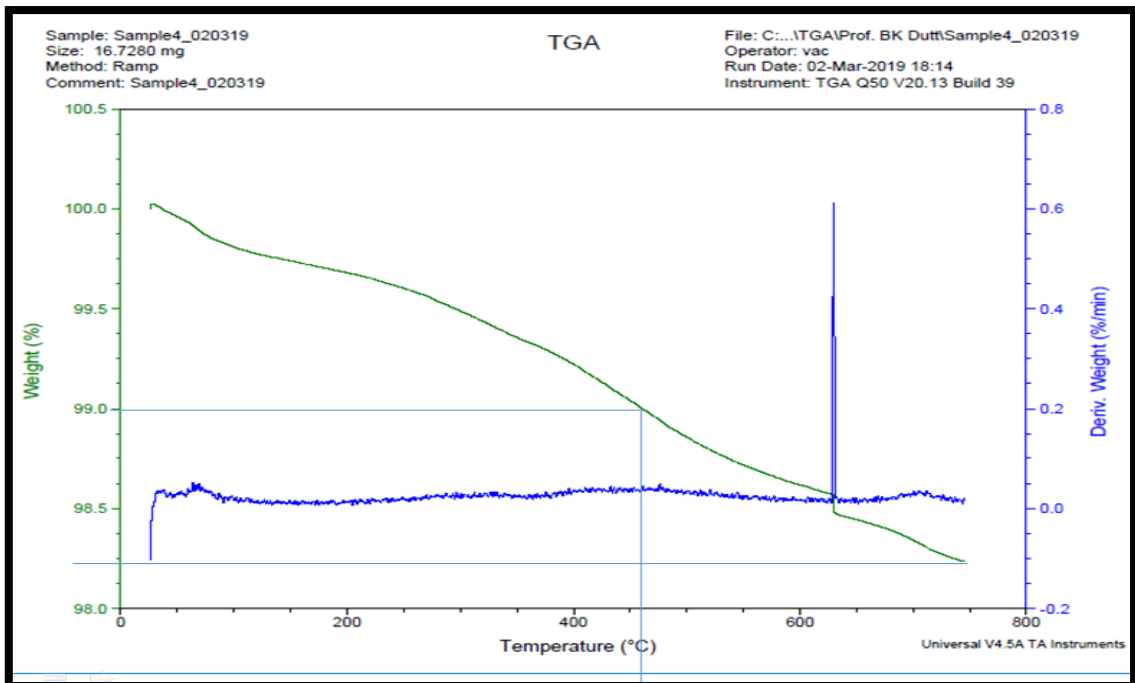


Figure 5. TGA of Furan-bonded (MR) 1:50 sand

Remarks- 1% degradation temperature is higher in case of new sand then MR sand



18th INTERNATIONAL FOUNDRYMEN CONFERENCE

Coexistence of material science and sustainable technology in economic growth

Sisak, May 15th-17th, 2019

<http://www.simet.hr/~foundry/>

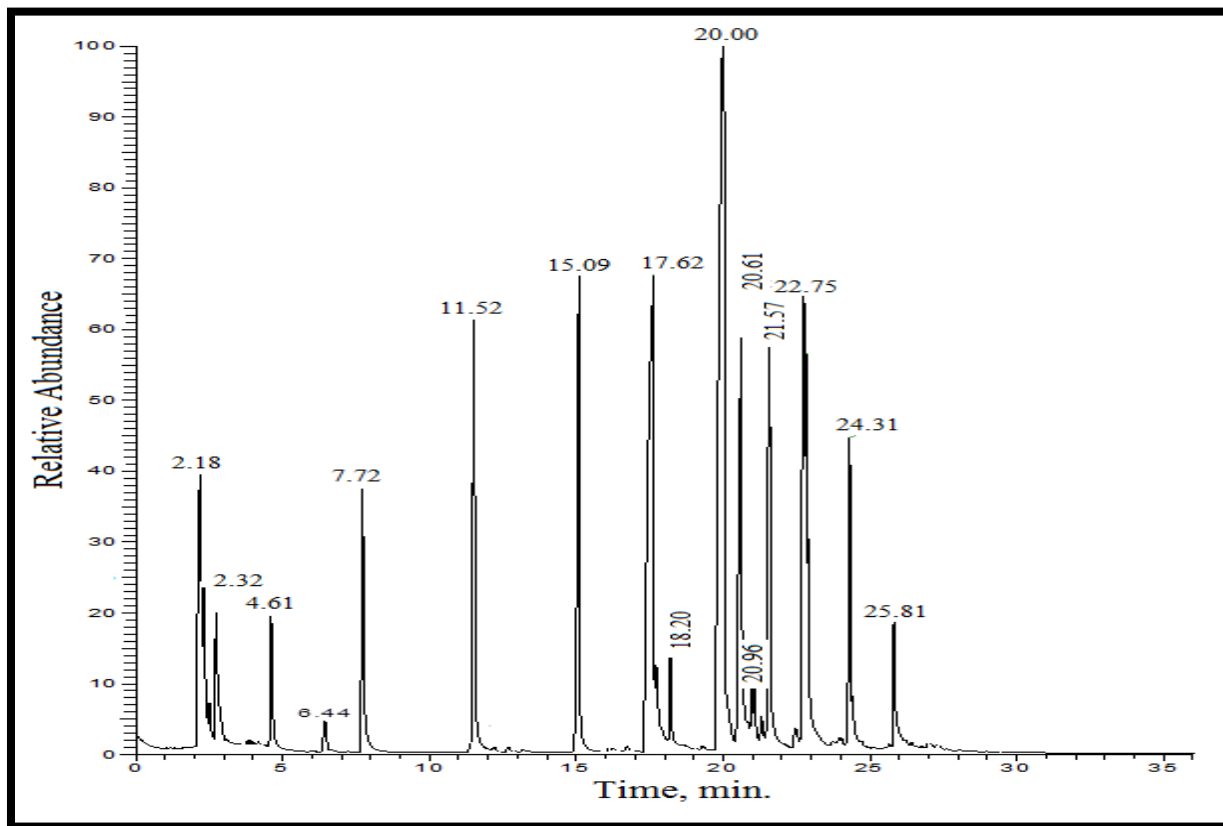


Figure 6. Py-GC-MS for Cured Mass of Alphasat with 20% Hardener at 900 °C

Table 1. Compounds detected and identified by GC-MS released during pyrolysis of cured mass of Alphasat with 20% wt. Hardener at 900 °C

Retention Time (RT)	Name of compound	Structural	CAS No.	Molecular weight
2.18	Isopropyl amine C ₃ H ₉ N		75-31-0	59
2.32	Cyclopropyl carbinol C ₄ H ₈ O		2516-33-8	72
4.61	Benzene C ₆ H ₆		71-43-2	78
7.72	Toluene C ₇ H ₈		108-88-3	92
11.52	m-Xylene C ₈ H ₁₀		108-38-3	106



18th INTERNATIONAL FOUNDRYMEN CONFERENCE

Coexistence of material science and sustainable technology in economic growth

Sisak, May 15th-17th, 2019

<http://www.simet.hr/~foundry/>

15.09	Benzene, 1,2,4-trimethyl C_9H_{12}		95-63-6	120
17.62	Phenol C_6H_6O		108-95-2	94
18.20	Benzene, 2-ethyl-1,4 dimethyl $C_{10}H_{14}$		1758-88-9	134
20.00	Phenol, 2-methyl o-Cresol C_7H_8O		108-39-4	108
20.61	p-Cresol C_7H_8O		106-44-5	108
20.97	2-Propenal, 3-phenyl- C_9H_8O		104-55-2	132
21.57	Phenol, 2,6-dimethyl- $C_8H_{10}O$		576-26-1	122
22.75	Phenol, 2,4-dimethyl- $C_8H_{10}O$		105-67-9	122
23.96	Phenol, 2-ethyl-4 methyl $C_9H_{12}O$		3855-26-3	136
24.31	Phenol, 2,3,6 - trimethyl 2,3,6 Trimethylphenol $C_9H_{12}O$		2416-94-6	136
25.81	Hexadecanoic acid, dimethyl ester $C_8H_{14}O_2$		627-93-0	174



18th INTERNATIONAL FOUNDRYMEN CONFERENCE

Coexistence of material science and sustainable technology in economic growth

Sisak, May 15th-17th, 2019

<http://www.simet.hr/~foundry/>

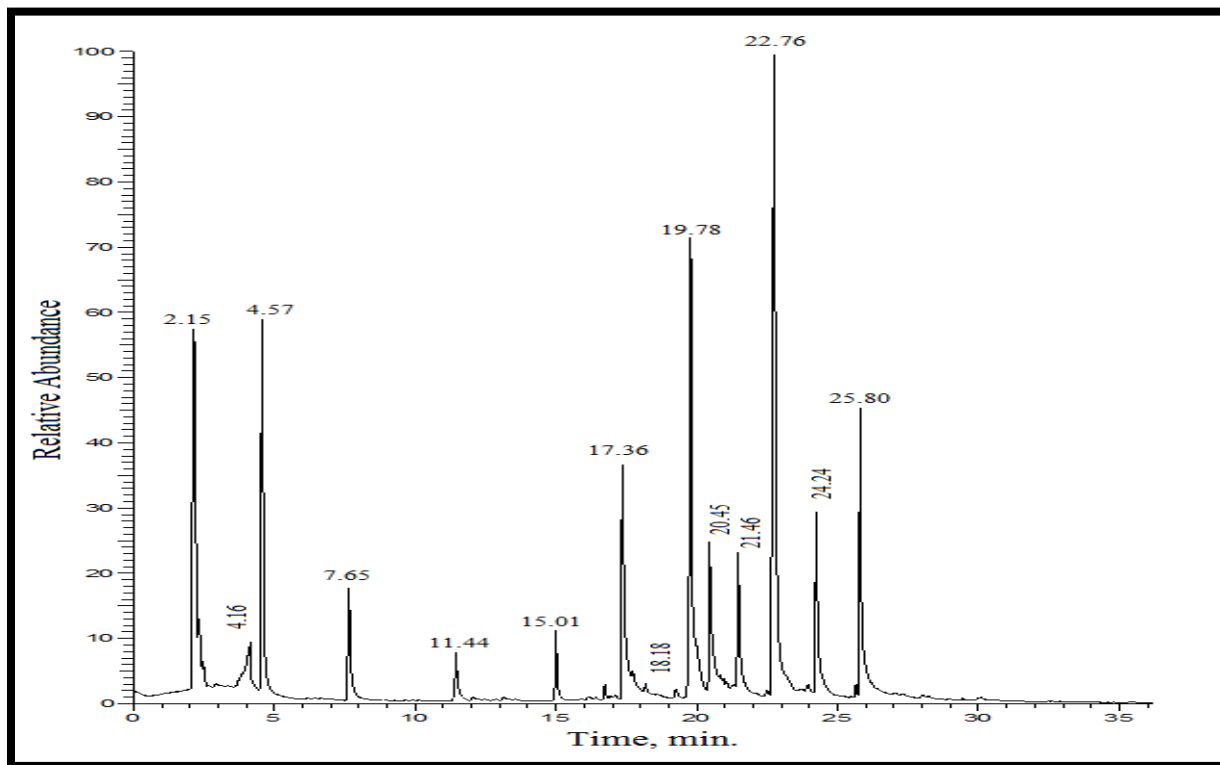


Figure 7. Py-GC-MS for cured mass of Alphaset with 20% wt. Hardener at 1100^oC

Table 2. Compounds detected and identified by GC-MS released during pyrolysis of Py-GC-MS for cured mass of Alphaset with 20% Hardener at 1100^oC

Retention Time (RT)	Name of compound	Structural	CAS No.	Molecular weight
2.15	Carbon dioxide CO ₂	$O=C=O$ 116.3 pm	124-38-9	44
4.16	Acetic acid C ₂ H ₄ O ₂		64-19-7	60
4.57	Benzene C ₆ H ₆		71-43-2	78
7.65	Toluene C ₇ H ₈		108-88-3	92
11.44	Benzene 1,2 dimethyl o-Xylene C ₈ H ₁₀		95-47-6	106

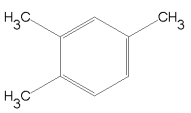
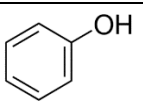
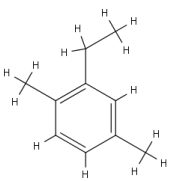
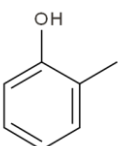
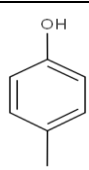
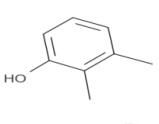
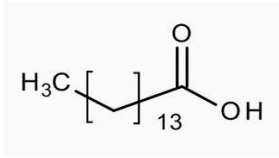
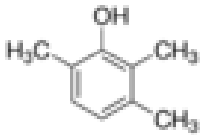
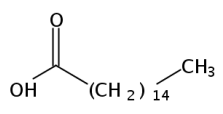


18th INTERNATIONAL FOUNDRYMEN CONFERENCE

Coexistence of material science and sustainable technology in economic growth

Sisak, May 15th-17th, 2019

<http://www.simet.hr/~foundry/>

15.01	Benzene, 1,2,4-trimethyl C_9H_{12}		95-63-6	120
17.36	Phenol C_6H_6O		108-95-2	94
18.18	2 ethyl -1,4-dimethyl benzene $C_{10}H_{14}$		1758-88-9	134
19.78	Phenol, 2-methyl o-Cresol C_7H_8O		108-39-4	108
20.45	p-Cresol C_7H_8O		106-44-5	108
21.46	Phenol, 2,3-dimethyl $C_8H_{10}O$ 2,3 Xylenol		526-75-0	122
22.76	Pentadecanoic acid, dimethyl ester Glutaric acid, dimethyl ester $C_7H_{12}O_4$		1119-40-0	160
24.24	Phenol, 2,3,6 tri methyl $C_9H_{12}O$		2416-94-6	136
25.81	Hexadecanoic acid, dimethyl ester $C_8H_{14}O_2$		627-93-0	174



18th INTERNATIONAL FOUNDRYMEN CONFERENCE

Coexistence of material science and sustainable technology in economic growth

Sisak, May 15th-17th, 2019

<http://www.simet.hr/~foundry/>

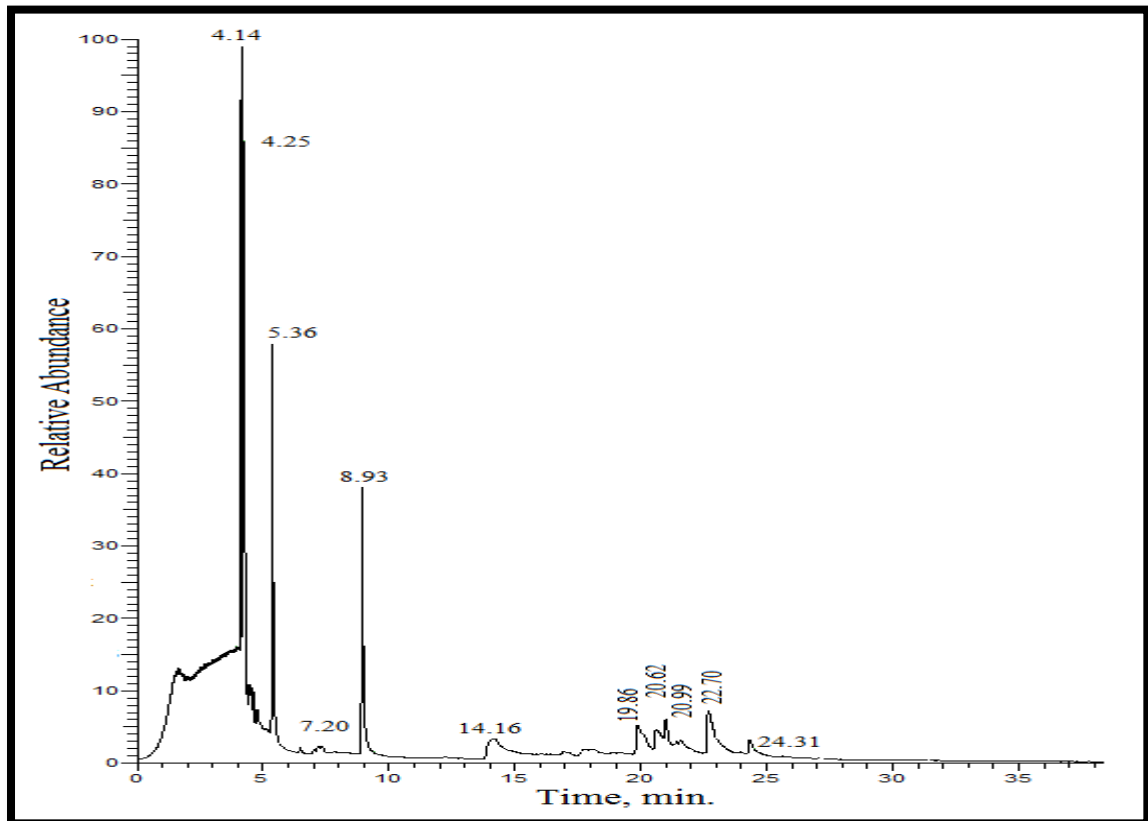


Figure 8. Py-GC-MS for Cured mass of Furan with 50% Catalyst at 1100 °C

Instrumental part

1. GC (Figure 1) of liquid portion of ester hardened Alphaset shows presence of formaldehyde
2. TGA (Figure 3 and 4) of curves show that 1% degradation temperature is higher for new sand than reclaimed sand for both FNB (525 °C Vs 460 °C) and APNB (600 °C Vs 350 °C)
3. Thermal stability improvement in new sand is 71.4% $\{(600-350)/350 \times 100\}$ in case of APNB bonded sand and same is 14.1% $\{(525-460)/460 \times 100\}$ in case of FNB bonded sand
4. Char residue for APNB bonded new sand, MR sand and FNB bonded new and MR sand are 98.8, 97.75, 98.75 and 98.25 % respectively
5. Nature of gases released on pyrolysis of cured APNB and FNB as studied by Py-GC-MS mostly tally with those studied by early researchers. However, presence of N bearing compound in APNB cured mass tested at 900 °C (Table 1) and absence at 1100 °C (Table 2) is beyond explanation
6. In practice, pyrolysis of cured binders of molds take place both in oxidative (surface) and inert (subsurface) atmosphere, whereas experiments were carried out in inert atmosphere. Ultimate products of pyrolysis are oxides of elements, most of which are less harmful than BTEX and PAH generated under inert atmosphere.



18th INTERNATIONAL FOUNDRYMEN CONFERENCE

Coexistence of material science and sustainable technology in economic growth

Sisak, May 15th-17th, 2019

<http://www.simet.hr/~foundry/>

Table 3. Compounds detected and identified by GC/MS released during pyrolysis of Cured mass of Furan with 50% Catalyst at 1100 °C

Retention Time (RT)	Name of compound	Structural	CAS No.	Molecular weight
4.14	Carbon dioxide CO ₂		124-38-9	44
4.25	Sulphur dioxide SO ₂		7446-09-5	64
5.36	Furan, 2 -methyl C ₅ H ₆ O		534-22-5	82
7.20	Furan, 2,5-dimethyl- C ₆ H ₈ O		625-86-5	96
8.93	Toluene C ₇ H ₈		108-88-3	92
14.16	2-Furanmethanol, Furfuryl alcohol, Tetra hydro C ₅ H ₁₀ O ₂		97-99-4	102
19.86	Phenol, 3-methyl m-Cresol C ₇ H ₈ O		108-39-4	108
20.62	p-Cresol C ₇ H ₈ O		106-44-5	108
20.99	Phenol, 2, -(2-methyl-2-propenyl)- Phenol, o-(2 methyl allyl)- C ₁₀ H ₁₂ O		20944-88-1	148
22.70	Phenol, 3,4-dimethyl C ₈ H ₁₀ O 2,3 Xylenol		95-65-8	122
24.31	Phenol, 2,3,6 Tri-methyl C ₉ H ₁₂ O		2416-94-6	136



18th INTERNATIONAL FOUNDRYMEN CONFERENCE

Coexistence of material science and sustainable technology in economic growth

Sisak, May 15th-17th, 2019

<http://www.simet.hr/~foundry/>

Sand tests

Two binder systems with three varieties of sand (New, MR and TR) were collected from two foundries in India and sand mix properties were studied in laboratory of Forace Polymers P. Ltd, India in recipe being followed in respective foundries.

Strength parameters required in molds and cores at different stages during movement were identified as follows:

- At the time of stripping which is 2-7.5 kg/cm² (depending upon mold geometry, weight, flaked or flaskless etc.) of samples in box without exposure to atmosphere
- Handling of stripped molds at different stages without coating (18-25 kg/cm²)
- Strength of molds after application of coating, without drying
- Recovered strength after drying of coating
- Hot strength after metal pouring
- Retained strength after solidification of metal

In this study, dry compression values of 50X50 mm samples were measured at different time interval from discharge of sand from 4 kg laboratory mixer. Samples were stripped from 12 cavity gang sample box when a small sample of mixed sand kept in polythene bag in tight condition became hard while pressing by hand. Dry compression strength of samples were tested immediately on stripping and 2 hrs, 4 hrs and 24 hrs from discharge. 24 hrs samples were baked, cooled and applied thinner based wash by brush. Samples were lighted off (checked for compression), cooled (checked for compression) and soaked in furnace at 450°C (this temperature has been chosen after several trial to get amplified values and resin burning as well) for 5, 10 and 15 mts and then tested for compression, both in hot (hot strength) and cold (retained strength) conditions in an attempt to simulate mold strength during and post pouring.

One set of samples were baked after 1 hr of strip in case of APNB and 2hrs in case of PNB at 135°C for 10 mts. Samples were tested for compressions on cooling.



APNB:

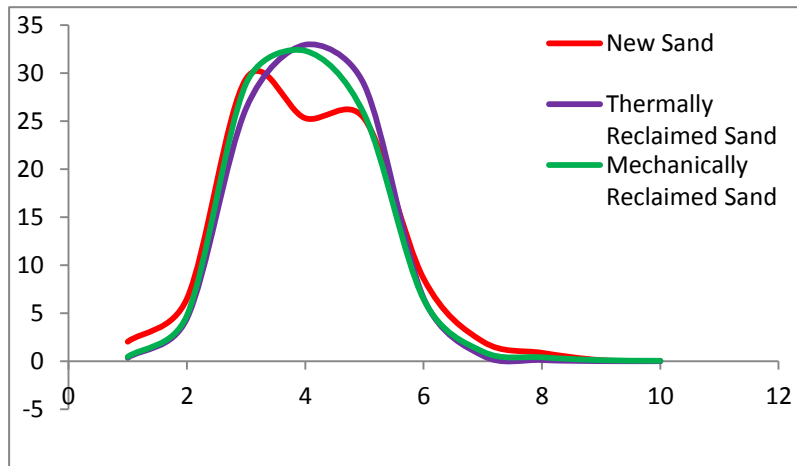


Figure 9. ASTM sieve no vs % retention

Table 4. Properties of used sand

Parameter	New Sand	Thermally Reclaimed Sand	Mechanically Reclaimed Sand
AFS	42.53	41.69	41.78
LOI (%)	0.786	0.583	2.36
ADV	1.60 ml 0.1 (N) NaOH/100 Gm	24.55 ml 0.1 (N) HCl/100 Gm	22.09 ml 0.1 (N) HCl/100 Gm

Table 5. Properties of used Resin, Hardener and Coating

Properties	Resin	Hardener	Coating (Zircon Thinner Based)
Viscosity (B-4, 30°C)	24 Sec.	13 Sec.	14 Sec.
Viscosity (Brookfield, 30°C)	60 cps	Less than 20 cps	NA
Non-Volatile (%)	47.38	NA	59.63
Sp. Gr. (30°C)	1.190	1.230	NA
Free Formaldehyde (%)	Not traceable	NA	NA
Appearance	Brownish red liquid	Light Brown transparent Liquid	Light Greenish Liquid
PH	12.40	NA	NA
Baume	NA	NA	52
Free Phenol (%)	0.93	NA	NA
Alkalinity as KOH (%)	11.56	NA	NA



18th INTERNATIONAL FOUNDRYMEN CONFERENCE
 Coexistence of material science and sustainable technology in economic growth

Sisak, May 15th-17th, 2019

<http://www.simet.hr/~foundry/>

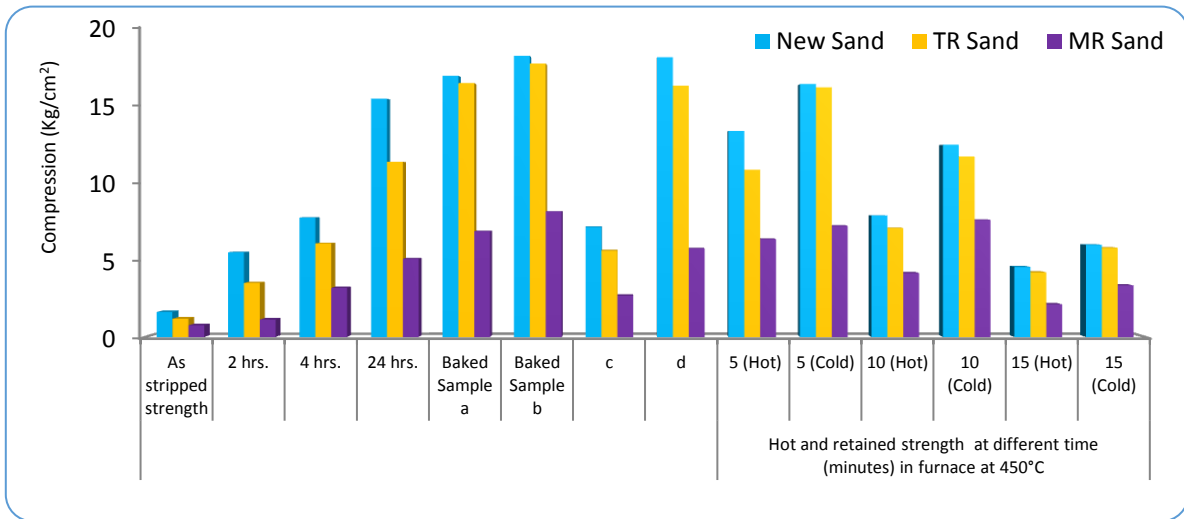


Figure 10. Recipe: 1.6:20 Medium Fast Hardener RT-20°C, RH-45%

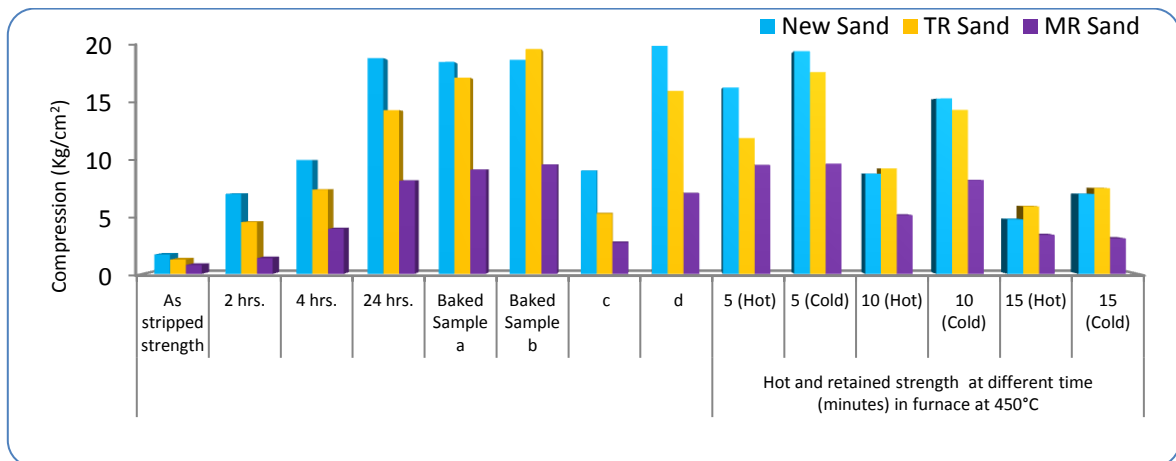


Figure 11. Recipe: 1.8:20 Medium Fast Hardener RT-20°C, RH-45%

Codes versus strength	
a	1 hr. samples baked @ 135°C for 10', cooled at RT & tested for compression
b	24 hr. samples baked @ 135°C for 10', cooled at RT & tested for compression
c	Samples b dipped in thinner based Zircon wash, lighted off, tested hot for compression
d	Samples b dipped in thinner based Zircon wash, lighted off, tested for compression after cooling

Table 6. Gas value (850 °C)

Sand	New Sand		TR Sand		MR Sand	
Recipe	1.6 :20	1.8 :20	1.6 :20	1.8 :20	1.6 :20	1.8 :20
Gas Value (ml/gm)	7.5	9.2	8.0	9.0	9.5	11.0



18th INTERNATIONAL FOUNDRYMEN CONFERENCE

Coexistence of material science and sustainable technology in economic growth

Sisak, May 15th-17th, 2019

<http://www.simet.hr/~foundry/>

FNB

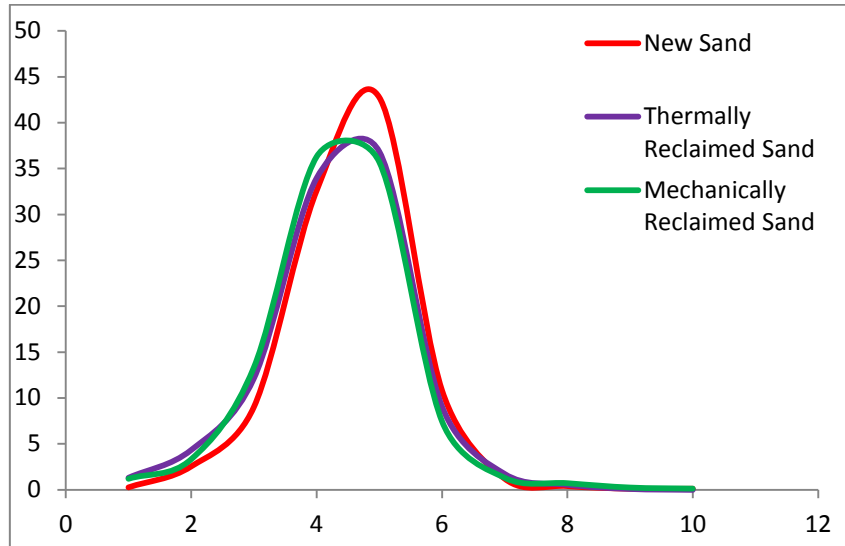


Figure 12. ASTM sieve no vs % retention

Table 7. Properties of sand used

ASTM No.	New Sand	Thermally Reclaimed Sand	Mechanically Reclaimed Sand
AFS	47.66	45.69	45.6
LOI (%)	0.484	0.568	2.47
ADV (%)	0.733 ml 0.1 (N) HCL/100 Gm	1.41 ml 0.1 (N) HCL/100 Gm	12.01 ml 0.1 (N) NaOH/100 Gm

Table 8. Properties of used Resin, Hardener and Coating

Properties	Resin	Hardener	Coating (Zircon Thinner Base)
Viscosity (B-4, 30°C)	14 Sec.	13 Sec.	14 Sec.
Viscosity (Brookfield)	Less than 20 cps	Less than 20 cps	NA
Non-Volatile (%)	31.24	NA	59.63
Sp. Gr. (30°C)	1.130	1.140	NA
Free Formaldehyde (%)	0.121	NA	NA
Appearance	Light Yellowish Liquid	Colorless Liquid	Light Greenish Liquid
PH	7.12	NA	NA
Baume	NA	NA	52
Free Phenol (%)	2.10	NA	NA



18th INTERNATIONAL FOUNDRYMEN CONFERENCE
 Coexistence of material science and sustainable technology in economic growth

Sisak, May 15th-17th, 2019

<http://www.simet.hr/~foundry/>

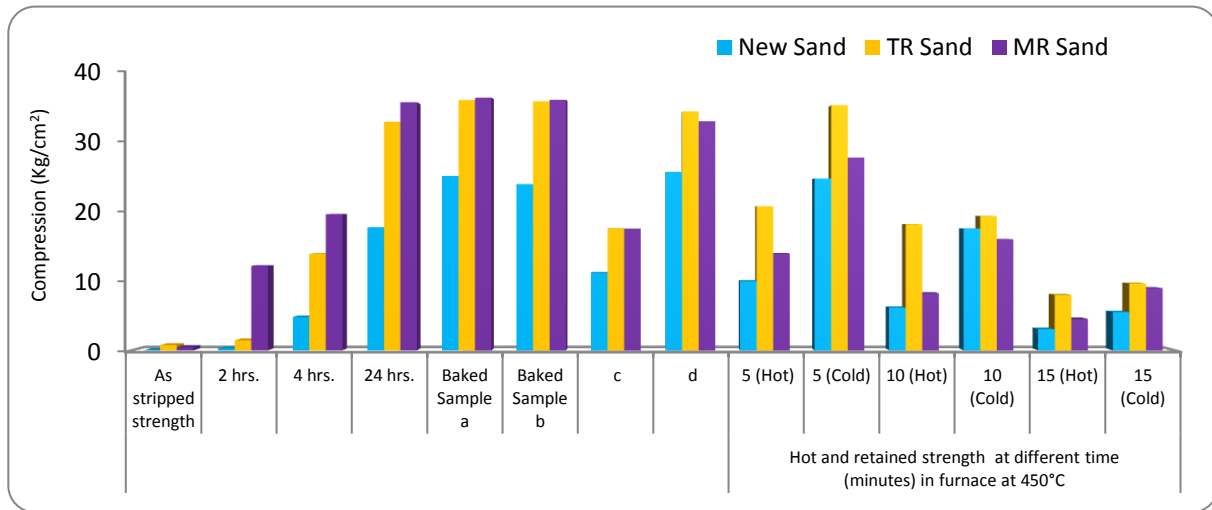


Figure 13. Recipe: 1.0:50 Medium Fast Catalyst RT-20°C, RH-47%

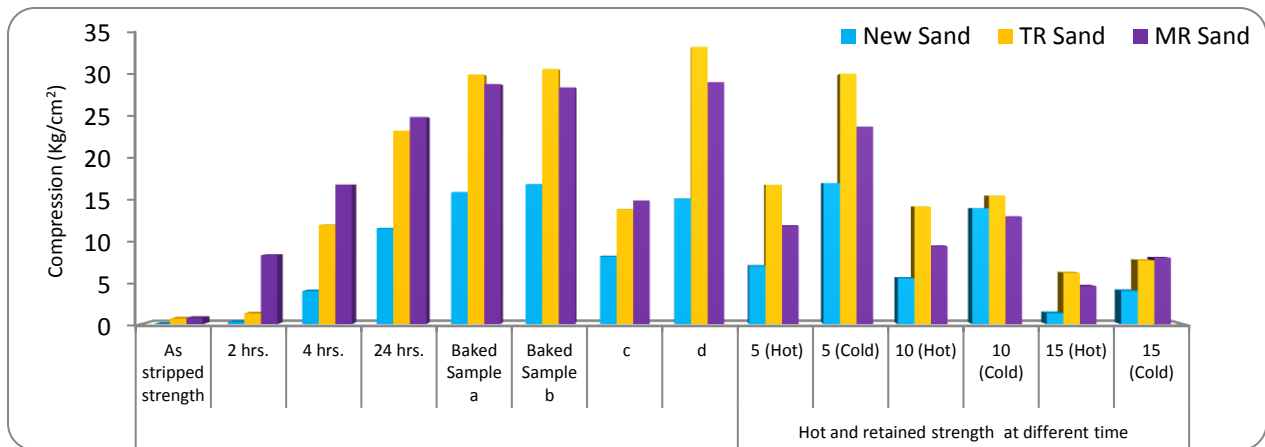


Figure 14. Recipe: 0.8:50 Medium Fast Catalyst RT-20°C, RH-47%

Codes versus strength

a : 2 hrs. samples baked @ 135°C for 10', cooled at RT & tested for compression
b : 24 hr. samples baked @ 135°C for 10', cooled at RT & tested for compression
c : Samples **b** dipped in thinner based Zircon wash, lighted off, tested hot for compression
d : Samples **b** dipped in thinner based Zircon wash, lighted off, tested for compression after cooling

Table 9. Gas value (850 °C)

Sand	New Sand		TR Sand		MR Sand	
Recipe	0.8:50	1.0 :50	0.8:50	1.0 :50	0.8:50	1.0 :50
Gas Value (ml/gm)	6.5	7.2	7.5	7.9	8.0	8.7



18th INTERNATIONAL FOUNDRYMEN CONFERENCE

Coexistence of material science and sustainable technology in economic growth

Sisak, May 15th-17th, 2019

<http://www.simet.hr/~foundry/>

Sand test part

- Baking for time as low as 10 mts and temperature as low 135 °C at any point of time after strip increase strength of molds to ultimate values for both systems
- Dry strength and handling strength of Furan bonded molds in working addition level are more than that of Alphasat bonded sands.
- In general, thermally reclaimed furan sand shows better strength than new sand and in case of Alphasat it is otherwise.
- Strength wise mechanically reclaimed furan bonded sand is far better than Alphasat bonded sand.
- Thinner based wash degrades mold strength in hot condition which is mostly recovered on cooling.
- Both hot and retained strength for both binder systems drop with soaking time in furnace at 450 °C.
- APNB bonded sand is more resistant to thermal degradation in both inert (TGA) and oxidative (450 °C in furnace) atmosphere
- Total gas evolution in working addition level is more in APNB bonded sand than in FNB

CONCLUSIONS

- Studies of strength (unwashed and washed, hot and cold) of samples made out of molding sand simulating different stages of mold movement can be used as a tool to have better control on mold strength and casting quality.
- Choice between two binders for green field foundries primarily depend on many factors, main being metal to be cast, compatibility with cheap and available sand and investment capability for mechanical and thermal reclaimer.
- With current stringent regulations for protection of Ecology and Environment, modern binder formulations have gone through changes like reduction in monomer contents, use of hybrid formulations, formulations with lower binder demand, increase in reclaimability of used sand so many.
- Modern Alphasat and Furan formulations are capable of working as clean binder systems at optimum addition level with reclamation, still meeting functional requirements of modern foundries.

Finally, modern formulations of FNB and APNB are capable of meeting most of the requirements of foundries right from BL of mixed sand and ease of de-coring of molds, post pouring and also stringent emission norms of local bodies.

Foundry World will keep on looking for inorganic self-sets which will match functional properties of these two self-sets and offering work place environment like any other manufacturing industry.



18th INTERNATIONAL FOUNDRYMEN CONFERENCE

Coexistence of material science and sustainable technology in economic growth

Sisak, May 15th-17th, 2019

<http://www.simet.hr/~foundry/>

One possibility is to use functionally modified silicate with slower liquid hardener like butylene carbonate, which is not available in commercial grade in today's market.

Acknowledgements

- My beloved professor Dr. B.K.Dutta for getting TGA done at his facilities at IIT, Kharagpur, India
- Prof. Mariusz Holtzer and his team of AGH University, Krakow for getting Py-CG-MS done at their facilities
- Management of Forace Polymers P Ltd, Hardwar, India for allowing me author to carry out sand tests at their facilities and allowing to submit this paper for presentation at IFC, Sisak, Croatia during 15-17th May'19.

REFERENCES

- [1] A. Kmita, A. Roczniak, M. Holtzer, Identification of pyrolysis products of the alphaset binder with gas chromatography/mass spectrometry, *Metalurgija*, 56(2017)1-2, pp. 21-24.
- [2] 50th Census of World casting production, *Modern casting* Dec 2016, Accessible on internet: <http://www.foundryinfo-india.org/statistics/Census-2016-Modern-Casting.pdf>, 06/03/2019
- [3] IIF Bulletin, Accessible on internet: http://www.foundryinfo-india.org/profile_of_indian.aspx, 06/03/2019
- [4] C. Cozzi, Ester cured sodium silicate a valid process for sand reclamation, 59th IFC Chandigarh, 2011, Accessible on internet: <http://foundryinfo-india.org/images/pdf/TS-2A-II.pdf>, 06/03/2019
- [5] M. Holtzer, Influence of Reclaim addition to the molding sand matrix obtained in the Alphasets technology on the emission of gases - Comparison with molding sand with Furfuryl Resin, *Archives of Foundry Engineering*, 15(2015)1, pp. 121-125.
- [6] M. Lucarz & J. Jezierski et al, Comparison of the properties of the Alkaline- Phenolic binders for the molding sand for the steel castings, 73rd World Foundry Congress, 23-27 Sep 2018, Krakow, Poland, pp. 1-2.
- [7] A. Kmita, A. Roczniak, M. Holtzer, Identification of pyrolysis products of the alphaset binder with gas chromatography/mass spectrometry, *Metalurgija*, 56(2017)1-2, pp. 21-24.
- [8] International patent publication number WO2017/10556 A1 dt 22/06/17
- [9] M. Holtzer, R. Danko, Molds and cores systems in foundry, DOI 10.1007/978-3-319-14583-9_2.
- [10] C. E. Bates, W. D. Scots WD, Decomposition of resin binders and the relationship between gases formed and casting surface quality-part 3, *AFS Transactions*, 85(1977), pp. 209-226.



18th INTERNATIONAL FOUNDRYMEN CONFERENCE

Coexistence of material science and sustainable technology in economic growth

Sisak, May 15th-17th, 2019

<http://www.simet.hr/~foundry/>

- [11] R. L. Naro, Porosity defects in iron castings from mold metal interface reactions, AFS Casting Congress, March 15, 1999, St. Louis- Missouri, USA, pp. 4.
- [12] M. Hosadyna et al, The diffusion of sulphur from molding sand to cast and methods of its elimination, Archives of Foundry Engineering, 9(2009)4, pp. 73-76.
- [13] W. Bauer, Investigations on the disturbance of spheroidal graphite formation in the marginal zone of GGG during casting in para toluene sulfonic acid-cured furan sand foundry practice, (1982), pp. 175-183.
- [14] E. Ireland, K. Chang, J. Kroker, New Horizon in Nobake Binder Technology, AFS Transactions, 02-025(2002), pp. 1-7.



18th INTERNATIONAL FOUNDRYMEN CONFERENCE

Coexistence of material science and sustainable technology in
economic growth

Sisak, May 15th-17th, 2019

<http://www.simet.hr/~foundry/>

APPROPRIATE MATHEMATICAL MODEL FOR STRESS CALCULATION BASED ON THE MEASURED VALUES OF DEFORMATION AND TEMPERATURE CHANGES

Ivan Jandrlić^{1*}, Stoja Rešković¹, Ladislav Lazić¹, Tin Brlić¹, Dušan Ćurčija²

¹ University of Zagreb Faculty of Metallurgy, Sisak, Croatia

² Croatian Metallurgical Society, Zagreb, Croatia

Oral presentation

Original scientific paper

Abstract

Presented mathematical model determines the stresses depending on the measured temperature changes and the associated deformations of the samples. Investigations were conducted by tensile testing machine Zwick 50 kN on the samples from low-carbon niobium microalloyed steel. The values of measured parameters were determined by using the methods of thermography and digital image correlation. The model is formulated on the basis of a multiple regression analysis of the relations between measured and calculated parameters. Verification and validation of the model showed a good agreement between the model and the system modeled.

Keywords: *stress, mathematical model, thermography, digital image correlation*

*Corresponding author: ijandrli@simet.hr

INTRODUCTION

The rapid development of technologies requires manufacturers to quickly adapt to new products, which have to meet the growing demands of the market. The development of materials used in the production of components goes hand in hand with development of the technologies. The best example for this is the automotive industry which, in addition to maintaining or increasing safety and dimensions, also requires a lower mass of the final product. For this reason, manufacturers are increasingly turning to the new types of materials. To maintain the reliability of the built-in components, it is of utmost importance to conduct detailed mechanical testings of newly installed components. Along with the application of different testing methods, the modeling and testing of components by using models formulated on the basis of the finite element method are increasingly in use [1-3].



18th INTERNATIONAL FOUNDRYMEN CONFERENCE

Coexistence of material science and sustainable technology in
economic growth

Sisak, May 15th-17th, 2019

<http://www.simet.hr/~foundry/>

Models for modeling mechanical behavior of various metal system components that are under load are especially complex. These models have certain limitations in terms of predicting all factors that may affect final values. They require knowledge of a significant number of parameters of the material to simulate the real behavior of certain components in the system as accurately as possible [4-8]. In order to obtain the reliable information of the material, there are also different models used in research to determine the interdependence between different parameters [4,5]. The wide knowledge on the material flow and stress distribution in the observed sample under load is also necessary [6,9]. Existing modeling methods are constantly subjected to improvements [8,9], as well as the ability of devices for the model verification [7]. What is valid for all models is a large number of metal testing, such as static tensile test, shear test, or some other method.

From the literature it is evident that there is a need for extensive research in order to develop the reliable models for determining stress distribution in the deformation zone. Lately the idea and need for a different and perhaps simpler approach to the modeling have emerged. It is well known that during the plastic deformation of the metals there is a change in the internal energy of the deformed metal, and this is manifested with the temperature change of the test sample in the deformation zone [10,11]. This change can be detected and measured by an infrared camera, and subsequent thermal analysis provides a clearer picture of the temperature distribution, i.e. the metal flow, throughout the deformation zone [11-14]. Thermography thus provides rapid and accurate measurements from which the distribution of temperature can be analyzed, and thus stress and deformation distribution during deformation of the test samples may be determined [13,14].

It is a reasonable assumption that the maximum temperature change occurs at the place of the maximum deformation. For this reason, it is necessary to obtain the accurate information on deformation distribution throughout the deformation zone. This can be achieved by the method of Digital Image Correlation (DIC), which is frequently used today as a method for displacement and deformation analysis [15-17]. With this method it is possible to measure very small changes in displacements, thus measuring very small non-homogeneous deformations [14,15]. The advantage of the method is also the insensitivity of the method considering the shape of the sample and it is possible to conduct the testings on the samples with non-standard shapes and sizes [18]. The method has been developed to such an extent that it begins to be used for the validation of models tested in real conditions [16].

The aim of this paper is to formulate a mathematical model which will be able to calculate the values of acting stresses from the experimentally determined values of deformation (strains) and corresponding temperature changes. The model will be formulated on the basis of experimentally determined values of strain and temperature changes detected by the methods of Digital Image Correlation and thermography. Maximum values of strains, temperature changes and stresses determined by a static tensile test, were used for the modeling. It is realistic to assume that they occur in places of maximum acting stresses. Once formulated, the model will be validated and verified by experimentally measured values.



18th INTERNATIONAL FOUNDRYMEN CONFERENCE
**Coexistence of material science and sustainable technology in
 economic growth**

Sisak, May 15th-17th, 2019

<http://www.simet.hr/~foundry/>

MATERIALS AND METHODS

For the proposed model, at first it was necessary to experimentally determine the stresses, strains and temperature changes in the deformation zone during the stretching of samples. For this purpose, at the same time, during the static tensile testing on the Zwick 50 kN testing machine, the deformation of samples was recorded with an infrared and optical digital camera. The maximum stress values during the experiment were obtained from the diagram recorded by the static tensile testing machine. By a subsequent analysis of recorded deformations, using the methods of thermography and DIC, the values of temperature changes and strains were determined during the testing period. The maximum values of temperature changes and strains at the points of maximum stresses were determined. The arrangement of the measuring equipment as well as the deformation zone analyzed by the thermography and DIC methods are shown in Figure 1.



Figure 1. The arrangement of the measuring equipment as well as the deformation zone analyzed by the thermography and DIC methods

Tests were performed at two different testing speeds of 10 and 15 mm · min⁻¹. The samples for static tensile testing were taken in the rolling direction from a 3 mm thick hot-rolled strip. Tests were performed on samples with rectangular cross-section, with gauge length of 45 mm and gauge width of 20 mm. The chemical composition of the tested steel is given in Table 1.

Table 1. Chemical composition of the tested steel, wt. %

Element	C	Mn	Si	P	S	Al	Nb	N
Micro-alloyed steel	0.12	0.78	0.18	0.011	0.018	0.02	0.048	0.008

To formulate the model, it was necessary to determine the interdependence of the measured values using the MathCAD and OriginPro software packages. Data obtained from the thermography and Digital Image Correlation analysis, due to the high frequency of measurement, had a certain noise, which would present a problem during the modeling



18th INTERNATIONAL FOUNDRYMEN CONFERENCE
**Coexistence of material science and sustainable technology in
economic growth**

Sisak, May 15th-17th, 2019

<http://www.simet.hr/~foundry/>

process. Therefore, a certain smoothing of the measured values of measured strains and temperature changes was made before the modeling with the use of the Savitzky - Golay method within OriginPro, and the fourth-order polynomial function. Subsequently, the multiple linear regression analysis with the application programs was performed on adjusted values of measurement results.

RESULTS AND DISCUSSION

In the first step of formulating the model, the interdependence of measured values was studied. First, the influence of temperature change on the increase of strain during stretching of samples was determined. The analysis was performed at both used testing speeds. The results are shown in Figure 2.

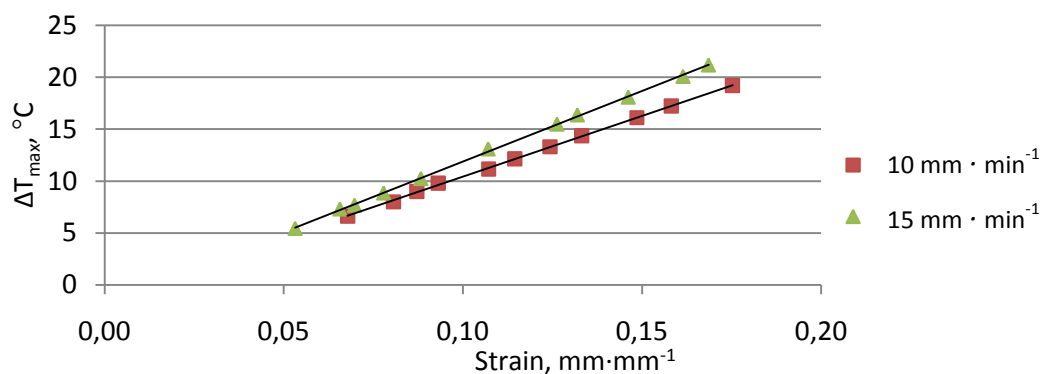


Figure 2. Dependence of temperature change on strain at different testing speeds

The analysis of the influence of the increase in strains on the temperature change during the stretching of samples, made of 0.048% Nb microalloyed steel, shows that the increase in strain causes an increase of the temperature changes. From the obtained diagrams it is clear that the increase in temperature is linear in relation to the strains increase. Linear growth indicates a close association of strains and temperature changes. It is logical to conclude that a greater amount of deformation causes a greater temperature change.

Linear growth was achieved at both used testing speeds. In the case of 15 mm · min⁻¹, the temperature increase is higher than at the lower testing speed (10 mm · min⁻¹). This indicates that the testing speed has an effect on the temperature change. It is expected that this increment will grow with a further increase in the testing speed, which should be explored in further research.

However, the question is how the temperature change is influenced by the increase in stress. For this reason, this dependence was also examined. The obtained diagram of the dependence of the temperature change on the increase in stress is shown in Figure 3.



18th INTERNATIONAL FOUNDRYMEN CONFERENCE
Coexistence of material science and sustainable technology in
economic growth
 Sisak, May 15th-17th, 2019
<http://www.simet.hr/~foundry/>

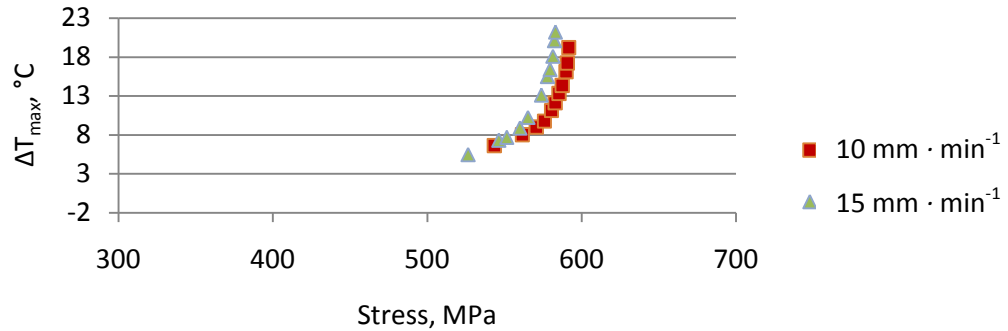


Figure 3. Dependence of the temperature change on the stress at different test speeds

As can be seen in the above correlation diagram, the increase in stress has a significant effect on the temperature change. This functional relationship is represented by an exponential function. The influence of deformation velocity is in this case weaker, but is still present.

From the analysis as well as previous investigations, it can be concluded that the measured temperature changes are closely related to the values of stresses and strains achieved during the tensile test. Accordingly, the following relation can be set:

$$\Delta T = f(\sigma, \varepsilon) \quad (1)$$

where: σ – stress,
 ε – strain (i.e. deformation).

Starting from this assumption, using the multiple linear regression analysis, the functional relationships between the temperature change on one side and the strain and stress on the other side, at both the test speeds, were determined separately. The following general function dependency was obtained:

$$\Delta T = a + b \cdot \varepsilon + c \cdot \sigma \quad (2)$$

From this function, we gain two separate functions for each testing speed:

$$\Delta T = 1.6 + 140.2 \cdot \varepsilon - 0.0077 \cdot \sigma \quad (3)$$

$$\Delta T = 2 + 157.2 \cdot \varepsilon - 0.0104 \cdot \sigma \quad (4)$$

Depending on the used testing speed, different parameter values of a , b , c were achieved, Table 2.



18th INTERNATIONAL FOUNDRYMEN CONFERENCE
**Coexistence of material science and sustainable technology in
economic growth**

Sisak, May 15th-17th, 2019

<http://www.simet.hr/~foundry/>

Table 2. Parameter values a , b and c at different testing speeds

Testing speed (mm · min ⁻¹)	a	b	c
10	1.6	140.2	-0.0077
15	2	157.2	-0.0104

By transformation of equation 4, it is possible to express the stress as the function of temperature change and achieved deformation:

$$\sigma = \frac{\Delta T - (a + b \cdot \varepsilon)}{c} \quad (5)$$

By entering the parameters assigned to each test speed, the following equations are achieved:

$$\sigma = \frac{\Delta T - (1.6 + 140.2 \cdot \varepsilon)}{-0.0077} \quad (6)$$

$$\sigma = \frac{\Delta T - (2 + 157.2 \cdot \varepsilon)}{-0.0104} \quad (7)$$

The mathematical model for the stress calculation formulated on the basis of the above achieved regression equations was validated and verified with the measured values of deformations and temperature changes. It has been achieved a good agreement between computed values by the developed model and the experimentally measured values of maximum stresses, for both of the used testing speeds.

CONCLUSIONS

By the experimental studies and analysis of obtained data on the adequate application programs it was established that there is interdependence between temperature changes, strains (i.e. deformations) and stresses in the deformation zone of the tested samples.

Using multiple linear regression analysis, the functional relationships between the two independent (predictive) variables, the temperature changes and strains, and the dependent (criterion) variable – stresses, were determined.

The mathematical model formulated on the basis of the achieved regression equations enables the calculation of stresses knowing the experimentally measured values of temperature changes and deformations in the deformation zone. Model was validated and verified by comparing the calculated and experimentally determined values.



18th INTERNATIONAL FOUNDRYMEN CONFERENCE

Coexistence of material science and sustainable technology in
economic growth

Sisak, May 15th-17th, 2019

<http://www.simet.hr/~foundry/>

Acknowledgements

This work has been fully supported by the Croatian Science Foundation under the project number IP-2016-06-1270.

REFERENCES

- [1] M. Seif, J. Main, J. Weigand, T. P. McAllister, W. Luecke, Finite element modeling of structural steel component failure at elevated temperatures, *Structures* 6(2016), pp. 134-145.
- [2] S. Izadpanah, S. Hadi Ghaderi, M. Gerdooei, Material parameters identification procedure for BBC2003 yield criterion and earing prediction in deep drawing, *International Journal of Mechanical Sciences*, 115–116(2016), pp. 552-563.
- [3] R. Padma Priya, S. Kandasamy, Study on the behavior of cold-formed steel angle tension members, 20th International Specialty Conference on Cold-Formed Steel Structures, (Roger A. LaBoube and Wei-Wen Yu), Department of Civil, Architectural & Environmental Engineering Missouri University of Science and Technology, November 3 & 4, 2010, St. Louis, Missouri, pp. 589-604.
- [4] M. Abspoel, M. E. Scholting, M. Lansbergen, Y. An, H. Vegter, A new method for predicting advanced yield criteria input parameters from mechanical properties, *Journal of Materials Processing Technology*, 248(2017), pp. 161-177.
- [5] C. Li, E. Daxin, N. Yi, Analysis on fracture initiation and fracture angle in ductile sheet metal under uniaxial tension by experiments and finite element simulations, *Journal of Materials Research*, 31(2016)24, pp. 3991-3999.
- [6] A. Nasser, A. Yadav, P. Pathak, T. Altan, Determination of the flow stress of five AHSS sheet materials (DP 600, DP 780, DP 780-CR, DP 780-HY and TRIP 780) using the uniaxial tensile and the biaxial Viscous Pressure Bulge (VPB) tests, *Journal of Materials Processing Technology*, 210(2010)3, pp. 429-436.
- [7] M. Merklein, M. Biasutti, Development of a biaxial tensile machine for characterization of sheet metals, *Journal of Materials Processing Technology*, 213(2013)6, pp. 939-946.
- [8] Y. Ling, Uniaxial true stress-strain after necking, *AMP Journal of Technology*, 5(1996), pp. 37-48.
- [9] H. Vegter, H. Mulder, P. van Liempt, J. Heijne, Work hardening descriptions in simulation of sheet metal forming tailored to material type and processing, *International Journal of Plasticity*, 80(2016), pp. 204-221.
- [10] A. Rusinek, J. R. Klepaczko, Experiments on heat generated during plastic deformation and stored energy for TRIP steels, *Materials and Design*, 30(2009), pp. 35-48.
- [11] M. M. Kutin, S. S. Ristić, M. R. Prvulović, M. M. Prokolab, N. M. Marković, M. R. Radosavljević; Application of Thermography during Tensile Testing of Butt Welded Joints, *FME Transactions*, 39(2011), pp. 133-138.



18th INTERNATIONAL FOUNDRYMEN CONFERENCE

Coexistence of material science and sustainable technology in
economic growth

Sisak, May 15th-17th, 2019

<http://www.simet.hr/~foundry/>

- [12] J. Hyun Ryu, J. In Kim, H. S. Kim, C. S. Oh, H. K. D. H. Bhadeshia, D.-W. Suh, Austenite stability and heterogeneous deformation in fine-grained transformation-induced plasticity assisted steel, *Scripta Materialia*, 68(2013), pp. 933-936.
- [13] T. Brlić, S. Rešković, I. Jandrlić, Study of inhomogeneous plastic deformation using thermography, 16th International Scientific Conference on Production Engineering - CIM 2017, (E. Abele, T. Udiljak, D. Ciglar), Zagreb: HUPS, 08-10.06., 2017, Zadar, Croatia, pp. 65-68.
- [14] I. Jandrlić, S. Rešković, T. Brlić, Distribution of stress in deformation zone of niobium microalloyed steel, *Metals and Materials International*, 24(2018)4, pp. 746-751.
- [15] M. Eskandari, A. Zarei-Hanzaki, M. Yadegari, N. Soltani, A. Asghari, In situ identification of elastic-plastic strain distribution in a microalloyed transformation induced plasticity steel using digital image correlation, *Optics and Lasers in Engineering*, 54(2014), pp. 79-87.
- [16] P. Lava, S. Cooreman, D. Debruyne, Study of systematic errors in strain fields obtained via DIC using heterogeneous deformation generated by plastic FEA, *Optics and Lasers in Engineering*, 48(2010)4, pp. 457-468.
- [17] I. Jandrlić, S. Rešković, T. Brlić, L. Lazić, T. Aleksandrov Fabijanić, Investigation of deformation by digital image correlation, 16th International Foundrymen Conference, Global Foundry Industry - Perspectives for the Future, (Z. Zovko Brodarac, N. Dolić, A. Begić Hadžipašić), University of Zagreb Faculty of Metallurgy, 15.-17.05.2017, pp. 115-121.
- [18] P. Lava, S. Coppieters, R. Van Hecke, P. Van Houtte and D. Debruyne, Digital image correlation in the classroom: determining stress concentration factors with webcams, http://www.matchid.org/pascal/Articles/plava_classroomfinal2.pdf (25.3.2015)



18th INTERNATIONAL FOUNDRYMEN CONFERENCE
**Coexistence of material science and sustainable technology in
economic growth**

Sisak, May 15th-17th, 2019

<http://www.simet.hr/~foundry/>

**COOLING RATE ASSESSMENT DURING NONEQUILIBRIUM SOLIDIFICATION OF
COMPLEX Al–Mn-BASED ALLOYS**

Blaž Leskovar^{*}, Boštjan Markoli, Iztok Naglič

University of Ljubljana Faculty of Natural Sciences and Engineering, Ljubljana, Slovenia

Oral presentation
Original scientific paper

Abstract

This work deals with the influence of alloying elements on the cooling rate and microstructure in complex Al–Mn-based alloys. Alloys were synthesized at 880 °C and cast into a copper mould with cylindrical casting cavity. The castings were characterized by light microscopy (LOM), scanning electron microscopy (SEM) and energy-dispersive x-ray spectroscopy (EDS). X-ray diffraction (XRD) and electron backscattered diffraction (EBSD) were used to determine the structure of the phases. The solidus and liquidus temperatures and enthalpies were determined with the differential scanning calorimetry (DSC). Cooling rate at the start of solidification was calculated by one-dimensional transient-heat-conduction analysis. Calculations showed negligible difference in the average cooling rate between investigated alloys. Nevertheless, the volume fraction of primary icosahedral quasicrystalline (iQc) phase, which had almost the same chemical composition in all investigated alloys, was far higher for the Al–Mn–Si–Zn–Ca–Sr alloy. Results showed significant difference in the solidification rate between investigated alloys. Solidification rates were estimated by measuring the secondary dendrite arm spacing (SDAS) and content of manganese in solid solution of α -Al. The highest solidification rate was estimated for the Al–Mn–Si–Zn–Ca–Sr alloy. Additional elements such as magnesium, calcium and strontium have a big influence on the solidification path of investigated alloys. Higher mean solidification rate in alloy containing calcium, strontium and zinc was also calculated using Chvorinov's rule.

Keywords: *aluminium alloys, microstructure, cooling rate, solidification rate, Chvorinov's rule*

*Corresponding author (e-mail address): blaz.leskovar@omm.ntf.uni-lj.si



18th INTERNATIONAL FOUNDRYMEN CONFERENCE

Coexistence of material science and sustainable technology in economic growth

Sisak, May 15th-17th, 2019

<http://www.simet.hr/~foundry/>

INTRODUCTION

Complex metallic alloy (CMA) is a compound, or a phase, or an alloy, essentially made of metals. This does not mean that the alloy is a metal itself, but it simply means that the major part of the constituents belongs to *sp* or *d* metals. Based on crystal structures we can state that CMAs are characterized by giant unit cells containing several tens up to more than a thousand atoms. Inside the unit cell, atoms usually form geometrical cluster units of high symmetry. Prominent role for example represents icosahedral (5-fold symmetry) or decagonal (10-fold symmetry) clusters. There has been a renewed interest in CMAs especially on aluminium based ones, since the discovery of metastable quasicrystals (Qcs) in 1984 [1-5]. According to their diffraction symmetry, Qcs are classified as icosahedral (i-), octagonal (o-), decagonal (d-) or dodecagonal (dd-) phases. The atomic positions are ordered, but with rotational symmetries, e. g. five- (i-), eight- (o-), ten- (d-) or twelfold (dd-), which are not found in standard crystals. These symmetries forbid a periodic structure and, instead, enforce quasi-periodicity explained by Fibonacci sequence [6-9]. There is a large number of metastable Qcs known, which can only be prepared by rapid solidification techniques [10-14].

Stable iQcs were discovered soon after in various alloys [15,16]. Conditions under which quasicrystals (Qcs) can form were explained by the Hume-Rothery rules where electron to atom ratio plays the most important role [17,18]. Recently, Naglič et al. showed that in addition to appropriate electron to atom ratio an average metallic radius is also important factor in formation of Qcs [19].

Addition of assorted alloying elements to Al–Mn alloy system, which incorporate into a metastable iQc phase, affect the cooling rate needed for their formation and stability of iQc. Two elements, among many other, which proved to be very efficient and decreased the cooling rate needed for the formation of metastable iQc were silicon and beryllium [20-24]. Bončina et al. found that around 30 at.% of beryllium got incorporated into the primary iQc phase [20].

Elements which are present in the same group as beryllium and possess similar electron to atom ratio as beryllium are calcium and strontium [25]. Metallic radius for these two elements is 0.197 and 0.215 nm. Both are much larger in comparison to beryllium that has the radius of 0.113 nm. This goes for aluminium, manganese and silicon with 0.143, 0.126 and 0.137 [26] nm, too. [27] On the other hand, zinc is also an element with similar electron to atom ratio as beryllium [25]. Its metallic radius is in the range of those found for aluminium and manganese, yielding 0.135 nm and is essentially similar that of silicon [27]. Electron to atom ratio for antimony is closer to silicon, but metallic radius is quite larger with 0.161 nm [28]. Large metallic radius of antimony, calcium and strontium are not favourable for the incorporation into the primary iQc phase, but in spite of that, those elements can have big influence on the solidification path of investigated alloys.

This was also the ground on which our choice for the antimony, calcium, strontium and zinc was made. Yet, recent research in facilitating the growth of iQcs has led us to investigate



18th INTERNATIONAL FOUNDRYMEN CONFERENCE

Coexistence of material science and sustainable technology in economic growth

Sisak, May 15th-17th, 2019

<http://www.simet.hr/~foundry/>

the influence of purely technological parameters of solidification, such as cooling rate, solidification rate, undercooling etc. It has been shown by Gillesen et al. [29] and Battezzati et al. [30] that the undercooling sparked by the cooling rate can fundamentally change the course of solidification of Al–Mn-based alloys and lead to increased amount of iQc phase in these alloys. In work by Ichikawa et al. [31] the effect of the undercooling and cooling rate on the solidified structures of Al–Mn alloys was studied. They discovered that undercooling is increasing with the manganese content and cooling rate.

We have therefore decided to introduce antimony, calcium, strontium and zinc into Al–Mn–Si-based alloys in order to evaluate the change in the formation ability of the iQc phase and provide a comprehensive explanation of the most influential parameters on the constitution of the quasicrystal forming alloys.

MATERIALS AND METHODS

Three aluminium alloys, first containing manganese and silicon, second containing manganese, silicon and antimony, and third containing manganese, silicon, zinc, calcium and strontium, were prepared in a chamber furnace. We used pure aluminium (99.8 wt.%), manganese (99.9 wt.%), zinc (99.99 wt.%), silicon (99.99 wt.%), antimony (99.9 wt.%) and the master alloys AlSr10 KBM and AlCa6 KBM. Alloys were melted and cast into a copper mould at 880 °C. The mould was made of copper block with dimensions of 100×100×120 mm and with a cylindrical casting cavity of 5 mm in diameter. The chemical compositions of the prepared alloys are presented in Table 1. The castings were cut, mount and prepared by grinding and polishing for characterization of microstructure.

Table 1. Chemical compositions of the alloys in at.% with corresponding experimental uncertainties

Alloy	Al	Mn	Si	Sb	Zn	Ca	Sr
Al–Mn–Si	93.5 ± 0.6	5.4 ± 0.5	1.1 ± 0.3	-	-	-	-
Al–Mn–Si–Sb	93.8 ± 0.7	4.3 ± 0.6	1.6 ± 0.2	0.4 ± 0.1	-	-	-
Al–Mn–Si–Zn–Ca–Sr	92.3 ± 0.6	4.3 ± 0.5	1.2 ± 0.2	-	1.0 ± 0.1	0.7 ± 0.1	0.5 ± 0.1

Characterization of microstructure was performed using a light optical microscope (LOM), ZEISS Axio Imager A1m, equipped with a digital camera AxioCam ICc 3 (3.3 million pixels) and AxioVision software. The primary iQc phase area fraction was determined using LOM images captured over the surface of the sample at magnification of 100x. The uncertainty of measured results based on the colour determination was assessed to be ±5 %.

X-ray diffraction (XRD) technique was used to identify the phases present in investigated alloys. PANalytical X'Pert PRO diffractometer with non-monochromated x-rays produced by Empréan Cu anode tube operating at 45 kV and 40 mA were used in this work.



18th INTERNATIONAL FOUNDRYMEN CONFERENCE
**Coexistence of material science and sustainable technology in
economic growth**

Sisak, May 15th-17th, 2019

<http://www.simet.hr/~foundry/>

A field-emission-gun scanning electron microscope JEOL JSM-7600F equipped with energy-dispersive x-ray spectroscopy (EDS) and electron backscatter diffraction (EBSD) was used for the microstructural characterization. The analyses were performed using Oxford Instruments INCA Microanalysis Suite, with an X-Max 20 SDD-EDS detector and CHANNEL5 EBSD software with a Nordlys detector. The elemental compositions of the iQc phases were measured using an optimized quantitative EDS approach at a 15 kV accelerating voltage. The crystallinity of the samples was studied by EBSD analysis using a 20 kV.

In order to identify and evaluate the variables that have the most influence on the amount of the iQc phase in investigated alloys we have employed several different approaches. First method used to calculate the cooling rate of our alloys was the one-dimensional transient-heat-conduction analyses. This was used to assess the cooling rate at the point of beginning of the solidification course as the liquidus temperatures (L_s) for Al–Mn–Si, Al–Mn–Si–Sb and Al–Mn–Si–Zn–Ca–Sr alloy were estimated using ternary Al–Mn–Si system and found to be between $L_s = 770$ °C and $L_s = 820$ °C. This gave us a difference of 110 °C and 60 °C if the casting temperature of 880 °C for the melt is considered. Such a difference could play an important role in influencing the amount of iQc phase but the calculations yielded a difference in cooling rate only around 20 K/s. This difference is negligible if actual values for cooling rates are taken into account, which are in range of 650 K/s as calculated. This leads to a suggestion that almost negligible difference in average cooling rate due to different liquidus temperatures does not play a dominant role influencing the content of iQc phase. Other physical properties for our alloys, such as the specific heat capacity for the alloys' melt, density of the melt, thermal conductivity of the melt and the heat-transfer coefficient were taken from the ref. [19], yielding, 1060 J kg⁻¹ K⁻¹, 2400 kg m⁻³, 100 W m⁻¹ K⁻¹, 2500 W m⁻² K⁻¹ and 25 °C for the copper mould was used.

We have also employed direct method to assess the solidification rate for non-equilibrium solidification conditions by measuring the secondary dendrite arm spacing (SDAS) of α -Al. We executed measurements using backscattered electron (BE) images. SDAS were measured in the centre of the cylindrical cross-section and on its edge. Then our SDAS measurements were used to make an estimate of the cooling rate for our alloys based on SDAS-cooling rate relation devised by Cho et al.[32]. This approach provided us with the average solidification rate according to Cho et al. and will be referred to hence forth as the Cho model.

To confirm results based on SDAS we then further assessed the average solidification rate based on the measured manganese content in the solid solution of α -Al as determinate by Ichikawa et al. (which will be referred to as the Ichikawa model) [31].

These two different methods for assessing the solidification rate are both focused on α -Al dendrites formed during nonequilibrium solidification. For that reason, we used independent method for calculating the mean solidification rate by using a modified Chvorinov's rule [33, 34]. This rule enables us to calculate solidification time for melt cast into a simple cylindrical mould by equation:



18th INTERNATIONAL FOUNDRYMEN CONFERENCE

Coexistence of material science and sustainable technology in
economic growth

Sisak, May 15th-17th, 2019

<http://www.simet.hr/~foundry/>

$$t = B \times \left(\frac{A_s}{A}\right)^{1.31} \times V^{0.67} \quad (1)$$

In Equation 2 t represents the solidification time, B is the mould constant, A_s is the surface area of the sphere having the same volume as the casting, A is the surface area of the casting that is in contact with the mould and V is the volume of the casting. The mould constant is defined as:

$$B = \left[\frac{\rho_m L}{(T_l - T_s)}\right]^2 \times \left[\frac{\pi}{4k\rho c}\right] \times \left[1 + \left(\frac{c_m \Delta T_s}{L}\right)^2\right] \quad (2)$$

where T_l is liquidus temperature of the alloy (K), T_s is solidus temperature of the alloy (K), ΔT_s is superheat (K), L is heat of fusion or heat of solidification ($\text{J}\cdot\text{kg}^{-1}$), k is a thermal conductivity of the mould ($\text{W}\cdot\text{m}^{-1}\cdot\text{K}^{-1}$), ρ is a density of the mould ($\text{kg}\cdot\text{m}^{-3}$), c is specific heat of the mould ($\text{J}\cdot\text{kg}^{-1}\cdot\text{K}^{-1}$), ρ_m is a density of the alloy ($\text{kg}\cdot\text{m}^{-3}$), and c_m is a specific heat of the alloy ($\text{J}\cdot\text{kg}^{-1}\cdot\text{K}^{-1}$).

Differential scanning calorimetry (DSC) technique was used to determine the temperature interval of solidification and heat of solidification (solidification enthalpies). A NETZSCH Jupiter 449c was used in this work and the experiments were performed in an Ar atmosphere up to the 880 °C (1150 K), at heating and cooling rates of 10 K/min.

RESULTS AND DISCUSSION

LOM images presented in Figure 1 show that a primary phase with dendritic morphology is present over the whole cross-section of the castings. These phases often possess five branches which is a characteristic for the icosahedral space group.[35] The primary dendritic phases in the central region of the samples (Figure 1b, 1d and 1f) are larger, with longer dendritic branches compared to those found near the contact surface of the casting (Figure 1a, 1c and 1e). The contact surface is referred to the outer surface of the casting being in contact with the mould. In the central region of the Al–Mn–Si alloy phase with a needle-like morphology dominate. Regarding to the phase diagram this is the β -Al–Mn–Si[21] phase, Figure 1b.



18th INTERNATIONAL FOUNDRYMEN CONFERENCE
Coexistence of material science and sustainable technology in
economic growth

Sisak, May 15th-17th, 2019

<http://www.simet.hr/~foundry/>

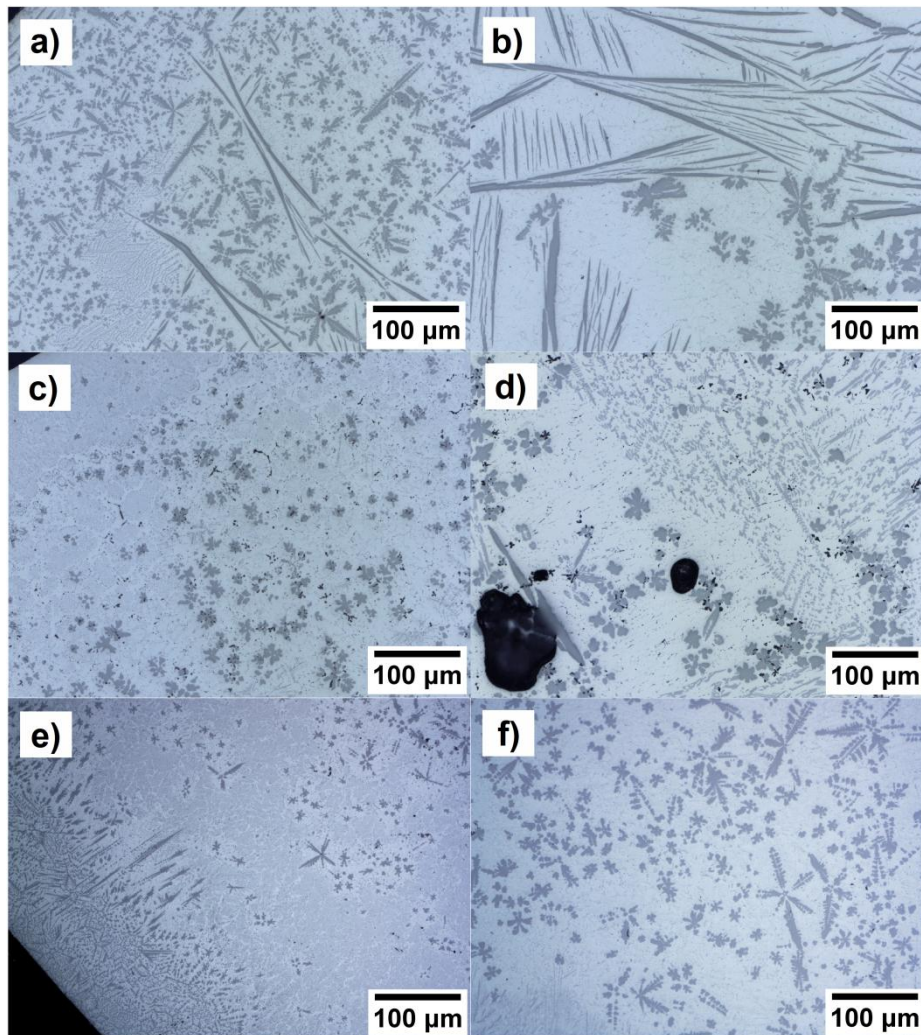


Figure 1. LOM microstructure of the Al–Mn–Si, a), b); Al–Mn–Si–Sb, c), d); and Al–Mn–Si–Zn–Ca–Sr, e), f), alloys in the as-cast state. Area near the contact surface of the casting a), c), e), and central region of the casting b), d), f), is shown

XRD technique was used to determine the phases present in the investigated alloys as presented in Figure 2.

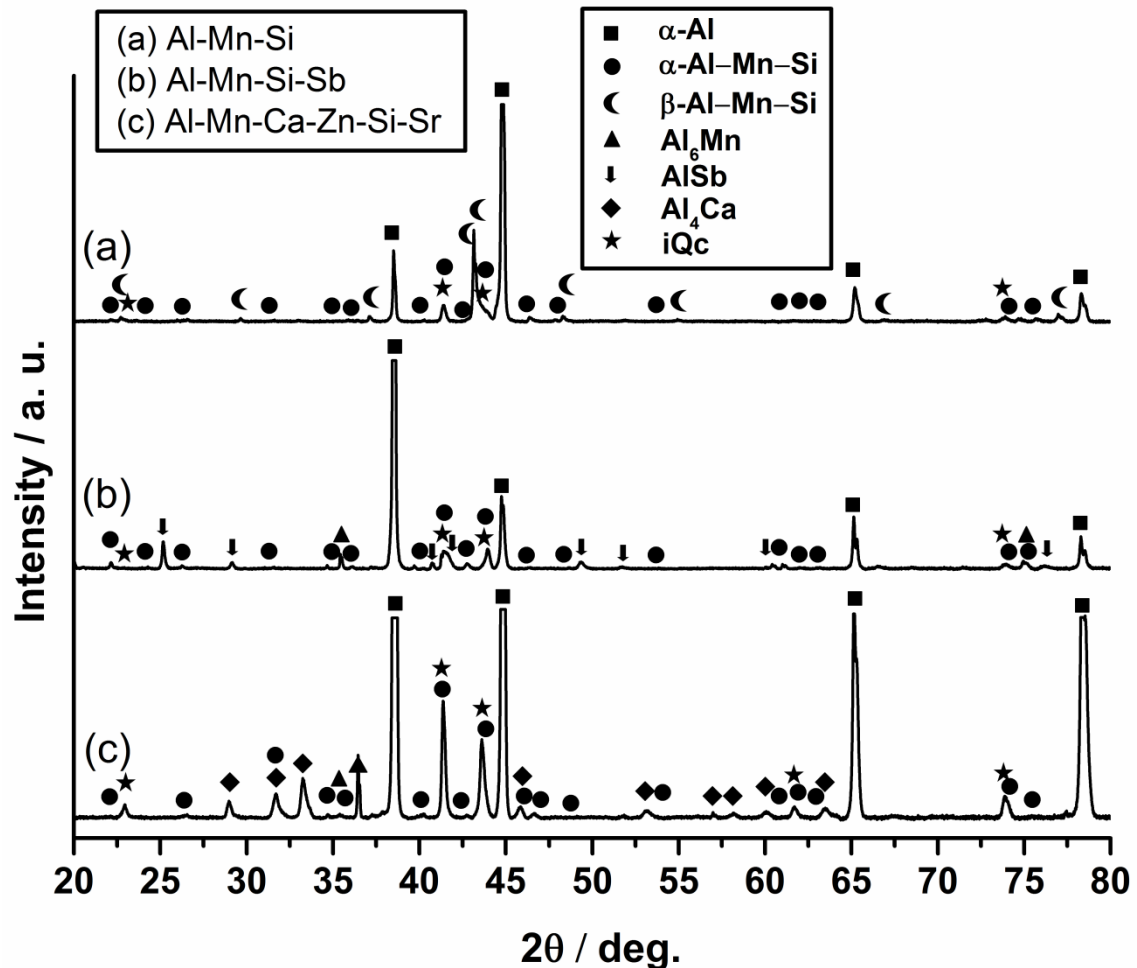


Figure 2. XRD patterns of bulk Al-Mn-Si, a), Al-Mn-Si-Sb, b), and Al-Mn-Si-Zn-Ca-Sr, c), alloys

The Al-Mn-Si alloy consists of α -Al [36], α -Al-Mn-Si [37], β -Al-Mn-Si [38] and iQc [39, 40] phase. The Al-Mn-Si-Sb alloy, which contains less manganese and more silicon, consists mainly of α -Al [36], α -Al-Mn-Si [37], AlSb [36], and iQc [39, 40] phase, whereas the Al-Mn-Si-Zn-Ca-Sr alloy consists of α -Al[36], iQc [39,40], Al₄Ca [36], α -Al-Mn-Si [37] and a small amount of Al₆Mn [36].

BE images of characteristic phases present in investigated alloys and corresponding electron backscattered diffraction (EBSD) patterns [41] are presented in Figure 3. EBSD patterns confirm that primary phases near the contact surface in all alloys were iQcs.

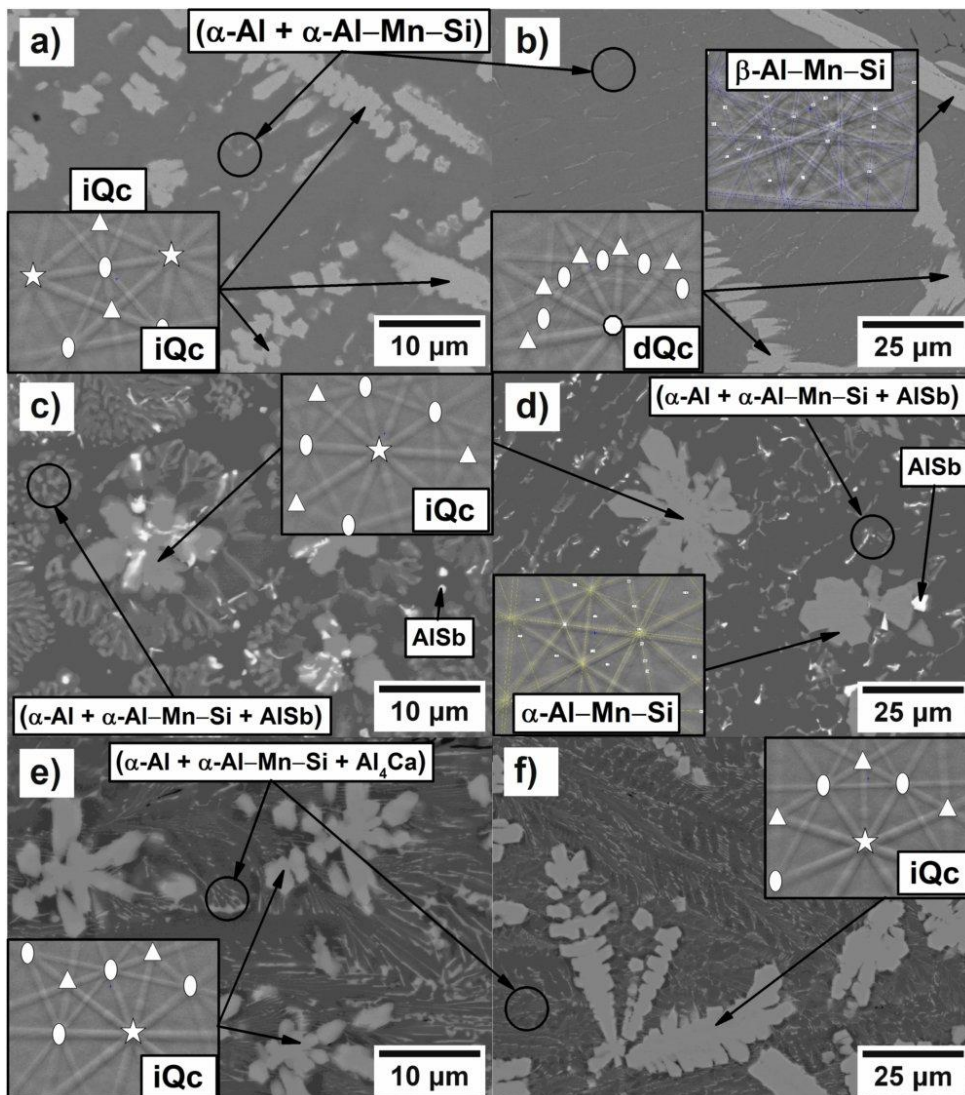


Figure 3. BE images of the Al–Mn–Si, Al–Mn–Si–Sb and Al–Mn–Si–Zn–Ca–Sr alloys in the as-cast state. Area near the contact surface of the casting a), c), e) and central region of the casting b), d), f) are presented. EBSD patterns presented in the inset have marked 10-fold (white circle), 5-fold (white pentagon), 3-fold (white triangle) and 2-fold (white ellipse) symmetry axes, indicating iQc and dQc phases

BE image of the Al–Mn–Si alloy indicates, that in addition to primary iQc phase (α -Al + α -Al–Mn–Si) heterogeneous structure is present over the whole cross-section. Primary iQc phase was observed in the area near the contact surface. In the central region β -Al–Mn–Si [38] phase was confirmed to have needle-like morphology and a small amount of dQc phase was also present. Microstructure of the Al–Mn–Si–Sb alloy indicates that in addition to primary iQc phase (α -Al + α -Al–Mn–Si + AlSb) heterogeneous structure is present over the whole cross-section. In the central region α -Al–Mn–Si [37] phase was also found. In



18th INTERNATIONAL FOUNDRYMEN CONFERENCE

Coexistence of material science and sustainable technology in economic growth

Sisak, May 15th-17th, 2019

<http://www.simet.hr/~foundry/>

addition to primary iQc phase in the Al–Mn–Si–Zn–Ca–Sr alloy (α -Al + α -Al–Mn–Si + Al₄Ca) heterogeneous structure was also identified.

Form microstructures and XRD results it is clear that the volume fraction of iQc phase is the largest in the case of the Al–Mn–Si–Zn–Ca–Sr alloy. For comparison between alloys volume fraction of primary iQc phase were determined on LOM images for all investigated alloys. The mean value of volume fraction of the iQc phase and the content found near the contact surface and in the central region of castings are presented in Table 2.

Table 2. The area fraction (volume fraction) of the primary iQc phase (%), near the contact surface, in the central region of the sample and the mean value with the standard deviations

Alloy	Near the contact surface	In the central region	Mean value
Al–Mn–Si	16.7 ± 5.5	7.5 ± 5.0	12.0 ± 7.0
Al–Mn–Si–Sb	9.5 ± 3.5	8.5 ± 2.5	9.0 ± 3.0
Al–Mn–Si–Zn–Ca–Sr	13.0 ± 4.0	19.0 ± 2.5	16.0 ± 4.5

The average volume fraction of the primary metastable iQc phase over the whole cross-section is the largest in the Al–Mn–Si–Zn–Ca–Sr alloy. A very important issue which could affect the formation of metastable iQc phase is incorporation of alloying elements into the iQc phase. In order to evaluate this, we determined the composition of the primary iQc phases in our alloys. Compositions of the iQc phases as determined by EDS analysis are presented in Table 3.

Table 3. Chemical composition of primary iQc phase in the middle and near the contact surface of investigated alloys in at.% with corresponding experimental uncertainties

Alloy		Al	Mn	Si	Zn
Al–Mn–Si	In the central region	79.8 ± 0.3	17.7 ± 0.2	2.5 ± 0.2	-
	Near the contact surface	80.3 ± 0.3	17.4 ± 0.2	2.3 ± 0.2	-
Al–Mn–Si–Sb	In the central region	78.1 ± 0.3	17.2 ± 0.2	4.7 ± 0.2	-
	Near the contact surface	78.7 ± 0.3	17.1 ± 0.2	4.2 ± 0.2	-
Al–Mn–Si–Zn–Ca–Sr	In the central region	79.8 ± 0.3	17.1 ± 0.2	2.8 ± 0.2	0.3 ± 0.1
	Near the contact surface	80.3 ± 0.3	16.6 ± 0.2	2.8 ± 0.2	0.3 ± 0.1



18th INTERNATIONAL FOUNDRYMEN CONFERENCE
**Coexistence of material science and sustainable technology in
economic growth**

Sisak, May 15th-17th, 2019

<http://www.simet.hr/~foundry/>

Results show that the iQc phase in the Al–Mn–Si–Sb alloy in comparison to other investigated alloys contains ~2.0 at.% more silicon. This slightly higher amount could be attributed to the formation of α -Al–Mn–Si phase in the central region of casting, as confirmed by EBSD and large interaction volume of EDS analyses in comparison to small iQc particles near the contact surface of the casting. The iQc phase in the Al–Mn–Si–Zn–Ca–Sr alloy in comparison to others contains also ~0.3 at.% of zinc. Antimony, calcium and strontium were not found in the primary iQc phase of investigated alloy. Incorporation of only 0.3 at.% Zn and a slight difference in content of aluminium, manganese and silicon in primary iQc is not likely to be the main reason for such differences in the volume fraction of the iQc phase.

It is well known that the cooling rate at the start of solidification can have an effect on the formation of iQc phase. On the other hand, the calculations of the average cooling rate at the start of solidification by one-dimensional transient-heat-conduction analysis showed that for alloys having liquidus temperature difference of 50 °C the cooling rates will differ for only around 20 K/s. This almost negligible difference in average cooling rate due to various liquidus temperatures in alloys suggest that these differences could not be the cause for volume fraction of the iQc phase.

Since the only marked difference between the investigated alloys is much higher volume fraction of iQc in the Al–Mn–Si–Zn–Ca–Sr alloy we further focused on the influence of the solidification rate. Primary solidification of iQc phase is usually followed by reactions where heterogeneous structures (comprising of two, three or more phases) form. In all alloys these structures contain α -Al phase. Solidification rate assessment was based on secondary dendrite arm spacing (SDAS) of α -Al phase (Cho model) and manganese content based on EDS analyses (Ichikawa model).

Cho model

Smaller secondary dendrite arm spacing (SDAS) or the distance between secondary dendrite arms in a specific alloy system indicates that the solidification rate was high [32][42]. The SDAS were measured on dendritic α -Al and results are presented in Table 4.

Table 4. The SDAS measured near the contact surface, in the center and the mean value in μm with corresponding experimental uncertainties

Alloy		Near the contact surface	In the central region	Mean value
Al–Mn–Si	SDAS (μm)	1.3 ± 0.3	4.4 ± 0.7	2.85 ± 0.9
	Sol. rate (K/s)	-	-	200
Al–Mn–Si–Sb	SDAS (μm)	1.3 ± 0.3	4.4 ± 0.6	2.85 ± 0.8
	Sol. rate (K/s)	-	-	200
Al–Mn–Si–Zn–Ca–Sr	SDAS (μm)	1.3 ± 2.5	2.0 ± 0.4	1.65 ± 0.5
	Sol. rate (K/s)	-	-	400



18th INTERNATIONAL FOUNDRYMEN CONFERENCE

Coexistence of material science and sustainable technology in economic growth

Sisak, May 15th-17th, 2019

<http://www.simet.hr/~foundry/>

Results show that the average solidification rate were approximately 200 K/s in Al–Mn–Si and Al–Mn–Si–Sb alloys, where in the Al–Mn–Si–Zn–Ca–Sr alloy average solidification rate was around 400 K/s.

Ichikawa model

An estimated solidification rate has been also verified by evaluating the content of manganese in solid solution of α -Al phase. Beside manganese, also silicon and zinc are soluble in α -Al. Higher solidification rate leads to larger content of soluble elements in solid solution of α -Al. Table 5 represents the concentration of alloying elements in solid solution of α -Al near the contact surface, in the central region of the casting and the mean value.

Table 5. Measured content of manganese, silicon and zinc in α -Al in the central region, near the contact surface and mean value for Al–Mn–Si, Al–Mn–Si–Sb and Al–Mn–Si–Zn–Ca–Sr alloys in at.%

Element	Al–Mn–Si			Al–Mn–Si–Sb			Al–Mn–Si–Zn–Ca–Sr			
	Al	Mn	Si	Al	Mn	Si	Al	Mn	Si	Zn
In the central region	98.7 ± 0.2	1.1 ± 0.1	up to 0.2	99.0 ± 0.2	0.8 ± 0.1	up to 0.2	98.1 ± 0.2	1.2 ± 0.1	up to 0.1	0.7 ± 0.2
Near the contact surface	98.0 ± 0.2	1.8 ± 0.1	up to 0.2	98.0 ± 0.2	1.8 ± 0.1	up to 0.2	97.3 ± 0.2	1.9 ± 0.1	up to 0.2	0.7 ± 0.2
Mean value	98.35 ± 0.2	1.45 ± 0.1	up to 0.2	98.5 ± 0.2	1.3 ± 0.1	up to 0.2	97.65 ± 0.2	1.6 ± 0.1	up to 0.15	0.7 ± 0.2

The average solidification rates, estimated according to Ichikawa et al.[31] yield 200 K/s for the Al–Mn–Si and Al–Mn–Si–Sb alloys and around 300 K/s for the Al–Mn–Si–Zn–Ca–Sr alloy.

These results confirm that the solidification rate is considerably higher in the case of the Al–Mn–Si–Zn–Ca–Sr alloy. Comparison of these solidification rates with previously evaluated based on SDAS shows that solidification rates evaluated on the base of manganese content are similar in the case of Al–Mn–Si and Al–Mn–Si–Sb alloys and lower in the case of Al–Mn–Si–Zn–Ca–Sr alloy. The difference between solidification rates estimated by two evaluation methods in the case of the Al–Mn–Si–Zn–Ca–Sr alloy can be attributed to the fact that beside manganese, also silicon and zinc are soluble in α -Al phase. Presence of additional elements (third and fourth elements) dissolved in α -Al phase decreases the solubility of manganese in comparison to pure binary Al–Mn system and consequently the evaluated solidification rate is lower. Both ternary phase diagrams Al–Mn–Si and Al–Mn–Zn confirm that fact.

Chvorinov's rule

Values used for calculation of solidification time according to Equations 1 and 2 are presented in Table 6. Mean solidification rate can be calculated by dividing the temperature interval of solidification ($T_l - T_s$) and the solidification time t . Table 6 has properties of copper mould and aluminium alloys which can be found in reference books [28]. Heat of solidification, liquidus and solidus temperature and consequently superheat of the alloys were determined by DSC technique at heating and cooling rate of 10 K/min. DSC heating and cooling curves are presented in Figure 4.

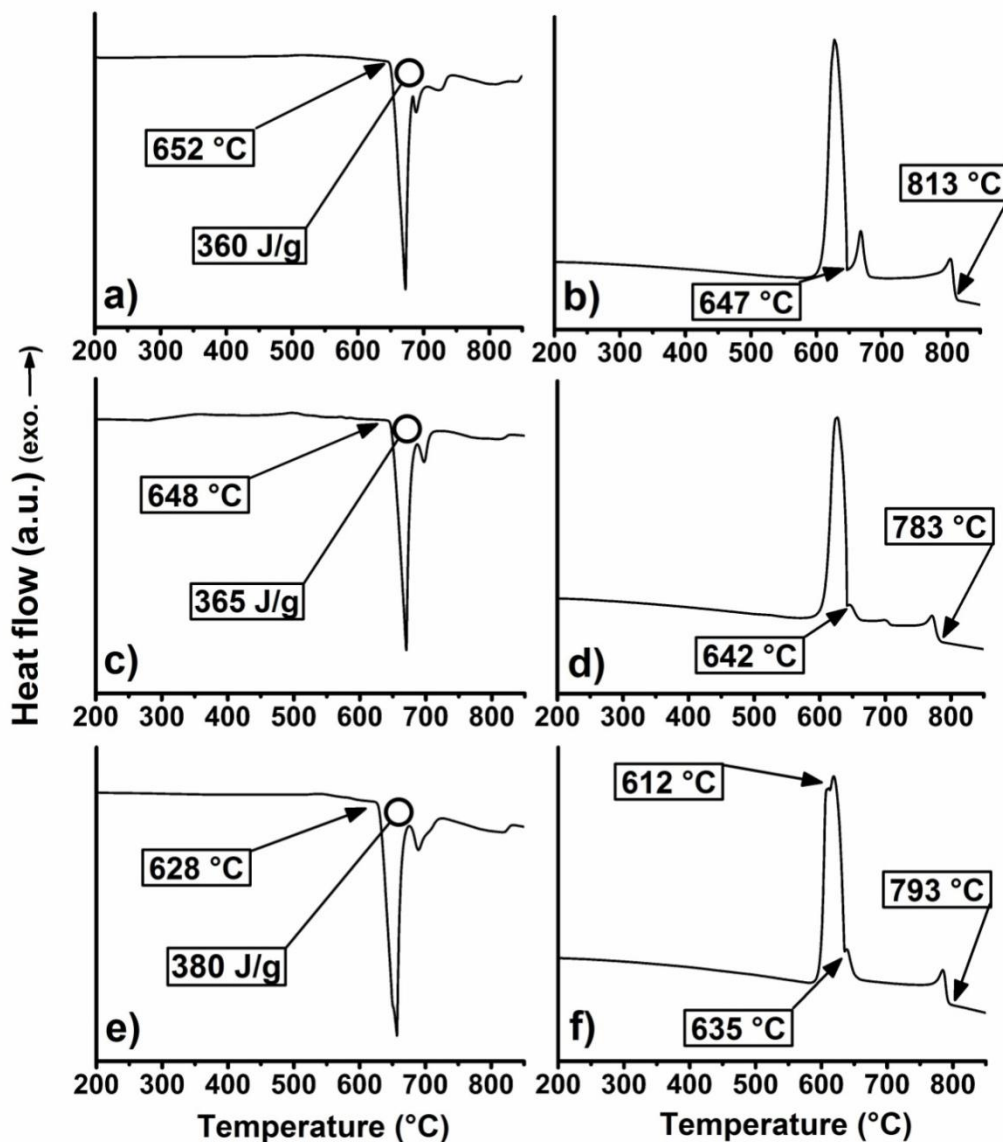


Figure 4. DSC heating and cooling curves of Al-Mn-Si a), b); Al-Mn-Si-Sb c), d); and Al-Mn-Si-Zn-Ca-Sr e), f) alloys



18th INTERNATIONAL FOUNDRYMEN CONFERENCE
**Coexistence of material science and sustainable technology in
economic growth**

Sisak, May 15th-17th, 2019

<http://www.simet.hr/~foundry/>

Solidus and liquidus temperatures for all investigated alloys were determined on a cooling curve while heat of solidification on the heating curve. The reason for using heating curve instead of a cooling curve is that in the case of heating curve present phases are nonequilibrium ones, which would not form in the case of cooling curve.

By using properties presented in Table 6 we can find that time of solidification and mean solidification rate in the case of Al–Mn–Si and Al–Mn–Si–Zn–Ca–Sr alloys are very close having 1.13 s (147 °K/s) and 1.06 s (170 °K/s), while the Al–Mn–Si–Sb alloy yield solidification time 1.64 s and 86 K/s.

Table 6. Parameters used in the calculation of solidification time and average solidification rate by using the Chvorinov's rule

Alloy	Al–Mn–Si	Al–Mn–Si–Sb	Al–Mn–Si–Zn–Ca–Sr
T_l (K)	1086 (813 °C)	1056 (783 °C)	1066 (793 °C)
T_s (K)	920 (647 °C)	915 (642 °C)	885 (612 °C)
ΔT_s (K)	67	97	87
L (J·kg ⁻¹)	360000	365000	380000
k (W·m ⁻¹ ·K ⁻¹)	398	398	398
ρ (kg·m ⁻³)	8960	8960	8960
c (J·kg ⁻¹ ·K ⁻¹)	385	385	385
ρ_m (kg·m ⁻³)	2961	2925	2943
c_m (J·kg ⁻¹ ·K ⁻¹)	1080	1080	1080
A_s/A	0.579355	0.579355	0.579355
V (m ³)	9.8125E-7	9.8125E-7	9.8125E-7

These results are not consistent with the previous findings that a mean solidification rate in the Al–Mn–Si alloy is significantly lower than the one evaluated for Al–Mn–Si–Zn–Ca–Sr alloy. The main reason for the difference is probable connected to the transformation of the iQc phase into crystalline approximant phase, which have higher latent heat. Further modification of Chvorinov's rule is necessary for better prediction of solidification time and mean solidification rate.

It is clear that the alloying elements have an important impact on the solidification rate and consequently on the formation of metastable phases in alloys with similar cooling rate before the onset of solidification.



18th INTERNATIONAL FOUNDRYMEN CONFERENCE

Coexistence of material science and sustainable technology in economic growth

Sisak, May 15th-17th, 2019

<http://www.simet.hr/~foundry/>

CONCLUSIONS

It was found that the Al–Mn–Si–Zn–Ca–Sr alloy contains more primary iQc phase compared to Al–Mn–Si and Al–Mn–Si–Sb alloys. The primary iQc phase in all alloys contains aluminium, manganese and silicon and in the case of Al–Mn–Si–Zn–Ca–Sr alloy also 0.3 at.% of zinc. The average solidification rate by SDAS of α -Al was found to be 200 K/s in the case of Al–Mn–Si and Al–Mn–Si–Sb alloys, while for the Al–Mn–Si–Zn–Ca–Sr alloy was higher being 400 K/s. Assessed cooling rates by the content of manganese dissolved in solid solution of α -Al were found to be similar for the Al–Mn–Si and Al–Mn–Si–Sb alloys with 200 K/s. For the Al–Mn–Si–Zn–Ca–Sr alloy solidification rate was higher with around 300 K/s. Higher solidification rate which was found in Al–Mn–Si–Zn–Ca–Sr alloy can explain the higher content of metastable primary iQc phase in this alloy. The average solidification rate across the whole solidification range determined by a modified Chvorinov's rule was found to be inconsistent with previous findings. Further modification is needed for better matching.

Acknowledgements

The authors would like to thank the Department of Materials and Metallurgy and Center for electron microscopy and microanalysis (CEMM) for all the help in the preparation of samples and the interpretation of results.

REFERENCES

- [1] J.-M. Dubois, Properties-and applications of quasicrystals and complex metallic alloys, Chemical Society Reviews, 41(2012), pp. 6760-6777.
- [2] J.-M. Dubois, Useful Quasicrystals, World Scientific, 2005.
- [3] K. Urban, Complex metallic alloys: fundamentals and applications, John Wiley & Sons, 2010.
- [4] K. Urban, M. Feuerbacher, Structurally complex alloy phases, Journal of non- crystalline solids, 334(2004), pp. 143-150.
- [5] S. Kenzari, D. Bonina, J.M. Dubois, V. Fournée, Complex metallic alloys as new materials for additive manufacturing, Science and technology of advanced materials, 15(2014), pp. 024802.
- [6] R.W. Cahn, P. Haasen, Physical metallurgy. vol. 1, North-Holland, 1996.
- [7] W. Steurer, Twenty years of structure research on quasicrystals. Part I. Pentagonal, octagonal, decagonal and dodecagonal quasicrystals, Zeitschrift für Kristallographie-Crystalline Materials, 219(2004), pp. 391-446.
- [8] W. Steurer, S. Deloudi, Fascinating quasicrystals, Acta Crystallographica Section A: Foundations of Crystallography, 64(2008), pp. 1-11.



18th INTERNATIONAL FOUNDRYMEN CONFERENCE

Coexistence of material science and sustainable technology in
economic growth

Sisak, May 15th-17th, 2019

<http://www.simet.hr/~foundry/>

- [9] W. Steurer, Why are quasicrystals quasiperiodic?, *Chemical Society Reviews*, 41(2012), pp. 6719-6729.
- [10] T. Masumoto, A. Inoue, K. Odera and M. Ogushi, High strength, heat resistant aluminum-based alloys, Patent US 5368658, Nov. 29 (1994).
- [11] K. Kita, Aluminum-based alloy with high strength and heat resistance containing quasicrystals, Patent US5419789, May 30 (1995).
- [12] T. Masumoto, A. Inoue, H. Kimura, Y. Shinodara, K. Kita, High strength aluminum-base alloy, Patent US5593515, Jan. 14 (1997).
- [13] E. Buchler, K. Kita, High-strength and high-ductility aluminum-base alloy, Patent US5900210, May 4 (1999).
- [14] I. Naglic, K. Delijic, Z. Samardzija, F. Bikic, B. Leskovar, B. Markoli, Microstructure and mechanical properties of Al-alloys with quasicrystals, *Proceedings and Book of Abstracts*, (2015), pp. 67.
- [15] A.-P. Tsai, A. Inoue, T. Masumoto, A stable quasicrystal in Al-Cu-Fe system, *Japanese Journal of Applied Physics*, 26(1987), L1505.
- [16] A.-P. Tsai, Discovery of stable icosahedral quasicrystals: Progress in understanding structure and properties, *Chemical Society Reviews*, 42(2013), pp. 5352-5365.
- [17] A.-P. Tsai, A test of Hume-Rothery rules for stable quasicrystals, *Journal of non-crystalline solids*, 334(2004), pp. 317-322.
- [18] A.P. Tsai, Icosahedral clusters, icosahedral order and stability of quasicrystals—a view of metallurgy, *Science and technology of advanced materials*, 9(2008), pp. 013008.
- [19] I. Naglič, Z. Samardžija, K. Delijić, S. Kobe, J.-M. Dubois, B. Leskovar, B. Markoli, Metastable quasicrystals in Al-Mn alloys containing copper, magnesium and silicon, *Journal of Materials Science*, 52(2017), pp. 13657-13668.
- [20] T. Bončina, B. Markoli, F. Zupanič, Characterization of cast Al₈₆Mn₃Be₁₁ alloy, *Journal of microscopy*, 233(2009), pp. 364-371.
- [21] H.-J. Chang, E. Fleury, G. Song, M. Lee, W.-T. Kim, D. Kim, Microstructure modification and quasicrystalline phase formation in Al-Mn-Si-Be cast alloys, *Materials Science and Engineering: A*, 375(2004), pp. 992-997.
- [22] N. Rozman, T. Boncina, I. Anzel, F. Zupanic, The influence of cooling rate on the microstructure of an Al-Mn-Be alloy, *Materiali in tehnologije*, 42(2008), pp. 65-68.
- [23] G. T. De Laissardière, D. Nguyen-Manh, D. Mayou, Electronic structure of complex Hume-Rothery phases and quasicrystals in transition metal aluminides, *Progress in materials science*, 50(2005), pp. 679-788.
- [24] H. Kang, T. Wang, Y. Lu, J. Jie, X. Li, Y. Su, J. Guo, Controllable 3D morphology and growth mechanism of quasicrystalline phase in directionally solidified Al-Mn-Be alloy, *Journal of Materials Research*, 29(2014), pp. 2547-2555.
- [25] U. Mizutani, H. Sato, M. Inukai, Y. Nishino, E.S. Zijlstra, Electrons per atom ratio determination and hume-rothery electron concentration rule for P-based polar compounds studied by FLAPW-Fourier calculations, *Inorganic chemistry*, 54(2014), pp. 930-946.
- [26] H. Axon, W. Hume-Rothery, The lattice spacings of solid solutions of different elements in aluminium, *Proc. R. Soc. Lond. A*, 193(1948), pp. 1-24.



18th INTERNATIONAL FOUNDRYMEN CONFERENCE
**Coexistence of material science and sustainable technology in
economic growth**

Sisak, May 15th-17th, 2019

<http://www.simet.hr/~foundry/>

- [27]R. J. Tilley, Understanding solids: the science of materials, John Wiley & Sons, 2004.
- [28]W. F. Gale, T.C. Totemeier, Smithells metals reference book, Elsevier, 2003.
- [29]F. Gillessen, D. Herlach, Nucleation and formation of quasicrystalline phases in undercooled Al-Mn melts, Materials Science and Engineering: A, 134(1991), pp. 1220-1224.
- [30]L. Battezzati, C. Antonione, F. Marino, Some thermodynamic and kinetic aspects of icosahedral phase nucleation in Al-Mn, Journal of materials science, 24(1989), pp. 2324-2330.
- [31]R. Ichikawa, T. Ohashi, T. Ikeda, Effects of cooling rate and supercooling degree on solidified structures of Al-Mn, Al-Cr and Al-Zr alloys in rapid solidification, Transactions of the Japan Institute of Metals, 12(1971), pp. 280-284.
- [32]J.-I. Cho, C.-W. Kim, The relationship between dendrite arm spacing and cooling rate of Al-Si casting alloys in high pressure die casting, International Journal of Metalcasting, 8(2014), pp. 49-55.
- [33]P. Jelinek, T. Elbel, Chvorinov's rule and determination of coefficient of heat accumulation of moulds with non-quartz base sands, Archives of foundry engineering, 10(2010), pp. 77-82.
- [34]M. Tiryakioglu, E. Tiryakioglu, D. Askeland, Statistical Investigation of the Effects of Shape, Size and Superheat on Solidification Times of Castings, TRANSACTIONS-AMERICAN FOUNDRYMENS SOCIETY, (1998), pp. 907-914.
- [35]F. Zupanic, T. Boncina, N. Rozman, B. Markoli, Morphologies of icosahedral quasicrystals in Al-Mn-Be-(Cu) alloys, (V. Puckermann, E. Beth E. (eds.)), Quasicrystals: types, systems, and techniques, Hauppauge, Nova Science Publishers, New York, 2010, str. 195-217.
- [36]J. L. C. Daams, P. Villars, J. H. N. Vucht, Atlas of Crystal Structure Types for Intermetallic Phases, ASM International, 1991.
- [37]K. Sugiyama, N. Kaji, K. Hiraga, Re-Refinement of $[\alpha]$ -(AlMnSi), Acta Crystallographica Section C, 54(1998), pp. 445-447.
- [38]K. Robinson, The structure of β (AlMnSi)-Mn₃SiAl₉, Acta Crystallographica, 5(1952), pp. 397-403.
- [39]J. Dubois, C. Janot, J. Pannetier, Preliminary diffraction study of icosahedral quasicrystals using isomorphous substitution, Phys. Lett. A, 115(1986), pp. 177-181.
- [40]P. A. Bancel, P. A. Heiney, P. W. Stephens, A. I. Goldman, P. M. Horn, Structure of Rapidly Quenched Al-Mn, Physical Review Letters, 54(1985), pp. 2422-2425.
- [41]D. Naumović, P. Aebi, L. Schlapbach, C. Beeli, K. Kunze, T. A. Lograsso, D. Delaney, Formation of a stable decagonal quasicrystalline Al-Pd-Mn surface layer, Physical review letters, 87(2001), pp. 195506.
- [42]P. Anyalebechi, Effects of alloying elements and solidification conditions on secondary dendrite arm spacing in aluminum alloys, Proceedings of EPD Congress, 2004, pp. 217-233.



18th INTERNATIONAL FOUNDRYMEN CONFERENCE

Coexistence of material science and sustainable technology in
economic growth

Sisak, May 15th-17th, 2019

<http://www.simet.hr/~foundry/>

THERMODYNAMIC DESCRIPTION OF THE TERNARY Ge-Sn-Ag, In, Zn

Milena Premović^{1*}, Duško Minić¹, Dragan Manasijević², Aleksandar Djordjević¹

¹ University of Priština Faculty of Technical Science, Kosovska Mitrovica, Serbia

² University of Belgrade Technical Faculty in Bor, Bor, Serbia

Oral presentation

Original scientific paper

Abstract

This paper presents results of experimental examinations of alloys from ternary Ag-Ge-Sn, Ge-Sn-In and Ge-Sn-Zn systems. Differential thermal analysis (DTA), scanning electron microscope with energy dispersive spectroscopy (SEM-EDS) and x-ray diffraction (XRD) were used for the experimental investigation of the prepared samples. Alloys were from isothermal sections and vertical sections. Based on the experimental results, a thermodynamic description of the ternary Ag-Ge-Sn, Ge-Sn-In and Ge-Sn-Zn systems have been developed by using CALPHAD method. Reasonable agreement between experimental data and the calculated phase diagrams has been reached. The liquid projection and invariant equilibria have been calculated by using obtained thermodynamic parameters.

Keywords: ternary Ag-Ge-Sn system, ternary Ge-Sn-In system, ternary Ge-Sn-Zn system, experimental tests, CALPHAD method

*Corresponding author (e-mail address): milena.premovic@gmail.com

INTRODUCTION

Focus on those alloys are due to the technical importance of the Ge-based alloys [1,2] and their special application as a phase change memory materials (PCM materials) [3-6]. The ternary systems are selected because they have not been tested before. Selected alloys for experimental tests were from three vertical sections and one isothermal section. As-cast samples from three vertical sections were experimentally studied by using differential thermal analysis (DTA). Annealed samples at 200 °C were experimentally studied by using scanning electron microscopy (SEM) with energy dispersive spectrometry (EDS) and X-ray powder diffraction (XRD). Experimentally determined results were used for thermodynamic modeling of the ternary systems. Calculation was done by using Pandat software [7]. Thermodynamic data for all seven sub-binary systems were taken from literature [8-18].



18th INTERNATIONAL FOUNDRYMEN CONFERENCE
Coexistence of material science and sustainable technology in
economic growth

Sisak, May 15th-17th, 2019

<http://www.simet.hr/~foundry/>

MATERIALS AND METHODS

All ternary samples were prepared from high purity elements (99.999 at. %) produced by Alfa Aesar (Germany). Obtained samples were melted and re-melted five times in order to improve homogeneity. The average weight loss of the samples during melting was about 1 mass % and total masses of the ternary alloy samples were about 3 g. After melting, one group of samples were put into quartz ampoules, sealed under vacuum, and placed in a furnace at 200 °C for three weeks. After that, annealed samples were subsequently quenched in the ice water to preserve the equilibrium compositions at the designated temperatures. Such prepared samples were subjected to the SEM-EDS and XRD examinations. Second group as samples were tested with DTG-60H (Shimadzu, China) using alumina crucibles and under flowing nitrogen atmosphere. Sample mass and heating rate were determined by analyzing one sample under different testing conditions and chosen heating rate was 5 °C/min. Samples weights were between 30 and 40 mg and the reference material was the empty alumina crucible. Overall uncertainty of the determined phase transformation temperatures, determined from the repeated measurements, was estimated to be ±1 °C.

RESULTS AND DISCUSSION

Twelve ternary samples per ternary system were analyzed by using DTA. Determination of phase transition temperatures from DTA results (Table 1) were compared with calculated vertical sections. Figure 1, presents comparison of DTA results and calculated vertical sections for ternary Ge-Sn-In system.

Table 1. Experimentally determined phase transition temperatures for the examined Ge-Sn-In alloys

Nominal composition (at.%)	Temperatures of phase transformation (°C)		
	Reaction and transformation		Liquidus
Vertical section Sn-GeIn			
Ge40Sn20In40	60	134	705
Ge30Sn40In30	119	143	671
Ge20Sn60In20	119	203	603
Ge10Sn80In10	87	197	516
Vertical section In-GeSn			
Ge40Sn40In20	115	178	714
Ge30Sn30In40	120		667
Ge20Sn20In60	135		606
Ge10Sn10In80	151		511
Vertical section Ge-InSn			
Ge20Sn40In40	117		592
Ge40Sn30In30	120		695
Ge60Sn20In20	117		787
Ge80Sn10In10	118		859



18th INTERNATIONAL FOUNDRYMEN CONFERENCE
Coexistence of material science and sustainable technology in
economic growth

Sisak, May 15th-17th, 2019

<http://www.simet.hr/~foundry/>

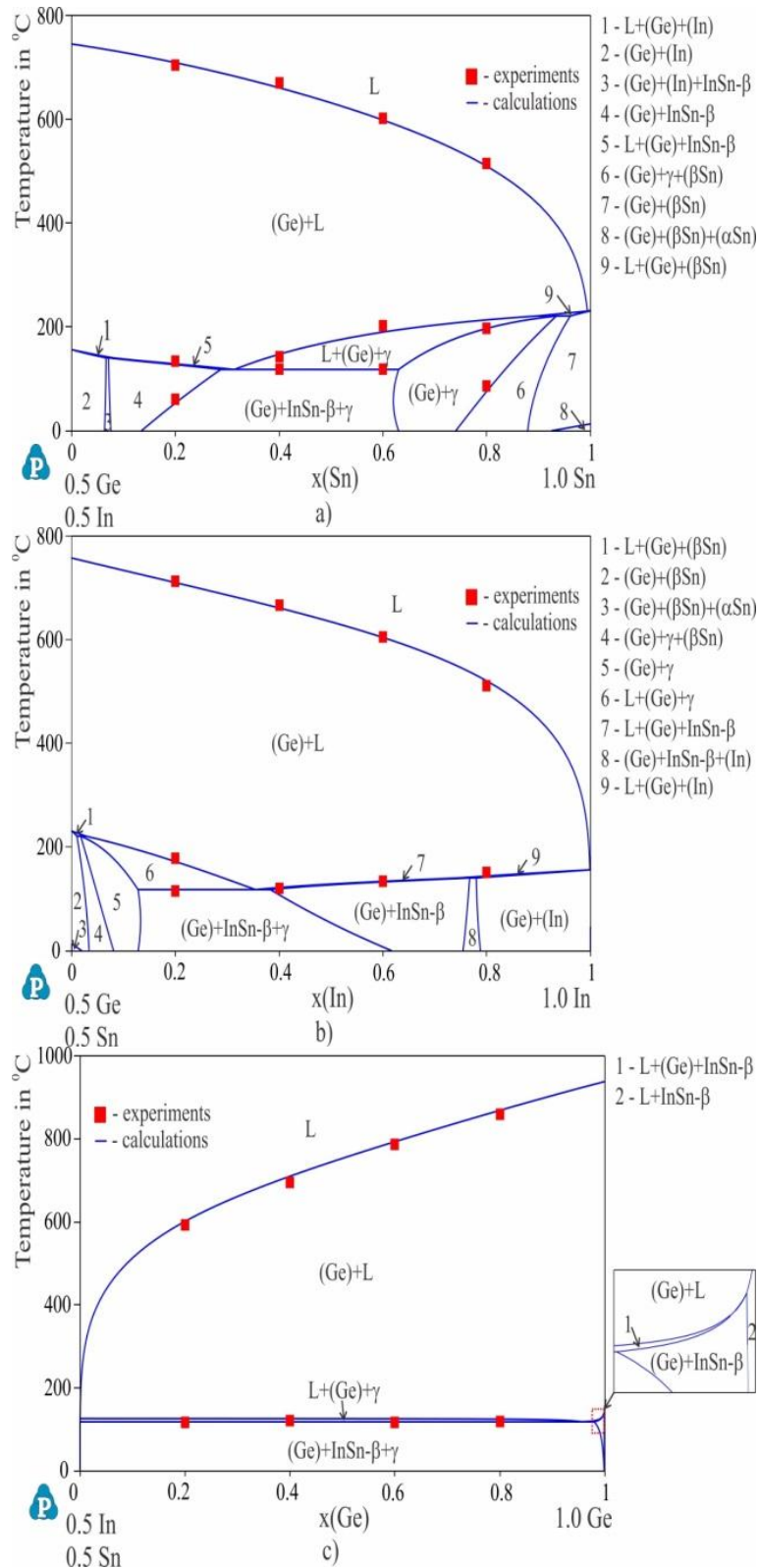


Figure 1. Comparison between experimental DTA results and calculated vertical sections: a) Sn-GeIn, b) In-GeSn and c) Ge-InSn



18th INTERNATIONAL FOUNDRYMEN CONFERENCE
**Coexistence of material science and sustainable technology in
economic growth**

Sisak, May 15th-17th, 2019

<http://www.simet.hr/~foundry/>

From results of calculation and experimental data, good agreement is noticeable. Figure 2, shows comparative review of DTA results (Table 2) and calculated vertical sections of ternary Ge-Sn-Zn system.

Table 2. Experimentally determined phase transition temperatures for the examined Ge-Sn-Zn alloys

Nominal composition (at.%)	Temperatures of phase transformation (°C)		
	Reaction and transformation		Liquidus
Vertical section Zn-GeSn			
Ge40Sn40Zn20	200	283	709
Ge30Sn30Zn40	200	346	628
Ge20Sn20Zn60	204	364	563
Ge10Sn10Zn80	203	374	463
Vertical section Sn-GeZn			
Ge40Sn20Zn40	205	354	703
Ge30Sn30Zn30	197	318	626
Ge20Sn60Zn20	203	265	574
Ge10Sn80Zn10	202		490
Vertical section Ge-ZnSn			
Ge20Sn40Zn40	205	329	606
Ge40Sn30Zn30	195	331	692
Ge60Sn20Zn20	205	324	796
Ge80Sn10Zn10	204	322	856



18th INTERNATIONAL FOUNDRYMEN CONFERENCE
Coexistence of material science and sustainable technology in economic growth

Sisak, May 15th-17th, 2019

<http://www.simet.hr/~foundry/>

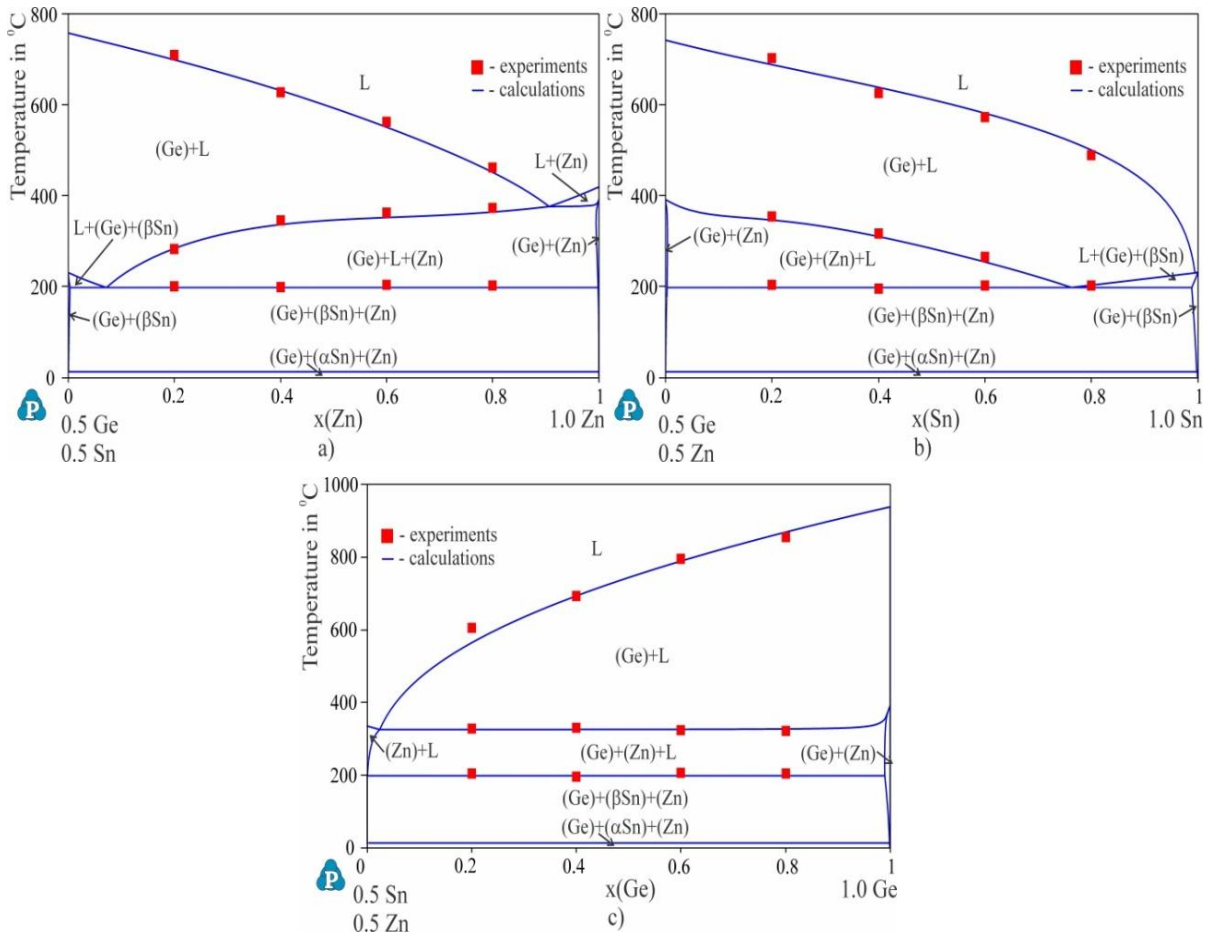


Figure 2. Comparison between experimental DTA results and calculated vertical sections: a) Zn-GeSn, b) Sn-GeZn and c) Ge-ZnSn

Same can be concluded for this ternary system, that agreement of calculation and experiments is satisfactory. Next ternary Ag-Ge-Sn systems results in higher temperature of liquid curve (Table 3) and it was necessary to add new ternary parameters for description of liquid curve.



18th INTERNATIONAL FOUNDRYMEN CONFERENCE
**Coexistence of material science and sustainable technology in
economic growth**

Sisak, May 15th-17th, 2019

<http://www.simet.hr/~foundry/>

Table 3. Experimentally determined phase transition temperatures for the investigated alloys from the ternary Ag-Ge-Sn system

Nominal composition (at.%)	Temperatures of phase transitions (°C)				
	Invariant reaction (DTA)			Other phase transitions	Liquidus
	*(221.11)	** (476.87)	*** (533.72)		
Vertical section Ag-Ge ₅₀ Sn ₅₀					
Ag ₁₀ Ge ₄₅ Sn ₄₅	220.5			359.5	770.5
Ag ₂₀ Ge ₄₀ Sn ₄₀	222.0			417.5	789.0
Ag ₃₀ Ge ₃₅ Sn ₃₅	220.0			455.5	788.0
Ag ₄₀ Ge ₃₀ Sn ₃₀	219.5	481.5		507.0	788.0
Ag ₅₀ Ge ₂₅ Sn ₂₅	221.5	478.5	535.5		771.0
Ag ₆₀ Ge ₂₀ Sn ₂₀	221.5	482.5		590.5	731.0
Ag ₇₀ Ge ₁₅ Sn ₁₅				239.0; 507.0; 565.0; 627.5	642.0
Ag ₈₀ Ge ₁₀ Sn ₁₀				362.0; 642.0	724.0
Ag ₉₀ Ge ₅ Sn ₅				489.0; 714.0	849.5
Vertical section Ge-Ag ₅₀ Sn ₅₀					
Ag ₄₀ Ge ₂₀ Sn ₄₀	222.0	467.0			727.0
Ag ₃₀ Ge ₄₀ Sn ₃₀	219.0	476.5			811.5
Ag ₂₀ Ge ₆₀ Sn ₂₀	222.0	468.0			824.5
Ag ₁₀ Ge ₈₀ Sn ₁₀	221.5	468.5			870.0
Vertical section Sn-Ag ₅₀ Ge ₅₀					
Ag ₄₅ Ge ₄₅ Sn ₁₀				507.0; 521.5; 633.5	822.5
Ag ₄₀ Ge ₄₀ Sn ₂₀	221.5	478.5	537.5		816.5
Ag ₃₅ Ge ₃₅ Sn ₃₀	220.0	482.0			802.0
Ag ₃₀ Ge ₃₀ Sn ₄₀	222.5			444.5	778.5
Ag ₂₅ Ge ₂₅ Sn ₅₀	220.5			429.0	727.0
Ag ₂₀ Ge ₂₀ Sn ₆₀	221.5			394.0	679.5
Ag ₁₅ Ge ₁₅ Sn ₇₀	224.0			353.5	607.0
Ag ₁₀ Ge ₁₀ Sn ₈₀	221.5			313.0	518.5
Ag ₅ Ge ₅ Sn ₉₀	224.5			244.0	454.5

Optimization of the parameters for liquid phase was conducted using the PARROT module based on a least square procedure.

The thermodynamic parameters for liquid phase obtained in this work are:

$${}^0L_{Ag,Ge,Sn}^L = 100403.41 - 76.52 * T \quad (1)$$

$${}^1L_{Ag,Ge,Sn}^L = 15443.03 + 55.13 * T \quad (2)$$

$${}^2L_{Ag,Ge,Sn}^L = 8058.02 \quad (3)$$

By using thermodynamic data for constitutive binary systems and new ternary parameter three vertical sections were calculated in Pandat software and compared with experimental results (Figure 3).

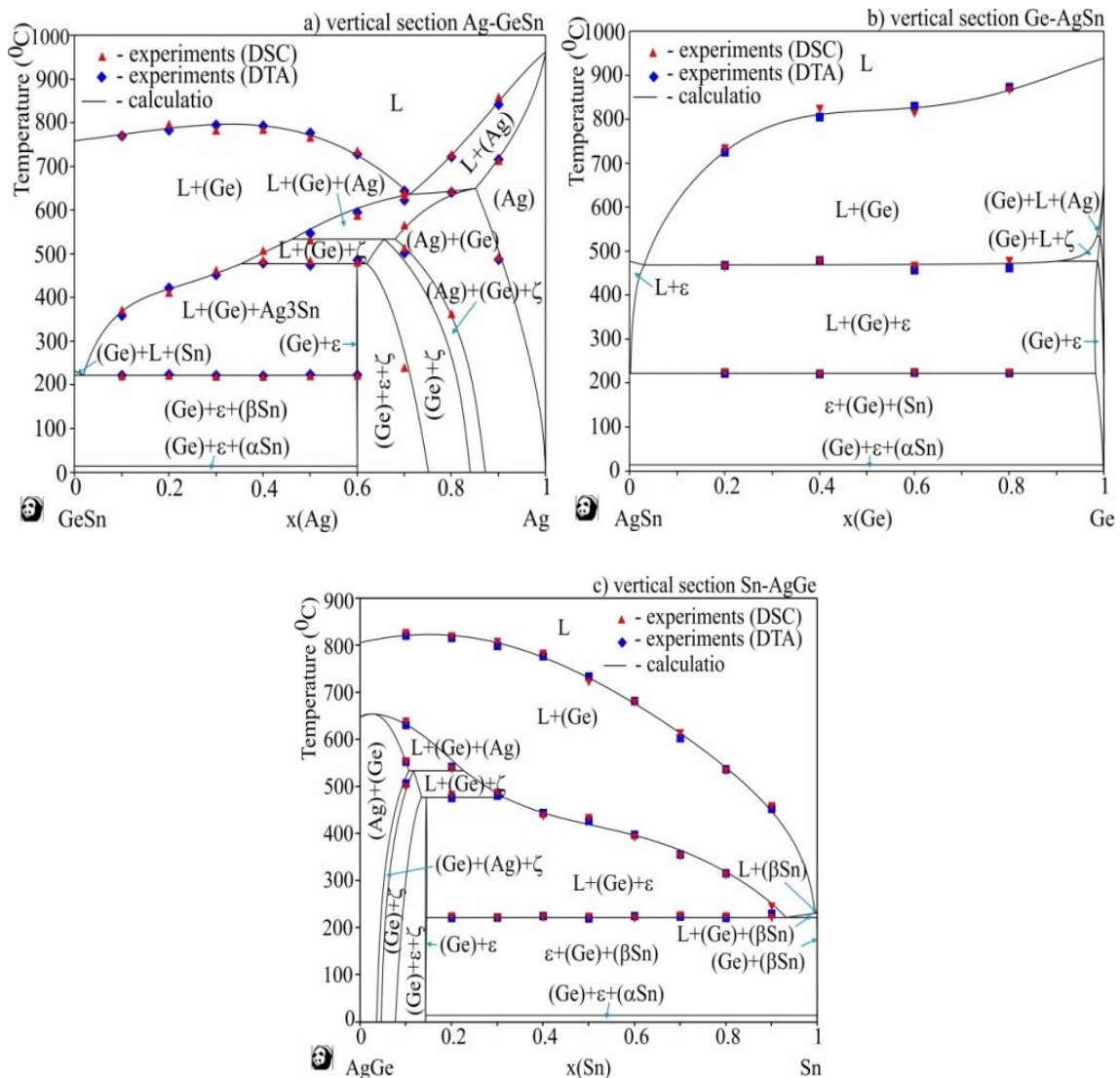


Figure 3. Comparison between experimental DTA results and calculated vertical sections of the Ag-Ge-Sn ternary system: a) Ag-GeSn, b) Ge-AgSn and c) Sn-AgGe

By using thermodynamic data sets for all three ternary systems, EDS results of samples annealed at 200 °C, were compared with calculated isothermal section at 200 °C. Figure 4, shows comparison of results.

Isothermal sections show different phase regions. In all three cases most of them are experimentally confirmed by EDS. EDS composition of phases shows good agreement with calculated composition of the phases and according to this it is not necessary to add new parameters except already defined.

By using proposed thermodynamic set of data three liquids surface are predicted and shown in Figure 5.



18th INTERNATIONAL FOUNDRYMEN CONFERENCE
 Coexistence of material science and sustainable technology in
 economic growth

Sisak, May 15th-17th, 2019

<http://www.simet.hr/~foundry/>

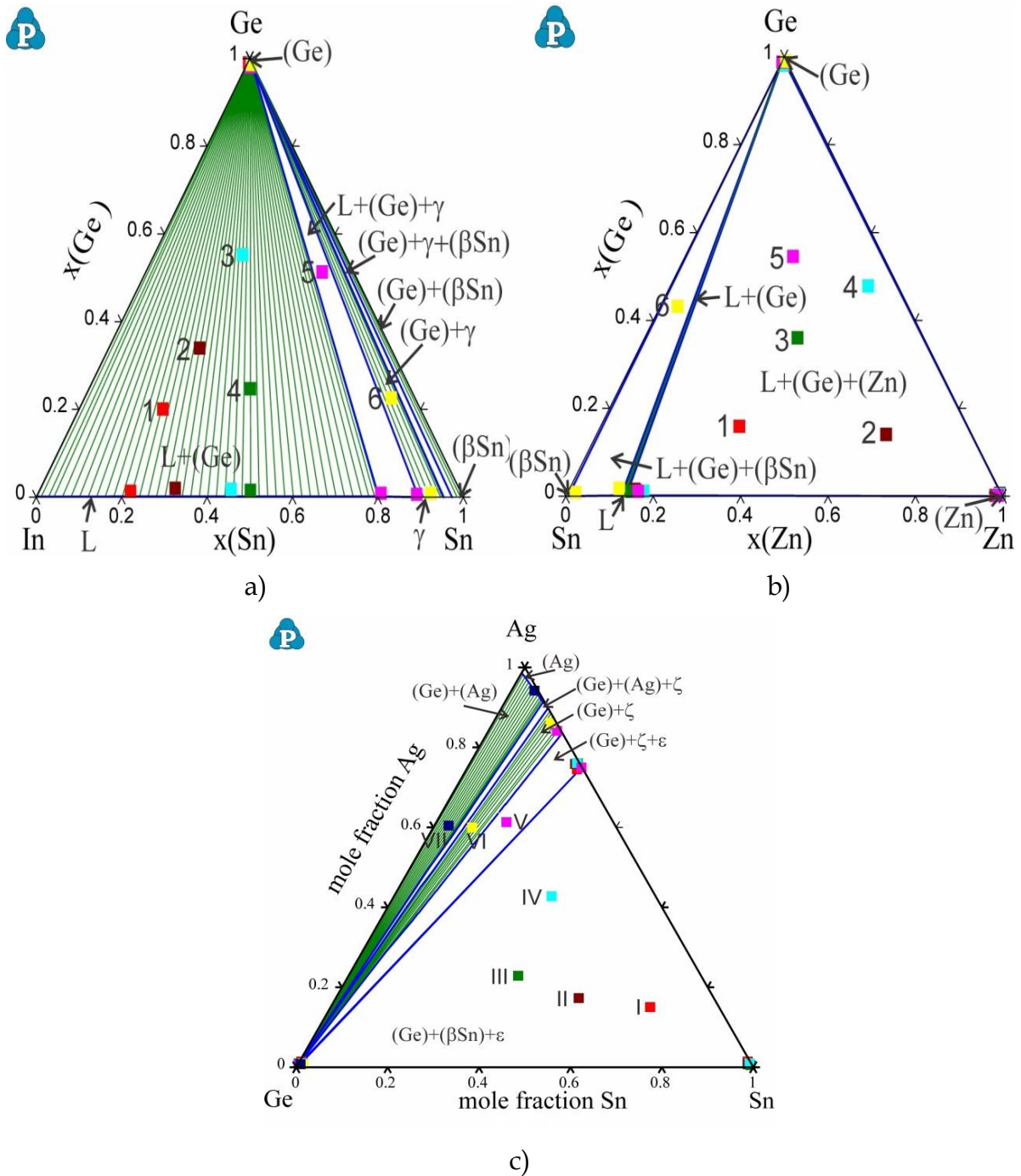


Figure 4. The calculated isothermal section at 200 °C compared with the experimental data
 a) Ge-Sn-In, b) Ge-Sn-Zn and c) Ag-Ge-Sn



18th INTERNATIONAL FOUNDRYMEN CONFERENCE
 Coexistence of material science and sustainable technology in
 economic growth

Sisak, May 15th-17th, 2019

<http://www.simet.hr/~foundry/>

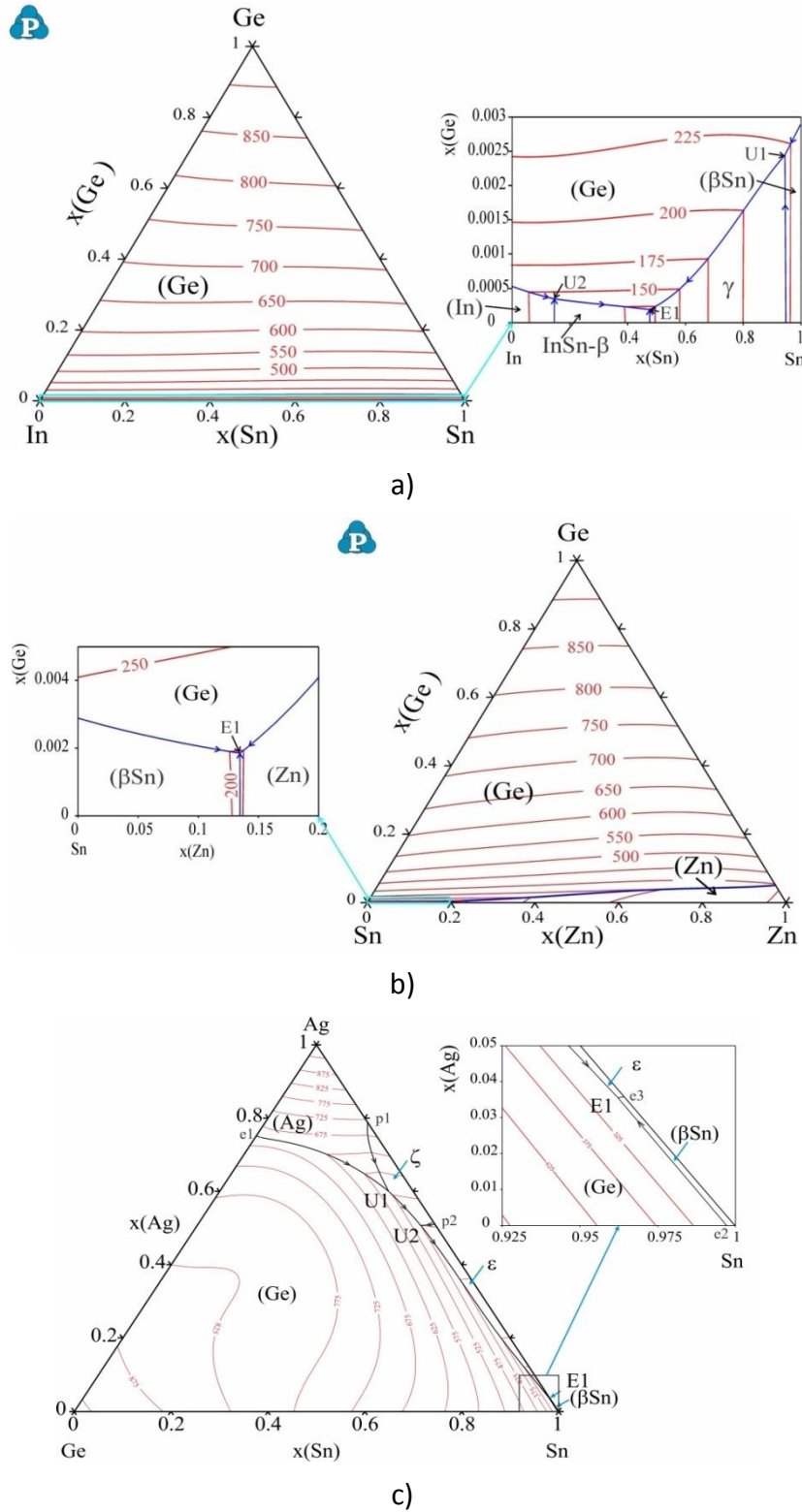


Figure 5. Predicted liquidus projection of the ternary: a) Ge-Sn-In, b) Ge-Sn-Zn and c) Ag-Ge-Sn



18th INTERNATIONAL FOUNDRYMEN CONFERENCE

Coexistence of material science and sustainable technology in economic growth

Sisak, May 15th-17th, 2019

<http://www.simet.hr/~foundry/>

Ternary Ag-Ge-Sn and Ge-Sn-In system each have three invariant reactions while ternary Ge-Sn-Zn system is the simplest one and has only one ternary eutectic reaction.

CONCLUSIONS

Alloys from the ternary Ag-Ge-Sn, Ge-Sn-In and Ge-Sn-Zn systems were investigated experimentally by DTA, SEM-EDS and XRD analysis and modeled by CALPHAD method. Prepared samples for experimental test were from three vertical sections and one isothermal section. Calculated phase diagrams of ternary Ge-Sn-In and Ge-Sn-Zn were in good agreement with experimental results and thermodynamic parameters of binary sub-system were enough for description of those ternary systems. While for description of phase diagrams of the ternary Ag-Ge-Sn system it was necessary to introduce new thermodynamic parameters. By using obtained experiment results of DTA test thermodynamic modeling of the Ag-Ge-Sn system was performed. Based on thermodynamic data for constituent binary systems and assessed ternary parameters for liquid phase, good agreement with calculated phase diagrams and experimental data is reached. This study showed reliable thermodynamic set of data for calculations of phase diagrams for the all three studied ternary systems.

Acknowledgements

This work has been supported by the Ministry of Education, Science and Technological Development of the Republic of Serbia (Grant No. OI172037).

REFERENCES

- [1] N. Agrawal, M. Sarkar, M. Chawda, V. Ganesan, Carrier induced magnetism in dilute Fe doped Ge_{1-x}Sb_x thin films, *Mater. Chem. Phys.*, 143(2013), pp. 330-335.
- [2] Y. Zeng, H. Li, Y. Du, Y. Pan, Y. Peng, P. Zhou, M. Premovic, Experimental investigation of the Co-Ge phase diagram, *J. Phase Equilib. Diffus.*, 38(2017)5, pp. 843-852.
- [3] S. L. Ou, C. P. Cheng, C. Y. Yeh, C. J. Chung, K. S. Kao, R. C. Lin, Characteristics of In-Ge-Sb-Sn-Te thin film used for phase change optical recording media, *Adv. Mater. Res.*, 189-193(2011), pp. 4430-4433.
- [4] D. Ielmini, A. L. Lacaita, Phase change materials in non-volatile storage, *Mater. Today.*, 14(2011)12, pp. 600-607.
- [5] E. M. Vinod, R. Naik, R. Ganesan, K. S. Sangunni, Signatures of Ge₂Sb₂Te₅ film at structural transitions, *J. Non-Cryst. Solids.*, 358(2012), pp. 2927-2930.
- [6] P. Nemeč, V. Nazabal, A. Moreac, J. Gutwirth, L. Benes, M. Frumar, Amorphous and crystallized Ge-Sb-Te thin films deposited by pulsed laser: Local structure using Raman scattering spectroscopy, *Mater. Chem. Phys.*, 136(2012), pp. 935-941.



18th INTERNATIONAL FOUNDRYMEN CONFERENCE

Coexistence of material science and sustainable technology in
economic growth

Sisak, May 15th-17th, 2019

<http://www.simet.hr/~foundry/>

- [7] W. Cao, S. L. Chen, F. Zhang, K. Wu, Y. Yang, Y. A. Chang, R. Schmid-Fetzer, W. A. Oates, PANDAT Software with PanEngine, *Calphad*, 33(2009), pp. 328-342.
- [8] J. Wang, Y. J. Liu, C. Y. Tang, L. B. Liu, H. Y. Zhou, Z. P. Jin, Thermodynamic description of the Au–Ag–Ge ternary system, *Thermochim. Acta.*, 512(2011), pp. 240-246.
- [9] W. Gierlotka, Thermodynamic description of the quaternary Ag–Cu–In–Sn system, *J. Electron. Mater.*, 41(2012)1, pp. 86-108.
- [10] Z. J. Liu, Y. Inohara, Y. Takaku, I. Ohnuma, R. Kainuma, K. Ishida, Z. Moser, W. Gasior, J. Pstrus, Experimental determination and thermodynamic calculation of the phase equilibria and surface tension in the Sn–Ag–In system, *J. Electron. Mater.*, 31(2002) pp. 1139-1151.
- [11] C. Luef, H. Flandorfer, H. Ipster, Lead-free solder materials: experimental enthalpies of mixing in the Ag–Cu–Sn and Cu–Ni–Sn ternary systems, *Z. Metallkd.*, 93(2004) , pp. 151-163.
- [12] X. J. Liu, H. S. Liu, I. Ohnuma, R. Kainuma, K. Ishida, S. Itabashi, K. Kameda, K. Yamaguchi, Experimental determination and thermodynamic calculation of the phase equilibria in the Cu–In–Sn system, *J. Electron. Mater.*, 30(2001)9, pp. 1093-1103.
- [13] Y. Feutelais, B. Legendre, S. G. Fries, Thermodynamic evaluation of the system Germanium–Tin, *Calphad*. 20(1996)1, pp. 109-123.
- [14] P. Y. Chevalier, A thermodynamic evaluation of the Ge–In, Ge–Pb, Ge–Sb, Ge–Tl, and Ge–Zn systems, *Thermochim. Acta*, 155(1989), pp. 227-240.
- [15] B. J. Lee, C. S. Oh, J. H. Shim, Thermodynamic assessments of the Sn–In and Sn–Bi binary systems, *J. Electron. Mater.*, 25(1996), pp. 983-991.
- [16] N. Moelans, K. C. Hari Kumar, P. Wollants, Thermodynamic Optimization of the Lead-Free Solder System Bi–In–Sn–Zn, *J. Alloys Compd.*, 360(2003), pp. 98-106.
- [17] P. Y. Chevalier, A thermodynamic evaluation of the Germanium–Indium, Germanium–Lead, Germanium–Antimony, Germanium–Thallium and Germanium–Zinc systems, *Thermochim. Acta*, 155(1989), pp. 227-240.
- [18] A. T. Dinsdale, A. Watson, A. Kroupa, J. Vrestal, A. Zemanova, J. Vizdal, *Atlas of Phase Diagrams for Lead-Free Soldering*, 1st ed., COST Office, Ed., 2008, Brno, Czech Republic, pp. 133-136 (ISBN 978-80-86292-28-1).



18th INTERNATIONAL FOUNDRYMEN CONFERENCE
**Coexistence of material science and sustainable technology in
economic growth**

Sisak, May 15th-17th, 2019

<http://www.simet.hr/~foundry/>

**EFFECT OF SUBSEQUENT HEATING ON THE MICROSTRUCTURE AND
MECHANICAL PROPERTIES OF Nb MICROALLOYED STEEL**

Ljerka Slokar Benić^{*}, Ivan Jandrić, Stoja Rešković

University of Zagreb Faculty of Metallurgy, Sisak, Croatia

Oral presentation

Original scientific paper

Abstract

Effect of subsequent heating on the microstructure and mechanical properties of hot rolled niobium microalloyed steel was researched in this paper. Low carbon steel was microalloyed with 0.048 % niobium and it was heated at 1150 °C followed by cooling in the air. Researches were performed on two types of samples: low carbon steel microalloyed with niobium and subsequently heated microalloyed steel in the rolling direction as well as in the direction perpendicular to the rolling direction. Mechanical properties of all samples were determined by the static tensile test at testing rate of 5 mm/min. After that their microstructure was observed by scanning electron microscope. Results have shown a significant effect of subsequent heating on the microstructure, i.e. grain size as well as on the mechanical properties.

Keywords: *subsequent heating, niobium microalloyed steel, microstructure, mechanical properties*

*Corresponding author (e-mail address): slokar@simet.hr

INTRODUCTION

The microalloyed steels nowadays are used for wide applications, such as constructions, automotive industry and shipbuilding. They are achieved by means of a suitable combination of chemical composition and thermomechanical treatment parameters. The aim of microalloying of steels is to ensure better mechanical properties and/or resistance to atmospheric corrosion than conventional carbon steels. This enhancement of properties may be achieved by dispersed precipitates that are obtained by addition of niobium, titanium, vanadium or aluminum. Namely, it is known that these elements form stable nitrides, carbides or carbonitrides [1-4]. The phases available in the microstructure of steel are determined by solidification and subsequent processing, such as hot or cold working,



18th INTERNATIONAL FOUNDRYMEN CONFERENCE

Coexistence of material science and sustainable technology in
economic growth

Sisak, May 15th-17th, 2019

<http://www.simet.hr/~foundry/>

heat treatment and solid-state phase transformation as well as by chemical composition [5,6]. In this work niobium has been chosen as microalloying element since it significantly improves the mechanical properties and reduces final ferrite grain size. Refinement of microstructure, in terms of reduced grain size offers possibilities for increasing both strength and ductility [7,8].

MATERIALS AND METHODS

In this work, effect of subsequent heating on the microstructure and mechanical properties of hot rolled niobium microalloyed steel was studied. Chemical composition of studied steel is given in Table 1. It can be seen that low carbon steel was microalloyed with 0.048 % niobium and that 0.008 % of nitrogen is present. Namely, niobium is known as strong carbide and carbonitride forming element. By the formation of niobium carbides or niobium carbonitrides it may be achieved precipitation strengthening, grain refinement and control of transformation temperature. Also, the possible embrittlement caused by nitrogen is minimized in that way [1,4]. Steel of given composition was heated at 1150 °C followed by cooling in the air with purpose to obtain the bigger size of niobium precipitates that effects cold deformation flow and stress distribution in the deformation zone.

Table 1. Chemical composition of studied Nb microalloyed steel

Element	C	Mn	Si	P	S	Al	Nb	N
Wt.%	0.12	0.78	0.18	0.011	0.018	0.02	0.048	0.008

Therefore, investigations were performed on two types of samples: low carbon steel microalloyed with niobium and subsequently heated microalloyed steel. Mechanical properties of all samples were determined by the static tensile test at testing rate of 5 mm/min at room temperature on the universal tensile testing machine Zwick 50kN. Tested samples were of rectangular cross-section taken in the rolling direction and in the direction perpendicular to the rolling direction from hot rolled strips with 3 mm thickness. For microstructural observations, samples were metallographically prepared by standard procedure at Buehler PHENIXBETA GRINDING/POLISHER and etched in nital reagent. After that, their microstructure was observed by scanning electron microscope TESCAN VEGA 5136MM.

RESULTS AND DISCUSSION

Mechanical properties of Nb microalloyed steel were determined by static tensile test at testing rate of 5 mm/min. Figure 1 shows force-elongation diagrams of Nb microalloyed steel tested in the rolling direction (Figure 1a) and in the direction perpendicular to the rolling direction (Figure 1b). It can be seen very similar curves for both test directions. They

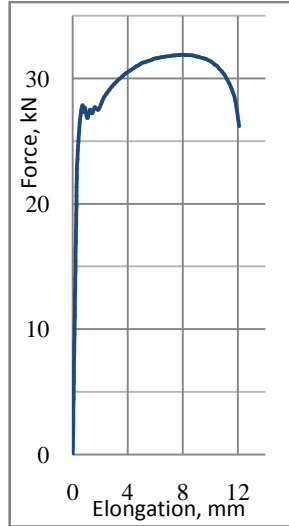


18th INTERNATIONAL FOUNDRYMEN CONFERENCE
**Coexistence of material science and sustainable technology in
economic growth**

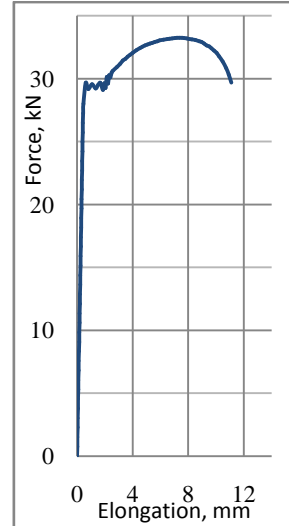
Sisak, May 15th-17th, 2019

<http://www.simet.hr/~foundry/>

show that after reaching the yield stress, values of force decrease and oscillated for one period.



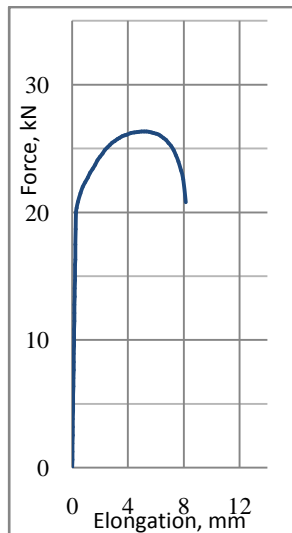
a) tested in the rolling direction



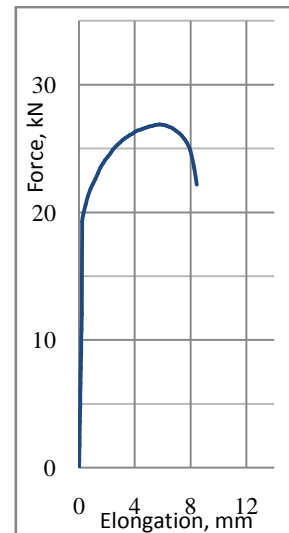
b) tested in the direction perpendicular to
the rolling direction

Figure 1. Force-elongation diagrams of Nb microalloyed steel

Figure 2 shows force-elongation diagrams of heated Nb microalloyed steel tested in the rolling direction (Figure 2a) and in the direction perpendicular to the rolling direction (Figure 2b). It can be seen also very similar curves for both test directions.



a) tested in the rolling direction



b) tested in the direction perpendicular to
the rolling direction

Figure 2. Force-elongation diagrams of heated Nb microalloyed steel



18th INTERNATIONAL FOUNDRYMEN CONFERENCE

Coexistence of material science and sustainable technology in economic growth

Sisak, May 15th-17th, 2019

<http://www.simet.hr/~foundry/>

When comparing Figures 1 and 2, it can be seen that by subsequent heating carried out at 1150 °C steel shows decrease of the yield stress values as well as oscillations of force values.

Results given in Table 2 were obtained from above diagrams (Figure 1). They show very similar data for Nb microalloyed steel in both tested directions. These values are high in comparison with values of conventional carbon steels [1].

Table 2. Mechanical properties of Nb microalloyed steel obtained by static tensile test

Test direction / mechanical property	Yield stress, MPa	YS mean value, MPa	Tensile strength, MPa	TS mean value, MPa	Elongation, %	Mean value of elongation, %
in the rolling direction	515	511	581	583	25.45	26.33
	508		581		27.32	
	509		586		26.22	
in the direction perpendicular to the rolling direction	518	524	583	588	26.35	25.96
	534		595		25.27	
	520		585		26.26	

As well as for the hot rolled but non-heated steel, values of mechanical properties of steel subsequently heated are very similar and relatively high (Table 3).

Table 3. Mechanical properties of heated Nb microalloyed steel obtained by static tensile test

Test direction / mechanical property	Yield stress, MPa	YS mean value, MPa	Tensile strength, MPa	TS mean value, MPa	Elongation, %	Mean value of elongation, %
in the rolling direction	401	404	508	508	19.01	17.96
	411		507		15.87	
	401		508		19.01	
in the direction perpendicular to the rolling direction	400	403	506	513	15.12	15.57
	404		516		15.80	
	404		516		15.80	

In comparison of values of mechanical properties for two types of studied steel (Table 2 and 3), it can be seen that subsequent heating resulted in decreasing of mechanical properties values. Further, heated steel has lost expressed yield point and there was no specific slowdown in the stress zone.

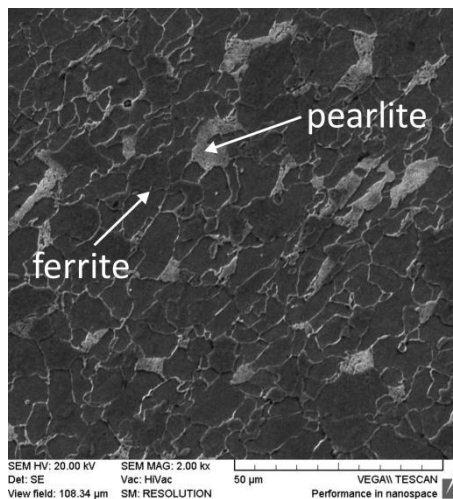


18th INTERNATIONAL FOUNDRYMEN CONFERENCE
**Coexistence of material science and sustainable technology in
economic growth**

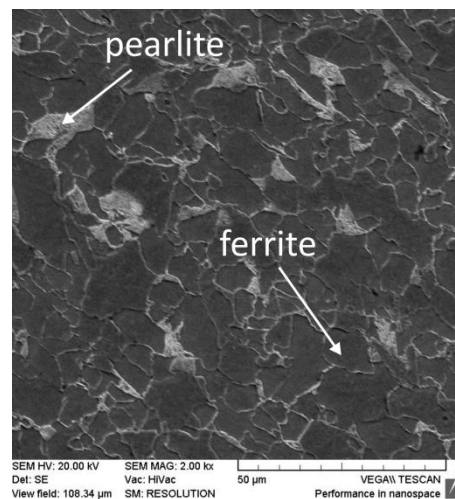
Sisak, May 15th-17th, 2019

<http://www.simet.hr/~foundry/>

The reason for such behavior could be found in the microstructures of studied steel. Namely, Figure 3 shows that microstructure of hot rolled steel microalloyed with 0.048 % niobium in both tested directions consist of polygonal ferrite, characterized by equiaxed and homogenous grains, and coarse lamellar pearlite. The banded ferrite pearlite structure has been commonly observed in hot rolled steels [8]. Formation of these microconstituents, primarily of polygonal ferrite could be attributed to the lowering of the niobium content in solid solution due to the strain-induced precipitation of niobium carbonitrides [9]. The consequence of similar microstructure in tested directions is a very similar mechanical properties showed above.



a) tested in the rolling direction



b) tested in the direction perpendicular to the rolling direction

Figure 3. SEM micrographs of Nb-microalloyed steel, 2000x

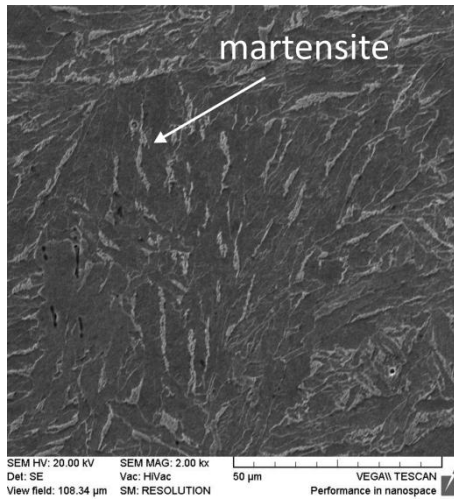
Figure 4 shows that microstructure of hot rolled steel Nb microalloyed subsequently heated at 1150 °C followed by air cooling in both tested directions is martensitic. Grains are coarser than in microstructure of hot rolled non-heated steel. This grain increasing could be attributed to the subsequent heating of hot rolled steel Nb microalloyed. Since there is no clear difference in microstructure observed in the rolling direction and in the direction perpendicular to the rolling direction, there is also negligible difference in mechanical properties values (Table 3).



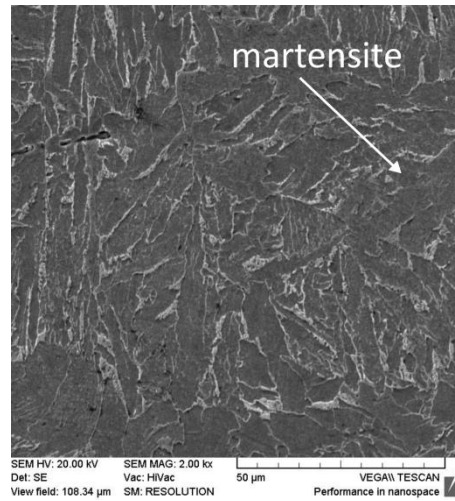
18th INTERNATIONAL FOUNDRYMEN CONFERENCE
**Coexistence of material science and sustainable technology in
economic growth**

Sisak, May 15th-17th, 2019

<http://www.simet.hr/~foundry/>



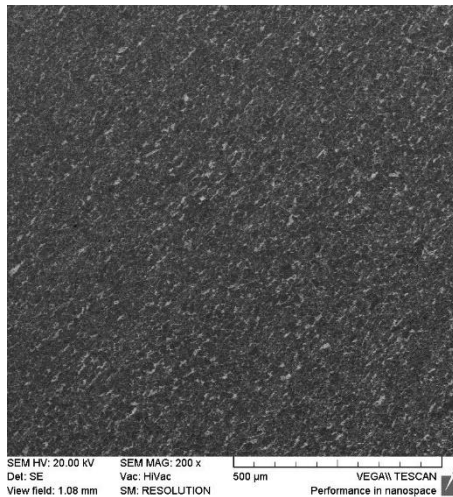
a) tested in the rolling direction



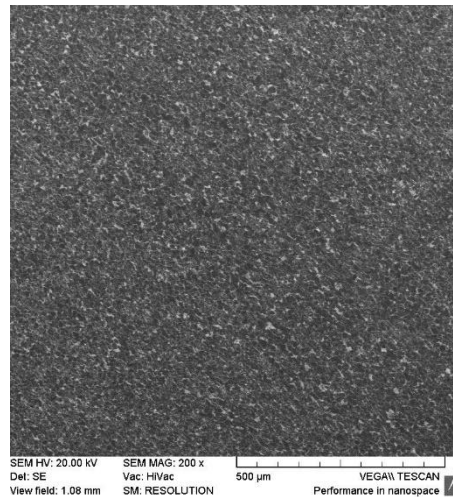
b) tested in the direction perpendicular
to the rolling direction

Figure 4. SEM micrographs of heated Nb-microalloyed steel, 2000x

But microstructural comparison of two types of studied steel shows that above stated loss of emphasize yield stress could be attributed to the increase of grain size after subsequent heating that may be seen in Figs. 5 and 6.



a) tested in the rolling direction



b) tested in the direction perpendicular
to the rolling direction

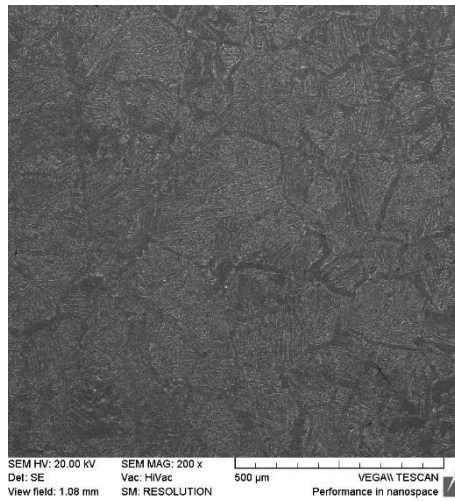
Figure 5. SEM micrographs of Nb-microalloyed steel, 200x



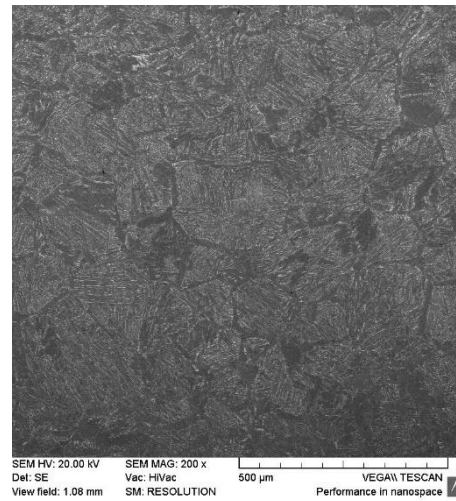
18th INTERNATIONAL FOUNDRYMEN CONFERENCE
**Coexistence of material science and sustainable technology in
economic growth**

Sisak, May 15th-17th, 2019

<http://www.simet.hr/~foundry/>



a) tested in the rolling direction



b) tested in the direction perpendicular
to the rolling direction

Figure 6. SEM micrographs of heated Nb-microalloyed steel, 200x

Microconstituents that are evident in Figure 5 are ferrite and pearlite, while in Figure 6 is martensite visible. That means that again there is no significant difference against the testing direction regarding the microstructure.

CONCLUSIONS

Based on the obtained results it can be concluded as follows:

- Microstructure of hot rolled Nb microalloyed steel is ferritic-pearlit. Microstructure of this steel after heating at 1150 °C followed by cooling in the air is martensitic.
- Microstructure and therefore mechanical properties does not depend on the rolling direction.
- Subsequent heating of Nb microalloyed steel revealed the coarsing of grains and consequently loss of mechanical properties.

Acknowledgements

This work was fully supported by the Croatian Science Foundation under the Project Number IP-2016-06-1270.



18th INTERNATIONAL FOUNDRYMEN CONFERENCE

Coexistence of material science and sustainable technology in economic growth

Sisak, May 15th-17th, 2019

<http://www.simet.hr/~foundry/>

REFERENCES

- [1] D. A. Skobir, High-strength low-alloy (HSLA) steels, *Materials and technology*, 45(2011)4, pp. 295-301.
- [2] I. Jandrić, S. Rešković, T. Brlić, Distribution of stress in deformation zone of niobium microalloyed steel, *Metals and Materials International*, 24(2018), pp. 746-751.
- [3] M. Kalantar, H. Najafi, M.R. Afshar, Comparison between vanadium and niobium effects on the mechanical properties of intercritically heat treated microalloyed cast steels, *Metals and Materials International*, 25(2019), pp. 229.
- [4] B. M. Whitley, J. G. Speer, R. Cryderman, J. Klemm-Toole, Understanding microstructural evolution during rapid heat treatment of microalloyed steels through computational modeling, advanced physical simulation, and multiscale characterization techniques, *Journal of Materials Engineering and Performance*, (2019)3.
- [5] A. R. Subhani, D. K. Mondal, Effect of repeated austenitisation and cooling on the microstructure, hardness and tensile behavior of 0.16 wt% carbon steel, *Archives of Metallurgy and Materials*, 63(2018)3, pp. 1141-1152.
- [6] X. Gan, G. Xu, G. Zhao, M. Zhou, Z. Cai, Composition optimization of Nb-Ti microalloyed high strength steel, *Journal of Wuhan University of Technology*, 33(2018)5, pp. 1193-1197.
- [7] D. Pe´rez Escobar, C. S. Batista Castro, E. Cavichioli Borba, A. P. Oliveira, K. Camey, E. Taiss, A. Costa E Silva, M. Spangler Andrade, Correlation of the solidification path with as-cast microstructure and precipitation of Ti,Nb(C,N) on a high-temperature processed steel, *Metallurgical and Materials Transactions A*, 49(2018)8, pp. 3358-3372.
- [8] C. Gupta, J. Nagchaudhury, J. K. Chakravartty, R. C. Prasad, Cyclic stress–strain characteristics of two microalloyed steels, *Materials Science and Technology*, 25(2009)6, pp. 760-769.
- [9] P. Cizek, Transformation behavior and microstructure of an API X80 linepipe steel subjected to simulated thermomechanical processing, *Proceedings of 10th International Metallurgical and Materials Conference METAL 2001, Tanger, 15.-17.5.2001., Ostrava, Czech Republic*, 1.



18th INTERNATIONAL FOUNDRYMEN CONFERENCE

Coexistence of material science and sustainable technology in
economic growth

Sisak, May 15th-17th, 2019

<http://www.simet.hr/~foundry/>

INFLUENCE OF MEDIUM ON CORROSION AND MICROSTRUCTURAL PROPERTIES OF HTCS-130 TOOL STEEL FOR HOT WORK

Sandra Brajčinović¹, Anita Begić Hadžipašić^{1*}, Jožef Medved², Stjepan Kožuh¹

¹ University of Zagreb Faculty of Metallurgy, Sisak, Croatia

² University of Ljubljana Faculty of Natural Sciences and Engineering, Ljubljana, Slovenia

Poster presentation

Original scientific paper

Abstract

In this paper the corrosion resistance of tool steel for hot work in the industrial emulsion medium (Lenox Band-Ade semi-synthetic oil + water, in ratio 1:10), water and 3.5% NaCl medium was tested. By Tafel's extrapolation from polarization curves it was established that the tested tool steel showed extremely high corrosion rate in water and 3.5% NaCl medium in contrast to medium of Lenox Band-Ade emulsion. The double higher corrosion rate of tool steel is recorded in the chloride medium as opposed to that obtained in water, indicating that the tested steel is more corrosion resistant in water. The obtained results were confirmed by the method of electrochemical impedance spectroscopy. The sample of tool steel in the Lenox Band-Ade emulsion medium showed far greater value of charge transfer resistance R_{ct} than that obtained in the water medium and 3.5% NaCl, which means that the Lenox Band-Ade emulsion formed a thicker oxide layer that has the role of barrier in further penetration of aggressive ions from the solution.

The conducted SEM analysis after electrochemical measurements in 3.5% NaCl medium indicate the occurrence of pitting corrosion caused by breaking the passive surface of the material as a result of the action of aggressive ions from the solution. The EDS analysis of formed pits has been shown the increased oxygen content, but also the higher presence of sodium and chlorine, which accumulate in the pits, and come from the medium. Molybdenum and tungsten showed the highest presence in white deposits on the sample surface, which represent parts that did not completely cover with oxide layer, which is why the smallest oxygen content was recorded at these sites.

The obtained corrosion rate values in the water medium and the chloride medium indicate that the studied tool steel is poorly stable in water and chloride media, and because of that it can only be used in exceptional cases under conditions in which it will come into contact with water or chloride medium.

Keywords: tool steel for hot work, pitting corrosion, corrosion rate, impedance, microstructure

*Corresponding author (e-mail address): begic@simet.hr



18th INTERNATIONAL FOUNDRYMEN CONFERENCE

Coexistence of material science and sustainable technology in
economic growth

Sisak, May 15th-17th, 2019

<http://www.simet.hr/~foundry/>

INTRODUCTION

Tool steels for hot work are designed for tools, which are heated during operation to a temperature higher than 200 °C. In such conditions, this group of tool steels is exposed to sudden temperature changes, high mechanical and impact loads, so extremely good properties are required from tool steels for hot work. The most important property of tool steels for hot work is tempering resistance [1].

Tempering resistance involves the phenomena that may occur during exposure to elevated temperatures, such as hardness reduction, microstructural changes and thermal fatigue. Also high impact strength, good shape and dimension stability, high wear resistance, good tempering resistance, high resistance to thermal fatigue and high-temperature corrosion resistance [2,3] are also required from tool steels for hot work. These properties are achieved by alloying tool steels with alloying elements that create the carbide phases (W, Mo, Cr, V) and with low carbon content.

In addition, by alloying it is trying to achieve the better corrosion resistance of the material. The corrosion resistance is achieved by alloying with chromium, which besides that increases the fire resistance and resistance to hydrogen. Molybdenum in combination with chromium prevents pitting corrosion. Nickel does not produce carbides because it has a low carbon affinity, but it is used in the production of corrosion resistant steels, especially for steels designed to work at elevated temperatures [1,4]. Some properties may be deteriorated by alloying, which is why it is necessary to know relationship and the effect of alloying elements. In addition to the alloying elements, there are elements which are usually combined with carbon in carbides, but they can also be substituted in the iron crystal grid and create undesirable intermetallic compounds, i.e. phases with a structure different from the structure of the starting metals [5].

The tool steel structure depends on the condition of the alloying and on the condition of the thermal processing. The metal base with high carbon content is pearlite, but a share of ferrite may also be present. Also, isolated carbide phases (primary, secondary or tertiary) and eutectic compounds [6,7] are present. For this group of tool steels, it is characteristic that during operation they must be resistant to high temperatures. Namely, machine parts are subjected to continuous heating and cooling of the surface, which is in contact with heated metals. Therefore, tensile stress can occur in tool steels for hot work, resulting in cracks [8]. If the tool steels for hot work are sufficiently tough, cracks spread more slowly and do not penetrate into the depth of the material. Otherwise, because of insufficient toughness, cracks are spreading very rapidly, but their number is also growing intense, so a visible mesh of cracks can be detected on the surface of the tool. In special cases, the depth of the cracks can also cause the breakage of the material [9,10]. The cracking is affected by the chemical composition, microstructure (negative effect has separated ferrite or carbide phases of larger dimensions and sharp shapes), lower hardness values which also contribute to thermal fatigue, tool form and surface roughness, the existence of notches etc. [11].

Tool steels for hot work are mainly intended for making molds (forgings, moldings, die-castings) or for cutting (blades, saws, drills, milling machines etc.). In addition to the above-mentioned requirements expected from this group of steel, it is very important to know the



18th INTERNATIONAL FOUNDRYMEN CONFERENCE

Coexistence of material science and sustainable technology in economic growth

Sisak, May 15th-17th, 2019

<http://www.simet.hr/~foundry/>

influence of medium in which they are exposed. If used in various metal treatments, they are most often exposed to oil and water based emulsions. Also, it is of great importance to explore the additional capabilities of these materials, such as corrosion resistance testing in various media, to which these tool steels could be exposed in practice.

It is generally known that corrosion shortens the service life of the tools, which results in work stoppages and reduced production capacity. Electrochemical corrosion can occur in water, aqueous solutions of acids, alkalis, salts, in the soil, atmospheres, etc. Although the atmosphere is not an electrolyte, the condensate resulting from the metal surface as a result of air humidity leads to the formation of an electrolyte and thus the electrochemical corrosion process starts [12].

Due to the insight into the corrosion behavior of the HTCS-130 tool steel for hot work under the conditions of exposure to the marine atmosphere or in the conditions of contact with sea water, in this paper the influence of 3.5% NaCl on the corrosion and microstructure properties of the tested tool steel was studied and compared with obtained results in water and Lenox Band-Ade emulsion.

MATERIALS AND METHODS

For testing the influence of medium and microstructure on the corrosion resistance of tool steel, a sample of HTCS-130 tool steel for hot work was used, whose chemical composition is shown in Table 1.

Table 1. Chemical composition of tested HTCS-130 tool steel for hot work (mas. %)

C	S	Si	Cr	Ni	V	W	Co	Al	Fe
0.31	0.001	0.07	0.1	0.04	0.01	1.9	0.01	0.012	rest
Cu	Mn	Mo	P	Sn	Ti	Nb	B	N	
0.04	0.08	3.2	0.007	0.005	0.01	0.01	0.001	0.001	

Tool steel HTCS-130 contains low carbon content and tungsten (W) and molybdenum (Mo) are added as alloying elements for purpose of producing the carbides, which favorably affect the properties of tool steels. Tungsten and molybdenum are classified into elements that are the strong carbide makers. Tungsten creates carbides that are resistant to wear and allows the increase of yield strength and tensile strength. Molybdenum also affects the increase of yield strength, tensile strength and creep limit, increases the hardenability and strength of steel, creates carbides and increases the wear resistance of steel [13,14].

Electrochemical testings (E_{corr} , EIS, Tafel)

To obtain data on the corrosion behavior of samples, the method for determining the corrosion potential E_{corr} , electrochemical impedance spectroscopy (EIS) and Tafel's extrapolation method were used. For these measurements, a three-electrode glass cell was



18th INTERNATIONAL FOUNDRYMEN CONFERENCE

Coexistence of material science and sustainable technology in
economic growth

Sisak, May 15th-17th, 2019

<http://www.simet.hr/~foundry/>

used with a working electrode (with surface of 0.5 cm²), a counter electrode and a reference electrode along with the potentiometer and a computer to measure and record the data. The working electrode represents a test sample of tool steel which is immersed in the working medium. The counter electrode is a platinum electrode, which represents a conductor that closes the electric circuit. The reference electrode is an electrode of known potential and does not participate in the electric circuit, but it is used to measure the potential of the working electrode [15,16]. In laboratory conditions as a reference electrode mainly a saturated calomel electrode is used, with a standard electrode potential of +0,242 V with respect to a hydrogen electrode. Potential stabilization at open circuit E_{ocp} was performed at room temperature (19±2) ° C using computer-controlled potentiostat/galvanostat (Parstat 2273). As a working medium in electrochemical experiments, water, 3.5% NaCl medium and industrial emulsion (Lenox Band-Ade semi-synthetic oil + water, in ratio 1:10) were used for simulating working conditions in practice. The measured pH for water was 6.7, and for 3.5% NaCl pH was 6.75. For electrochemical testings, the tool steel sample is cut and pressed in conductive mass by device for hot pressing (SimpliMet® 1000). Before each series of electrochemical measurements the sample was prepared by machine grinding (gradations No. 240, 400, 600 and 800) and polishing (Al₂O₃ suspension in water) on the automatic grinding and polishing machine (Bühler) and then washed in distilled water and degreased in ethanol [15,16].

Determination of corrosion potential E_{corr}

For the tool steel sample, the time corrosion dependence of the corrosion potential was first tested. Prior to the polarization measurement, the metal electrolyte system should be stabilized. The corrosion potential or the open circuit potential is determined in such a way that the current circuit between the working electrode and the counter electrode is kept open and the potential difference between the working electrode and the counter electrode is measured over a period of 1800 seconds. After a certain time, an approximate stationary state at certain potential value is established. Along with the observation of time changes of the stationary potential of the open circuit E_{ocp} , data on the corrosion behavior of the sample in the tested medium are obtained [16].

Determination of corrosion parameters by the method of electrochemical impedance spectroscopy (EIS)

Electrochemical impedance spectroscopy is a method based on the application of alternating current by supplying the electrode with alternating potential of low amplitude (5 mV) and wide range of frequencies (100 kHz - 10 mHz). As the response, the amplitude and the phase shift of the alternating current of the same frequency are followed. The impedance parameters were analyzed by ZSIMPWin 3.21 software using the appropriate electric circuit models [15]. The obtained data are presented graphically in different shapes, and the most commonly used display of the EIS results is Nyquist's diagram.



18th INTERNATIONAL FOUNDRYMEN CONFERENCE

Coexistence of material science and sustainable technology in
economic growth

Sisak, May 15th-17th, 2019

<http://www.simet.hr/~foundry/>

The Nyquist's view of the impedance spectrum represents the dependence of the imaginary impedance component Z_{imag} (Z''), relative to the real component Z_{real} (Z'), for each frequency, and consists of a capacitive and inductive loop. By analysis of results the following values of parameters are obtained: the electrolyte resistance R_{el} , a constant phase element of double-layer Q_{dl} , measure of the surface heterogeneity n and charge transfer resistance R_{ct} [16].

Detremination of corosion parameters by the method of Tafel's extrapolation

Tafel's extrapolation method is performed by means of potentiodynamic polarization in the potential range of -250 mV to +250 mV vs E_{corr} , with the rate of potential change of 1 mV/s, and the corrosion parameters are determined using the software application PowerCorrTM according to Tafel's extrapolation method and the Faraday's law. The electrode is polarized to a certain potential, and then the anode and cathode curves are recorded. By extrapolating the anode and cathode Tafel's linear section of the curves, the values of corrosion current density I_{corr} and corrosion potential E_{corr} are determined. This method provides corrosion parameters (corrosion potential E_{corr} , corrosion rate v_{corr} , anode slope b_a and cathode slope b_c) that give insight into the corrosion behavior of the material in the tested medium [17].

Metallographic analysis

For the purposes of metallographic analysis, the HTCS-130 tool steel sample was prepared by pressing into the conductive mass with a hot pressing device (SimpliMet® 1000). The sample was then grinded by waterproof abrasive paper gradation No. 240, 400, 600 and 800 and polished (Al_2O_3 suspension in water) on the automatic grinding and polishing machine (Bühler), after which it was washed in distilled water and degreased in ethanol. The thus prepared sample was etched by 3% Nital solution (97 ml of ethyl alcohol and 3 ml of nitric acid) to highlight the microstructure.

The sample was observed on an optical microscope with a digital camera (Olympus GX 51) and the Automatic Image Processing System (AnalySIS® Materials Research Lab), followed by a scanning electron microscope (Tescan Vega LSH (TS 5130 LS)) after etching in Nital solution and after corrosion in the investigated media [15,16]. Also, energy dispersion spectroscopy (EDS) was carried out to determine the chemical composition.

RESULTS AND DISCUSSION

After measuring the open circuit potential E_{ocp} , electrochemical impedance spectroscopy at the value of open circuit potential was performed. The time dependences of open circuit potential for the tested tool steel in different media are shown in Figure 1, and Figure 2 shows a comparative view of Nyquist's EIS diagrams obtained for tested tool steel in various media.



18th INTERNATIONAL FOUNDRYMEN CONFERENCE
**Coexistence of material science and sustainable technology in
economic growth**

Sisak, May 15th-17th, 2019

<http://www.simet.hr/~foundry/>

The modeling of the obtained EIS diagrams is derived by the model of the equivalent electric circuit $R(Q(R(QR)))$. The simulated curves were well matched with experimental curves, and the registered deviation was of the order of 10^{-4} . By modeling EIS diagrams the following impedance parameters were obtained: electrolyte resistance R_{el} , the resistance of the oxide layer R_{ox} , a constant phase element of double-layer Q_{dl} , measure of the surface heterogeneity n and charge transfer resistance R_{ct} (Table 2).

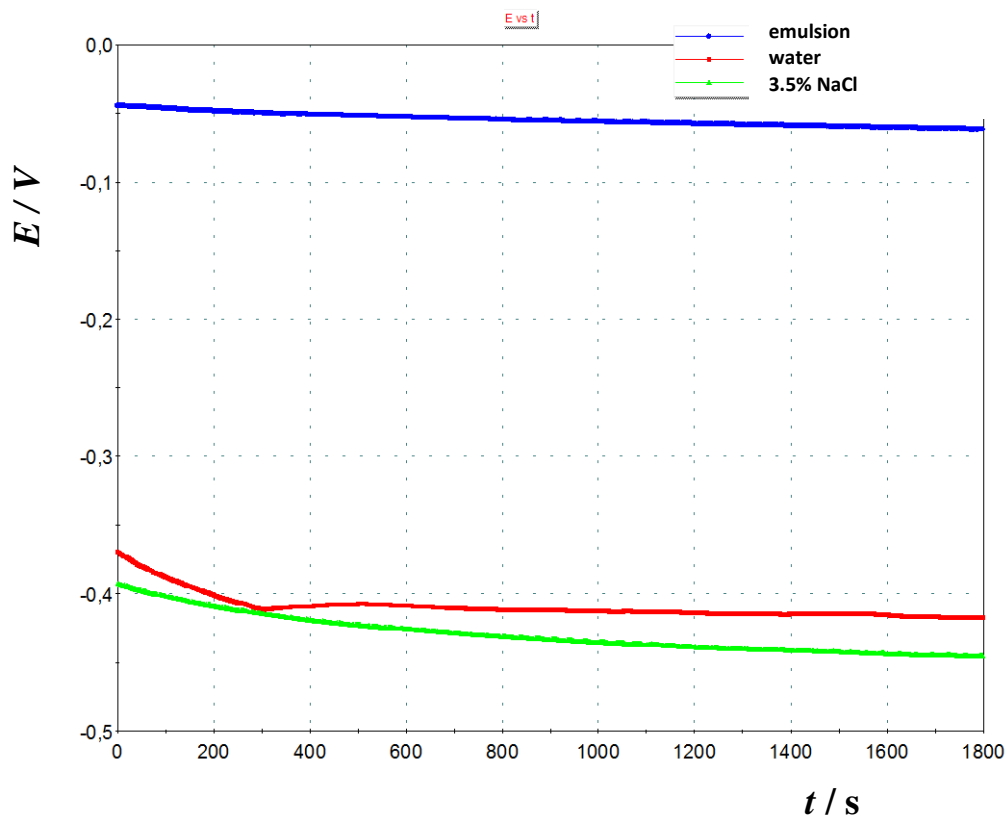


Figure 1. Time dependance of open circuit potential for HCTS-130 tool steel in medium of Lenox Band-Ade emulsion, water and 3.5% NaCl



18th INTERNATIONAL FOUNDRYMEN CONFERENCE
Coexistence of material science and sustainable technology in economic growth

Sisak, May 15th-17th, 2019

<http://www.simet.hr/~foundry/>

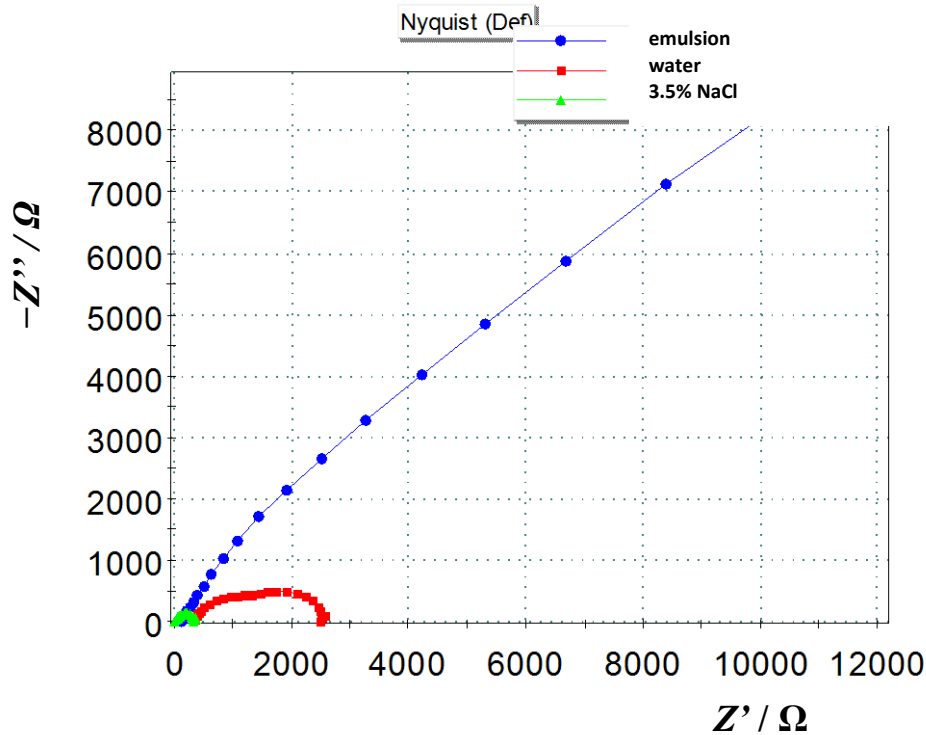


Figure 2. The comparative view of Nyquist's EIS diagrams obtained for HCTS-130 tool steel in medium of Lenox Band-Ade emulsion, water and 3.5% NaCl

Table 2. Impedance parameters of tested HTCS-130 tool steel for hot work

Medium	E_{corr} vs. SCE	R_{el}	$Q_{dl} \times 10^6$	n	R_{ox}	$Q_{dl} \times 10^6$	n	R_{ct}
	mV	Ωcm^2	$\Omega^1 \text{s}^n \text{cm}^{-2}$		Ωcm^2	$\Omega^1 \text{s}^n \text{cm}^{-2}$		Ωcm^2
Lenox Band-Ade emulsion	-61.6	129.4	197.1	0.70	4953.0	185.9	0.40	327000.0
Water	-417.0	343.2	35.4	0.73	1172.0	400.1	0.79	1067.0
3.5% NaCl	-445.0	8.8	1028.0	0.75	20.1	1244.0	0.79	351.1

From Figure 1 it is apparent that the sample tested in the selected media (Lenox Band-Ade emulsion, water, 3.5% NaCl) rapidly achieves its stationary potential, i.e. open circuit potential. In water and medium of 3.5% NaCl, the potentials are shifted to negative values indicating the presence of corrosion or instability of the electrode, so that the sample dissolves. In the Lenox Band-Ade emulsion medium, the potential is shifted to positive values, meaning the electrode is stable. For the stability of the electrodes in the emulsion, the inhibitor contained in the emulsion is partly responsible, because its task is to slow down the corrosion process.



18th INTERNATIONAL FOUNDRYMEN CONFERENCE

Coexistence of material science and sustainable technology in
economic growth

Sisak, May 15th-17th, 2019

<http://www.simet.hr/~foundry/>

From Figure 2 it can be seen that Nyquist's impedance display in the water medium and 3.5% NaCl are actually depression semicircles with a center above the real axis, which is characteristic for solid electrodes. In this respect, the charge transfer resistance R_{ct} and the double-layer capacity C_{dl} are connected parallel in the passive electrode system. The impedance measurements result in a deviation of the mentioned double-layer capacity and instead it a surface-constant phase element of the double-layer Q_{dl} introduces, which represents a combination of surface roughness properties and inhomogeneities of metal electrodes [15,16].

From the data in Table 2, it is apparent that the tool steel in the Lenox Band-Ade emulsion showed a much higher oxide layer resistance R_{ox} and the charge transfer resistance R_{ct} than that in the water medium and 3.5% NaCl. The reason is that in the Lenox Band-Ade emulsion a thicker oxide layer formed on tested sample, which has a protective role, and acts as a barrier to further penetration of the aggressive ions from the solution.

Lower values of charge transfer resistance in the water and 3.5% NaCl indicate that the surface of the formed oxide layer is thinner, and cannot prevent the penetration of aggressive ions from the solution, so the consequence of this is increase in the corrosion rate. Furthermore, from Table 2, it can be seen that the highest value of the surface constant phase element of the double layer Q_{dl} is recorded on the tool steel in the medium of 3.5% NaCl, indicating that the resulting passive layer growing on the surface of the tested tool steel is not enough compact in the chloride medium, due to which the capacity of the intermediate layer metal/oxide layer or inside the passive layer increases [15,16].

The resulting passive layer on the studied tool steel is three times thinner in the chloride medium in comparison with the water medium. The above facts can be explained by the fact that dissolved oxygen and hydrogen cations play an important role in aqueous electrolytes. If the water contains enough O_2 , Fe^{2+} can be oxidized to Fe^{3+} , before Fe^{2+} ions diffuse from the metal surface to the solution. Therefore, a layer of $Fe(OH)_3$ is formed on the surface. However, if sufficient amount of chloride ions entering the formed layer is present, the corrosion rate continues to increase [18].

Results obtained by electrochemical impedance spectroscopy correspond to the parameters resulting from the Tafel's extrapolation method. Potentiodynamic polarization in the range of potentials from -250 mV to +250 mV vs. E_{corr} was performed for the determination of corrosion parameters such as corrosion potential E_{corr} , corrosion rate v_{corr} , anode slope b_a and cathode slope b_c . The polarization curves of the tested tool steel sample in all three tested media are shown in Figure 3, and the obtained corrosion parameters are listed in Table 3.

From Figure 3 it can be seen that as the polarization curve is shifted to the left, the corrosion rate density and thus the corrosion rate will be smaller. Table 3 shows a very small value of corrosion rate registered for tool steel in the Lenox Band-Ade emulsion medium, while in the water and 3.5% NaCl medium a much higher corrosion rate was recorded.



18th INTERNATIONAL FOUNDRYMEN CONFERENCE
Coexistence of material science and sustainable technology in economic growth

Sisak, May 15th-17th, 2019

<http://www.simet.hr/~foundry/>

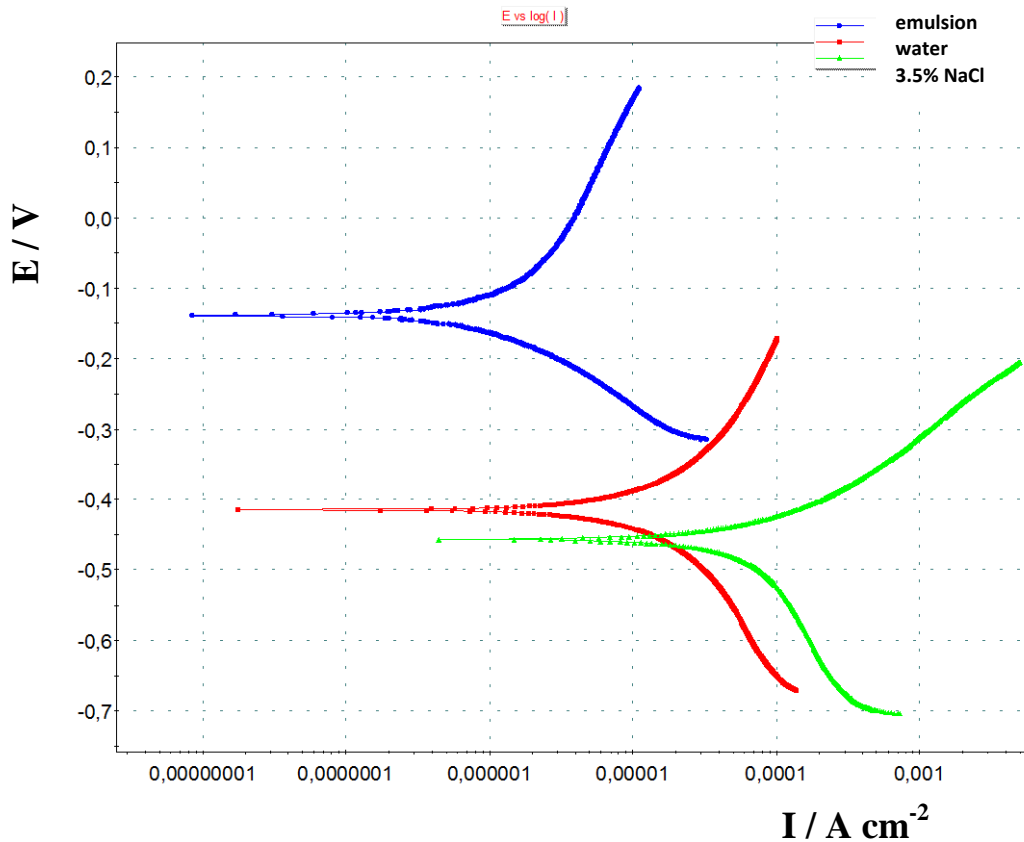


Figure 3. Polarization curves of tested tool steel obtained in medium of Lenox Band-Ade emulsion, water and 3.5% NaCl

Table 3. Corrosion parameters of tested tool steel in medium of Lenox Band-Ade emulsion, water and 3.5% NaCl

Medium	E_{corr} vs. SCE	b_a	b_c	v_{corr}
	mV	mV dec ⁻¹	mV dec ⁻¹	mm god ⁻¹
Lenox Band-Ade emulsion	-138.8	441.2	171.7	0.05
Water	-414.4	664.0	718.0	1.28
3.5% NaCl	-456.2	154.1	629.4	2.79

However, it is important to emphasize that corrosion rate of tested tool steel is more than double higher in the chloride medium, compared to those registered in the water, which points to the fact that investigated tool steel is more corrosion resistant in water, although the pH value for both solutions is approximately the same. It is to be expected, since chloride ions are very aggressive and selectively etches the surface of the material. The Lenox Band-Ade emulsion has the role of cooling liquid in the processing of materials and its primary function is to extend the working life of the tool and reduce the wear of the machine parts, so the obtained corrosion rate was expected. As for the anode and cathode slope, a higher



18th INTERNATIONAL FOUNDRYMEN CONFERENCE
**Coexistence of material science and sustainable technology in
economic growth**

Sisak, May 15th-17th, 2019

<http://www.simet.hr/~foundry/>

value of the anode slope has been obtained in the emulsion medium, indicating that the metal dissolution reaction is more pronounced in this medium. However, since the corrosion potential of the tested tool steel in the emulsion media is shifted to more positive values, this means that the metal dissolution reaction is of very low intensity, which also resulted in less corrosion rates. In water media and chloride media, cathode reactions are more pronounced, as evidenced by the greater number of cathode slopes compared to the anode slope. On the other hand, the corrosion potential of tool steel in water medium and chloride media has been shifted to more negative values, which means that corrosion reaction and dissolution of the tested sample occur.

Based on the obtained values of corrosion rate between 1 and 10 mm/year it can be concluded that the tested tool steel is poorly stable in water and chloride medium, which can be used only in exceptional cases in conditions in which it will come into contact with water or chloride medium [12].

The cause of this corrosion behavior was also studied in the microstructure of the tested tool steel, obtained by etching in Nital (Figure 4).

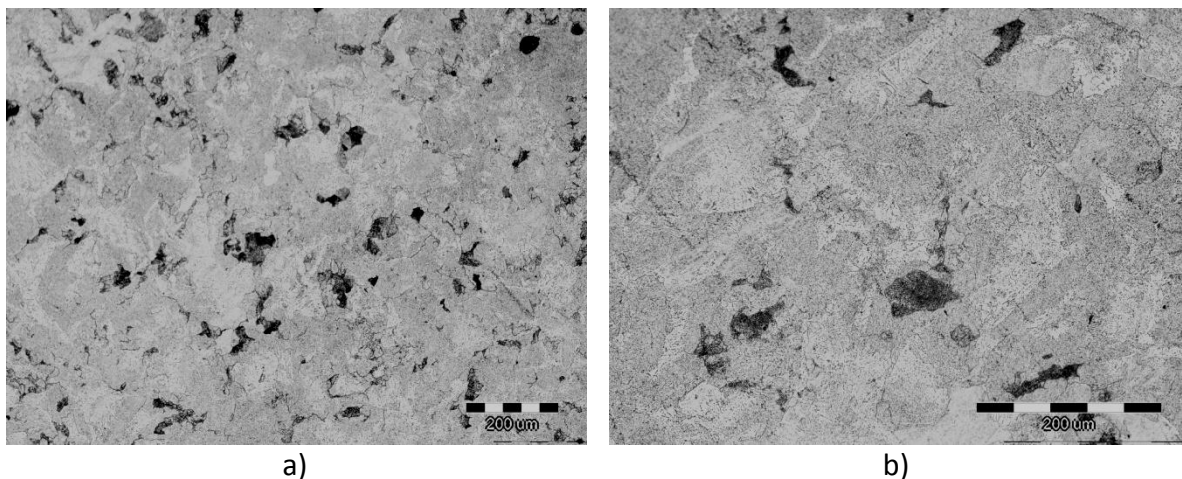


Figure 4. Microstructure of HTCS-130 tool steel for hot work after etching in Nital:
a) magnification 100x and b) magnification 200x

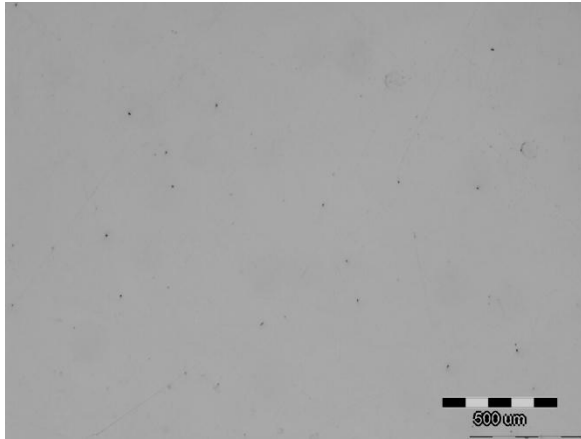
Figure 4 shows that the studied tool steel has a ferrite-pearlite structure. The darker parts of the picture represent pearlite and lighter ferrite. Given the carbon content in the chemical composition, the studied tool steel belongs to the group of hypoeutectoid steel because it contains less than 0.8% C [1]. According to the chemical composition of the tested steel, it can be seen that this is a high quality steel, because the proportion of sulfur and phosphorus is low. Therefore, the surface of the examined tool steel observed "on white" was very pure, with no registered inclusions. For the purpose of observing the microstructural changes of the examined tool steel, the sample was observed using an optical microscope before and after exposure to various media (Figure 5).



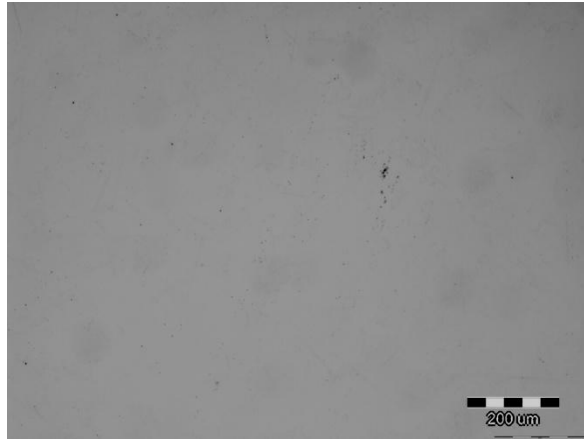
18th INTERNATIONAL FOUNDRYMEN CONFERENCE
**Coexistence of material science and sustainable technology in
economic growth**

Sisak, May 15th-17th, 2019

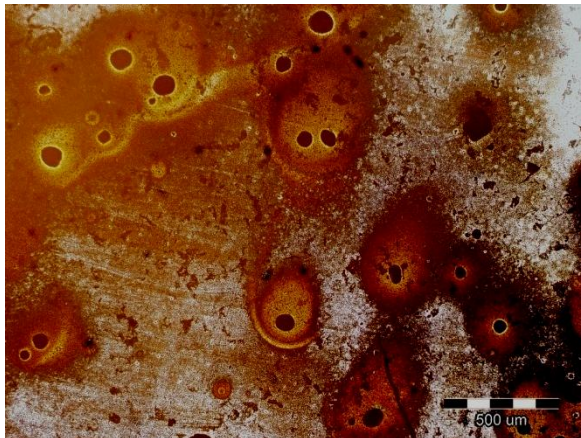
<http://www.simet.hr/~foundry/>



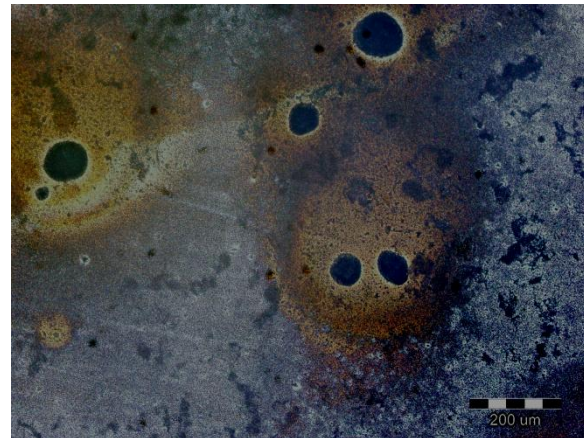
a) emulsion: magnification 50x



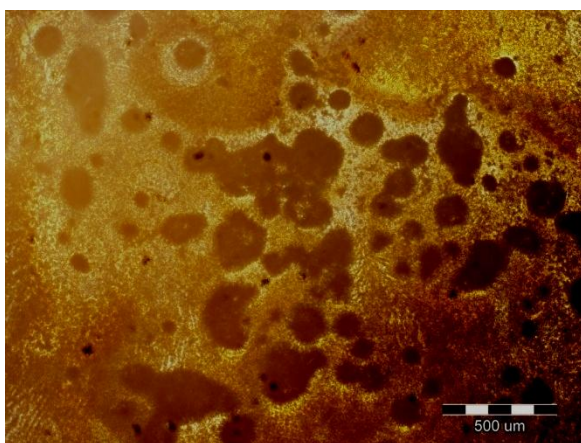
b) emulsion: magnification 100x



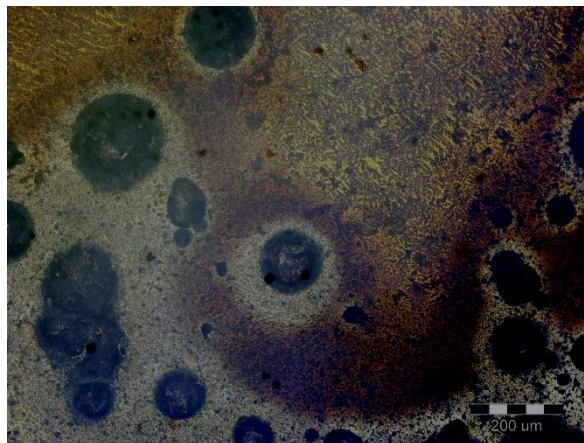
c) water: magnification 50x



d) water: magnification 100x



e) 3.5% NaCl: magnification 50x



f) 3.5% NaCl: magnification 100x

Figure 5. Microstructure of HTCS-130 tool steel for hot work in medium of Lenox Band-Ade emulsion, water and 3.5% NaCl



18th INTERNATIONAL FOUNDRYMEN CONFERENCE

Coexistence of material science and sustainable technology in
economic growth

Sisak, May 15th-17th, 2019

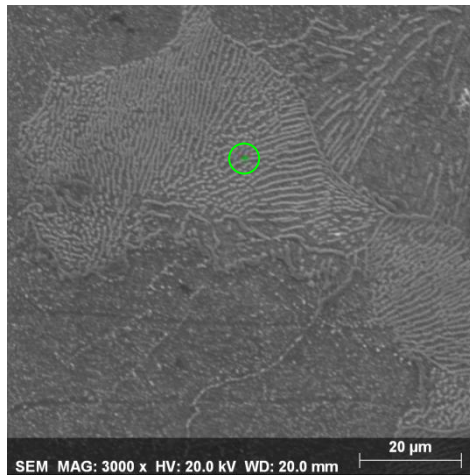
<http://www.simet.hr/~foundry/>

Figure 5 shows that the microstructure of the HTCS-130 tool steel after electrochemical testing in the Lenox Band-Ade emulsion medium remained unchanged. However, in water and 3.5% NaCl, corrosion products were deposited on the surface of the sample, which means that the mentioned media strongly attacked the metal base.

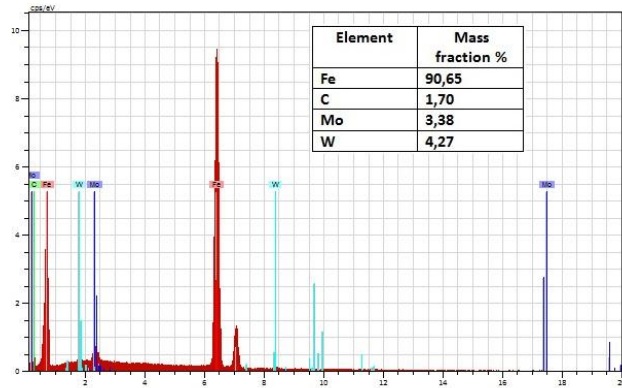
Namely, the corrosion products do not have a protective role in the corrosion process, which can be confirmed by results obtained after electrochemical measurements. It can be concluded that local corrosion takes place, i.e. pitting corrosion, because the occurred holes (pits) are characteristic for pitting corrosion. Generally, the pitting corrosion caused by the existence of large cathode and small anode surfaces, which is why the severity of attack on the anode is large. The potential difference can be caused by mechanical damage, thin coating oxide, acidic media, and corrosion due to salt, holes or cracks [18,19]. In a highly aggressive medium such as 3.5% NaCl, this kind of corrosion occurs at the destruction of the passive layer on the metal surface in the middle of the chloride action. Chloride accumulates in the destroyed pits, which encourages deeper material destruction.

Because of the aggressiveness of chloride ions, from Figure 5 it is apparent that the holes are thicker and larger on the surface of the tested sample, than in the case of water media. Therefore, by combining different alloying elements in tool steels, the aim is to achieve better corrosion resistance. Nickel increases corrosion resistance, and molybdenum with chromium increases the resistance to the occurrence of pitting corrosion. However, the low chromium and nickel content in the investigated tool steel points to the fact that insufficient corrosion resistance is ensured in the tested media.

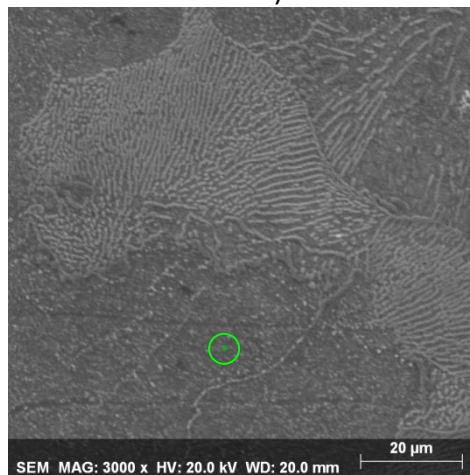
Results of testing the surface condition of the HCTS-130 tool steel conducted by scanning electron microscopy after etching in Nital are shown in Figure 6, and after the electrochemical measurements in a medium of 3.5% NaCl are shown in Figure 7.



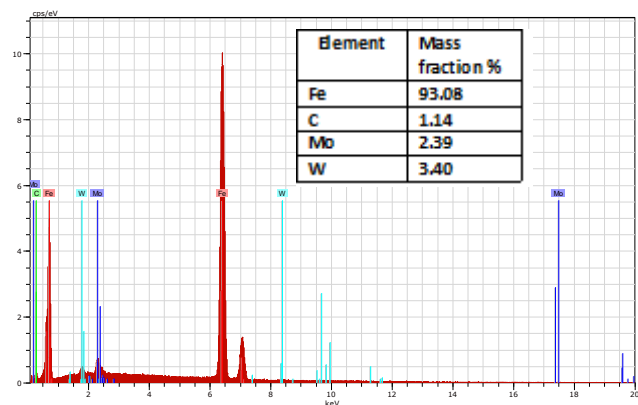
a)



b)



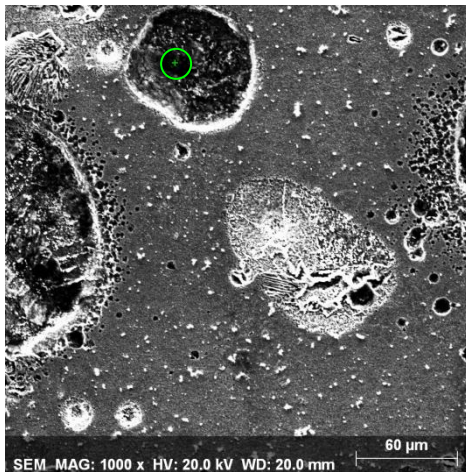
c)



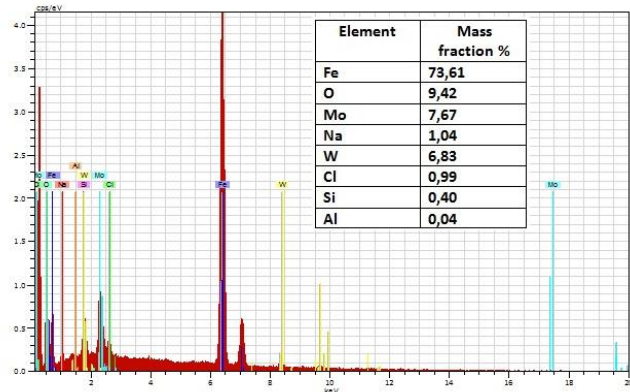
d)

Figure 6. a) c) SEM micrographs of HTCS-130 tool steel surface after etching in Nital (magnification 3000x) and b) d) EDS analyzes

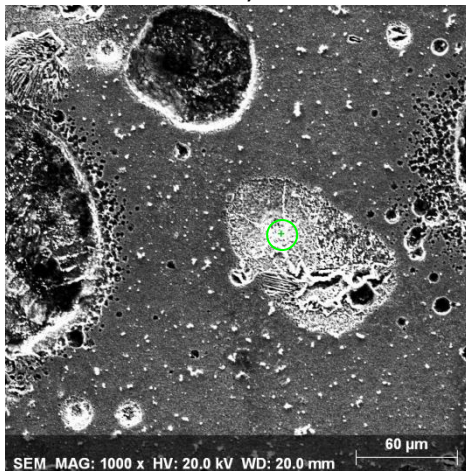
SEM micrographs of the sample after etching in Nital showed the presence of a ferrite-pearlite phase (Figure 6). Pearlite structure is composed of alternately stacked white or matrix base ferrite and cementite thin tiles. The results of the EDS analysis (Figure 6b) indicate the increased content of molybdenum and tungsten, i.e. the presence of their carbides. Namely, molybdenum and tungsten as alloying elements are considered to be strong carbide forming elements, which form Mo_6C and W_6C types of carbides.



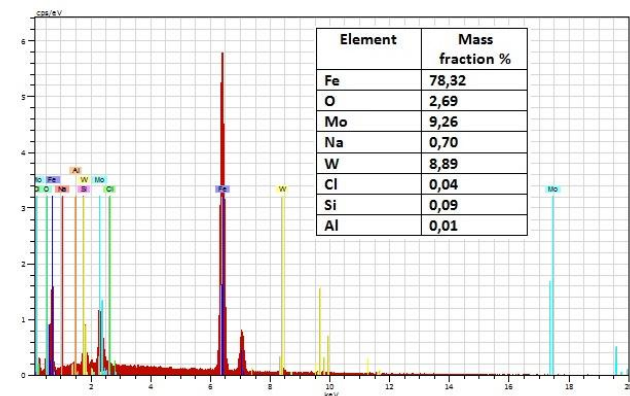
a)



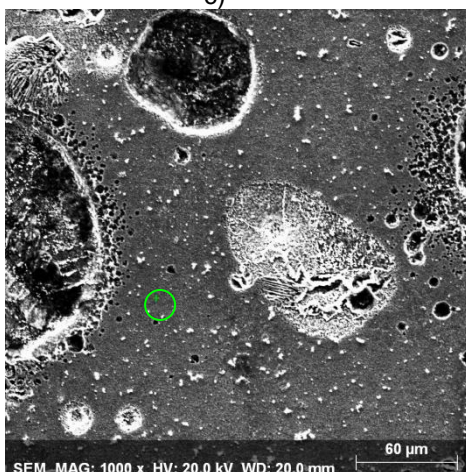
b)



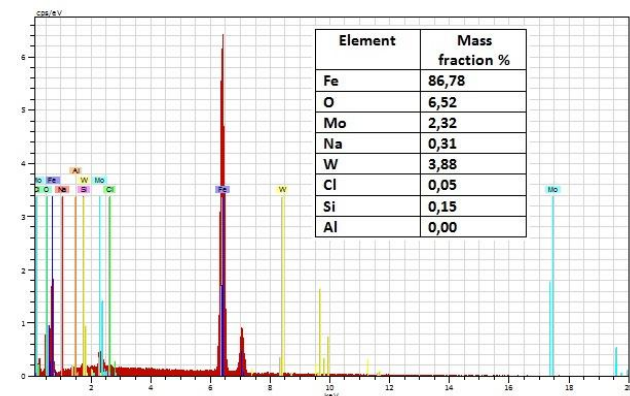
c)



d)



e)



f)

Figure 7. a),c),e) SEM micrographs of HTCS-130 tool steel surface after electrochemical measurements in the medium of 3.5 % NaCl (magnification 1000x) and b),d),f) EDS analyzes



18th INTERNATIONAL FOUNDRYMEN CONFERENCE

Coexistence of material science and sustainable technology in
economic growth

Sisak, May 15th-17th, 2019

<http://www.simet.hr/~foundry/>

The SEM images in Figure 7 show pitting corrosion or local corrosion caused by the breaking of the passive metal surface and can be identified by the large black holes/pits formed on the sample. The breaking of the passive layer was most likely due to the presence of chloride ions, and the additional factors that might have contributed to it were: the difference in the amount of oxygen, the pH value, the flow rate and the physical and chemical inhomogeneity of the passive layer.

The chemical composition determined by EDS analysis after electrochemical testing in the medium of 3.5% NaCl shows the elevated oxygen content at the metal base (Figure 7e), indicating that the sample is covered with an oxide layer. However, the oxide layer is not compact but is filled with black holes/pits, in which is also the oxygen content increased, but there is a higher presence of sodium, chlorine, molybdenum and tungsten inside the pits, than outside the pits. Chlorine and sodium come from the tested medium and it is logical that they accumulate more in the pits than on the sample surface.

Molybdenum and tungsten showed the highest presence on white deposits on the sample surface, which represent parts that did not completely cover by the oxide layer, which is the reason why the smallest oxygen content was recorded at these sites. Because of the low chromium content in the chemical composition of the tested steel, creating a passive layer on the surface was not entirely possible, i.e. no insoluble surface layer was created that would prevent further oxygen diffusion on the surface and thus prevent oxidation of the iron in the material matrix.

CONCLUSIONS

1. By the electrochemical measurements corrosion resistance of HTCS-130 tool steel for hot work of in medium of Lenox Band-Ade emulsion, water and 3.5% NaCl was investigated.
2. The potentiodynamic polarization of the tool steel in the Lenox Band-Ade emulsion medium has resulted in a low corrosion rate relative to the water medium and 3.5% NaCl, where the corrosion rate was significantly higher. The Lenox Band-Ade emulsion has the role of coolant in the processing of materials and its primary function is to extend the service life of the tool and reduce the wear of machine parts, therefore the obtained corrosion rate was expected.
3. In the chloride medium there is more than double higher the value of corrosion rate registered in tool steel than that obtained in the water, indicating that the tested steel is more corrosion resistant in water, although the pH value for both solutions is approximately the same. The cause of this behavior is aggressive chloride ions that destroy the newly formed oxide layer and reduce its protective role in the fight against corrosion.
4. From the impedance parameters obtained by modeling the EIS spectrum, a much higher value of charge transfer resistance R_{ct} was noted in the Lenox Band-Ade emulsion medium than that in the water medium and 3.5% NaCl, which means that a thicker oxide layer formed that acts as a barrier and prevents further penetration of



18th INTERNATIONAL FOUNDRYMEN CONFERENCE

Coexistence of material science and sustainable technology in
economic growth

Sisak, May 15th-17th, 2019

<http://www.simet.hr/~foundry/>

potential aggressive ions from the solution. Conversely, the lower charge transfer resistance recorded in the chloride medium indicates the formation of a thin oxide layer on the tool steel, which cannot be further expanded and strengthened due to the aggressive action of chloride ions.

5. SEM micrographs of the sample after etching in Nital showed the presence of ferrite-pearlite phase. Pearlite structure is composed of alternately stacked white or matrix base ferrite and cementite thin tiles. EDS analysis showed an elevated content of molybdenum and tungsten, i.e. the presence of their carbides.
6. The metallographic analysis of the tool steel exposed to the Lenox Band-Ad emulsion medium showed no microstructural changes. However, corrosion products on the surface of the tested tool steel were observed in the medium of water and chloride media. The resulting corrosion products suggest that iron oxidation has occurred in the material matrix, which is why an elevated oxygen content is registered.
7. SEM analysis of tool steel exposed to the chloride medium has shown a bigger distribution of pitting corrosion rather than in a water medium attributed to the presence of chloride ions, which lead to the destruction of the passive layer on the metal surface and the formation of pits. EDS analysis of pits characteristic for the appearance of pitting corrosion has been shown the increased content of oxygen, but also the higher presence of sodium and chlorine, which accumulate in the pits, and result from the tested medium. Molybdenum and tungsten showed the highest presence on white deposits on the sample surface, which represent parts that did not completely cover by the oxide layer, which is the reason why the smallest oxygen content was recorded at these sites.
8. The obtained values of corrosion rate in the water and 3.5% NaCl medium indicate to the fact that the investigated tool steel for hot work is poorly stable in water and chloride medium, and it can be used only in exceptional cases in conditions in which it will come into contact with water or chloride medium.

Acknowledgements

Investigations were performed within the research topic "Design and Characterization of Innovative Engineering Alloys", Code: TP167 funded by University of Zagreb within the Framework of Financial Support of Research, scientific-research project within Croatian-Slovenian collaboration "Design and Characterization of Innovative Aluminum - Magnesium - Lithium alloy (2018-2019) funded by Ministry of Science and Education and infrastructural scientific project: Center for Foundry Technology, Code: KK.01.1.1.02.0020 funded by European Regional Development Fund, Operational programme Competitiveness and cohesion 2014 - 2020.



18th INTERNATIONAL FOUNDRYMEN CONFERENCE

Coexistence of material science and sustainable technology in
economic growth

Sisak, May 15th-17th, 2019

<http://www.simet.hr/~foundry/>

REFERENCES

- [1] G. Roberts, G. Krauss, R. Kennedy, Tool Steels, 5th ed., ASM International, Materials Park, 1998.
- [2] M. Novosel, F. Cajner, D. Krumes, Alatni materijali, Strojarski fakultet u Slavonskom Brodu, Slavonski Brod, 1996.
- [3] W. E. Bryson, Heat treatment, selection and application of tool steels, 2nd Edition, Hanser Publications, Cincinnati, 2013.
- [4] S. J. Huang, Tribological properties of the low-carbon steels with different micro-structure processed by heat treatment and severe plastic deformation, Wear, 271(2011), pp. 705-711.
- [5] S. Kožuh, Specijalni čelici, Skripta, Sveučilište u Zagrebu, Metalurški fakultet, Sisak, 2010.
- [6] A. F. Rousseau, Metallurgical characterization and performance of high speed steel tool materials used in metal cutting applications, School of Applied Sciences College of Science, Engineering and Health, RMIT University, Melbourne, 2016.
- [7] J. Szumera, The tool steel guide, Industrial Press Inc., New York, 2013.
- [8] R. W. Staehle, Engineering with advanced and new materials, Materials Science and Engineering: A, 198(1995)1-2, pp. 245-256.
- [9] D. J. Young, High temperature oxidation and corrosion of metals, School of Materials Science and Engineering, University of New South Wales, Sydney, 2016.
- [10] N. Birks, G. H. Meier, F. S. Pettit, Introduction to the high-temperature oxidation of metals, 2nd Edition, University of Pittsburgh, Cambridge, 2006.
- [11] C. R. Sohar, Lifetime controlling defects in tool steels, Doctoral Thesis, Vienna University of Technology, Austria, 2011.
- [12] V. Alar, Kemijska postojanost metala, Sveučilište u Zagrebu, Fakultet strojarstva i brodogradnje, Zagreb, 2015.
- [13] T. Kostadin, Čelici i željezni ljevovi, Materijali II, Interna skripta, Veleučilište u Karlovcu, Karlovac, 2017.
- [14] H. Kim, J. Kang, D. Son, T. Lee, K. Cho, Evolution of carbides in cold-work tool steels, Materials Characterization, 107(2015), pp. 376-385.
- [15] S. Mitić, A. Begić Hadžipašić, G. Gojsević Marić, Z. Zovko Brodarac, Utjecaj medija i mikrostrukture na korozijsko ponašanje nodularnog lijeva, Proceedings of 16th International Foundrymen Conference, (ur.: Z. Zovko Brodarac, N. Dolić, A. Begić Hadžipašić), University of Zagreb Faculty of Metallurgy, 15-17.5.2017, Opatija, Croatia, pp. 173-188.
- [16] A. Begić Hadžipašić, S. Brajčinović, G. Gojsević Marić, Z. Zovko Brodarac, Utjecaj medija i mikrostrukture na korozijsko ponašanje sivog lijeva, Proceedings of 17th International Foundrymen Conference, (ur.: N. Dolić, Z. Zovko Brodarac, A. Begić Hadžipašić), University of Zagreb Faculty of Metallurgy, 16-18.5.2018, Opatija, Croatia, pp. 98-112.
- [17] E. Stupnišek-Lisac, Korozija i zaštita konstrukcijskih materijala, Sveučilište u Zagrebu Fakultet kemijskog inženjerstva i tehnologije, Zagreb, 2007.



18th INTERNATIONAL FOUNDRYMEN CONFERENCE

**Coexistence of material science and sustainable technology in
economic growth**

Sisak, May 15th-17th, 2019

<http://www.simet.hr/~foundry/>

- [18] N. Bakula, Zaštita konstrukcijskog ugljičnog čelika inhibitorima korozije, diplomski rad, Fakultet kemijskog inženjerstva i tehnologije, Zagreb, 2005.
- [19] H. Ezuber, A. Alshater, S. O. Nisar, A. Gonsalvez, S. Aslam, Effect of surface finish on the pitting corrosion behavior of sensitized AISI 304 austenitic stainless steel alloys in 3.5% NaCl solutions, Surface Engineering and Applied Electrochemistry, 54(2018), pp. 73-80.
- [20] M. Atapour, H. Sarlak, M. Esmilzadeh, Pitting corrosion susceptibility of friction stir welded lean duplex stainless steel joints, Int. J. Adv. Many Technol, 83(2016)5, pp. 721-728.



18th INTERNATIONAL FOUNDRYMEN CONFERENCE

Coexistence of material science and sustainable technology in
economic growth

Sisak. May 15th-17th. 2019

<http://www.simet.hr/~foundry/>

CORRELATION OF MECHANICAL AND MICROSTRUCTURAL PROPERTIES IN AS-CAST CONDITION OF EN AW-5083 ALUMINIUM ALLOY USING STATISTICAL ANALYSIS

Natalija Dolić^{1*}, Ivana Bunjan², Franjo Kozina¹

¹ University of Zagreb Faculty of Metallurgy, Sisak, Croatia

² Master degree student at University of Zagreb Faculty of Metallurgy, Sisak, Croatia

Poster presentation

Original scientific paper

Abstract

In the frame of this investigation, six (6) ingots of EN AW-5083 alloy have been casted by semi-continuous vertical Direct Chill process (DC). The idea behind the process was correlating mechanical properties (tensile strength) with microstructure of ingots (number of grains per unit area) in as-cast state using statistical analysis. The Latin square experimental design was used for statistical analysis. The ingot cross-sectional grain sizes and the mean grain number per unit area were determined at precise, statistically defined locations in the slice by means of semi-automatic method for measuring mean lineal intercept lengths. Additionally, determination of the ultimate tensile strength across the cross-sectioned slices of ingots was made. It revealed differences between ingots' fronts and rears for both microstructure and ultimate tensile strength. Comparison of obtained differences enabled the correlation between ultimate tensile strength and number of grains per unit and hypothesis was based on impact of disposition and number of grains on ultimate tensile strength. The results were processed using the StatSoft® STATISTICA 13.2. software package using charge, slice height and slice width as sources of variability. Comparison of obtained statistical results for both number of grains per unit and tensile strength in respect to the sampling position enabled further correlation between these two properties and it explained how casting process has direct impact on microstructure and, ultimately, on mechanical properties.

Keywords: aluminium alloy EN AW-5083, direct chill casting, statistical analysis, microstructure, tensile strength

*Corresponding author (e-mail address): ndolic@simet.hr



18th INTERNATIONAL FOUNDRYMEN CONFERENCE

Coexistence of material science and sustainable technology in
economic growth

Sisak. May 15th-17th. 2019

<http://www.simet.hr/~foundry/>

INTRODUCTION

According to the wrought aluminium alloys designation system, alloys of this series are designated as 5xxx. Magnesium is major alloying element and is used for solid solution hardening. These alloys can also contain chromium, titanium, vanadium, beryllium and gallium as minor alloying elements. The 5xxx series have moderate to high mechanical strength combined with high ductility in annealed condition, good corrosion resistance and weldability. Because of these properties, 5xxx series are used for high strength foil, petrol tanks, marine structures and fittings, architectural components and automotive trim [1]. The AlMg alloy 5083 (EN AW-5083), which contains 4 - 4.9 wt% Mg has exceptional combination of economy of fabrication, weldability, and corrosion resistance [2]. Microstructure development followed by obtained mechanical properties is significantly dependent on the interaction between commonly present elements. Elements introduced by melt treatment can influence microstructure development and mechanical properties, respectively [3].

Direct Chill (DC) Casting is a vertical semi-continuous casting process used for fabrication of cylindrical billets or rectangular ingots/blooms from non-ferrous metals. More than a half of aluminium in the world is cast by this process [4]. At the start of the DC process, a starter block is partially inserted into a water-cooled copper or aluminium mould (the starter block is slightly above the lower lip of the mould). The mould is then filled with molten metal until the desired metal level is reached. Bottom block is gradually lowered into a casting pit carrying with it the solidifying ingot. Cooling water circulated in the water manifold and the heat was transferred from the liquid metal to the mould. This removal of the heat through the mould wall is called primary cooling. Majority part of cooling takes place in the secondary cooling region below the mould where a water film is streamed over the ingot surface (80 percent of heat extraction). The microstructure, chemical composition and the homogeneity of the ingot are directly impacted by temperature, effect of metal level, effect of molten metal pouring temperature, etc [5].

Homogeneity of as-cast structure is essential for ingots made of high-quality wrought aluminium alloys. Fine and equiaxed grain structure as well as uniformly precipitated intermetallic phases warrant numerous technological and economic advantages. One of them are improved mechanical properties, fewer surface defects and diminished propensity for occurrence of hot and cold tears in the outer regions of the ingot [3,6,7]. With increasing demand for better mechanical performance of aluminium alloys, various technologies were applied during the past decades for achieving higher strength as well as ductility of aluminium alloys. Purifying and grain refinement were two keys issued according to their outstanding effects on mechanical properties improvement. Grain refinement becomes a preferred method to improve simultaneously the strength and plasticity of metallic materials [8].

In this study, influence of casting parameters was evaluated using statistical analysis. Statistical analysis was used in order to correlate obtained mechanical properties results in as-cast state with number of grains per unit. Comparison of the obtained results enabled the homogeneity of the ingots' front and rear sections (slices) properties determination and their mutual comparison.



18th INTERNATIONAL FOUNDRYMEN CONFERENCE

Coexistence of material science and sustainable technology in economic growth

Sisak. May 15th-17th. 2019

<http://www.simet.hr/~foundry/>

MATERIALS AND METHODS

Correlation between microstructural and mechanical properties was carried out in six ingot castings by the Direct Chill Process. The ingots 1430 x 520 x 5100 mm in size were manufactured from six different charges of alloy EN AW-5083 (designations 3157, 3158, 3159, 3160, 3162, 3163). Homogenization was not performed.

First step before casting was to refine melt with an argon and chlorine mixture in an Alpur unit. The Al-Ti5-B1 master alloy was used for grain refinement in an average amount of 1.9 kg/t melt. Small bars of the master alloy were added to the casting furnace, and a master alloy wire was introduced in a launder positioned in front of the Alpur unit [9].

Investigation model plan was based on "Latin square" [10]. There was no expectation that sources of variability - process factors will interact. Ingot dimensions (length, width and height) are potential sources of variability, without mutual interaction, this model is applicable for investigation. Melt charge is considered to be main cause of inhomogeneity. It is presumed that slice height and slice width would be sources of variability between charges.

Figure 1 is a schematic representation of Latin square based sampling design, i is slice height/ingot depth and j is slice width/ingot width. The specimens cut from the slice carry the following designation: specimen number, letters F (ingot front section) or R (ingot rear section). Investigation of samples in as-cast condition were carried out at the lower half of the board.

The 36 samples from the ingots' fronts and rears were taken according to the statistical design of the experiment, respectively. The 72 samples were taken in total. For ultimate tensile strength UTS two parallel samples A and B were taken from every designated position and test samples were prepared according to the EN 10002-1 [11]. The mean value of result was taken. UTS investigation was performed on AMSLER testing machine, type 10THZ722, with maximum stretching force up to 100 kN.

Processing of UTS has been performed using StatSoft® 13.2 program. Statistical analysis was based on regression analysis (F -test) in order to define if the means between two populations are significantly different. P value is used for defining the area in the tail of a probability distribution. P value indicates the hypothesis acceptance and therefore variability source influence. Performed statistical analysis enables the comparison of mechanical properties for the ingots' fronts and rears as well as comparison at indicated positions on particular slice [3,9]. Comparison of obtained results for both UTS and number of grain size per unit area enabled estimation of number of grain size per unit area influence on UTS . The major outcome of obtained properties fluctuation is possibility of quantitative prediction of feature behavior in whole ingot.

Grain size was determined by semiautomatic measurement of mean lineal intercept length (the intercept procedure). From the computed mean lineal intercept length \bar{l} (μm), the mean number of grains per unit area \bar{N}_A ($\text{No.}/\text{mm}^2$), for the n measured fields, was calculated by linear approximation [12,13]. For the results to be statistically justifiable, manual determination of grain boundary intersections was repeated until at least 500 intercept lengths were measured.



18th INTERNATIONAL FOUNDRYMEN CONFERENCE
Coexistence of material science and sustainable technology in
economic growth

Sisak, May 15th-17th, 2019

<http://www.simet.hr/~foundry/>

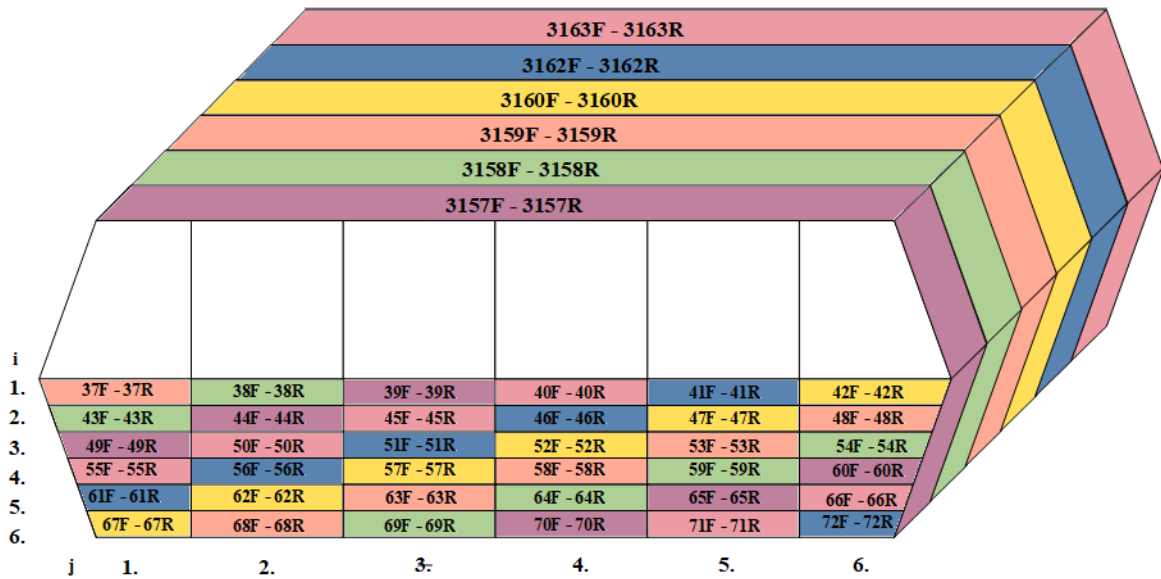


Figure 1. Sampling from EN AW-5083 ingots following the Latin square experiment design

RESULTS AND DISCUSSION

Table 1 shows the chemical compositions of the examined charges determined by optical emission spectrometry. Specimens were taken during casting, from ingots of about 0.5 m in length.

Table 1. Chemical compositions of charges of Alloy EN AW-5083

Chemical Composition [wt%]									
Charge	Si	Fe	Cu	Mn	Mg	Cr	Zn	Ti	Be
3157	0.160	0.420	0.01	0.450	4.410	0.100	0.004	0.024	0.003
3158	0.140	0.350	0.01	0.445	4.325	0.070	0.004	0.021	0.003
3159	0.150	0.385	0.01	0.470	4.175	0.090	0.005	0.025	0.003
3160	0.160	0.430	0.01	0.440	4.390	0.080	0.005	0.024	0.004
3162	0.160	0.350	0.01	0.425	4.350	0.100	0.004	0.022	0.003
3163	0.175	0.375	0.01	0.435	4.490	0.090	0.004	0.023	0.004

Results of the ultimate tensile strength *UTS* and number of grains per unit area N_A for as-cast samples are given in Table 2.



18th INTERNATIONAL FOUNDRYMEN CONFERENCE
**Coexistence of material science and sustainable technology in
 economic growth**

Sisak. May 15th-17th. 2019

<http://www.simet.hr/~foundry/>

Table 2. Results of measurement of ultimate tensile strength UTS and number of grains per unit area N_A of samples alloy EN AW-5083

Sample	\overline{UTS} [MPa]	$\overline{N_A}$ [No./mm ²]	Sample	\overline{UTS} [MPa]	$\overline{N_A}$ [No./mm ²]
37F	261.5	88.11	37R	260.0	115.68
38F	249.0	88.79	38R	240.5	60.70
39F	232.0	80.76	39R	229.0	61.08
40F	244.5	78.89	40R	235.0	52.22
41F	248.0	83.87	41R	242.5	69.73
42F	264.5	85.71	42R	236.5	101.08
43F	262.5	105.97	43R	263.0	118.89
44F	239.0	67.89	44R	246.5	67.92
45F	252.0	59.76	45R	254.0	50.44
46F	247.5	80.08	46R	253.5	74.60
47F	255.0	84.77	47R	255.0	81.89
48F	260.0	86.22	48R	260.0	122.10
49F	250.0	102.80	49R	260.5	122.00
50F	258.5	72.81	50R	259.5	63.74
51F	254.0	87.49	51R	255.0	87.12
52F	259.0	68.56	52R	260.5	73.88
53F	257.5	89.75	53R	258.0	86.51
54F	262.5	101.53	54R	269.0	85.41
55F	262.5	92.59	55R	262.5	73.73
56F	259.5	118.80	56R	261.5	86.82
57F	261.5	113.63	57R	264.0	108.32
58F	264.5	97.43	58R	263.0	95.88
59F	265.0	83.27	59R	265.5	83.31
60F	253.5	93.79	60R	263.5	87.39
61F	261.0	119.36	61R	262.0	119.86
62F	264.5	115.89	62R	269.0	121.35
63F	265.0	93.24	63R	267.0	133.75
64F	266.5	131.08	64R	255.0	103.75
65F	256.0	133.71	65R	266.5	118.35
66F	262.5	86.03	66R	273.0	108.34
67F	261.0	137.55	67R	272.5	155.99
68F	262.0	154.69	68R	261.0	168.65
69F	265.5	137.31	69R	261.0	157.89
70F	262.5	154.82	70R	265.0	132.49
71F	263.0	126.71	71R	265.5	122.97
72F	264.0	117.17	72R	272.0	144.74

Comparison of EN AW-5083 alloy samples for front and rear sections of as-cast ingots state on characteristic positions with significantly different cooling conditions resulted in



18th INTERNATIONAL FOUNDRYMEN CONFERENCE
**Coexistence of material science and sustainable technology in
economic growth**

Sisak, May 15th-17th, 2019

<http://www.simet.hr/~foundry/>

differentiation of number of grains per unit area. Figure 2 represents micrographs of front and rear sections of as-cast ingots.

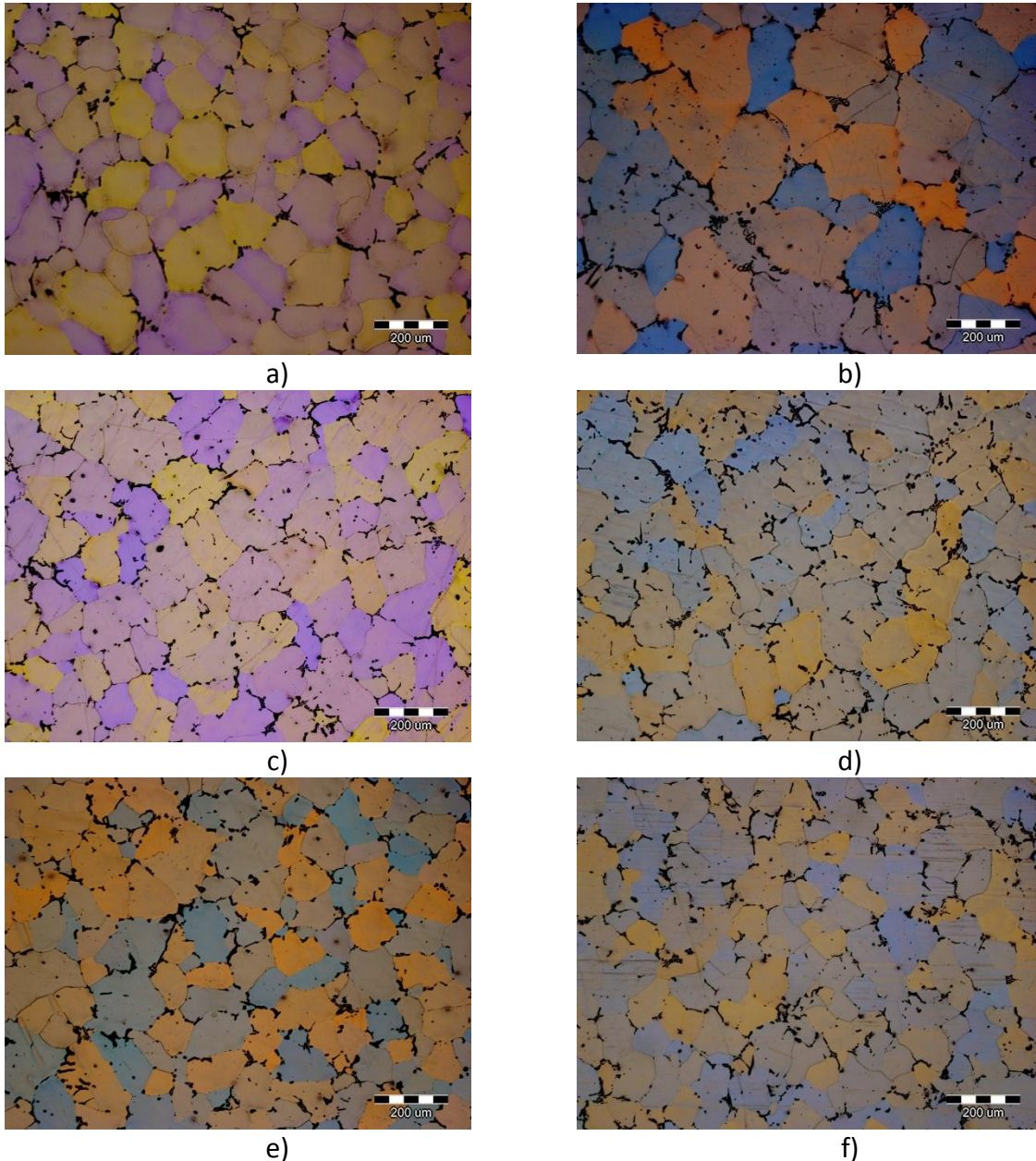


Figure 2. Micrographs of EN AW-5083 alloy samples from characteristic positions at ingot front - F (left side) and rear positions - R (right side)
a) sample 39F; b) sample 39R; c) sample 49F; d) sample 49R; e) sample 65F; f) sample 65R



18th INTERNATIONAL FOUNDRYMEN CONFERENCE

Coexistence of material science and sustainable technology in
economic growth

Sisak, May 15th-17th, 2019

<http://www.simet.hr/~foundry/>

Number of grains per unit area significantly depends on local cooling parameters and therefore from the position in charge and ingot, respectively. Samples from Figure 2 belong to charge 3157 according to the Figure 1.

Influence of individual variables on number of grains per unit area

Figure 3 is a graphic representation of relationship between individual variables (charge, slice height/ingot depth and slice width/ingot width) and the mean number of grains per unit area in as-cast state in EN AW-5083 specimens.

Graphic representation of the relationship between individual variables and mean number of grains per unit area in as-cast state for the:

a) ingot front section

- The effect of *charge* for ingot front section shows large variations in both directions in relation to the local arithmetic mean for the ingot front ($\overline{N_{A,F}} = 100.334 \text{ No./mm}^2$);
- The influence of the *slice height* (*i*) shows deviation of number of grains per unit area from total arithmetic mean as a very pronounced increase from $-15.9792 \text{ No./mm}^2$ for $i = 1$ (ingot center) to $+37.7075 \text{ No./mm}^2$ for $i = 6$ (ingot edge);
- The influence of the *slice width* (*j*) shows deviation for $i = 6$ (ingot edge), as expected. In that area there is a larger amount of grains per unit because of heat extraction. On the beginning of the melting is non-stationary state of the melt and long time is needed for casting parameters to stabilize. Solidification process is disrupted.

b) ingot rear section

- The effect of *charge* for ingot rear section shows large variations in both directions in relation to the local arithmetic mean for the ingot rear ($\overline{N_{A,R}} = 101.412 \text{ No./mm}^2$);
- The influence of the *slice height* (*i*) shows deviation of number of grains per unit area from total arithmetic mean as a very pronounced increase from $-24.6633 \text{ No./mm}^2$ for $i = 1$ (ingot center) to $+45.7050 \text{ No./mm}^2$ for $i = 6$ (ingot edge);
- The influence of the *slice width* (*j*) shows linear growth of number of grains per unit area at the edge of the ingot. Number of grains rise from the center of the ingot to the edge which implies larger heat extraction on the edge of the ingot, especially in the means of *slice height/ingot depth*, rather than *slice width/ingot width*.



18th INTERNATIONAL FOUNDRYMEN CONFERENCE
Coexistence of material science and sustainable technology in economic growth

Sisak, May 15th-17th. 2019

<http://www.simet.hr/~foundry/>

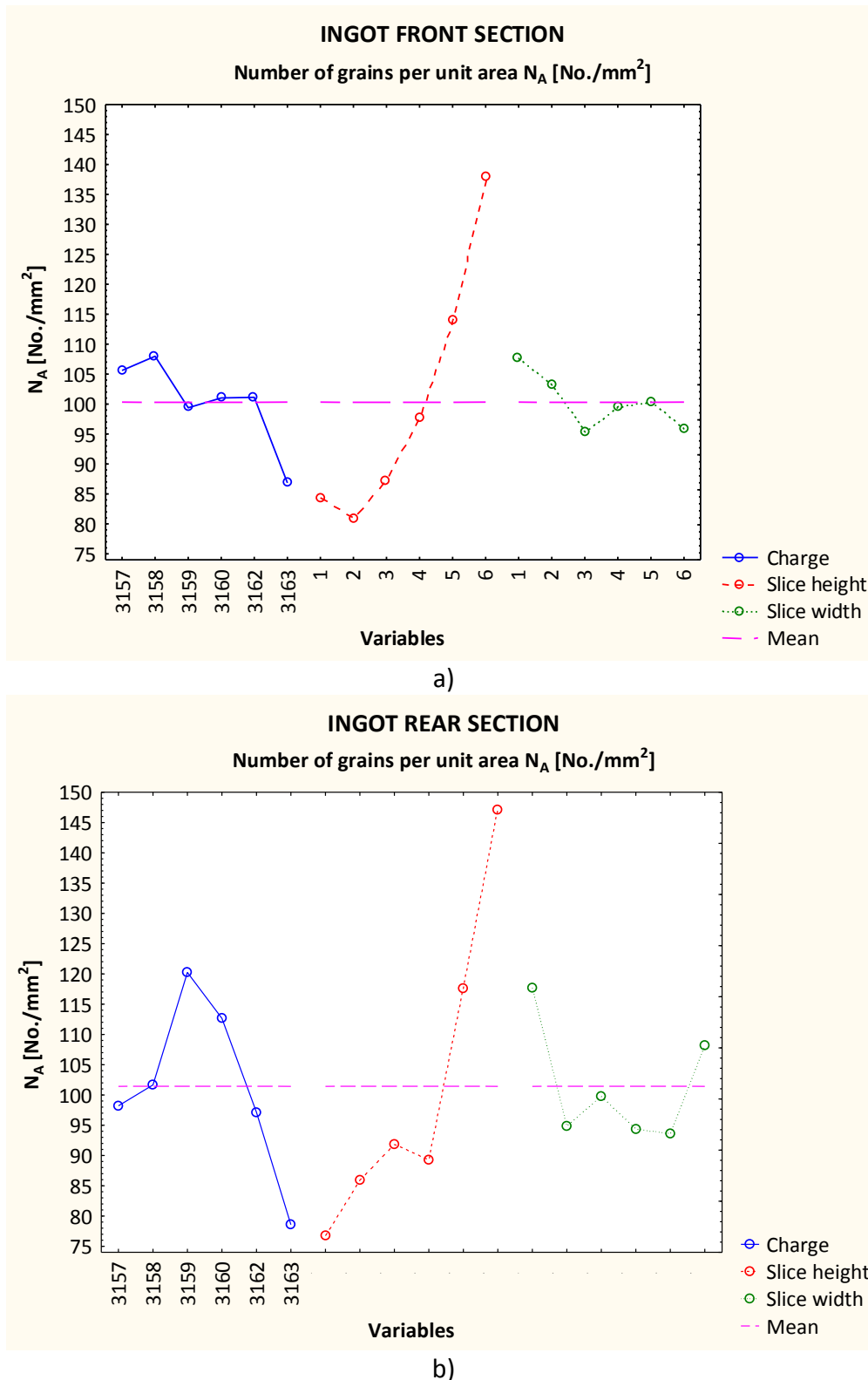


Figure 3. Graphic representation of the relationship between individual variables and mean number of grains per unit area (as-cast state): a) ingot front section; b) ingot rear section



18th INTERNATIONAL FOUNDRYMEN CONFERENCE
**Coexistence of material science and sustainable technology in
economic growth**

Sisak. May 15th-17th. 2019

<http://www.simet.hr/~foundry/>

The variance analysis is variability analysis between the means expressed as the variance. The results obtained by the *F*-test for the number of grains size per unit area for the ingots' front and rear sections in as-cast state are shown in Table 3.

Table 3. Analysis of variance of the Latin square for the number of grains - ingots' front and rear sections

Variables	Sum of Squares		Degrees of Freedom		Mean Squares		F-Test		Significance P	
	F	R	F	R	F	R	F	R	F	R
Charge	1623.89	6186.82	5	5	324.779	1237.365	1.60089	7.85224	0.205504	0.000314
Slice height	14548.27	20619.59	5	5	2909.655	4123.918	14.34221	26.17012	0.000005	0.000000
Slice width	650.79	2800.92	5	5	130.158	560.185	0.64157	3.55490	0.670798	0.018392
Residual	4057.47	3151.62	20	20	202.874	157.581				

From Table 3 is evident that differences in number of grains are highly significant in respect to *slice height* for ingot front and all three sources of variability for ingot rear due to significance value ($P < 0.05$).

Correlation coefficients for the number of grains between the ingots' fronts and rears for different charges $r_c(N_A)$, shown in Table 4 indicate a high number of grains homogeneity within each particular ingot, with correlation coefficients being lower for charges 3158 and 3162.

Table 4. Correlation coefficients for the number of grains for investigated charge samples $r_c(N_A)$ and total correlation coefficient $r(N_A)$

Charge	3157	3158	3159	3160	3162	3163	$r(N_A)$
$r_c(N_A)$	0.882563	0.665256	0.825879	0.931949	0.746140	0.871213	0.765105

Given the total coefficient of correlation for the number of grains for all charges $r(N_A) = 0.765105$ between the ingots' fronts and rears, it is apparent that applied casting technology and melt treatment provides satisfying microstructural homogeneity of the ingots as a whole. The number of grains per unit area depends only on the casting local cooling rates defined with the position within the ingot and/or slice (i, j).

Influence of individual variables on ultimate tensile strength

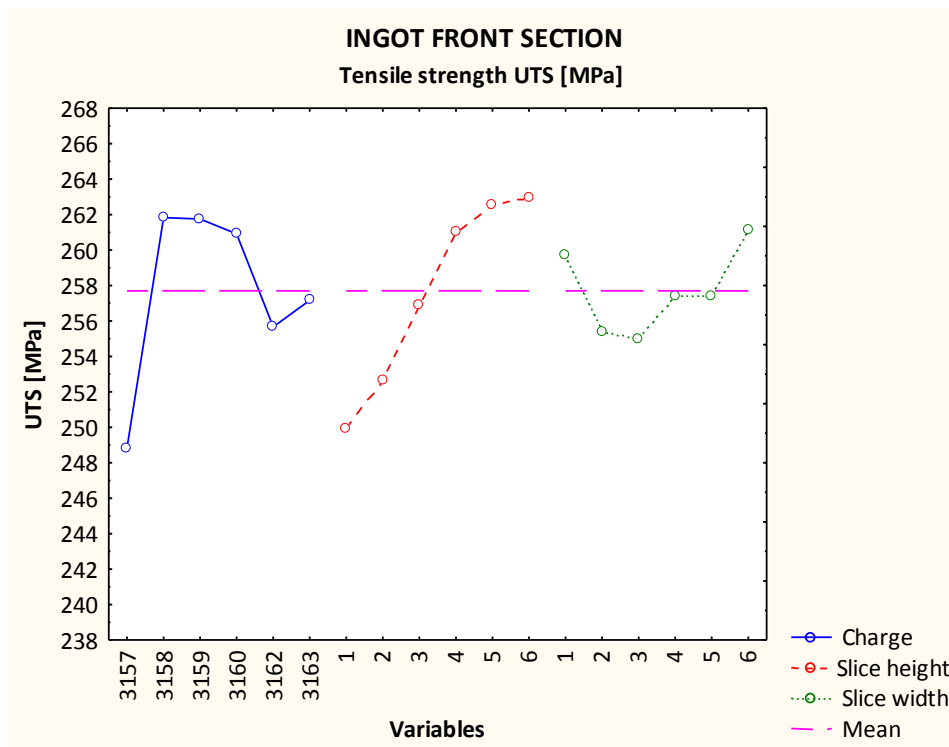
Figure 4 is a graphic representation of the relationship between individual variables mentioned before. and *the mean ultimate tensile strength* in as-cast state in EN AW-5083 specimens.



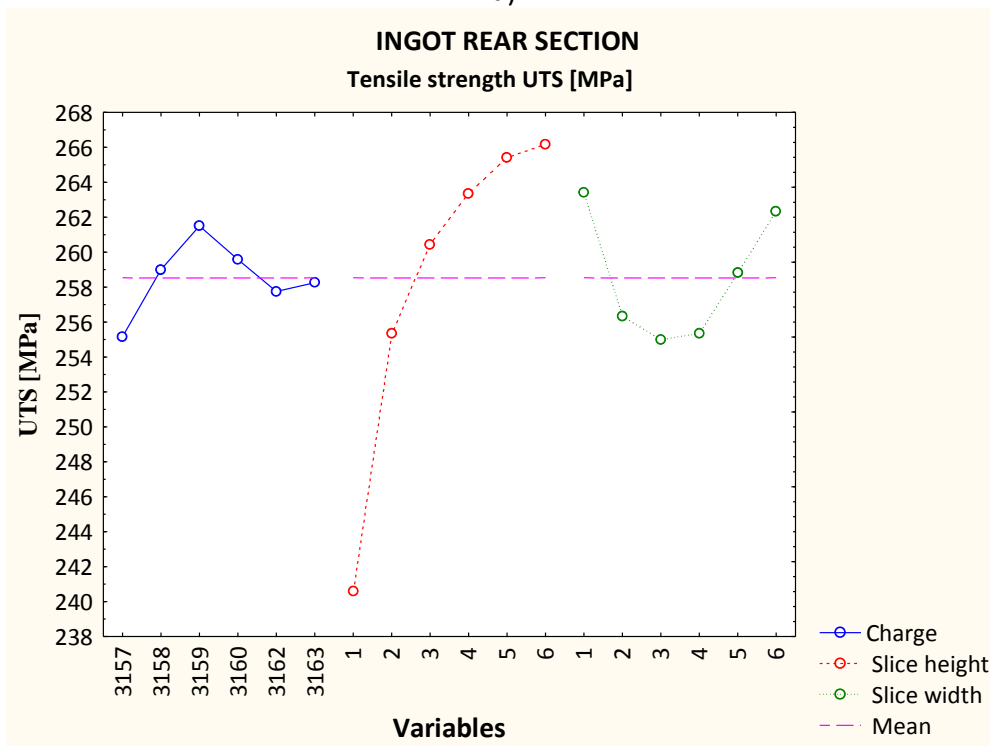
18th INTERNATIONAL FOUNDRYMEN CONFERENCE
Coexistence of material science and sustainable technology in
economic growth

Sisak, May 15th-17th. 2019

<http://www.simet.hr/~foundry/>



a)



b)

Figure 4. Graphic representation of the relationship between individual variables and mean ultimate tensile strength (as-cast state): a) *ingot front section*; b) *ingot rear section*



18th INTERNATIONAL FOUNDRYMEN CONFERENCE
**Coexistence of material science and sustainable technology in
economic growth**

Sisak. May 15th-17th. 2019

<http://www.simet.hr/~foundry/>

Graphic representation of the relationship between individual variables and mean ultimate tensile strength in as-cast state for the:

a) ingot front section

- The effect of *charge* shows large variations of ultimate tensile strength in both directions in relation to the total arithmetic mean for the ingot front ($\overline{UTS}_F = 257.694$ MPa);

- The influence of the *slice height* (*i*) shows deviation of ultimate tensile strength from total arithmetic mean as a very pronounced increase from -7.77778 MPa for *i* = 1 (ingot center) to +5.30556 MPa for *i* = 6 (ingot edge);

- The influence of the *slice width* (*j*) indicates deviation of ultimate tensile strength from total arithmetic means with the parabolic trend - minimum of -2.69444 MPa positioned in the middle slice section and maximum of +3.47222 at the slice edge.

b) ingot rear section

- The effect of *charge* shows large variations of ultimate tensile strength in both directions in relation to the total arithmetic mean for the ingot rear ($\overline{UTS}_R = 258.542$ MPa);

- The influence of *slice height* (*i*) shows deviation of ultimate tensile strength from total arithmetic means as a very pronounced increase from -17.95830 MPa for *i* = 1 (ingot center) to +7.62500 MPa for *i* = 6 (ingot edge), same as the effect of *slice height* on ingots' front;

- The influence of *slice width* (*j*) indicated deviation of ultimate tensile strength from total arithmetic means with the parabolic trend- minimum of -3.5417 MPa positioned in the middle slice section and maximum of +4.8750 MPa at the slice edge.

The variance analysis is variability analysis between the means, expressed as the variance. The results obtained by the *F*-test for the ultimate tensile strength for the ingots' front and rear sections in as-cast state are shown in Table 5.

Table 5. Analysis of variance of the Latin square for the ultimate tensile strength - ingots' front and rear sections

Variables	Sum of Squares		Degrees of Freedom		Mean Squares		F-Test		Significance P	
	F	R	F	R	F	R	F	R	F	R
Charge	761.2222	132.896	5	5	152.2444	26.5792	7.534264	0.82984	0.000405	0.543521
Slice height	899.4722	2788.063	5	5	179.8944	557.6125	8.902605	$\frac{17.4095}{2}$	0.000142	0.000001
Slice width	173.3056	395.646	5	5	34.6611	79.1292	1.715307	2.47054	0.177105	0.067363
Residual	404.1389	640.583	20	20	20.2069	32.0292				



18th INTERNATIONAL FOUNDRYMEN CONFERENCE

Coexistence of material science and sustainable technology in
economic growth

Sisak, May 15th-17th, 2019

<http://www.simet.hr/~foundry/>

From Table 5 it is evident that differences in ultimate tensile strength are highly significant in respect to *charge* and *slice height* for ingot front and *slice height* for ingot rear due to significance value ($P < 0.05$). Other sources of variability showed they are not significant.

Correlation coefficients for the number of grains between the ingots' fronts and rears for different charges r_c (UTS) shown in Table 6 indicate a high number of grains homogeneity within each particular ingot with correlation coefficients being lower for charges 3158 and 3160.

Table 6. Correlation coefficients for the number of grains for investigated charge samples r_c (UTS) and total correlation coefficient r (UTS)

Charge	3157	3158	3159	3160	3162	3163	r (UTS)
r_c (UTS)	0.943691	0.772787	0.900377	0.086135	0.905123	0.947683	0.715537

Given the total coefficient of correlation for the ultimate tensile strength for all charges r (UTS) = 0.715537 between the ingots' fronts and rears, it is apparent that applied casting technology and melt treatment provides satisfying microstructural homogeneity of the ingots as a whole.

CONCLUSIONS

Microstructural and mechanical investigations were performed at six (6) EN AW-5083 alloy ingots' fronts and rears in as-cast state. series 2 of it (3157 - 3163). Obtained mechanical properties, specifically ultimate tensile strength, were correlated with number of grains per unit area. Quantification and statistical processing of obtained results enabled determination of following conclusions:

-Heat extraction and casting parameters had highest impact on number of grains per unit area and proper use of inoculants (AlTiB). Main source of variability for number of grains per unit area for both ingots' fronts and rears was *slice height*. All three sources of variability influenced only ingots' rears.

-The total coefficient of correlation for the number of grains for all charges r (N_A) = 0.765105 between the ingots' fronts and rears implied that used casting technology and melt treatment was relatively adequate for given charge samples.

-Main source of variability for ultimate tensile strength for both ingots' fronts and rears was *slice height* - same as for number of grains per unit area. All three sources of variability were not present neither for ingots' fronts nor rears.

-The total coefficient of correlation for the ultimate tensile strength for all charges r (UTS) = 0.715537 between the ingots' fronts and rears implied that used casting technology and melt treatment was relatively adequate for given charge samples. The total coefficients of correlations for both the number of grains and UTS were similar implying that given



18th INTERNATIONAL FOUNDRYMEN CONFERENCE

Coexistence of material science and sustainable technology in
economic growth

Sisak. May 15th-17th. 2019

<http://www.simet.hr/~foundry/>

results for *UTS* are relatively correlated with results of number of grains per unit area for these six (6) ingots.

Acknowledgements

Formed in collaboration with former Company TLM Ltd Šibenik Croatia. Investigations were performed within Complex technological research – development project HITRA-STIRP with the research topic “Improved process of casting of wrought aluminium alloy ingots and slabs”, Code: TP-02-0124-04 funded by the Ministry of Science and Education Republic of Croatia; “Design and Characterization of Innovative Engineering Alloys”, Code: TP167 funded by University of Zagreb within the Framework of Financial Support of Research; scientific-research project within Croatian-Slovenian collaboration "Design and Characterization of Innovative Aluminum - Magnesium - Lithium alloy" (2018-2019) funded by Ministry of Science and Education and infrastructural scientific project: Center for Foundry Technology, Code: KK.01.1.1.02.0020 funded by European Regional Development Fund, Operational programme Competitiveness and cohesion 2014 - 2020.

REFERENCES

- [1] D. Kopeliovich, Wrought aluminium-magnesium alloys (5xxx), Accessible on Internet: http://www.substech.com/dokuwiki/doku.php?id=wrought_aluminum-magnesium_alloys_5xxx (21.3.2019.)
- [2] C. Huang. Z. Wu. R. Huang. W. Wang. L. Li, Mechanical properties of AA5083 in different tempers at low temperatures, IOP Conf. Series: Materials Science and Engineering, 279(2017).
- [3] N. Dolić. Z. Zovko Brodarac, Evaluation of EN AW-5083 aluminium alloy homogeneity using statistical analysis of mechanical properties, Journal of Mining and Metallurgy, 53B(2017)3, pp. 429 -439.
- [4] D. Kopeliovich, Direct Chill (DC) casting. Accessible on Internet: http://www.substech.com/dokuwiki/doku.php?id=direct_chill_dc_casting (21.3.2019.)
- [5] R. E. Ortega Pelayo, Master's Thesis Direct Chill and FusionTM Casting of Aluminium Alloys, University of Waterloo, Ontario, Canada, 2012.
- [6] H. E. Vatne, Efficient grain refinement of ingots of commercial wrought aluminium alloys. Part I: Methods for grain refining, Aluminium, 75(1999)1/2, pp. 84-90.
- [7] H. E. Vatne, Aluminium, 75(1999)3, pp. 200-203.
- [8] R-G. Guan, D. Tie, A Review on grain refinement of aluminium alloys: progresses, challenges and prospects, Acta Metallurgica Sinica, 30(2017)5, pp. 409-432.
- [9] N. Dolić, Homogenost blokova Al-slitine 5083 proizvedenih vertikalnim DC postupkom (Homogeneity of 5083 Al-alloy Slabs Produced by Vertical DC Process), Master's thesis, University of Zagreb Faculty of Metallurgy, Sisak, Croatia, 2006 (in Croatian).



18th INTERNATIONAL FOUNDRYMEN CONFERENCE

**Coexistence of material science and sustainable technology in
economic growth**

Sisak. May 15th-17th. 2019

<http://www.simet.hr/~foundry/>

- [10] N. Šakić, Planiranje i analiza pokusa u istraživačkom radu (Planning and analysis of experiments in research work), University of Zagreb Faculty of Mechanical Engineering and Naval Architecture, Zagreb, 2002 (in Croatian).
- [11] ISO 6892-1: 2016, Metallic materials - Tensile testing - Part 1: Method of Test at Room Temperature, European Committee for Standardization (CEN), Brussels, 2016.
- [12] N. Dolić, A. Markotić, F. Unkić, Structural homogeneity of direct-chill cast ingots of aluminium alloy EN AW-5083, Metallurgical and Materials Transactions B, 38(2007)3, pp. 491-495.
- [13] E 112-96: Standard Test Methods for Determining Average Grain Size, American National Standard Institute/ASTM, 2000.



18th INTERNATIONAL FOUNDRYMEN CONFERENCE
Coexistence of material science and sustainable technology in economic growth

Sisak, May 15th-17th, 2019
<http://www.simet.hr/~foundry/>

**MODERNIZATION OF THE LADLE TO IMPROVE FERROALLOY
REFINING CONDITIONS**

Stanisław Gil^{1*}, Wojciech Bialik¹, Bolesław Machulec¹, Sławomir Kozłowski²

¹ Silesian University of Technology Faculty of Materials Engineering and Metallurgy, Katowice, Poland

² Re Alloys Ltd., Łaziska Górne, Poland

Poster presentation
Original scientific paper

Abstract

A potential for reduction of heat losses from a refining ladle due to the use of refractory lining with higher thermal resistance as well as proposed modification of liquid ferrosilicon ladle refining with technical gases to improve its purity have been presented in the paper. It includes calculation results for insulation materials with low conductivity. Instead of Al 44 chamotte [1], two insulating materials, Promacrete PF 145/20 [2] and Carath FL 1500 [3] refractory concretes, have been selected and it is suggested that chamotte brick is replaced with porous chamotte in the insulation layer. Compressed gas should be delivered to liquid metal through a gas lance or, optionally, through a specially designed porous plug located in the ladle bottom (the gas lance was used in the experiments). Physical model studies have shown that the optimal depth of lance immersion should be 2/3 of the metal height in the refining ladle.

Keywords: *casting ladles, ferroalloys, improving purity of alloy*

*Corresponding author (e-mail address): stanislaw.gil@polsl.pl

INTRODUCTION

Current global economy trends require continuous improvement of a product and reduced costs of its production. These policies also refer to the metallurgical industry, although the need of product improvement is more difficult to satisfy in this field. Implementation of sometimes minor innovations may significantly improve the product quality and result in



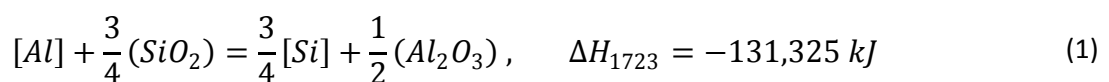
18th INTERNATIONAL FOUNDRYMEN CONFERENCE

Coexistence of material science and sustainable technology in economic growth

Sisak, May 15th-17th, 2019

<http://www.simet.hr/~foundry/>

considerable economic benefits. Due to their properties, ferroalloys (ferrosilicon, ferromanganese, ferrochrome) are widely used in the metallurgical and chemical industries [4,5]. The most popular ferroalloys are ferrosilicons (FeSi65 and FeSi75), used in the steel industry for steel deoxidation and as alloy additives. Silicon is a component of many steel and alloy types, including spring, bearing, stainless, heat-resistant and electrical steels as well as structural steels for the construction industry. Industrial-type ferrosilicons also contain small amounts of other elements, such as Al, Ca, Mg, Mn, Cr, Ti, P or S, which are impurities. Their fractions depend of the quality of raw materials and physicochemical processes that occur during electrothermal reduction of silica with carbon in a submerged arc furnace [6,7]. One of the ways of non-metallic inclusion content reduction in liquid metal is its refining in a ladle through technical gas purging. Gas bubbles, moving to the liquid metal surface, facilitate flow of non-metallic inclusions. Depending on the type of process, refining gases can be inert gases or their mixtures with other gases as well as nitrogen, oxygen, air or oxygen-enriched air. In addition to metal bath stirring, gas can participate in oxidation of additives, which generates extra energy flow in exothermic reactions. Reduction of heat losses in the refining ladle due to the use of refractory lining with higher thermal resistance and occurring exothermic reactions ensure longer stay of liquid alloy in the ladle and improved ferroalloy refining conditions. Based on the mechanism of carbide inclusion removal from the metal bath (mediated by slag resulting from ferrosilicon-dissolved Al, Ca, Mg oxidation), natural air, oxygen-enriched air or pure oxygen can be the best refining gases. Industrial experiences from previous years, related to liquid ferrosilicon dealumination with the use of INJECT oxidising refining method [4], show that with application of appropriate silica-based synthetic slags, oxygen use for Al, Mg, Ca oxidation is not necessarily associated with silicon loss. This is due to chemical reactions between slag and liquid metal in the oxidising environment [4]:



Reactions (1) and (2) are highly exothermic, which additionally improves the thermal balance of refining process and enables its longer duration. Therefore, combination of ferrosilicon decarbonisation and dealumination processes is worth considering. Smaller additive contents in ferrosilicon are beneficial for its durability, which is related to formation of a smaller 0 – 3 mm subgrain amount in the mechanical milling process. Additionally, reduced Al contents in the alloy may result in a higher sale price. The above considerations show that the use of inert gas for the refining process is not advisable because the same effect of metal bath stirring in the ladle can be achieved when compressed air is applied for liquid metal purging.



18th INTERNATIONAL FOUNDRYMEN CONFERENCE
Coexistence of material science and sustainable technology in economic growth

Sisak, May 15th-17th, 2019
<http://www.simet.hr/~foundry/>

REDUCTION OF HEAT LOSSES FROM THE REFINING LADLE

To analyse the potential for improving thermal insulation of the ladle refractory lining, results of calculations for insulation materials with low thermal conductivity are presented below. Instead of Al 44 ($\lambda = 1.4 \text{ W/(mK)}$) chamotte, two types of insulating refractory concrete were selected: Promacrete PF 145/20 ($\lambda = 1.03 \text{ W/(mK)}$ for $T = 1273 \text{ K}$) [2] and Carath FL 1500 ($\lambda = 0.7 \text{ W/(mK)}$ for $T = 1273 \text{ K}$) [3]. It is suggested that chamotte brick ($\lambda = 1.7$) in the insulation layer should be replaced with porous chamotte ($\lambda = 0.15 \text{ W/(mK)}$ for $T = 873 \text{ K}$) [1]. The thicknesses of the lining layers are the same as before the retrofit to obtain the same amount of liquid alloy during refining. Figures 1 and 2 show a ladle with a cover containing a thermal insulation layer and a thermogram of ladle shell temperature distribution. Table 1 presents calculation results for overall heat losses to the environment at 1773 K and 1623 K for the previous ('old') refractory lining. Mean heat loss in the case of discussed temperatures and refining time of 1800 s was 378.3 MJ.



Figure 1. Ladle and its cover with a thermal insulation layer

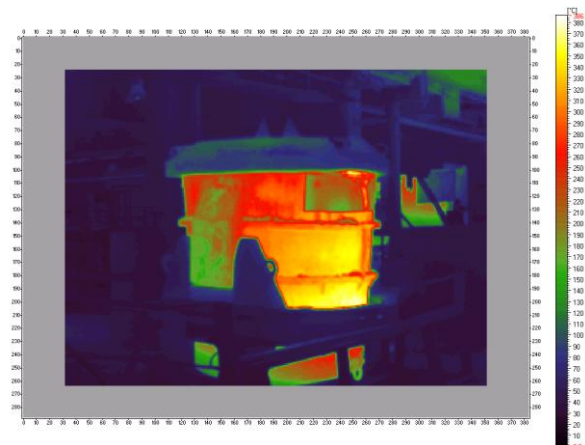


Figure 2. Thermogram of the ladle shell temperature distribution

Table 1. Heat losses from the ladle to the environment for the FeSi75 refining time of 1800 s for the previous lining

Heat losses	Symbol	Value	Unit
Heat loss (1773 K)	Q_{1773}	389.9	MJ
Heat loss (1623 K)	Q_{1623}	366.7	MJ
Mean heat losses for 1623 K – 1773 K	Q_m	378.3	MJ
Mean heat loss rate	\dot{q}_m	12.61	MJ/min

It was assumed that thickness of the ladle refractory lining walls did not change and it was the same as in the existing project. Table 2 presents calculations results for overall heat losses from the ladle to the environment with Promacrete PF 145/20 refractory concrete and porous chamotte while Table 3 presents these results for Carath FL 1500 refractory concrete. The other process conditions were the same as for the previous lining.



18th INTERNATIONAL FOUNDRYMEN CONFERENCE
Coexistence of material science and sustainable technology in economic growth

Sisak, May 15th-17th, 2019

<http://www.simet.hr/~foundry/>

Table 2. Overall heat losses from the ladle to the environment for the time of 1800 s (PF 145/20 insulation)

Heat losses	Symbol	Value	Unit
Heat loss (1773 K)	Q_{1773}	236.4	MJ
Heat loss (1623 K)	Q_{1623}	230.4	MJ
Mean heat losses for 1623 K – 1773 K	Q_m	233.4	MJ
Mean heat loss rate	\dot{q}_m	7.78	MJ/min

Table 3. Overall heat losses from the ladle to the environment for the time of 1800 s (Carath FL 1500 insulation)

Heat losses	Symbol	Value	Unit
Heat loss ($T_{cl} = 1773$ K), $t = 1800$ s, FeSi75 refining	Q_{1773}	241.4	MJ
Heat loss ($T_{cl} = 1623$ K), $t = 1800$ s, FeSi75 refining	Q_{1623}	235.1	MJ
Mean heat losses for 1623 K – 1773 K	Q_m	238.2	MJ
Mean heat loss rate	\dot{q}_m	7.94	MJ/min

The above results show that the new lining is characterised by higher thermal resistance and smaller weight (by about 2000 kg of ladle weight with an old liner, which was about 7,500 kg), which significantly reduces its heat capacity. As a result, the overall heat loss rate for the ladle refractory lining is lower by approximately 40 % compared to the previous lining. Higher thermal resistance of the lining will affect lower temperature decrease of the alloy in the ladle.

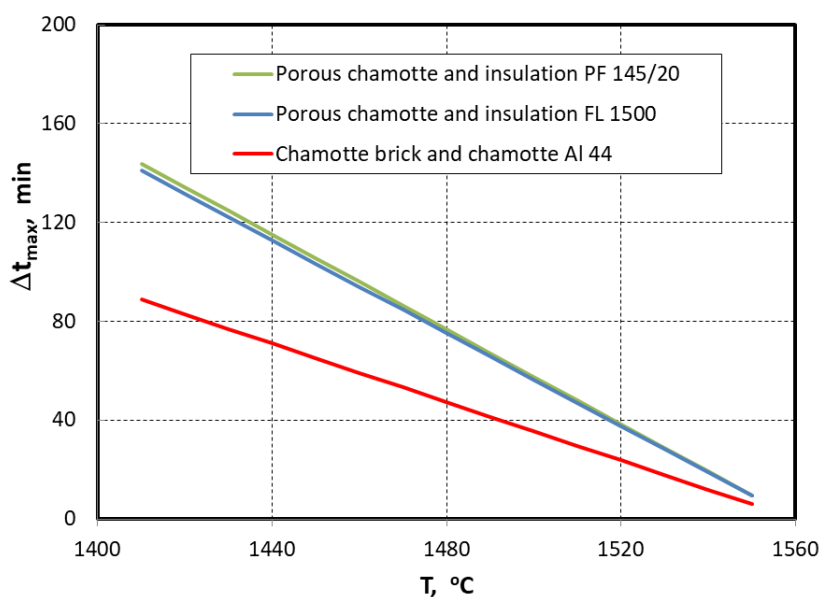


Figure 3. Maximum metal holding time versus its temperature



18th INTERNATIONAL FOUNDRYMEN CONFERENCE

Coexistence of material science and sustainable technology in economic growth

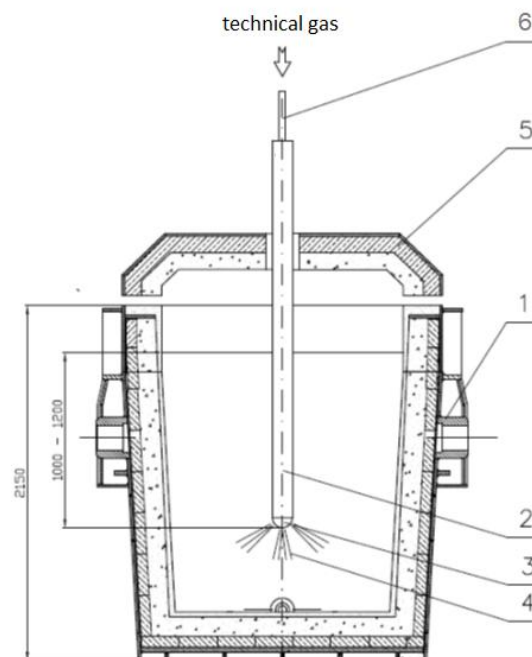
Sisak, May 15th-17th, 2019

<http://www.simet.hr/~foundry/>

Figure 3 shows the maximum time of metal holding in the refining ladle versus its initial temperature for three cases considered: the previous lining as well as the use of Promacrete PF 145/20 and Carath FL 1500 refractory concretes in the inner layer and the porous chamotte insulation layer. When modern insulation materials are used, the time of alloy staying in the refining ladle is longer by 40 %.

PARAMETERS OF GASE SOLUTION BLOWN INTO THE REFINING LADLE

One of the ways of non-metallic inclusion content reduction in liquid metal is its refining in a ladle through technical gas purging. Gas bubbles, moving to the liquid metal surface, facilitate flow of non-metallic inclusions. Depending on the type of process, refining gases can be inert gases or their mixtures with other gases as well as nitrogen, oxygen, air or oxygen-enriched air. In addition to stirring of metal bath alone or metal bath with refining slag, gas can participate in oxidation of additives. Compressed gas can be delivered to liquid metal through a porous plug located in the bottom of the refining ladle or through a gas lance. The scheme of a ferrosilicon refining system with a gas lance immersed in liquid metal is presented in Figure 4.



1 refining ladle, 2 gas lance in a thermal cover, 3 gas lance head, 4 refining gas stream, 5 cover of the ladle, 6 refinery gas connector

Figure 4. Scheme of a refining ladle with a gas lance



18th INTERNATIONAL FOUNDRYMEN CONFERENCE

Coexistence of material science and sustainable technology in economic growth

Sisak, May 15th-17th, 2019

<http://www.simet.hr/~foundry/>

Physical model studies [5] have shown that the optimal depth of lance immersion should be 2/3 of the metal height in the refining ladle. Assuming that for the ladle with 8 Mg of FeSi75 ferrosilicon, the height of metal surface is about 1600 mm, the gas lance head should be located at the depth of approximately 1000 to 1200 mm. Due to the decarbonisation process, a non-graphite lance is recommended. Therefore, an air-cooled lance is suggested. In addition, to ensure a properly high gas outflow velocity enabling volume penetration of liquid metal by gas streams, the lance should be fitted with a replaceable head (3) with holes of appropriate diameter and shape. Pressure of gas delivered to the lance must overcome hydrostatic pressure of the metal bath and flow resistance of the lance head nozzles resulting from required outflow velocity.

Hydrostatic pressure can be calculated using the following formula:

$$p = g \cdot h \cdot (\rho_a - \rho_g), \quad (3)$$

where: p – hydrostatic pressure, Pa; g – gravitational acceleration m s^{-2} ; h – depth of lance immersion in liquid, m; ρ_a – alloy density, kg m^{-3} ; ρ_g – gas density, kg m^{-3} . Because the gas density in formula (1) is far smaller than the alloy density, it can be neglected in engineering calculations. Assuming the FeSi75 ferrosilicon density at 1450 °C is 3400 kg m^{-3} , the formula (3) result suggests that hydrostatic pressure does not exceed 0.04 MPa, but in the case of lance fitted with a nozzled head, a higher pressure of 0.15 to 0.25 MPa is required to overcome nozzle resistance and to ensure properly high gas outflow velocity. In industrial practice, to achieve the effect of smooth metal bath stirring with no metal splashing out of the ladle, gas pressure should be adjusted in an experimental manner by observation of liquid bath surface in the ladle. To reduce radiation heat loss to the environment, the ladle is fitted with a cover (5) containing a slot for outflowing gases. In addition to pressure, another important parameter to determine is the intensity of refining gas stream. With no exothermic reactions, gas that flows through liquid metal leads to its cooling. It has been confirmed by results of previous attempts to purge liquid metal with compressed oxygen-enriched air using a bath-immersed lance of the 45 mm inner diameter [6]. The report does not contain detailed data on refining gas consumption or composition but the measurement values demonstrated a faster metal temperature decrease of about 3.5 K/min during the refining process while the same parameter during smelting with no gas purging reached a mean value of 2.0 K/min. The tests did not result in expected refining improvement compared to smelting without refining gas purging. Therefore, it is suggested that pure oxygen is used in further refining attempts by means of gas purging. To estimate the quantitative gaseous oxygen requirements, it was assumed that after the refining process in oxidising environment, a higher Al and Ca content reduction should be achieved to ensure a final Al content in the alloy of less than 0.5 %.



18th INTERNATIONAL FOUNDRYMEN CONFERENCE

Coexistence of material science and sustainable technology in economic growth

Sisak, May 15th-17th, 2019

<http://www.simet.hr/~foundry/>

CONCLUSIONS

1. To reduce heat losses to the environment, it is suggested that refractory materials with higher thermal resistance should be used for the ladle refractory lining. Instead of Al 44 chamotte, refractory concrete materials were selected: Promacrete PF 145/20 and Carath FL 1500. It is proposed to replace the chamotte brick with porous chamotte. This ensures that the overall heat losses to the environment are reduced from 210.2 kW to below 130 kW and the refractory lining weight decreases by about 2000 kg.
2. For gas purging, a ceramic-coated, air-cooled lance of the 45 mm inner diameter is recommended. To ensure a properly high gas outflow velocity, enabling volume penetration of liquid metal by gas streams, it is recommended that the lance is fitted with a replaceable head with holes of appropriate diameter and shape.
3. At the optimal immersion depth of the lance in the metal bath (1 - 1.2 m), hydrostatic pressure of metal does not exceed 0.04 MPa. When the lance is fitted with a nozzled head, higher pressure of 0.15 to 0.25 MPa will be required to overcome nozzle resistance and to ensure properly high gas outflow velocity.

Acknowledgement

The authors acknowledge the support of research project "Innovative technology for the production of ferrosilicon with silicon content min. 75% and ultra-low carbon content max. 0.02% " (Project No POIR.01.01.01-00-0052/17), funded by the Intelligent Development Operational Program 2014-2020.

REFERENCES

- [1] E. Kostowski, Przepływ ciepła, Wydawnictwo Politechniki Śląskiej, Gliwice, 2000.
- [2] www.promat-hpi.com/pl
- [3] www.rath.com.pl.
- [4] A. J. Schei, J. Kr. Tuset, H. Tveit, Production of High Silicon Alloys, Trondheim, 1998.
- [5] V. L. Zubov, M. I. Gasik, Electrometallurgy of ferrosilicon, Physical Chemistry and Technology, System Technologies Publication, Dnepropetrovsk, 2002.
- [6] S. Kozłowski, Raport z procesu rafinacji odwęglającej FeSi75, Re Alloys, 2016 (not published, Project No POIR.01.01.01-00-0052/17).
- [7] M. Gasik, [red.], Handbook of ferroalloys theory and technology, Elsevier Ltd. (Butterworth-Heinemann), Waltham, 2013.



18th INTERNATIONAL FOUNDRYMEN CONFERENCE

Coexistence of material science and sustainable technology in
economic growth

Sisak, May 15th-17th, 2019

<http://www.simet.hr/~foundry/>

INFLUENCE OF Mn ON THE CORROSION BEHAVIOR OF CuAlMn ALLOY IN NaCl SOLUTION

Senka Gudić^{1*}, Blanka Rakuljić¹, Ladislav Vrsalović¹, Milan Bizjak², Ivana Ivanić³, Stjepan Kožuh³, Mirko Gojić³

¹ University of Split Faculty of Chemistry and Technology, Split, Croatia

² University of Ljubljana Faculty of Natural Sciences and Engineering, Ljubljana, Slovenia

³ University of Zagreb Faculty of Metallurgy, Sisak, Croatia

Poster presentation

Original scientific paper

Abstract

The corrosion behavior of different CuAlMn shape memory alloys (Cu-12%Al-4%Mn, Cu-12.3%Al-5.2%-Mn and Cu-12%Al-6%Mn) in 0.9% NaCl solution at pH = 7.4 and T = 37°C was investigated using open circuit potential measurements, polarization and electrochemical impedance spectroscopy methods. It has been found that the corrosion resistance of the tested samples at open circuit potential increases with increasing Mn content in the alloy, i.e. growing in the order of: Cu-12%Al-4% Mn < Cu-12.3%Al-5.2%Mn < Cu-12%Al-6% Mn. Namely, the corrosion current decreases in same order, while the polarization resistance and the resistance, thickness and compactness of the surface oxide layer increase. However, at high anodic potentials ($E > 0.1$ V), the corrosion rate increases with Mn content in the alloy, and light microscopy investigations reveal pits on the surface of Cu-12.3%Al-5.2%-Mn and Cu-12%Al-6%Mn alloys, while Cu-12%Al-4%Mn surface is almost clear of any corrosion damage.

Keywords: shape memory alloys, CuAlMn alloy, corrosion, polarization, electrochemical methods

*Corresponding author (e-mail address): senka@ktf-split.hr

INTRODUCTION

Shape memory alloys (SMA) are significant and growing group of intelligent materials which have ability to “remember” their original shape and return to it by heating above a certain temperature due to its crystallographic structure changes between low temperature martensite and the high temperature austenite phase [1-4]. Mainly three alloy systems



18th INTERNATIONAL FOUNDRYMEN CONFERENCE

Coexistence of material science and sustainable technology in
economic growth

Sisak, May 15th-17th, 2019

<http://www.simet.hr/~foundry/>

which are known to exhibit the shape memory phenomena have been in the focus of research and development: Ni-Ti, Cu-Al and Fe based alloys [5]. Nickel-titanium alloys (Nitinol) possess the unique thermal shape memory and superelasticity effects as well as excellent corrosion resistance and biocompatibility, that make these alloys very attractive for medical use [6,7]. However, their difficulty in production and processing, high cost and low transformation temperatures prohibit their use where Cu-based shape memory alloys fill in the need [5,8]. The main advantages of Cu-based shape memory alloys are their low price, relatively simple fabrication procedure, higher range of potential transformation temperatures, high thermal and electrical conductivity. Shortcoming of Cu-based shape memory alloys are brittleness and low mechanical strength which are close related to the microstructure characteristics of Cu-SMAs, such as coarse grain size, high elastic anisotropy and the segregation of secondary phases [9-11]. Some research has shown that CuAlMn alloy possess good strain recovery, better ductility, higher shape memory strain, larger recovery power, and higher damping capacity than CuAlNi [11-14]. Investigated CuAlMn alloys were produced by melt spinning methods which enables the formation of homogeneous solution and have unique advantages in refining the microstructure [15-17]. Most research on influence of alloying elements in CuAlMn shape memory alloys have focused on its microstructure and mechanical properties, however little attention has been devoted to their influence to the electrochemical behavior [5,8,18]. Thus some studies have shown that additions of Mn to the binary Cu-Al alloy stabilize the β -phase and widen the single-phase region to lower temperature and lower Al contents [18]. With the increase in the aluminum and manganese concentration of the alloy, the martensite morphology is modified and the transformation temperature decrease [8]. Also, increase in the Al:Mn ratio leads to increase in grain size as well as cast hardness [5]. This paper deals with the influence of Mn content on corrosion behavior of CuAlMn alloy in NaCl solution.

MATERIALS AND METHODS

The CuAlMn alloys used in this study were Cu-12%Al-4%Mn (A), Cu-12.3%Al-5.2%-Mn (B), and Cu-12%Al-6%Mn (C). Alloy ribbons were manufactured with the single roll melt spinning apparatus. The cast precursors were inserted into the graphite crucible, inductively melted in Ar atmosphere and sprayed through the nozzle onto a rotating cooled copper wheel. The obtained ribbons were 4-5 mm wide and 30-100 μ m thick. The as-prepared specimens were cut at the proper dimensions and solder to an isolated copper wire to insure good electrical contact. Solder joints were isolated with polyacrilate resin and prepared electrodes were degreased ultrasonically in ethanol, rinsed in deionized water and immersed in 0.9% NaCl solution (pH = 7.4, T = 37 °C). Since melt-spin alloys are rather thin, the surface of the ribbons was not mechanically polished.

Experiments were performed with a PAR 273A potentiostat/galvanostat and a PAR M5210 lock-in amplifier. A double walled three-electrode glass cell was used, thermostated at 37 °C, with Pt-plate auxiliary electrode and saturated calomel electrode (SCE) as a reference



18th INTERNATIONAL FOUNDRYMEN CONFERENCE
**Coexistence of material science and sustainable technology in
economic growth**

Sisak, May 15th-17th, 2019

<http://www.simet.hr/~foundry/>

electrode. Prior the electrode immersion, solution was deaerated with Ar for a 20 min and the deaeration continued during the experiment.

The corrosion behaviour of CuAlMn alloys in 0.9% NaCl solution was performed by open circuit potential measurements (E_{OC}) in 60 min time period, linear polarisation method in the potential region of ± 20 mV vs. E_{OC} with the scan rate of 0.2 mV s^{-1} and potentiodynamic polarisation method in the range of -0.250 V from E_{OC} to 0.7 V with scan rate of 0.5 mV s^{-1} . Electrochemical impedance spectroscopy measurements were carried out at E_{OC} using the signal amplitude of 10 mV and a frequency interval from 50 kHz to 30 mHz . All electrochemical measurements were performed after 60 min electrode stabilisation on E_{OC} . After the potentiodynamic polarization measurements electrode surfaces were cleaned ultrasonically in deionized water, dry in desiccator and investigated with light microscope MXFMS-BD, Ningbo Sunny Instruments co., with magnifications of 100 times.

RESULTS AND DISCUSSION

Figure 1 shows the variation of E_{OC} of investigated alloys with time in the NaCl solution. The open circuit potential reflects the composite results of the electrochemical reactions which take place at the electrode/solution interface. As can be seen, all investigated samples shows similar changes of E_{OC} . Namely, immediately after immersing each electrode in NaCl solution, values of E_{OC} were shifted towards negative values due to the adsorption of chloride ions on the surface of the electrode [19]. After the initial drop, E_{OC} for all alloys increases gradually towards positive values which indicate the formation and thickening of the protective passive film on their surfaces during the immersion. The stabilization of E_{OC} for all alloys occurs in period of 20 minutes. It can also be noted that by increasing the Mn content in alloy, the final E_{OC} value become more negative.

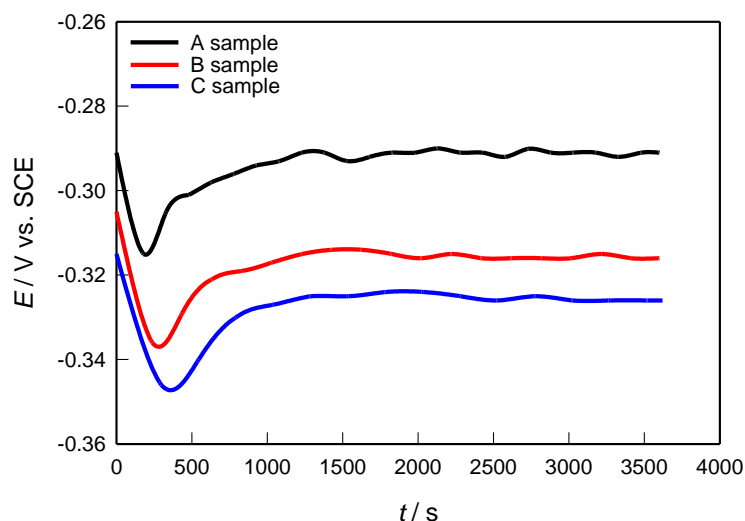


Figure 1. Evolution of open circuit potential as a function of time for investigated CuAlMn alloys in a 0.9% NaCl solution



18th INTERNATIONAL FOUNDRYMEN CONFERENCE
**Coexistence of material science and sustainable technology in
 economic growth**

Sisak, May 15th-17th, 2019

<http://www.simet.hr/~foundry/>

The general corrosion behavior of tested CuAlMn alloys in NaCl solution was investigated by recording the polarization curves in wide potential range. The purpose of these measurements was to evaluate influence of Mn on anodic and cathodic behaviour of alloy and determination of corrosion current density (i_{corr}) and corrosion potential (E_{corr}). Obtained results are presented on Figure 2 and Table 1.

Significant differences in corrosion behavior of tested samples can be noticed. The slight increases of the anodic current density in Tafel region and gradually reduction of cathodic current density along with the slight changes the values of corrosion potential in the cathodic side can be observed with increasing Mn content in alloy. This direction of change ultimately leads to a reduction in the corrosion rate.

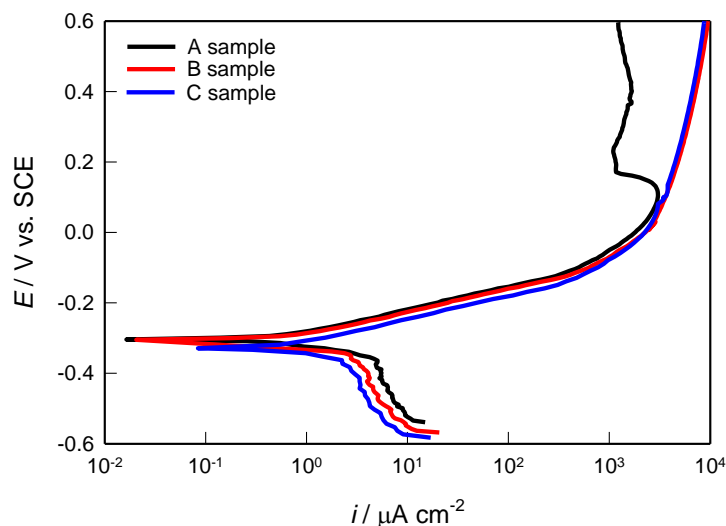


Figure 2. Potentiodynamic polarization curves for investigated CuAlMn alloys in 0.9% NaCl solution

Table 1. Corrosion parameters of investigated CuAlMn alloys in 0.9% NaCl solution

sample	E_{corr} / V	$i_{corr} / \mu A \text{ cm}^{-2}$	$R_p / k\Omega \text{ cm}^2$
A	-0.29	3.17	5.24
B	-0.31	2.54	6.53
C	-0.33	2.09	7.18

As can be seen from Table 1 the lowest i_{corr} and the most negative E_{corr} have been obtained for C sample (alloy with the largest Mn content) which also have the highest polarization resistance, R_p (i.e. resistance of metal to corrosion). The R_p data were determined from the slope of linear part of polarization curves obtained by measurements in the potential range close to E_{OC} (Figure 3). Thus, it can be concluded that the corrosion resistance of the tested samples at open circuit potential increases with increasing Mn content in the alloy (i.e. growing in the order of: A < B < C).

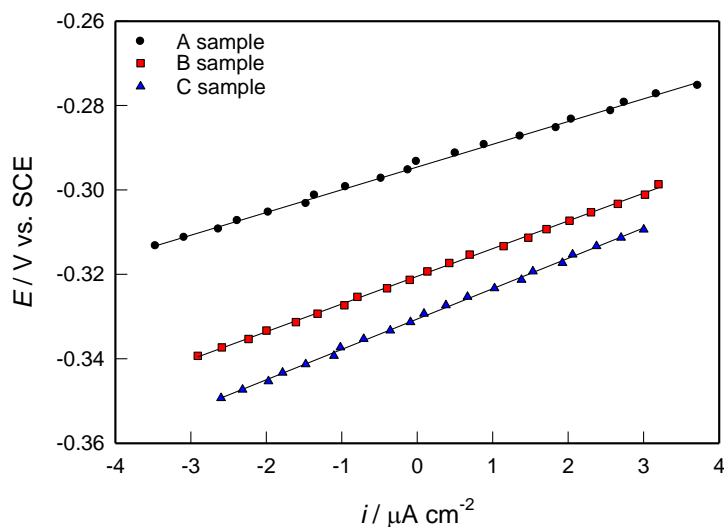


Figure 3. Linear parts of polarization curves for investigated CuAlMn alloys in 0.9% NaCl solution

However, at high anode potentials (after passing through Tafel area, $E > 0.1$ V) the opposite trend is noticed. Anodic current density, and thus the corrosion are increased with the increase of Mn content in the alloy. After polarization measurement (which ended at 0.7 V) electrode surfaces were examined with light microscope with magnification of 100 times, and obtained results have shown on Figure 4 (a-c). Pits are visible on the surface of samples C and B, while surface of sample A is almost clear of any pitting corrosion damages.

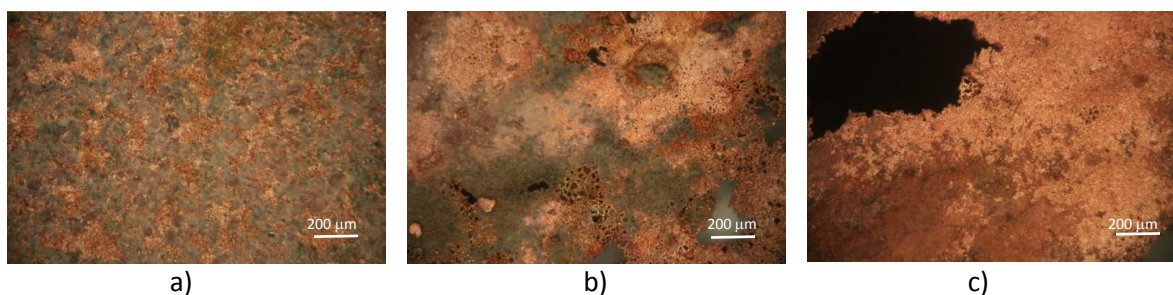


Figure 4. Light microscopy images of the electrode surfaces after potentiodynamic polarization measurements for a) sample A, b) sample B and c) sample C

Impedance measurements were undertaken in order to obtain physical insight into the processes occurring at the CuAlMn alloys/solution phase boundary. Figure 5 shows the Nyquist plots for CuAlMn electrodes in NaCl solution obtained after 60 minutes stabilization at E_{OC} . The response of the systems in the Nyquist complex plane was a semicircle that can be correlated with the dielectric properties of the naturally formed oxide film on alloy surface, which mostly consists of aluminum and manganese oxides [20,21]. The diameter of capacitive loop increases with the increase of the Mn content in the alloy.

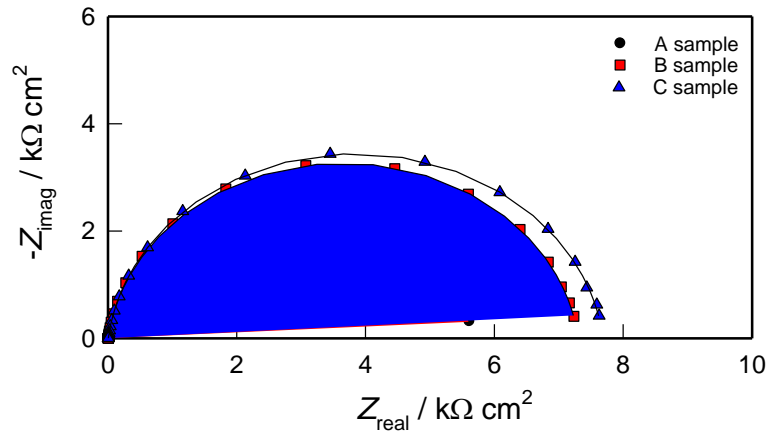


Figure 5. Nyquist plots for investigated CuAlMn alloys in 0.9% NaCl solution

In mathematical analysis of impedance diagrams the constant phase element, CPE, was used instead of an "ideal" capacitor to account for the deviations observed as capacitive loops are depressed. The impedance, Z_{CPE} , of CPE is described by the expression [22]:

$$Z_{CPE} = [Q(j\omega)^n]^{-1} \quad (1)$$

with n and Q constants, that can be used in data fitting when interpreting frequency dispersions. When the value of n is close to 1, the CPE behaves like an ideal capacitance. The equivalent circuit, shown in the Figure 6 was used to fit the experimental data. R_{el} represents the resistance of electrolyte. R is the resistance and Q is the capacitance of the surface oxide film ($n \approx 1$; $Q \approx C$).

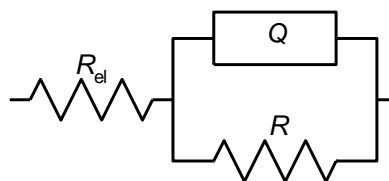


Figure 6. Proposed equivalent circuits for modeling the impedance data

The parameters of the equivalent circuit R_{el} , R and Q were evaluated using a simple least square fit procedure and are presented in Table 2.



18th INTERNATIONAL FOUNDRYMEN CONFERENCE
Coexistence of material science and sustainable technology in
economic growth

Sisak, May 15th-17th, 2019

<http://www.simet.hr/~foundry/>

Table 2. Impedance parameters of investigated CuAlMn alloys in 0.9% NaCl solution

sample	$R_{el} / \Omega \text{ cm}^2$	$Q \times 10^6 / \Omega^{-1} \text{ s}^n \text{ cm}^{-2}$	n_1	$R / \text{k}\Omega \text{ cm}^2$
A	8.31	44.75	0.91	5.24
B	8.04	38.62	0.93	6.53
C	7.78	34.21	0.93	7.18

Increase in Mn content lead to the increase in alloy surface film resistance (R), while the surface layer capacity (Q) decreases. This is attributed to the increase of protective properties of the surface oxide layer on the electrode.

According to the plate capacitor model, the surface film capacity, C , is inversely proportional to its thickness, d (according to $C = \varepsilon_0 \varepsilon / d$; ε_0 is the permittivity of vacuum; and ε the relative permittivity of the film). Hence, the reduction of Q (from 44.75 to 34.21 $\Omega^{-1} \text{ s}^n \text{ cm}^{-2}$), with the increase of Mn content matches the corresponding increase in the thickness of the surface layer, which additionally corresponds to an enhancement in the protective properties of the surface layer. This indicates that Mn (with constant content of Al) increases the stability of oxide layer on the surface and effectively prevents alloy corrosion at E_{OC} .

Properties of the oxide films which are formed on the alloy surfaces primarily depend on the chemical composition of the based metal, i.e. the content of the individual alloying elements in the investigated samples. If the alloying element facilitates alloy passivation, the properties of the oxide film will be better (higher resistance and thickness, more compact structure), which will ultimately increase the corrosion resistance of the metal, i.e. less corrosion currents and greater polarization resistance.

Cu-Al alloys represent the base material for production of copper shape-memory alloys. The role of Al is primarily in reducing weight and increasing corrosion resistance of the alloy. High corrosion resistance of Cu-Al alloys is primarily due to the presence of a protective layer which, according to the data in the literature, has a two layer structure and consists of an inner thin, compact layer (mainly containing Cu_2O and Al_2O_3) and an exterior enriched porous layer [23]. Inner compact layer decelerate the passage of Cu^+ cations and prevent surface alloy dissolution [24,25]. It should be emphasized that Al has an extremely high affinity for oxygen and that Al_2O_3 is one of the most stable oxides found in nature. At standard conditions, Al_2O_3 has more than 11 times high stability over Cu_2O .

However, Cu-Al alloys manufactured by conventional procedures are often very fragile that is related to their large anisotropy and a crushed microstructure [1,2,4]. The microstructure can be affected by micro-alloying and by applying a rapid cooling process (resulting in a large number of limited-diameter crystal chips) [10].

As already noted, the addition of Mn to the binary Cu-Al alloy further increases the corrosion resistance of the alloy (Table 1 and 2). According to literature, addition of Mn in small amounts influences the microstructure of the alloy, i.e. reduces the size of the crystal grain. Specifically, Mn diffuses easily and rapidly disperses through the mass of alloy, and accumulates on the grain boundaries and thus prevents further growth of grain [21,26]. Studies have shown that such refining of microstructures, with the improvement of



18th INTERNATIONAL FOUNDRYMEN CONFERENCE

Coexistence of material science and sustainable technology in
economic growth

Sisak, May 15th-17th, 2019

<http://www.simet.hr/~foundry/>

mechanical properties, significantly increases corrosion resistance of alloys [21]. This fine microstructure positively affects the compactness and stability of the passive oxide film formed on the alloy.

CONCLUSIONS

In this paper, corrosion behavior of different CuAlMn shape memory alloys (Cu-12%Al-4%Mn, Cu-12.3%Al-5.2%-Mn and Cu-12%Al-6%Mn) was studied in 0.9% NaCl solution. From the analysis of the obtained results can be concluded as follows:

- By increasing the Mn content in alloy, the final E_{OC} value becomes more negative.
- Significant differences in corrosion behavior of tested samples at open circuit potential and at high anodic potentials can be noticed by polarization measurements.
- The corrosion resistance of the tested samples at open circuit potential is following the order: Cu-12%Al-4%Mn < Cu-12.3%Al-5.2%Mn < Cu-12%Al-6%Mn. Namely, the corrosion current decreases in same order, while the polarization resistance increases.
- The corrosion resistance of the CuAlMn alloys is a consequence of the oxide layer formation whose properties depend on the Mn content in the samples. Namely, impedance measurements carried out on open circuit potential have shown that Mn facilitates passivation of tested alloys and improve surface film properties (higher resistance and thickness, more compact structure).
- At high anodic potentials (after passing Tafel's region, $E > 0.1$ V), the corrosion rate increases with Mn content in the alloy, and light microscopy investigations reveal pits on the surface of Cu-12.3%Al-5.2%-Mn and Cu-12%Al-6%Mn alloys, while Cu-12%Al-4%Mn surface is almost clear of any corrosion damage.

Acknowledgements

This work was fully supported by the Croatian Science Foundation under the project HRZZ-IP-2014-09-3405.

REFERENCES

- [1] I. Ivanić, M. Gojić, S. Kožuh, Slitine s prisjetljivosti oblika (I. dio): najznačajnija svojstva, Kem. Ind., 63(2014), pp. 323-330.
- [2] I. Ivanić, M. Gojić, S. Kožuh, Slitine s prisjetljivosti oblika (II. dio): podjela, proizvodnja i primjena, Kem. Ind., 63(2014), pp. 331-344.
- [3] M. Čolić, R. Rudolf, D. Stamenković, I. Anžel, D. Vučević, M. Jenko, V. Lazić, G. Lojen, Relationship between microstructure, cytotoxicity and corrosion properties of Cu-Al-Ni shape memory alloy, Acta Biomater., 6(2010), pp. 308-317.



18th INTERNATIONAL FOUNDRYMEN CONFERENCE

Coexistence of material science and sustainable technology in
economic growth

Sisak, May 15th-17th, 2019

<http://www.simet.hr/~foundry/>

- [4] S. Sathish, U. S. Mallik, T. N. Raju, Microstructure and shape memory effect of Cu-Zn-Ni shape memory alloys, *JMMCE*, 2(2014), pp. 71-77.
- [5] A. K. Jain, S. Hussain, P. Kumar, A. Pandey, Effect of varying Al/Mn ratio on phase transformation in CuAlMn shape memory alloys, *Trans. Indian Inst. Met.*, 69(2016), pp. 1289-1295.
- [6] S. Shabalovskaya, J. Anderegg, J. Van Humbeeck, Critical overview of nitinol surfaces and their modifications for medical applications, *Acta Biomater.*, 4(2008), pp. 447-467.
- [7] S. Kožuh, L. Vrsalović, M. Gojić, S. Gudić, B. Kosec, Comparison of the corrosion behavior and surface morphology of NiTi alloy and stainless steels in sodium chloride solution, *J. Min. Metall. Sect. B-Metall.*, 52(2016), pp. 53-61.
- [8] U. S. Mallik, V. Sampath, Influence of aluminium and manganese concentration on the shape memory characteristics of Cu-Al-Mn shape memory alloys, *J. Alloy Compd.*, 459(2008), pp. 142-147.
- [9] A. O. Moghaddam, M. Ketabchi, R. Bahrami, Kinetic grain growth, shape memory and corrosion behavior of two Cu-based shape memory alloys after thermomechanical treatment, *Trans. Nonferrous Mat. Soc. China*, 22(2013), pp. 2896-2904.
- [10] K. K. Alaneme, E. A. Okotete, M. O. Bodunrin, Microstructural analysis and corrosion behavior of Fe, B, and Fe-B-modified Cu-Zn-Al shape memory alloys, *Corros. Rev.*, 35(2017), pp. 3-11.
- [11] S. Kožuh, M. Gojić, I. Ivanić, T. Holjevac Grgurić, B. Kosec, I. Anžel, The effect of heat treatment on the microstructure and mechanical properties of Cu-Al-Mn shape memory alloy, *Kem. Ind.*, 67(2018), pp. 11-17.
- [12] M. R. Rezvani, A. Shokuhfar, Synthesis and characterization of nano structured Cu-Al-Mn shape memory alloy by mechanical alloying, *Mater. Sci. Eng. A*, 532(2012), pp. 282-286.
- [13] U. S. Mallik, V. Sampath, Influence of quaternary alloying additions on transformation temperatures and shape memory properties of Cu-Al-Mn shape memory alloy, *J. Alloys Comp.*, 469(2009), pp. 156-163.
- [14] J. Chen, Z. Li, Y. Y. Zhao, A high-working-temperature CuAlMnZr shape memory alloy, *J. Alloys Comp.*, 480(2009), pp. 481-484.
- [15] H. Morawiec, J. Lełątko, D. Stróż, M. Gigla, Structure and properties of melt-spun Cu-Al-Ni shape memory alloys, *Mat. Sci. Eng. A*, 273-275(1999), pp. 708-712.
- [16] M. Izadinia, K. Dehghani, Structure and properties of nanostructured Cu-13.2Al-5.1Ni shape memory alloy produced by melt spinning, *Trans. Nonferrous Met. Soc. China*, 21(2011), pp. 2037-2043.
- [17] G. Lojen, I. Anžel, A. Kneissl, A. Križman, E. Unterweger, B. Kosec, M. Bizjak, Microstructure of rapidly solidified Cu-Al-Ni shape memory alloy ribbons, *J. Mater. Process. Technol.*, 162-163(2005), pp. 220-229.
- [18] R. Kainuma, S. Takahashi, K. Ishida, Thermoelastic martensite and shape memory effect in ductile Cu-Al-Mn alloys, *Metal. Mater. Trans.*, 27(1996), pp. 2187-2195.
- [19] L. Vrsalović, E. Oguzie, M. Kliškić, S. Gudić, Corrosion inhibition of CuNi10Fe alloy with phenolic acids, *Chem. Eng. Comm.*, 198(2011), pp. 1380-1393.



18th INTERNATIONAL FOUNDRYMEN CONFERENCE

Coexistence of material science and sustainable technology in
economic growth

Sisak, May 15th-17th, 2019

<http://www.simet.hr/~foundry/>

- [20] L. Vrsalović, M. Matulić, S. Kožuh, I. Ivanić, M. Gojić, Effect of pH on corrosion of CuAlMn alloy in 0.9% NaCl solution, Proceedings of the MTSM 2017, (S. Jozić, B. Lela), Croatian society for mechanical technologies, 21.-22. September, 2017., Split, Croatia, 159-163.
- [21] S. N. Saud, E. Hamzah, T. Abubakar, H. R. Bakhsheshi-Rad, Correlation of microstructural and corrosion characteristics of quaternary shape memory alloys Cu-Al-Ni-X (X=Mn or Ti), Trans. Nonferrous Met. Soc. China, 25(2015), pp. 1158-1170.
- [22] D. D. Raistrick, J. R. Macdonald, D. R. Franceschetti, in: J. R. Macdonald (Ed.), Impedance Spectroscopy, J. Wiley & Sons, New York, 1987.
- [23] W. A. Badawy, M. El-Rabeiee, N. H. Hilal, H. Nady, Electrochemical behavior of Mg and some Mg alloys in aqueous solutions of different pH, Electrochim. Acta, 55(2010), pp. 1880-1887.
- [24] H. Nady, N. H. Hilal, M. M. Rabeiee, W. A. Badawy, The role of Ni content on the stability of Cu-A-Ni ternary alloy in neutral chloride solutions, Mater. Chem. Phys., 134(2012), pp. 945-950.
- [25] W. A. Badawy, M. El-Rabeiee, N. H. Hilal, H. Nady, Effect of nickel content on the electrochemical behavior of Cu-A-Ni alloys in chloride free neutral solutions, Electrochim. Acta, 56(2010), pp. 913-918.
- [26] G. N. Sure, L. C. Brown, The mechanical properties of grain refined β -CuAlNi strain memory alloys, Metall. Trans. A, 15A(1984), pp. 1613-1621.



18th INTERNATIONAL FOUNDRYMEN CONFERENCE

Coexistence of material science and sustainable technology in
economic growth

Sisak, May 15th-17th, 2019

<http://www.simet.hr/~foundry/>

MICROSTRUCTURAL ANALYSIS OF COLD DRAWN CuAlMn SHAPE MEMORY ALLOY WIRE

Ivana Ivanić^{1*}, Stjepan Kožuh¹, Nikolina Pavičić², Dijana Čubela³, Omer Beganović⁴, Borut
Kosec⁵, Mirko Gojić¹

¹ University of Zagreb Faculty of Metallurgy, Sisak, Croatia

² Master degree student at University of Zagreb Faculty of Metallurgy, Sisak, Croatia

³ University of Zenica Faculty of Metallurgy and Technology, Zenica, Bosnia and Herzegovina

⁴ University of Zenica Metallurgical Institute Kemal Kapetanović, Zenica, Bosnia and Herzegovina

⁵ University of Ljubljana Faculty of Natural Sciences and Engineering, Ljubljana, Slovenia

Poster presentation

Original scientific paper

Abstract

The Cu-11.9Al-2.5Mn (wt. %) shape memory alloy was produced by vertically continuous casting technique obtaining bars of 8 mm in diameter which is applicable for plastic deformation. With the process of hot rolling and forging the 4.80 mm bar was produced. Afterwards, the obtained 4.80 mm bar was subjected to cold drawing process. After first run and after fourth run of cold drawing process the wire with diameter of 4.47 mm and 3.22 mm was produced, respectively. Optical microscopy (OM) and scanning electron microscopy (SEM) equipped with energy dispersive spectroscopy (EDS) shown the insight in the samples microstructure. The as-cast state sample has two phase ($\alpha+\beta$) microstructure. After cold working process the two-phase (martensite+ α) microstructure appears. As the result of the cold working process it can be noticed a texture inside the sample depending on cold drawing direction. The microhardness of samples increases as the wires diameter decreases.

Keywords: CuAlMn wire, shape memory alloy, microstructure, hot working, cold working

*Corresponding author (e-mail address): iivanic@simet.hr

INTRODUCTION

Cooper based shape memory alloys (SMAs) are very interesting material for industrial application due to its good shape memory effect (SME), relatively low cost, good machinability and damping capacity in comparison to the properties that NiTi alloy obtain.



18th INTERNATIONAL FOUNDRYMEN CONFERENCE

Coexistence of material science and sustainable technology in
economic growth

Sisak, May 15th-17th, 2019

<http://www.simet.hr/~foundry/>

Its excellent thermal stability and very high martensite transformation temperature makes them rapidly become one of the most promising high temperature shape memory alloys [1,2].

CuZnAl and CuAlNi shape memory alloys have been extensively investigated due to its previously mentioned properties. However, these shape memory alloys are too brittle for cold working because of coarse grain structure and high elastic anisotropy [3]. The large grain size problem can be solved by using grain size refinements (as titanium and boron for example) or production by rapid solidification techniques. This type of production ensures shaping and forming procedures easier [4-6]. Mechanical properties improvement, preferably meaning ductility, can be provided by adding alloying elements and by heat treatment as well [7].

Addition of manganese to binary CuAl alloy can significantly improve alloys properties by stabilizing the bcc phase, widening the single β -phase region to lower temperatures and improving ductility in low Al alloys (less than 18 at. %) [8,9]. The austenitic β -phase arranged to the lower order system β_1 (L21; Cu₂AlMn) and martensitic phase stabilization of unstable β'_3 (18R) to stable γ'_3 (2H) ratio can be adjusted by quenching and the amount of aluminium (Al) and manganese (Mn) [10].

The CuAlMn alloys exhibit shape memory effect and superelasticity based on cubic β_1 (L21) to monoclinic β_1' (6M) martensitic transformation. The shape memory characteristics (superelasticity and shape memory effect) of CuAlMn SMAs can be enhanced by the addition of alloying elements and the application of microstructure control achieved by thermomechanical treatment. It has been reported that those characteristics strongly depend on grain size and the development of texture [11]. Some investigations have been demonstrated that low thermal expansion can be obtained in CuAlMn shape memory alloys by controlling stress-induced martensitic transformation due to cold-rolling [8,11].

Due to the fact that CuAlMn shape memory alloy possesses significant ductility the aim of this paper is to produce a ductile CuAlMn shape memory alloy wire for possible industrial application with favorable microstructural properties by hot/cold plastic deformation process.

MATERIALS AND METHODS

Copper-based SMA with the nominal composition of Cu-11.9Al-2.5Mn (wt. %) was prepared in a vacuum induction furnace. The bar of 8 mm in diameter (Figure 1) was obtained and it was used for hot/cold plastic deformation process to obtain wire. Firstly, the bar was subjected to hot working process which was performed by a combination of hot rolling and hot forging. The forging was performed as free forging and forging in a profiled tool (Figure 2). The obtained bar after first run of rolling and forging was presented at Figure 3. The forging and rolling procedures were performed alternately till the cross section of the bar was 4.80 mm. Afterwards, the obtained bars were taken to recrystallization annealing at 580 °C for 60 minutes. After annealing, surface of the samples is brushed for elimination of possible surface defects propagation during cold working process. After first run of cold



18th INTERNATIONAL FOUNDRYMEN CONFERENCE
Coexistence of material science and sustainable technology in
economic growth

Sisak, May 15th-17th, 2019

<http://www.simet.hr/~foundry/>

drawing the wire with diameter of 4.47 mm was obtained. Followed by three more runs the wire with \varnothing 4.02 mm, 3.61 mm and 3.22 mm was produced. Between last two runs (\varnothing 3.61 mm and 3.22 mm) the recrystallization annealing at 580 °C for 60 minutes was performed. The exact procedure of plastic deformation process can be seen in Table 1. Samples selected for investigation were in as-cast state (Figure 1) and after cold working process with dimensions \varnothing 4.47 mm and \varnothing 3.22 mm (Figure 4), marked bold and underlined in the Table 1. Insight into samples microstructure was obtained by optical microscopy (OM) equipped with digital camera and scanning electron microscopy (SEM) along with energy dispersive x-ray spectroscopy (EDS). The alloys hardness was determined by Vickers method.



Figure 1. Photograph of CuAlMn shape memory alloy bar \varnothing 8 mm after casting

Table 1. Procedure of plastic deformation process on CuAlMn SMA bars

Deformation process	Dimensions (mm)	Schematic illustration of crosssection
Sample in as-cast state		
HOT WORKING PROCESS - hot rolling and forging		
Hot rolling (880 – 900 °C) 2 runs	6.10x8.50	
Hot forging (880 – 900 °C) in a profiled tool	Square side length 6.00	
Hot rolling (880 – 900 °C) 1 run	4.50x9.50	
Hot forging (880 – 900 °C) in a profiled tool	Square side length 5.20	
Hot rolling (880 – 900 °C) 1 run	4.00x8.70	
Hot forging (880 – 900 °C) in a profiled tool	Square side length 4.60	
Hot forging (880 – 900 °C) in a profiled tool	Square side length 4.80	
COLD WORKING PROCESS - cold drawing		
Cold drawing	\varnothing 4.47	
Cold drawing	\varnothing 4.02	
Cold drawing	\varnothing 3.61	
Annealing at 580 °C/60'		
Cold drawing	\varnothing 3.22	



18th INTERNATIONAL FOUNDRYMEN CONFERENCE
**Coexistence of material science and sustainable technology in
economic growth**

Sisak, May 15th-17th, 2019

<http://www.simet.hr/~foundry/>

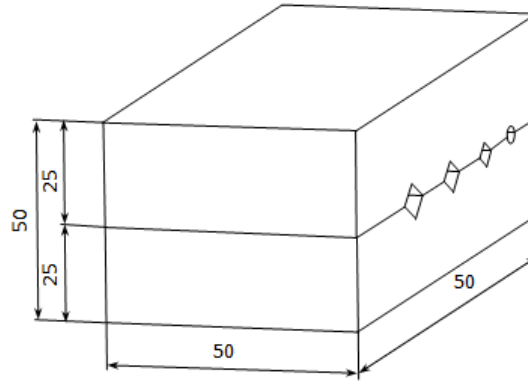


Figure 2. Schematic illustration of a profiled forging tool



Figure 3. Photograph of CuAlMn shape memory alloy bar after first run of hot rolling and forging



Figure 4. Photograph of CuAlMn shape memory alloy wire \varnothing 4.47 mm (a) and \varnothing 3.22 mm (b)

RESULTS AND DISCUSSION

By hot and cold plastic deformation process CuAlMn shape memory alloy wire was successfully produced. The ductility as a useful property of this copper based shape memory alloy enables exhibition of better pseudoelasticity and therefore better hot or cold workability. It has been reported [8-11] that alloying additions play a very significant role in the properties of Cu-based shape memory alloys and required properties can be achieved by proper designing/selection of the alloying elements.

Figure 5 and 6 shows results of metallographic analysis by OM and SEM method of CuAlMn selected samples.

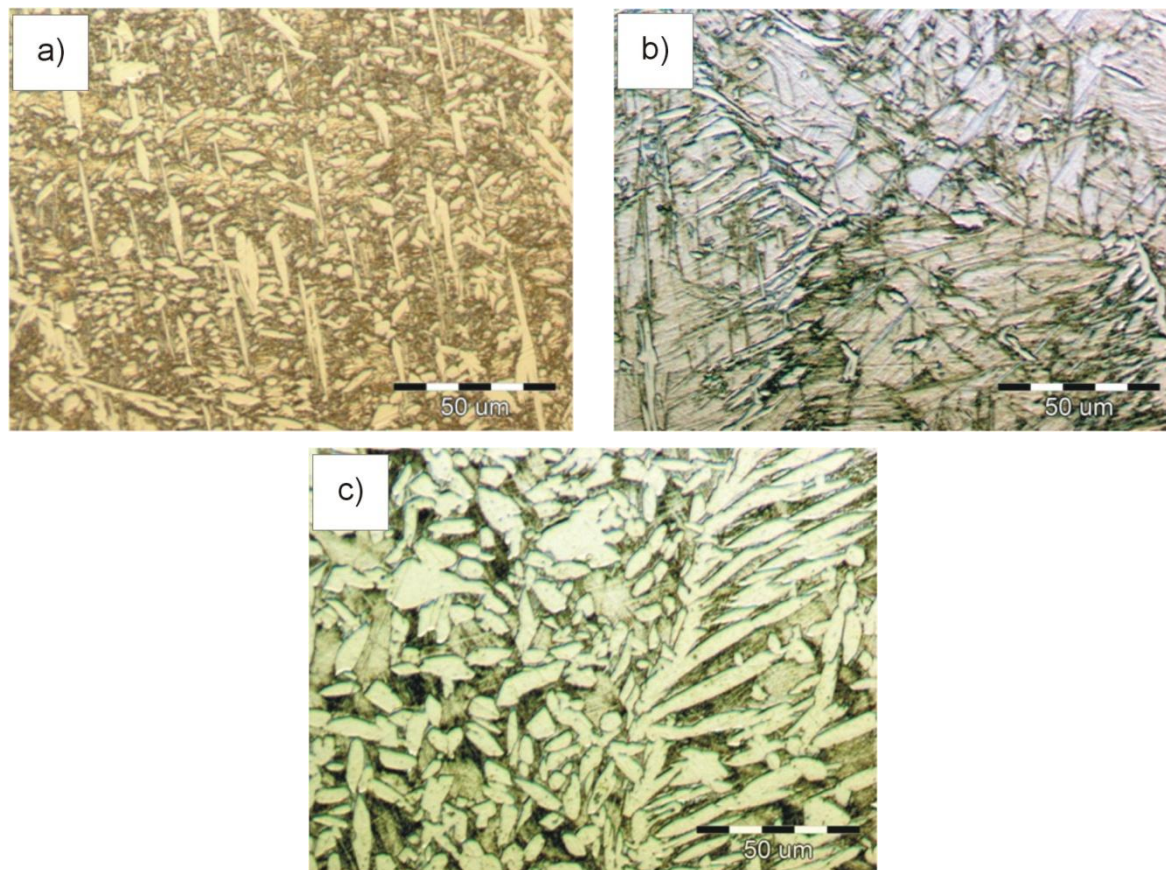


Figure 5. Optical micrographs of CuAlMn SMA in as-cast state (a), after cold drawing: \varnothing 4.47 mm (b), \varnothing 3.22 mm (c)

As can be seen, the CuAlMn as-cast bar has two-phase ($\alpha+\beta$) microstructure (Figure 5a and 6a). It is known that in vertical section of phase diagram of Cu-Al-10 at.% Mn the single phase region is broadened by addition of Mn and $\alpha+\beta$ microstructure exists [12]. Grain structure with $\alpha+\beta$ phases a prerequisite for martensite formation after quenching. This clearly indicates that all the alloys have potential to exhibit the shape memory behaviour [13].

The influence of plastic deformation process can be seen on microstructures at the obtained \varnothing 4.47 mm and \varnothing 3.22 mm wires after cold working (Figure 5b, 5c, 6b and 6c). In both cases after cold working process the martensite appears in some places inside the microstructure. Considering that the β phase exists in the alloy in as-cast state, during plastic deformation process transforms into the martensite, probably came to appearance of stress-induced martensite. The stress induced martensite transformation occurs during loading under the almost constant stress [14].



18th INTERNATIONAL FOUNDRYMEN CONFERENCE
**Coexistence of material science and sustainable technology in
economic growth**

Sisak, May 15th-17th, 2019

<http://www.simet.hr/~foundry/>

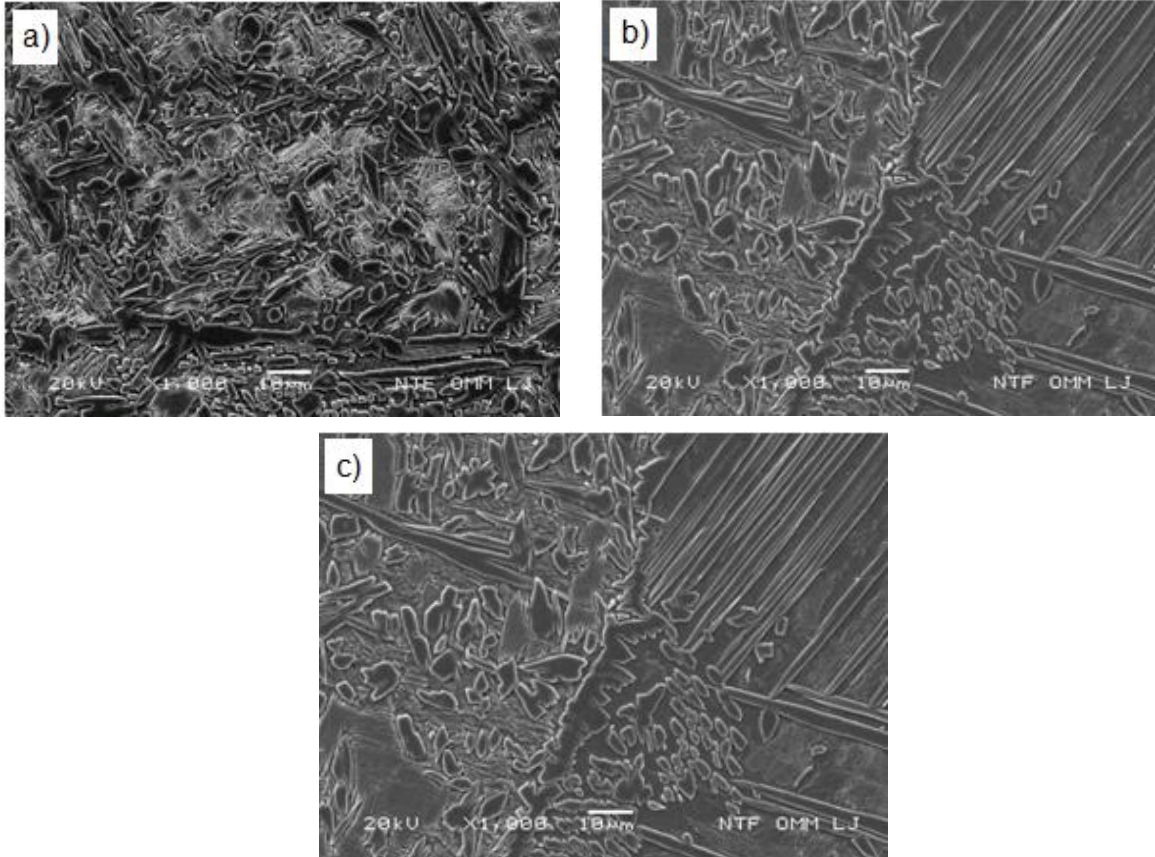


Figure 6. SEM micrographs of CuAlMn SMA in as-cast state (a), after cold drawing: \varnothing 4.47 mm (b), \varnothing 3.22 mm (c)

Figures 7 and 8 shows SEM micrographs along with the marked positions for EDS analysis of CuAlMn wire \varnothing 4.47 mm and \varnothing 3.22 mm, respectively. The results of the EDS analysis for cold drawn wire with diameter \varnothing 4.47 mm show the difference between position 1 which shows higher amount of aluminum (7.45 wt.%) in comparison to positions 2 and 3 with amount of aluminum of (5.30 and 5.03 wt. %), Figure 7 and Table 2. Similar composition difference is noticed for wire with \varnothing 3.22 mm, Figure 8 and Table 3. The difference between positions 1 and 2 has higher amount of aluminum (6.93 and 6.76 wt. %) in comparison to position 3 with amount of aluminum of (4.92 wt. %). It can be assumed that the aluminum enriched phase presents α phase. Sutou et al. [2] reported existence of two-phase microstructure (martensite + α) in Cu-Al-Mn-Ni-Si alloy after heat treatment at 850 °C. Due to the fact that the samples between the cold drawing runs were heat treated at 580 °C/60 minutes, the martensite + α microstructure is possible.



18th INTERNATIONAL FOUNDRYMEN CONFERENCE
Coexistence of material science and sustainable technology in
economic growth

Sisak, May 15th-17th, 2019

<http://www.simet.hr/~foundry/>

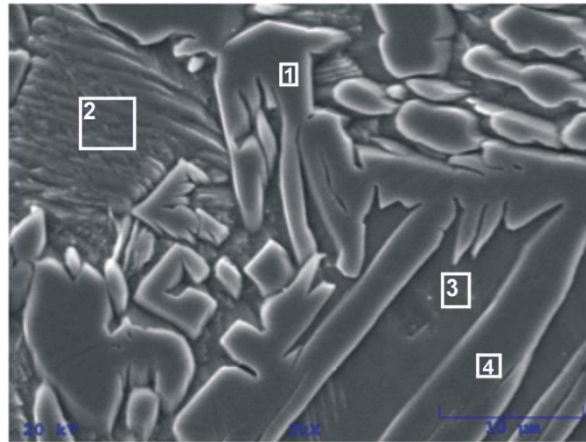


Figure 7. SEM micrograph of CuAlMn SMA wire ϕ 4.47 mm

Table 2. Chemical composition of CuAlMn SMA wire ϕ 4.47 mm positions marked at the Fig.7, wt. %

	Cu	Al	Mn
Position 1	82.74	7.45	9.81
Position 2	86.27	5.30	8.43
Position 3	86.47	5.03	8.50
Position 4	86.16	5.17	8.68

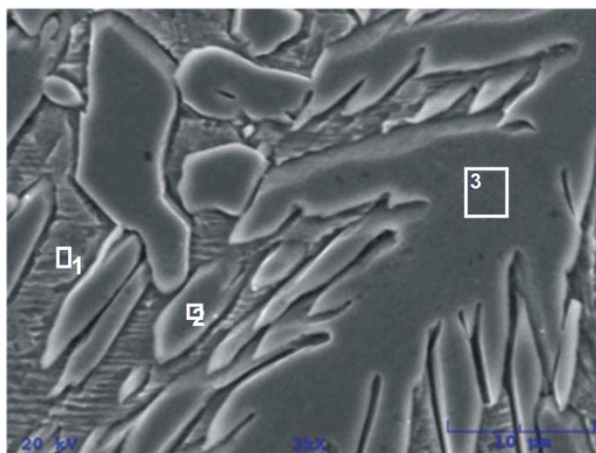


Figure 8. SEM micrograph of CuAlMn SMA wire ϕ 3.22 mm



18th INTERNATIONAL FOUNDRYMEN CONFERENCE
Coexistence of material science and sustainable technology in
economic growth

Sisak, May 15th-17th, 2019

<http://www.simet.hr/~foundry/>

Table 3. Chemical composition of CuAlMn SMA wire ϕ 3.22 mm positions marked at the Figure 8, wt. %

	Cu	Al	Mn
Position 1	82.66	6.93	10.41
Position 2	83.17	6.76	10.09
Position 3	86.63	4.92	8.45

The hardness values of the investigated samples are given as mean value of three measurements and the results can be seen at Figure 9. It is obvious that the hardness of the alloy increases through the process of cold drawing. The hardness of the alloy in as-cast state was 268 HV 0.05. Increase in alloys hardness is noticed for wire with ϕ 4.47 mm (318 HV 0.05) and for wire with ϕ 3.22 mm (341 HV 0.05), respectively.

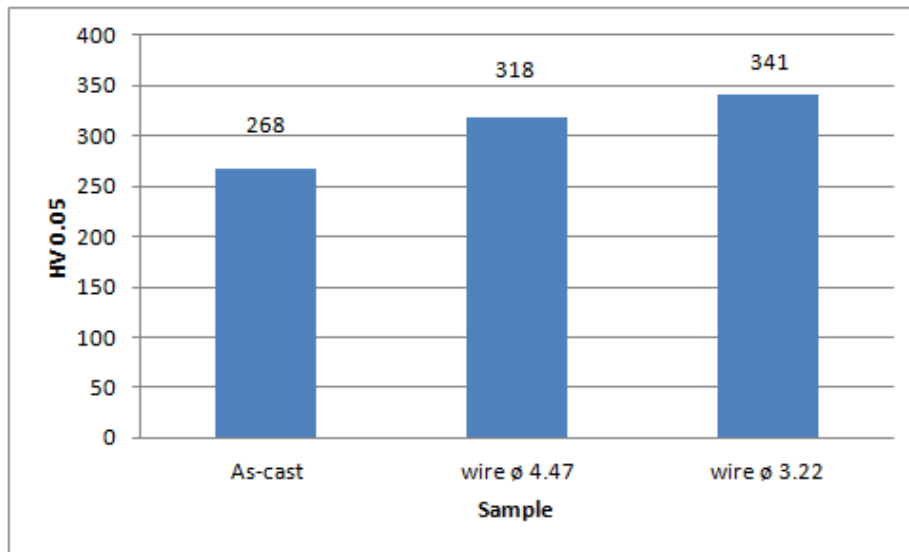


Figure 9. Hardness of CuAlMn shape memory alloy before and after cold working process

CONCLUSIONS

With hot and cold plastic deformation process it was successfully produced the CuAlMn shape memory wire with ϕ 4.47 mm and ϕ 3.22 mm in diameter from continuously casted ϕ 8mm CuAlMn shape memory alloy bar. From the results of microstructural characterization and hardness measurements can be withdrawn following conclusions:

- From the optical and SEM micrographs obtained grain structure with $\alpha+\beta$ phases is visible in the as-cast condition of the CuAlMn shape memory alloy. This



18th INTERNATIONAL FOUNDRYMEN CONFERENCE

Coexistence of material science and sustainable technology in
economic growth

Sisak, May 15th-17th, 2019

<http://www.simet.hr/~foundry/>

microstructure is a prerequisite for martensite formation after quenching indicating that the alloy has potential to exhibit the shape memory behaviour.

- In some places the martensite formation is observed in CuAlMn alloy wires (\varnothing 4.47 mm and \varnothing 3.22 mm) produced by cold drawing process. During hot and cold working process appear favorable conditions for appearance of stress induced martensite.
- The results of EDS analysis for cold drawn wires with diameter \varnothing 4.47 mm and \varnothing 3.22 mm shows the difference between the positions enriched with aluminum content indicating the existence of the α phase in the microstructure.
- The hardness of the alloy increases through the process of cold drawing from 268 HV 0.05 in as-cast state to 318 HV 0.05 wire with \varnothing 4.47 mm and 341 HV 0.05 for wire with \varnothing 3.22 mm.

REFERENCES

- [1] Q. Wang, F. Han, C. Cui, S. Bu, L. Bai, Effect of ageing on the reverse martensitic phase transformation behaviors of a CuAlMn shape memory alloy, *Materials Letters* 61(2007), pp. 5185-5187.
- [2] Y. Sotou, N. Koeda, T. Omori, R. Kainuma, K. Ishida, Effects of aging on stress-induced martensitic transformation in ductile Cu-Al-Mn – based shape memory alloys, *Acta Materialia*, 57(2009), pp. 5759-5770.
- [3] T. Omori, N. Koeda, Y. Sotou, R. Kainuma, K. Ishida, Superplasticity of Cu-Al-Mn-Ni shape memory alloy, *Materials Transactions*, 48(2007)11, pp. 2914-2918.
- [4] C. E. Sobrero, P. La Roca, A. Roatta, R. E. Bolmaro., J. Malarría, Shape memory properties of highly textured Cu-Al-Ni-(Ti) alloys, *Materials Science and Engineering A*, 536(2012), pp. 207-215.
- [5] I. Ivanić, M. Gojić, I. Anžel, S. Kožuh, M. Rimac, O. Beganović, K. Begović, B. Kosec, Microstructure and properties of casted CuAlNi and CuAlNiMn shape memory alloys, *Proceedings Book 13th International Foundrymen Conference*, (eds. Z. Glavaš, Z. Zovko Brodarac, N. Dolić), University of Zagreb Faculty of Metallurgy, 2013, Sisak, Croatia, pp. 153-162.
- [6] Z. Wang, X. F. Liu, J. X. Xie, Effects of solidification parameters on microstructure and mechanical properties of continuous columnar-grained Cu-Al-Ni alloy, *Progress in Natural Science: Materials International*, 21(2011), pp. 368-374.
- [7] U. Sari, T. Kirindi, Effects of deformation on microstructure and mechanical properties of a Cu-Al-Ni shape memory alloy, *Materials Characterization*, 59(2008), pp. 920-929.
- [8] Y. Sutou, T. Omori, R. Kainuma, K. Ishida, Ductile Cu-Al-Mn based shape memory alloys: General properties and applications, *Materials Science and Technology*, 24(2008)8, pp. 896-901.
- [9] U. S. Mallik, V. Sampath, Effect of composition and ageing on damping characteristics of Cu-Al-Mn shape memory alloys, *Materials Science Engineering A*, 478(2008), pp. 48-55.



18th INTERNATIONAL FOUNDRYMEN CONFERENCE

**Coexistence of material science and sustainable technology in
economic growth**

Sisak, May 15th-17th, 2019

<http://www.simet.hr/~foundry/>

- [10] U. Arlica, H. Zak, B. Weidenfeller, W. Riehemann, Impact of alloy composition and thermal stabilization on martensitic phase transformation structures in CuAlMn shape memory alloys, *Materials Research*, 21(2018), pp. 1-6.
- [11] Y. Sutou, T. Omori, J.J. Wang, R. Kainuma, K. Ishida, Characteristics of Cu–Al–Mn-based shape memory alloys and their applications, *Materials Science and Engineering A*, 378(2004), pp. 278-282.
- [12] Y. Sutou, T. Omori, R. Kainuma, N. Ono, K. Ihida, Enhancement of superelasticity in Cu-Al-Mn-Ni shape-memory alloys by texture control, *Metallurgical and Materials Transactions A*, 33(2002), pp. 2817-2824.
- [13] M. Reza Rezvani, A. Shokuhfar, Synthesis and characterization of nano structured Cu-Al-Mn shape memory alloy by mechanical alloying, *Materials Science and Engineering A*, 532(2012), pp. 282-286.
- [14] H. Sakamoto, Distinction between thermal and stress-induced martensitic transformations and inhomogeneity in internal stress, *Materials Transactions*, 43(2002)9, pp. 2249-2255.



18th INTERNATIONAL FOUNDRYMEN CONFERENCE

Coexistence of material science and sustainable technology in
economic growth

Sisak, May 15th-17th, 2019

<http://www.simet.hr/~foundry/>

THE IMPACT OF MULTIWALL CARBON NANOTUBES ON THE PHOTOCATALYTIC PROPERTIES OF IMOBILIZED TiO₂

Igor Jajčinović^{1*}, Ivan Brnardić¹, Stjepan Kožuh¹, Kristina Tolić²

¹ University of Zagreb Faculty of Metallurgy, Sisak, Croatia

² University of Zagreb Faculty of Chemical Engineering and Technology, Zagreb, Croatia

Poster presentation

Preliminary note

Abstract

Industry development, Earth's population growth, ever increasing need for greater pharmaceuticals production causes irreversible changes in the environment. Photocatalysis is a process that leads to complete decomposition of pharmaceuticals to non-hazardous degradation products under the influence of solar radiation in the presence of a photocatalyst. A photocatalyst, such as titanium dioxide (TiO₂), is required for photocatalysis. The efficiency of using TiO₂ is limited due to the high energy banned zone (3-3.2 eV) so only UV-A light, which makes up 5% of solar radiation, activates the photocatalyst. In order to overcome the problem of prohibited zones and to shift the light response threshold of TiO₂ into the visible part of the spectrum, different methods can be used. One of the methods showing the potential is the use of multiwall carbon nanotubes (MWCNT).

In this paper a TiO₂ / MWCNT composites with various concentrations of MWCNT were prepared. The concentrations of MWCNT ranged from 1.5, 5, 10, 25, 50 and 100 wt. % MWCNT relative to the mass of TiO₂. It was observed that the concentration of MWCNT affects the photocatalytic activity of the composite obtained. Photocatalytic activity was followed by a degradation of salicylic acid, in a pilot reactor followed by UV-VIS spectrometry, as a modal solution and an example of a pharmaceuticals present in the water. The prepared catalysts were characterized by scanning electron microscopy (SEM) equipped with an energy dispersive X-ray spectroscopy (EDX).

Keywords: photocatalysis, TiO₂, multiwall carbon nanotubes

*Corresponding author (e-mail address): ijajcinovic@simet.hr



18th INTERNATIONAL FOUNDRYMEN CONFERENCE

Coexistence of material science and sustainable technology in
economic growth

Sisak, May 15th-17th, 2019

<http://www.simet.hr/~foundry/>

INTRODUCTION

Environmental pollution and destruction are very serious problems [1]. Quality of water available for human use is increasingly deteriorated due to anthropogenic activities. Much of the pharmaceuticals used for treatment or as dietary supplements are not fully metabolized in the human body, and the vast majority of these endpoints end up in the environment. It has been found that pharmaceuticals are present in waste water after treatment also found in lakes and rivers, groundwater and drinking water. Except for wastewater, pharmaceuticals can enter the environment in a variety of ways, including disposal of unused medicines, waste disposal sites, veterinary use and fertilizer application and waste sludge from the wastewater treatment process in agriculture [2]. Conventional drinking water preparation techniques utilize physical-chemical processes to eliminate pathogens, reduce turbidity, and control taste and odor problems. These processes have a partial impact on reducing the contamination of micropollutant in ready to drink water, but incomplete, need to find new economically viable methods [3]. Two process of purification of micropollutants are used in the industrial process, which, due to their cost, requires finding new cheaper solutions. One of the solutions is an advanced oxidation process of photocatalysis where complete degradation of pollutions. Photocatalysts are used for this purpose and one of the most common is titanium (IV) oxide (TiO_2) due to their low cost, chemical and thermal stability, low toxicity and relatively high catalytic activity [4-6]. UV radiation of TiO_2 photocatalysts create hydroxyl radicals, $\bullet\text{OH}$ [7] which, as non-selective oxidants, with its oxidation potential almost completely degrade the organic matter into water and CO_2 [8,9]. Because of that fact, TiO_2 photocatalysis has recently found application to wastewater treatment [10]. Although TiO_2 is most often used in suspended form, the catalyst immobilization is considered to be more useful for easier removal of TiO_2 from the system and the ability to reuse the immobilized catalyst [11]. The efficiency of using TiO_2 is limited due to the high energy banned zone (3-3.2 eV) which causes only UV-A lights, which makes up 5 % of solar radiation to activate the photocatalyst. In order to overcome the problem of banned zones and to shift the light response threshold of TiO_2 into the visible part of the spectrum, different methods can be used. One way is to use chemical methods such as coupling with secondary semiconductors, photosensitizing and doping with transitional metals (Au, Pd, Pt, Rh) or non-metallic elements (N, S, I, F). Another way is to use physical methods such as introducing microwave or ultrasonic radiation into the photocatalysis process. The method of catalyzing the activity of the catalyst for which the scientists show an increasing interest is the use of carbon nanotubes, multiwall nanotube (MWCNT) and graphene. Significant efforts are directed towards obtaining TiO_2 / carbon nanotubes and TiO_2 / graphene composite materials. For the synthesis of the composite, the sol-gel process, the physical mixing technique and the nano-application can be used [12-14]. In this paper a TiO_2 / MWCNT composites with various concentrations of MWCNT were prepared with sol-gel method. The photocatalytic properties and morphology of the immobilized layer of the photocatalyst will be determined.



18th INTERNATIONAL FOUNDRYMEN CONFERENCE

Coexistence of material science and sustainable technology in
economic growth

Sisak, May 15th-17th, 2019

<http://www.simet.hr/~foundry/>

MATERIALS AND METHODS

Multiwall carbon nanotubes (MWCNT), Chengdu Organic Chemicals, P.R. China with outer diameter of 10 – 30 nm, TiO₂, Aeroxide® P25, Evonik, Germany, tetraethoxysilane (TEOS), VWR Cemical, USA, acetic acid from VWR Chemicals, France, salicylic acid (SA), Kemika Croatia and ethanol, GramMol, Croatia used as received. As a carrier the glass mesh from Keltex, Croatia (CM 300/300, $\rho = 610 \text{ g / m}^2$) was purchased.

TiO₂ and MWCNT is applied to the glass mesh using sol-gel method, for the preparation of the immobilized layer. Glass meshes are cut into the reactor's dimension and weighed. The suspension from which TiO₂ and MWCNT is applied to the glass mesh is prepared by mixing TiO₂ and MWCNT with distilled water and ethanol (water: ethanol = 1 : 1) on a magnetic stirrer. Six different solutions with different concentrations of MWCNT were produced. The concentrations of MWCNT ranged from 1.5, 5, 10, 25, 50 and 100 wt. % MWCNT relative to the mass of TiO₂. The pH of the suspension was adjusted by adding acetic acid with stirring to pH 1.5-2. After achieving the desired pH, the suspension was mixed for a period of 15 minutes, after which the homogenization was performed with ultrasound for 6 minutes (ultrasonic bath 120W, frequency 40 kHz). After homogenization, TEOS was added and further stirred over a period of 60 minutes at a temperature of 50 °C. Glass mesh is immersed in the prepared suspension and dried. Drying was carried out in a 70 °C drier for 30 minutes. The immersion and drying procedure was repeated 4 times. Schematic illustration of preparing immobilized layer on glass mesh is show on Figure 1. The prepared glass meshes were left in air for 7 days, after which they were washed with distilled water, dried and weighed to determine the mass of the applied layer. Clean meshes and meshes with TiO₂ / MWCNT obtained by the described procedure were recorded by scanning electron microscope (SEM, TESCAN VEGA 5136MM) operated at 20kV. The presence of TiO₂ and/or MWCNT on fiber glass mesh was determined by using energy dispersion spectroscopy (EDX) mapping analysis. For mapping analysis SEM microscope was operating at 20 kV while working distance was set at 20 mm. Mesh for SEM / EDX analysis were previously fixed to the carrier using double-sided self-adhesive carbon-guided stripes and a gold-platinum layer. The photocatalytic properties of the catalyst were investigated through the degradation of salicylic acid in the prepared 0.2 mmol / dm³ model solution. The UV-VIS spectrophotometer (Perkin Elmer LAMBDA 35, 200-700 nm with a recording speed of 480 nm / min) was used to monitor the photocatalytic degradation reaction. Tests for photocatalytic properties were carried out in a batch pilot photoreactor of rectangular geometry (size 4.5 x 17.5 cm) with recirculation with peristaltic pumps with a flow rate of 48 cm³ / min. The source of the simulated solar radiation (UV-B 2% / 13 W) is placed 7 cm above the surface of the reaction solution and is covered with a shadow / reflective surface of Al-sheet in order to evenly illuminate the reactor space.

The immobilized photocatalyst meshes was placed at the bottom of the reactor and a model solution of SA 100 cm³ was added. At the beginning of the procedure, a sample of SA 2 cm³ was taken, after which the reactor was left in the dark for 30 minutes and the sampling was repeated. At the end of the phase in the dark, the source of the simulated solar radiation was included, and the samples were taken periodically 15, 30, 60, 90 minutes. Also, tests of a

blank probe without a catalyst, that is, the influence of light radiation on the potential photolysis of salicylic acid, were conducted.

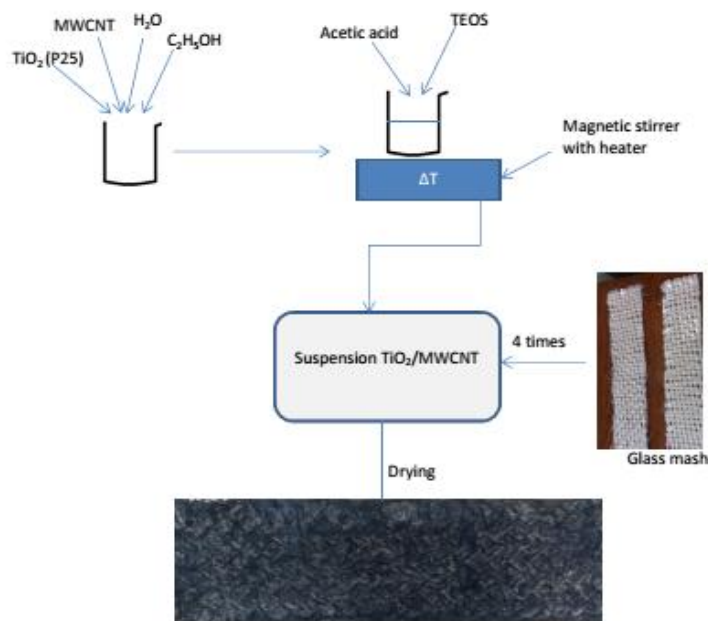


Figure 1. Schematic illustration of immobilization TiO_2 / MWCNT on glass mesh

RESULTS AND DISCUSSION

To demonstrate the immobilized of TiO_2 and TiO_2 / MWCNT composite on the surface of glass mesh samples were recorded with SEM (Figure 2) after photocatalysis.

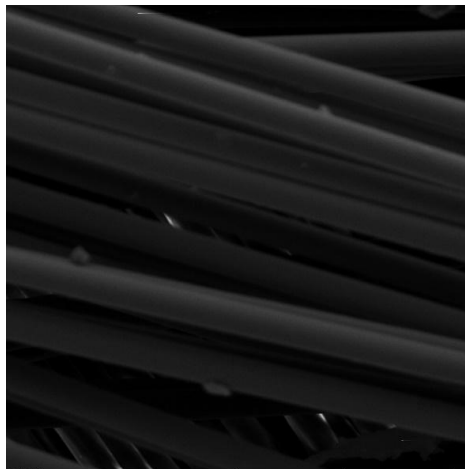
Comparing Figures 2a, 2b and 2c it can be concluded that TiO_2 and TiO_2 / MWCNT immobilization on glass mesh with sol-gel methods was successful. Furthermore, from Figures 2b and 2c it can be seen that particles are of similar size. The presence of TiO_2 / MWCNT was determined by EDX analysis on the glass meshes after immobilization. Results of EDX analysis showed on Figure 3. On Figures 3b it can see results EDX analysis where showed presence TiO_2 and carbon. Presence of carbon is results of immobilization MWCNT.



18th INTERNATIONAL FOUNDRYMEN CONFERENCE
**Coexistence of material science and sustainable technology in
economic growth**

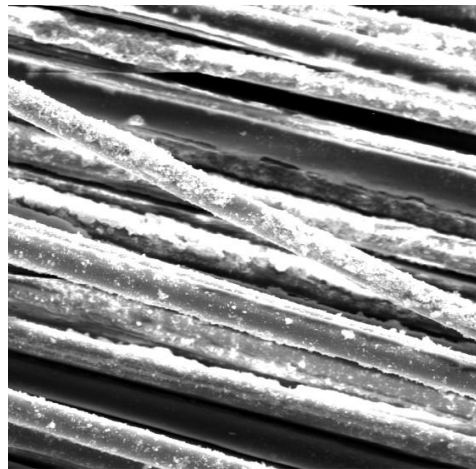
Sisak, May 15th-17th, 2019

<http://www.simet.hr/~foundry/>



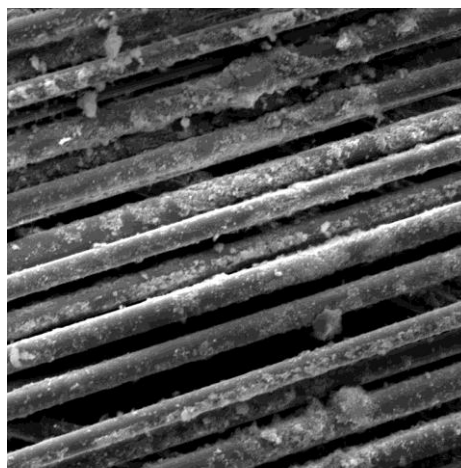
Det: SE
SEM MAG: 1.00 kx SEM HV: 20.00 kV
Date(m/d/y): 03/20/18 Name: M-1000X.jpg
VEGA\\ TESCAN
Performance in nanospace

(a)



Det: SE
SEM MAG: 1.00 kx SEM HV: 20.00 kV
Date(m/d/y): 03/20/18 Name: Mrezica-1000x-2.jpg
VEGA\\ TESCAN
Performance in nanospace

(b)



SEM HV: 20.00 kV SEM MAG: 1.00 kx
Date(m/d/y): 02/28/19 Stef
Det: SE Stef
VEGA\\ TESCAN
Performance in nanospace

(c)

Figure 2. SEM images: (a) clean glass mesh, (b) glass mesh with TiO₂,
(c) glass mesh with TiO₂ / MWCNT

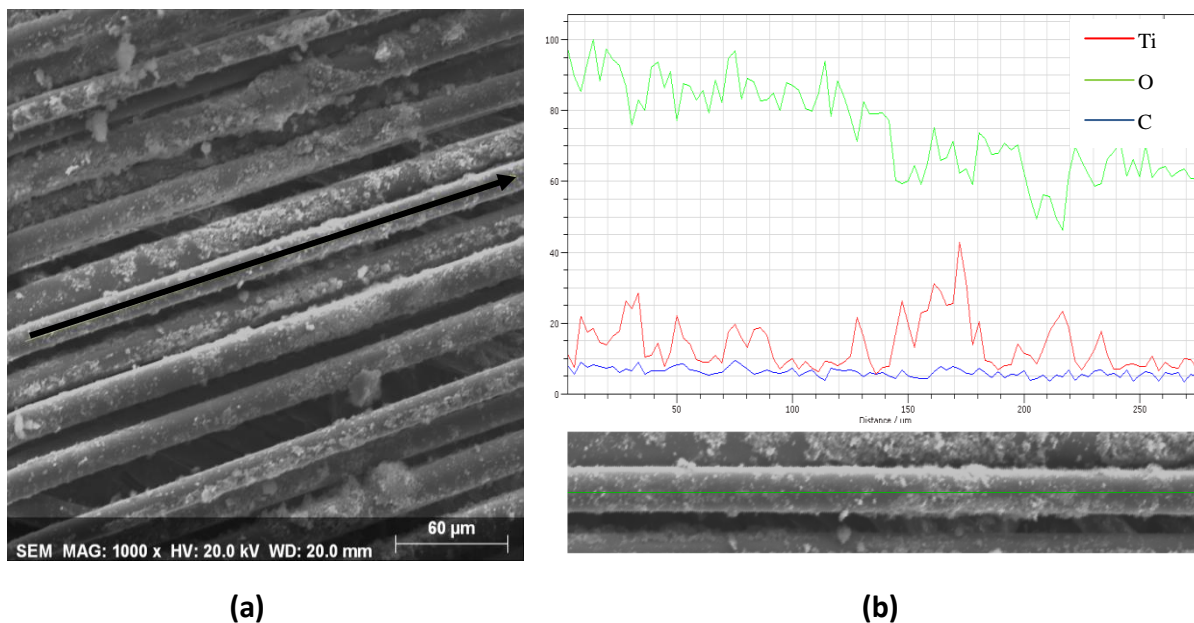


Figure 3. (a) SEM image for EDX analysis, (b) results EDX analysis

The photocatalytic properties were carried out in a batch pilot photoreaction with recirculation were investigated through the degradation of salicylic acid (SA). On Figure 4 is show degradation of SA with TiO₂ and TiO₂ / MWCNT composites with various concentrations of MWCNT.

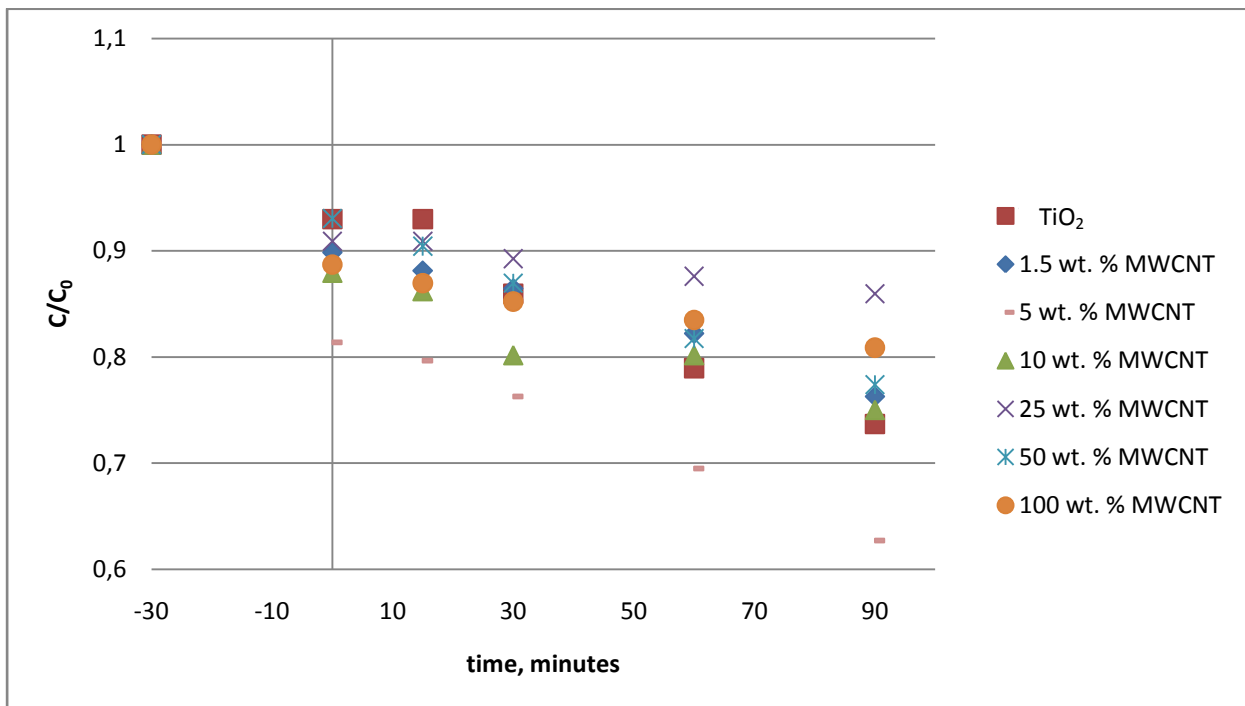


Figure 4. Photocatalytic degradation of SA over TiO₂ and TiO₂ / MWCNT under visible light irradiation



18th INTERNATIONAL FOUNDRYMEN CONFERENCE

Coexistence of material science and sustainable technology in
economic growth

Sisak, May 15th-17th, 2019

<http://www.simet.hr/~foundry/>

Results are given as normalized SA concentration vs irradiation time. Negative time is the time spent in the dark for the decrease of the concentration resulting from adsorption to the photocatalyst as described in the chapter of materials and methods.

Comparing the results of the photocatalytic degradation of salicylic acid it is concluded that it is the best result achieved when using the composite TiO₂ / MWCNT with 5 wt. % MWCNT concentrations while the weakest degradation when using the composite with higher concentrations MWCNT. Comparing the results of the photocatalysis with the mass of the immobilized layer (Table 1), it can be seen that photocatalysis doesn't depend on the mass of the immobilized layer but on the concentration of MWCNT.

Table 1. Mass of immobilization layer

Concentrations of wt.% MWCNT	m (glass mesh clean)/ g	m (glass mesh + TiO ₂ /MWCNT)/g	m (immobilization layer)/g
0	5.7764	5.9781	0.2017
1.5	6.4251	6.6492	0.2241
5	4.5922	4.8158	0.2236
10	5.9035	6.1226	0.2191
25	7.5188	7.6999	0.1811
50	5.7496	6.1090	0.3594
100	5.4641	5.9050	0.4409

CONCLUSIONS

In this paper a new photocatalysts, glass meshes with the immobilized TiO₂ and TiO₂ / MWCNT with various concentrations of MWCNT, were prepared and subsequently compared. The concentrations of MWCNT ranged from 1.5, 5, 10, 25, 50 and 100 wt. % MWCNT relative to the mass of TiO₂. After preparation, photocatalytic properties were investigated through the degradation of salicylic acid in pilot reactor. Comparing the results of the photocatalysis it was concluded that the best result is achieved using the composite TiO₂ / MWCNT with 5 wt. % MWCNT.

After photocatalysis, SEM and EDX analysis of prepared photocatalysts demonstrated the presence of TiO₂ and MWCNT on glass meshes that confirm the stability of immobilized TiO₂ and TiO₂ / MWCNT.

REFERENCES

- [1] N. R. Khalid, A. Majid, M. Bilal Tahir, N.A. Niaz, S. Khalid, Carbonaceous-TiO₂ nanomaterials for photocatalytic degradation of pollutants: A review, *Ceramics International*, 43(2017)17, pp. 14552-14571.



18th INTERNATIONAL FOUNDRYMEN CONFERENCE

Coexistence of material science and sustainable technology in
economic growth

Sisak, May 15th-17th, 2019

<http://www.simet.hr/~foundry/>

- [2] P. M. Thomas, G. D. Foster, Tracking acidic pharmaceuticals, caffeine, and triclosan through the wastewater treatment process, *Environmental Toxicology and Chemistry*, 24(2015)1, pp. 25-30.
- [3] J. Benner, D. E. Helbling, H. P. E. Kohler, J. Wittebol, E. Kaiser, C. Prasse, T. A. Ternes, C. N. Albers, J. Amand, B. Horemans, D. Springael, E. Walravens, N. Boon, Is Biological Treatment a Viable Alternative for Micropollutant Removal in Drinking Water Treatment Processes?, *Water Research*, 13(2013)16, pp. 5955-5976.
- [4] J. Altmann, A. S. Ruhl, F. Zietzschmann, M. Jekel, Direct comparison of ozonation and adsorption onto powdered activated carbon for micropollutant removal in advanced wastewater treatment, *Water Research*, 55(2014), pp. 185-193.
- [5] B. Plavac, I. Grčić, I. Brnardić, V. Grozdanić, S. Papić, Kinetic study of salicylic acid photocatalytic degradation using sol-gel anatase thin film with enhanced long-term activity, *Reaction Kinetics, Mechanisms and Catalysis*, 120(2017)1, pp. 385-401.
- [6] H. D. Traid, M. L. Vera, A. E. Ares, M. I. Litter, Porous titanium dioxide coatings obtained by anodic oxidation for photocatalytic applications, *Procedia Materials Science*, 9(2015), pp. 619-626.
- [7] D. Mukherjee, S. Barghi, A. K. Ray, Preparation and characterization of the TiO₂ immobilized polymeric photocatalyst for degradation of aspirin under UV and solar light, *Processes*, 2(2014)1, pp. 12-23.
- [8] P. R. Gogate, A. B. Pandit, A review of imperative technologies for wastewater treatment I: oxidation technologies at ambient conditions, *Advances in Environmental Research*, 8(2004)3-4, pp. 501-551.
- [9] Y. Wang, Y. He, Q. Lai, M. Fan, Review of the progress in preparing nano TiO₂: An important environmental engineering material, *Journal of environmental sciences*, 26(2014)11, pp. 2139-2177.
- [10] G. Lusvardi, C. Barani, F. Giubertoni, G. Paganelli, Synthesis and characterization of TiO₂ nanoparticles for the reduction of water pollutants, *Materials*, 10(2017)1208.
- [11] S. Souzanchi, F. Vahabzadeh, S. Fazel, S. N. Hosseini, Performance of an annular sieve-plate column photoreactor using immobilized TiO₂ on stainless steel support for phenol degradation, *Chemical Engineering Journal*, 223(2013), pp. 268-276.
- [12] N. Abdullahi, E. Saion, A. H. Shaari, N. M. Al-Hada, A. Keiteb, Optimisation of the photonic efficiency of TiO₂ decorated on MWCNTs for methylene blue photodegradation, *PLoS ONE*, 10(2015)5.
- [13] J. Hu, H. Li, S. Muhammad, Q. Wu, Y. Zhao, Q. Jiao, Surfactant -assisted hydrothermal synthesis of TiO₂ / reduced graphene oxide nanocomposites and their photocatalytic performances, *Journal of Solid State Chemistry*, 253(2017), pp. 113-120.
- [14] J. Li, S. Zhou, G. Hong, C. Chang, Hydrothermal preparation of P25-graphene composite with enhanced adsorption and photocatalytic degradation of dyes, *Chemical Engineering Journal*, 219(2013), pp. 486-491.



18th INTERNATIONAL FOUNDRYMEN CONFERENCE

Coexistence of material science and sustainable technology in
economic growth

Sisak, May 15th-17th, 2019

<http://www.simet.hr/~foundry/>

INVESTIGATION OF IRON CONTAINING INTERMETALLICS IN AISi12 ALLOY WITH $w(\text{Mn}/\text{Fe}) = 0.99$

Franjo Kozina^{1*}, Zdenka Zovko Brodarac¹, Dalibor Drobňjak², Ivan Jukić³

¹University of Zagreb Faculty of Metallurgy, Sisak, Croatia

²Almos Ltd, Kutina, Croatia

³Mosdorfer GmbH, Weiz, Austria

Poster presentation

Original scientific paper

Abstract

The precipitation of iron-rich intermetallic phases in AISi12 alloy with manganese/iron weight ratio $w(\text{Mn}/\text{Fe}) = 0.99$ was investigated. Calculation of solidification sequence under equilibrium conditions, obtained using Computer Aided Thermodynamic Diagram Calculation, comprehended precipitation of $\alpha\text{-Al}_{15}(\text{FeMn})_3\text{Si}_2$ and $\beta\text{-Al}_5\text{FeSi}$. However, the microstructural investigations performed using light and electron microscopy indicated the lack of $\beta\text{-Al}_5\text{FeSi}$ in needle-like morphology. The intermetallic phases in Chinese script, transitional and polyhedral morphology were found, respectively. The results of Energy Dispersive Spectroscopy showed the minimum difference in the chemical composition between the intermetallic phases in Chinese script and polyhedral morphology due to high $w(\text{Mn}/\text{Fe})$ weight ratio.

Keywords: AISi12, solidification sequence calculation, morphology of iron-rich intermetallic phases, $w(\text{Mn}/\text{Fe})$ ratio

*Corresponding author (e-mail address): fkozin@simet.hr

INTRODUCTION

The mechanical properties and development of microstructural constituents during solidification of aluminum-silicon (Al-Si) cast alloys are the result of chemical composition, melt treatment conditions, solidification rate [1], casting processes [2] and the application of, or the lack of, thermal treatment [3]. Chemical composition is designed in order to produce required performance capabilities including good specific strength and stiffness, low density, wear resistance, high temperature strength and improved damping capacity.



18th INTERNATIONAL FOUNDRYMEN CONFERENCE

Coexistence of material science and sustainable technology in
economic growth

Sisak, May 15th-17th, 2019

<http://www.simet.hr/~foundry/>

Interactions between alloying elements [4] promote development of microstructural constituents and affect solid solution of the matrix [5]. The alloying elements are classified as major or minor alloying elements and impurities, respectively [6]. Silicone, copper and magnesium are major alloying elements that control castability and properties development. Silicone is responsible for good castability, low density and abrasion resistance. While copper additions affect strength and hardness of Al-Si cast alloys, magnesium provides strength and corrosion resistance [6]. As minor alloying elements, titanium, boron, strontium, beryllium, manganese and chromium, influence solidification behavior, modify eutectic structure, refine primary phases and grain size morphology, promote or suppress phase formation and reduce oxidation [5]. Iron and zinc are impurity elements that can be partially dissolved into a solid solution of the matrix or form insoluble intermetallic phases. However, they are not homogeneously distributed between solid solution and intermetallic phases [6]. Besides impurities, the form and distribution of insoluble intermetallic phases is controlled by the addition of silicone, magnesium and copper [7]. In Al-Si-Mg alloys, zinc promotes precipitation at the grain boundaries increasing alloy susceptibility to stress corrosion cracking and crack propagation [8].

A major impurity element in Al-Si cast alloys that promotes intermetallic phase precipitation is iron. The iron is frequently acquired at levels of 0.4 wt. % to 0.8 wt. % during melting and casting processes [9], particularly when aluminum scrap and recycled materials are used [10]. Although the presence of iron prevents die soldering in high pressure die casting [11], the excess amount of iron has been found detrimental for mechanical properties of Al-Si, Al-Si-Cu and Al-Si-Mg cast alloys [12]. In order to avoid soldering effect and production of defect castings with short end of life [13], the iron must be maintained at or above its saturation point in the liquid aluminum [14]. However, the reduction of iron content in cast Al-alloys is necessary, due to the precipitation of Fe-rich intermetallic phases. The effect of Fe-rich intermetallic phases on the mechanical properties of cast Al-alloys depend on their type, size and distribution in the microstructure [15].

Although iron is highly soluble in liquid aluminum (L) and its alloys, it has a low solubility in aluminum solid solution (α_{Al}) of 0.052 wt. %. As a result iron tends to form intermetallic phases of various types. Equilibrium solubility of iron in L can reach 2.5 wt. % at a melting temperature of 700 °C and up to 5 wt. % at 800 °C [16].

Equilibrium Al-Fe phase diagram is characterized by eutectic interaction between the α_{Al} and stable Al_3Fe phase [16]. However, at higher cooling rates, due to the increased supercooling and changes in nucleation and growth conditions, precipitation of metastable phases is expected. Al-rich corner of stable and metastable Al-Fe phase diagram is given in Figure 1. The metastable phases that precipitate in Al-Fe system are Al_xFe (Al_6Fe) [17] and Al_mFe (Al_9Fe_2) [18], respectively.

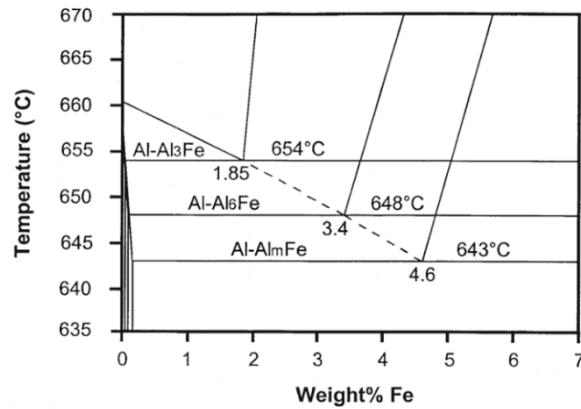


Figure 1. Al-rich corner of the stable and metastable Al-AlFe phase diagram [19]

The stable Al_3Fe phase solidifies at 1.85 wt. % Fe and 655 °C (Figure 1). At the commercial cooling rates of $10^{-1} - 10^2$ K/s the solidification of stable and metastable phases occurs. The cooling rate of $10^{-1} - 10$ K/s promotes solidification of Al_6Fe intermetallic phase at 3.4 wt. % Fe and 648 °C (Figure 1). The metastable Al_9Fe_2 phase precipitates at 4.6 wt. % Fe and 643 °C with cooling rate of 20 K/s [19] (Figure 1).

Thermodynamic description of Al-Fe-Si phase diagram comprehends solidification of eutectic ($\alpha_{\text{Al}} + \beta_{\text{Si}}$), α_{Al} , as well as Al_3Fe , $\alpha\text{-Al}_8\text{Fe}_2\text{Si}$, $\beta\text{-Al}_5\text{FeSi}$, $\gamma\text{-Al}_3\text{FeSi}$ and $\delta\text{-Al}_4\text{FeSi}_2$ intermetallic phases [20].

The liquidus projection of the Al - corner of the Al-Fe-Si system is given in Figure 2. The corresponding invariant reactions are given in Table 1.

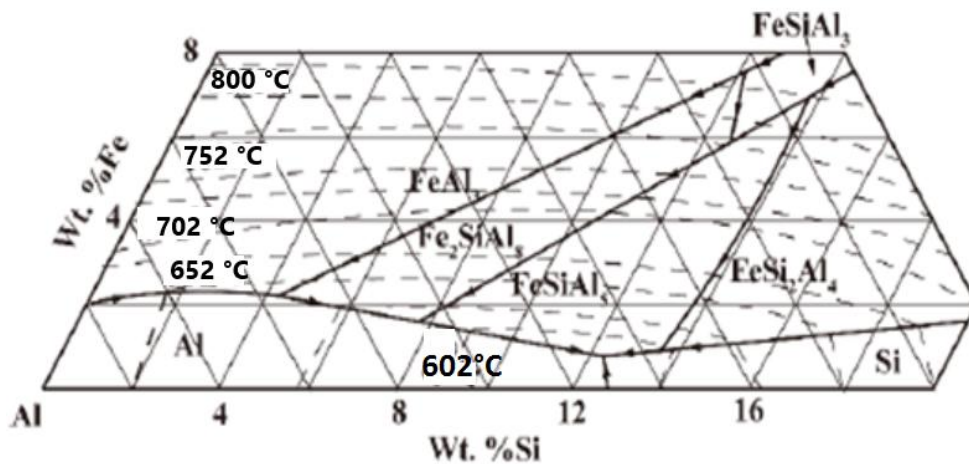


Figure 2. Liquidus projection in the Al corner of Al-Fe-Si ternary phase diagram [20]



Table 1. Invariant equilibrium reactions in the Al corner of Al-Fe-Si phase diagram [22]

Reaction No.	Reaction	Concentration in liquid phase, wt. %		Temperature, °C
		Fe	Si	
1	$L + Al_3Fe \rightarrow \alpha-Al_8Fe_2Si + \gamma-Al_3FeSi$	7.5	12.5	710
2	$L + \gamma-Al_3FeSi + \delta-Al_4FeSi_2 \rightarrow \beta-Al_5FeSi$	7.2	14.0	700
3	$L + \gamma-Al_3FeSi \rightarrow \alpha-Al_8Fe_2Si + \beta-Al_5FeSi$	6.0	13.0	675
4	$L + Al_3Fe \rightarrow \alpha_{Al} + \alpha-Al_8Fe_2Si$	2.0	4.2	632
5	$L + \alpha-Al_8Fe_2Si \rightarrow \alpha_{Al} + \beta-Al_5FeSi$	1.8	6.2	613
6	$L + \delta-Al_4FeSi_2 \rightarrow \beta-Al_5FeSi + \beta_{Si}$	1.5	14.3	600
7	$L \rightarrow \alpha_{Al} + \beta-Al_5FeSi + \beta_{Si}$	0.5	11.7	573

Based on the liquidus projection of Al-rich corner given in Figure 2, eutectic ($\alpha_{Al} + \beta_{Si}$), α_{Al} , Al_3Fe , $\alpha-Al_8Fe_2Si$, $\beta-Al_5FeSi$, $\gamma-Al_3FeSi$ and $\delta-Al_4FeSi_2$ are in equilibrium with L [23].

According to the Table 1, $\alpha-Al_8Fe_2Si$ and $\gamma-Al_3FeSi$ intermetallic phases are the first to solidify during peritectic reaction between L and Al_3Fe phase at 710 °C (reaction no. 1). The solidification of $\gamma-Al_3FeSi$ phase introduces a partial disorder to the α_{Al} dendritic network due to the partial substitution of aluminum and silicone atoms. The partial substitution of atoms is a result of large homogeneity of $\gamma-Al_3FeSi$ phase [24]. Solidification of $\beta-Al_5FeSi$ at 700 °C involves peritectic reaction of L, $\gamma-Al_3FeSi$ and $\delta-Al_4FeSi_2$ phase (reaction no. 2). Dissolution of previously precipitated $\gamma-Al_3FeSi$ and $\delta-Al_4FeSi_2$ phases increases the amount of silicone in L from 12.5 wt. % to 14.0 wt. %. The amount of silicone in L still remains high (13 wt. %) at 675 °C during solidification of $\alpha-Al_8Fe_2Si$ and $\beta-Al_5FeSi$ phase. At this stage solidification of $\alpha-Al_8Fe_2Si$ and $\beta-Al_5FeSi$ phase involves dissolution of $\gamma-Al_3FeSi$ (reaction no. 3). Transformation of α_{Al} dendritic network starts at 632 °C parallel to solidification of $\alpha-Al_8Fe_2Si$ phase (reaction no. 4). This reaction causes significant drop of silicone in L phase from 13 wt. % to 4.2 wt. %. The silicone content in L increases to 6.2 wt. % during solidification of $\beta-Al_5FeSi$ at 613 °C (reaction no. 5). The increase in silicone content from 6.2 wt. % to 14 wt. % if followed by solidification of $\beta-Al_5FeSi$ and primary β_{Si} (reaction no. 6) from silicone bulked L. The sequence ends with solidification of eutectic ($\alpha_{Al} + \beta_{Si} + \beta-Al_5FeSi$) at 573 °C (reaction no. 7).

The solid solubility of iron and silicone in α_{Al} related to temperatures is given in Figure 3. The solid solubility of iron and silicone in α_{Al} is indicated in Table 2.

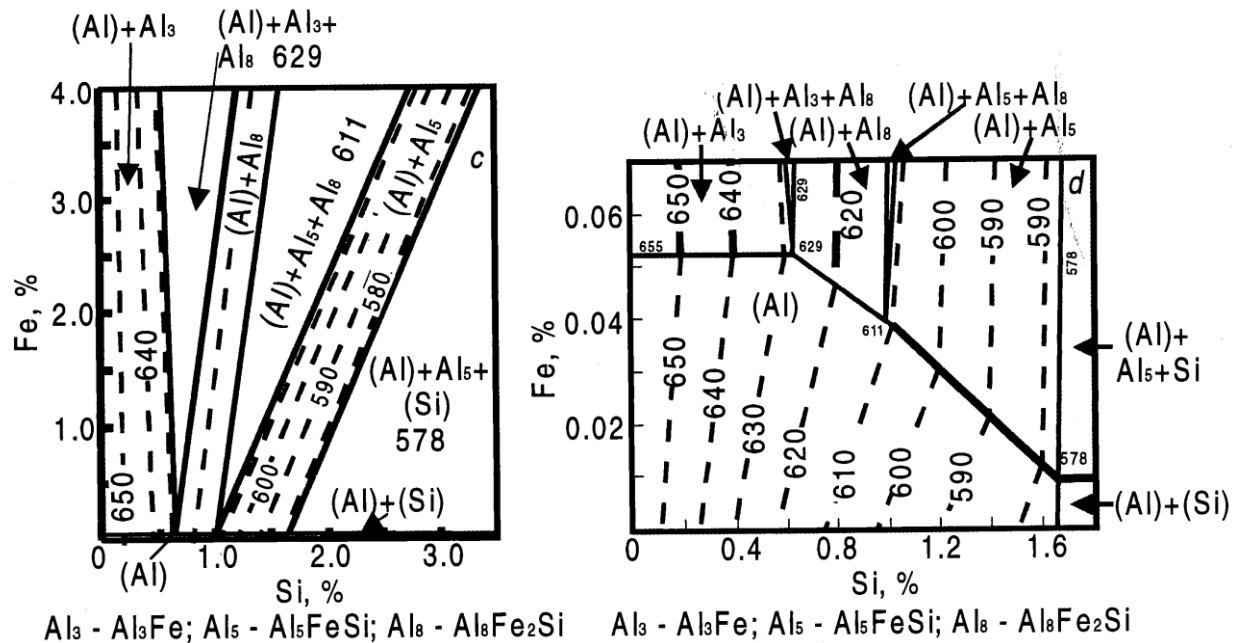


Figure 3. Solidus projection of primary iron intermetallic phases [25]

Table 2. Solid solubility of iron and silicone in α_{Al} at different temperatures [25]

T, °C	$\alpha_{Al} + Al_3Fe + \alpha-Al_8Fe_2Si$		$\alpha_{Al} + \beta-Al_5FeSi + \alpha-Al_8Fe_2Si$		$\alpha_{Al} + \beta-Al_5FeSi + \beta_{Si}$	
	Fe, wt. %	Si, wt. %	Fe, wt. %	Si, wt. %	Fe, wt. %	Si, wt. %
629	0.052	0.64	--	--	--	--
611	--	--	0.040	0.82	--	--
600	0.033	0.40	0.033	0.82	--	--
550	0.0016	0.20	0.016	0.42	0.008	1.30
400	0.002	0.03	0.002	0.06	0.002	0.30

Based on the solidus projection of Al-rich corner in Al-Fe-Si phase diagram, Al₃Fe, α -Al₈Fe₂Si, β -Al₅FeSi and eutectic ($\alpha_{Al} + \beta_{Si}$) are in equilibrium with α_{Al} dendritic network (Figure 3) [26].

When silicone content in solid solution is 0.64 wt. %, Al₃Fe and α -Al₈Fe₂Si phase solidify at 629 °C (Figure 3). Increasing silicone content to 0.83 wt. % causes solidification of ternary β -Al₅FeSi and α -Al₈Fe₂Si phase at 611 °C. The eutectic ($\alpha_{Al} + \beta_{Si} + \beta$ -Al₅FeSi) solidify at 590 °C and silicone content of 1.20 wt. % [25].

Taking into account phase transformation and solidification in liquid and solid state (Table 1 and 2), there are five main Fe-rich intermetallic phases: Al₃Fe, α -Al₈Fe₂Si, β -Al₅FeSi, γ -Al₃FeSi and δ -Al₄FeSi₂. Solidification of Fe-rich intermetallic phases originates from low solubility of iron in α_{Al} solid solution. The δ -Al₄FeSi₂ phase solidifies in aluminum alloys with silicone content of 14 wt. %, while γ -Al₃FeSi phase is present in alloys with high silicone (12.5 wt. %) and iron (7.5 wt.%) content [27]. The thermodynamic stability of α -Al₈Fe₂Si phase is only achieved in high purity Al-Fe-Si alloys. The presence of other alloying elements, such as



18th INTERNATIONAL FOUNDRYMEN CONFERENCE

Coexistence of material science and sustainable technology in economic growth

Sisak, May 15th-17th, 2019

<http://www.simet.hr/~foundry/>

manganese, chromium [28] and vanadium, introduce changes into the lattice of α -Al₈Fe₂Si phase [29]. The changes in lattice of α -Al₈Fe₂Si phase originate from iron and alloying element substitution as well as mutual substitution of silicon and aluminum [30]. The β -Al₅FeSi intermetallic phase solidifies during pre-eutectic reaction in liquid/solid range [31]. The brittle β -Al₅FeSi intermetallic phase has needle-like or plate-like morphology [32]. This type of morphology acts as a crack initiator and has a negative effect on mechanical properties [33] as well as on castability [34]. Poor castability originates from increased content of porosities. The β -Al₅FeSi intermetallic phase increases the porosity content by blocking dendritic flow and therefore acting as a nucleation site [35]. Also β -Al₅FeSi intermetallic phase enables growth of large Al-Si eutectic grains [36].

Neutralizing negative effect of β -Al₅FeSi intermetallic phase comprehends modification of its needle-like morphology to less deleterious form of Chinese script. Neutralizing effect is achieved by adding soluble neutralizer elements such as manganese, chromium, beryllium or strontium [37]. Manganese is the most frequent neutralizing element [38] that promotes precipitation of α -Al₁₅(FeMn)₃Si₂ phase [27] during peritectic reactions [39]. Precipitation of β -Al₅FeSi intermetallic phase is suppressed, respectively. The invariant equilibrium reactions in Al-rich corner of Al-Fe-Mn-Si diagram are given in Table 3.

Table 3. The invariant equilibrium reactions in Al-rich corner of Al-Fe-Mn-Si diagram [25]

Reaction	Composition of Liquid			Temperature, °C
	Fe, wt. %	Mn, wt. %	Si, wt. %	
$L + Al_3Fe + Al_6(FeMn) \rightarrow \alpha_{Al} + \alpha-Al_{15}(FeMn)_3Si_2$	2.0	0.35	1.75	648
$L + Al_3Fe \rightarrow \alpha_{Al} + \alpha-Al_8Fe_2Si + \alpha-Al_{15}(FeMn)_3Si_2$	2.0-2.5	<0.2	3.0-5.0	627-632
$L + \alpha-Al_8Fe_2Si \rightarrow \alpha_{Al} + \beta-Al_5FeSi + \alpha-Al_{15}(FeMn)_3Si_2$	1.0-2.0	0.1-0.5	5.0-10.0	597-607
$L + \beta-Al_5FeSi \rightarrow \alpha_{Al} + \beta_{Si} + \alpha-Al_{15}(FeMn)_3Si_2$	0.6	0.2	11.7	575

According to Table 3, transformation of α_{Al} dendritic network and solidification of α -Al₁₅(FeMn)₃Si₂ phase are first reactions to occur. Their solidification is a result of peritectic reaction between L, Al₃Fe and Al₆(FeMn) phase at 648 °C. The transformation of α_{Al} dendritic network and solidification of α -Al₁₅(FeMn)₃Si₂ phase are continuous till the end of liquid state reactions. In the temperature range from 627 °C to 632 °C, primary α -Al₈Fe₂Si phase begins to solidify. The solidification of primary α -Al₈Fe₂Si enables peritectic reaction, in the temperature range from 597 °C to 607 °C and solidification of β -Al₅FeSi. Liquid state reactions end with transformation of α_{Al} dendritic network, solidification of eutectic ($\alpha_{Al} + \beta_{Si}$) and α -Al₁₅(FeMn)₃Si₂. The solidification of eutectic ($\alpha_{Al} + \beta_{Si}$) is a result of increased amount of silicone in L. The eutectic ($\alpha_{Al} + \beta_{Si}$) solidifies at 11.7 wt. % of silicone. The amounts of iron and manganese in L decrease towards the end of liquid state reactions (Table 3), respectively.

The Al₆Mn, eutectic ($\alpha_{Al} + \beta_{Si}$) and α -Al₁₅(FeMn)₃Si phases are in equilibrium with α_{Al} solid solution. In the α -Al₁₅(FeMn)₃Si phase, iron can replace up to 90 % of manganese. The metastable Al₆Fe and Al₂₀Fe₅Si₂ phase only occur in rapidly quenched alloys [40].



18th INTERNATIONAL FOUNDRYMEN CONFERENCE

Coexistence of material science and sustainable technology in economic growth

Sisak, May 15th-17th, 2019

<http://www.simet.hr/~foundry/>

The solidification of Fe-rich intermetallic phase can occur in different morphologies: needle-like, Chinese script and polyhedral or star-like morphology. The morphology of precipitated phases is influenced by manganese/iron weight ratio (w (Mn/Fe)). The exact w (Mn/Fe) necessary for neutralizing effect of manganese and the transition of needle-like to Chinese script morphology is not fully established. With the w (Mn/Fe) at 0.35 the partial transformation of needle-like to Chinese script morphology was observed. At w (Mn/Fe) of 0.5 transformation of β -Al₅FeSi to α -Al₁₅(FeMn)₃Si₂ was fully achieved [41]. However, α -Al₁₅(FeMn)₃Si₂ with Chinese script morphology was observed at w (Mn/Fe) as low as 0.17 [27]. Increasing the w (Mn/Fe) additionally causes precipitation of α -Al₁₅(FeMn)₃Si₂ with polyhedral morphology. The precipitation of α -Al₁₅(FeMn)₃Si₂ phase with polyhedral morphology occurs at w (Mn/Fe) of 0.65 [41].

The goal of the research is to identify the Fe-rich intermetallic phases during solidification of AlSi12 alloy with w (Mn/Fe) of 0.99.

MATERIALS AND METHODS

The AlSi12 alloy was prepared in induction melting furnace from the ingot and return material. After melting at the temperature of 770 °C the melt treatment was performed through inoculation with AlTi5B master alloy and modification with AlSr10 master alloy. High-pressure die casting was used. The chemical composition was determined spectroscopically using Spectro machine.

The calculations of Fe-rich intermetallic phase development under equilibrium conditions were enabled using CALPHAD. The CALPHAD enabled calculation of aluminum, iron, silicone and manganese interaction with bulked α_{Al} as well as solidification sequence calculations and reactions in both liquid and solid state, respectively.

Samples for metallographic analysis were prepared using grinding/polishing machine Pheonix Beta Biller SAD. In order to observe microstructural constituents, samples were etched using Keller's etching solutions as well as caustic chemical etching. The caustic chemical etching was performed using 30 % aqueous solution of sodium hydroxide (NaOH) and 0.1 M hydrochloric acid (HCl). The application of caustic chemical etching enabled dissolution of α_{Al} dendritic network. The rest of microstructural constituents were not affected. The Olympus GX51 inverted metallographic microscope was used to perform light microscopy. Electron microscopy was made on Tescan, Vega TS 5136 MM equipped with energy dispersive spectrometer (EDS). Backscatter electron (BSE) imaging was used in order to obtain better distinction between the elements based on atomic weight. The EDS measurements were performed on at least ten different details. Details for EDS measurements were determined based on phase morphology.



18th INTERNATIONAL FOUNDRYMEN CONFERENCE
**Coexistence of material science and sustainable technology in
 economic growth**

Sisak, May 15th-17th, 2019

<http://www.simet.hr/~foundry/>

RESULTS AND DISCUSSION

The chemical composition of the casting is given in Table 4.

Table 4. Chemical composition of the casting, wt. %

Si	Fe	Cu	Mn	Mg	Cr	Ni	Zn	Ti	B	Bi
11.69	0.443	0.149	0.438	0.0250	0.011	0.011	0.0410	0.0270	0.003	0.0022

The AlSi12 alloy is hypoeutectic alloy with Si content of 11.69 wt. %. The w (Mn/Fe) is 0.99. The w (Mn/Fe) is sufficient to avoid solidification of β -Al₅FeSi intermetallic phase with needle-like morphology. Instead, the iron should solidify as α -Al₁₅(FeMn)₃Si₂ with Chinese script morphology. Given the w (Mn/Fe), solidification of α -Al₁₅(FeMn)₃Si₂ with polyhedral morphology is expected, as well. The additions of copper, chromium, nickel, zinc, titanium, boron and bismuth are higher than their solid solubility in α_{Al} dendritic network.

Phase transformation and precipitations under equilibrium conditions were determined using Thermo-Calc 2019a software support with TCAL 4 database. The thermodynamic calculations included elements from the chemical composition given in Table 4. The calculations concerning Fe-rich intermetallic phases as well as diffusion of aluminum, silicone, iron and manganese components were emphasized.

The amount of phases developed during solidification is given in Figure 4 a and b. The following reactions are shown in Table 5.

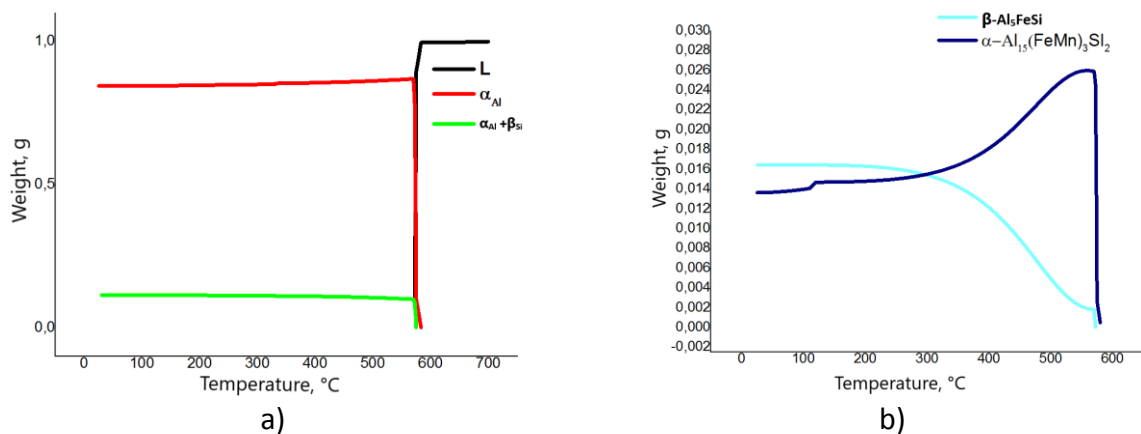


Figure 4. The amount of phases developed during solidification:
 a) Transformation of α_{Al} dendritic network and solidification of eutectic ($\alpha_{Al} + \beta_{Si}$),
 b) Solidification of Fe-rich and α -Al₁₅(FeMn)₃Si₂ phase



18th INTERNATIONAL FOUNDRYMEN CONFERENCE
**Coexistence of material science and sustainable technology in
 economic growth**

Sisak, May 15th-17th, 2019

<http://www.simet.hr/~foundry/>

Table 5. Solidification sequence according to Thermo-Calc calculations

Reaction no.	Reaction	Temperature, °C
1	$L \rightarrow \alpha_{Al}$	581
2	$L + \alpha_{Al} \rightarrow \alpha-Al_{15}(FeMn)_3Si_2$	580
3	$L \rightarrow \alpha_{Al} + \beta_{Si}$	574
4	$\alpha_{Al} + \alpha-Al_{15}(FeMn)_3Si_2 \rightarrow \beta-Al_5FeSi$	570

The calculations of solidification sequence in equilibrium conditions comprehend solidification of $\alpha-Al_{15}(FeMn)_3Si_2$ and $\beta-Al_5FeSi$. The solidification sequence begins with transformation of α_{Al} dendritic network at 581 °C followed by solidification of $\alpha-Al_{15}(FeMn)_3Si_2$ at 580 °C. The eutectic ($\alpha_{Al} + \beta_{Si}$) solidifies from L at 574 °C. The $\beta-Al_5FeSi$ phase solidifies at 570 °C reducing the amount of $\alpha-Al_{15}(FeMn)_3Si_2$ phase, respectively. The additional decrease in the amount of $\alpha-Al_{15}(FeMn)_3Si_2$ phase occurs at 110 °C.

The amount of components in L phase is given in Figure 5, a and b.

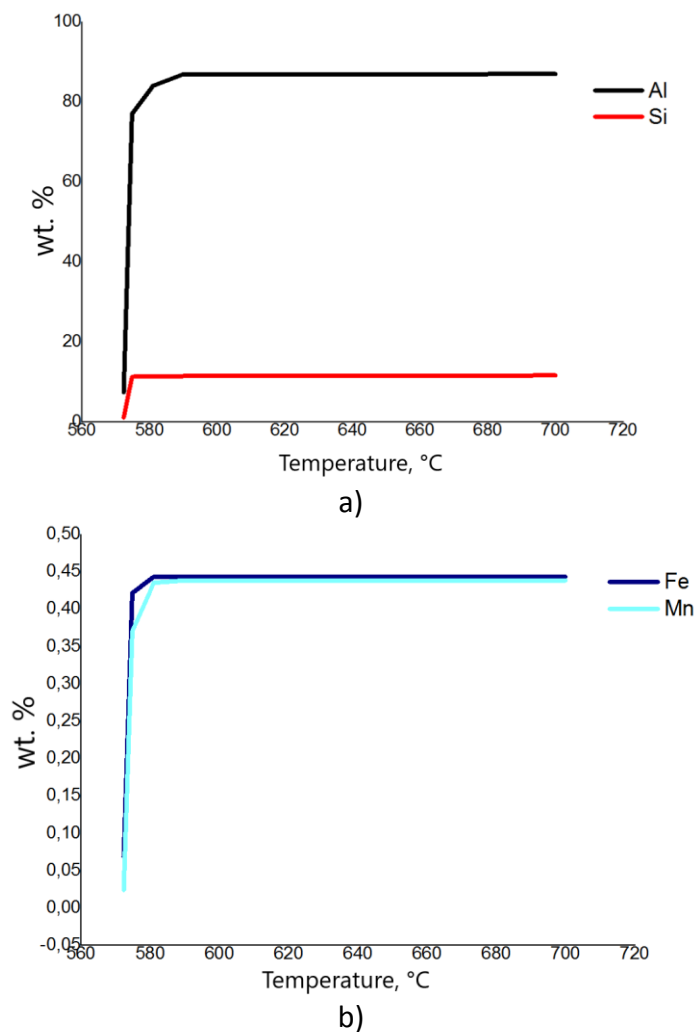


Figure 5. The component ratio in L: a) Al and Si, b) Fe and Mn



18th INTERNATIONAL FOUNDRYMEN CONFERENCE

Coexistence of material science and sustainable technology in economic growth

Sisak, May 15th-17th, 2019

<http://www.simet.hr/~foundry/>

The average aluminum content of 86.88 wt. % in L phase stays constant till the temperature of 581 °C when it drops to 83.92 wt. % as α_{Al} dendritic network starts to transform. The solidification of eutectic ($\alpha_{Al} + \beta_{Si}$) reduces the amount of aluminum in L phase 574 °C when it reaches its minimum of 7.38 wt. %. The average silicone content of 11.63 wt. % in L phase drops at the 570 °C towards its minimum of 1.08 wt. % due to the solidification of eutectic ($\alpha_{Al} + \beta_{Si}$). The average content of iron and manganese follow the same pattern as aluminum. The significant drop in average content of manganese (0.44 wt. %) is recorded at the temperature of 580 °C as a result of $\alpha-Al_{15}(FeMn)_3Si_2$ phase solidification, while average Fe content (0,44 wt. %) drops at the temperature of 570 °C. The drop in iron content is caused by solidification of $\beta-Al_5FeSi$ phase.

The amount of components in α_{Al} is given in Figure 6, a and b.

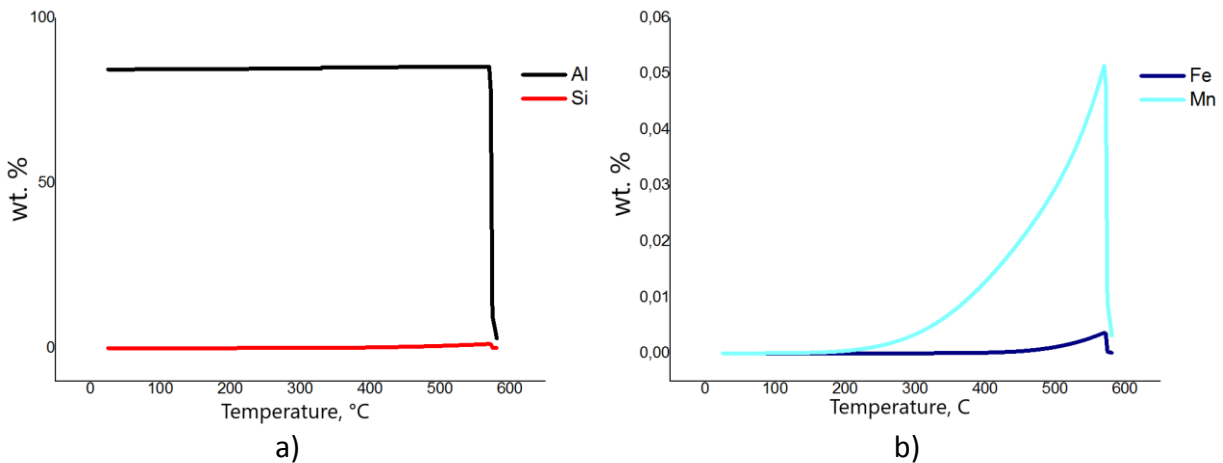


Figure 6. The component ratio in α_{Al} solid solution:
a) Al and Si, b) Fe and Mn

The average amount of aluminum in α_{Al} solid solution reaches maximum value of 85.22 wt. % at 570 °C and remains constant till the end of solidification sequence. The maximum average amount of silicone in α_{Al} solid solution is 1.27 wt. % at 572 °C. At the end of solidification sequence the average value of silicone in α_{Al} solid solution drops to $4.76 \cdot 10^{-4}$ wt. %. The solid solubility of manganese in α_{Al} solid solution reaches its maximum of 0.05 wt. % at 570 °C, and drops significantly to $3.23 \cdot 10^{-7}$ wt. %. The maximum solid solubility of iron in α_{Al} solid solution is 0.004 wt. % at 570 °C. At the end of solidification sequence the amount of iron in α_{Al} solid solution is $1.75 \cdot 10^{-10}$ wt. %.

Elements amount in $\alpha-Al_{15}(FeMn)_3Si_2$ phase in correlation to the temperature are shown in Figure 7.



18th INTERNATIONAL FOUNDRYMEN CONFERENCE
Coexistence of material science and sustainable technology in economic growth

Sisak, May 15th-17th, 2019

<http://www.simet.hr/~foundry/>

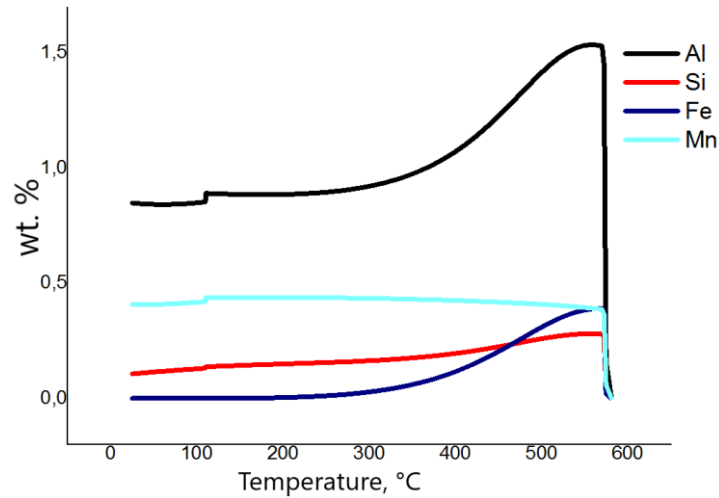


Figure 7. The solid solubility of Al, Si, Fe and Mn in $\alpha\text{-Al}_{15}(\text{FeMn})_3\text{Si}_2$ phase

The starting average content of aluminum is 0.023 wt. % and silicone is 0.005 wt. % in $\alpha\text{-Al}_{15}(\text{FeMn})_3\text{Si}_2$ phase at 580 °C respectively. The maximum amount of aluminum is 1.53 wt. % and silicone is 0.28 wt. % at 570 °C. Towards the end of solidification $\alpha\text{-Al}_{15}(\text{FeMn})_3\text{Si}_2$ phase contains average 0.85 wt. % of aluminum and 0.11 wt. % of silicone. The maximum iron content of 0.39 wt. % is reached at 570 °C. At the end of solidification sequence amount of iron drops slowly and reaches average amount of $2.61 \cdot 10^{-6}$ wt. %. The maximum manganese amount of 0.39 wt. % in $\alpha\text{-Al}_{15}(\text{FeMn})_3\text{Si}_2$ phase is achieved at 570 °C. The amount of manganese remains constant till the temperature of 110 °C. At the temperature of 110 °C the average amounts of aluminum (0.85 wt. %), silicone (0.13 wt. %) and manganese (0.41953 wt. %) slightly drop.

The amount of components in $\beta\text{-Al}_5\text{FeSi}$ phase is given in Figure 8.

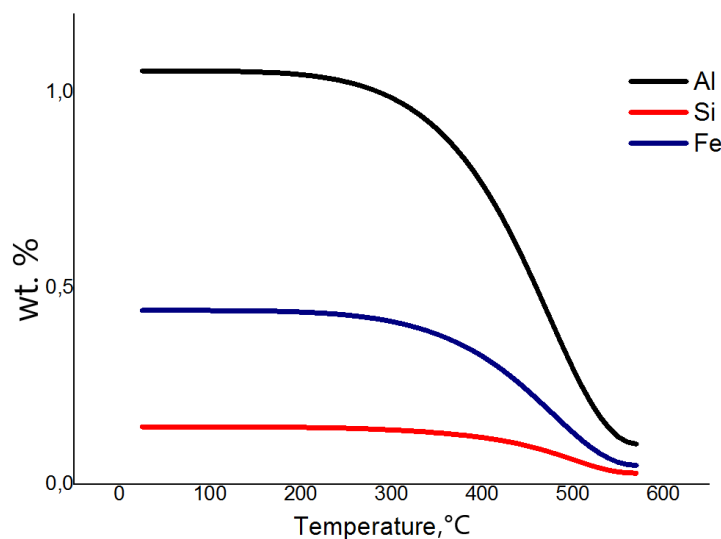


Figure 8. The solid solubility of Al, Si, Fe and Mn in $\beta\text{-Al}_5\text{FeSi}$ phase



18th INTERNATIONAL FOUNDRYMEN CONFERENCE

Coexistence of material science and sustainable technology in
economic growth

Sisak, May 15th-17th, 2019

<http://www.simet.hr/~foundry/>

The starting average content of aluminum is 0.10 wt. % and silicone is 0.029 wt. % in β - Al_5FeSi phase at 570 °C respectively. At the end of solidification β - Al_5FeSi phase contains in average 1.053 wt. % of aluminum and 0.146 wt. % of silicone. The average content of iron in α phase grows from starting 0.048 wt. % to 0.443 wt. % at the end of solidification sequence. The manganese content is not influenced by solidification of β - Al_5FeSi phase.

Decrease in the aluminum and silicone content in L is caused by transformation of α_{Al} dendritic network at 581 °C followed by solidification of α - $\text{Al}_{15}(\text{FeMn})_3\text{Si}_2$ at 580 °C. The amount of aluminum is reduced additionally by solidification of β - Al_5FeSi phase at 570 °C. The reduction of manganese amount in L is caused by α - $\text{Al}_{15}(\text{FeMn})_3\text{Si}_2$ solidification at 580 °C. Although the amount of iron begins to drop during solidification of α - $\text{Al}_{15}(\text{FeMn})_3\text{Si}_2$, the more significant loss is noticed at 570 °C during β - Al_5FeSi phase solidification. Both aluminum and silicone content in α_{Al} solid solution stay unaffected till the end of solidification. The amounts of iron and manganese in α_{Al} solid solution are depleted during α - $\text{Al}_{15}(\text{FeMn})_3\text{Si}_2$ and β - Al_5FeSi phase solidification, respectively. The amounts of aluminum, silicone and iron in α - $\text{Al}_{15}(\text{FeMn})_3\text{Si}_2$ are reduced by solidification of β - Al_5FeSi phase. The manganese amount is unaffected by β - Al_5FeSi phase solidification. However, the amounts of aluminum and manganese are reduced in α - $\text{Al}_{15}(\text{FeMn})_3\text{Si}_2$ phase after 110 °C due to the precipitation of $\text{Al}_{16}\text{Mn}_3\text{Ni}$. The β - Al_5FeSi phase grows till the end of solidification sequence.

The microstructure of the samples at the magnification of 500 X is given in Figure 9.

The results of light microscopy indicated the presence of Fe-rich intermetallic phases in Chinese script (Figure 9 a), transitional (Figure 9 b) and polyhedral morphology (Figure 9c). The intermetallic phases in needle-like morphology were not detected. The intermetallic phases in Chinese script morphology envelopes α_{Al} dendritic network (Figure 9a). The intermetallic phases with transitional morphology can be found at the border $\alpha_{\text{Al}}/\beta_{\text{Si}}$ (Figure 9b). The phases with polyhedral morphology are surrounded by eutectic ($\alpha_{\text{Al}} + \beta_{\text{Si}}$) (Figure 9c).



18th INTERNATIONAL FOUNDRYMEN CONFERENCE
**Coexistence of material science and sustainable technology in
economic growth**

Sisak, May 15th-17th, 2019

<http://www.simet.hr/~foundry/>

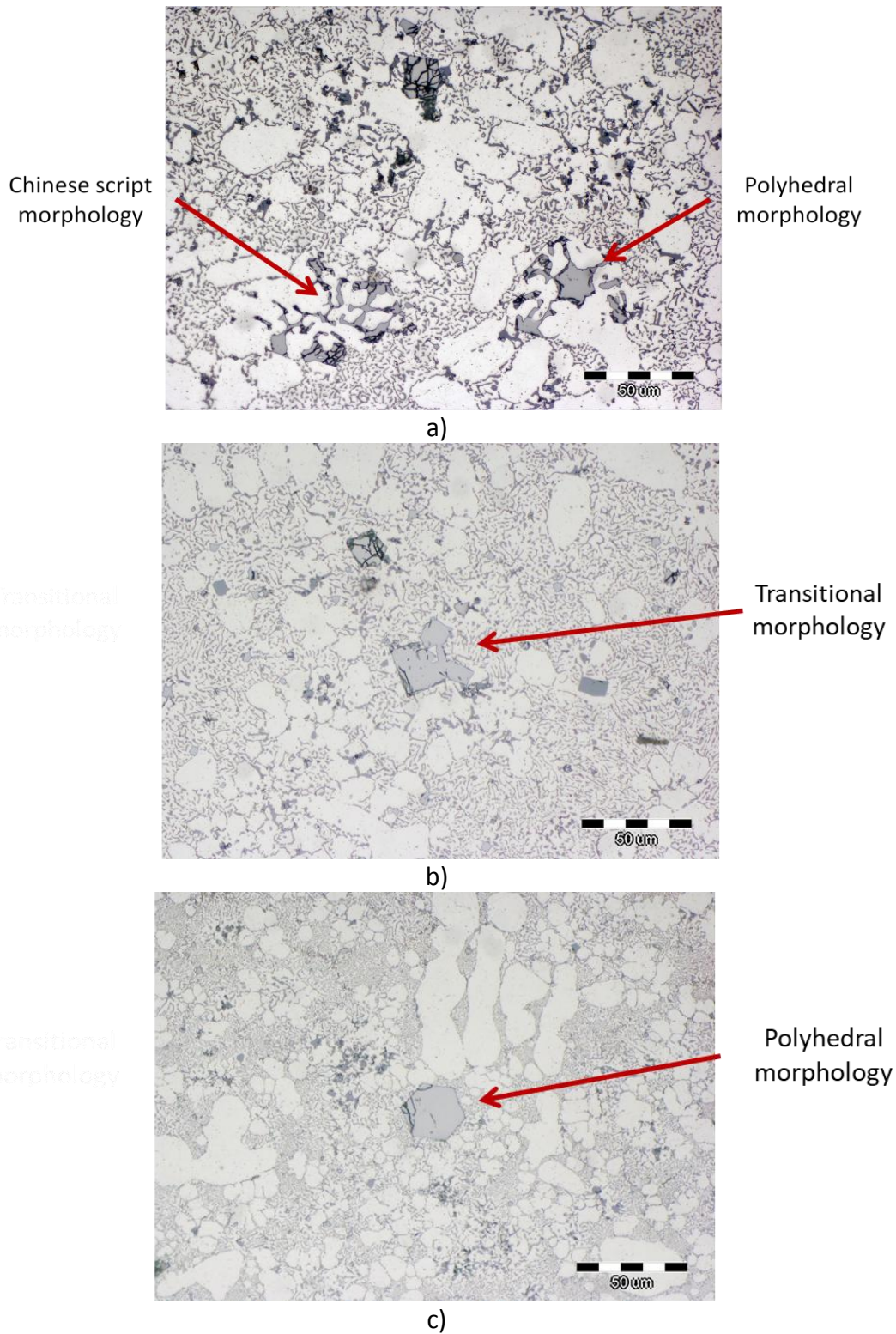


Figure 9. Microstructure of the samples showing: a) Chinese script morphology, b) Transitional morphology, c) Polyhedral morphology



18th INTERNATIONAL FOUNDRYMEN CONFERENCE
**Coexistence of material science and sustainable technology in
economic growth**

Sisak, May 15th-17th, 2019

<http://www.simet.hr/~foundry/>

The BSE images of intermetallic phases in Chinese script and polyhedral morphology with corresponding EDS analysis are given in Figure 10.

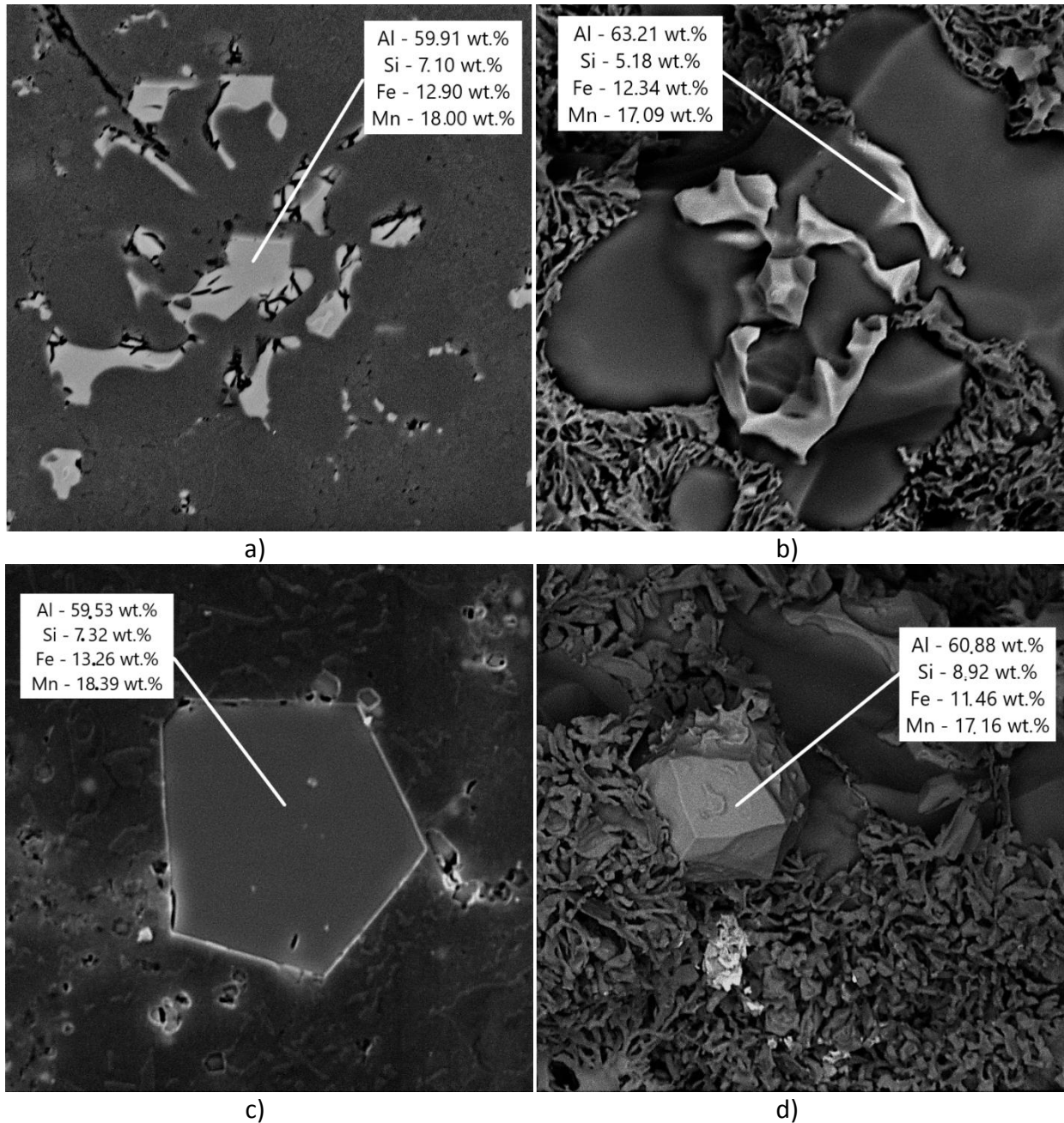


Figure 10. The SEI of:
a) Intermetallic phase in Chinese script morphology,
b) Intermetallic phase in Chinese script morphology after caustic chemical etching,
c) Intermetallic phase in polyhedral morphology,
d) Intermetallic phase in polyhedral morphology after caustic chemical etching



18th INTERNATIONAL FOUNDRYMEN CONFERENCE
**Coexistence of material science and sustainable technology in
 economic growth**

Sisak, May 15th-17th, 2019

<http://www.simet.hr/~foundry/>

The Chinese script morphology of intermetallic phases is not typical (Figure 10a). The branches of intermetallic phase with Chinese script morphology surround α_{Al} dendritic network (Figure 10b). The polyhedral iron morphology is more compact (Figure 10c). The intermetallic phase in polyhedral morphology is surrounded by main eutectic ($\alpha_{Al} + \beta_{Si}$) (Figure 10d).

The results of EDS analysis performed on intermetallic phases in Chinese script and polyhedral morphology are shown in Figure 11.

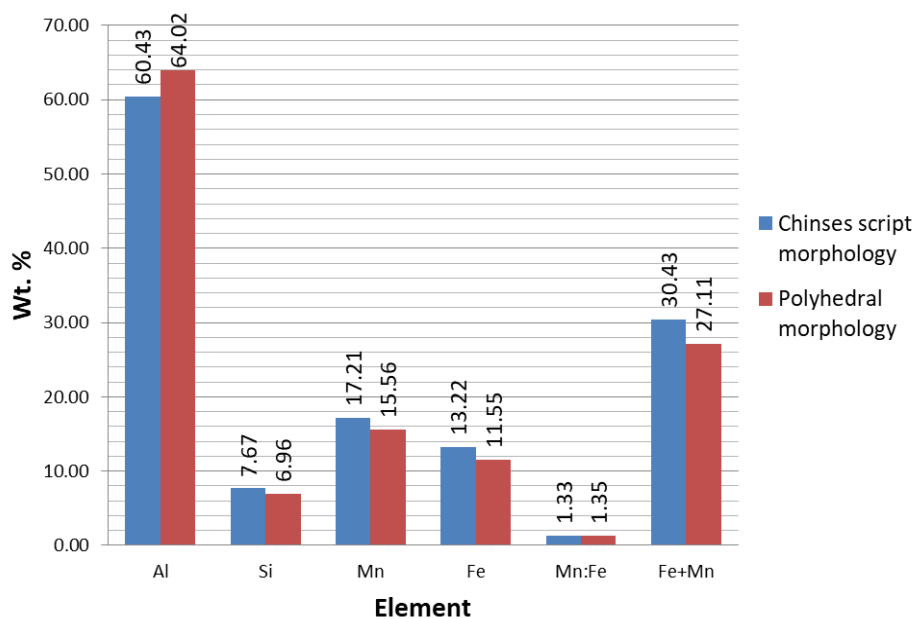


Figure 11. The average wt. % of elements in intermetallic phases in Chinese script and polyhedral morphology

The results shown in Figure 10 indicate small difference in average content of elements between intermetallic phases in Chinese script and polyhedral morphology. The intermetallic phases in Chinese script morphology have higher average amount of silicone, manganese, and iron. The total amount Fe + Mn is higher for Chinese script morphology, while polyhedral morphology has higher w (Mn/Fe).

The aluminum, silicone, manganese, iron wt. % as well as w (Mn/Fe) and total amount Mn + Fe for intermetallic phases in Chinese script and polyhedral morphology are given in Table 5.



18th INTERNATIONAL FOUNDRYMEN CONFERENCE

Coexistence of material science and sustainable technology in
economic growth

Sisak, May 15th-17th, 2019

<http://www.simet.hr/~foundry/>

Table 5. Results of EDS analysis of intermetallic phases in Chinese script and polyhedral morphology

Element, wt.%	Chinese script morphology		Polyhedral morphology	
	Mid value	Standard deviation	Mid value	Standard deviation
Al	64.02	6.10	60.43	1.39
Si	6.96	1.31	7.67	2.17
Fe	11.55	2.12	13.22	1.37
Mn	15.56	2.81	17.21	2.68
Mn/Fe	1.35	0.04	1.33	0.27
Fe + Mn	27.11	4.91	30.43	1.63

The intermetallic phases in Chinese script morphology contain: 64.02 wt. % of aluminum, 6.96 wt. % of silicone, 11.55 wt. % of iron and 15.65 wt. % of manganese. The Mn/Fe ratio is 1.35, while the Mn + Fe is 27.11. The intermetallic phases with polyhedral morphology contain: 60.43 wt. % of aluminum, 7.67 wt. % of silicone, 13.22 wt. % of iron and 17.21 wt. % of manganese. The Mn/Fe ratio in polyhedral shaped intermetallics is 1.33 while Fe + Mn total is 30.43. The intermetallic phases in Chinese script morphology have higher Al content. The content of silicone, iron and manganese is higher in polyhedral shaped intermetallic. The Mn/Fe ratio and Fe + Mn are higher in polyhedral intermetallics.

CONCLUSIONS

The transformation and solidification of Fe-rich intermetallic phases during solidification sequence of AlSi12 alloy with w (Mn/Fe) ratio of 0.99 were investigated.

The equilibrium solidification calculations comprehended solidification of α -Al₁₅(FeMn)₃Si₂ and β -Al₅FeSi Fe-rich intermetallic phases. The solidification sequence begins with transformation of α _{Al} dendritic network at 581 °C followed by solidification of eutectic α -Al₁₅(FeMn)₃Si₂ from the L at 580 °C. The eutectic (α _{Al} + β _{Si}) solidifies from the L at 574°C. The β -Al₅FeSi phase solidifies at 570 °C reducing the amount of α -Al₁₅(FeMn)₃Si₂. The additional reduction in α -Al₁₅(FeMn)₃Si₂ phase content occurs at 110 °C during precipitation of Al₁₆Mn₃Ni.

Under realistic conditions the solidification sequence begins with solidification of primary Al₃Fe, Al₆(FeMn) and α -Al₈Fe₂Si Fe-intermetallic phases. The solidification of α -Al₁₅(FeMn)₃Si₂ phase involves peritectic reaction between L, Al₃Fe and Al₆(FeMn) at 648 °C. The β -Al₅FeSi phase solidifies in the interval of 597 °C to 607 °C during peritectic reaction engaging L and α -Al₈Fe₂Si.

The intermetallic phases with Chinese script and polyhedral morphology were identified by light microscopy. The β -Al₅FeSi phase in needle-like morphology was not found.

The EDS analysis indicated similarities between intermetallic phases with Chinese script and polyhedral morphology. The indicated similarity in chemical composition points towards the



18th INTERNATIONAL FOUNDRYMEN CONFERENCE

Coexistence of material science and sustainable technology in
economic growth

Sisak, May 15th-17th, 2019

<http://www.simet.hr/~foundry/>

high w (Mn/Fe) ratio. The w (Mn/Fe) ratio of 0.99 enabled solidification of α -Al₁₅(FeMn)₃Si₂ phase in polyhedral morphology.

Acknowledgements

Investigations were performed within the research topic "Design and Characterization of Innovative Engineering Alloys", Code: TP167 funded by University of Zagreb within the Framework of Financial Support of Research, scientific-research project within Croatian-Slovenian collaboration "Design and Characterization of Innovative Aluminum - Magnesium - Lithium alloy (2018-2019) funded by Ministry of Science and Education and infrastructural scientific project: Center for Foundry Technology, Code: KK.01.1.1.02.0020 funded by European Regional Development Fund, Operational programme Competitiveness and cohesion 2014 - 2020.

Personal gratitude goes to the colleagues from foundry Almos Ltd. (Kutina, Croatia) and Mosdorfer GmbH (Weiz, Austria) for allowing this research to take place.

REFERENCES

- [1] S. Seifeddine, S. Johansson, I. L. Svensson, The influence of cooling rate and magnesium content on the β -Al₅FeSi phase formation and mechanical properties of Al-Si – based alloys, *Materials Science and Engineering A*, 490(2008)1-2, pp. 385-390.
- [2] L. Hurtalová, E. Tillová, M. Chalupová, E. Ďuríníková, Effect of chemical composition of secondary al-si cast alloy on intermetallic phases, *Scientific Proceedings IX International Congress "Machines, Technologies, Materials"*, Scientific Technical Union of Mechanical Engineering, 19th-21th of September, Varna, Bulgaria, pp. 23-26.
- [3] L. Hurtalová, J. Belan, E. Tillová, M. Chalupová, Changes in structural characteristics of hypoeutectic Al-Si cast alloy after age hardening, *Materials Science*, 18(2012)3, pp. 228-233.
- [4] S. Gowri and F. H. Samuel, Effect of alloying elements on the solidification characteristics and microstructure of Al-Si-Cu-Mg-Fe 380 alloy, *Metallurgical and Materials Transactions A*, 25(1994)2, pp. 437-448.
- [5] J. G. Kaufman, E. L. Rooy, *Aluminum Alloy Castings: Properties, processes, and applications*, ASM International, Peoria, 2004.
- [6] S. Belmares-Perales, M. Castro-Román, M. Herrera-Trejo, and L. E. Ramírez-Vidaurri, Effect of cooling rate and Fe/Mn weight ratio on volume fractions of α -AlFeSi and β -AlFeSi phases in Al-7.3Si-3.5Cu alloy, *Metals and Materials International*, 14(2008)3, pp. 307-314.
- [7] R. S. Rana, R. Purohit, S. Das, Reviews on the influences of alloying elements on the microstructure and mechanical properties of aluminum alloy composites, *International Journal of Scientific and Research Publications*, 2(2012)6, pp. 2250-3153.



18th INTERNATIONAL FOUNDRYMEN CONFERENCE

Coexistence of material science and sustainable technology in
economic growth

Sisak, May 15th-17th, 2019

<http://www.simet.hr/~foundry/>

- [8] M. M. Makhlouf, D. Apelian, L. Wang, Microstructures and properties of aluminum die casting alloys, North American Die Casting Association, Rosemont, 1998.
- [9] C. Puncrebutr, A. B. Phillion, J. L. Fife, P. Rockett, A. P. Horsfield, P. D. Lee, In situ quantification of the nucleation and growth of Fe-rich intermetallics during Al alloy solidification, *Acta Materialia*, 79(2014)1, pp. 292-303.
- [10] J. Shouxun, Y. Wenchao, F. Gao, D. Watson, Z. Fan, Effect of iron on the microstructure and mechanical property of Al–Mg–Si–Mn and Al–Mg–Si diecast alloys, *Materials Science & Engineering A*, 564(2013)1, pp. 130-139.
- [11] G. B. Winkelman, Z. W. Chen, D. H. StJohn, M. Z. Jahedi, Morphological features of interfacial intermetallics and interfacial reaction rate in Al-11Si-2.5Cu-(0.15/0.60)Fe cast alloy/die steel couples, *Journal of Materials Science*, 39(2004)1, pp. 519-528.
- [12] S. Ji, W. Yang, F. Gao, D. Watson, Z. Fan, Effect of iron in Al-Mg-Si-Mn ductile die cast alloy, *Light Metals 2013*, Springer, Cham, 2013.
- [13] K. A. Nazari, S. G. Shabestari, Effect of micro alloying elements on the interfacial reactions between molten aluminum alloy and tool steel, *Journal of Alloys and Compounds*, 478(2009), pp. 523-530.
- [14] C. H. Cáceres, I. L. Svensson, J. A. Taylor, Strength-Ductility Behaviour of Al-Si-Cu-Mg Casting Alloys in T6 Temper, *International Journal of Cast Metals Research*, 15(2003)5, pp. 531-543.
- [15] M. Pokusová, I. Berta, M. Murgašová, Metallurgical processing of Al-Si alloys with increased iron content using sodium, strontium, and tellurium, *Journal of Casting & Materials Engineering*, 2(2019)1, pp. 9-13.
- [16] H. W. L. Phillips, Annotated equilibrium diagrams of some aluminium alloy systems, Institute of Metals, Michigan, 1959.
- [17] M. W. Meredith, A. L. Greer, P. V. Evans, R. G. Hamerton, The generation of Al_mFe in ductile aluminium alloys with different grain refining additions, *Light Metals 1998*, The Minerals, Metals & Materials Society, 1998.
- [18] A. Aliravci, M. Pekgüeryüz, Calculation of phase diagrams for the metastable Al-Fe phases forming in direct-chill (DC)-cast aluminum alloy ingots, *Calphad*, 22(1998)2, pp. 147-155.
- [19] C. A. Aliravci, J. E. Gruzleski, M. Pekgüeryüz, A thermodynamic study of metastable Al-Fe phase formation in direct chill (DC)-cast aluminum alloy ingots, *Light Metals 1998*, The Minerals, Metals & Materials Society 2016, 1998.
- [20] Z. K. Liu, Y. A. Chang, Thermodynamic assessment of the Al-Fe-Si system, *Metallurgical and Materials Transactions A*, 30A(1999), pp. 1081-1095.
- [21] M. Gnatko, C. Li, A. Arnold, B. Friedrich, Purification of aluminium cast alloy melts through precipitation of Fe-containing intermetallic compounds, *Metals*, 8(2018)10, pp. 796-808.
- [22] N. A. Belov, D. G. Eskin, A. A. Aksenov, Multicomponent phase diagrams: Application for commercial aluminum alloys, Elsevier Science, 2005.
- [23] S. Ji, W. Yang, F. Gao, D. Watson, Z. Fan, Effect of iron on the microstructure and mechanical property of Al–Mg–Si–Mn and Al–Mg–Si diecast alloys, *Materials Science & Engineering A*, 564(2013)1, pp. 130-1390.



18th INTERNATIONAL FOUNDRYMEN CONFERENCE

Coexistence of material science and sustainable technology in
economic growth

Sisak, May 15th-17th, 2019

<http://www.simet.hr/~foundry/>

- [24] J. Roger, E. Jeanneau, J. C. Viala, Crystal structure of the ternary compound γ -Al₃FeSi, *Zeitschrift für Kristallographie Crystalline Materials*, 226(2011)11, pp. 805-813.
- [25] N. A. Belov, A. A. Aksenov, D. G. Eskin, *Iron in Aluminum Alloys*, Taylor & Francis Group, London, 2002.
- [26] G. Effenberg, S. Ilyenko, *Light metal ternary systems: phase diagrams, crystallographic and thermodynamic data*, Springer, Berlin, 2005.
- [27] X. Cao, J. Campbell, Morphology of β -Al₅FeSi phase in Al-Si cast alloys, *Materials Transactions*, 47(2006)5, pp. 1303-1312.
- [28] M. Mahta, M. Emamy, A. Daman, A. Keyvani, J. Campbell, Precipitation of Fe rich intermetallics in Cr- and Co-modified A413 alloy, *International Journal of Cast Metals Research*, 18(2005)2, pp. 73-79.
- [29] X. Cao and J. Campbell, The Solidification characteristics of Fe-rich intermetallics in Al-11.5Si-0.4Mg cast alloys, *Metallurgical and Materials Transactions A*, 35(2004)5, pp. 1425-1435.
- [30] M. Warmuzek, J. Sieniawski, K. Wicher, G. Mrowka, The study of the distribution of the transition metals and Si during primary precipitation of the intermetallic phases in Al-Mn-Si alloys, *Journal of Materials Processing Technology*, 175(2006)1, pp. 421-426.
- [31] M. Mahta, M. Emamy, X. Cao, J. Campbell, Overview of β -Al₅FeSi phase in Al-Si alloys, *Materials Science Research Trends*, Nova Science Publishers Inc., Ontario, 2008.
- [32] C. Puncreobutr, D. P. Lee, K. M. Kareh, T. Connelley, J. L. Fife, A. B. Phillion, Influence of Fe-rich intermetallics on solidification defects in Al-Si-Cu alloys, *Acta Materialia*, 68(2014)1, pp. 42-51.
- [33] J. Z. Yi, Y. X. Gao, P. D. Lee, T. C. Lindley, Effect of Fe-content on fatigue crack initiation and propagation in a cast aluminum-silicon alloy (A356-T6), *Materials Science and Engineering A*, 386(2004)1, pp. 396-407.
- [34] L. Lu and A. K. Dahle, Iron-rich intermetallic phases and their role in casting defect formation in hypoeutectic Al-Si alloys, *Metallurgical and Materials Transactions A*, 36A(2005)1, pp. 819-835.
- [35] N. Roy, A. M. Samuel, F. H. Samuel, Porosity formation in Al-9 wt. % Si-3 wt. % Cu alloy systems: metallographic observations, *Metallurgical and Materials Transactions A*, 27(1996)2, pp. 415-429.
- [36] C. M. Dinnis, J. A. Taylor, A. K. Dahle, Interactions between iron, manganese, and the Al-Si eutectic in hypoeutectic Al-Si alloys, *Metallurgical and Materials Transactions A*, 37(2006)11, pp. 3283-3291.
- [37] S. G. Shabestari, S. Ghodrat, Assessment of modification and formation of intermetallic compounds in aluminum alloy using thermal analysis, *Materials Science and Engineering A*, 467(2007)1, pp. 150-158.
- [38] C. Bidmeshki, V. Abouei, H. Saghafian, S. G. Shabestari, M. T. Noghani, Effect of Mn addition on Fe-rich intermetallics morphology and dry sliding wear investigation of hypereutectic Al-17.5%Si alloys, *Journal of Materials Research and Technology*, 5(2016)3, pp. 250-258.



18th INTERNATIONAL FOUNDRYMEN CONFERENCE

**Coexistence of material science and sustainable technology in
economic growth**

Sisak, May 15th-17th, 2019

<http://www.simet.hr/~foundry/>

- [39] T. Gao, K. Hu, L. Wang, B. Zhang, X. Liu, Morphological evolution and strengthening behavior of α -Al(Fe,Mn)Si in Al-6Si-2Fe-xMn alloys, *Results in Physics*, 7(2017)1, pp. 1051-1054.
- [40] A. Darvishi, A. Maleki, M. M. Atabaki, M. Zargami, Mutual effect of iron and manganese on microstructure and mechanical properties of aluminium-silicon alloy, *Metallurgical & Materials Engineering*, 16(2010)1, pp. 11-24.
- [41] Z. Zhang, H. Tezuka, E. Kobayashi, T. Sato, Effects of the Mn/Fe ratio and cooling rate on the modification of Fe intermetallic compounds in cast A356 based alloy with different Fe contents, *Materials Transactions*, 54(2013)8, pp. 1484-1490.



18th INTERNATIONAL FOUNDRYMEN CONFERENCE

Coexistence of material science and sustainable technology in
economic growth

Sisak, May 15th-17th, 2019

<http://www.simet.hr/~foundry/>

THE EFFECT OF ANNEALING TIME ON MICROSTRUCTURE AND IMPACT ENERGY OF STAINLESS STEEL AISI 316L

Stjepan Kožuh^{1*}, Katarina Pavičić², Ivana Ivanić¹, Milan Bizjak³, Mirko Gojić¹

¹ University of Zagreb Faculty of Metallurgy, Sisak, Croatia

² Master degree student at University of Zagreb Faculty of Metallurgy, Sisak, Croatia

³ University of Ljubljana Faculty of Natural Sciences and Engineering, Ljubljana, Slovenia

Poster presentation

Original scientific paper

Abstract

In this work the results of microstructural analysis and impact energy testing of austenitic stainless steel AISI 316L were carried out. Investigations were performed before and after annealing at 850 °C. Annealing time in this investigation varied from 30 to 90 minutes. After annealing, the samples were cooled in room temperature air. Microstructural analysis of initial rolled and different annealed states was performed by optical microscopy (OM) and scanning electron microscopy (SEM) equipped with device for energy dispersive spectroscopy (EDS). Impact tests were performed on Charpy V-notch specimens at room temperature. Initial rolled state of investigated steel showed the presence of typical elongated polygonal grains austenite and delta ferrite while annealed states showed the presence and evolution of sigma phase in microstructure. Impact energy value of initial rolled state was 260 J and by increasing annealing time it decreases.

Keywords: *stainless steel, microstructure, heat treatment, annealing, impact energy*

*Corresponding author (e-mail address): kozuh@simet.hr

INTRODUCTION

Stainless steels (SS) are based on the binary Fe-Cr systems, the properties of which are modified by the additional alloying elements like nickel, molybdenum and manganese. Molybdenum is added usually to type 316 steel to enhance the corrosion properties, primarily the pitting and crevice corrosion resistance [1]. In the world's total stainless steel production austenitic type steels take about 60% [2]. Austenitic stainless steels are often used in nuclear power plants, boilers, heat exchangers, chemical reactors etc. because their



18th INTERNATIONAL FOUNDRYMEN CONFERENCE

Coexistence of material science and sustainable technology in
economic growth

Sisak, May 15th-17th, 2019

<http://www.simet.hr/~foundry/>

high resistance to corrosion and high temperature [3-5]. Also, stainless steel offers exceptional advantages for applications in construction [6]. Mostly stainless steels are used for construction as flat products and bars. Besides acceptable yield strength and tensile strength austenitic stainless steels are characterized by high impact energy and relatively low hardness. When considering the operational performance of austenitic stainless steel, the most important points to be taken into account are corrosion resistance, mechanical properties and the integrity of the welded joint in the case of welding these steels. Their high corrosion resistance resulted from formation of a continuous and protective surface oxide layer (passive film). This film is only a few nanometers thick and enriched in Cr (III) oxide/hydroxide species.

To reduce or prevent of microfissures in austenitic stainless steel, a minimum delta ferrite is required. Beneficial effect of delta ferrite is in dissolving more of harmful elements such as sulfur, phosphorus and boron in austenite [7]. But, this ferrite can be transformed in sigma phase. Austenitic steels may undergo microstructural changes when they are exposed to elevated temperature for a shorter or longer period of time. Microstructural variations caused by heat treatment are responsible for changes in the mechanical properties and corrosion resistance. Usually, three intermetallic phases which can be occurred in austenitic stainless steels are sigma phase, chi phase and Laves phase [8-10]. The precipitation mechanism in austenitic stainless steels has been the subject of many investigations motivated by the detrimental effects of the precipitated phases on impact energy and corrosion resistance of steels [11-13]. Padilha et al. [11] and Sourmail [13] reported the precipitation of carbides ($M_{23}C_6$, MC, M_6C , M_7C_3), primary nitrides (MN, M = Zr, Ti, Nb and V), and secondary nitrides (M_2N , M = Cr, Fe) in austenitic stainless steels during thermal treatment (annealing) or welding. Dománková et al. [10] mentioned the following sigma phase composition in AISI 316 which observed after ageing at 800 °C: 56–61%Fe, 21–26%Cr, 12–21%Mo and 1–5%Ni. As the sigma phase composition tends to vary it is difficult to define it by a formula but it is certain that it negatively affects on the steel properties.

The sigma phase has significant influence on properties of stainless steels and has been researched for some time [14]. Generally, the sigma phase forms via thermal ageing but also can be formed via radiation-induced segregation in FeCr alloys. Sigma phase is an intermetallic compound with a complex tetragonal crystalline structure and a typical sigma phase composition for the AISI 316L steel type is 44 % Fe - 29 % Cr - 8 % Mo. Sigma phase can be responsible for reduction in impact energy at room temperature.

Due to AISI 316L stainless steel can be particularly useful at very high temperatures (e.g. in nuclear reactor) it becomes important to study the material microstructure and impact energy at elevated temperatures. The aim of the present work is to show possibility the sigma phase appearance and whether relative short annealing time (up to 90 minutes) can have an influence on microstructure and impact energy of austenitic stainless steel AISI 316L.



18th INTERNATIONAL FOUNDRYMEN CONFERENCE
**Coexistence of material science and sustainable technology in
economic growth**

Sisak, May 15th-17th, 2019

<http://www.simet.hr/~foundry/>

MATERIALS AND METHODS

The material used in this study was AISI 316L type stainless steel which was delivered in hot rolled state. The chemical composition of the investigated steel is listed in Table 1. Specimens for investigation were produced from steel plates of 15 mm thickness. Austenitic stainless steel AISI 316L was studied before and after heat treatment. Heat treatment consisted from annealing at 850 °C for 30, 60 and 90 minutes followed by cooling in the air. Microstructural analysis was carried out by optical microscopy Olympus GX 51 (OM) and scanning electron microscopy TESCAN VEGA 5136 MM (SEM) equipped with device for energy dispersive spectroscopy (EDS). Samples used for microstructural characterization were subsequently ground (papers grid 240-1200), polished (0.3 μ Al₂O₃) and electrolytically etched in two different solutions. To expose austenite boundaries the etching solution 1 containing 60 ml HNO₃ and 40 ml water solution was used at 1V DC for 20 s. Sigma phase were identified with etching solution 2 composed from 56 g KOH in 100 ml water at 2V DC for 10 s. Impact tests were performed on Charpy V-notch specimens (7.5x10x55 mm) at room temperatures on device MLF System PSW 300.

Table 1. Chemical composition of investigated austenitic stainless steel AISI 316L, wt.%

C	Mn	Si	Cu	V	Mo	Al	Cr	Ni	W	Ti	Nb	Fe
0.018	1.50	0.33	0.39	0.078	1.91	0.006	17.34	10.56	0.121	0.003	0.025	balance

RESULTS AND DISCUSSION

From the results of this paper it was possible to establish a correlation between the microstructure, impact energy and various annealing time at 850 °C for investigated AISI 316L stainless steel. The material in delivered (hot rolled) and thermal treated (annealed) state was microstructural characterized firstly after electrolytically etching to expose austenite boundaries (etching solution 1). Figures 1-3 show a typical microstructure of the austenitic stainless steel of the present study. Optical micrographs (Figure 1a) and SEM micrographs (Figures 2a and 3) of microstructure of rolled state exhibited typical elongated grains of polygonal austenite and delta ferrite. Stringers of delta ferrite are elongated in the direction of rolling. In AISI 300 series stainless steels, during casting firstly is formed delta ferrite, and then this ferrite transforms to austenite by diffusion of chromium and nickel between the phases. Chromium diffuses to the ferrite and nickel to the advancing austenite. The austenite grains nucleate and grow into delta ferrite grains. The presence of residual delta ferrite retained at room temperature can be ascribed to the slow diffusion of chromium and nickel. The microstructure, according to Schaeffler diagram (Figure 4) [15], consisted of austenite and up to 10% of delta ferrite because the Cr_{eq}/Ni_{eq} ratio was 1.69 (Equations 1 and 2).



18th INTERNATIONAL FOUNDRYMEN CONFERENCE
**Coexistence of material science and sustainable technology in
economic growth**

Sisak, May 15th-17th, 2019

<http://www.simet.hr/~foundry/>

$$Cr_{eq} = \%Cr + 1.5\%Si + \%Mo + 0.5\%(Ta+Nb) + 2\%Ti + \%W + \%V + \%Al \quad (1)$$

$$Ni_{eq} = \%Ni + 30\%C + 0.5\%Mn + 0.5\%Co \quad (2)$$

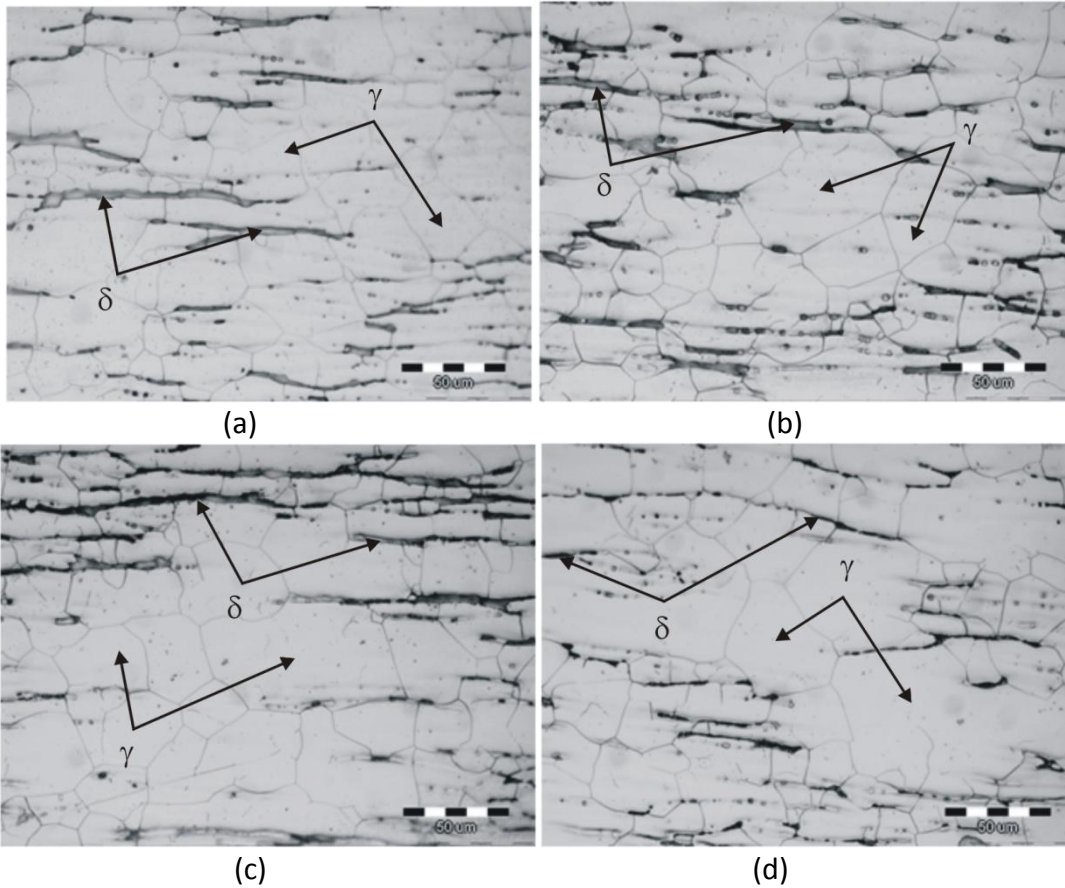


Figure 1. Optical micrographs of AISI 316L stainless steel in rolled (delivered) state (a), annealed state 850 °C/30 min (b), annealed state 850 °C/60 min (c), annealed state 850 °C/90 min (d); etching solution 1



18th INTERNATIONAL FOUNDRYMEN CONFERENCE
Coexistence of material science and sustainable technology in
economic growth

Sisak, May 15th-17th, 2019

<http://www.simet.hr/~foundry/>

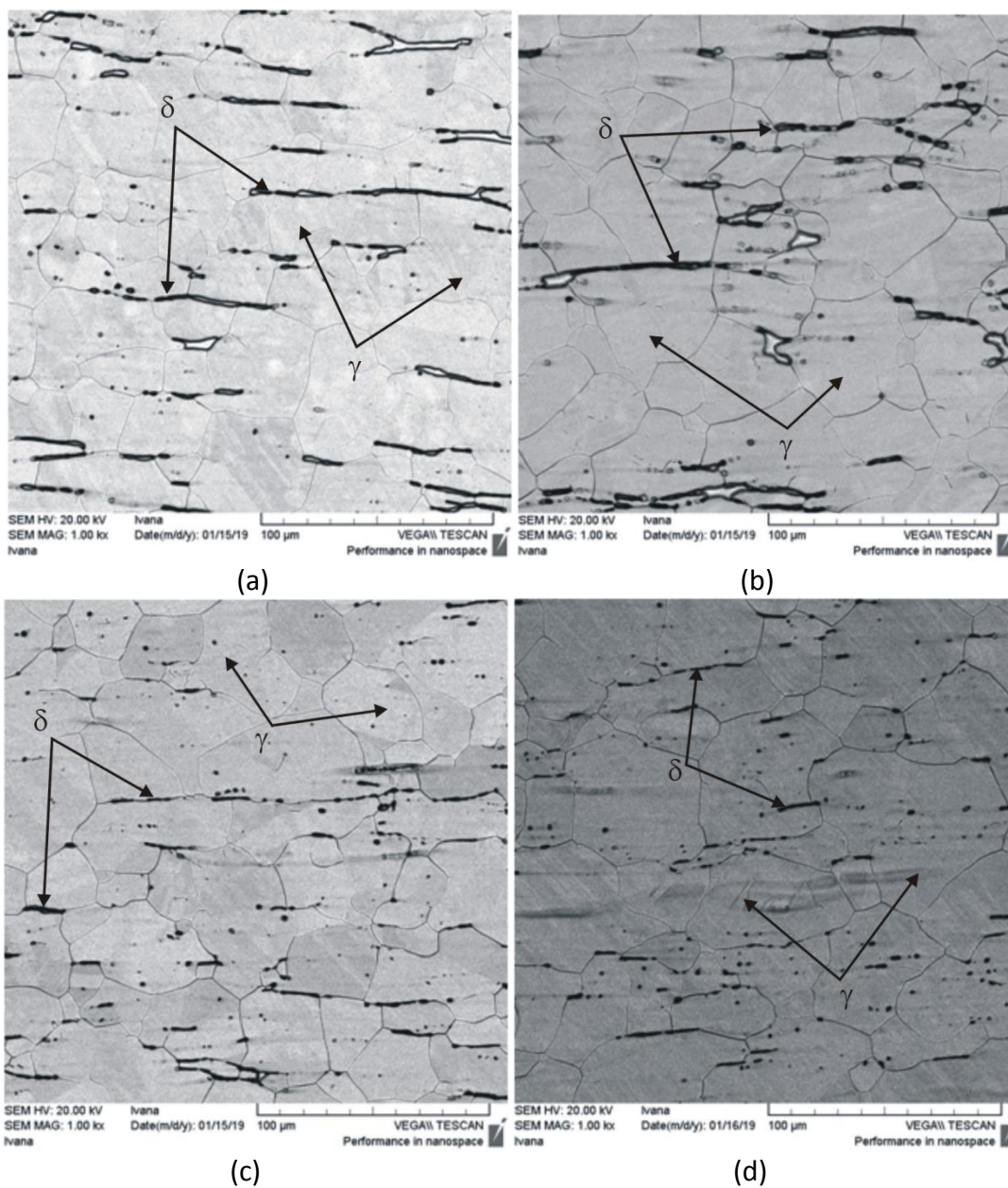


Figure 2. SEM micrographs of AISI 316L stainless steel in rolled (delivered) state (a), annealed state 850 °C/30 min (b), annealed state 850 °C/60 min (c), annealed state 850 °C/90 min (d); etching solution 1



18th INTERNATIONAL FOUNDRYMEN CONFERENCE
Coexistence of material science and sustainable technology in economic growth

Sisak, May 15th-17th, 2019

<http://www.simet.hr/~foundry/>

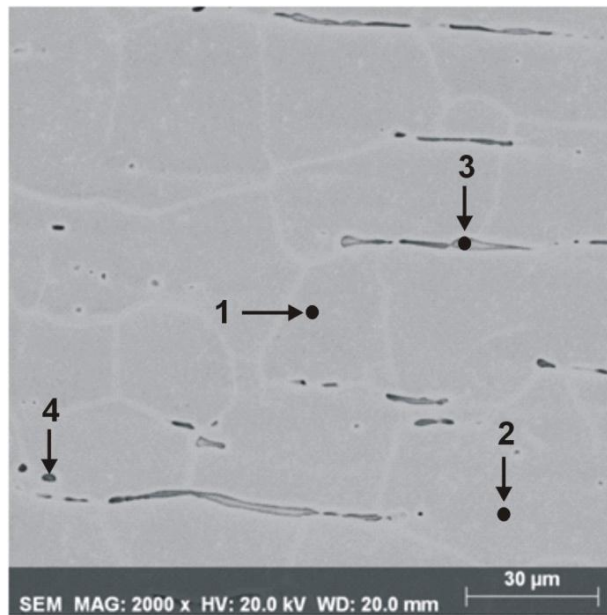


Figure 3. SEM micrograph of AISI 316L stainless steel in rolled (delivered) state with marked positions for EDS analysis; etching solution 1

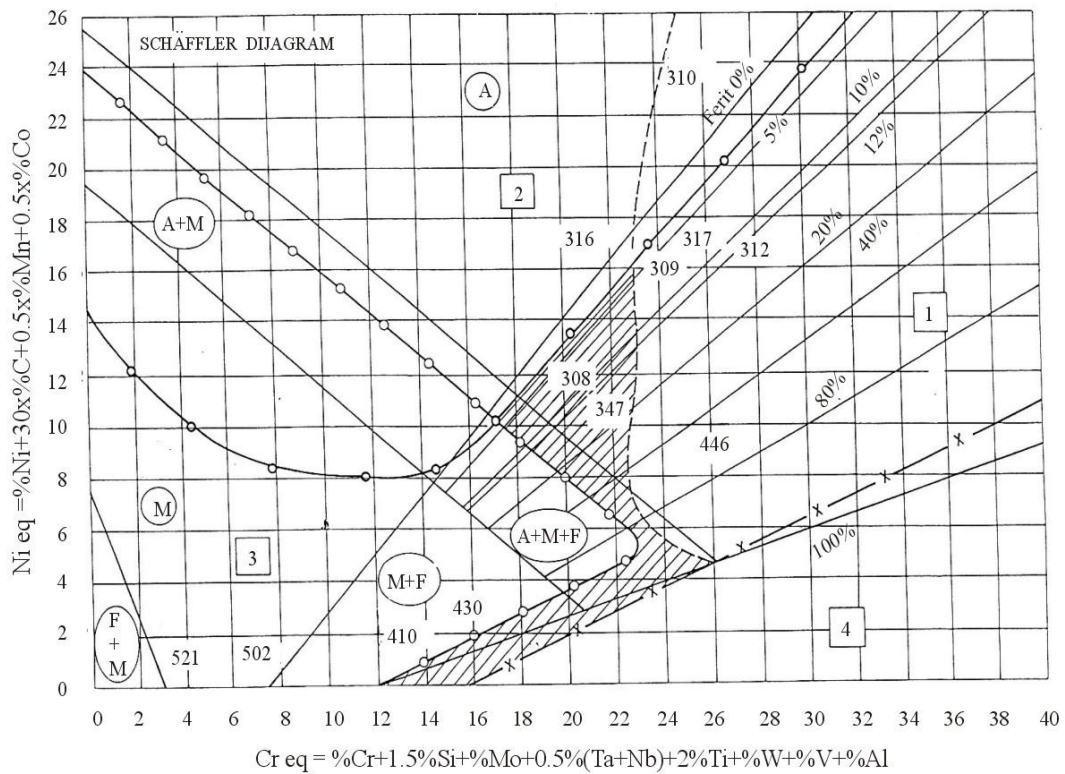


Figure 4. Schaeffler diagram [15]



18th INTERNATIONAL FOUNDRYMEN CONFERENCE

Coexistence of material science and sustainable technology in
economic growth

Sisak, May 15th-17th, 2019

<http://www.simet.hr/~foundry/>

It is generally held that up to 10% of delta ferrite in microstructure of austenitic stainless steel is an effective means of offsetting a grain boundary weakness that develops in austenite at high temperatures and leads to fissuring. From detailed analysis of optical and SEM micrographs (Figures 1b, 1c, 1d and 2b, 2c, 2d) can be obtained similar microstructures in OM micrographs. In contrast, SEM micrographs show that increase in the annealing time results in a decrease content of elongated ferrite stringers. Annealing time was too short for visible changes at OM micrographs, probably. Figure 3 show SEM micrograph of AISI 316L stainless steel in as-rolled state with marked positions for EDS analysis. The results of the EDS analysis (Table 2) show similar content of chromium (16.44-16.87 wt.%), nickel (11.19-11.82 wt.%), manganese (1.77-2.00 wt.%), molybdenum (1.77-2.24 wt.%), and silicon (0.23-0.33 wt.%) for all positions.

Table 2. Results of EDS analysis of different positions in as-rolled state AISI 316L stainless steel; positions marked at the Figure 3

Positions	Chemical composition, wt.%					
	Fe	Cr	Ni	Mn	Mo	Si
1	67.19	16.50	11.74	2.00	2.24	0.33
2	67.81	16.44	11.82	1.88	1.77	0.27
3	67.53	16.66	11.75	1.97	1.84	0.26
4	67.87	16.87	11.19	1.77	2.07	0.23

Also, the investigated steel in rolled and annealed state was microstructural characterized after electrolytically etching to expose sigma phase (etching solution 2). Figures 5-7 show a microstructure of the austenitic stainless steel AISI 316L after etching in solution 2. The presence of sigma phase was observed. Optical and SEM micrographs show that the content of the sigma phase is increasing by increasing annealing time. In rolled (delivered) state (Figures 5a and 6a) the sigma phase is not present since it only occurs by exposing the steel to high temperatures. Sigma phase is intermetallic phase which usually forms in the Fe-Cr systems at high temperatures (550-900 °C). The mechanism of sigma phase nucleation can be described by transformation of delta ferrite. Transformation of delta ferrite into sigma phase was a function of the chemical composition and the kinetics of its precipitation which was governed by the rate of diffusion sigma-forming elements, especially chromium and molybdenum. Figure 7 show SEM micrograph of AISI 316L stainless steel in as-annealed 850 °C/90 min state with marked positions for EDS analysis. The results of the EDS analysis show similar content of manganese (1.96-1.98 wt.%), molybdenum (1.88-2.74 wt.%), and silicon (0.24-0.27 wt.%) for all analyzed positions. By contrast, the chromium content is higher at position 2 (Figure 7, Table 3). Based on this it can be assumed that position 2 presents probably a sigma phase evolution with chromium content 21.42 wt.% and nickel content 6.79 wt.%.



18th INTERNATIONAL FOUNDRYMEN CONFERENCE
Coexistence of material science and sustainable technology in
economic growth

Sisak, May 15th-17th, 2019

<http://www.simet.hr/~foundry/>

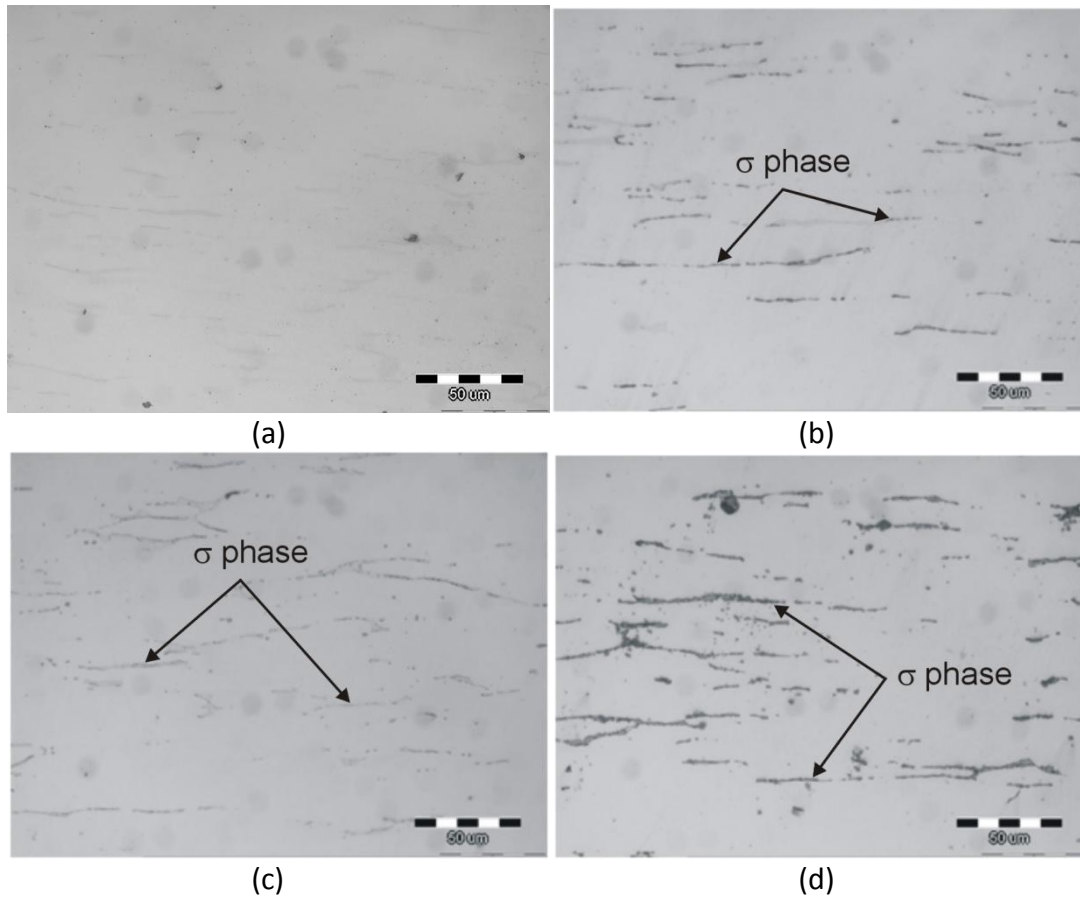


Figure 5. Optical micrographs of AISI 316L stainless steel in rolled (delivered) state (a), annealed state 850 °C/30 min (b), annealed state 850 °C/60 min (c), annealed state 850 °C/90 min (d); etching solution 2



18th INTERNATIONAL FOUNDRYMEN CONFERENCE
**Coexistence of material science and sustainable technology in
economic growth**

Sisak, May 15th-17th, 2019

<http://www.simet.hr/~foundry/>

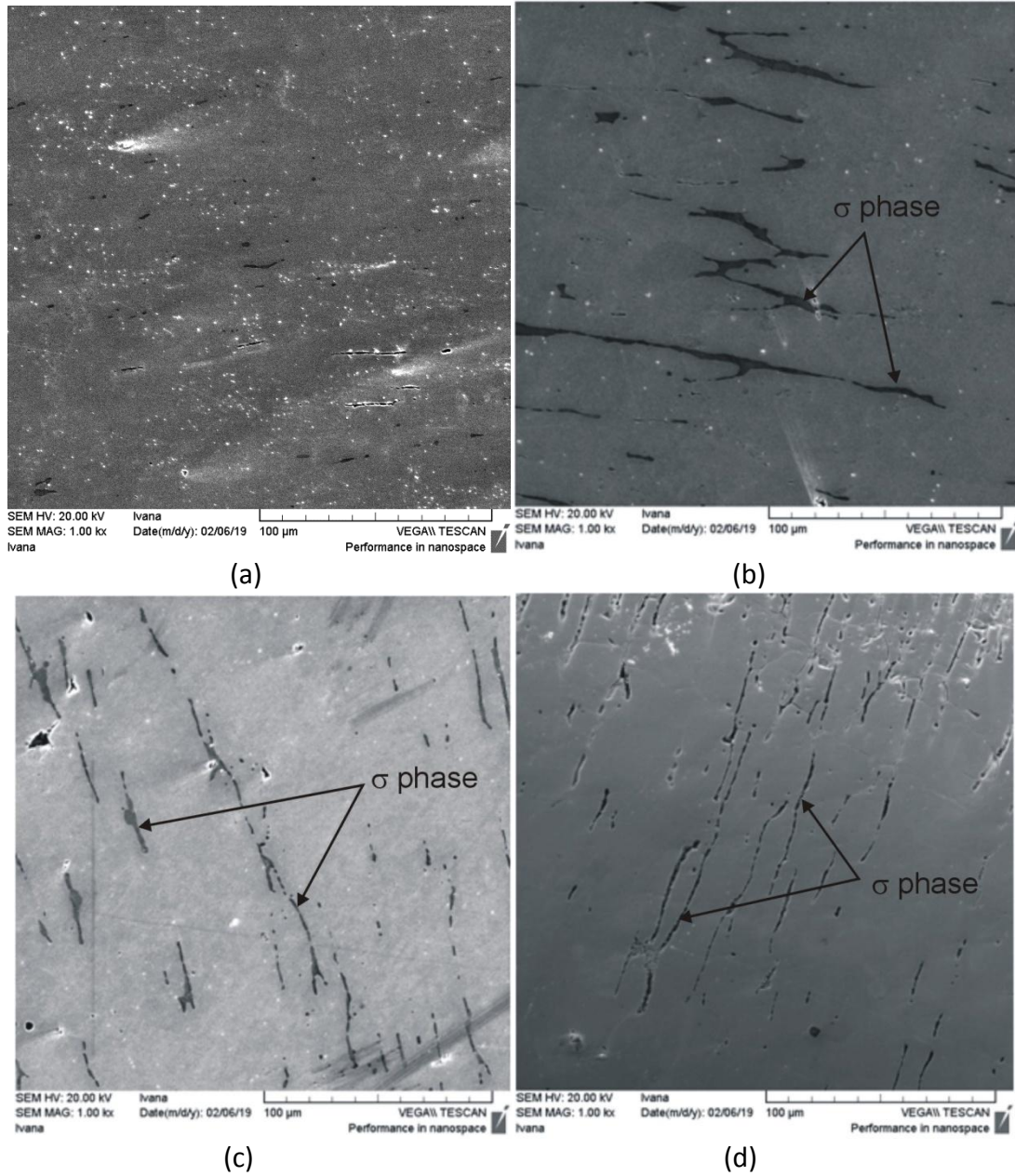


Figure 6. SEM micrographs of AISI 316L stainless steel in rolled (delivered) state (a), annealed state 850 °C/30 min (b), annealed state 850 °C/60 min (c), annealed state 850 °C/90 min (d); etching solution 2



18th INTERNATIONAL FOUNDRYMEN CONFERENCE
**Coexistence of material science and sustainable technology in
 economic growth**

Sisak, May 15th-17th, 2019

<http://www.simet.hr/~foundry/>

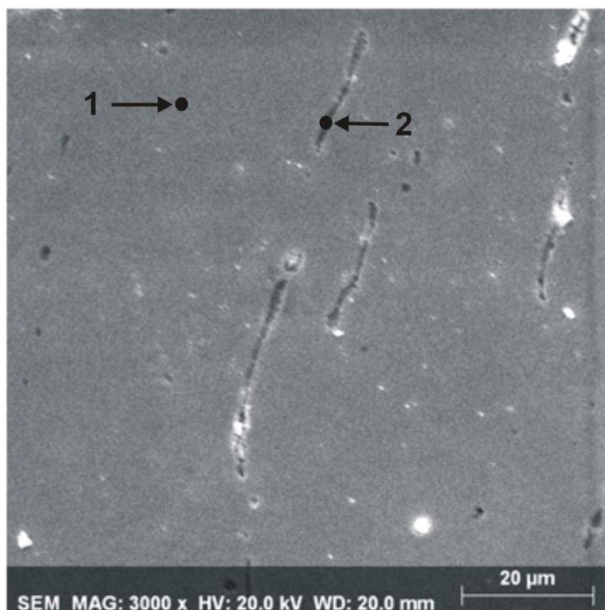


Figure 7. SEM micrograph of AISI 316L stainless steel in annealed state 850 °C/90 min with marked positions for EDS analysis; etching solution 2

Table 3. Results of EDS analysis of different positions in as-annealed state 850 °C/90 min; positions marked at the Figure 6

Positions	Chemical composition, wt.%					
	Fe	Cr	Ni	Mn	Mo	Si
1	68.86	15.81	11.23	1.96	1.88	0.27
2	66.82	21.42	6.79	1.98	2.74	0.24

Figure 8 show the average values of impact energy testing of the investigated AISI 316L stainless steel before and after heat treatment (annealing). The values of impact energy are given as means of mostly three determinations. With a more detailed analysis of the impact energy values it can be seen that increasing annealing time (30-90 min) caused decreasing in impact energy. Before heat treatment impact energy value of AISI 316L stainless steel was 260 J. Heat treated state 850 °C/30 min/air have impact energy 224.5 J and it decreased to 166 J in heat treated state 850 °C/90 min/air. This decrease in impact energy can be related to microstructural changes i.e. occurrence and evolution of sigma phase by increasing annealing time.



18th INTERNATIONAL FOUNDRYMEN CONFERENCE
**Coexistence of material science and sustainable technology in
economic growth**

Sisak, May 15th-17th, 2019

<http://www.simet.hr/~foundry/>

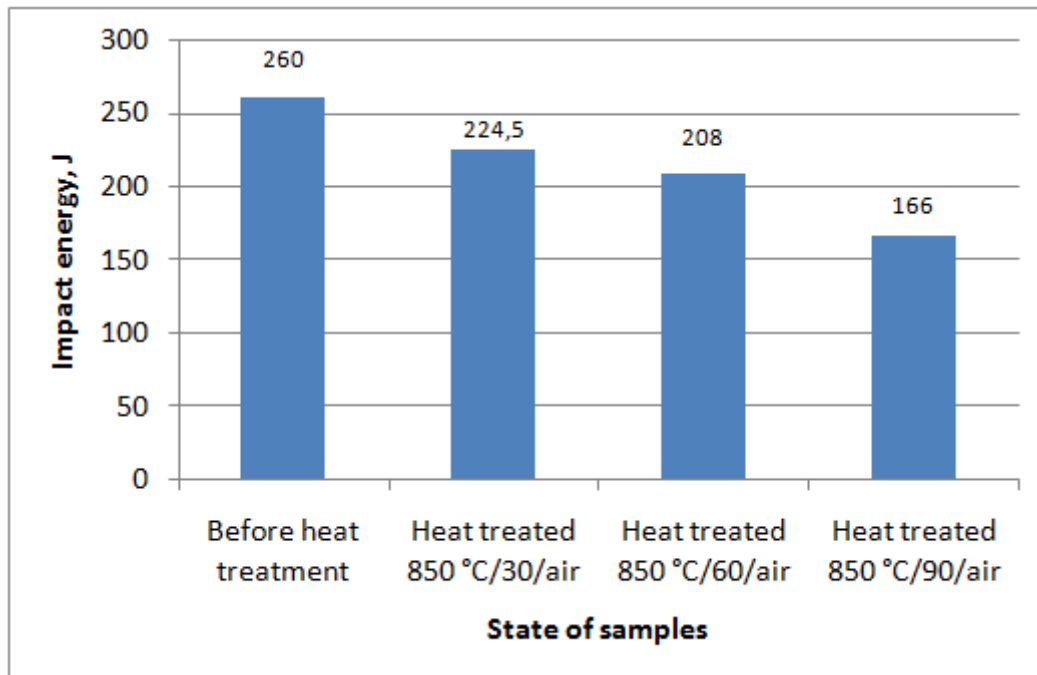


Figure 8. Impact energy vs. annealing time for stainless steel AISI 316L

CONCLUSIONS

Results of investigation the effect of annealing time on microstructure and impact energy of austenitic stainless steel AISI 316L suggest the following:

- Optical micrographs and SEM micrographs of microstructure of initial rolled state confirmed the presence of typical elongated polygonal grains of austenite and delta ferrite stringers.
- Increase in the annealing time from 30 to 90 minutes resulted in a decrease of elongated ferrite stringers content.
- EDS analysis showed similar content of chromium (16.44-16.87 wt.%), nickel (11.19-11.82 wt.%), manganese (1.77-2.00 wt.%), molybdenum (1.77-2.24 wt.%), and silicon (0.23-0.33 wt.%) for different positions in delivered rolled state.
- Optical and SEM micrographs showed the presence of sigma phase in annealed states. According to micrographs the content of the sigma phase is increasing by increasing annealing time.
- EDS analysis of annealed states showed position with higher chromium content (21.42 wt.%) and this position presents a sigma phase evolution, probably.
- Increasing annealing time from 30 to 90 minutes caused a decrease in impact energy. Impact energy value of stainless steel AISI 316L in initial rolled state was 260 J while after 90 minutes of annealing time impact energy decrease to 166 J. This decreasing can be result of occurrence and evolution of sigma phase during annealing.



18th INTERNATIONAL FOUNDRYMEN CONFERENCE

Coexistence of material science and sustainable technology in
economic growth

Sisak, May 15th-17th, 2019

<http://www.simet.hr/~foundry/>

Acknowledgements

This work was supported by the CRO-SLO bilateral scientific-research project „Analysis of fracture surfaces of microalloyed steels“.

REFERENCES

- [1] Z. Begum, A. Poonguzhali, R. Basu, C. Sudha, H. Shaikh, R.V. Subba Rao, A. Patil, R. K. Dayal, Studies of the tensile and corrosion fatigue behavior of austenitic stainless steels, *Corrosion Science*, 53(2011), pp. 1424-1432.
- [2] R. T. Loto, C. A. Loto, I. Ohijeagbon, Effect of heat treatment processes on the localized corrosion resistance of austenitic stainless steel type 301 in chloride/sulphate solution, *Results in Physics*, 11(2018), pp. 570-576.
- [3] L. Chang, M. G. Burke, F. Scenini, Stress corrosion crack initiation in machined type 316L austenitic stainless steel in simulated pressurized water reactor primary water, *Corrosion Science*, 138(2018), pp. 54-65.
- [4] S. S. Rezaei-Nejad, A. Abdollah-Zadeh, M. Hajian, F. Kargar, R. Seraj, Formation of nanostructure in AISI 316L austenitic stainless steel by friction stir processing, *Procedia Materials Science*, 11(2015), pp. 397-402.
- [5] R. K. Desu, H. N. Krishnamurthy, A. Balu, A. K. Gupta, S. K. Singh, Mechanical properties of austenitic stainless steel 304L and 316L at elevated temperatures, *Journal of Materials Research and Technology*, 5(2016)1, pp. 13-20.
- [6] N. R. Baddoo, Stainless steel in construction: A review of research, applications, challenges and opportunities, *Journal of Constructional Steel Research*, 64(2008), pp. 1199-1206.
- [7] Y. Cui, C. D. Lundin, Austenite-preferential corrosion attack in 316 austenitic stainless steel weld metals, *Materials and Design*, 28(2007), pp. 324-328.
- [8] Y. Song, N. A. Mcpherson, T. N. Baker, The effect of welding process on the Chi phase precipitation in as-welded 317L weld metal, *ISIJ International*, 36(1996)11, pp. 1392-1396.
- [9] I. Hrivňák, Metallography of austenitic and dual phase stainless steels, *Acta Metallurgica Slovaca*, 10(2004), pp. 91-102.
- [10] M. Dománková, V. Magula, Study of grain boundary structure on precipitation in 316 austenitic stainless steel, *Acta Metallurgica Slovaca*, 10(2004), pp. 234-238.
- [11] A. F. Padilha, R. L. Plaut, P. R. Rios, Annealing of cold-worked austenitic stainless steels, *ISIJ International*, 43(2003)2, pp. 135-143.
- [12] D. N. Wasnik, G. K. Dey, V. Kain, I. Samajdar, Precipitation stages in a 316L austenitic stainless steel, *Scripta Materialia*, 49(2003)2, pp. 135-141.
- [13] T. Sourmail, Precipitation in creep resistant austenitic stainless steels, *Materials Science and Technology*, 17(2001)1, pp. 1-14.
- [14] K. H. Lo, C. H. Shek, J. K. L. Lai, Recent developments in stainless steels, *Material Science and Engineering R*, 65(2009), pp. 39-104.



18th INTERNATIONAL FOUNDRYMEN CONFERENCE
**Coexistence of material science and sustainable technology in
economic growth**

Sisak, May 15th-17th, 2019

<http://www.simet.hr/~foundry/>

[15] M. Gojić, Tehnike spajanja i razdvajanja, Metalurški fakultet, Sveučilište u Zagrebu, Sisak, 2003.



18th INTERNATIONAL FOUNDRYMEN CONFERENCE

Coexistence of material science and sustainable technology in
economic growth

Sisak, May 15th-17th, 2019

<http://www.simet.hr/~foundry/>

SELECTED PARAMETERS THAT INFLUENCE EMISSION FORMATION DURING ALUMINUM MELTING

Ladislav Lukáč^{1*}, Ján Kizek¹, Augustín Varga¹, Ladislav Lazić², Róbert Dzurňák¹

¹ Technical University of Košice Faculty of Materials, Metallurgy and Recycling, Košice, Slovakia

² University of Zagreb Faculty of Metallurgy, Sisak, Croatia

Poster presentation

Original scientific paper

Abstract

The aim of the present paper is to point out the emissions generated by the aluminum melting process in melting furnaces, especially CO, CO₂, NO_x, based on the analysis of selected parameters. Measurements were made on the experimental equipment to analyze such a process. One of the available methods for reducing emissions is the oxygen enrichment of the combustion air. The results of the study show that the enrichment of the combustion air with oxygen leads to a reduction in CO₂ emissions, but undesirable CO emissions have been observed throughout the aluminum heating and melting process. The conclusions of this particular investigation are very useful for practice and point to the importance of analysis of this kind of processes.

Keywords: *combustion, enrichment of the air, melting of aluminum, drum furnace, emissions*

*Corresponding author (e-mail address): ladislav.lukac@tuke.sk

INTRODUCTION

Melting of metallic materials is carried out in thermal aggregates of various designs. Gaseous, liquid and also solid fuel can be used as a fuel in the combustion process. In addition to the melting process, it is also necessary to pay attention to the efficiency of the combustion processes as well as generating associated emissions of pollutants.

Combustion processes are in many cases influenced by many factors that significantly affect not only the economy but also the efficient operation of such an aggregate. The Commission's conclusions on a common EU energy policy show that each operator has an obligation to increase the energy efficiency of the thermal aggregates in its possession (more detailed in the literature [1]).



18th INTERNATIONAL FOUNDRYMEN CONFERENCE

Coexistence of material science and sustainable technology in economic growth

Sisak, May 15th-17th, 2019

<http://www.simet.hr/~foundry/>

In this context, EU energy policy also focuses on emerging emissions in the operation of thermal aggregates and the possibilities of their reduction. One way to intensify the combustion process is to use the oxy-combustion method (more detailed in the literature [2, 3]).

The charge of the tilting rotary melting furnaces consists of slag, aluminum swabs or high alumina and aluminum scrap. Aluminum swabs are being produced during the production of primary aluminum by electrolysis or in the production of aluminum and its alloys. Aluminum swabs consist of aluminum metal, alumina, chlorides, fluorides and other impurities and contaminants. The aim is to homogenize the input material in order to achieve the desired chemical composition in the final product. Paints and varnishes are particularly problematic as they burn and contribute to metal loss in the melting process. Additionally, they form chemical compounds in the flue gases which must be collected on the filtering devices [4].

Emissions in the monitored aluminum melting process can be divided into two groups. The first group consists of so-called technological emissions, which arise, for example, during a downtime, blasting through openings and leaks (Figure 1), taphole heating and casting channels and other technological operations. The second group of emissions can be incorporated into emissions from fuel combustion, such as: poorly set combustion ratios, false air intake to the furnace, improper burner system and others.



Figure 1. Blasting of emissions through openings

In this paper, the processes of emission formation during melting of metallic materials were monitored, as part of the VEGA project. The experimental equipment for melting aluminum and monitoring the intensification of heat exchange during oxygen enrichment was designed for this purpose. The thermal quantities required for the analysis of the equipment's work and the melting processes were observed during the melting process.



18th INTERNATIONAL FOUNDRYMEN CONFERENCE
**Coexistence of material science and sustainable technology in
economic growth**

Sisak, May 15th-17th, 2019

<http://www.simet.hr/~foundry/>

MATERIALS AND METHODS

The experimental equipment (Figure 2) was constructed to monitor the melting and intensification processes of the gaseous fuel combustion process. Natural gas was used as a fuel for the combustion process. For the design of the physical model, the real tilting rotary melting furnace was used at a geometrical scale of 1:5.2, but the working space of the laboratory equipment was reduced by 129 times compared to the furnace dimensions.

The experimental equipment with a burner system is rated for 10 kW of thermal input. The thermal input of the real furnace is 400 kW, which corresponds to the thermal input ratio of 1:40.

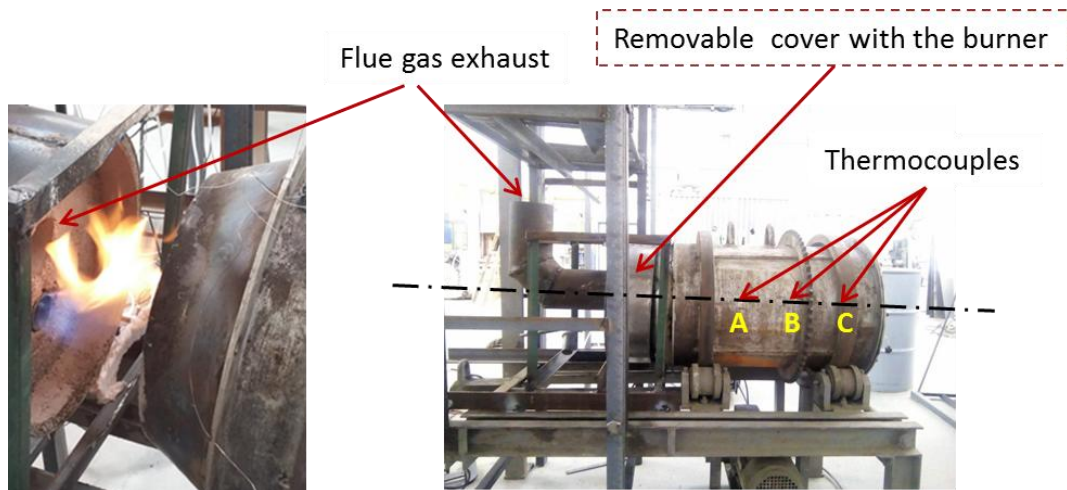


Figure 2. View of experimental equipment - tilting rotary furnace

Through experimental measurements the amount of input material in the furnace was also observed depending on the heating time at different O₂ contents in the air from 21 to 45%. The decisive criterion for melting termination was the achievement of the melt temperature of 740°C and the temperature in the furnace chamber.

The thermocouples used to measure all temperatures were type K. Temperatures were recorded with a COMET MS5 measuring panel. The flue gas analysis was performed using a Testo 350 M analyzer.

RESULTS AND DISCUSSION

In Figure 3 it is possible to monitor the temperature increase in the axis of the experimental device during a single melting process. 15 kg of aluminum was used as the charge for the melting process. The heat input at the burner was maintained at 13.2 kW. Natural gas as a fuel and enriched air were used in the combustion process. The O₂ content in the air was maintained at 45%.



18th INTERNATIONAL FOUNDRYMEN CONFERENCE
**Coexistence of material science and sustainable technology in
economic growth**

Sisak, May 15th-17th, 2019

<http://www.simet.hr/~foundry/>

It is possible to monitor the fluctuation of the temperature field in the axis of the device caused by the regulation of the combustion ratio depending on the oxygen content in the flue gases at the beginning of the heating.

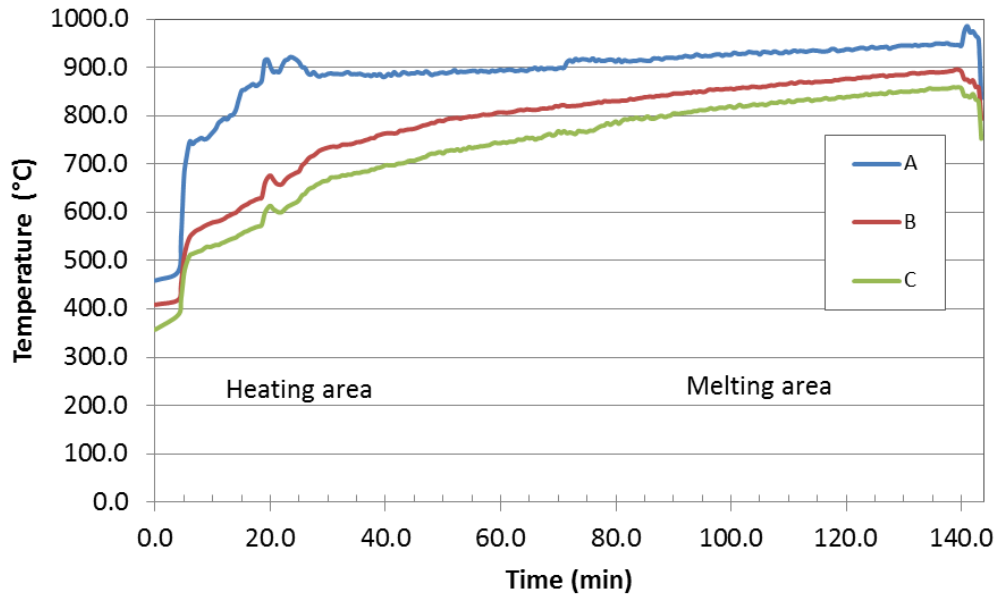


Figure 3. Temperature course for three measuring points (A, B, C) during experimental measurements in the furnace axis, according to the location of the thermocouples A -12 cm distance from burner; B - 27cm distance from burner; C - 57cm distance from burner

Figure 3 shows the course of the contents of the selected flue gas components during the experimental measurement. It was necessary to adjust the combustion ratio after inserting the burner with cover (Figure 2) and sealing the cover at the start of heating phase. Cover sealing is an important factor that influenced the amount of air being sucked and thus the furnace atmosphere composition.

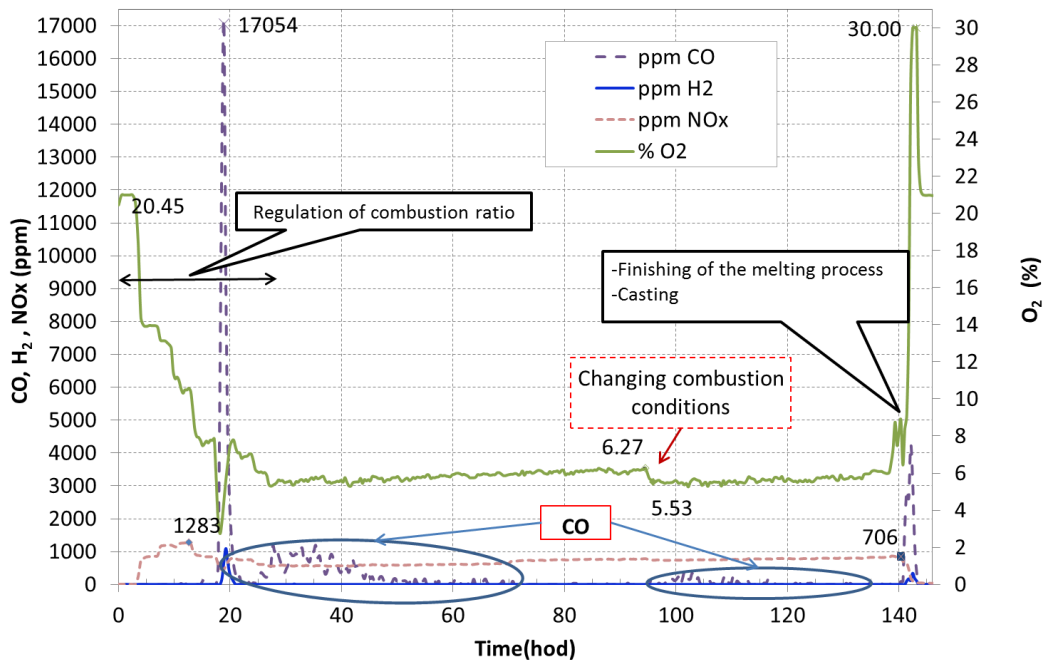


Figure 4. Graphical representation of CO, H₂, NO_x and O₂ content during a single melting process

Figure 4 shows changes in CO, H₂ and NO_x emissions generated by the combustion process obtained from the experimental measurement during a single aluminum melting process. It is possible to observe the decrease in CO content and an increase in oxygen content after setting the combustion ratios in the first stages of heating and melting. This effect was explained in some literature by the oxidation-forming melt and thus by the consumption of part of the supplied oxygen. As a result, the oxidation of the melt also affects to some extent the combustion process (more detailed in the literature [4, 5, 6]). It can be assumed from the course of individual emissions that if more than 6% of O₂ is being kept in the flue gases, hazardous CO can be excluded in the flue gas. A maximum NO_x concentration of 1283 ppm was measured at the start of the experimental measurement at the 13th minute of the measurement. In the next minutes of measurement, the NO_x concentration was about 700 ppm.

The composition of the flue gases at the outlet of the aggregates not only indicates the perfection of the combustion, but also the efficiency of the heat exchange between the flue gases, the charge and the walls in a aggregate. This issue is described in more detail in the literature [2, 7 - 10]. This knowledge can be applied to stationary types of remelting furnaces, which are more described in the literature [11].



18th INTERNATIONAL FOUNDRYMEN CONFERENCE

Coexistence of material science and sustainable technology in economic growth

Sisak, May 15th-17th, 2019

<http://www.simet.hr/~foundry/>

CONCLUSIONS

Partial conclusions can be in the case of aluminum melting in the experimental equipment:

- 1) Combustion processes took place without the formation of CO emissions at O₂ content in flue gas above 6% during experimental measurements.
- 2) The impact of a significant reduction on the specific fuel consumption and the melting time has been proven only to 35% of the O₂ enrichment limit. Above this limit of oxygen enrichment, it had not longer a significant impact.
- 3) Cover sealing contributes to prevention of the infiltration of environmental air into the combustion process, thereby providing better control of combustion conditions.
- 4) During heating and melting of the metal-bearing charge it is also necessary to incorporate into the control model the initial conditions of temperature of the equipment and charge as well as purity or composition of the charge.

The conclusions of the COP21 Climate Changes Conference in Paris (2015) as well as the last COP24 conference in Katowice (2018) and the National Action Plans revealed the need to analyze thermal aggregates for smelting scrap to reduce emissions. Similarly, explore solutions to reduce excessive emissions to reduce excess emissions by adjusting the parameters of technological processes, adjusting or changing the burner system to use the air enriched with oxygen.

The submitted information is only partial results of the grant project solution.

Acknowledgements

This work was supported by the project VEGA 1/0691/18 and obtained results are part of the solution from this grant project.

REFERENCES

- [1] European Parliament. Energy efficiency. Accessible on internet <http://www.europarl.europa.eu/factsheets/sk/sheet/69/energeticka-efektivnost>, 10.10.2018
- [2] CH. E. Baukal, Oxygen- Enhanced Combustion, 2nd ed., CRC Press, Boca Raton, USA, 2013.
- [3] G. Jablonský, M. Pástor, R. Dzurňák, Enrichment of combustible mixture with oxygen in practice, First edition, TU of Košice, Košice, 2015.
- [4] J. Trpčevská, M. Laubertová, Metal waste and its processing, First edition, TU of Košice, Košice, 2015.
- [5] A. Varga et al., Energy balance of Al waste remelting, Report TU of Košice, Faculty of Metallurgy, Department Furnace and Thermal Technology, TU of Košice, Košice, 2010.



18th INTERNATIONAL FOUNDRYMEN CONFERENCE

**Coexistence of material science and sustainable technology in
economic growth**

Sisak, May 15th-17th, 2019

<http://www.simet.hr/~foundry/>

- [6] T. Liptáková, J. Jandačka, M. Malcho, M. Vojsovičová, Corrosion-erosion waste of metals in the duct system of the recycling aluminium, Communications: Scientific Letters of the University of Žilina, 14(2012)4 , pp. 37-42.
- [7] A. Varga, G. Jablonský, L. Lukáč, J. Kizek, Thermal technology for metallurgists, TU of Košice, Košice, 2013.
- [8] M. Rimár, M. Fedák, Combustion processes, First edition, TU of Košice, Košice, 2014.
- [9] K. Ferstl, M. Masaryk, Heat transfer book, STU Bratislava, Bratislava, 2011.
- [10] A. Varga et al., Energy analysis of tilting rotary furnace for Al scrap processing, Report TUKE, Faculty of Metallurgy, Department Furnace and Thermal Technology, TU of Košice, Košice, 2011.
- [11] V. Lunkin, A. Varga, J. Kizek, L. Lazić, Analysis of aluminium scrap melting, 13th International Foundrymen Conference: Innovative Foundry Processes and Materials, (eds. Z. Glavaš, Z. Zovko Brodarac, N. Dolić), University of Zagreb Faculty of Metallurgy, 16. - 17. May, 2013, Opatija, Croatia, pp. 193-198.



18th INTERNATIONAL FOUNDRYMEN CONFERENCE

Coexistence of material science and sustainable technology in
economic growth

Sisak, May 15th-17th, 2019

<http://www.simet.hr/~foundry/>

INVESTIGATION OF THERMAL PROPERTIES OF THE Ga–In AND Ga–Sn EUTECTIC ALLOYS

Ivana Manasijević^{1*}, Ljubiša Balanović¹, Tamara Holjevac Grgurić²,
Emi Govorčin Bajsić³

¹ University of Belgrade Technical Faculty in Bor, Bor, Serbia

² University of Zagreb Faculty of Metallurgy, Sisak, Croatia

³ University of Zagreb Faculty of Chemical Engineering and Technology, Zagreb, Croatia

Poster presentation

Original scientific paper

Abstract

The application of phase change materials (PCMs) has grown rapidly in the field of thermal management and thermal energy storage. Low melting point metals (LMPMs) and eutectic alloys represent new category of PCMs, which has certain advantages over commercial nonmetallic PCMs like high thermal conductivity and high volumetric latent heat. Two most important criteria for PCMs selection are melting point and the latent heat of melting. In this study, melting and solidification temperatures and latent heat of melting and solidification of the Ga–In and Ga–Sn eutectic alloys were measured using differential scanning calorimetry (DSC). Undercooling tendency of the studied alloys, which is also important criterion for the PCMs selection, was investigated using heating and cooling DSC cycles. Experimentally determined results were compared with the results of thermodynamic calculations according to the CALPHAD (calculation of phase diagram) method and good agreement was observed.

Keywords: Ga–In alloy, Ga–Sn alloy, eutectic alloy, latent heat of melting

*Corresponding author (e-mail address): ivanamanasijevic80@gmail.com

INTRODUCTION

Low-melting alloys based on gallium have found wide usage in many practical applications, including soldering, thin-film coatings and fuse applications [1-3]. They are usually used instead of toxic mercury in heat transfer systems, thermostats, switches and barometers [3].



18th INTERNATIONAL FOUNDRYMEN CONFERENCE

Coexistence of material science and sustainable technology in
economic growth

Sisak, May 15th-17th, 2019

<http://www.simet.hr/~foundry/>

Gallium and its alloys own a variety of properties that make them an excellent choice for microelectronic interconnects, including low melting point, non-toxicity, and the ability to wet without fluxing most materials used in microelectronics [4]. Gallium-based liquid alloys have excellent thermal and electrical conductivities with low viscosity [5].

In recent years there has been a lot of research regarding the usage of low-melting metals and eutectic alloys as a phase change materials (PCMs), in the field of thermal management and thermal energy storage [6-10]. Phase change materials (PCMs) are defined as materials with high heat of fusion which undergo melting/solidification process at a constant or nearly constant temperature and absorb/release thermal energy from/to the surroundings [9,10]. Many different classes of materials have been investigated so far and commercially used in the field of PCMs for heat storage [7-12]. The usual drawback of commercial nonmetallic PCMs is their low thermal conductivity, which considerably limits the heat transfer in the material [11,12]. In order to improve the thermal conductivity, intensive research is being carried out on a variety of metals and eutectic alloys as potential PCMs for heat accumulation [7-12]. Low-melting point metals (LMPMs) and eutectic alloys represent relatively new category of PCMs [7-10]. The main advantages of low-melting metallic materials usage as PCMs are their high thermal conductivity and high volumetric latent heat [10,12].

From that point of view, the low-melting eutectic alloys based on gallium represent the most promising candidates for low (operating temperature below 40 °C) temperature PCMs [6]. However, literature data for numerous essential thermo-physical properties such as melting point, latent heat of fusion, specific heat capacity, thermal conductivity, supercooling tendency for many low melting gallium based eutectics are rare and not consistent [6,7].

The aim of the present study is experimental and theoretical investigation of melting and solidification temperatures and latent heat of melting and solidification for the eutectic Ga–In and Ga–Sn binary alloys. For this purpose, the analysis of melting and solidification processes of investigated alloys was carried out using DSC method. Experimentally obtained results were compared with the results of phase equilibria calculations according to the CALPHAD method.

LITERATURE REVIEW

Phase equilibria and thermodynamic properties of the Ga–In and Ga–Sn binary systems have been widely investigated both experimentally and by thermodynamic calculations.

Experimental investigations of thermodynamic properties of the Ga–In binary system have been published in a larger number of studies. Mixing enthalpies of the liquid Ga–In were determined by Bros [13], Predel and Stein [14], Ansara et al. [15], and Girard et al. [16]. Phase equilibria in the Ga–In system have been investigated by French et al. [17], Denny et al. [18], Svirbeley et al. [19], Heubner et al. [20], Hayes and Kubaschewski [21], and Kuznetsova et al. [22].

Based on the available experimental data, Anderson and Ansara [23] performed thermodynamic assessment of the Ga–In binary system and calculated optimized phase diagram given in Figure 1.



18th INTERNATIONAL FOUNDRYMEN CONFERENCE

Coexistence of material science and sustainable technology in
economic growth

Sisak, May 15th-17th, 2019

<http://www.simet.hr/~foundry/>

According to the presented phase diagram of the Ga-In binary system, Ga and In form simple eutectic phase diagram with eutectic reaction at 15.3 °C, composition of eutectic point at 14.2 at. % In, and small solubility of Ga in (In) solid solution phase.

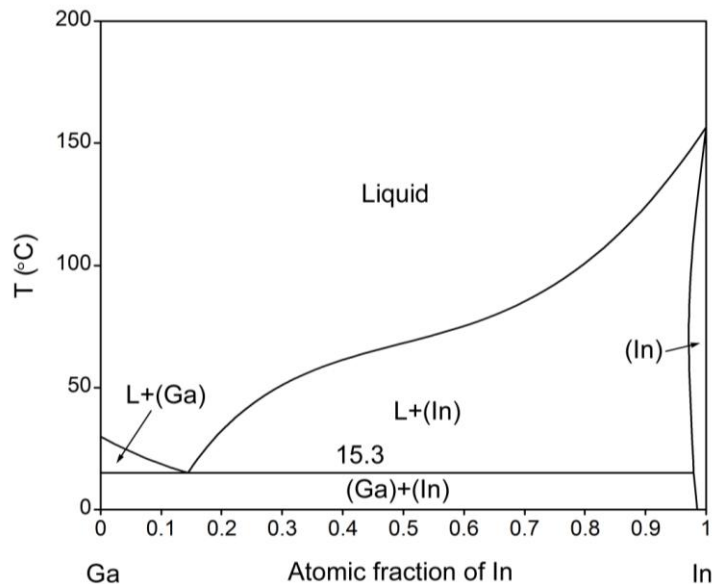


Figure 1. Calculated phase diagram of the Ga–In binary system using thermodynamic parameters from Anderson and Ansara [23]

Thermodynamic optimization of the Ga-Sn phase diagram has been performed by Anderson and Ansara [24]. The experimental data from [24-29] were the basis for thermodynamic modeling. Ga and Sn form eutectic phase diagram with eutectic reaction at 20.7 °C on the Ga- rich side (Figure 2). The solubility of Sn in Ga is negligible. The solubility of Ga in Sn at the eutectic temperature is about 6.4 at. %. No experimental data are reported for equilibria including low temperature (α Sn) phase. Calculated phase diagram of the Ga–Sn binary system is shown in Figure 2.



18th INTERNATIONAL FOUNDRYMEN CONFERENCE

Coexistence of material science and sustainable technology in economic growth

Sisak, May 15th-17th, 2019

<http://www.simet.hr/~foundry/>

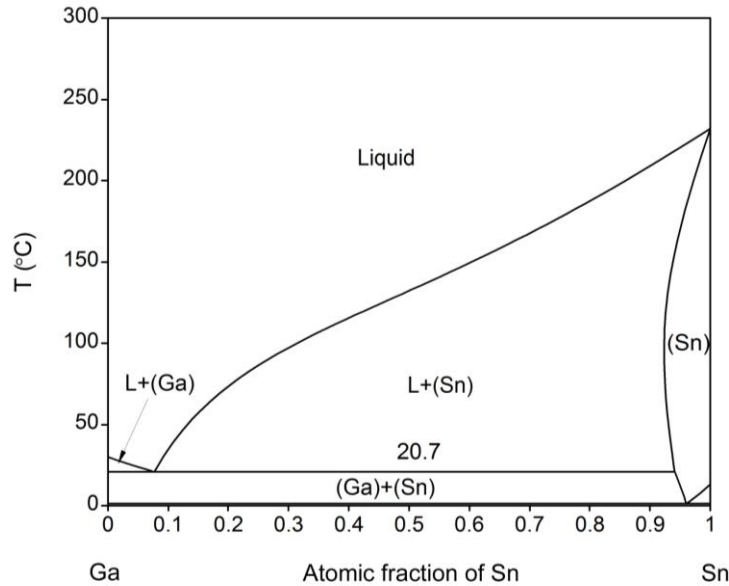


Figure 2. Calculated phase diagram of the Ga–Sn binary system using thermodynamic parameters from Anderson and Ansara [24]

Values of thermophysical properties for the constitutive pure metals Ga, In, and Sn are available in the reference literature [30]. Melting point and latent heat of fusion values for the elements Ga, In and Sn are given in Table 1. It can be seen that among this elements, Ga has the lowest melting point and the highest latent heat of fusion.

Table 1. Melting points and latent heat of fusion of the pure metals Ga, In and Sn [30]

Metal	Melting point (°C)	Latent heat of fusion (Jg ⁻¹)
Ga	29.8	80.2
In	156.61	28.47
Sn	231.9	59.6

Although the phase diagrams of many binary Ga-based systems have been well established, investigations of the thermophysical properties of the Ga-based eutectic alloys are rare in the existing literature [31,32]. Therefore, the results presented in this study should contribute to the better understanding of thermal behavior of eutectic Ga-In and Ga-Sn alloys.

MATERIALS AND METHODS

The Ga–In and Ga–Sn alloys with target eutectic compositions (Ga-14.20 at. % In and Ga–7.70 at. % Sn) were prepared by melting of high purity elements (In 99.995 %, Sn 99.99 %, Ga



18th INTERNATIONAL FOUNDRYMEN CONFERENCE

Coexistence of material science and sustainable technology in
economic growth

Sisak, May 15th-17th, 2019

<http://www.simet.hr/~foundry/>

99.999 %, Alfa Aesar) in the graphite crucibles under argon atmosphere. The masses of the prepared samples were about 1 g. The total mass losses of the samples after melting were less than 0.2 % so the nominal compositions were accepted for further analysis.

Melting and solidification temperatures and latent heat of melting and solidification were studied using DSC analyzer Mettler Toledo 822e. Measurements were done in argon atmosphere, through 5 heating/cooling cycles from -50 to 100 °C with heating/cooling rates 5 °Cmin⁻¹. Samples' masses were about 80 mg. Before performing DSC experiments, temperature and heat calibrations were done using the pure metal standards (In and Ga) under the measurement conditions.

RESULTS AND DISCUSSION

Thermodynamic calculations

Thermodynamic calculations of phase equilibria and enthalpy of fusion were carried out using CALPHAD (calculation of phase diagrams) method [33,34]. Calculations were performed using optimized thermodynamic parameters from [23,24]. Calculated results, obtained by using Pandat software [35], include diagrams of phase fractions of stable phases as a function of temperature and temperature dependencies of enthalpy for two investigated eutectic alloys.

Calculated diagrams of phase fractions of stable phases as a function of temperature for the eutectic alloys are presented in Figures 3a-b.

Temperature dependence of phase fractions for the Ga-14.20 at. % In alloy under equilibrium conditions is given in Fig. 3a. Above eutectic temperature (15.3 °C) Ga-14.20 at. % In alloy is fully liquid. At the eutectic temperature liquid phase isothermally transforms according to the eutectic reaction Liquid \rightarrow (Ga)+(In) into (Ga) and (In) phases. Below the eutectic temperature microstructure of the eutectic alloy includes (Ga) and (In) phases. It can be seen that phase fraction of (Ga) phase is much larger (about 85 %) than the phase fraction of (In) phase (about 15 %).

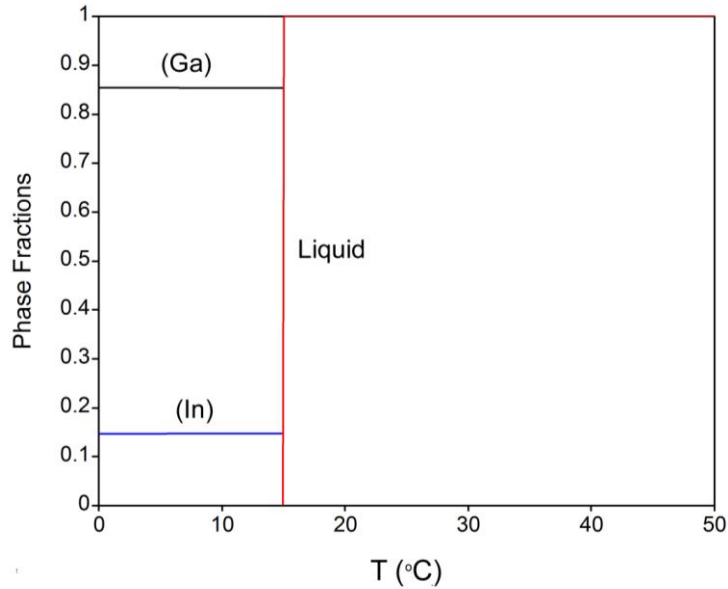
Calculated temperature dependence of phase fractions for the Ga-7.70 at. % Sn alloy under equilibrium conditions is presented in Fig. 3b. By reaching the eutectic temperature (20.7 °C), Ga-rich liquid phase isothermally converts to (Ga) and (Sn) solid solution phases according to the Liquid \rightarrow (Ga)+(Sn) eutectic reaction. Below the liquidus temperature (Ga) and (Sn) phases are stable phases. The phase fraction of the (Ga) phase is much larger (over 90%) than the phase fraction of (Sn) phase.



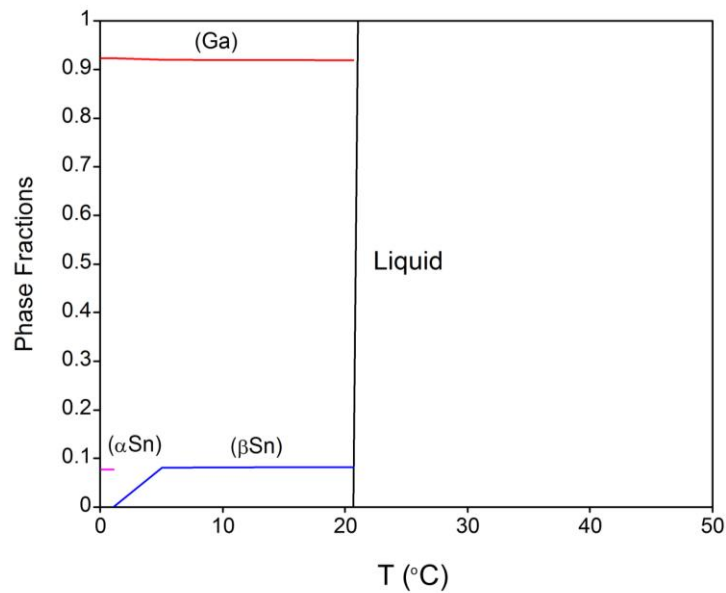
18th INTERNATIONAL FOUNDRYMEN CONFERENCE
**Coexistence of material science and sustainable technology in
economic growth**

Sisak, May 15th-17th, 2019

<http://www.simet.hr/~foundry/>



(a)



(b)

Figure 3. Calculated phase fractions of stable phases as a function of temperature for the investigated eutectic alloys: (a) Ga-14.20 at. % In; (b) Ga-7.70 at. % Sn

Figure 4 shows calculated dependences of enthalpy vs. temperature for the investigated Ga-14.20 at. % In alloy (Figure 4a) and Ga-7.70 at. % Sn alloy (Figure 4b).

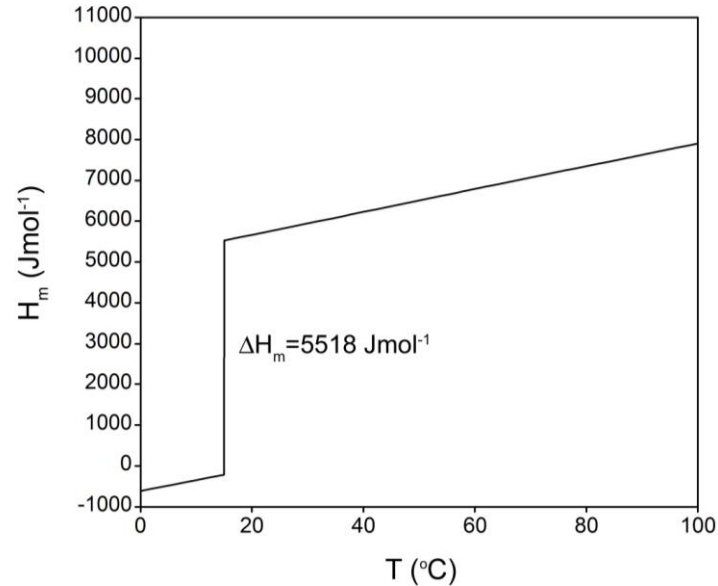


18th INTERNATIONAL FOUNDRYMEN CONFERENCE

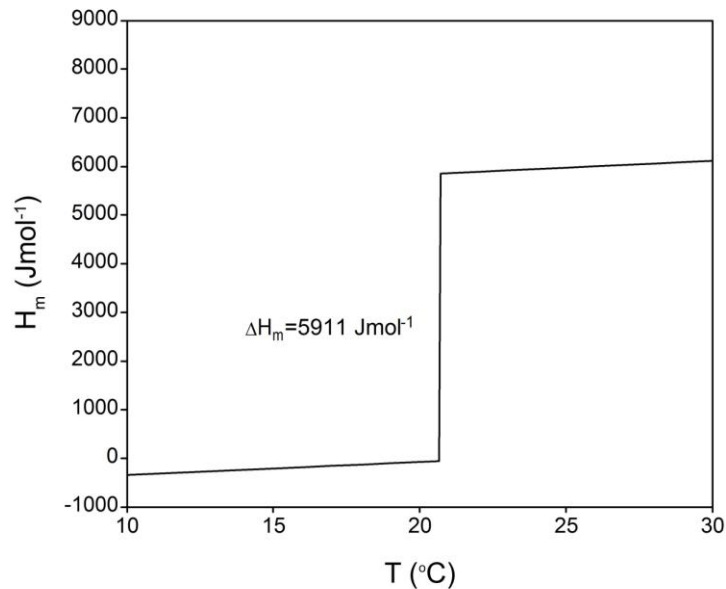
Coexistence of material science and sustainable technology in economic growth

Sisak, May 15th-17th, 2019

<http://www.simet.hr/~foundry/>



(a)



(b)

Figure 4. Temperature dependence of enthalpy calculated under equilibrium conditions for the eutectic alloy: (a) Ga-14.20 at. % In; (b) Ga-7.70 at. % Sn

Enthalpy change during the melting phase transformation represents enthalpy of melting (ΔH_m) or latent heat of melting and is equal to the enthalpy difference between the liquid and solid phases at the melting temperature. According to the results of calculation, calculated latent heat of melting for the Ga-14.20 at. % In alloy is 5518 Jmol^{-1} (72.4 Jg^{-1}) and for the Ga-7.70 at. % Sn alloy is 5911 Jmol^{-1} (80.4 Jg^{-1}).



18th INTERNATIONAL FOUNDRYMEN CONFERENCE

Coexistence of material science and sustainable technology in
economic growth

Sisak, May 15th-17th, 2019

<http://www.simet.hr/~foundry/>

Summary of the results obtained by thermodynamic calculation, including compositions of eutectic alloys, calculated eutectic temperatures, and related calculated enthalpies of fusion, is given in Table 2.

Table 2. Calculated eutectic temperatures, compositions of eutectic alloys and related enthalpies of melting using the optimized thermodynamic parameters from [23,24]

T (°C)	Invariant eutectic reaction	Composition in mole fractions		Calculated enthalpy of fusion (Jmol ⁻¹)
		x(Ga)	x(In)	
15.3	Liquid → (Ga)+(In)	x(Ga)=0.8580	x(In)=0.1420	5518
20.7	Liquid →(Ga)+(Sn)	x(Ga)=0.9230	x(Sn)=0.0770	5911

Thermal analysis

Differential scanning calorimetry (DSC) was used for measurements of melting and solidification temperatures and latent heat of melting and solidification of the investigated Ga–In and Ga–Sn eutectic alloys. The temperature of the peak onset was used for determination of eutectic temperature [36]. Associated latent heat can be calculated as the integral of the heat flow curve for each studied alloy. The heating/cooling curves were recorded using scanning velocities of 5 °Cmin⁻¹.

Examples of DSC thermograms (taken from the third heating and cooling runs) for the investigated eutectic alloys are shown in Figure 5.

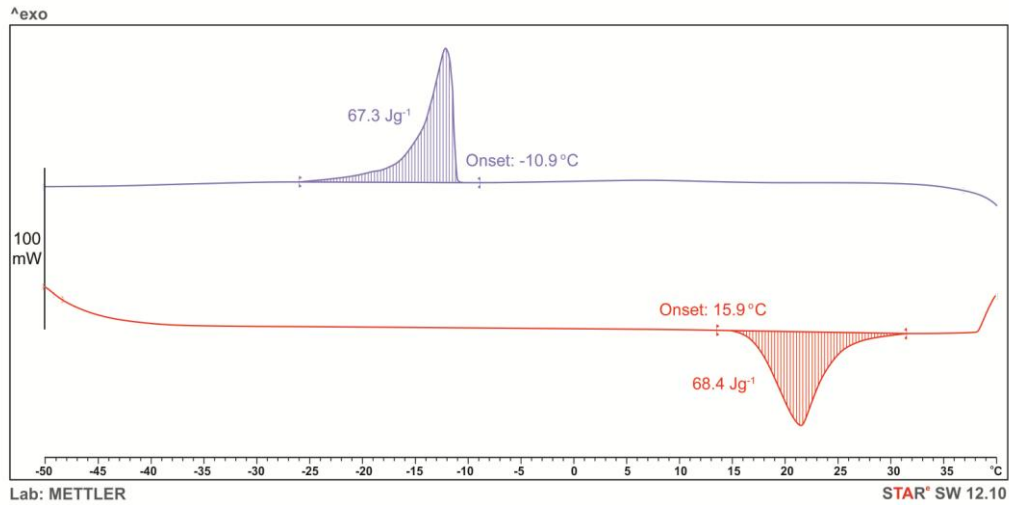
Figure 5a shows DSC heating/cooling thermogram for the Ga-14.20 at. % In alloy. One exothermic peak is observed during cooling and one endothermic peak occurs during heating of the sample. The endothermic peak observed during heating is related to the melting transformation of the Ga-14.20 at. % In alloy. Experimentally determined melting temperature for the Ga-14.20 at. % In eutectic alloy (15.9±0.1 °C) from this study, obtained in heating regime, is to some extent higher than the corresponding calculated value (15.3 °C) obtained by thermodynamic assessment. Experimentally determined latent heat of melting for the Ga-14.20 at. % In eutectic alloy, 68.4±0.2 Jg⁻¹, is noticeably smaller than related calculated value (72.4 Jg⁻¹). The identified exothermic peak, with the onset temperature - 10.9±0.2 °C is determined to be alloy's solidification temperature. Released heat (67.3±0.2 Jg⁻¹) is somewhat smaller but still comparable to the heat absorption during the alloy melting. It can be concluded that, under measurement conditions, investigated alloy exhibits significant undercooling (supercooling) effect which could negatively affect its potential application in the field of low operating PCMs. It is known that pure Ga also displays large undercooling on solidification [37].



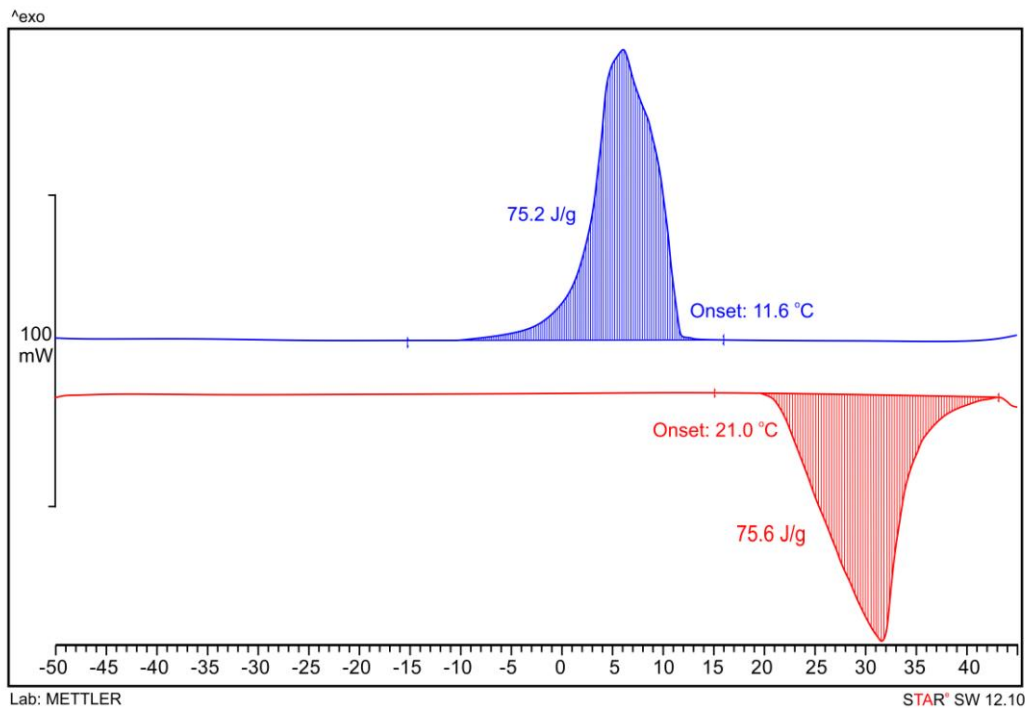
18th INTERNATIONAL FOUNDRYMEN CONFERENCE
Coexistence of material science and sustainable technology in economic growth

Sisak, May 15th-17th, 2019

<http://www.simet.hr/~foundry/>



(a)



(b)

Figure 5. DSC heating/cooling curves:
(a) Ga-14.20 at. % In eutectic alloy; (b) Ga-7.70 at. % Sn eutectic alloy

Figure 5b represents DSC thermogram for the Ga-7.70 at. % Sn eutectic alloy. One well defined endothermic peak was detected during heating and one exothermic peak was observed during cooling of the investigated sample. The mean onset temperature of the peak obtained during heating runs is 21.0 ± 0.1 °C, which is only slightly higher than related



18th INTERNATIONAL FOUNDRYMEN CONFERENCE

Coexistence of material science and sustainable technology in
economic growth

Sisak, May 15th-17th, 2019

<http://www.simet.hr/~foundry/>

calculated melting temperature (20.7 °C). The measured onset temperature of the exothermic peak obtained during cooling runs is 11.6 ± 0.2 °C and it represents solidification temperature for the Ga–7.70 at. % Sn eutectic alloy. It is noticeable that this alloy also shows undercooling on solidification but the undercooling value is not so prominent as in the case of Ga-14.20 at. % In alloy. Experimentally determined heat of melting is 75.6 ± 0.1 Jg⁻¹ and related heat of solidification 75.2 ± 0.1 Jg⁻¹. These results are in reasonable agreement with the results of Pan et al. [32], who have reported measured values of 78.3 and 79.2 Jg⁻¹ for the Ga–8.4 at. % Sn and Ga–5.0 at. % Sn alloys, respectively.

Average values of eutectic temperatures and latent heat of melting and solidification together with related standard uncertainties obtained from five repeated DSC heating/cooling cycles are presented in Table 3. The results of thermodynamic calculation are also shown in Table 3 for comparison.

Table 3. Comparison between DSC results and results of thermodynamic calculation for the investigated Ga-14.20 at. % In and Ga–7.70 at. % Sn eutectic alloys

Alloy composition (at.%)	Calculation		Experimental results			
	Melting temperature (°C)	Latent heat of fusion (Jg ⁻¹)	Melting temperature (°C)	Latent heat of fusion (Jg ⁻¹)	Solidification temperature (°C)	Latent heat of solidification (Jg ⁻¹)
Ga-14.20 In	15.3	72.4	15.9 ± 0.1	68.4 ± 0.1	-10.9 ± 0.2	67.3 ± 0.2
Ga–7.70 Sn	20.7	80.4	21.0 ± 0.1	75.6 ± 0.1	11.6 ± 0.2	75.2 ± 0.2

CONCLUSIONS

In the present study, an investigation of thermal properties of the low melting Ga-14.20 at. % In and Ga–7.70 at. % Sn eutectic alloys as candidate PCMs were performed by using differential scanning calorimetry (DSC) and thermodynamic calculations according to the CALPHAD method. Experimentally determined melting temperatures were found to be in good agreement with the results of thermodynamic calculation. Experimentally determined solidification temperatures for both investigated eutectic alloys are considerably lower than related determined melting temperatures, especially for the Ga-14.20 at. % In alloy. These results reveal that both investigated alloys are very susceptible to undercooling, which could have negative effect on their potential application as PCMs. It was determined that Ga–7.70 at. % Sn alloy has very high latent heat of melting (75.6 ± 0.1 Jg⁻¹), close to the latent heat of melting of pure gallium (80.2 Jg⁻¹). Ga-14.20 at. % In alloy has somewhat lower latent heat of melting (68.4 ± 0.1 Jg⁻¹) comparing to the Ga–7.70 at. % Sn alloy.

The results of this study represent contribution to the better understanding of thermal properties of the low melting Ga-In and Ga-Sn eutectic alloys as candidate metallic PCMs.



18th INTERNATIONAL FOUNDRYMEN CONFERENCE

Coexistence of material science and sustainable technology in
economic growth

Sisak, May 15th-17th, 2019

<http://www.simet.hr/~foundry/>

Acknowledgement

This work has been supported by the Ministry of Education, Science and Technological Development of the Republic of Serbia, project No. OI172037.

REFERENCES

- [1] <http://www.indium.com/low-temperature-alloys/>. Accessed 25 July 2018.
- [2] X. C. Tong, Advanced materials for thermal management of electronic packaging, Springer Science & Business Media, LLC, 2011.
- [3] D. Manasijević, D. Minić, M. Premović, Lj. Balanović, D. Živković, I. Manasijević, S. Mladenović, Thermodynamic calculations and characterization of the Bi-Ga-In ternary alloys, *J. Alloys Compd.*, 664(2016), pp. 199-208.
- [4] S. Liu, K. Sweatman, S. McDonald and K. Nogita, Ga-based alloys in microelectronic interconnects: A review, *Materials*, 11(2018)8, pp. 1384.
- [5] G. Bo, L. Ren, X. Xu, Y. Du and S. Dou, Recent progress on liquid metals and their applications, *Advances in Physics: X*, 3(2018)1, pp. 412-442.
- [6] H. Ge, H. Li, S. Mei, J. Liu, Low melting point liquid metal as a new class of phase change material: An emerging frontier in energy area, *Renew. Sust. Energ. Rev.*, 21(2013), pp. 331-346.
- [7] A. Sharma, V. V. Tyagi, C. R. Chen, D. Buddhi, Review on thermal energy storage with phase change materials and applications, *Renew Sustain Energy Rev.*, 13(2009)2, pp. 318-345.
- [8] X. H. Yang, S. C. Tan, Y. J. Ding, L. Wang, J. Liu, Y. X. Zhou, Experimental and numerical investigation of low melting point metal based PCM heat sink with internal fins, *Int. Commun. Heat Mass.*, 87(2017), pp. 118-124.
- [9] X. H. Yang, S. C. Tan, J. Liu, Numerical investigation of the phase change process of low melting point metal, *Int. J. Heat Mass Tran.*, 100(2016), pp. 899-907.
- [10] I. Manasijević, Lj. Balanović, T. Holjevac Grgurić, D. Minić, M. Gorgievski, Study of microstructure and thermal properties of the low melting Bi-In-Sn eutectic alloys, *Materials Research*, 21(2018)6, e20180501.
- [11] M. M. Kenisarin, High-temperature phase change materials for thermal energy storage *Renew. Sustain. Energy. Rev.*, 14(2010)3, pp. 955-970.
- [12] J. Rodriguez-Aseguinolaza, P. Blanco-Rodríguez, E. Risueno, M. J. Tello, S. Doppiu, Thermodynamic study of the eutectic Mg₄₉-Zn₅₁ alloy used for thermal energy storage, *J Therm Anal Calorim.*, 117(2014)1, pp. 93-99.
- [13] J. P. Bros, Enthalpy of mixture of liquid gallium-indium alloys, *C. R. Seances Acad. Sci., Ser. C*, 263(1966), pp. 977-980 (in French).
- [14] B. Predel, D. W. Stein, Thermodynamic Properties of the Gallium-Indium Systems, *J. Less-Common Met.*, 18(1969), pp. 49-57.
- [15] I. Ansara, M. Gambino, J. P. Bros, A thermodynamic study of the ternary system gallium-indium-antimony, *J. Cryst. Growth*, 32(1976), pp. 101-110.



18th INTERNATIONAL FOUNDRYMEN CONFERENCE

Coexistence of material science and sustainable technology in
economic growth

Sisak, May 15th-17th, 2019

<http://www.simet.hr/~foundry/>

- [16] C. Girard, R. Baret, J. P. Bros, P. Leydet, Enthalpy of formation of Al+Ga+In liquid ternary alloy, *J. Chim. Phys.*, 74(1977)10, pp. 1061-1068 (in French).
- [17] S. J. French, D. J. Saunders, G. W. Ingle, The System Gallium-Indium, *J. Phys. Chem.*, 42(1938), pp. 265-274.
- [18] J. P. Denny, J. H. Hamilton, J. R. Lewis, Constitution of the system gallium-indium, *Trans. AIME*, 194(1952), pp. 39-42.
- [19] W. J. Svirbely, S. M. Read, The thermodynamic properties of liquid ternary zinc, indium, and gallium solutions, *J. Phys. Chem.*, 66(1962), pp. 658-662.
- [20] U. Heubner, P. Wincierz, In-Ga phase diagram, *Metall (Berlin)*, 20(1966), pp. 703-707.
- [21] F. H. Hayes, O. Kubaschewski, A reassessment of the system indium-gallium, *J. Inst. Met.*, 97(1969), pp. 381-383.
- [22] S. K. Kuznetsova, K. I. Chshkalkova, G. M. Kuznetsov, Study of the system Ge-In-Ga, *Izv. Akad. Nauk SSSR Neorg. Mater.*, 11(1975), pp. 1016-1019.
- [23] T. J. Anderson, I. Ansara, The Ga-In (gallium-indium) system, *J. Phase Equilib*, 12(1991)1, pp. 64-72.
- [24] T. Anderson, I. Ansara, The Ga-Sn (gallium-tin) system, *J. Phase Equilib.*, 13(1992)2, pp. 181-189.
- [25] W. Kroll, Alloys of Ga, *Metallwirtschaft*, 2(1932), pp. 435-437 (in German).
- [26] N. A. Puschin, S. Stepanovic, V. Stajic, Alloys of gallium with zinc, cadmium, mercury, tin, lead, bismuth and aluminum, *Z. Anorg. Chem.*, 209(1932), pp. 329-334 (in German).
- [27] L. Bosio, A. Defrain, M. Erny, S. Lignel, and I. Epelboin, Influence of impurities on supercooling, solidification and melting of Ga, *Mém. Sci. Rev. Métall.*, 58(1961), pp. 43-5143-5143-51 (in French).
- [28] S. Delcroix, A. Defrain, I. Epelboin, Alloy diagrams of Ga(I) or (II) with Sn, Zn or In, *J. Phys. Radium*, 24(1963), pp. 17-20 (in French).
- [29] B. Predel, Constitution diagram and properties of Ga-Sn alloys, *J. Less-Common Met.*, 7(1964), pp. 347-355 (in German).
- [30] ASM Handbook Volume 2: Properties and selection: Nonferrous alloys and special-purpose materials, ASM International, 1990. ISBN: 978-0-87170-378
- [31] S. Yu, M. Kaviany, Electrical, thermal, and species transport properties of liquid eutectic Ga-In and Ga-In-Sn from first principles, *The Journal of Chemical Physics*, 140(2014)6, 064303.
- [32] A. Pan, J. Wang, X. Zhang, Prediction of melting temperature and latent heat for low-melting Metal PCMs, *Rare Metal Mat Eng*, 45(2016)4, pp. 874-880.
- [33] N. Saunders, A.P. Miodownik, *CALPHAD (A Comprehensive Guide)*, Elsevier, London, 1998.
- [34] H. L. Lukas, S. G. Fries, B. Sundman, *Computational thermodynamics: the Calphad method*, Cambridge University Press, Cambridge, 2007.
- [35] W. Cao, S. L. Chen, F. Zhang, K. Wu, Y. Yang, Y. A. Chang, R. Schmid-Fetzer, W. A. Oates, PANDAT software with PanEngine, PanOptimizer and PanPrecipitation for multi-component phase diagram calculation and materials property simulation, *Calphad*, 33(2009), pp. 328-342.



18th INTERNATIONAL FOUNDRYMEN CONFERENCE

**Coexistence of material science and sustainable technology in
economic growth**

Sisak, May 15th-17th, 2019

<http://www.simet.hr/~foundry/>

- [36] W. J. Boettinger, U. R. Kattner, K. W. Moon, J. H. Perepezko, DTA and heat-flux DSC measurements of alloy melting and freezing, NIST Special Publication 960-15, Washington, 2006.
- [37] J. H. Perepezko, Nucleation in undercooled liquids, Materials Science and Engineering, 65(1984), pp. 125-135.



18th INTERNATIONAL FOUNDRYMEN CONFERENCE

Coexistence of material science and sustainable technology in economic growth

Sisak, May 15th-17th, 2019

<http://www.simet.hr/~foundry/>

PERMANENT MOULD CASTING OF ALUMINIUM ALLOY FORK

Ivana Mihalic Pokopec, Ines Mance, Davor Cesarec, Branko Bauer*

University of Zagreb Faculty of Mechanical Engineering and Naval Architecture, Zagreb, Croatia

Poster presentation

Professional paper

Abstract

Permanent mould casting process is used for its high productivity of castings with high requirements on mechanical properties and surface quality. Carefully set technological parameters lead to efficient and defect-free castings. Computer simulations have nowadays become a necessary tool in both industrial design and manufacturing. Simulation of filling and solidification was carried out using ESi QuikCAST software to determine influence of casting parameters on final quality of cast fork. AlSi10Mg alloy was used. The results of computer simulations were then analysed and compared with the actual castings.

Keywords: permanent mould casting, aluminium alloy, casting simulation

*Corresponding author (e-mail address): branko.bauer@fsb.hr

INTRODUCTION

Permanent mould casting is highly used casting process for aluminium alloys but despite of its many advantages there are still problems that may emerge in the process. Automotive, electro, metal processing industry etc., use permanent mould casting in their production. Permanent mould casting offers high accuracy in its products with a good quality surface finish which is suitable for many products without the need for extra machining. Permanent mould casting first requires the creation of a steel mould, of the part to be cast. These moulds once created are fitted to the permanent mould casting machine and gravity poured with the desired molten metal or alloy of choice. The quality of the finished casting is influenced by every step of the process from the design of the casting suitable for a certain process, the gating and feeding system that will enable rapid filling without turbulence, proper melting and melt treatment and mould preparation including preheating and coating [1-7].



18th INTERNATIONAL FOUNDRYMEN CONFERENCE

Coexistence of material science and sustainable technology in
economic growth

Sisak, May 15th-17th, 2019

<http://www.simet.hr/~foundry/>

Simulations are carried out in order that optimal tooling and process parameters are selected to get products right first time-avoiding time-consuming and costly physical experimentation or to obtain a deeper understanding of the effect of varying process parameters towards optimizing a process [3,4].

During preparation of casting process, it is necessary to consider many different aspects of casting process. At this stage numerical simulation may help engineer to make right decisions to produce casting with good quality. Engineer can virtually test different shapes of mould, pouring temperatures, types of insulation etc. and decide which setup will be the most economical and guarantee sound casting [5,7].

The construction of metal moulds for gravity casting is a significant structural challenge and requires a combination of knowledge and experience in design and fabrication. Many criteria should be met when designing and manufacturing metal moulds. Casting parameters also play a significant role in obtaining high quality castings. Casting simulations are continually becoming better and more reliable tool for defect prediction and elimination. Visualization of mould filling, cooling, solidification and porosity occurrence saves time and reduces cost.

MATERIALS AND METHODS

The CAD model of the AISi10Mg aluminium alloy fork casting was obtained using 3D scanner ATOS (Figure 1). The STL file was created from 3D scan data to perform the casting and solidification simulation in ESI QuikCAST software. 2D drawing from 3D scan data is shown in Figure 2.

Simplified steel mould of one piece was used in the simulation, which is sufficient to obtain the initial insight of the influence of the variables. More precise results can be obtained by simulating a two-piece mould with two cores, when the whole casting cycle can be set, i.e., mould opening time, spraying and cooling time and closing time of the mould. Temperature field of the mould is then more accurate. Filling simulation was not performed. Solidification simulation was performed from the fulfilled mould with the same initial melt temperature.

Four simulations were carried out combining two melt temperatures with two different mould preheating temperatures, as shown in Table 1. Melt temperatures were 720 °C and 640 °C, and the mould preheating temperatures were 300 °C and 200 °C. The same parameters were used and controlled when casting process was performed in foundry laboratory in order to compare simulated results with experimental results.



18th INTERNATIONAL FOUNDRYMEN CONFERENCE
Coexistence of material science and sustainable technology in economic growth

Sisak, May 15th-17th, 2019

<http://www.simet.hr/~foundry/>

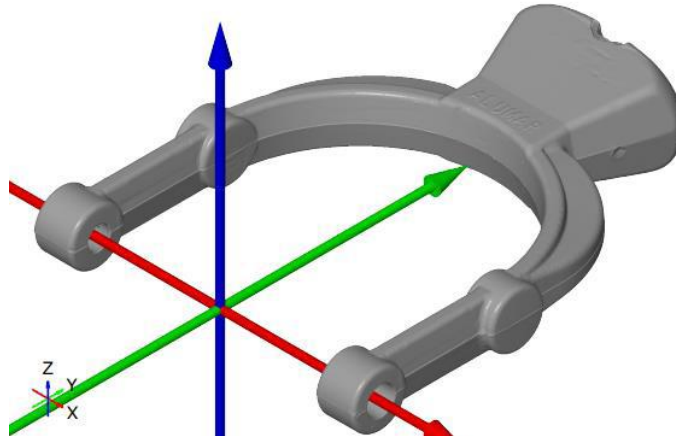


Figure 1. 3D model of aluminium fork

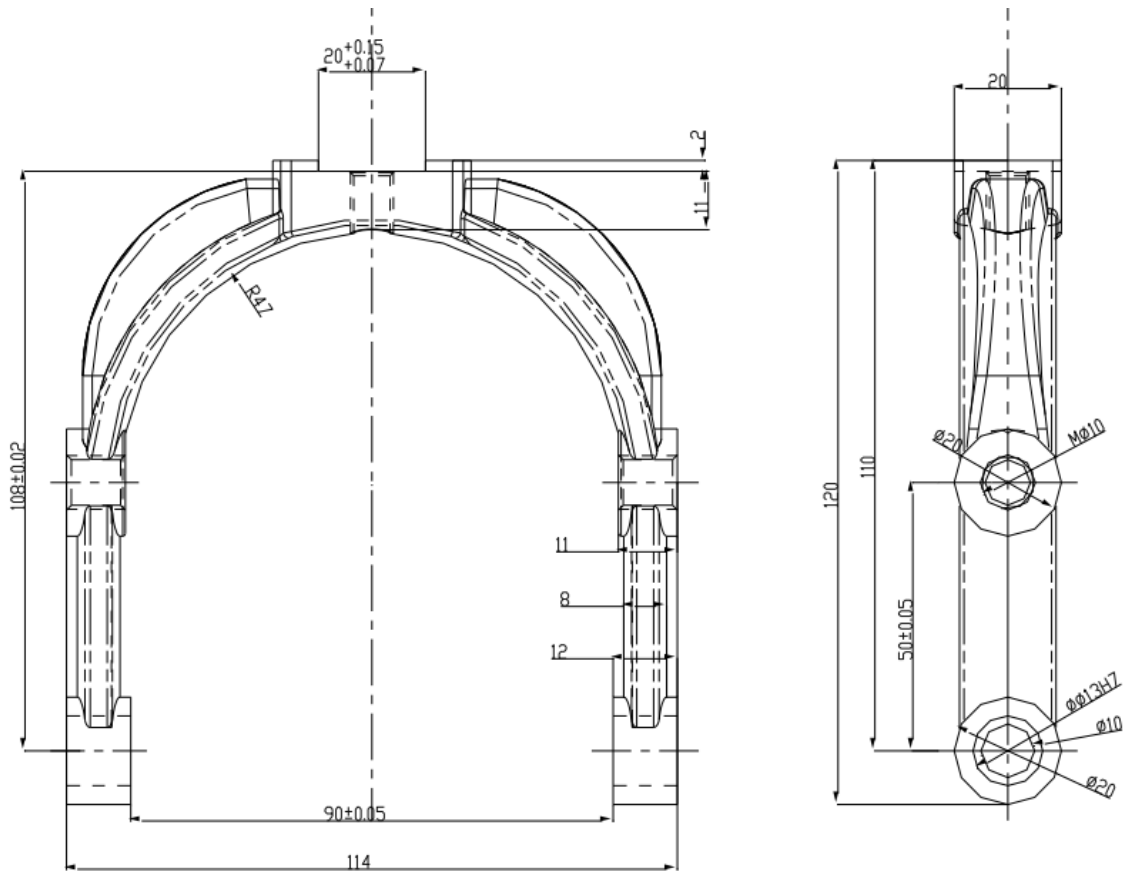


Figure 2. 2D drawing of aluminium fork



18th INTERNATIONAL FOUNDRYMEN CONFERENCE
Coexistence of material science and sustainable technology in economic growth

Sisak, May 15th-17th, 2019

<http://www.simet.hr/~foundry/>

Table 1. Four combinations of two melt temperatures and two die temperatures

		MELT TEMPERATURE	
		720°C	640°C
MOULD TEMPERATURE	300°C	VARIANT 1 (V1)	VARIANT 3 (V3)
	200°C	VARIANT 2 (V2)	VARIANT 4 (V4)

Three characteristic points were selected on casting for simulation requirements and for obtaining the cooling curve of all four combinations of melt temperature and mould preheating temperature.

Casting was done in a Foundry laboratory at the Faculty of Mechanical Engineering and Naval Architecture at the University of Zagreb. Aluminium ingots AlSi10Mg were melted in an electric furnace, Figure 3, and heated to a temperature of 840 °C. The temperature was controlled by a contact pyrometer, Figure 4.

Aluminium slag was carefully removed before the melt was poured from the furnace to the ladle, Figure 5. Foundry pot was also preheated before transfer and pouring.



Figure 3. Aluminium ingot in furnace



Figure 4. Measuring melt temperature



Figure 5. Removing slag from the melt

Permanent mould halves are attached to the electro-hydraulic device for opening, closing and securing during gravity casting. One half of the mould is stationary and the another one moves horizontally pushed by the hydraulic cylinder.

Before pouring of the melt, both halves of the mould were preheated with gas torches to 150°C and coated with DYOCOTE DBN120, Figure 6, using the pneumatic spraying device.

After pouring, cooling and solidification, metal cores were removed, the mould was opened, and the casting was manually removed from the mould, Figure 7. Finished casting was visually inspected for surface quality and radiographed for shrinkage porosity testing and comparison with simulation result.



18th INTERNATIONAL FOUNDRYMEN CONFERENCE
Coexistence of material science and sustainable technology in economic growth

Sisak, May 15th-17th, 2019

<http://www.simet.hr/~foundry/>



Figure 6. Coated mould surface before casting cycles



Figure 7. Removing casting out from the mould

RESULTS AND DISCUSSION

Figure 8 shows the casting cross-section with three characteristic points for which cooling curves were simulated and recorded.

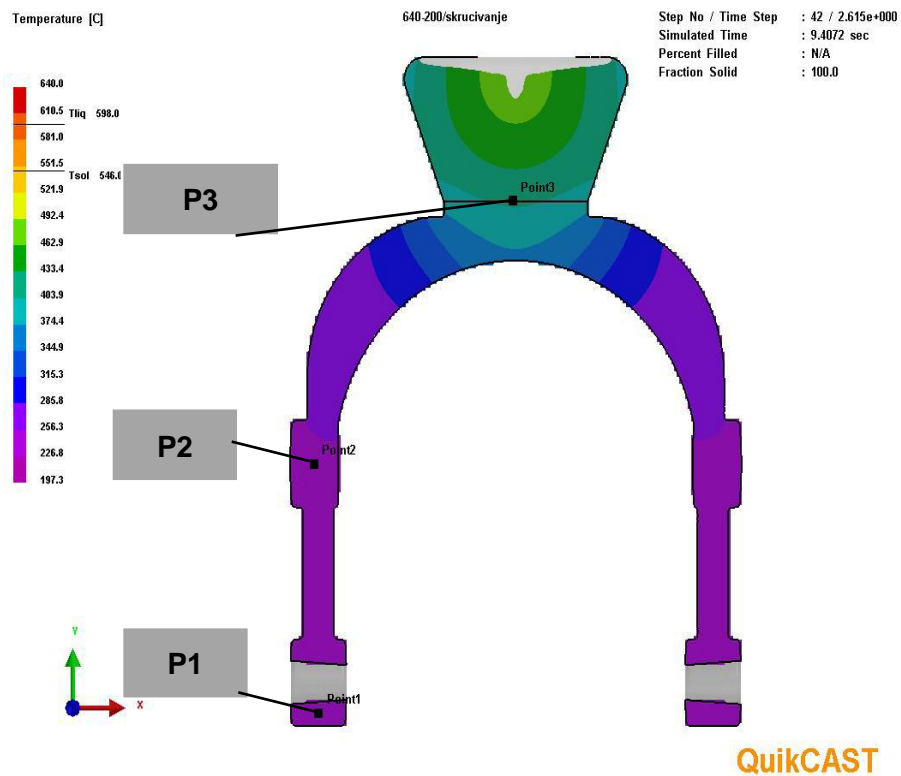


Figure 8. Cross section of casting with characteristic cooling points



18th INTERNATIONAL FOUNDRYMEN CONFERENCE

Coexistence of material science and sustainable technology in economic growth

Sisak, May 15th-17th, 2019

<http://www.simet.hr/~foundry/>

In Figures 9-12 the cooling curves of three characteristic points and four combinations of melt temperatures and die temperatures are shown.

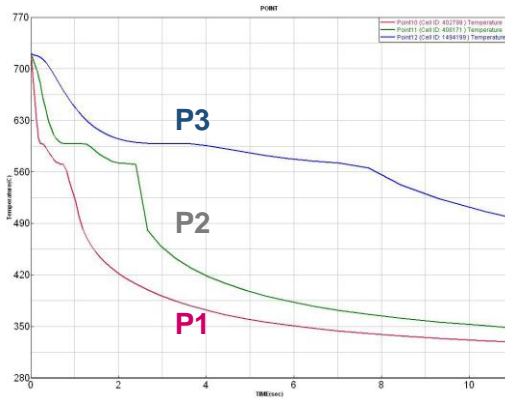


Figure 9. Cooling curves, V1: 720°/300°C

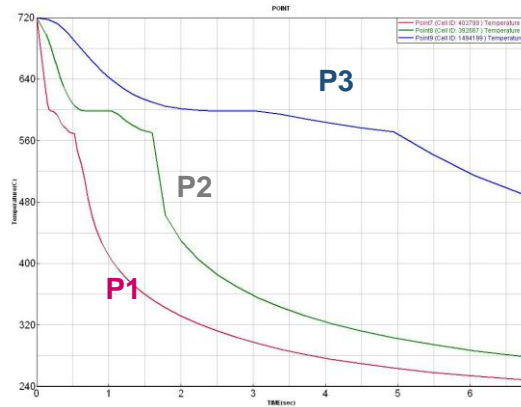


Figure 10. Cooling curves, V2: 720°/200°C

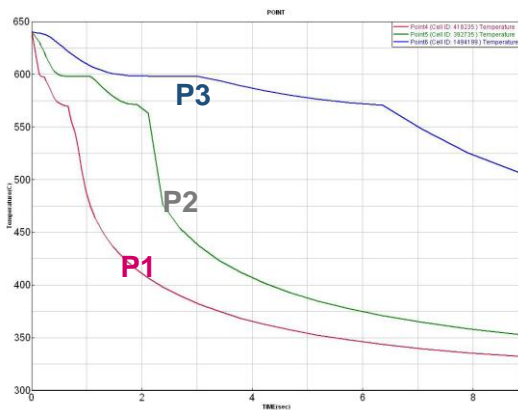


Figure 11. Cooling curves, V3: 640°/300°C

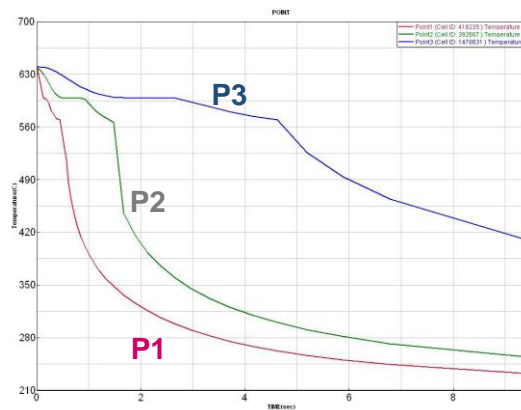


Figure 12. Cooling curves, V4: 640°/200°C

The specific moment 0,7 seconds after start of solidification in which core is at its highest temperature of about 470°C was selected and temperature field at that moment is shown in Figure 13. The temperature field of the mould and casting at the end of solidification (5.2 seconds after start of solidification) is shown in Figure 14.



18th INTERNATIONAL FOUNDRYMEN CONFERENCE

Coexistence of material science and sustainable technology in economic growth

Sisak, May 15th-17th, 2019

<http://www.simet.hr/~foundry/>

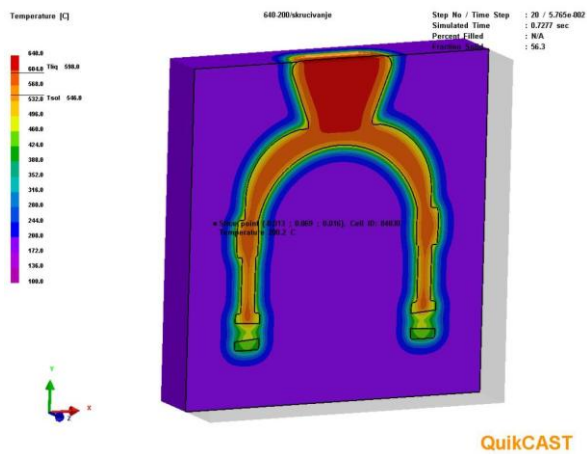


Figure 13. Temperature field in the mould 0.7 second after solidification start

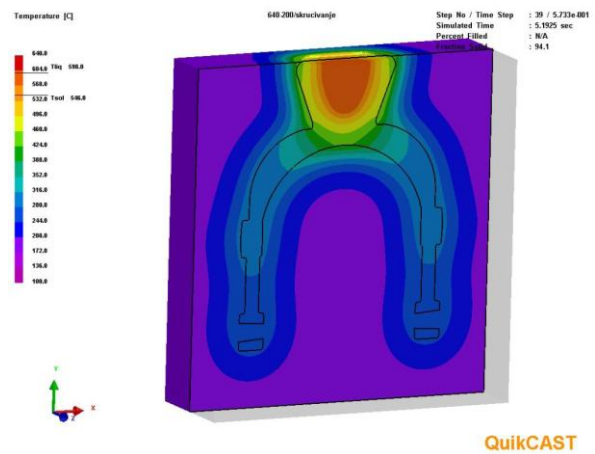


Figure 14. Temperature field in the mould at the end of solidification

The simulation provides a visual representation of the temperature fields in the casting and in the mould, from melt pouring to fully solidified casting which also allows for each process segment to be analysed in detail.

Figure 15 shows the places where the curves of temperature changes in the mould were recorded.

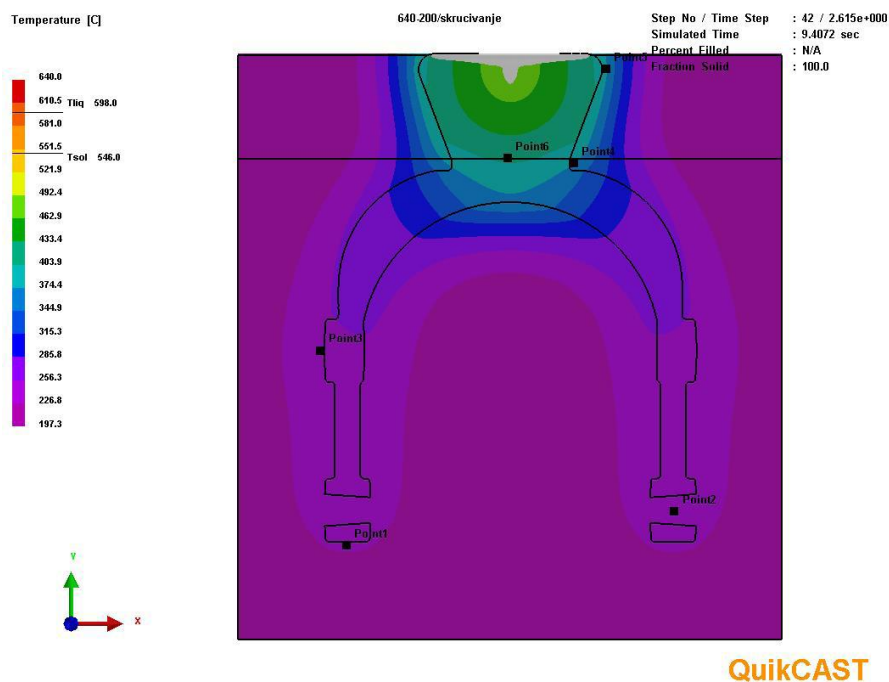


Figure 15. Characteristic locations where temperature changes were recorded in the mould (1-5) and in the casting (6)



18th INTERNATIONAL FOUNDRYMEN CONFERENCE
Coexistence of material science and sustainable technology in economic growth

Sisak, May 15th-17th, 2019

<http://www.simet.hr/~foundry/>

Figure 16 shows curves of temperature changes in the mould and in the casting for variant 2, melt temperature 720 °C and preheat temperature 200 °C.

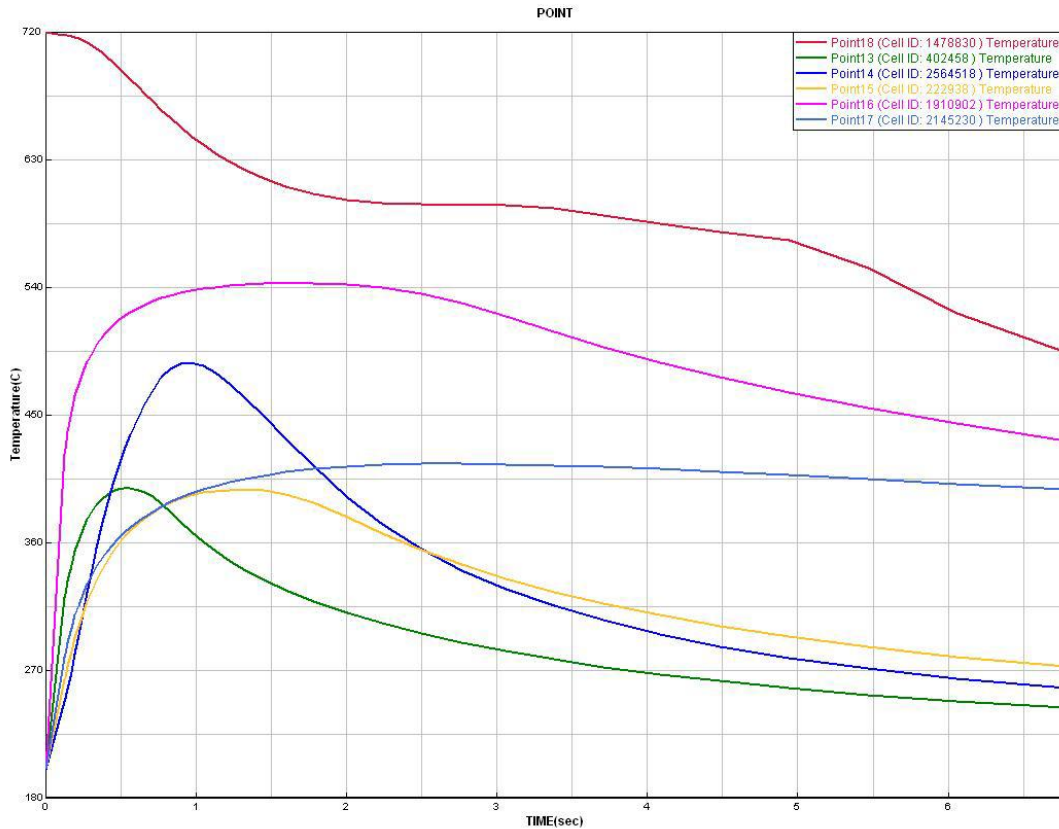


Figure 16. Temperature changes in the mould (1-5) and in the casting (6), V2 720-200

Table 2 shows maximum temperatures at characteristic locations in the mould for all four variants.

Table 2. Maximum temperatures at characteristic locations in the mould

LOCATION IN THE MOULD	TEMPERATURE VARIANTS			
	V1	V2	V3	V4
1.BOTTOM	457	398	450	392
2.CORE	532	487	520	462
3.MIDDLE	487	390	480	430
4.FEEDER BOTTOM	557	540	542	518
5.FEEDER TOP	495	430	488	442

According to the simulation results the metal core location and feeder bottom get heated the most.



18th INTERNATIONAL FOUNDRYMEN CONFERENCE
Coexistence of material science and sustainable technology in economic growth

Sisak, May 15th-17th, 2019

<http://www.simet.hr/~foundry/>

Figure 17 shows casting cross-section with different solidification times for the variant 720-300, V1.

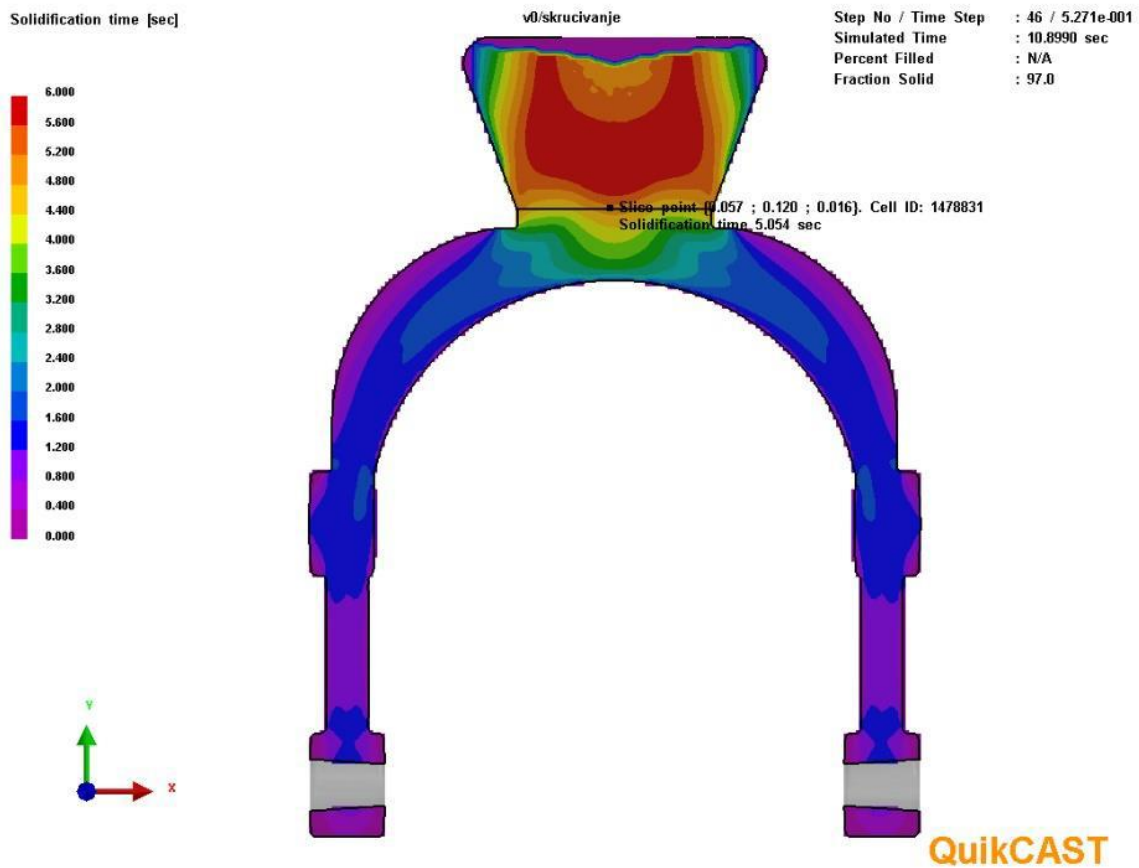


Figure 17. Solidification time at cross-section of the casting, V1

In Table 3 and in histogram in Figure 18, solidification times of the characteristic locations in casting; top, middle and bottom, for all four combinations of melt temperature-preheating temperature are presented.

Table 3. Solidification times for characteristic locations in casting

		SOLIDIFICATION TIMES [s]			
		V1	V2	V3	V4
LOCATION IN THE CASTING	TOP	5.05	2.67	4.85	2.58
	MIDDLE	1.52	0.86	1.45	0.83
	BOTTOM	0.66	0.32	0.58	0.30



18th INTERNATIONAL FOUNDRYMEN CONFERENCE

Coexistence of material science and sustainable technology in economic growth

Sisak, May 15th-17th, 2019

<http://www.simet.hr/~foundry/>

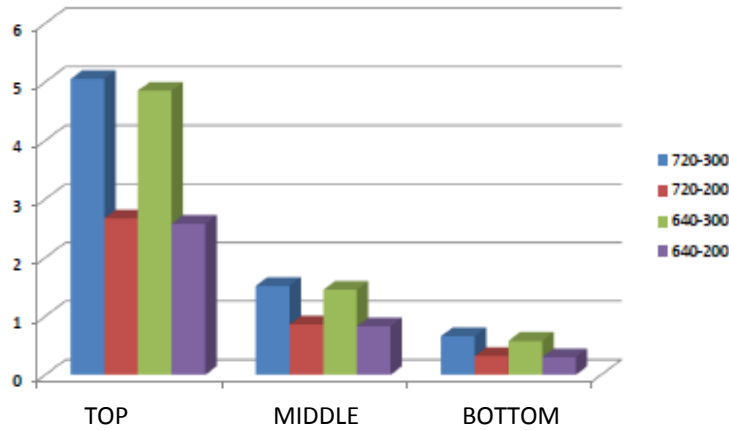


Figure 18. Solidification times at different locations in the casting

The first place to solidify in all combinations is the bottom of the fork, but as expected the solidification in the mould preheated to 200 °C is faster than in the mould preheated to 300 °C.

The solidification time of the fork-top in a mould preheated to 200 °C is less than half of time recorded for the fork-top in a mould preheated to 300 °C.

Figure 19 shows fraction solid results as a radiographic view for a temperature combination V1 720-300 1.6 seconds after filling. Solidification of the casting is directional and starts from the thin bottom part of the casting and progresses to the feeder on top. The solidification sequence is the same for all four temperature combinations.

In Figures 19 and 20, the solidification is shown after 1.6 s and 5.2 seconds after filling. The quantity of the solid phase is greater in the lower area of the casting and, as observed, decreases into the thicker cross sections and the feeder.



Figure 19. Fraction solid result after 1.6 seconds in radiographic view

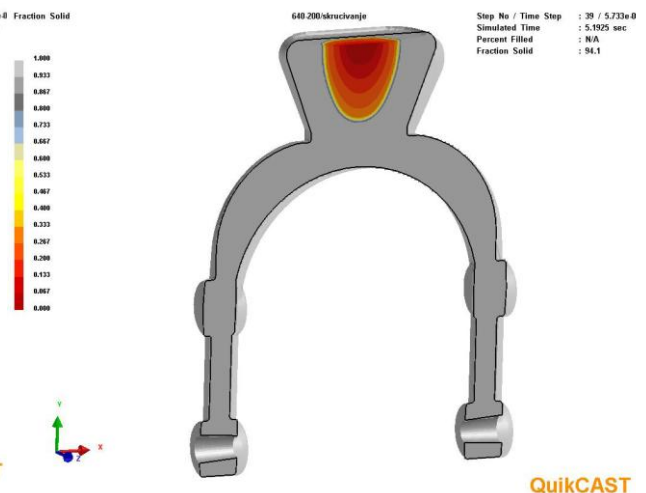


Figure 20. Fraction solid result after 5.2 seconds in cross-section



18th INTERNATIONAL FOUNDRYMEN CONFERENCE
Coexistence of material science and sustainable technology in economic growth

Sisak, May 15th-17th, 2019

<http://www.simet.hr/~foundry/>

Figure 21 shows shrinkage porosity in 3D view. Three specific locations can be spotted on the casting where the melt supply from feeder to isolated liquid areas is interrupted causing shrinkage porosity occurrence in these areas. Figure 22 shows probability of shrinkage porosity occurrence in vertical symmetry plane for variant V4, the lowest melt temperature and the lowest preheat temperature.

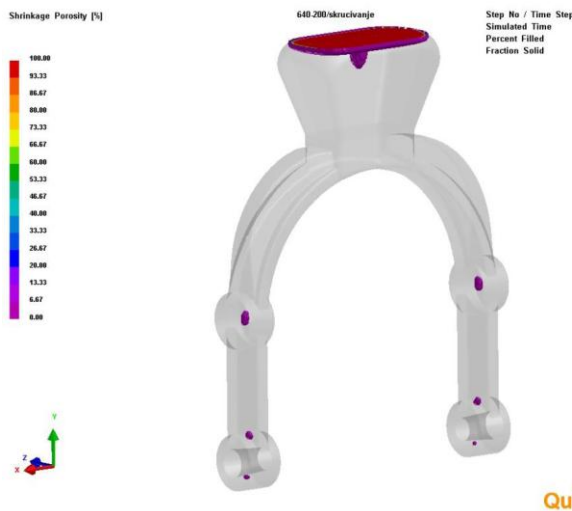


Figure 21. Shrinkage porosity 3D view

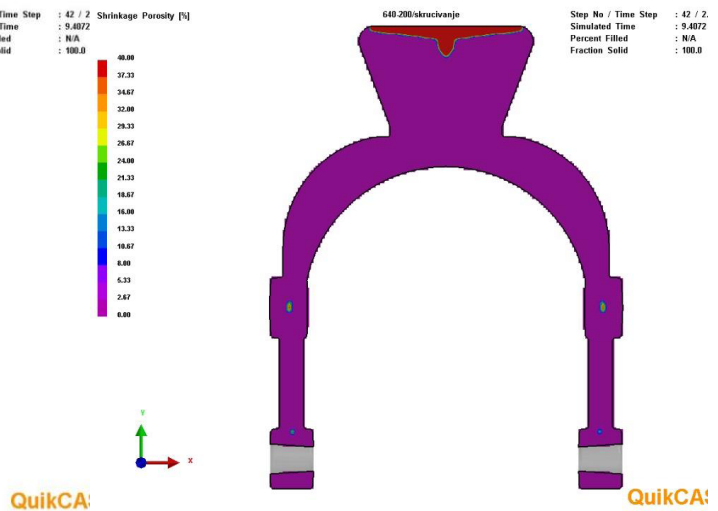


Figure 22. Probability of shrinkage porosity in vertical symmetry plane

For all four melt-mould temperature combinations at three characteristic locations in the casting the probability of the shrinkage porosity occurrence is presented in the histogram in Figure 23.

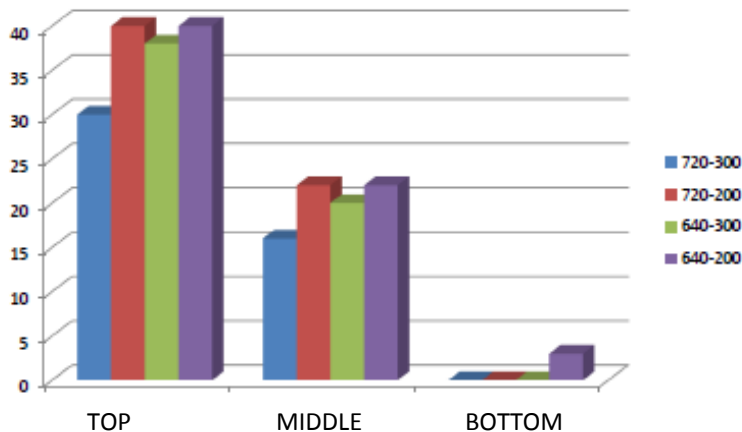


Figure 23. Probability of porosity occurrence histogram



18th INTERNATIONAL FOUNDRYMEN CONFERENCE

Coexistence of material science and sustainable technology in economic growth

Sisak, May 15th-17th, 2019

<http://www.simet.hr/~foundry/>

The lowest probability of porosity is at the bottom of the fork, regardless of the temperature. In the middle and top area, the highest probability of porosity occurs in moulds with lower preheat temperature (V2 and V4). The lowest probability of porosity is in combination with the highest melt temperature and highest preheat temperature (V1).

Simulation results showed that the occurrence of porosity depends more on the mould temperature than on the melt temperature. Higher mould temperatures resulted in less porosity, while higher melt temperature for the same mould temperature resulted in approximately the same porosity.

Experimental castings

Visual control of real castings showed that the surface of the first casting (casted in preheated mould on 200 °C) is not smooth. Surface defects in the form of lines occurred due to higher cooling rate caused by colder mould, Figure 24.

After ten casting cycles, a stable mould temperature field was achieved, which can be noticed in a higher quality of the casting surface compared to the quality of a first casting from a cooler mould.



Figure 24. First casting in preheated mould on 200 °C and casting from a mould with stabilised temperature field (higher mould temperature)

Castings were radiographed in order to determine the internal porosity. Figure 25 shows the radiograms of the first casting from the preheated mould (left) and casting made in a mould with stable temperature field (right).

Porosity is present in both castings. In the first casting (left) porosity is more accentuated as a result of higher cooling rate and progressive solidification that interrupted the melt flow from the feeder.

Pouring in a cooler mould results in higher cooling rate, faster solidification of the casting and greater porosity.



18th INTERNATIONAL FOUNDRYMEN CONFERENCE

Coexistence of material science and sustainable technology in economic growth

Sisak, May 15th-17th, 2019

<http://www.simet.hr/~foundry/>

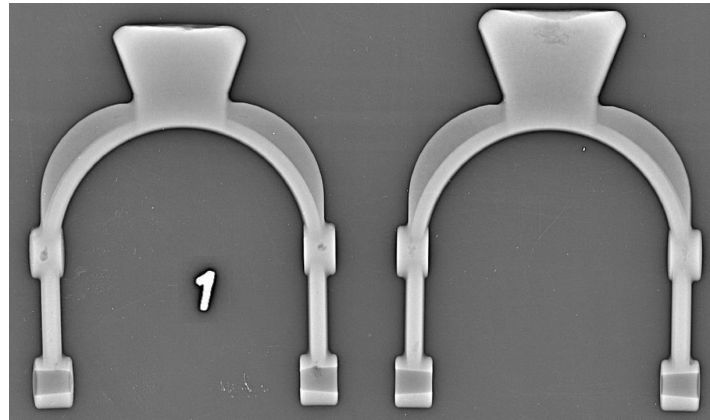


Figure 25. Radiograms of first casting in preheated mould on 200 °C and casting from a mould with stabilised temperature field (higher mould temperature)

Porosity was significantly decreased when warmer moulds were used, right casting on Figure 24. Due to the higher temperature of the mould, cooling rate was lower and progressive solidification slower.

CONCLUSIONS

Casting simulation of permanent mould casting process was performed for aluminium alloy fork. Melt temperature and mould temperature were investigated at two levels as the two parameters influencing the size and location of the porosity. Subsequently casting was done at the foundry laboratory and simulation results were compared to actual casting. Radiogram reveals the occurrence of porosity on critical parts of the castings. The simulation results match the results of actual casting. Simulations have shown that the appearance of porosity does not depend so much on melt temperature as it depends on the temperature of the mould. At lower mould temperature, higher cooling rate results in faster solidification and greater porosity. Higher mould temperatures resulted in less porosity, while higher melt temperature for the same mould temperature resulted in approximately the same porosity. The lowest probability of porosity is in combination with the highest melt temperature and highest preheat temperature.

Acknowledgements

This work was supported by the companies Alumar, Ljevaonica Bujan and Topomatika.



18th INTERNATIONAL FOUNDRYMEN CONFERENCE

Coexistence of material science and sustainable technology in economic growth

Sisak, May 15th-17th, 2019

<http://www.simet.hr/~foundry/>

REFERENCES

- [1] ..., Casting, ASM Handbook, Vol. 15., 2008.
- [2] ..., Accessible on Internet: <https://www.esi-group.com/software-solutions/virtual-manufacturing/casting-simulation-software>, 12.03.2019.
- [3] B. Ravi, Casting simulation and optimization: Benefits, bottlenecks, and best practices, Technical Paper for Indian Foundry Journal, 2008, pp. 1-12.
- [4] D. R. Gunasegaram, D. J. Farnsworth, T. T. Nguyen, Identification of critical factors affecting shrinkage porosity in permanent mold casting using numerical simulations based on design of experiments, Journal of Materials Processing Technology, 209(2009), pp. 1209-1219.
- [5] S. Gondkar, K. H. Inamdar, Optimization of casting process parameters through simulation, International Journal of Application or Innovation in Engineering & Management, 3(2014)6.
- [6] C. Hallam, W. Griffiths, A model of the interfacial heat-transfer coefficient for the aluminium gravity die casting process, Metall. Mater. Trans. B, 35(2004), pp. 721-733.
- [7] A. Hamasaiid, M. S. Dargusch, C. J. Davidson, S. Tovar, T. Loulou, F. Rezai-Aria, G. Dour, Effect of mould coating materials and thickness on heat transfer in permanent mould casting of aluminium alloys, Metall. Mater. Trans. A, 38A(2007), pp. 1303-1316.



18th INTERNATIONAL FOUNDRYMEN CONFERENCE

Coexistence of material science and sustainable technology in
economic growth

Sisak, May 15th-17th, 2019

<http://www.simet.hr/~foundry/>

EFFECT OF UV IRRADIATION ON THERMAL AND MECHANICAL PROPERTIES OF MATERIALS

Vesna Ocelić Bulatović^{1*}, Dajana Kučić², Antonio Ivančić³, Lucija Kefurt³

¹ University of Zagreb Faculty of Metallurgy, Sisak, Croatia

² University of Zagreb Faculty of Chemical Engineering and Technology, Zagreb, Croatia

³ Master degree student at University of Zagreb Faculty of Metallurgy, Sisak, Croatia

Poster presentation

Original scientific paper

Abstract

Due to environmental concern and environmental protection a great attention has been developed for degradable polymers, especially in packaging industries that is greatly responsible for large accumulation of polymer waste. A possible solution to reduce the considerable amount of polymer waste while maintaining low prices and good quality of the products is to induce a certain level of biodegradability by blending synthetic polymers with biodegradable polymers such as starch. So, on the other hand it is very important to accelerate and enhancement their biodegradability. One of the well-known and simple methods is UV irradiation or heat treatment that leads to the formation of functional groups in hydrophobic polymer chains making them sensitive to further microbial attack thus accelerating their biodegradability.

The objective of this work is to investigate the effects of UV irradiation on the properties of biodegradable blends of low-density polyethylene, LDPE, and thermoplastic starch, TPS. The thermoplastic starch was prepared by melting with glycerol as a plasticizer in a single screw Brabender extruder, while the biodegradable blends, LDPE/TPS, were prepared using a Brabender kneading chamber and compression molded in a hydraulic press. The prepared biodegradable blends with a different proportion of individual components were submitted to treatment with UV irradiation (wavelength 290 nm) for 30 days. The changes in mechanical properties, such as tensile strength and elongation at break have been investigated. Also, thermal changes of the biodegradable blends have been measured using the differential scanning calorimetry and the thermogravimetric analysis. UV irradiation causes photooxidative degradation mainly in the amorphous regions of the blends due to the direct absorption of photons on the surface of the polymer chain which results in breaking of the polymer chains, branching, networking, producing free radicals and reducing the molecular weight, causing deterioration of thermal and mechanical properties.

Keywords: *biodegradable blends, UV irradiation, thermal properties, mechanical properties*

Corresponding author (e-mail address): vocelicbu@simet.hr



18th INTERNATIONAL FOUNDRYMEN CONFERENCE

Coexistence of material science and sustainable technology in
economic growth

Sisak, May 15th-17th, 2019

<http://www.simet.hr/~foundry/>

INTRODUCTION

The wide use of non-degradable conventional petroleum-based plastics and their environmental impact due to their inappropriate disposal are already alarming. Approximately, about 300 million tons of polymer materials based on fossil raw materials are manufactured each year for packaging, construction, appliances, and other technical goods [1,2]. The majority of these polymers end up together with communal waste in landfills. The dumping of plastic waste into the environment has caused serious problems to flora and fauna, affecting the balance of ecosystems. To reduce the amount of landfill waste, and due to environmental and economic reasons, finding durable plastic substitutes, especially for short-term packaging and disposable application has become very important. Clearly, plastic waste, whose major source is packaging, is one of the contributors to the waste management problem. Polyethylene plastic is among the most dominant packaging materials and its main problem is that it is not capable of self-decomposition. Further, the burning of polyethylene plastics causes serious health issues as it leads to the evolution of noxious gases, thus contributing to additional air pollution. Like other packaging products, when products reach the end of their useful life, most are discarded in open dumps, landfills, or as simple litter [3,4]. As alternatives to conventional non-degradable polymers such as polyethylene, polypropylene and polystyrene could be use of biodegradable polymers as a promising route of development [3,4]. Biopolymers based on renewable raw materials, which are proven to be biodegradable, can be further recycled using biological processes, such as composting (aerobic degradation) or fermentation (anaerobic degradation) and converted into useful products such as humus and/or methane [4]. Melt blending of TPS with synthetic polymer, such as polyethylene, has been considered an excellent alternative for the development of low-cost, sustainable materials [5-7]. To achieve biodegradability, thermoplastic starch is added to LDPE. The main goal of blending LDPE and TPS is to achieve biodegradability, maintain low cost and retaining good properties. Microorganisms will consume the primary starch, which will lead to loss of LDPE structural integrity, enhancing other mechanisms of degradation and possibly deteriorating mechanical properties. However, as the amount of starch increases, the degradability characteristics will increase and the mechanical properties may remain unchanged. The degradation process of the polymers is a result of many chemical reactions that cause irreversible losses in the properties of the polymeric material; this deterioration generally depends on the nature of the materials and the conditions to which they are subjected [8]. Degradation of the polymer can be initiated by the absorption of UV irradiation, heat and /or tension, resulting in loss in polymer molecular weight due to breakage of the molecular chains leaving a remaining of low molecular weight on which must be capable of developing a process of degradation when exposed to environmental conditions [8]. Degradation of the polymer is related to the photooxidation and thermooxidation reactions, chain decomposition and crosslinking of the polymer skeleton [8-11]. There is formation of a carbonyl ($C = O$) and a vinyl ($CH_2 = CH$) group, accompanied by a change in polymer conformation and crystallinity [8]. Studies on the photodegradation of polyethylene and their blends are important for developing



18th INTERNATIONAL FOUNDRYMEN CONFERENCE

Coexistence of material science and sustainable technology in
economic growth

Sisak, May 15th-17th, 2019

<http://www.simet.hr/~foundry/>

methods to prevent photodegradation indoors and simultaneously to enhance photodegradation outdoors when they become waste or as litter.

The aim of this paper is to investigate the effect of UV irradiation on thermal and mechanical properties of the blends prepared of low density polyethylene and thermoplastic starch.

MATERIALS AND METHODS

Materials

A low-density polyethylene resin, LDPE, Dow 150E from Dow Chemical Company was used. Wheat starch "Srpanjka" (harvest 2008) was obtained from the Agricultural Institute, Osijek, Croatia. Glycerol from Gram Mol, Zagreb, Croatia was used as plasticizer for wheat starch to obtain thermoplastic starch. The some characteristic properties of LDPE are shown in Table 1.

Preparation of LDPE/TPS blends

In order to obtain different ratio of binary LDPE/TPS blends, an extrusion system laboratory single- screw extruder, Model 19/20DN, Brabender GmbH, Germany and a Brabender kneading chamber was used. A suspension of wheat starch / glycerol (70:30) was extruded with a laboratory single-screw extruder to prepare thermoplastic starch, TPS. The extrusion parameters were as follows: screw 1 : 1; die 4 mm; temperature profile in the first (dosing), second (compression) and third (ejection) zone 100/100/130 °C; screw speed 40 rpm; dosing speed 15 rpm. Pelletized samples of TPS were air-dried overnight and stored in sealed plastic bags to avoid contact with environment moisture. On the other hand, LDPE/TPS blends were prepared using a Brabender kneading chamber. The pellets of LDPE/TPS were mixing in the chamber at a temperature of 160 °C and with rotor rate of 60 rpm and with mixing time 6 minute. TPS was blended with LDPE in a five different levels of TPS (10, 20, 30, 40, 50 wt%). After homogenization, the blends were moulded in laboratory hydraulic press Fortune, Holland, SRB 140, at a temperature of 150 °C, a pressure of 25 kPa for 5 minutes with a preheating of 1 min.

Table 1. Properties of low density polyethylene (LDPE)

Properties	LDPE
Density, kg/m ³	921 (ASTM D792)
Melt Index (190 °C/2.16 kg)	0.25 g/10min (ISO 1133)
Tensile strength, MPa	21.0 (ISO 527-3)
Tensile modulus, MPa	128 (ISO 527-3)

Exposure of the LDPE/TPS blends to UV irradiation

UV irradiation of the LDPE/TPS blends was performed in a SUNTEST CPS UV chamber equipped with Xenon lamp and temperature sensor was used as the source for artificial sunlight. Polymers and blends were exposed to UV irradiation at constant temperature



18th INTERNATIONAL FOUNDRYMEN CONFERENCE

Coexistence of material science and sustainable technology in
economic growth

Sisak, May 15th-17th, 2019

<http://www.simet.hr/~foundry/>

(25°C) and constant relative humidity (65 %) for 30 days. On the top of the chamber, there was Xenon lamp wavelength of 290 nm. The exposure chamber was 20 cm wide x 45 cm long and the film surface was at 15 cm from the lamp; they were irradiated continuously for 720 h.

Differential Scanning Calorimetry (DSC)

Testing of thermal properties of LDPE/TPS and LDPE/TPS_UV blends were analysed using Differential Scanning Calorimetry (DSC), DSC 823^e (Mettler Toledo) calibrated with Indium. The following conditions were used: weight of the samples ~ 10mg, nitrogen atmosphere with a flow rate 60 mL min⁻¹, heating rate 10 °C min⁻¹ and temperature range from – 90 °C to 150 °C. Thermograms for LDPE/TPS and LDPE/TPS_UV blends were recorded in three consecutive runs:

- (1) first heating from 25 to 150 °C, followed by
- (2) cooling from 150 °C to -90 °C, and
- (3) a second heating from -90 °C to 150 °C.

The degree of crystallinity (χ_c) of the LDPE in the blends was calculated based on a heat of fusion (ΔH_m°) value of 290 J g⁻¹ for 100 % crystalline LDPE [12-14] according to following equation:

$$\chi_c = \frac{\Delta H_m}{\Delta H_m^\circ (1-w)} * 100 \% \quad (1)$$

Thermogravimetric analysis (TGA)

The thermal degradation of LDPE/TPS and LDPE/TPS_UV blends was monitored by thermogravimetric analysis (TGA) using a TA Instrument Q500. Samples of ~10 mg were heated from room temperature to 700 °C at a rate of 10 °C min⁻¹ in a nitrogen gas flow of 100 ml min⁻¹.

Mechanical properties

The mechanical properties of LDPE/TPS and LDPE/TPS_UV blends were tested using a Zwick Testing Machine (model 1445) at a constant, ambient, temperature of 23 °C and the humidity of 65% RH. The gauge lengths of 50 mm, crosshead speed of 50 mm min⁻¹ and sample size (100.0 × 15.0 × 1.0) mm were used to determine tensile strength and elongation at break. The results of mechanical properties are given as the average values of five sample measurements.

RESULTS AND DISCUSSION

Differential Scanning Calorimetry

DSC measurements were performed to assess the temperature characteristic of melting (T_m) as well as enthalpy of fusion (ΔH_m) of LDPE and LDPE/TPS blends before and after UV irradiation. The degree of crystallinity, quantification of the amount of ordered regions in



18th INTERNATIONAL FOUNDRYMEN CONFERENCE

Coexistence of material science and sustainable technology in
economic growth

Sisak, May 15th-17th, 2019

<http://www.simet.hr/~foundry/>

semicrystalline LDPE polymer and its changes during UV irradiation were calculated on the basis of ΔH_m , according to equation (1). As was mentioned in Experimental section, the two DSC scan cycles were performed. With first scanning the thermal history of the materials was erased and DSC curves of the second run are shown in Figures 1 and 2. Table 2 shows a summary of the thermal properties obtained from the DSC thermograms. From the Fig. 1 that shows DSC thermograms of cooling-heating of LDPE (before) and LDPE_UV (after UV irradiation) a sharp endothermic peaks is visible which indicates the melting temperature of LDPE. Melting temperature (T_m) of the LDPE before UV irradiation exhibits a maximum at 114.7 °C and decreases to 111.5 °C after 30 days of exposure to UV irradiation (Figure 1 and Table 2). Similar behaviour is also observed for all LDPE/TPS blends (Figure 2(b) and Table 2). The greatest T_m reduction from 114.2 °C before UV irradiation to 99.3 °C after 30 days UV irradiation is observed in the blend that having 40 wt% TPS (LDPE/40TPS). Fig. 2(b) shows the effect of UV irradiation on the ΔH_m values of LDPE/TPS_UV blends. UV irradiated blends with a lower content of added TPS (up to 20 wt% TPS) show a dramatic reduction of ΔH_m from 105.3 J g⁻¹ and 99.2 J g⁻¹, before UV irradiation, to 89.9 and 94.9 J g⁻¹, after exposure to UV irradiation. Conversely, LDPE/TPS blends with 30, 40 and 50 wt% TPS show different trend, ΔH_m increases after 30 days of UV irradiation (Figure 2(b)). Also, the increase in ΔH_m after UV irradiation is bound for neat LDPE (Figure 1, Table 2). According to some authors, the increasing values of ΔH_m for samples with a higher content of TPS after UV irradiation may be the consequence of recrystallization caused by initial Norrish II oxidative chain scission in competition with subsequent crosslinking and extensive Norrish I chain scissions [15,16]. Oxidative scission enables polymer chain relaxation to occur as well as formation of nucleating polar sites and so recrystallization may dominate the physical consequences of degradation. Subsequently, excessive oxidative chain scission reduces crystallinity and may lead to decrease in elongation at break and significant increase in carbonyl index [15,16]. The ΔH_m results clearly show that exposure to UV irradiation produces structural changes in the LDPE polymer. From this, it can be concluded that the initial degradative changes take place in the amorphous regions of the polymer, leaving the crystalline regions unaffected. The changes in the enthalpy of fusion could be attributed to the changes in crystallite sizes and molecular weight reductions due to chain breaking and secondary crystallization which may occur because of chain scission of LDPE during UV expose [17].

The degree of crystallinity is proportional to enthalpy of fusion, so the same trend of change as in the ΔH_m is expected (Table 2). The degree of crystallinity increases for pure LDPE as well as for the blends with a higher TPS content. At a lower TPS content the degree of crystallinity decreases. The higher the content of the added TPS, the smaller changes in the degree of crystallinity after UV radiation are evident. The highest change in the degree of crystallinity after UV irradiation is indicated for the blends with 30 wt% of TPS (LDPE/30TPS_UV), while the slightest change shows blends with 50 wt% of TPS (LDPE/50TPS_UV). According to literature, some authors have similar results, increasing the degree of crystallinity of LDPE during UV irradiation [5,17] while other authors have found that the degree of crystallinity of LDPE decreases during UV irradiation [5,16,18,19]. The change in the degree of crystallinity for the investigation samples take place during



18th INTERNATIONAL FOUNDRYMEN CONFERENCE
Coexistence of material science and sustainable technology in
economic growth

Sisak, May 15th-17th, 2019

<http://www.simet.hr/~foundry/>

photooxidation via UV irradiation. The increase in the degree of crystallinity is probably due to scission of tie molecules traversing the amorphous regions. The chain scission allows the resulting freed segments to crystallize [5]. The creation of new intermolecular polar bonds, due to carbonyl groups may also lead to this effect [5,20]. The reduction in the degree of crystallinity for LDPE/TPS_{UV} blends that having lower wt% of TPS is probably due to disruption of the crystalline order. Also, the UV irradiation can lead to formation of functional groups (such as hydroxyls, ketones, branching) during photooxidative degradation usually disturbing macro-chain order and losing compact polymeric structure, which manifests itself in reduction of the crystallinity degree [8].

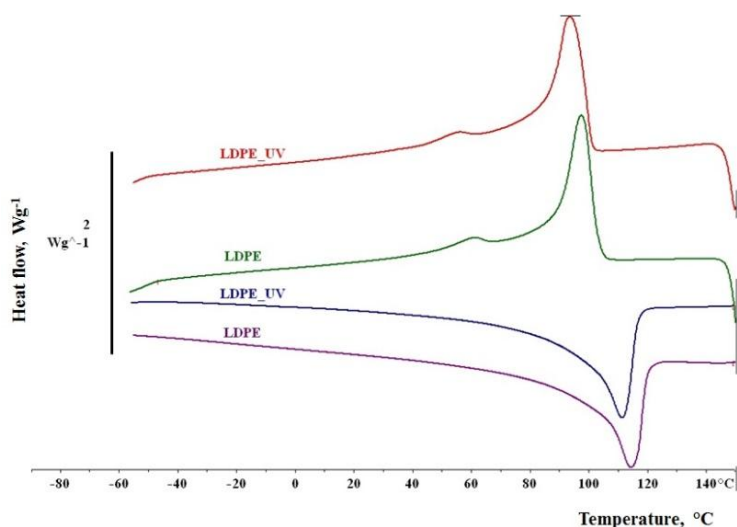


Figure 1. DSC thermograms of cooling-heating of LDPE and LDPE_{UV} samples

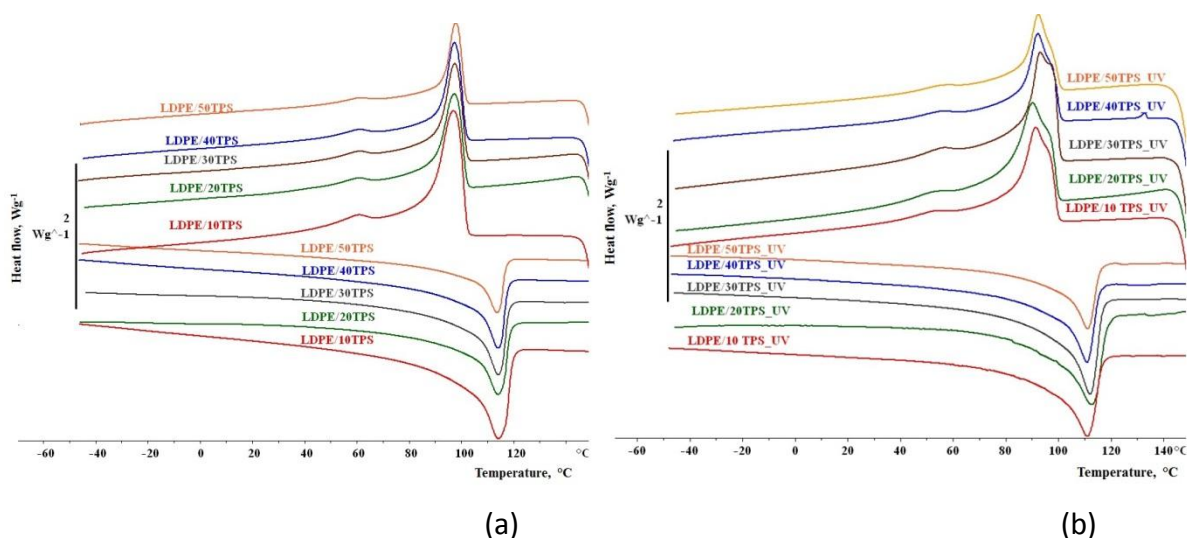


Figure 2. DSC thermograms of cooling-heating of (a) LDPE/TPS and (b) LDPE/TPS_{UV} blends



18th INTERNATIONAL FOUNDRYMEN CONFERENCE
Coexistence of material science and sustainable technology in
economic growth

Sisak, May 15th-17th, 2019

<http://www.simet.hr/~foundry/>

Table 2. Results of DSC analysis

Sample	T _m /°C	ΔH _m /Jg ⁻¹	χ _c /%
LDPE	114.7	114.0	39.3
LDPE_UV	111.5	129.4	44.6
LDPE/10TPS	114.2	105.3	40.4
LDPE/10TPS_UV	110.5	89.9	31.9
LDPE/20TPS	113.7	99.2	42.7
LDPE/20TPS_UV	112.3	94.9	40.9
LDPE/30TPS	114.3	74.5	36.7
LDPE/30TPS_UV	112.2	91.7	45.2
LDPE/40TPS	114.2	63.1	36.3
LDPE/40TPS_UV	99.3	73.3	42.1
LDPE/50TPS	113.7	48.4	33.4
LDPE/50TPS_UV	100.3	55.4	38.2

Thermogravimetric Analysis

Thermogravimetric analysis of neat polymers LDPE, TPS and their LDPE/TPS blends before and after UV irradiation was performed to investigate the thermal stability. Thermogravimetric analysis (TG) provides quantitative information about the thermal decomposition of the polymeric materials, from which the thermal stability can be evaluated. Thermal stability was evaluated through several parameters from the TG/DTG curves; by: the onset decomposition temperature (T_{onset}, °C), the temperature at maximum degradation rate (T^{max}, °C) (from DTG curve), weight loss (Δm, %) and final degradation temperature (T_{end}, °C).

Table 3 summarizes the all values taking from the corresponding TG (TG/DTG curves) thermograms. From the TG curves of TPS (Figure 3) the mass loss up to 250 °C associated to the evaporation of water, glycerol, and other volatile compounds present in TPS is noticeable, while the thermal degradation of polysaccharide (i.e. starch and cellulose) occurred between 250 and 350 °C with the highest degradation rate recorded at a temperature of 338.0 °C. TPS exhibited the lower peak degradation temperature compared to the LDPE. Figures 4 and 5 show the TG/DTG curves of the LDPE and LDPE/TPS blends before and after UV irradiation. Single step degradation is visible for pure LDPE which is also retained after UV irradiation of LDPE. As opposed to that, two-step degradation is manifested in LDPE/TPS blends, which is associated with the addition of TPS (Figure 4). The first degradation step at lower temperatures is linked to the decomposition of TPS and the second degradation step above 470 °C corresponds to the decomposition of LDPE [12]. It is obviously from Table 3 that the blending of starch with LDPE decreases the thermal stability of blends due to the weak points in starch inducing structure defects and/or irregularities as weak points in LDPE. These weak points decrease the thermal stability with the addition of starch.



18th INTERNATIONAL FOUNDRYMEN CONFERENCE

Coexistence of material science and sustainable technology in
economic growth

Sisak, May 15th-17th, 2019

<http://www.simet.hr/~foundry/>

After UV irradiation it is observed that the onset decomposition temperatures of the thermal degradation (T_{onset}) of the irradiated TPS, LDPE, and blends are lower than that of the samples before UV irradiation (Figure 4). The T_{onset} of the irradiated samples such as TPS decreased by 18 °C, whereas that of LDPE decreased by 8 °C. In contrast, some of the irradiated blends showed an insignificant decrease of the T_{onset} (LDPE/30TPS_UV), while some blends showed a significant decreased that for 31.2 °C (LDPE/20TPS_UV) (Figures 4 and 5). Exposure starch to UV irradiation bring the photooxidative degradation of starch, resulting in the cleavage of glycosidic bonds accompanied by the shortening of the amylose chain and a debranching of the amylopectin chain, due to the formation of free radicals, also facilitating the production of free radicals, which may react with a monomer to form a grafted co-polymer in the free radical-initiated graft co-polymerization of starch [21]. From the TG/DTG curves (Figure 5) it can be observed that the LDPE/TPS_UV irradiated sample initiated degradation at lower temperatures which further proceeded to steep degradation up to cc. 330 °C, resulting in increased weight loss in the first degradation step which is associated with thermoplastic starch. Also, from the Table 3 it is obvious that the second maximum temperature (T_2^{max}) related to the LDPE in the blends it is shifted to higher temperatures. According to the literature, the possible reason is linked to the amorphous regions of LDPE which are more susceptible to photooxidative degradation via UV light exposure than the densely packed crystalline regions. The amorphous regions that are more prone to oxidation act as a buffer for the crystalline regions, and therefore protect them from thermal degradation at the beginning of degradation. Probably the formation of carbonyl groups increase the degree of crystallinity of polyethylene, which may be related to the increase of LDPE degradation temperature (the second maximum temperature, T_2^{max}) after UV irradiation [22].

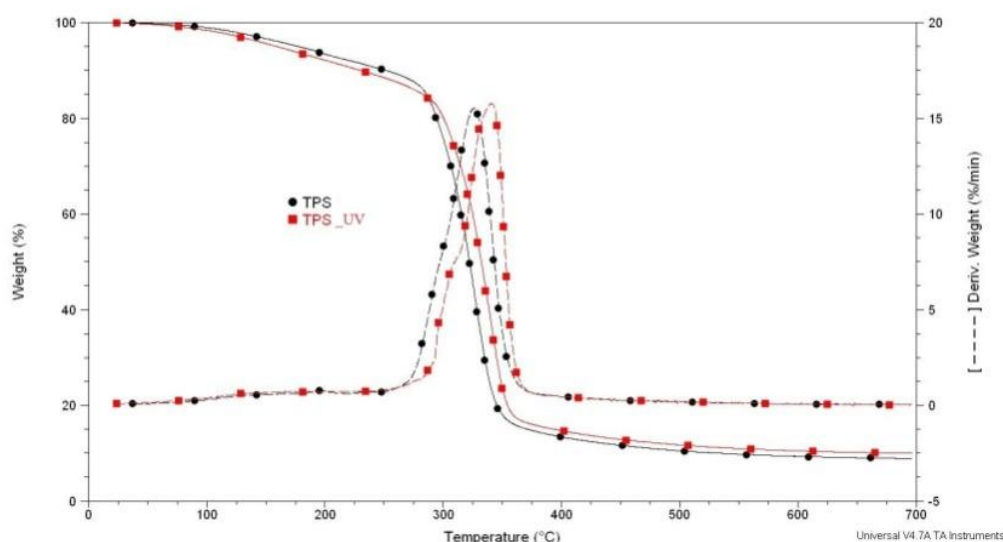


Figure 3. TG/DTG curves of TPS and TPS_UV



18th INTERNATIONAL FOUNDRYMEN CONFERENCE
Coexistence of material science and sustainable technology in
economic growth

Sisak, May 15th-17th, 2019

<http://www.simet.hr/~foundry/>

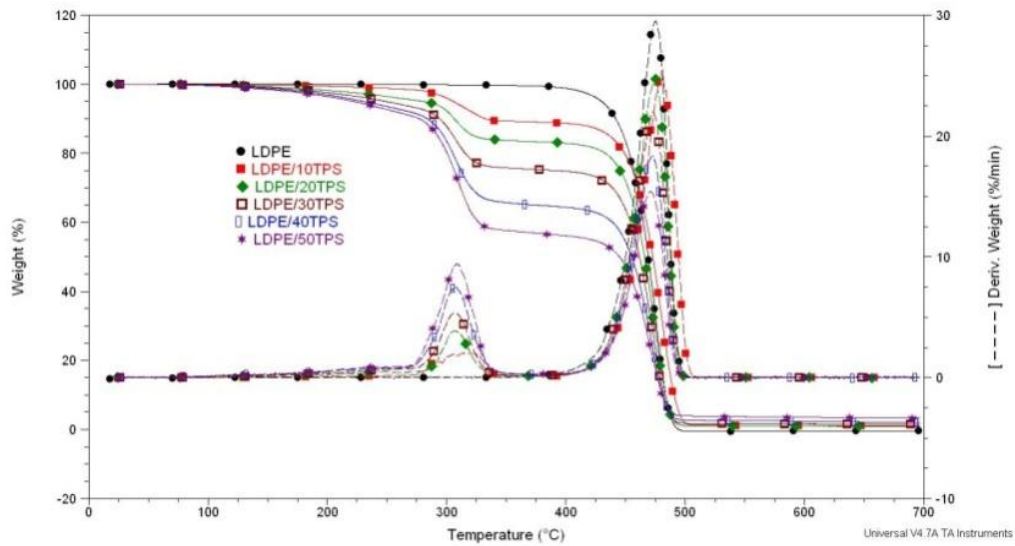


Figure 4. TG/DTG curves of LDPE/TPS blends

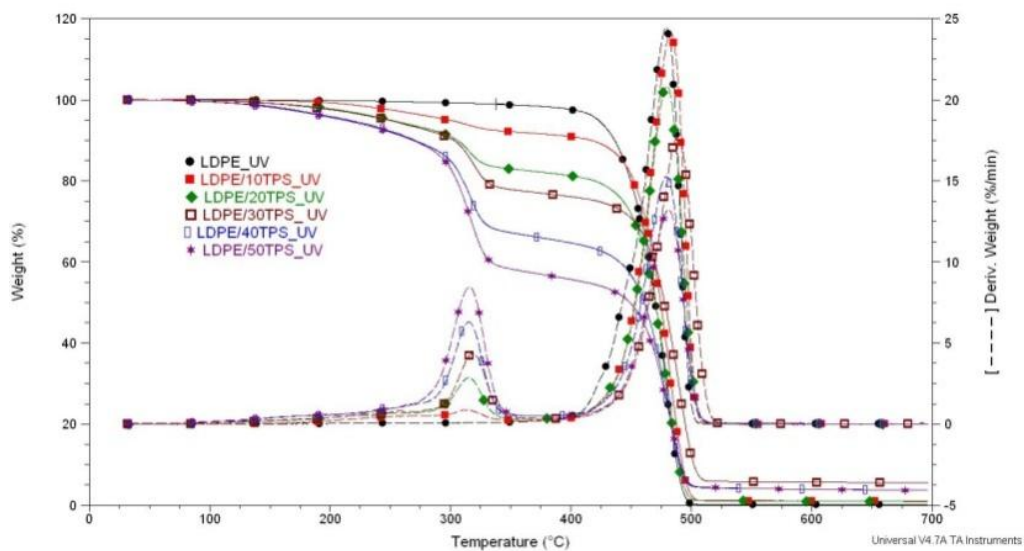


Figure 5. TG/DTG curves of LDPE/TPS_UV blends



18th INTERNATIONAL FOUNDRYMEN CONFERENCE
Coexistence of material science and sustainable technology in
economic growth

Sisak, May 15th-17th, 2019

<http://www.simet.hr/~foundry/>

Table 3. Results of TG analysis

Sample	T _{onset} , °C	T ₁ ^{max} , °C	Δm ₁ , %	T ₂ ^{max} , °C	Δm ₂ , %	T _{end} , °C
LDPE	430.1	N/A	N/A	474.7	100.0	495.3
LDPE_UV	422.6	N/A	N/A	479.1	98.7	492.2
LDPE/10TPS	305.7	317.1	9.1	479.9	88.2	491.2
LDPE/10TPS_UV	298.8	315.8	8.3	482.8	90.3	495.2
LDPE/20TPS	281.0	307.0	11.6	474.2	82.8	488.0
LDPE/20TPS_UV	249.8	314.8	15.8	479.6	81.0	492.8
LDPE/30TPS	249.6	310.0	18.5	472.8	74.1	484.9
LDPE/30TPS_UV	249.0	318.4	18.4	488.6	70.9	502.1
LDPE/40TPS	230.9	308.0	26.9	471.9	63.0	484.1
LDPE/40TPS_UV	215.4	315.1	28.5	479.2	61.6	494.1
LDPE/50TPS	222.5	308.8	35.9	470.7	53.3	483.5
LDPE/50TPS_UV	211.3	315.7	37.9	481.0	52.9	494.2
TPS	177.1	325.9	85.7	N/A	N/A	360.2
TPS_UV	159.5	338.0	77.9	N/A	N/A	356.4

Mechanical properties

Mechanical properties are of great importance for any application because the material must be able to maintain stable conditions and withstand all loads from the environment. The law of blends states that when polymers are miscible, the resultant blend properties are close to the sum of the polymer properties (as a function of their proportions); however, when polymers are not miscible, their properties are even lower [23, 24].

The mechanical properties, tensile strength and elongation at break of the neat LDPE, TPS polymers and LDPE/TPS blends were evaluated from stress-strain curves before and after UV irradiation, and results are presented in Table 4. LDPE is a tough and rigid material, presented low value of tensile strength ($11.8 \pm 0.3 \text{ N mm}^{-2}$) but high value of elongation at break ($664.0 \pm 39.4\%$). On the other hand, TPS exhibited extremely poor mechanical properties, low value of tensile strength and elongation at break. According to the obtained mechanical properties, TPS can be described as an extremely fragile polymeric material, whose fragility limits its wider application (Table 4). From the Table 4 it is apparent that the addition and increase in TPS content in LDPE/TPS blends results in a decreased in tensile strength and elongation at break. Possible explanation is related to the physical incorporation of TPS in the LDPE matrix, which weakens London's force between LDPE layers. Another reason is related with TPS as molecules with low molecular weight and withstands lower elongation at break compared to LDPE [24]. Table 4 shows a decrease in the tensile strength of the LDPE/TPS blends before UV irradiation with increasing the ratio of TPS. This decrease can be related with the incompatibility of the LDPE/TPS blends, due to the coarse dispersed particle and poor interfacial adhesion. After UV irradiation for 30 days the mechanical properties of LDPE/TPS_UV blends decrease. Decrease of the tensile strength and elongation of the break for all LDPE/TPS_UV blends after UV irradiation may be caused



18th INTERNATIONAL FOUNDRYMEN CONFERENCE

Coexistence of material science and sustainable technology in
economic growth

Sisak, May 15th-17th, 2019

<http://www.simet.hr/~foundry/>

by photooxidation via UV irradiation of the polymer with a formation of small molecular products which act as plasticisers, which is in agreement with the DSC and TGA results. Besides the increase in density of crosslinking and degradation, longer exposure causes oxidation, destruction of the crystal regions and formation of new order range as the effect of chemicrystallisation. All these phototransformations may deteriorate or improve the mechanical properties, depending on the relation of efficiency of individual transformation [25].

Table 4. Results of mechanical properties

Sample	Tensile strength/ Nmm ⁻²	Elongation at break/ %
LDPE	11.8 ± 0.3	664.0 ± 39.4
LDPE_UV	9.7 ± 0.4	456.1 ± 23.1
LDPE/10TPS	9.8 ± 0.2	81.3 ± 8.3
LDPE/10TPS_UV	8.1 ± 0.1	63.1 ± 3.4
LDPE/20TPS	9.3 ± 0.4	16.3 ± 2.3
LDPE/20TPS_UV	7.9 ± 0.3	14.1 ± 1.3
LDPE/30TPS	8.8 ± 2.3	15.5 ± 0.5
LDPE/30TPS_UV	7.5 ± 0.4	13.1 ± 0.3
LDPE/40TPS	8.3 ± 0.5	8.7 ± 1.2
LDPE/40TPS_UV	7.1 ± 0.1	7.1 ± 0.1
LDPE/50TPS	7.4 ± 0.8	5.5 ± 1.0
LDPE/50TPS_UV	6.1 ± 0.1	4.1 ± 0.1
TPS	4.1 ± 0.1	4.7 ± 2.3
TPS_UV	3.2 ± 0.3	3.2 ± 0.3

CONCLUSIONS

The effect of UV irradiation of low density polyethylene blends containing a different content of thermoplastic starch, LDPE/TPS, were analyzed through thermal and mechanical properties. From the DSC results, the degree of crystallinity LDPE/TPS_UV blends with higher content of TPS increased after UV irradiation. Increase of the crystalline region led to deterioration of the mechanical properties due to the reduction of the polymer chain, preferably the amorphous region, and the rearrangement of molecules causing a larger organization of the chain. Based on the investigation results, it can be concluded that the UV irradiation of the blends influenced both the molecular structure of the LDPE chains as well as its degree of crystallinity because the photooxidation occurs mainly in the amorphous region of the LDPE polymers. More research needs to focus on the application and large scale production of such environmentally-friendly materials with the aim of developing



18th INTERNATIONAL FOUNDRYMEN CONFERENCE
**Coexistence of material science and sustainable technology in
economic growth**

Sisak, May 15th-17th, 2019

<http://www.simet.hr/~foundry/>

completely degradable plastics. This study aids in the development of degradable plastics that can limit the amount of plastic pollution.

However, the widespread practical application of LDPE/TPS blends requires further studies aimed on improving their compatibility and other properties relevant to its applications.

Acknowledgements

This work was supported by the Ministry of Science and Education of the Republic of Croatia.

REFERENCES

- [1] M. Lackner, Biopolymers, in: Handbook of climate change mitigation and adaptation, W.-Y. Chen et al. (eds.), Springer Science and Business Media, New York, 2015.
- [2] S. Jovanović, J. V. Džunuzović, Ž. Stojanović, Polymers based on renewable raw materials – Part II, *Kemija u Industriji*, 9-10(2013)62, pp. 315-326.
- [3] V. A. Carmona, A. C. Correia, J. M. Marconcini, L. H. Capparelli Mattoso, Properties of a biodegradable ternary blend of thermoplastic starch (TPS), poly(ϵ -Caprolactone) (PCL) and poly(Lactic Acid) (PLA), *Journal of Polymer Environmental*, 23(2015)1, pp. 83-89.
- [4] A. Martínez-Romo, R. González-Mota, J. J. Soto-Bernal, I. Rosales-Candelas, Investigating the degradability of HDPE, LDPE, PE-BIO, and PE-OXO films under UV-B radiation, *Journal of Spectroscopy*, (2015), Article ID 586514, pp. 1-6.
- [5] M. L. Méndez-Hernández, C. S. Tena-Salcido, Z. Sandoval-Arellano, M. C. González-Cantú, M. Mondragón, F. J. Rodríguez-González, The effect of thermoplastic starch on the properties of HDPE/TPS blends during UV accelerated aging, *Polymer Bulletin*, 67(2011)5, pp. 903-914.
- [6] F. J. Rodriguez-Gonzalez, B. A. Ramsay, B. D. Favis, High performance LDPE/thermoplastic starch blends: a sustainable alternative to pure polyethylene, *Polymer*, 44(2003)5, pp. 1517-1526.
- [7] A. Taguet, M. A. Huneault, B. D. Favis, Interface/morphology relationship in polymer blends with thermoplastic starch, *Polymer*, 50(2009)24, pp. 5733-5743.
- [8] E. Yousif, R. Haddad, Photodegradation and photostabilization of polymers, especially polystyrene: review, *Springerplus*, 2(2013), pp. 398-430.
- [9] D. C. Wright, Failure of polymer products due to thermo-oxidation, iSmithers Rapra Publishing, Shrewsbury, United Kingdom, 2001.
- [10] F. Khabbaz, A.-C. Albertsson, S. Karlsson, Chemical and morphological changes of environmentally degradable polyethylene films exposed to thermo-oxidation, *Polymer Degradation and Stability*, 63(1999)1, pp. 127-138.
- [11] A. Tidjani, Comparison of formation of oxidation products during photo-oxidation of linear low density polyethylene under different natural and accelerated weathering conditions, *Polymer Degradation and Stability*, 68(2000)3, pp. 465-469.



18th INTERNATIONAL FOUNDRYMEN CONFERENCE

Coexistence of material science and sustainable technology in
economic growth

Sisak, May 15th-17th, 2019

<http://www.simet.hr/~foundry/>

- [12] V. Ocelić Bulatović, I. Borković, D. Kučić Grgić, A. Jozinović, Toplinska i mehanička svojstva na bazi termoplastičnog škroba, *Kemija u industriji*, 67(2018)13, pp. 21-31.
- [13] B. G. Girija, R. R. N. Sailaja, Low - density polyethylene / plasticized tapioca starch blends with the low - density polyethylene functionalized with maleate ester: Mechanical and thermal properties, *Journal of Applied Polymer Science*, 101(2006), pp. 1109-1120.
- [14] A. Gupta, V. Kumar, M. Sharma, Formulation and characterization of biodegradable packaging film derived from potato starch & LDPE grafted with maleic anhydride - LDPE composition, *Journal of Polymer Environmental*, 18(2010), pp. 484-491.
- [15] A. Adelhafidia, I. M. Babaghayou, S. F. Chabira, M. Sebaa, Impact of solar radiation effects on the physicochemical properties of polyethylene (PE) plastic film, *Procedia - Social and Behavioral Sciences*, 195(2015), pp. 2210-2217.
- [16] M. Gardette, A. Perthue, J.-L. Gardette, T. Janecska, E. Földes, B. Pukánszky, S. Therias, Photo- and thermal-oxidation of polyethylene: Comparison of mechanisms and influence of unsaturation content, *Polymer Degradation and Stability*, 98(2013)11, pp. 2383-2390.
- [17] E. Eltayeb, M. Barikani, A. Mahdavian, H. Honarkar, An investigation into the UV-photo-oxidative degradation of LDPE by using cobalt naphthenate as photosensitizer, *Polymer-Plastics Technology and Engineering*, 49(2010)7, pp. 718-724.
- [18] P. K. Roy, P. Surekha, R. Raman, C. Rajagopal, Investigating the role of metal oxidation state on the degradation behavior of LDPE, *Polymer Degradation and Stability*, 94(2009)7, pp. 1033-1039.
- [19] H. Kaczmarek, D. Oldak, The effect of UV-irradiation on composting of polyethylene modified with cellulose, *Polymer Degradation and Stability*, 91(2006)10, pp. 2282-2291.
- [20] F. Khabbaz, A.-C. Albertsson, S. Karlsson, Chemical and morphological changes of environmentally degradable polyethylene films exposed to thermo-oxidation, *Polymer Degradation and Stability*, 63(1999)1, pp. 127-138.
- [21] R. Bhat, A. A. Karim, Impact of radiation processing on starch, *Comprehensive Reviews in Food Science and Food Safety*, 8(2009)2, pp. 44-58.
- [22] R. T. Thomasa, N. Sandhyarani, Enhancement in the photocatalytic degradation of low density polyethylene-TiO₂ nanocomposite films under solar irradiation, *RSC Advances*, 3(2013)33, pp. 14080-14087.
- [23] S. Ali Akbari Ghavimi, M. H. Ebrahimzade, M. Solati-Hashjin, N. A. Abu Osman, Polycaprolactone/starch composite: Fabrication, structure, properties, and applications, *Journal of Biomedical Materials Research Part A*, 103(2015)7, pp. 2482-2498.
- [24] S. Korman, F. Korman, M. D. H. Beg, Effect of plasticizer on physical and mechanical properties of LDPE/sago starch blend, *Journal of Physics: Conf. Series*, 1150 (2019)012032.
- [25] A. Sionkowska, M. Wisniewski, J. Skopinska, S. Vicini, E. Marsano, The influence of UV irradiation on the mechanical properties of chitosan/poly(vinyl pyrrolidone) blends, *Polymer Degradation and Stability*, 88 (2005)2, pp. 261-267.



18th INTERNATIONAL FOUNDRYMEN CONFERENCE

Coexistence of material science and sustainable technology in
economic growth

Sisak, May 15th-17th, 2019

<http://www.simet.hr/~foundry/>

WASTE OIL MANAGEMENT IN CROATIA FOR THE PERIOD 2007 – 2016

GOSPODARENJE OTPADNIM ULJIMA U HRVATSKOJ U RAZDOBLJU 2007. – 2016.

Tahir Sofilić¹, Ivan Brnardić^{1*}, Una Sofilić-Šimić², Laila Gumhalter-Malić³

¹ University of Zagreb Faculty of Metallurgy, Sisak, Croatia

² STSI - Integrated Technical Services, Ltd., Zagreb, Croatia

³ Croatian Agency for Environment and Nature, Zagreb, Croatia

Poster presentation

Review

Abstract

This paper describes the course of introducing and implementing regulations ensuring efficient waste oil (lubricating oils and edible oils) management, as well as results obtained based on ten years of experience in monitoring and reporting on the management of this special waste category. According to the results for period from 2007 to 2016, between 5 390 t (5 989 000 L) and 7 068 t (7 853 000 L) of waste lubricating oils were collected in the Republic of Croatia.

The quantities of waste edible oil collected in the same period indicate low amounts compared to the estimated annual quantities of fresh edible oil placed on the market, i.e. supposed quantities of waste edible oil collected vary, from 718 t (798 000 L) to 2 145 t (2 383 000 L).

Keywords: waste oils, lubricating oils, edible oils, waste management

*Corresponding author (e-mail address): brnardic@simet.hr

Sažetak

U ovom radu je opisan tijek uvođenja i primjene legislative u Republici Hrvatskoj kojima je bio cilj osigurati učinkovito upravljanje otpadnim uljima (otpadno mazivo i otpadno jestivo ulje). Prikazani su rezultati dobiveni na temelju desetogodišnjeg iskustva u praćenju i izvještavanju o upravljanju ovom posebnom skupinom otpada. Prema rezultatima od 2007. do 2016. godine, u Republici Hrvatskoj prikupljeno je između 5 390 t i 7 068 t ulja za mazanje.

Rezultati sakupljanja otpadnog jestivog ulja u istom razdoblju ukazuju na relativno male količine u odnosu na procijenjene godišnje količine svježeg jestivog ulja stavljanog na tržište, tj. količine sakupljenih količina otpadnog jestivog ulja varirale su od 718 t do 2 145 t.

Ključne riječi: otpadna ulja, maziva ulja, jestiva ulja, gospodarenje otpadom



18th INTERNATIONAL FOUNDRYMEN CONFERENCE

Coexistence of material science and sustainable technology in
economic growth

Sisak, May 15th-17th, 2019

<http://www.simet.hr/~foundry/>

UVOD

Na temelju dostupnih literaturnih podataka Eurostat ureda za statistiku Europske komisije [1], koji se odnose na ukupnu količinu otpada nastalog tijekom 2014. godine u svim ekonomskim djelatnostima i kućanstvima na području EU-28, količina obrađenog otpada iznosila je 2.503 milijuna tona što je bio i najveći iznos obrađenog otpada u razdoblju od 2004. do 2014. godine. Gotovo pola od navedene obrađene količine (47,4 %) unutar EU-28, bilo je zbrinuto odlaganjem, prije svega na odlagalištima, 10,2 % otpada bilo je odloženo u blizini rudnika ili u samim rudnicima, a jedan dio je i ispušten u vode. Ostatak otpada koji čini 42,4 % ukupne količine nastalog otpada u EU u 2014. godini uglavnom je recikliran (36,2 %), dok je ostalo (6,2 %) obrađeno spaljivanjem u spalionicama sa ili bez iskorištenja toplinske energije.

Rastući trend količine nastalog otpada, kao i aktivnosti vezane uz njegovu obradu i/ili zbrinjavanje, ukazuju na značaj gospodarenja otpadom koje zauzima posebno mjesto u strategijama zaštite okoliša u svim europskim zemljama. Strategije razvijenih zemalja koje naglašavaju zahtjeve za smanjenjem, oporabom i recikliranjem otpada, doprinose zatvaranju kruga uporabe materijala na svim poljima gospodarstva stvarajući materijale nastale iz otpada kao ulazni materijal za novu proizvodnju. U novije vrijeme razmatranje životnog ciklusa sve se više uvodi kao vodeće načelo gospodarenja resursima, a utjecaji na okoliš promatraju se tijekom cijelog životnog ciklusa proizvoda kako bi se, gdje god je to moguće, izbjeglo ili na najmanju moguću mjeru svelo premještanje problema okoliša iz jedne u drugu fazu životnog ciklusa ili pak premještanja iz jedne u drugu zemlju pomoću tržišnih instrumenata.

Dobro izgrađen i učinkovit sustav gospodarenja otpadom bitna je sastavnica modernog društva, a za njegovo razvijanje i učinkovitost važne su gospodarske odrednice koje potiču smanjivanje količine otpada na mjestu nastajanja, odvojeno skupljanje, obradu, recikliranje i oporabu.

U Republici Hrvatskoj (RH) je zakonodavni dio sustava gospodarenja otpadom velikim dijelom riješen, iako još postoji izvjesna neusklađenost sa zahtjevima i standardima EU, međutim, veliki problem predstavlja neprovođenje propisa. Iako se u području gospodarenja otpadom u RH već niz godina provode aktivnosti i mjere koje pridonose približavanju zadanim strateškim ciljevima, ipak se u nekim segmentima ti ciljevi ne provode očekivanom dinamikom ili se bilježe poteškoće u provedbi. Iz tog razloga nužno je daljnje jačanje kapaciteta tijela nadležnih za gospodarenje otpadom, unapređenje rada tvrtki sudionika u gospodarenju otpadom, permanentno razvijanje i unapređenje ekonomskih instrumenata poput već uvedenih naknada za troškove sakupljanja i oporabe posebnih kategorija otpada te naknada za onečišćavanje okoliša otpadom, a posebno mjesto zauzima potreba obrazovanja stručnjaka koji će se baviti ovom problematikom.

U hrvatskom zakonodavnom okviru vrlo značajno mjesto zauzima gospodarenje posebnim kategorijama otpada koje je uređeno te su razvijeni sustavi odvojenog skupljanja i oporabe pojedinih posebnih kategorija otpada u koji se ubraja: biootpad, otpadni tekstil i obuća, otpadna ambalaža, otpadne gume, otpadna ulja, otpadne baterije i akumulatori, otpadna vozila, otpad koji sadrži azbest, medicinski otpad, otpadni električni i elektronički uređaji i



18th INTERNATIONAL FOUNDRYMEN CONFERENCE

Coexistence of material science and sustainable technology in
economic growth

Sisak, May 15th-17th, 2019

<http://www.simet.hr/~foundry/>

oprema, otpadni brodovi, morski otpad, građevni otpad, otpadni mulj iz uređaja za pročišćavanje otpadnih voda, itd.

Od svih navedenih posebnih kategorija otpada, organiziranim gospodarenjem se, kako u Europi, tako i u RH, najranije pristupilo gospodarenju otpadnim uljima, što predstavlja skup mjera koje obuhvaćaju sakupljanje otpadnih ulja radi materijalne oporabe ili korištenja u energetske svrhe ili nekog drugog načina konačnog zbrinjavanja kada ih nije moguće oporabiti. Stoga će i u ovom radu biti prikazani neki pokazatelji uspješnosti u ovoj djelatnosti kao i dosadašnja iskustva u gospodarenju otpadnim uljima u RH.

POVIJEST GOSPODARENJA OTPADNIM ULJIMA U RH

Krajem 60-tih godina prošlog stoljeća otpadna ulja počinju zanimati svjetske stručnjake i to najprije kao jedna od onečišćujućih tvari u okolišu koja je tada značajno ugrožavala kvalitetu vode i tla. U to vrijeme su se pod otpadnim uljima uglavnom podrazumijevala tzv. industrijska mineralna ulja i ulja korištena za podmazivanje. Spoznajama o štetnom utjecaju otpadnih ulja na okoliš, pojavila se potreba za uvođenjem mjera sprječavanja njihovog ispuštanja u vode i izlivanjem na tlo izradom odgovarajućih propisa za gospodarenje ovom vrstom otpada. Istovremeno, a s obzirom na sve veću uporabu svježih ulja u industriji i prometu, rastao je njihov značaj i nakon uporabe ta su se *korištena* ili *otpadna* ulja sve više počela koristiti i za preradu odnosno proizvodnju novih količina svježih ulja. Prema podacima [2] nekih studija Američkog naftnog instituta (engl. *American Petroleum Institute*, API) već krajem 60-tih i početkom 70-tih godina prošlog stoljeća zabilježeni su značajni rezultati organiziranog sakupljanja otpadnih mazivih ulja na američkim benzinskim crpkama kao i podaci o kretanju prodanih količina sakupljenih otpadnih ulja trećim osobama u svrhu obrade i proizvodnje svježih ulja. Naime, već tada su postojali komercijalizirani procesi za oporabu otpadnog ulja na način da se dobiju novi proizvodi ili da se pročišćavanjem omogući njihova ponovna uporaba ili su se otpadna ulja termički obrađivala na način da su se koristila kao gorivo.

U isto vrijeme su u RH pojedina pitanja zaštite okoliša bila uređena u okviru *Zakona o prostornom uređenju i korištenju građevinskog zemljišta* iz 1973. godine [3], što nije zadovoljavalo pitanja vezana uz otpad, pa tako niti otpadna ulja. No, već 1982. godine stupio je na snagu poseban *Zakon o postupanju s otpadnim tvarima* [4] u kojem se, između ostalog, prvi puta posvetila posebna pozornost otpadnim uljima. Naime, ovim Zakonom, su se otpadne tvari razvrstavale u četiri skupine i to: otpad iz proizvodnje i prometa, *otpadna mineralna i ostala ulja*, komunalni otpad i neiskorištena energija. Tim istim Zakonom bili su utvrđeni obveznici propisanog načina postupanja s navedenim vrstama otpada, kao i obveza određenih gospodarskih subjekata za preuzimanje otpadnih ulja, odnosno obveza registracije ostalih gospodarskih subjekata za obavljanje djelatnosti sakupljanja otpadnih ulja.

Iako su neke europske zemlje i tijekom 60-tih godina imale izvjesne rezultate u gospodarenju otpadnim uljima poput Velike Britanije, Njemačke, Italije itd. [2], sustavnim pristupom gospodarenja ovom posebnom kategorijom otpada može se smatrati druga polovica 70-tih



18th INTERNATIONAL FOUNDRYMEN CONFERENCE

Coexistence of material science and sustainable technology in
economic growth

Sisak, May 15th-17th, 2019

<http://www.simet.hr/~foundry/>

godina, kada je i objavljena Direktiva 75/439/EEC o odlaganju otpadnih ulja [5] (engl. *Council Directive on the disposal of waste oils*) koja se odnosila samo na otpadna maziva ulja. Ova direktiva je nadopunjavana u tri navrata Direktivama o dopunama direktive o odlaganju otpadnih ulja 1987/101/EEC, 1991/692/EEC i 2000/76/EC, a opozvana je izdavanjem Direktive 2008/98/EC o otpadu i stavljanju izvan snage određenih direktiva [6] (engl. *Directive of the European Parliament and of the Council on waste and repealing certain Directives*) u koju su prenesene sve relevantne odredbe koje su se odnosile na gospodarenje otpadnim uljima, te koja je danas transponirana u zakonodavstva zemalja članica EU.

U RH do promjena dolazi 1995. godine, kada stupa na snagu novi *Zakon o otpadu* [7] čime je izvan snage stavljen *Zakon o postupanju s otpadnim tvarima*. Iako se u tom novom zakonu, kojim se uređuju pitanja gospodarenja otpadom, otpadna ulja ne spominju izdvojeno, ipak je u provedbenom dokumentu toga zakona, a to je *Pravilnik o vrstama otpada* [8] otpadnim uljima dana velika pozornost. Naime, navedenim su Pravilnikom bile utvrđene vrste otpada, ovisno o svojstvima i mjestu nastanka, način postupanja s pojedinim vrstama otpada, način dostave podataka o postupanju s otpadom, ispitivanje kemijsko-fizikalnih svojstava opasnog otpada, uzorkovanje otpada, itd., a vrlo detaljno se propisuje način postupanja jedino s otpadnim uljima, dok za ostale vrste i kategorije otpada vrijede navedene općenite odredbe.

U ovom dokumentu je definiran pojam *otpadnih ulja*, način razvrstavanja prema stupnju onečišćenja, propisane su obveze proizvođača svježih ulja i onih koji ih stavljaju na tržište, kao i obveze proizvođača otpadnih ulja posebice u pogledu skupljanja (odvojeno skupljanje, posebni označeni spremnici,...), vođenje evidencije o nastalim količinama otpadnih ulja, itd. Zakonom o otpadu iz 1995., propisana je obveza hrvatskih proizvođača otpada, o načinu vođenja evidencije o vrstama i količinama nastalog otpada i dostave podataka u Katastar otpada koji je dio Katastra emisija u okoliš.

Sam sustav praćenja podataka o vrstama, količinama, mjestu nastanka, načinu zbrinjavanja otpada itd., uveden je 1997. godine čemu je prethodilo stupanje na snagu *Pravilnik o katastru emisije u okoliš* [9]. Ovaj Pravilnik bio je predviđen još 1994. godine i to *Zakonom o zaštiti okoliša* [10], a svrha mu je bila ustrojiti cjelovitu bazu podataka o onečišćenju okoliša emisijama u zrak, vode i more iz pojedinačnih izvora, kao i vrstama i količinama opasnoga otpada.

Pravilnikom o katastru emisija u okoliš bio je propisan obvezni sadržaj, metodologija i način vođenja katastra emisija u okoliš, način i rokovi prikupljanja i dostavljanja traženih podataka, uvjeti izdavanja ovlaštenja pravnim osobama zainteresiranim za obavljanje poslova vođenja katastra emisija u okoliš te kaznene odredbe za obveznike koji ne bi provodili odredbe ovoga pravilnika. Na ovaj način je počelo sustavno prikupljanje i vođenje podataka o izvorima, vrsti, količini, načinu i mjestu ispuštanja, istjecanja ili odlaganja štetnih tvari u okoliš iz određenog izvora u okoliš, a koji su se odnosili na razdoblje protekle kalendarske godine. Katastar emisija u okoliš bio je sastavni dio katastra onečišćavanja okoliša definiranog *Zakonom o zaštiti okoliša* [10].

Katastar emisije u okoliš (KEO) prikupljao je podatke o onečišćenju okoliša od 1997. do 2008. godine, kada ga je zamijenio Registar onečišćavanja okoliša (ROO) kao baza podataka o izvorima, vrsti, količini, načinu i mjestu ispuštanja, prijenosa i odlaganja onečišćujućih tvari i otpada u okoliš [7].



18th INTERNATIONAL FOUNDRYMEN CONFERENCE

Coexistence of material science and sustainable technology in
economic growth

Sisak, May 15th-17th, 2019

<http://www.simet.hr/~foundry/>

Precizniji način praćenja podataka o količinama, mjestu nastanka i načinu zbrinjavanja otpadnih ulja započeo je 2006. godine donošenjem *Pravilnika o gospodarenju otpadnim uljima* [12], čije donošenje je bila obveza odredbama tadašnjeg *Zakona o otpadu* iz 2004. godine [13]. Navedeni Pravilnik imao je za cilj uspostavljanje sustava sakupljanja otpadnih ulja radi oporabe i/ili zbrinjavanja, zaštite okoliša u cijelosti pa tako i zdravlja ljudi. Ovim pravilnikom je propisan način gospodarenja otpadnim uljima, određeni su obveznici plaćanja naknada, vrste i iznosi naknada, načini i rokovi obračunavanja i plaćanja naknada, iznosi naknada koje se plaćaju ovlaštenim osobama za sakupljanje otpadnih ulja kao i druga pitanja iz područja gospodarenja otpadnim uljima. Nadalje, propisano je i vođenje posebne evidencije o količinama proizvoda stavljenih na tržište RH (proizvedenih i/ili uvezenih) koji istekom životnog vijeka postaju jedna od posebnih kategorija otpada.

Odredbe ovog Pravilnika se ne odnose na gospodarenje otpadnim uljima koja sadrže poliklorirane bifenile (PCB) i poliklorirane terfenile (PCT) iznad 30 mg/kg, emulzijama i zauljenim tekućim otpadom koji sadrže u svom sastavu osim otpadnih emulzijskih ulja i ostalih otpadnih ulja i ostale onečišćujuće tvari i vodu, jer su to pitanja koja su uređena zasebnim Pravilnikom. Od tada do danas, *Pravilnik o gospodarenju otpadnim uljima* je doživio više izmjena i dopuna, a po stupanju na snagu *Zakona o održivom gospodarenju otpadom* iz 2013. godine [14], predstoji mu zamjena novim Pravilnikom.

POKAZATELJI USPJEŠNOSTI GOSPODARENJA OTPADNIM ULJIMA U RH

Kao što je već navedeno *Pravilnik o gospodarenju otpadnim uljima* [12], je korigirao dotadašnji način sakupljanja otpadnih ulja, njihovu oporabe i zbrinjavanje i to uspostavljanjem cjelovitog sustava gospodarenja otpadnim uljima. Do tada, nije bio jasno definiran niti pojam *otpadno ulje*, za koja se 1996. smatralo da su to *tekući ili polutekući proizvodi koji potječu iz različitih primjena, a koji su tijekom korištenja, skladištenja ili prijevoza postali neprikladni za upotrebu prema prvobitnoj namjeni* [8].

Europska Direktiva 2008/98/EC o otpadu i stavljanju izvan snage određenih direktiva [6] otpadna ulja definira kao *mineralna ili sintetička ulja za podmazivanje ili industrijska ulja koja su postala neprikladna za uporabu za koju su prvobitno bila namijenjena, primjerice ulja iz motora s unutarnjim izgaranjem i ulja reduktora, ulja za podmazivanje, ulja za turbine i hidraulička ulja*. Sukladno toj definiciji u legislativi RH tj. u *Zakonu o održivom gospodarenju otpadom* [14] otpadna ulja se definiraju na isti način tj. kao *mineralna ili sintetička ulja za podmazivanje ili industrijska ulja koja su postala neprikladna za uporabu za koju su prvobitno namijenjena, primjerice ulja iz motora s unutarnjim izgaranjem i ulja reduktora, ulja za podmazivanje, ulja za turbine i hidraulička ulja*.

Pri ovome se otpadna jestiva ulja ne spominju, no bitno je naglasiti da iako Direktiva 2008/98/EC o otpadu klasificira otpadno jestivo ulje u kategoriju neopasnog otpada kao *jestiva ulja i masti* (klj. br. 20 01 25) obvezuje sve države članice EU na poduzimanje mjera za poticanje odvojenog sakupljanja i obrade biootpada na način koji osigurava visoku razinu zaštite okoliša. Na temelju ovoga su u *Pravilniku o gospodarenju otpadnim uljima* [12], precizno definirani pojmovi vezani uz otpadno ulje na način kako slijedi:



18th INTERNATIONAL FOUNDRYMEN CONFERENCE

Coexistence of material science and sustainable technology in
economic growth

Sisak, May 15th-17th, 2019

<http://www.simet.hr/~foundry/>

- *Otpadno ulje* je otpadno mazivo ulje i otpadno jestivo ulje;
- *Otpadno mazivo ulje (OMU)* je svako mineralno i sintetičko mazivo, industrijsko, izolacijsko (ulje koje se rabi u elektroenergetskim sustavima) i/ili termičko ulje (ulje koje se rabi u sustavima za grijanje ili hlađenje) koje više nije za uporabu kojoj je prvotno bilo namijenjeno, posebice rabljena motorna ulja, strojna ulja, ulja iz mjenjačkih kutija, mineralna i sintetička maziva ulja, ulja za prijenos topline, ulja za turbine i hidraulička ulja osim ulja koja se primješavaju benzinima kod dvotaktnih motora s unutrašnjim izgaranjem i
- *Otpadno jestivo ulje (OJU)* je svako ulje koje nastaje obavljanjem ugostiteljske i turističke djelatnosti, industriji, obrtu, zdravstvenoj djelatnosti, javnoj upravi i drugim sličnim djelatnostima u kojima se priprema više od 20 obroka dnevno.

Unatoč spomenutoj obvezi, većina europskih država nema pokretače i motivaciju za široko rasprostranjene učinkovite sustave prikupljanja i uporabu OJU koja proizvode kućanstva. Slijedom toga, više od 60 % proizvedenih OJU nepropisno se zbrinjava što često uzrokuje štetne posljedice poput začepjenja kanalizacijskih sustava i onečišćenja voda. Istovremeno, postoji veliki potencijal u recikliranju OJU, što povećava interes za njihovo prikupljanje, posebno za njihovo korištenje u proizvodnji biodizela koji bi mogao zamijeniti 1,5 % potrošnje dizel goriva u EU28, a time pridonio postizanju cilja EU za smanjenje emisije CO₂ za 20 % do 2020. godine [15].

Imajući ovo na umu, kao i propuste u obveznika u pravovremenom dostavljanju podataka nadležnim institucijama o nastalom otpadu, pa tako i otpadnim uljima, ne postoje precizni podaci za 90-te godine prošlog stoljeća o kretanju nastalih količina otpadnih ulja, njihovom sakupljanju, obradi i zbrinjavanju na području RH.

Naime, u razdoblju od 1996. do 2004. godine obveznici su svoje podatke o vrsti, količini, načinu i mjestu ispuštanja, prijenosa i odlaganja onečišćujućih tvari i otpada u okoliš dostavljali županijskim uredima nadležnim za poslove zaštite okoliša. Nažalost, u dostupnoj literaturi ne postoje sistematizirani podaci o sakupljenim količinama otpada u navedenom razdoblju. Naime, do 2005. godine u RH je Katastar otpada vodilo tadašnje Ministarstvo zaštite okoliša, prostornog uređenja i graditeljstva, a od 2005. ga je vodila tadašnja Agencija za zaštitu okoliša (AZO) sukladno Zakonu o otpadu iz 2004. godine [13]. Tijekom 2005. godine AZO je započela zaprimati podatke o otpadu za 2004. godinu i tek tada uvela u praksu izradu *Pregleda podataka iz katastra otpada* [16-18], koji su između ostaloga sadržavali i zbirni podatak o količini sakupljenih otpadnih ulja.

Podaci koje su obveznici dostavljali u Katastar otpada često su bili nepotpuni i netočni što je obično bilo vezano na pogrešno odabrane ključne brojeve prijavljivanog otpada, nedostatku podataka o tokovima otpada, neadekvatnim mjernim jedinicama količina otpada, itd. Stoga se i obrađeni rezultati prikazani u tim prvim izvješćima, kako na županijskoj tako i na državnoj razini, moraju promatrati s rezervom.

Značajno je za napomenuti da je prvo izvješće u RH u kojem su bili prikazani detalji prikupljenih podataka o OMU bilo *Katastar otpada - Izvješće za 2005. godinu* [17], u kojem je utvrđeno da je količina otpadnih ulja od 9.461 tone (otpadna ulja i otpad od tekućih goriva – osim jestivih ulja i ulja iz poglavlja 05, 12 i 19), predstavljala gotovo 27 % ukupno prijavljene



18th INTERNATIONAL FOUNDRYMEN CONFERENCE

Coexistence of material science and sustainable technology in
economic growth

Sisak, May 15th-17th, 2019

<http://www.simet.hr/~foundry/>

količine nastalog opasnog otpada. Godinu dana kasnije, učešće ovih otpadnih ulja u ukupnoj količini nastalog opasnog proizvodnog otpada bilo je nešto manje i iznosilo je oko 25 % [18]. Ovdje je važno napomenuti da otpadna ulja za podmazivanje predstavljaju najveću količinu tekućeg, ne vodenog opasnog otpada na svijetu te industrija re-rafiniranja OMU potpuno integrira filozofiju kružnog gospodarstva u svakodnevnom poslovanju. Iz ovih razloga je nužno poduzimati svakodnevne aktivnosti kojima je cilj ušteda dragocjene sirovina (sirove nafte) za proizvodnju svježih mazivih ulja (SMU) preoblikovanjem istrošenih ulja i njihovim pretvaranjem u vrijednu sirovinu (bazno ulje) za tržište maziva, čija je kvaliteta jednaka kvaliteti svježih baznih ulja.

Iako su način gospodarenja otpadnim uljima kao i obveza plaćanja naknada i njihovi iznosi, bili propisani već 2006. godine *Pravilnikom o gospodarenju otpadnim uljima* [12], podatke o provedbi i učinkovitosti njegovih odredbi, bilo je moguće analizirati tek nakon stupanja na snagu novog *Zakona o zaštiti okoliša* iz 2007. godine [19], prema kojem je AZO bila dužna izrađivati godišnja *Izvešća o stanju okoliša u RH*.

U spomenutom *Pravilniku o gospodarenju otpadnim uljima*, kojem je osnovni cilj bio uspostavljanje sustava sakupljanja otpadnih ulja radi oporabe i/ili zbrinjavanja, zaštite okoliša i zdravlja ljudi, definirani su sakupljači, oporabitelji, kao i drugi koji se žele baviti nekom od aktivnosti unutar djelatnosti gospodarenja otpadom, te uvjet da moraju imati odgovarajuće dozvole izdane od nadležnog ministarstva.

Tijekom 2008. godine, stupanjem na snagu *Pravilnika o registru onečišćavanja okoliša*, u RH je propisan obvezni sadržaj i način vođenja registra onečišćavanja okoliša, propisani su obveznici dostave podataka u registar, način, metodologije i rokovi prikupljanja i dostavljanja podataka o ispuštanju, prijenosu i odlaganju onečišćujućih tvari u okoliš i otpadu, podaci o onečišćivaču, tvrtki, postrojenju, organizacijskoj jedinici u sastavu onečišćivača, rok i način obavještanja javnosti, način provjere i osiguranja kvalitete podataka, rok čuvanja podataka i obavljanje stručnih poslova vođenja registra. Ovim pravilnikom se u potpunosti osigurala primjena Uredbe 166/2006 EZ o uspostavi Europskog registra ispuštanja i prijenosa onečišćujućih tvari [20] (engl. *European Pollutant Release and transfer Register - E-PRTR*), a ulaskom RH u EU, AZO je postala dužna dostavljati podatke u E-PRTR.

U prvim službenim izvješćima o otpadu [16-18] obično su u prvom dijelu bili prikazani objedinjeni godišnji podaci za područje cijele RH, a u drugom dijelu bile su prikazane prijavljene količine proizvedenog, sakupljenog i obrađenog proizvodnog otpada po kategorijama, te su dati sažeti prikazi postupanja s nastalim, sakupljenim i obrađenim otpadom. Tako prikupljeni podaci su često bili nepotpuni i netočni, te se trebaju promatrati s rezervom. Tek u *Strategiji gospodarenja otpadom RH* [21], a na bazi podataka iz 2003. godine, bilo je procijenjeno je da u RH nastaje oko 51.000 t/god otpadnih mineralnih ulja od čega se manji dio zbrinjavao termičkom obradom suspaljivanjem kod proizvođača mineralnih ulja, u termoelektranama HEP-a, cementarama i u nekim industrijskim toplinama i kotlovnica. Prema istom izvoru, u razdoblju 1996.-2001., u termoelektranama se godišnje spaljivalo prosječno 350 t otpadnih mineralnih ulja (transformatorska, turbinska, hidraulička, kompresorska, kablovska i motorna ulja).

Prema prvom *Izvešću o otpadnim uljima* za 2007. godinu [22] koje je izradila AZO sukladno *Zakonu o zaštiti okoliša* i *Pravilniku o gospodarenju otpadnim uljima*, tijekom godine je u RH



18th INTERNATIONAL FOUNDRYMEN CONFERENCE

Coexistence of material science and sustainable technology in
economic growth

Sisak, May 15th-17th, 2019

<http://www.simet.hr/~foundry/>

proizvedeno i uvezeno, odnosno stavljeno na tržište ukupno 31.478 t SMU. Iste godine je sakupljeno 6.115 t OMU što je 39 % od ukupno nastalih OMU ili svega 19,4 % od količine SMU koja je stavljena na tržište, tablica 1.

U ovom izvješću, kao i u izvješćima koja su ga slijedila, prikazane su i količine sakupljenih OJU. Za 2007. godinu, ta je količina iznosila 1.132 t, dok podatak o količini svježeg jestivog ulja (SJU) stavljenog na tržište RH u toj godini, nije bio poznat jer proizvođači i uvoznici SJU u RH nisu bili obveznici plaćanja naknada za gospodarenje otpadnim uljima i nisu imali obvezu dostavljanja podataka o količinama SJU stavljenog na tržište u Fond za zaštitu okoliša i energetske učinkovitost (FZOEU). Od 1.132 t sakupljenog OJU, obrađivačima je predano 691 t ili 61 %. Ova prva zabilježena količina sakupljenog OJU, kao i sve druge količine za godine koje su slijedile, bile su puno manje od procijenjene godišnje količine nastalog OJU od 50.000 t/god, kako je procijenjeno u *Planu gospodarenja otpadom u Republici Hrvatskoj za razdoblje 2007-2015 godine* [23], tablica 2.

Valja napomenuti da su u prvim izvješćima o gospodarenju otpadnim uljima u RH, koja su izrađena na temelju podataka koje su ovlašteni sakupljači i oporabitelji dostavljali u FZOEU i AZO, primijećena određena neslaganja u podacima, a što je posljedica lošeg utvrđivanja ključnog broja nekog od otpada iz grupe 13 00 00, izjednačavanja jedinica litre (L) i kilograma (kg), itd.

Tablica 1. Pregled kretanja količina mazivih ulja u RH u razdoblju 2007.- 2016. [24-28]

MAZIVA ULJA	Godina									
	2007.	2008.	2009.	2010.	2011.	2012.	2013.	2014.	2015.	2016.
Stavljeno na tržište SMU (t)	31.478	35.576	24.061	20.488	24.667	21.219	31.126	22.791	32.786	34.881
Očekivano OMU (t)	15.739	17.788	12.031	10.244	12.334	10.610	15.563	11.396	16.393	17.441
Skupljeno OMU (t)	6.115	7.068	6.784	6.640	6.391	5.835	5.678	5.753	5.390	7.033
Skupljeno OMU (L/stanovnik)	1.53	1.77	1.70	1.67	1.66	1.52	1.48	1.51	1.42	1.87
Oporabljeno OMU (t)	6.364	7.131	6.842	6.535	5.906	5.125	4.821	5.244	6.830	6.830

SMU – svježe mazivo ulje; OMU – otpadno mazivo ulje

U proteklih deset godina provedbe *Pravilnika o gospodarenju otpadnim uljima* u RH, nažalost nisu zabilježena značajna poboljšanja i promjene u gospodarenju otpadnim uljima, a količine SMU koje su se stavljale na tržište RH, kretale su se od 20.488 t (2010) do 35.576 (2008), a rezultat su količina proizvedenih mazivih ulja koja je umanjena za količinu izvezenog i uvećana za količinu uvezenog mazivog ulja.

Prema posljednjim dostupnim podacima FZOEU o kretanju količina mazivih ulja, a to su podaci za 2016. godinu [24], u RH je uvezeno je 26.036 t SMU, proizvedeno je 16.876 t, a izvezeno 8.031 t. Prema tome, na tržište RH je ukupno stavljeno 34.881 t SMU. Od te ukupne količine SMU stavljenih na tržište, očekivalo se nastajanje OMU u količini od 50% tj. 17.441 t.



18th INTERNATIONAL FOUNDRYMEN CONFERENCE

Coexistence of material science and sustainable technology in
economic growth

Sisak, May 15th-17th, 2019

<http://www.simet.hr/~foundry/>

Ukoliko bi se u izračunu primijenio isti prosječni faktor sakupljanja OMU od 0,50 i to za sve vrste mazivih ulja, tada bi se dobile nešto veće količine OMU koje bi bilo moguće prikupiti od one navedene u tablici 1. Tako je bilo za očekivati da se za 2007. godinu u odnosu na količinu SMU stavljenih na tržište RH prikupi 7.870 t, a za 2016. godinu 8.721 t OMU.

Stopa sakupljanja OMU u razdoblju od 2007. do 2016. godine, izračunata kao odnos sakupljenih količina i procijenjenih nastalih količina OMU, kretala se je od 33 % (2015.) do 65% (2010.). Za usporedbu, prosječna stopa sakupljanja OMU u članicama EU15 je u 2000. godini iznosila 71 %, a kretala se je od 37 % (Grčka) do 86 % (Velika Britanija) dok je ta ista stopa 2007. godine u zemljama EU27 iznosila 75 % [29,30].

Dobro je poznato da su OMU opasni otpad jer jedna litra ulja može onečistiti milijun litara vode i trajno onečistiti tlo jer najvećim dijelom nisu biološki razgradiva. Stoga je značajno ovdje postaviti pitanje što se dogodilo i gdje je završilo oko 85 milijuna litara OMU koje je nastalo, a nije sakupljeno u razdoblju od 2007. do 2016. godine? Svakako je nužno spriječiti ovakve pojave nepoznatih tokova OMU jer osim što su štetne za okoliš u isto vrijeme su i vrijedna sirovina jer se mogu regenerirati i služiti u proizvodnji SMU, odnosno koristiti u proizvodnji sapuna, sredstava za pranje i slično ili pak koristiti kao energent u pojedinim energetskim i proizvodnim postrojenjima.

Ovo je jednostavno ilustrirati i podacima [31] Europske grupacije industrije za regeneraciju (fr. *Groupement Européen de l'Industrie de la Régénération*, GEIR) koji kažu kako je od ukupne količine baznih ulja za podmazivanje u 2017. godini oko 13% proizvedeno iz O, a 87 % iz svježje naftne sirovine.

Nažalost, sve navedeno još uvijek nije dovoljan razlog zbog kojeg bi učinkovitost njihovog sakupljanja bila adekvatna mogućoj koristi, jer stopa sakupljanja OMU u RH uvelike zaostaje za stopama u zemljama članicama EU, te se moraju poduzeti dodatne mjere u svrhu povećanja učinkovitosti sustava gospodarenja ovom vrstom otpada. Ovdje je potrebno uzeti u obzir i relativne odnose populacije, broja vozila i aktivnosti industrije, što u mnogome utječe na vrijednosti procijenjene količine OMU koje bi se mogle sakupiti na području RH. Vrijednosti stopa oporabe OMU u RH u odnosu na ukupno sakupljene količine su zadovoljavajuće (>95 %) i odnose se uglavnom na uporabu otpadnih ulja u energetske svrhe. U prikazu kretanja količina mazivih ulja od 2007. do 2016., za neke godine prikazane oporabljene količine prelaze sakupljene količine što se može pripisati uporabi količina OMU sakupljenih u prethodnoj kalendarskoj godini (količine sa skladišta).

Kako *Pravilnik o gospodarenju otpadnim uljima* u RH pod pojmom otpadna ulja podrazumijeva osim mazivih otpadnih ulja i jestiva otpadna ulja koja su definirana u prethodnom poglavlju, tako se i njima mora posvetiti dužna pozornost.

Prema podacima FZOEU [24,25] o količinama sakupljenih OJU u razdoblju od 2007. do 2016. godine u RH, sakupljene količine su vrlo male, u odnosu na procijenjene godišnje količine SJU stavljenog na tržište RH, tablica 2.



18th INTERNATIONAL FOUNDRYMEN CONFERENCE

Coexistence of material science and sustainable technology in
economic growth

Sisak, May 15th-17th, 2019

<http://www.simet.hr/~foundry/>

Tablica 2. Pregled kretanja količina jestivih ulja u RH u razdoblju 2007.- 2016. [24-28,32]

JESTIVA ULJA (JU)	Godina									
	2007.	2008.	2009.	2010.	2011.	2012.	2013.	2014.	2015.	2016.
Broj stanovnika RH	4.435.982	4.434.508	4.429.078	4.417.781	4.280.622	4.267.558	4.255.689	4.238.389	4.203.604	4.174.349
Potrošnja SJU (L/stanovnik)	13.8	13.2	13.1	13.5	13.2	NP	NP	12.9	NP	NP
Prosjek godišnje potrošnje SJU (L/stanovnik)	13.3									
Količina SJU utrošena za pripremu hrane / Minimalna količina SJU stavljena na tržište (t)	53.099	53.081	53.016	52.881	51.239	51.083	50.941	50.734	50.317	49.967
Očekivana količina nastalih OJU (t)	26.550	26.541	26.508	26.441	25.620	25.542	25.471	25.367	25.159	24.984
Obuhvaćena FZOEU – količina OJU (t)	13.275	13.271	13.254	13.221	12.810	12.771	12.736	12.684	12.580	12.492
Sakupljeno OJU (t)	1.132	1.606	2.145	1.260	1.196	911	718	721	759	825
Sakupljeno OJU (L/stanovnik)	0.28	0.40	0.54	0.32	0.31	0.24	0.19	0.19	0.20	0.22
Oporabljeno OJU (t)	691	1.033	1.507	683	785	678	691	706	761	1.307

NP – nema podataka



18th INTERNATIONAL FOUNDRYMEN CONFERENCE

Coexistence of material science and sustainable technology in economic growth

Sisak, May 15th-17th, 2019

<http://www.simet.hr/~foundry/>

S obzirom na to da ne postoje podaci o godišnjim količinama SJU stavljenog na tržište, jer i ne postoji obveza vođenja evidencije (proizvedeno + uvezeno – izvezeno), procjena minimalne količine ulja stavljenih na tržište svakako odgovara količina utrošenih SJU za proizvodnju hrane, a izračunata je kao umnožak prosječne godišnje potrošnje SJU po glavi stanovnika [32] i broja stanovnika u toj godini prema podacima Državnog zavoda za statistiku RH [26-28].

Prema podacima Europske i svjetske statistike [33] oko 50 % jestivog ulja upotrijebljenog za pripremu hrane utroši se u restoranima i industriji, a ostatak u kućanstvima, od čega se oko 50 % upije u hranu, a ostatak postane otpadno ulje. Ako se uzme u obzir da su obveznici izvještavanja FZOEU samo proizvođači hrane (industrija, restorani i sl.) tada proizlazi da potencijalna količina OJU iznosi oko 25 % od količine ulja koje se utroši za pripremu hrane.

U promatranom razdoblju od 2007. do 2016. godine u RH je godišnje sakupljeno od 718 t (2013.) do 2.145 t (2009.) OJU, a oporabljeno od 678 t (2012.) do 1.507 t (2009.) ili u odnosu na ukupno sakupljene količine OJU, stopa oporabe se kretala od 54,2 % (2010.) do 98 % (2014.).

Prema podacima navedenim u tablici 2, razvidno je da su količine sakupljenih otpadnih ulja u promatranom razdoblju po glavi stanovnika bile vrlo male i kretale su se od oko 0,2 do 0,5 L/stanovnik. Međutim, važno je napomenuti da ovi podaci nisu potpuni i odnose se samo na evidentirane količine sakupljenih otpadnih ulja koje su prijavljene od strane obveznika (profesionalni sektor) u bazu podataka FZOEU, a stvarne količine sakupljenih OJU su veće, čemu doprinose sakupljene količine OJU iz kućanstava.

Tako npr., iz podataka FZOEU-a navedenih u tablici 2, u 2016. godini ukupno je sakupljeno 825 t OJU i oporabljeno je 1.307 t od čega je 482 t otpadnih ulja bilo sakupljeno prethodne godine. Međutim, podaci HAOP-a o količinama sakupljenih otpadnih ulja prijavljenih u bazu ROO koji obuhvaćaju i dionike izvan sustava FZOEU-a, pokazuju da je u 2016. godini sakupljeno 5.323 t OJU (klj. br. 20 01 25) što obuhvaća profesionalni sektor tj. proizvodnju hrane u industriji, restoranima i sl. ali i kućanstva te je ova količina višestruko veća od količine prijavljene u istoj godini u FZOEU. Slično se dogodilo i godinu ranije kada je prema podacima FZOEU-a sakupljeno je 842.925 L (759 t) OJU, a prema podacima HAOP-a podaci dostavljeni u bazu ROO, koji obuhvaćaju i dionike izvan sustava FZOEU-a, pokazali su da je u 2015. godini bilo sakupljeno 4.163 t OJU što je bilo također višestruko veća količina sakupljenog jestivog ulja.

Posljedično ovome i podaci o količinama oporabljene jestivog ulja se razlikuju. Tako je prema HAOP u 2015. godini od sakupljenih 4.163 t OJU oporabljeno u RH 1.400 t, a 2.500 t izvezeno na uporabu u druge zemlje, a 2016. je od 5.323 t sakupljenih OJU oporabljeno u RH 1.840 t, a 2.340 t izvezeno na uporabu u druge zemlje. Preostale sakupljene količine (1.143 t) privremeno su bile uskladištene kod sakupljača i/ili oporabitelja.

Promotre li se navedeni objedinjeni podaci o količinama sakupljenih OJU (FZOEU i HAOP) tada se, za 2015. i 2016. godinu, dobije sasvim drugačija slika o sakupljenim količinama koja su sada značajno veće od 0,20 i 0,22 L/stanovniku i iznose 1,1 i 1,4 L/stanovniku. Usporede li se ovako izračunate količine sakupljenih OJU s vrijednostima sakupljenih količina ovih ulja po



18th INTERNATIONAL FOUNDRYMEN CONFERENCE

Coexistence of material science and sustainable technology in economic growth

Sisak, May 15th-17th, 2019

<http://www.simet.hr/~foundry/>

glavi stanovnika u zemljama članicama EU, tablica 3, daje se zaključiti da se RH može svrstati uz Švedsku, Češku i Francusku [34].

Ovi pokazatelji uspješnosti sakupljanja OJU i načini na koji je uređen sustav ukazuju još jednom na potrebu unaprjeđenja sustava gospodarenja posebnim kategorijama otpada, čime bi se trebalo bolje identificirati kako obveznike plaćanja naknade tako i unaprijediti sustav praćenja podataka o posebnim kategorijama otpada putem Informacijskog sustava gospodarenja otpadom te izradom Registra gospodarenja za posebne kategorije otpada.

Tablica 3. Kretanje količina OJU u nekim članicama EU za 2015. godinu [34,35]

Države članica EU	Proizvodnja hrane (industrija, restorani i sl.)			Kućanstva			Ukupno sakupljeno OJU L/stanovnik
	Procijenjena količina OJU (t)	Sakupljeno OJU (t)	Sakupljeno %	Procijenjena količina OJU (t)	Sakupljeno OJU (t)	Sakupljeno %	
Njemačka	161.000	140.000	86.9	65.000	1.209	1.9	1.93
Španjolska	78.000	65.000	83.3	232.000	5.000	2.2	1.67
Portugal	26.000	22.000	84.6	30.000	1.000	3.3	2.46
Nizozemska	69.000	60.000	87.0	12.000	3.600	30.0	4.18
Austrija	18.000	15.000	83.3	7.000	2.352	33.6	2.25
Švedska	10.000	8.000	50.0	3.000	1.400	46.7	1.07
Belgija	33.000	29.000	87,9	13.000	8.300	63.8	3.68
EU 28 ukupno	806.000	675.000	83.8	854.000	47.736	5.6	1.58

ZAKLJUČAK

U ovom radu opisan je tijek uvođenja i primjene legislative kojom se osigurava istodobno učenje, izgradnja i implementacija sustava gospodarenja otpadnim uljima u RH. Pokazana je opredijeljenost RH i njenih stručnjaka za sveobuhvatno sagledavanje ovog segmenta zaštite okoliša i zdravlja ljudi, što je i rezultiralo postojećom legislativom i desetogodišnjim iskustvom u izvještavanju o postignutim rezultatima gospodarenja otpadnim mazivim i jestivim uljima.

Prikazani su podaci FZOEU o kretanju količina mazivih ulja za razdoblje 2007.- 2016. koji govore da su u navedenom razdoblju na tržište RH stavljane količine SMU od 20.488 t (2010.) do 35.576 t (2008.) od čega je bilo za očekivati nastajanje 10.244 t (2010.) i 17.788 t (2008.) OMU.

Stope sakupljanja nastalih OMU u analiziranom razdoblju, izračunate kao odnos sakupljenih količina i procijenjenih količina OMU, kretale su se od 33 % (2015.) do 65 % (2010.).

U istom razdoblju od 2007. do 2016. godine, promatrano je i kretanje količina SJU stavljenog na tržište RH, nastajanje očekivanih količina OJU kao i uspješnost u njegovu sakupljanju. Godišnje količine sakupljenog OJU u ovom razdoblju kretale su se od 718 t (2013.) do 2.145 t (2009.), a oporabljene količine ovog otpadnog ulja iznosile su od 678 t (2012.) do 1.507 t



18th INTERNATIONAL FOUNDRYMEN CONFERENCE

Coexistence of material science and sustainable technology in
economic growth

Sisak, May 15th-17th, 2019

<http://www.simet.hr/~foundry/>

(2009.) tj. godišnje stope uporabe sakupljenog otpadnog ulja su se kretala od 54,2% (2010.) do 98 % (2014.).

Analizom prikupljenih podataka je utvrđeno da za razliku od podataka u bazi FZOEU-a, podaci HAOP-a o količinama sakupljenih otpadnih ulja prijavljenih u bazu ROO, pokazuju za 2015. i 2016. godinu znatno veće (5-6 puta) količine sakupljenih OJU jer su uz profesionalni sektor tj. proizvodnju hrane u industriji, restoranima i sl. u izvještavanju za ovu bazu podataka o sakupljenim OJU obuhvaćena i kućanstva.

Na temelju prikazanog u radu, a uzimajući u obzir činjenicu da OMU kao i OJU imaju visoki potencijal za uporabu, nameće se za potrebno u sustavu gospodarenja otpadnim uljima, intenzivirati njihovo sakupljanje i unaprijediti kontrolu sakupljanja i predaje ovlaštenim oporabiteljima.

Istovremeno je nužno osigurati dodatne kapacitete za uporabu OJU, a što je moguće postići razvojem sustava za biološku obradu otpada u postrojenjima za bioplinsku obradu.

Osim toga, potrebno je uvesti i intenzivirati obrazovanja o otpadnim uljima u okviru obrazovanja o okolišu - plansko, formalno i neformalno obrazovanje na različitim razinama i u različitim sektorima.

LITERATURA

- [1] URL: http://ec.europa.eu/eurostat/statistics-explained/index.php/Waste_management_indicators (23.2.2018.)
- [2] W. A. Irwin, R. A. Liroff, Used oil law in the United States and Europe, Office of Research and Development U.S. Environmental Protection Agency, EPA-600/5-74-025, USA, 1974.
- [3] Zakon o prostornom uređenju i korištenju građevinskog zemljišta (NN br. 14/73).
- [4] Zakon o postupanju s otpadnim tvarima (NN br. 42/82).
- [5] Council Directive 75/439/EEC on disposal of waste oil, Official Journal of the European Communities L 194/23, 25.7.1975.
- [6] Directive 2008/98/EC of the European Parliament and of the Council on waste and repealing certain Directives, Official Journal of the European Union L 312/3, 22.11.2008.
- [7] Zakon o otpadu (NN br. 34/95).
- [8] Pravilnik o vrstama otpada (NN br. 27/96).
- [9] Pravilnik o katastru emisije u okoliš (NN br. 36/96).
- [10] Zakon o zaštiti okoliša (NN br. 82/94).
- [11] Pravilnik o Registru onečišćavanja okoliša (NN br. 35/08).
- [12] Pravilnik o gospodarenju otpadnim uljima (NN br. 124/06, 121/08, 31/09, 156/09, 91/11, 45/12, 86/13, 95/15).
- [13] Zakon o otpadu (NN br. 178/04).
- [14] Zakon o održivom gospodarenju otpadom (NN br. 94/13, 73/17).
- [15] EUBIA - The European Biomass Industry Association, Transformation of used cooking oil into biodiesel: From waste to resource, UCO to Biodiesel 2030, Brussels, Belgium, 2015.



18th INTERNATIONAL FOUNDRYMEN CONFERENCE

Coexistence of material science and sustainable technology in
economic growth

Sisak, May 15th-17th, 2019

<http://www.simet.hr/~foundry/>

- [16] Pregled podataka iz katastra otpada/KEO za 2004., Agencija za zaštitu okoliša, Zagreb 2006.
- [17] Katastar otpada – Izvješće za 2005., Agencija za zaštitu okoliša, Zagreb, 2007.
- [18] Katastar otpada – Izvješće za 2006., Agencija za zaštitu okoliša, Zagreb, 2008.
- [19] Zakon o zaštiti okoliša (NN br. 110/07).
- [20] Regulation (EC) No 166/2006 of the European Parliament and of the Council concerning the establishment of a European Pollutant Release and Transfer Register and amending Council Directives 91/689/EEC and 96/61/EC, Official Journal of the European Union L 33/1, 4.2.2006.
- [21] Strategija gospodarenja otpadom Republike Hrvatske (NN br. 130/05).
- [22] Izvješće o otpadnim uljima za 2007. godinu, Agencija za zaštitu okoliša, Zagreb, 2008.
- [23] Plan gospodarenja otpadom u RH za razdoblje 2007. – 2015. godine (NN br. 85/07).
- [24] Plan gospodarenja otpadom u RH za razdoblje 2017. – 2022. godine (NN br. 3/17).
- [25] Pregled podataka za posebne kategorije otpada za 2016. godinu, Hrvatska agencija za okoliš i prirodu, Zagreb, 2017.
- [26] Procjena stanovništva Republike Hrvatske u 2010., Priopćenje, Državni Zavod za statistiku RH, Godina XLVIII, br. 7.1.4., Zagreb, 2011.
- [27] Procjena stanovništva Republike Hrvatske u 2015., Priopćenje, Državni Zavod za statistiku RH, Godina LIII, br. 7.1.4., Zagreb, 2016.
- [28] Procjena stanovništva Republike Hrvatske u 2016., Priopćenje, Državni Zavod za statistiku RH, Godina LIV, br. 7.1.3., Zagreb, 2017.
- [29] V. Monier, E. Labouze, Critical review of existing studies and life cycle analysis on the regeneration and incineration of waste oils, European Commission DG Environment A2 – Sustainable Resources Consumption and Waste, Montrouge, France, 2001.
- [30] URL: <http://www.geir-rerefining.org/documents/2.DallaGiovanna.pdf> (6.3.2018.)
- [31] URL: http://www.geir-rerefining.org/documents/GEIRpositionpaperWFD_2016_FINAL.pdf (6.3.2018.)
- [32] Statistički ljetopis 2016., Državni zavod za statistiku RH, godina 48., Zagreb, 2016.
- [33] J. Cvengroš, S. Cvengroševa, Used frying oils and fats and their utilization in the production of methyl esters of higher fatty acids, Biomass Bioenergy, 27(2004), pp. 173-181, DOI: <https://doi.org/10.1016/j.biombioe.2003.11.006>
- [34] Analysis of the current development of household UCO collection systems in the EU, EWABA European Waste to Advanced Biofuels Association, Brussels, Belgium, 2016.
- [35] URL: https://europa.eu/european-union/about-eu/figures/living_en (12.3.2018.)



18th INTERNATIONAL FOUNDRYMEN CONFERENCE

Coexistence of material science and sustainable technology in
economic growth

Sisak, May 15th-17th, 2019

<http://www.simet.hr/~foundry/>

THE CHARACTERISTICS AND ENVIRONMENTAL ASPECTS OF MAGNESIUM THIXOMOLDING VERSUS DIE CASTING PROCESS

Paul Sponsel¹, Irena Žmak^{2*}, Milan Vukšić²

¹ Technical University of Munich, Munich, Germany

² University of Zagreb Faculty of Mechanical Engineering and Naval Architecture, Zagreb, Croatia

Poster presentation

Review

Abstract

Magnesium is an increasingly popular metal used in the design of lightweight constructional components. The applications in the automobile and electronics sector are rising in the past several years. The common magnesium production technology is die casting. One of the advanced manufacturing processes for magnesium is thixomolding. The thixomolding process is applied to the metal in semi-solid state.

This paper describes the underlying chemical and physical phenomena of thixomolding, the technical process and machinery, the characteristics of the produced workpieces, and different applications of thixomolded parts. The number of thixomolding manufacturers by different regions and recent years is presented and an outlook on future developments is given.

Thixomolding is compared to die casting, which is the prevailing technology for magnesium processing. The difference in energy consumption is presented, as well as the cost of the used amounts of gasses. The environmental impact of different gasses used, expressed as the CO₂-equivalent or the gasses' toxicity is presented. Some gasses used in die casting have a strong environmental imprint: sulfur hexafluoride is a very potent greenhouse gas; sulfur dioxide is a well-known air pollutant and also corrosive for the equipment and hydrofluorocarbon HFC-134a has a high global-warming potential. On the other hand, the thixomolding process uses the inert gas argon, without a global warming potential.

Keywords: *thixomolding, die casting, magnesium, global warming, environment*

*Corresponding author (e-mail address): irena.zmak@fsb.hr



18th INTERNATIONAL FOUNDRYMEN CONFERENCE

Coexistence of material science and sustainable technology in
economic growth

Sisak, May 15th-17th, 2019

<http://www.simet.hr/~foundry/>

INTRODUCTION TO THIXOMOLDING

Magnesium is becoming more and more popular as a material to design and construct functional components. Especially in the automobile and electronics sector the demand is rising since several years. Compared to aluminum magnesium has only one third of the specific weight and compared to technical plastics it has higher stiffness, much higher thermal conductivity and better shielding against electromagnetic radiation. In large-scale production the prevailing production method for magnesium alloys is still the die casting process. But there are new manufacturing processes evolving in which magnesium is processed in a semi-solid state, using the so-called thixoforming processes. These processes include thixoforging, thixocasting, new rheocasting and thixomolding [1].

This paper focuses on the thixomolding technology. The name comes from the underlying phenomenon of thixotropy. Thixotropy describes the characteristics of materials which shear when the material flows but stay thick, or viscous, under static conditions. In the second chapter of this paper the technical process and machinery is explained. The third chapter focuses on the physical and chemical characteristics of the produced workpieces. Since die casting is still the prevailing technology for processing magnesium, it is compared to thixomolding in the fourth chapter. In the fifth chapter the manufacturers of thixomolding machines are presented. In the sixth chapter different applications are shown. The last chapter gives a summary and an outlook on future developments.

TECHNICAL BASICS OF THIXOMOLDING

Thixomolding is a semi-solid metal casting technique, which is mostly used for forming magnesium alloys. The used equipment is quite similar to injection molding. The raw material, i.e. magnesium alloy chips with a grain size from 0.5 to 5 mm, is fed into the back end of a heated cylinder. To prevent the oxidation of the magnesium chips, argon is used as an inert gas. The magnesium chips are transported and heated by a 3-zone-screw conveyor located inside the cylinder. The screw is divided into a feeding, a compression and a homogenization area. Subsequently a high-speed injection system presses the semi-solid magnesium slurry with up to 6 m s^{-1} into the mold. High injection speed is necessary due to the low thermal capacity and conductivity of magnesium. The cylinder, the screw and heater must be heated up to the operating temperature which can vary from 560 °C to 630 °C depending on the alloy used [2]. Figure 1 shows a schematic of a thixomolding machine.



18th INTERNATIONAL FOUNDRYMEN CONFERENCE
Coexistence of material science and sustainable technology in economic growth

Sisak, May 15th-17th, 2019

<http://www.simet.hr/~foundry/>

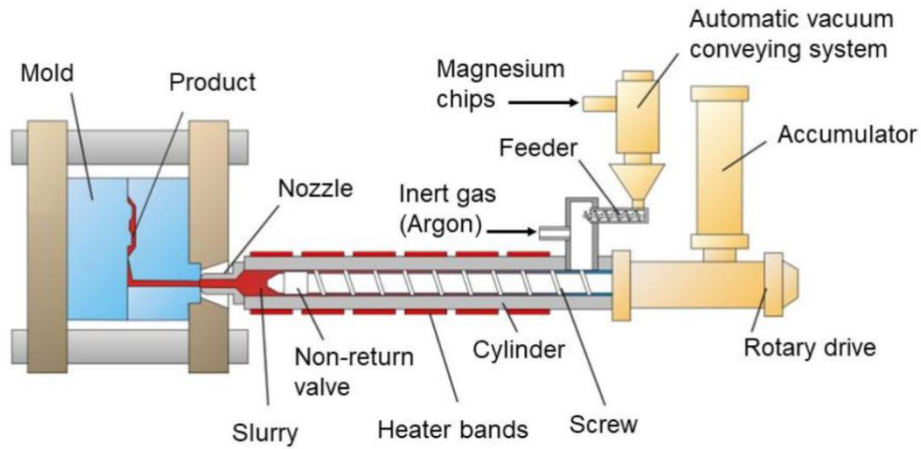


Figure 1. Thixomolding machine set-up [3]

Since the used machinery is quite similar to plastic injection molding, the process and operation cycle are similar as well. Figure 2 shows several steps of the operation cycle.

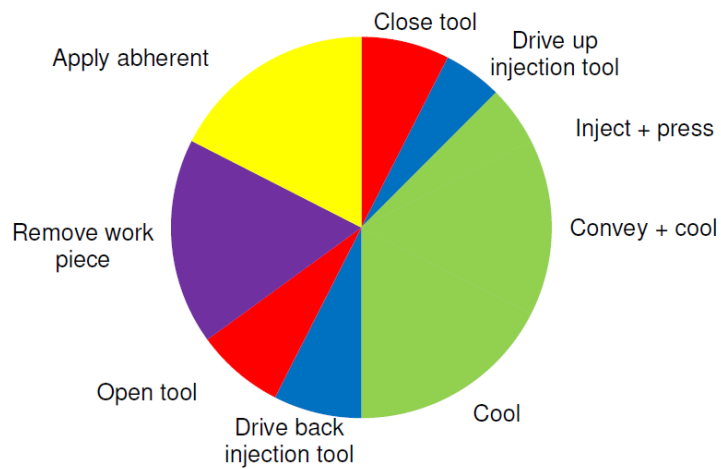


Figure 2. Thixomolding operation cycle [2]

CHEMICAL AND PHYSICAL BASICS OF THIXOMOLDING

Magnesium alloys are the most common alloys used for thixomolding. Under atmospheric pressure magnesium has a hexagonal structure with the stacking order ABAB as shown in Figure 3 [2].



18th INTERNATIONAL FOUNDRYMEN CONFERENCE
**Coexistence of material science and sustainable technology in
economic growth**
Sisak, May 15th-17th, 2019
<http://www.simet.hr/~foundry/>

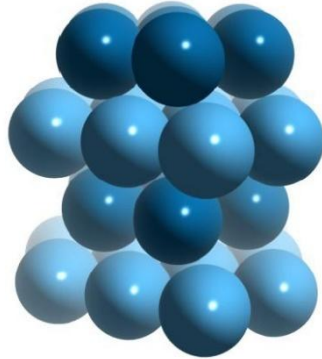


Figure 3. Hexagonal structure of magnesium [4]

To improve the low strength of pure magnesium several different alloying elements are added to magnesium alloys. The most common alloying element is aluminum. As shown in Figure 4, a eutectic is formed at 436 °C and 33 % aluminum, thereby better magnesium alloy castability is achieved through a lower melting point. The added aluminum also makes it possible to harden the magnesium finished products using heat treatment. Also, the aluminum oxide layer improves the corrosion protection. Technical magnesium alloys typically contain about 10 % of aluminum by mass even though 12.7 % is solvable [2].

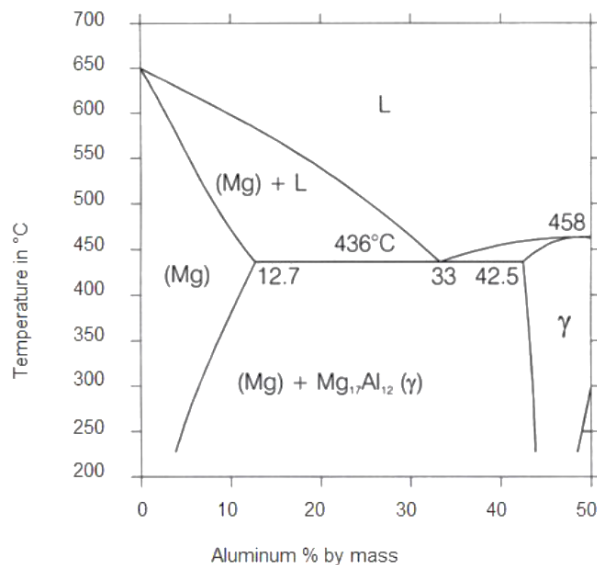


Figure 4. Phase diagram magnesium-aluminum [2]

Besides aluminum, zinc is often used as an additional alloying element for magnesium alloys. The low melting eutectic formed at 342 °C and 51.3 % zinc by mass additionally improves the castability of the alloy. In Figure 5 the ternary system between aluminum, magnesium and zinc is shown. Zinc provides more strength to the alloy and also makes the solid solution



18th INTERNATIONAL FOUNDRYMEN CONFERENCE
**Coexistence of material science and sustainable technology in
economic growth**

Sisak, May 15th-17th, 2019

<http://www.simet.hr/~foundry/>

hardening process possible. Furthermore, higher elongation properties add up to these alloys. Technical aluminum-zinc-magnesium alloys contain up to 1 % zinc by mass [2].

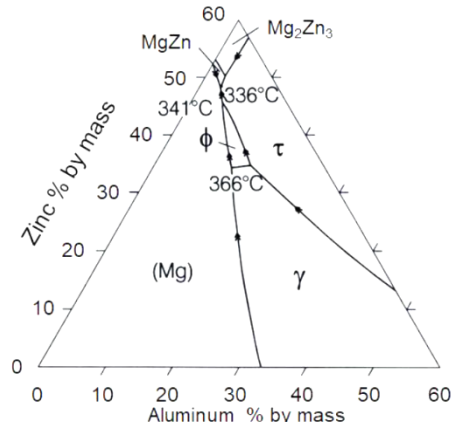


Figure 5. Phase diagram aluminum-magnesium-zinc [2]

Manganese is often used to reduce iron impurities which enter the material during the alloying process. Manganese binds the iron into Fe-Mn-Al compounds. Thereby the corrosion behavior of the alloy is improved. Technical alloys contain up to 0.4 % by mass of manganese [2]. Many other chemical elements may be used during the alloying process but aluminum, zinc and manganese are the most important.

The magnesium alloy slurry goes through different stages during the thixomolding process. At first, the magnesium granules are heated up to the solidus-liquidus temperature interval in the cylinder. This means that α -crystals and melt exist in thermodynamic equilibrium as shown in Figure 6 on the left-hand side. During and after the injection into the mold the melt cools down at high cooling rates, which gives the typical fine-grained casting structure [2].

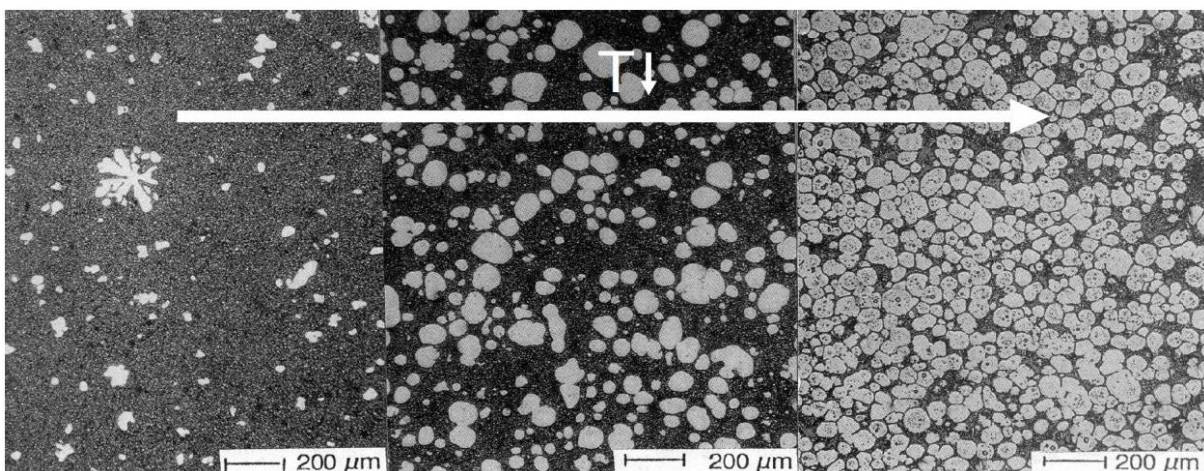


Figure 6. Microstructure during the thixomolding solidification process [2]



18th INTERNATIONAL FOUNDRYMEN CONFERENCE
**Coexistence of material science and sustainable technology in
economic growth**

Sisak, May 15th-17th, 2019

<http://www.simet.hr/~foundry/>

The viscosity of the magnesium slurry is crucial for the thixomolding process. If wrong parameters were chosen, the mold would not be filled completely, or the properties of the workpiece would not be satisfying. Figure 7 shows the three parameters which influence the viscosity (η) of thixotropic materials: shear time (t), shear rate ($\dot{\gamma}$) and temperature (T). Through higher shear time lower viscosity is achieved because the dendritic structure of the magnesium is transformed into equiaxed crystals. The viscosity can also be lowered by applying higher shear rates. But, with higher shear rates the solid phase of the material is accumulated in the middle of the work piece, and the liquid phase flows better at the cavity boundaries. Higher temperature lowers the solid phase content in the melt and also lowers the melt viscosity [2].

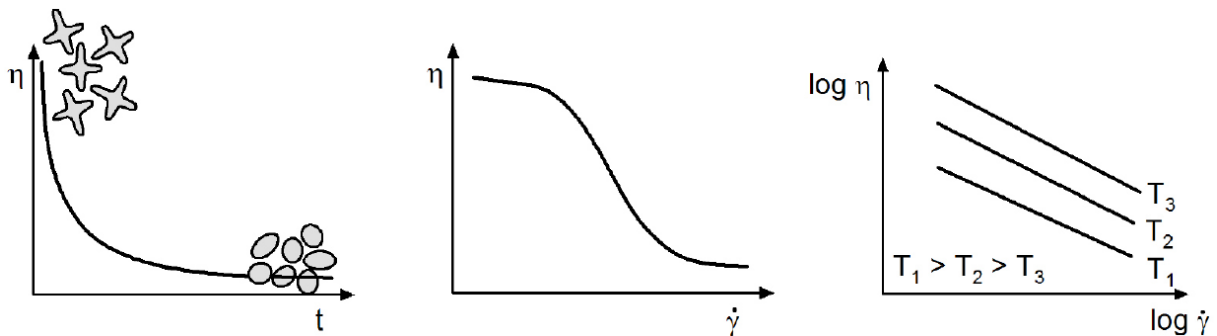


Figure 7. Influence of shear time (t), shear rate ($\dot{\gamma}$) and temperature (T) onto viscosity (η) [2]

THIXOMOLDING VERSUS DIE CASTING: STRUCTURE, PROPERTIES, ENERGY, ENVIRONMENT

The most common way to process magnesium is die casting. Figure 8 shows the difference between the microstructure of a workpiece produced with thixomolding and die casting. The fine-grained structure is more homogenous if thixomolding is used, which has a strong impact on the properties of the workpiece.



18th INTERNATIONAL FOUNDRYMEN CONFERENCE
**Coexistence of material science and sustainable technology in
economic growth**

Sisak, May 15th-17th, 2019

<http://www.simet.hr/~foundry/>

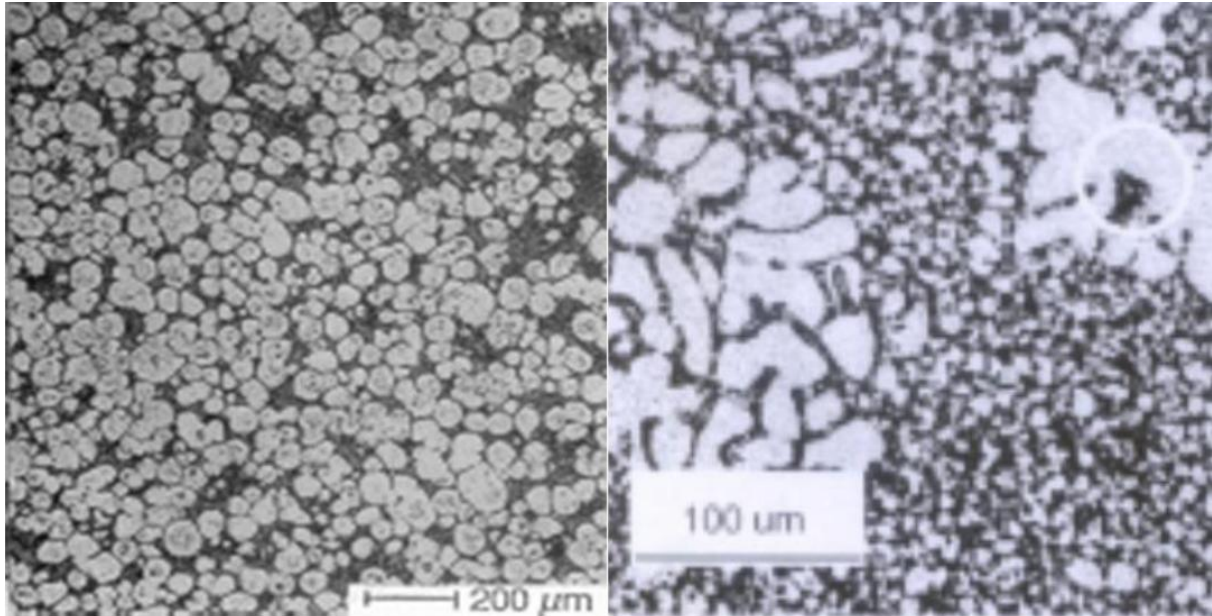


Figure 8. Thixomolding versus die casting microstructure [2]

Table 1 shows a comparison between the mechanical properties of workpieces manufactured with thixomolding and die casting. Throughout all listed alloys and mechanical properties, the workpieces created with thixomolding show better results in terms of tensile strength (R_m), yield strength ($R_{p0.2}$) and elongation (A).

Table 1. Properties of workpieces [5]

ASTM (EN) designation	Test. temp., °C	Thixomolding			Die casting		
		R_m , MPa	$R_{p0.2}$, MPa	A , %	R_m , MPa	$R_{p0.2}$, MPa	A , %
AZ91D (MgAl9Zn1)	RT	260	170	8	260	160	6
	150	175	130	19	160	100	18
AM60B (MgAl6Mn)	RT	253	150	11	247	123	12
	150	157	114	24	-	-	-
AZ70 (Mg7Al0.4Zn)	RT	259	150	11	-	-	-
	150	165	120	25	-	-	-
AJ52 (Mg5Al2Sr)	RT	245	151	10	212	134	6
	150	172	128	20	163	110	12
AJ62 (Mg6Al2Sr)	RT	257	151	11	239	142	8
	150	170	125	15	163	108	19
AS31 (Mg3Al1Si)	RT	251	145	13	216	130	8
	150	155	113	26	-	-	-
AS41 (Mg4Al1Si)	RT	265	152	13	240	130	10
	150	160	118	29	150	90	-



18th INTERNATIONAL FOUNDRYMEN CONFERENCE
Coexistence of material science and sustainable technology in economic growth

Sisak, May 15th-17th, 2019

<http://www.simet.hr/~foundry/>

The chosen process has also an impact on the porosity of the workpiece. Using less porous materials, thinner wall castings may be achieved. Figure 9 shows the comparison of porosities for two different magnesium alloys: AZ91 (MgAl9Zn1) and AJ62 (Mg91Al6Sr3).

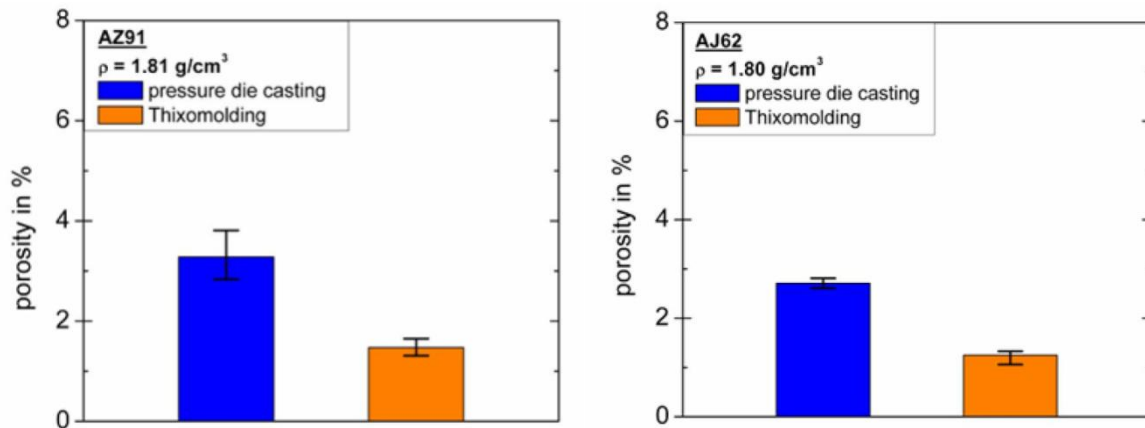


Figure 9. Porosity after die casting vs. thixomolding of AZ91 and AJ62 alloys [5]

Besides workpiece properties, energy consumption is an important parameter when comparing thixomolding to die casting. Namely, the low energy consumption is one of the very relevant advantages of thixomolding. Depending on the solid phase share in the slurry, thixomolding has significantly lower energy consumption compared to die casting [5]. Figure 10 shows the achievable energy consumption rates depending on the processing temperature for the AZ91 alloy.

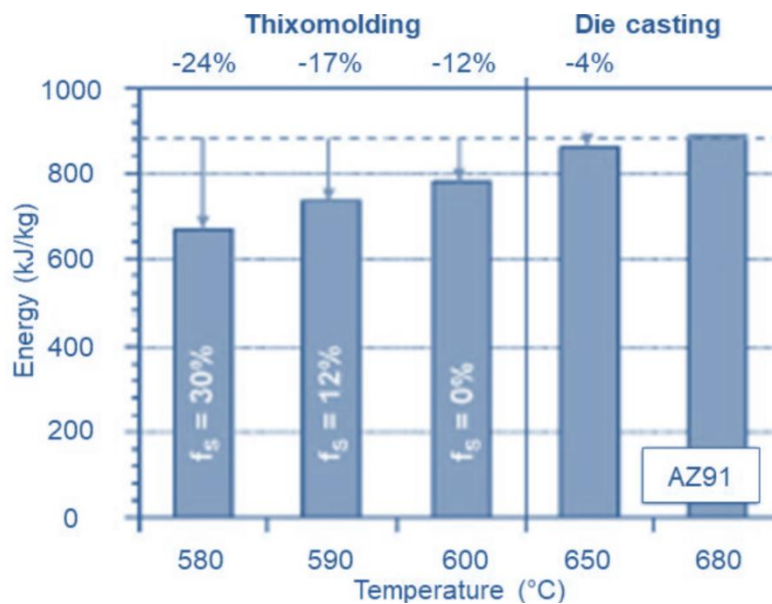


Figure 10. Lower energy consumption at higher solid phase content for thixomolded AZ91 [5]



18th INTERNATIONAL FOUNDRYMEN CONFERENCE

Coexistence of material science and sustainable technology in economic growth

Sisak, May 15th-17th, 2019

<http://www.simet.hr/~foundry/>

For example, required casting energy was 12 % lower for thixomolded parts with 0 % solid phase content, compared to die cast parts. When the solid phase content in thixomolding increased to 30 %, 24 % less energy was required compared to die casting.

Lower energy consumption of the thixomolding process makes it a greener option than die casting, as the overall CO₂-equivalent is lower. Even more, other important environmental aspects contribute to advantages of thixomolding, one of them are cover gases. Die casting uses a variety of gases which have an impact on the environment because of their CO₂-equivalent or are toxic [5]. Figure 11 shows the differences of the used inert gases, where thixomolding typically uses argon as a gas that prevents the oxidizing of the semi-molten magnesium alloy. On the other hand, die casting commonly uses a mixture of dry air, nitrogen or CO₂ as carrier gasses, with sulfur hexafluoride (SF₆), hydrofluorocarbon 1,1,1,2-tetrafluoroethane (HFC-134a) or sulfur dioxide (SO₂) [5].

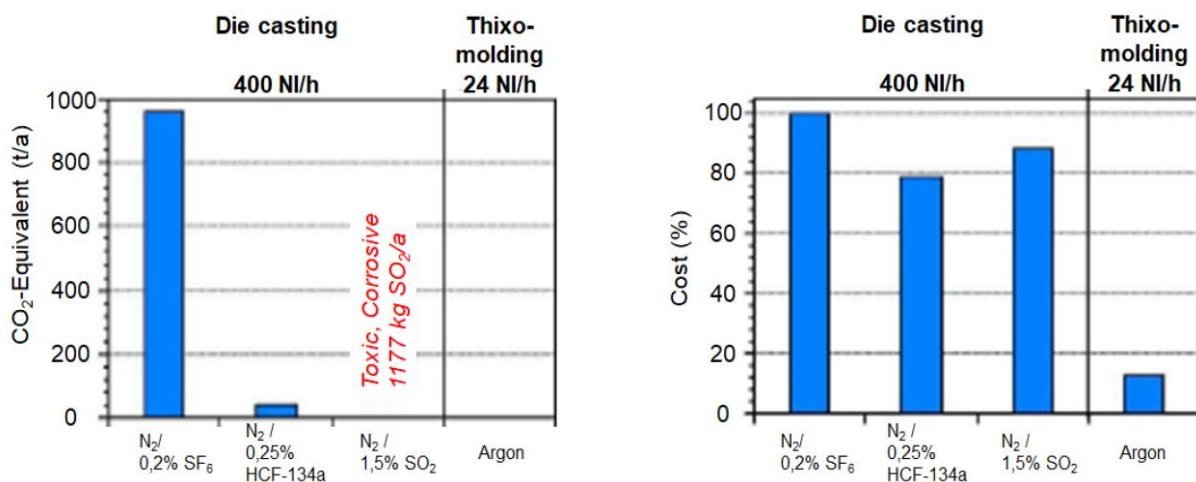


Figure 11. CO₂-footprints and costs of used cover gases for die casting vs. thixomolding [5]

Sulfur hexafluoride (SF₆) is an extremely potent greenhouse gas, having the Global Warming Potential (GWP) of 22,800, which means that 0.2 kg of SF₆ equals to 5 tons of CO₂ contributing to global warming [6]. European Union prohibited the use of SF₆ in magnesium die casting as of January 1st 2008 through the “2006 F-Gas Regulation”, except where the quantity involved was below 850 kg per year. In 2008 there were 19 die casting foundries below this SF₆-threshold in EU, half of which in Germany where also half of the SF₆ was used, Table 2 [7].



18th INTERNATIONAL FOUNDRYMEN CONFERENCE
Coexistence of material science and sustainable technology in
economic growth

Sisak, May 15th-17th, 2019

<http://www.simet.hr/~foundry/>

Table 2. SF₆ Consumption of SF₆ in die cast foundries by EU member states, 2008 [7]

EU member	Number of die casting foundries	Total SF ₆ consumption, kg/a
Germany	9	3.024
Italy	4	1.080
Sweden	2	825
Romania	1	420
UK	1	350
Spain	2	220
Total	19	5.919

After the legal ban, HFC-134a and SO₂ became the most accepted alternatives to SF₆ as cover gasses. SO₂ has become by far the most important cover gas (59 %). HFCs were applied as alternative cover gases in 21 % of the die casting industry, Figure 12. However, 20 % of produced magnesium amounts was still covered by SF₆ (9 % in foundries with an annual SF₆ consumption over 850 kg plus 11 % of the in foundries with a gas consumption of less than 850 kg/a), as for the production data from 2008 [7].

Mg Consumption 2008 in tonnes, by Melt Protection: Total 122,000 t Mg
[Result of 2006 F-Gas Regulation]

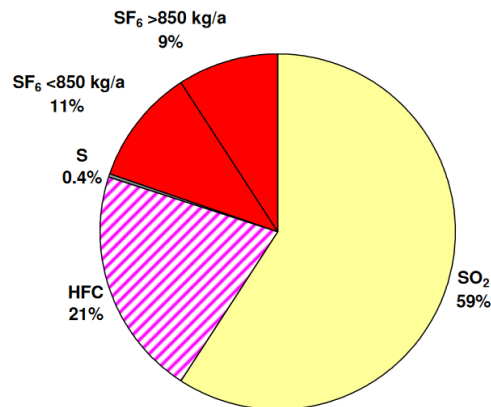


Figure 12. Protection gas in magnesium casting industry after 2006 F-Gas Regulation [7]

The novel EU f-gas regulation (EN 517/2014, Article 13) starting from January 1st 2018 prohibits the use of sulfur hexafluoride (SF₆) also in small magnesium foundries, i.e. with a demand less than 850 kg/a [8].

The Global Warming Potential of the hydrofluorocarbon 1,1,1,2-tetrafluoroethan (HFC-134a) is assumed to be 1430, i.e. 3.5 kg of HFC-134a equals to 5 tons of CO₂ [6]. These values are much lower than for SF₆, but are still considered important. Also, thermal disintegration of HFC-134a at high magnesium melting temperatures may result in the release of toxic hydrogen fluoride [5].



18th INTERNATIONAL FOUNDRYMEN CONFERENCE

Coexistence of material science and sustainable technology in
economic growth

Sisak, May 15th-17th, 2019

<http://www.simet.hr/~foundry/>

Sulfur dioxide (SO₂) is a colorless gas with a strong, pungent odor. Exposure of workers to SO₂ may be by breathing it in the air and it may affect the lungs, while high levels of SO₂ in the working area may lead to nose and throat burning, breathing difficulties and cause severe airway obstructions [9]. When the SO₂ reacts with the air humidity, sulfuric acid is formed. This eventually may lead to the corrosion of the casting machine parts and to the increase of maintenance costs of die casting equipment. SO₂ emissions contribute to atmospheric corrosion too, through the effect known as acid rain. The Global Warming Potential for SO₂ is not to be considered and the same applies to argon [5].

In the thixomolding process, argon is applied into the feed of the thixomolding machine in order to prevent the magnesium chips from oxidation. Since argon is an inert gas, it is considered safe for the environment and for the workers. Workplace exposure limits have not been established for argon. Argon exposure may pose a health risk in extreme cases, for example when high argon content would decrease the amount of available oxygen. Therefore oxygen content should be routinely measured to make sure there is at least 19.5 % oxygen available by volume [10].

MANUFACTURERS

Since thixomolding is a relatively new technology, the market worldwide is quite small. In total only approximately 300 thixomolding machines have been installed since 1991. There are only two manufacturers of thixomolding machines: Japan Steel Works Ltd. from Japan and Husky Injection Molding Ltd. located in Canada, which produce machines with clamp forces between 75 t and 1600 t. As for the thixomolding equipment installed in Europe, a very limited number of companies use this technology in Austria, Belgium, France and Germany [2]. Figure 13 shows the development of thixomolding machines by region.

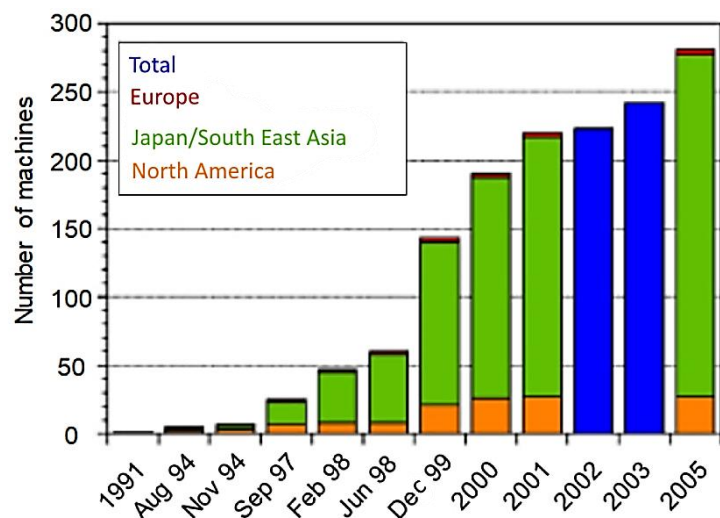


Figure 13. Number of thixomolding machines by region and time [2]



18th INTERNATIONAL FOUNDRYMEN CONFERENCE
**Coexistence of material science and sustainable technology in
economic growth**

Sisak, May 15th-17th, 2019

<http://www.simet.hr/~foundry/>

APPLICATIONS

Thixomolded parts can be used in several industries and applications. The main share of thixomolded components is used in the automobile industry, which requires good properties and suitability for mass production of high-quality products. Thixomolded parts are used for making seat frames, steering wheels, road wheels, oil pumps, key lock housings, transmission parts, navigation systems, etc., Figure 14 [1].

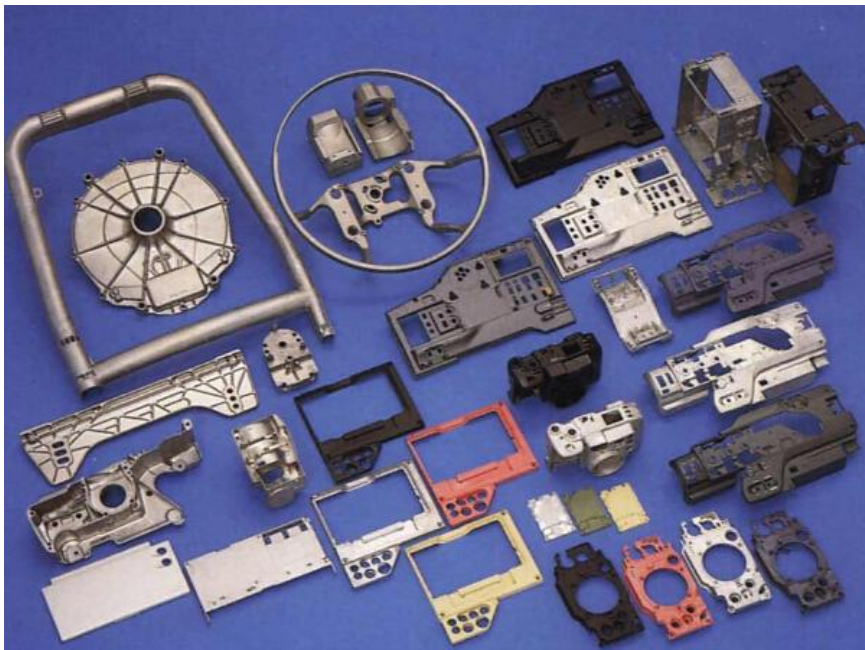


Figure 14. Applications in the automobile industry [11]

Also, the electronics industry recognized the advantages of the thixomolding technology. Parts manufactured by thixomolding are used in cameras, notebooks, mobile phones, monitors, heat sinks, LCD projectors and optical pickups, Figure 15. Light-weight, metallic, thin-walled shaping offers a huge advantage in these small applications [1].



18th INTERNATIONAL FOUNDRYMEN CONFERENCE

Coexistence of material science and sustainable technology in economic growth

Sisak, May 15th-17th, 2019

<http://www.simet.hr/~foundry/>



Figure 15. Applications in the electronics industry [1]

CONCLUSIONS

Thixomolding is still a rather new technology with the problems that come with it. The coverage of manufacturers and support is not completely developed and available worldwide, but the advantages of thixomolding are already very clear.

Mechanical properties of the workpieces show higher tensile strength, higher yield strength and higher elongation while being less porous when thixomolded parts are compared to die cast parts. Also, nearly no machining is needed after thixomolding as the workpieces are near net shaped.

Still a lot of research on different parameters and materials will have to be done. New technologies are currently developed to further improve the thixomolding process, for example particle reinforced magnesium alloys are expected to increase mechanical properties. One new option in the process improvement is the advanced production of magnesium granules. Lowering the processing temperature may be achieved by lowering the melting point through improved alloying. The process itself is going to be improved in several ways, for example, by a hot runner system, which preheats the mold, may reduce the shot weight per workpiece up to 35 %, etc.

Compared to die casting, thixomolding has several environmental benefits, some of which are very strong, compared to die casting. One of the most obvious benefits is lower energy consumption. Furthermore, thixomolding uses inert gasses, without global warming potential, while die casting requires the use of different protective gasses that have a strong negative impact to global warming. Different legal regulations are influencing the manufacturers in the European Union to switch to greener options recently. While novel cover gasses used in die casting have a neutral effect on global warming, they contribute to the corrosion of the equipment and to the air pollution.



18th INTERNATIONAL FOUNDRYMEN CONFERENCE

Coexistence of material science and sustainable technology in economic growth

Sisak, May 15th-17th, 2019

<http://www.simet.hr/~foundry/>

In total, thixomolding is a very promising technology for producing magnesium alloys, with high growth potential all over the world.

REFERENCES

- [1] H. Eibisch, A. Lohmüller, M. Scharrer, R. Jennings, M. Hilbinger, R. F. Singer, Neue Entwicklungen beim Thixospritzgießen von Magnesiumlegierungen, *Giessereiforschung*, 57(2005)1, pp. 2-9.
- [2] M. Scharrer, Thixospritzgießen von Magnesiumlegierungen - Gefüge und mechanische Eigenschaften, TIBKAT, Erlangen, 2008.
- [3] M. Franke, Herstellung von Magnesium-Bauteilen durch Thixospritzgießen, Accessible on Internet: <http://www.nmfgmbh.de/en/hauptnavigation/frth/fields-of-activity/injection-molding-of-magnesium-parts>, 2.5.2018.
- [4] Chemicalstructure.net, Magnesium and Aluminum, Accessible on Internet: <https://chemicalstructure.net/portfolio/magnesium-and-aluminum/>, 26.6.2018.
- [5] A. Lohmüller, M. Scharrer, R. Jennings, C. Rauber, M. Loos, N. Kömpel, M. Hilbinger, M. Hartmann, R.F. Singer, Advances in magnesium thixomolding, Proceedings of International Symposium of 15th Magnesium Automotive and User Seminar, Sep 27-28, 2007, Aalen, Germany.
- [6] Calculate the carbon dioxide equivalent quantity of an F gas - GOV.UK, Accessible on Internet: <https://www.gov.uk/guidance/calculate-the-carbon-dioxide-equivalent-quantity-of-an-f-gas>, 25.3.2019.
- [7] Service contract to assess the feasibility of options to reduce emissions of SF6 from the EU non-ferrous metal industry and analyse their potential impacts, Final Report, Accessible on Internet: https://ec.europa.eu/clima/sites/clima/files/f-gas/docs/report_sf6_en.pdf, 25.3.2019.
- [8] Regulation (EU) No 517/2014 of the European Parliament and of the Council of 16 April 2014 on fluorinated greenhouse gases and repealing Regulation (EC) No 842/2006 Text with EEA relevance, Accessible on Internet: <https://eur-lex.europa.eu/legal-content/EN/TXT/PDF/?uri=CELEX:32014R0517&from=EN>, 5.3.2019.
- [9] Agency for Toxic Substances and Disease Registry, Toxic Substances Portal - Sulfur Dioxide, Accessible on Internet: <https://www.atsdr.cdc.gov/toxfaqs/tf.asp?id=252&tid=46>, 26.3.2019.
- [10] Argon, Hazardous Substance Fact Sheet, New Jersey Department of Health, Accessible on Internet: <https://www.nj.gov/health/eoh/rtkweb/documents/fs/0151.pdf>, 26.3.2019.
- [11] The Japan Steel Works Ltd., Molding examples, Accessible on Internet: https://www.isw.co.jp/en/products/mg/molding_examples.html, 2.5.2018.



18th INTERNATIONAL FOUNDRYMEN CONFERENCE

Coexistence of material science and sustainable technology in
economic growth

Sisak, May 15th-17th, 2019

<http://www.simet.hr/~foundry/>

THE EFFECT OF THE AGING PROCESS ON THE DIFFERENT PROPERTIES OF THE EN AW-6082 ALUMINUM ALLOY

Uroš Stamenković*, Svetlana Ivanov, Ivana Marković, Vesna Grekulović, Jasmina Petrović,
Milica Bošković

University of Belgrade Technical Faculty in Bor, Bor, Serbia

Poster presentation

Original scientific paper

Abstract

The aim of this paper is the investigation of the effect of natural aging and pre-aging on an EN AW-6082 aluminum alloy by studying its mechanical, physical and microstructural properties. These properties were investigated during different aging treatments. Firstly, the effect of natural aging on investigated properties was studied, after which the influence of natural aging (room temperature pre-aging) on the artificial aging was investigated. The results showed that the hardness values increased gradually with the duration of natural aging. During the natural aging the hardness gradually increased up to around 30 %, while electrical conductivity decreased for about 1 MS/m in all naturally aged samples compared to the quenched one. Room temperature pre-aging had no effect or even negative effect on measured properties of subsequent artificially aged samples. This means that pre-aged samples during artificial aging had the same or lower hardness values compared to the only artificially aged samples. The same conclusions were drawn for the electrical conductivity measurements. Optical microscopy investigation confirmed the existence of precipitated phases and their distribution in the structure.

Keywords: *aluminum alloys, EN AW-6082, natural aging, pre-aging, artificial aging, hardness, electrical conductivity, microstructure*

*Corresponding author (e-mail address): ustamenkovic@tfbor.bg.ac.rs

INTRODUCTION

Aluminum alloys from 6XXX series (Al-Mg-Si) are those containing the Mg and Si as a two primary elements for alloying. These alloys are often chosen in automotive and other industries due to high resistance to corrosion followed by very good formability and strength [1-7]. The strengthening of Al-Mg-Si alloys is achieved through the formation of precipitates



18th INTERNATIONAL FOUNDRYMEN CONFERENCE

Coexistence of material science and sustainable technology in
economic growth

Sisak, May 15th-17th, 2019

<http://www.simet.hr/~foundry/>

during the aging process. This process includes solution heat treatment followed by quenching to below room temperature followed by natural (room temperature) or artificial (higher temperature) aging [1]. The precipitation has a complex sequence which is often given as: $\alpha_{SSSS} \rightarrow \text{Mg:Si clusters} \rightarrow \text{G.P. zones} \rightarrow \beta'' \rightarrow \beta' \rightarrow \text{Si}$ (if excess silicon is present) $\rightarrow \beta$ [4, 8-13]. All of the above precipitates form in the alloy's structure at the specific temperature range, exist until higher temperature is achieved, then dissolve. They influence the structure differently and uniquely. By the means of natural aging due to the room temperature storage only the clusters of magnesium and silicon are able to be present in the structure. Formation of clusters due to the natural aging and their influence on the subsequent artificial aging has attracted attention of many researchers [7]. There are essentially two main effects that natural aging can produce. The positive effect, which often appears in the so-called lean (low-alloyed) alloys that are used in the electric power industry. This positive effect means the higher values of peak-aged hardness after the subsequent artificial aging [14,15]. The negative effect is reversely proportional to the positive one giving lower hardness values after storage at room temperature (room temperature pre-aging) and it is often observed in the high solute alloys used in automotive and construction industries [1,2,6,16]. Regardless of many investigations of this subject, the influence of natural aging is still investigated. In this paper the high solute (EN AW-6082) alloy was investigated. The aim was to better understand the influence of room temperature storage (natural aging) on hardness, electrical conductivity and microstructural changes. Also, the investigation of positive or negative effects on subsequent artificial aging was performed.

MATERIALS AND METHODS

EN AW-6082 alloy was chosen for experimental investigation. The alloy was delivered from "AlCu metali d.o.o." company, in peak aged condition (T6 temper) in the form of extruded rectangular bars. Table 1 represents the chemical composition of investigated alloy determined by the optical emission spectrometer "Belec Compact Port". Annealing at 550 °C for 6 hours in the electric resistance furnace Heraeus K-1150/2 removed peak aged condition and obtained the O-temper for all of the samples. After that, solution heat treatment was performed at the same temperature for 1 hour followed by quenching in water with ice in order to obtain a super saturated solid solution (α_{SSSS}). After obtaining the super saturated solid solution, the samples were subjected to natural aging for a different time from 3 up to 70 days (referenced as NA samples). One sample was directly aged at 180 °C for 6 h without any room temperature storage in order to achieve peak hardness state (presented on graph as directly aged AA samples). In order to investigate the influence of natural aging on artificial aging (AA), samples that were naturally aged for 3, 10, 40 and 70 days were chosen and artificially aged in the same manner as the directly aged sample at 180 °C for 6 h (those samples are referenced as NA+AA samples). All the NA samples were compared to the quenched sample (quenched state on the presented graphs), while all the NA+AA samples were compared to only the artificially aged samples (AA samples).



18th INTERNATIONAL FOUNDRYMEN CONFERENCE

Coexistence of material science and sustainable technology in economic growth

Sisak, May 15th-17th, 2019

<http://www.simet.hr/~foundry/>

During the aging treatment, all samples were subjected to various characterization methods. Electrical conductivity was measured using the electrical conductivity tester Sigmatest 2.063. Hardness was measured on the VEB Leipzig Vickers hardness tester using a 10 kg load and a 15 s dwelling time. The ASTM E384 standard was followed during the hardness measurements [17]. Optical microscopy investigation of the samples at different magnifications was used to confirm the existence of precipitated phases and their distribution in the structure. Preparation of the samples included wet grinding on a series of SiC papers, polishing with alumina slurry with two different Al₂O₃ particle sizes; particle sizes of 0.3 μm and 0.05 μm. Dix-Keller reagent was used for etching of the samples by immersion to reveal fine dispersed particles.

Table 1. Chemical composition of the investigated alloy (mass%)

Si	Fe	Cu	Mn	Mg	Cr	Ni	Zn
0.807	0.354	0.042	0.453	0.696	<0.012	0.012	0.115
Ti	Pb	V	Co	Sn	Zr	Al	
0.025	0.01	<0.003	0.006	<0.003	<0.003	97.45	

RESULTS AND DISCUSSION

Presented results in Figure 1 show that natural aging causes the hardening of the samples. From the obtained hardness curve it can be concluded that hardness rapidly increases after only 3 days of aging. All of the NA samples had higher values of hardness in comparison to quenched state. Hardness saturation value is achieved after around 25 days of natural aging, after that hardness stays somewhat the same up to 70 days. The hardness is gradually increased up to around 30 % (after 25 days of NA).

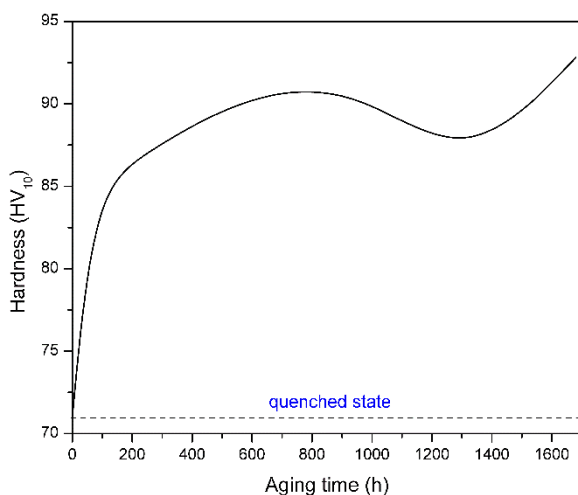


Figure 1. Hardness variations of quenched samples during natural aging

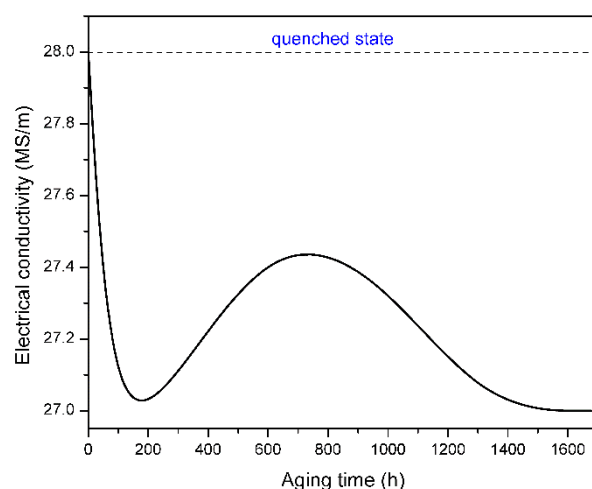


Figure 2. Electrical conductivity variations of quenched samples during natural aging



18th INTERNATIONAL FOUNDRYMEN CONFERENCE

Coexistence of material science and sustainable technology in economic growth

Sisak, May 15th-17th, 2019

<http://www.simet.hr/~foundry/>

An increment in hardness values is possible due to the Mg-Si atoms that originally dissolved into the Al matrix during solution heat treatment and remained in the matrix after quenching. After natural aging those atoms precipitated from the super saturated matrix, forming the Mg-Si clusters and Mg-Si co-clusters. This formation is causing the restriction of dislocation motion and increasing the hardness of the alloy [1,2,6,7]. L. Cao et al. discovered through 3D atom probe that clustering between Mg and Si occurs after several hours of natural aging explaining the steepness of the curve presented in Figure 1 [18]. These clusters, especially Si ones, are very durable at room temperature. They are able to dissolve only after reaching certain higher temperatures. This durability of clusters can explain the maximum value of hardness after 25 days of natural aging and the following plateau state up until 70 days of natural aging [7].

The results of the influence of natural aging on the electrical conductivity of the investigated alloy are presented in Figure 2. It can be concluded that all of the NA samples had lower values of electrical conductivity in comparison to the quenched samples. Knowing that during natural aging clusters and co-clusters are formed, electrical conductivity decrease can be expected. The decrease can be explained by the strong electron scattering effect that these clusters possess which is also mentioned by other authors [11,19,20].

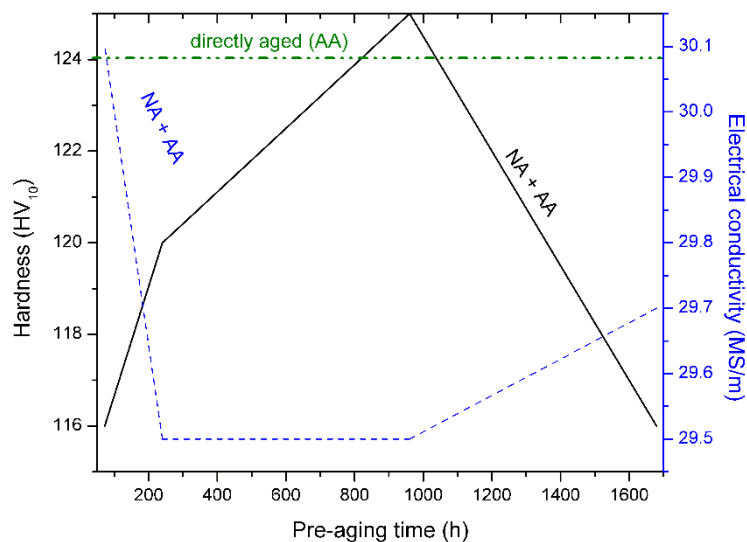


Figure 3. The influence of natural aging on artificial aging on hardness and electrical conductivity of investigated alloy

The influence of natural aging on the artificial aging has been documented in Figure 3. From Figure 3 it can be concluded that in the case of the investigated alloy the natural aging had no effect or even negative effect on hardness and electrical conductivity samples. All of the samples that were naturally aged before artificial aging show lower values of both hardness and electrical conductivity. In order to obtain the highest hardness values the samples need



18th INTERNATIONAL FOUNDRYMEN CONFERENCE
**Coexistence of material science and sustainable technology in
economic growth**

Sisak, May 15th-17th, 2019

<http://www.simet.hr/~foundry/>

to be peak aged. For the highest values of hardness in peak aged samples the β'' phase is responsible. Any obstruction of the precipitation of this phase results in lower hardness values. The investigated alloy belongs to the high solute alloys that experience the negative effect of natural aging [1,2,4,7]. The negative effect of room temperature pre-aging is caused by the formation of clusters and zones during natural aging. The β'' phase that forms in the peak aged samples (AA samples) can precipitate after the dissolution of clusters. In this case those clusters are very stable so they inhibit the formation of β'' phase causing the hardness to decrease in NA+AA samples [1,2]. In our case the negative effect was not so much pronounced as in other cases [1,2]. This can be attributed to the excess silicon in the alloy that can stimulate the precipitation of the small and fine clusters and zones. Those kinds of clusters and zones can't have high impact on later precipitation of β'' phase [4]. Even though the precipitation is somewhat inhibited, the β'' phase appears in the microstructure as finely dispersed particles, as shown in Figure 4. Size of these particles is approximately 1 μm or even below that.

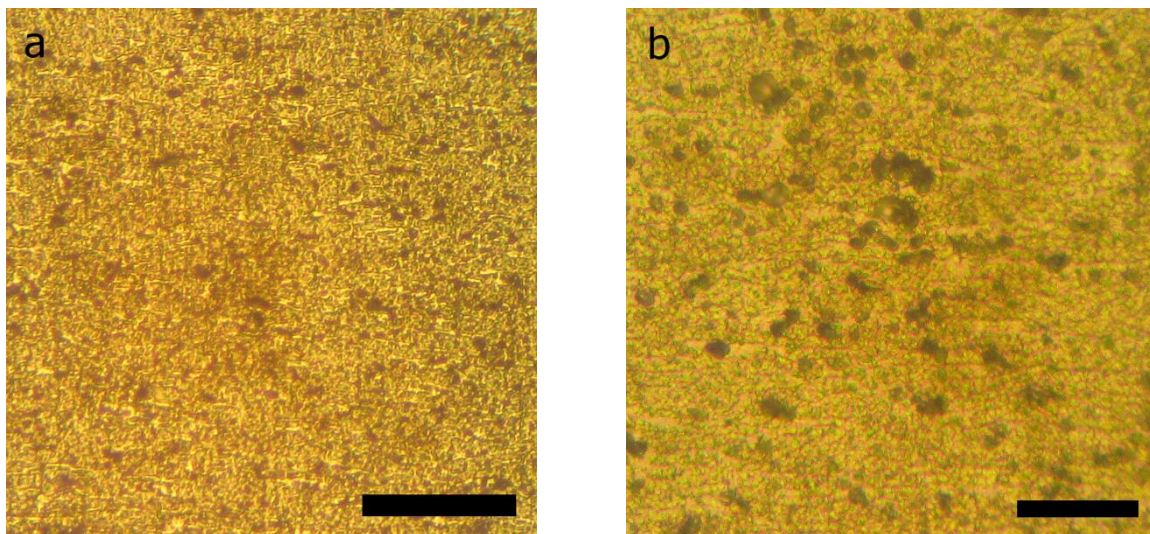


Figure 4. Microstructure at different magnifications of the sample naturally aged for 10 days and then peak aged for maximum hardness; a) 200x (scale bar is 50 μm);
b) 500x (scale bar is 15 μm)

CONCLUSIONS

The influence of natural aging on hardness, electrical conductivity and microstructure was investigated. The key conclusions can be outlined:

- The hardness of the samples naturally aged is higher than those in the quenched state. Maximal hardness is achieved after the 25 days of natural aging after which the



18th INTERNATIONAL FOUNDRYMEN CONFERENCE

Coexistence of material science and sustainable technology in economic growth

Sisak, May 15th-17th, 2019

<http://www.simet.hr/~foundry/>

hardness goes into the plateau state and hardness remains the same up to 70 days of natural aging.

- Naturally aged samples have lower values of electrical conductivity in comparison to the quenched one.
- Natural aging showed no effect or even negative effect on artificial aging. The strengthening effect of β'' phase wasn't influenced, probably due to the formation of small fine clusters and zones caused by the excess silicon in the alloys composition. Hardness and electrical conductivity values remained approximately the same as values achieved for only artificially aged sample. Hardness only changed for approximately 10 HV₁₀ while electrical conductivity for 0.6 MS/m.
- In the samples that were naturally and subsequently artificially aged, β'' phase appeared in the form of finely dispersed particles.

Acknowledgements

The research results were developed with the assistance of the Ministry of Education, Science and Technological Development of the Republic of Serbia under the projects OI 172037 and TR34003.

REFERENCES

- [1] A. Cuniberti, A. Tolley, M. V. Castro Riglos, R. Giovachini, Influence of natural aging on the precipitation hardening of an AlMgSi alloy, *Materials Science and Engineering: A*, 527(2010)20, pp. 5307-5311.
- [2] Y. Birol, The effect of processing and Mn content on the T5 and T6 properties of AA6082 profiles, *Journal of Materials Processing Technology*, 173(2006)1, pp. 84-91.
- [3] M. H. Farshidi, M. Kazeminezhad, H. Miyamoto, On the natural aging behavior of Aluminum 6061 alloy after severe plastic deformation, *Materials Science and Engineering: A*, 580(2013), pp. 202-208.
- [4] A. K. Gupta, D. J. Lloyd, S. A. Court, Precipitation hardening in Al–Mg–Si alloys with and without excess Si, *Materials Science and Engineering: A*, 316(2001)1–2, pp. 11-17.
- [5] G. Mrowka-Nowotnik, J. Sieniawski, Influence of heat treatment on the microstructure and mechanical properties of 6005 and 6082 aluminium alloys, *Journal of Materials Processing Technology*, 162–163(2005), pp. 367-372.
- [6] S. Pogatscher, H. Antrekowitsch, H. Leitner, T. Ebner, P.J. Uggowitzer, Mechanisms controlling the artificial aging of Al–Mg–Si Alloys, *Acta Materialia*, 59(2011)9, pp. 3352-3363.



18th INTERNATIONAL FOUNDRYMEN CONFERENCE

Coexistence of material science and sustainable technology in
economic growth

Sisak, May 15th-17th, 2019

<http://www.simet.hr/~foundry/>

- [7] S. Jin, T. Ngai, G. Zhang, T. Zhai, S. Jia, L. Li, Precipitation strengthening mechanisms during natural ageing and subsequent artificial aging in an Al-Mg-Si-Cu alloy, *Materials Science and Engineering: A*, 724(2018), pp. 53-59.
- [8] B. Milkereit, N. Wanderka, C. Schick, O. Kessler, Continuous cooling precipitation diagrams of Al-Mg-Si alloys, *Materials Science and Engineering: A*, 550(2012), pp. 87-96.
- [9] G. Mrowka-Nowotnik, Influence of chemical composition variation and heat treatment on microstructure and mechanical properties of 6xxx alloys, *Archives of Materials Science and Engineering*, 46(2010)2, pp. 98-107.
- [10] Y. Birol, Precipitation during homogenization cooling in AlMgSi alloys, *Transactions of Nonferrous Metals Society of China*, 23(2013)7, pp. 1875-1881.
- [11] G. A. Edwards, K. Stiller, G. L. Dunlop, M. J. Couper, The precipitation sequence in Al-Mg-Si alloys, *Acta Materialia*, 46(1998)11, pp. 3893-3904.
- [12] B. C. Shang, Z. M. Yin, G. Wang, B. Liu, Z. Q. Huang, Investigation of quench sensitivity and transformation kinetics during isothermal treatment in 6082 aluminum alloy, *Materials & Design*, 32(2011)7, pp. 3818-3822.
- [13] M. Vedani, G. Angella, P. Bassani, D. Ripamonti, A. Tuissi, DSC analysis of strengthening precipitates in ultrafine Al-Mg-Si alloys, *Journal of Thermal Analysis and Calorimetry*, 87(2007)1, pp. 277-284.
- [14] C. Chang, I. Wieler, N. Wanderka, J. Banhart, Positive effect of natural pre-ageing on precipitation hardening in Al-0.44 at% Mg-0.38 at% Si alloy, *Ultramicroscopy*, 109(2009)5, pp. 585-92.
- [15] K. Strobel, M. D. H. Lay, M. A. Easton, L. Sweet, S. Zhu, N. C. Parson, A. J. Hill, Effects of quench rate and natural ageing on the age hardening behaviour of aluminium alloy AA6060, *Materials Characterization*, 111(2016), pp. 43-52.
- [16] Y. Aruga, M. Kozuka, Y. Takaki, T. Sato, Formation and reversion of clusters during natural aging and subsequent artificial aging in an Al-Mg-Si alloy, *Materials Science and Engineering: A*, 631(2015), pp. 86-96.
- [17] Standard Test Method for Microindentation Hardness of Materials, Accessible on Internet: <https://www.astm.org/Standards/E384.htm>
- [18] L. Cao, P. A. Rometsch, M. J. Couper, Clustering behavior in an Al-Mg-Si-Cu alloy during natural ageing and subsequent under-ageing, *Materials Science and Engineering: A*, 559(2013), pp. 257-261.
- [19] L. Cui, Z. Liu, Xi. Zhao, J. Tang, K. Liu, X. Liu and C. Qian, Precipitation of metastable phases and its effect on electrical resistivity of Al-0.96Mg₂Si alloy during aging, *Transactions of Nonferrous Metals Society of China*, 24(2014)7, pp. 2266-2274.
- [20] T. R. Prabhu, Effects of ageing time on the mechanical and conductivity properties for various round bar diameters of AA2219 Al alloy, *Engineering Science and Technology, an International Journal*, 20(2017)1, pp. 133-142.



18th INTERNATIONAL FOUNDRYMEN CONFERENCE

Coexistence of material science and sustainable technology in
economic growth

Sisak, May 15th-17th, 2019

<http://www.simet.hr/~foundry/>

INFLUENCE OF DEEP CRYOGENIC TREATMENT ON THE MECHANICAL PROPERTIES OF ADI AUSTEMPERED AT THE LOWER AUSFERRITIC RANGE

UTJECAJ DUBOKOG HLAĐENJA NA MEHANIČKA SVOJSTVA ADI-A POBOLJŠANOG U PODRUČJU DONJEG AUSFERITA

Sanja Šolić^{1*}, Bojan Podgornik², Zdravko Schauerl³, Matjaž Godec², Branko Bauer³, Vlado
Tropša¹

¹ University North, Department of Mechanical Engineering, Varaždin, Croatia

² Institute of Metals and Technology, Ljubljana, Slovenia

³ University of Zagreb Faculty of Mechanical Engineering and Naval Architecture, Zagreb, Croatia

Poster presentation

Original scientific paper

Abstract

The application of deep cryogenic treatment in heat treatment processes showed excellent results in improving mechanical and tribological properties of variety of materials, especially tool steels, hard metals and grey iron and also nodular cast iron austempered in the upper ausferrite temperature range. This paper presents the results of the investigation of the influence of deep cryogenic treatment with subsequent tempering on the tensile strength and Charpy impact test at three different temperatures of the ductile cast iron grade EN-GJS-600-3 austempered at the lower ausferrite temperature range. The results show that austempering process influenced the tensile strength increase but deep cryogenic treatment with tempering did not have any significant influence on the tensile strength or the Charpy impact test results.

Keywords: *deep cryogenic treatment, ADI, lower ausferrite, tensile strength, Charpy impact test*

*Corresponding author (e-mail address): ssolic@unin.hr

Sažetak

Primjena dubokog hlađenja u postupcima toplinske obrade pokazala je izvrsne rezultate u pogledu poboljšanja mehaničkih i posebno triboloških svojstava kod velikog broja materijala, posebno alatnih čelika, tvrdih metala pa i sivog lijeva te nodularnog lijeva izotermički poboljšanog u području gornjeg ausferita. U ovom radu ispitan je utjecaj dubokog hlađenja uz naknadno popuštanje, na čvrstoću i udarni rad loma pri tri različite temperature, nodularnog lijeva EN-GJS-600-3 izotermički poboljšanog u području donjeg ausferita. Rezultati su pokazali značajno povećanje čvrstoće izotermičkim



18th INTERNATIONAL FOUNDRYMEN CONFERENCE

Coexistence of material science and sustainable technology in
economic growth

Sisak, May 15th-17th, 2019

<http://www.simet.hr/~foundry/>

poboljšavanjem, ali bez značajnijeg utjecaja dubokog hlađenja i naknadnog popuštanja na promjenu čvrstoće i udarnog rada loma.

Ključne riječi: duboko hlađenje, ADI, donji ausferit, čvrstoća, udarni rad loma

UVOD

Izvrсна kombinacija svojstava izotermički poboljšanog nodularnog lijeva svrstala su ga među važne inženjerske materijale posljednjih desetak godina. Posebno je zanimljiv za upotrebu u automobilskoj industriji kao zamjena za čelične dijelove radi odličnog omjera čvrstoće i mase, dobre žilavosti i otpornosti na trošenje te izvrsne dinamičke izdržljivosti u odnosu na relativno nisku cijenu, mogućnost optimiranja svojstava i dobru obradivost. Ta dobra kombinacija svojstava rezultat je specifične mikrostrukture izotermički poboljšanog nodularnog lijeva koja se sastoji od igličastog bainitnog ferita i visokougličnog austenita, a koja se naziva ausferitnom mikrostrukturom [1-6]. Dugi vremenski period pogrešno se smatralo da se mikrostruktura ADI-a sastoji od bainita. Razlog tome je u sličnosti postupka toplinske obrade i mikrostrukture, u usporedbi s izotermički poboljšanim čelicima, a koja je bainitna i sastoji se od igličastog ferita i karbida, dok kod pravilno toplinski obrađenog ADI-a nema prisutnih karbida u mikrostrukтури.

Toplinska obrada kojom se postiže ausferitna struktura matrice kod nodularnog lijeva sastoji se od austenitizacije, s ciljem postizanja potpuno austenitne strukture matrice, te gašenja na temperaturu izotermičke pretvorbe kako bi se izbjeglo formiranje perlita ili druge visokotemperaturne fazne transformacije. Temperatura izotermičkog poboljšavanja o kojoj ovise konačna mikrostruktura i svojstva najvažniji je parametar toplinske obrade ADI-a te se provodi uobičajeno u rasponu od 250 °C do 400 °C. Izotermičko poboljšavanje u donjem temperaturnom pojasu (250 °C – 320 °C) rezultira mikrostrukturom koja se sastoji od sitnozrnatog, igličastog ili acikularnog ferita i austenita, tzv. donji ausferit, koji daje višu čvrstoću i nižu udarnu žilavost i duktilnost. Izotermičko poboljšavanje u višem temperaturnom pojasu (320 °C – 400 °C) rezultira grubim, paperjastim feritom i austenitom tzv. gornji ausferit, s nižom čvrstoćom ali značajno boljom duktilnosti i udarnom žilavosti ADI-a.

Tijekom izotermičkog poboljšavanja ADI prolazi kroz dvije faze. U prvoj fazi dolazi do pretvorbe austenita u bainitni ferit, $\alpha_{(B)}$, i visokouglični austenit, γ_{HC} , tzv. ausferit.

$$\gamma = \alpha_{(B)} + \gamma_{HC} \quad (1)$$

Ukoliko se materijal drži na temperaturi izotermičkog poboljšavanja predugo, dolazi do daljnje mikrostrukturne pretvorbe visokougličnog austenita, pri čemu se u drugoj fazi visokouglični austenit raspada na ferit, α , i ϵ -karbide.

$$\gamma = \alpha + \epsilon \quad (2)$$



18th INTERNATIONAL FOUNDRYMEN CONFERENCE

Coexistence of material science and sustainable technology in
economic growth

Sisak, May 15th-17th, 2019

<http://www.simet.hr/~foundry/>

Optimalna kombinacija svojstava, čvrstoće i duktilnosti, postiže se ukoliko se izotermičko poboljšavanje prekine nakon prve faze mikrostrukturnih pretvorbi postizanjem ausferitne mikrostrukture matrice ADI-a, jer izlučivanje ϵ – karbida tijekom druge faze uzrokuje povećanje krhkosti materijala [7]. Daljnjim držanjem na temperaturi izotermičke pretvorbe dolazi do transformacije ϵ – karbida u nekoherentne Fe_3C karbide te materijal završava s bainitnom mikrostrukturom [6-10].

Duboko hlađenje je postupak toplinske obrade kod kojeg se materijal podvrgava djelovanju niskih temperatura prije popuštanja u svrhu eliminacije zaostalog austenita i postizanja dimenzijske stabilnosti, ali i u svrhu poboljšanja otpornosti na trošenje i poboljšanje dinamičke izdržljivosti materijala. U praksi postoje dva temperaturna područja hlađenja materijala. Pothlađivanje (*eng. cold treatment*), na temperaturama od cca $-80\text{ }^\circ\text{C}$ („suhi led“) do $-120\text{ }^\circ\text{C}$ dovoljno je za transformaciju zaostalog austenita iz kaljenog čelika u martenzit i u širokoj je komercijalnoj primjeni, posebno za uklanjanje zaostalog austenita u pougljičenim i površinski kaljenim slojevima. Duboko hlađenje (*eng. deep cryogenic treatment*) provodi se na temperaturi $-196\text{ }^\circ\text{C}$ (tekući dušik) i primarno utječe na povećanje otpornosti na trošenje materijala. To poboljšanje svojstava rezultat je potpune transformacije zaostalog austenita u martenzit i precipitacije sitnih nanometarskih η -karbida u popuštenom martenzitu. Duboko hlađenje vrlo je popularno u istraživanjima i koristi se danas u toplinskoj obradi alatnih i brzoreznih čelika, maraging čelika, čelika za poboljšavanje i sivog lijeva u svrhu povećanja otpornosti na trošenje i postizanja dimenzijske stabilnosti [10-15]. Istraživanja su također napravljena na izotermički poboljšanom nodularnom lijevu. Nekoliko autora istraživala su utjecaj dubokog hlađenja na mehanička svojstva ADI-a poboljšanom u donjem temperaturnom području ($288\text{ }^\circ\text{C}$) te su zaključili kako je duboko hlađenje utjecalo na povećanje vlačne čvrstoće, ali smanjenje istezljivosti uz nepromijenjenu lomnu žilavost [9,10]. U ovom radu prikazani su rezultati ispitivanja utjecaja dubokog hlađenja i naknadnog popuštanja na vlačnu čvrstoću i udarnu žilavost pri tri različite temperature izotermički poboljšanog nodularnog lijeva u temperaturnom pojasu donjeg ausferita.

MATERIJALI I POSTUPCI

Materijal korišten u ovom istraživanju je perlitno - feritni nodularni lijev oznake EN-GJS-600-3. Ispitni uzorci uzeti su iz Y-probe, slika 1.

Kemijski sastav nodularnog lijeva prikazan je u tablici 1. Kvantitativna analiza mikrostrukture pokazala je da se mikrostruktura nodularnog lijeva sastojala od približno 135 grafitnih nodula na mm^2 i ravnomjerno raspoređene perlitno-feritne matrice oko grafitnih nodula. Pomoću analizatora slike izmjeren je udio perlita od 67 %, ferita 19 % i grafitnih nodula 14 %.



18th INTERNATIONAL FOUNDRYMEN CONFERENCE
**Coexistence of material science and sustainable technology in
economic growth**

Sisak, May 15th-17th, 2019

<http://www.simet.hr/~foundry/>



Slika 1. Y-probe nodularnog lijeva EN-GJS-600-3 u ljevaonici MIV, Varaždin

Tablica 1. Kemijski sastav nodularnog lijeva EN-GJS-600-3

% C	% Si	% Mn	% P	% S	% Cu	% Mg	% Fe
3,52	2,58	0,375	0,031	0,011	0,475	0,035	ostatak

Iz Y-proba izrezani su ispitni uzorci za statičko vlačno ispitivanje, kratke standardne epruvete ($\phi 10$ mm x 50 mm), 9 kom, uzorci za ispitivanje udarnog rada loma na Charpy-jevom batu (10 mm x 10 mm x 55 mm, 18 kom) te uzorci za ispitivanje otpornosti na trošenje. Statičko vlačno ispitivanje nodularnog lijeva napravljeno je u samoj ljevaonici tijekom kontrole kvalitete odlivenih Y-proba.

Austenitizacija uzoraka provedena je u električnoj peći sa zaštitnom atmosferom argona na temperaturi 900 °C u trajanju 90 min. Uzorci su gašeni do temperature izotermičke pretvorbe od 250 °C. Izotermičko poboljšavanje provedeno je u solnoj kupki AS 160 na temperaturi 250 °C u trajanju od 120 min. Nakon izotermičkog poboljšavanja uzorci su hlađeni na zraku do sobne temperature. Dio uzoraka uronjen je kontroliranom brzinom u tekući dušik (-196 °C) u trajanju od 24 h nakon čega su sporo grijani do sobne temperature. Dio uzoraka je nakon dubokog hlađenja popušten na temperaturi 200 °C u trajanju 2 h. Tablica 2 prikazuje grupe uzoraka sa pripadnim oznakama i provedenim toplinskim obradama.

Tablica 2. Parametri toplinske obrade

Oznaka	Izotermičko poboljšavanje	Duboko hlađenje	Popuštanje
ADI	900 °C/90 min, 250 °C/120 min	-	-
DH0	900 °C/90 min, 250 °C/120 min	-196 °C/24 h	-
DH 1	900 °C/90 min, 250 °C/120 min	-196 °C/24 h	200 °C/2 h

Statičko vlačno ispitivanje provedeno je prema normi EN ISO 6892-1 A224 na kidalici tipa Instron 1255, na tri ispitne epruvete za svako stanje toplinske obrade. Udarni rad loma proveden je prema normi EN ISO 148-1:2017 na Charpy-jevom batu. Za svako stanje provedene toplinske obrade, po tri uzorka su ispitivana na sobnoj temperaturi, tri uzorka



18th INTERNATIONAL FOUNDRYMEN CONFERENCE
**Coexistence of material science and sustainable technology in
economic growth**

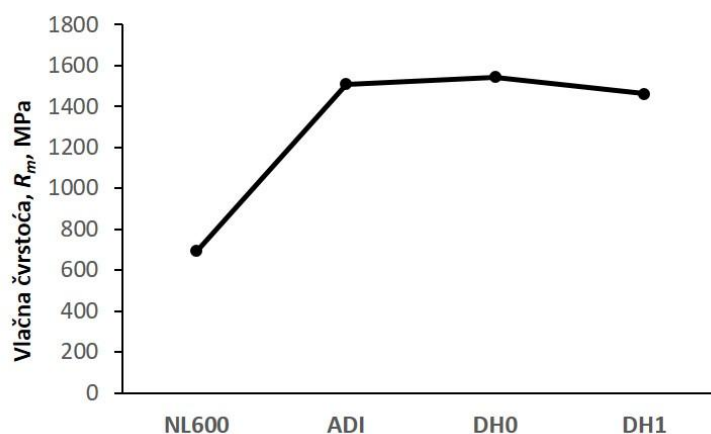
Sisak, May 15th-17th, 2019

<http://www.simet.hr/~foundry/>

hlađena su na temperaturu 0 °C te tri uzorka na -20 °C. Svi prikazani rezultati predstavljaju srednju vrijednost tri dobivena rezultata.

REZULTATI I RASPRAVA

Nakon provedene toplinske obrade ispitana je vlačna čvrstoća ispitnih uzoraka. Rezultati ispitivanja prikazani su u dijagramu na slici 2 zajedno s vrijednostima čvrstoće nodularnog lijeva prije postupka izotermičkog poboljšavanja.



Slika 2. Rezultati statičkog vlačnog ispitivanja

Iz dijagrama je vidljivo kako je izotermičko poboljšavanje utjecalo na značajno povećanje vlačne čvrstoće nodularnog lijeva, za 118 % u odnosu na lijevano stanje, a što je u skladu s postignutom mikrostrukturom matrice donjeg ausferita koji prema literaturi [3-6, 8-10] daje visoku čvrstoću, ali nisku duktilnost i žilavost u odnosu na perlitno-feritnu strukturu matrice nodularnog lijeva. Duktilnost se značajno smanjila, sa 9 % na samo 1 % za izotermički poboljšano stanje. Iz dijagrama i rezultata u tablici 3 vidljivo je da je duboko hlađenje utjecalo na minimalno povećanje vlačne čvrstoće, ali je zato popuštanje nakon dubokog hlađenja utjecalo na smanjenje vlačne čvrstoće bez utjecaja na istezljivost.

Tablica 3. Rezultati statičkog vlačnog ispitivanja i udarnog rada loma

	R_m , MPa	A, %	CVN, J, 20 °C	CVN, J, 0 °C	CVN, J, -20 °C
NL 600	692	9	-	-	-
ADI	1507	1	6,3	5,8	5,8
DH0	1542,5	1,5	6,7	6,2	6,8
DH1	1462	1	6,0	6,3	5,8



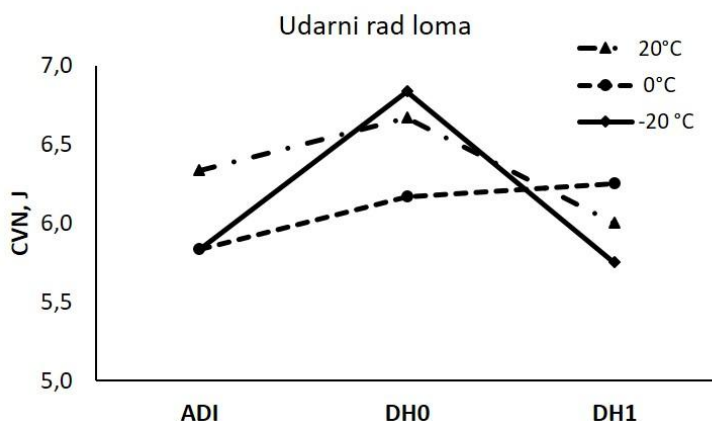
18th INTERNATIONAL FOUNDRYMEN CONFERENCE

Coexistence of material science and sustainable technology in
economic growth

Sisak, May 15th-17th, 2019

<http://www.simet.hr/~foundry/>

U istraživanjima drugih autora [9,10] duboko hlađenje je provedeno na temperaturi $-150\text{ }^{\circ}\text{C}$ u trajanju od 8 h s naknadnim popuštanjem na $150\text{ }^{\circ}\text{C}$ u trajanju od pola sata te su dobiveni slični rezultati kao i u ovom istraživanju. Time se može izvesti zaključak da sniženje temperature dubokog hlađenja te dulje držanje na toj temperaturi ne utječe značajno na promjenu vlačne čvrstoće i istezljivosti izotermički poboljšanog nodularnog lijeva. Rezultati ispitivanja udarnog rada loma na tri različite temperature prikazani su u dijagramu na slici 3.



Slika 3. Rezultati ispitivanja udarnog rada loma

Iz rezultata je vidljivo da je udarna žilavost nakon izotermičkog poboljšavanja u donjem ausferitnom temperaturnom rasponu u skladu s literaturnim izvorima gdje se navodi kako mikrostruktura matrice donjeg ausferita utječe na značajno povećanje čvrstoće, ali uz smanjenje žilavosti i duktilnosti. Vidljivo je da je duboko hlađenje utjecalo na povećanje udarnog rada loma u odnosu na izotermički poboljšano stanje pri sve tri temperature ispitivanja dok je naknadno popuštanje uzrokovalo značajno lošije rezultate u odnosu na početno stanje, osim pri ispitivanju na sobnoj temperaturi. Iz dobivenih rezultata moguće je zaključiti da duboko hlađenje ne utječe na promjenu ili eventualno značajnije povećanje udarnog rada loma te duktilnosti i žilavosti izotermički poboljšanog nodularnog lijeva u području donjeg ausferita.

ZAKLJUČAK

U ovom radu ispitan je utjecaj dubokog hlađenja na temperaturi $-196\text{ }^{\circ}\text{C}$ u trajanju 24 h s naknadnim popuštanjem na čvrstoću i udarni rad loma izotermički poboljšanog nodularnog lijeva u temperaturnom području donjeg ausferita jer se poboljšavanjem ADI-a u tom temperaturnom rasponu postižu visoke vrijednosti čvrstoće uz nisku duktilnost i žilavost. Iz dobivenih rezultata moguće je zaključiti da duboko hlađenje pri temperaturi $-196\text{ }^{\circ}\text{C}$ u trajanju od 24 h hlađenje minimalno utječe na povećanje vrijednosti vlačne čvrstoće uz



18th INTERNATIONAL FOUNDRYMEN CONFERENCE

Coexistence of material science and sustainable technology in
economic growth

Sisak, May 15th-17th, 2019

<http://www.simet.hr/~foundry/>

nepromijenjenu vrijednost istezljivosti. Popuštanje nakon dubokog hlađenja uzrokuje pad vlačne čvrstoće uz nepromijenjenu istezljivost. Iz rezultata ispitivanja udarnog rada loma moguće je zaključiti kako duboko hlađenje nije utjecalo na značajno povećanje rezultata udarnog rada loma pri svim temperaturama ispitivanja te u tom smjeru nije potrebno provoditi daljnja ispitivanja.

U okviru ovih ispitivanja pripremljeni su uzorci za ispitivanje otpornosti na trošenje koje se planira provesti kao nastavak na istraživanja utjecaja dubokog hlađenja na otpornost na trošenje izotermički poboljšanog nodularnog lijeva u području gornjeg ausferita [4].

ZAHVALE I PRIZNANJA

Ovo ispitivanje podržano je potporom znanstvenim istraživanjima Sveučilišta Sjever i bilateralnim hrvatsko – slovenskim projektom financiranim od strane MZO. Autori zahvaljuju tvrtki MIV iz Varaždina na lijevanju i izradi ispitnih uzoraka te dr.sc. Saši Kovačiću za podršku u provođenju toplinske obrade.

LITERATURA

- [1] M. Ferry, W. Xu, Microstructural and crystallographic features of ausferrite in as-cast gray iron, *Mater. Charact.*, 53(2004)1, pp. 43-49.
- [2] Y. Sahin, M. Erdogan, V. Kilicli, Wear behavior of austempered ductile irons with dual matrix structures, *Mater. Sci. Eng., A*, 444(2007), pp. 31-38.
- [3] J. M. Han, Q. Zou, G. C. Barber, T. Nasir, D. O. Northwood, X. C. Sun, P. Seaton, *Wear*, 201-202(2012), pp. 99-105.
- [4] S. Šolić, M. Godec, Z. Schauerl, Č. Donik, Improvement in abrasion wear resistance and microstructural changes with deep cryogenic treatment of austempered ductile cast iron (ADI), *Metallurgical and Materials Transactions A*, 47(2016), pp. 5058-5070.
- [5] L. Sidjanin, R. E. Smallman, Metallography of bainitic transformation in austempered ductile iron, *Mater. Sci. Technol.*, 8(1992), pp. 1095-1103.
- [6] W. J. Dubensky, K. B. Rundman, An electron microscope study of carbide formation in austempered ductile iron, *AFS Trans.*, 93(1985), pp. 389-394.
- [7] D. J. Moore, T. N. Rouns, K. B. Rundman, The effect of heat treatment, mechanical deformation and alloying elements on rate of bainitic formation in austempered ductile cast iron, *J. Heat Treat.* 4, 1(1985), pp. 7-24.
- [8] D. N. Collins, Cryogenic treatment of tool steels, *Adv. Mater. Process.*, 154(1998)6, pp. H23-H29.
- [9] S. Putatunda, C. Martis, R. Papp, F. Diekman, Proceedings of the 26th ASM Heat Treating Society Conference, 2011, pp. 44-49.
- [10] S. Panneerselvam, C. J. Martis, S. K. Putatunda, J. M. Boileau, An investigation on the stability of austenite in austempered ductile cast iron (ADI), *Mater. Sci. Eng., A*, 626(2015), pp. 237-246.



18th INTERNATIONAL FOUNDRYMEN CONFERENCE

**Coexistence of material science and sustainable technology in
economic growth**

Sisak, May 15th-17th, 2019

<http://www.simet.hr/~foundry/>

- [11] D. Mohan Lal, S. Renganarayanan, A. Kalanidhi, Cryogenic treatment to augment wear resistance of tool and die steels, *Cryogenics*, 41(2001)3, pp. 149-155.
- [12] A. Molinari, M. Pellizzari, S. Gialanella, G. Straffelini, K. H. Stiasny, Effect of deep cryogenic treatment on the mechanical properties of tool steels, *J. Mater. Process. Technol.*, 118(2001)1-3, pp. 350-355.
- [13] R. F. Barron, Cryogenic treatment of metals to improve wear resistance, *Cryogenics*, 22(1982), pp. 409-414.
- [14] S. Šolić, F. Cajner, V. Leskovšek, Effect of deep cryogenic treatment on mechanical and tribological properties of PM S390 MC high-speed steel, *Materials Testing*, 54(2012)10, pp. 688-693.
- [15] S. Šolić, Z. Schauerperl, M. Godec, V. Tropša, Microstructural changes in heat treatment of PM high speed steels, *Technical Journal*, 11(2017)4, 166-170.



18th INTERNATIONAL FOUNDRYMEN CONFERENCE

Coexistence of material science and sustainable technology in
economic growth

Sisak, May 15th-17th, 2019

<http://www.simet.hr/~foundry/>

CORROSION BEHAVIOR OF CuAlMn AND CuAlMnNi ALLOY IN 0.9% NaCl SOLUTION

Ladislav Vrsalović^{1*}, Ivana Ivanić², Stjepan Kožuh², Borut Kosec³, Milan Bizjak³, Senka Gudić¹, Mirko Gojić²

¹ University of Split Faculty of Chemistry and Technology, Split, Croatia

² University of Zagreb Faculty of Metallurgy, Sisak, Croatia

³ University of Ljubljana Faculty of Natural Sciences and Engineering, Ljubljana, Slovenia

Poster presentation

Original scientific paper

Abstract

Corrosion behavior of CuAlMn and CuAlMnNi alloy ribbons, produced by melt spinning method, were investigated by electrochemical methods such as open circuit potential measurement, linear and potentiodynamic polarization method. Investigations were performed in deaerated 0.9% NaCl solution (T = 37 °C pH = 7.4). Results of electrochemical investigations have shown that CuAlMnNi alloy have higher values of polarization resistance and smaller values of corrosion current density, but in higher anodic potentials region anodic current density for CuAlMn is lower than for CuAlMnNi alloy which indicates higher dissolution of CuAlMnNi alloy. After polarization measurements CuAlMn and CuAlMnNi ribbon surfaces were investigated with light microscope and with SEM/EDS analysis and results have shown that CuAlMnNi alloy is prone to pitting corrosion, while the surface of CuAlMn alloy is partially covered with corrosion product without existence of pits.

Keywords: corrosion, polarization, shape memory alloys, SEM/EDS analysis

*Corresponding author (e-mail address): ladislav@ktf-split.hr

INTRODUCTION

Cu-based shape memory alloys (Cu-SMA) have attracted considerable attention in order to be utilized in practical applications due to its favorable properties such as wide range of transformation temperature, relatively simple fabrication procedure, low production price and high thermal and electrical conductivity [1-4]. Cu-based SMAs are currently derived from three binary alloy systems i.e. Cu-Zn, Cu-Al and Cu-Sn [5]. Intensive investigations have been



18th INTERNATIONAL FOUNDRYMEN CONFERENCE

Coexistence of material science and sustainable technology in
economic growth

Sisak, May 15th-17th, 2019

<http://www.simet.hr/~foundry/>

performed on Cu-Zn based alloy containing alloying elements such as Al, Si, Sn, Ga or Mn as ternary alloy and Cu-Al based ternary alloys containing Ni, Be, Zn and Mn as alloying elements for their potential use [6-10].

Shortcoming of these alloys such as brittleness and low mechanical strength are closely related to the microstructural characteristics of Cu-based shape memory alloys such as coarse grain size, high elastic anisotropy and the segregation of secondary phases or impurities along the grain boundaries [11]. It has been found that CuAlMn alloy shows good strain recovery and better ductility than CuAlNi alloy which can be correlated to decreasing the degree of order of the β parent phase [4,12,13]. Also CuAlMn alloys have higher shape memory strain, larger recovery power, better ductility, and higher damping capacity [4,14].

Most of the commercial Cu-based shape memory alloys are produced by conventional casting methods. Generally there are four advantages of rapid solidification over the slow conventional solidification techniques. These are an ability to form metastable phases, increasing the solubility above the equilibrium solubility, decreasing the segregation of additions and refining the microstructure [15-17].

In this paper, results of corrosion behavior of CuAlMn and CuAlMnNi alloy ribbons, produced by melt spinning method, in 0.9% NaCl solution have been presented.

MATERIALS AND METHODS

Rapidly solidified ribbons of CuAlMn (Cu-8.3%Al-9.4%Mn in wt.%) and CuAlMnNi (Cu-13%Al-4%Ni-2.5Mn in wt.%) were manufactured with the single roll melt spinning apparatus. The cast precursors were inserted into the graphite crucible and inductively melted in Ar atmosphere and then ejected through the nozzle with the circular shape orifice on the outer surface of the cooled rotating copper wheel. The CuAlMn and CuAlMnNi alloy ribbon samples for the electrochemical measurements were prepared by cutting to the appropriate dimensions and then soldered on an insulated copper wire to gain proper electrical contact. Polirepar S protective mass was used to isolate soldered joint points to prevent the evaluation of galvanic corrosion in contact with the electrolyte. As ribbons have very small thickness its mechanical treatment by grinding and polishing could not be performed, so the surface of the electrodes was processed by ultrasonic degreasing in ethanol, washed with deionized water and immersed in the electrolyte.

Princeton Applied Research PAR M273A potentiostat/galvanostat connected with PC was used to perform electrochemical investigations. All measurements were taken in double wall glass cell which allowed maintenance of desired electrolyte temperature, equipped with saturated calomel electrode as reference electrode, Pt-sheet electrode as counter electrode and prepared working electrode. Investigations were performed in 0.9% NaCl solution pH = 7.4 and T = 37 °C. Electrolyte solution was purged with Ar for 20 minutes prior working electrode immersion in electrolyte, and purging were continued during the electrochemical measurement with very weak intensity.



18th INTERNATIONAL FOUNDRYMEN CONFERENCE
**Coexistence of material science and sustainable technology in
economic growth**

Sisak, May 15th-17th, 2019

<http://www.simet.hr/~foundry/>

The evaluation of corrosion behavior of CuAlMn and CuAlMnNi alloy in 0.9% NaCl solution was performed by open circuit potential measurements (E_{OC}) in 60 minutes time period, linear polarization method in the potential region of ± 20 mV around E_{OC} , with the scanning rate of 0.2 mV s^{-1} and potentiodynamic polarization method in the potential region of -0.250 V from open circuit potential to 0.7 V, with the scanning rate of 0.5 mV s^{-1} . After the polarization measurements electrode surfaces were cleaned ultrasonically in deionized water, dry in desiccator and investigated with optical and SEM/EDS analysis.

RESULTS AND DISCUSSION

Table 1 shows the results of open circuit measurements for the CuAlMn and CuAlMnNi alloy in 0.9% NaCl solution. Measurements were started immediately after electrode immersion in electrolyte with collecting the values of electrode potential every 30 sec in 60 minutes period of time. Tabular values refer to the electrode potential values in ten minutes intervals, Table 1.

Table 1. Open circuit potential changes for CuAlMn and CuAlMnNi in 0.9% NaCl solution

Time/ Alloy	0 min	10 min	20 min	30 min	40 min	50 min	60 min
CuAlMn	-0.313	-0.321	-0.323	-0.324	-0.325	-0.325	-0.325
CuAlMnNi	-0.342	-0.334	-0.325	-0.321	-0.319	-0.318	-0.317

From the Table 1 it can be observed the opposite trend in changes of open circuit values for CuAlMn and CuAlNiMn alloys, i.e. for the CuAlMn alloy values of open circuit potential change slowly with time towards negative direction while for CuAlMnNi changes of E_{OC} were observed towards more positive values. It is also clear that stabilization of E_{OC} for both alloys occurs in period of 40 minutes and that final E_{OC} values do not differ significantly.

Linear polarization measurements were performed in order to determine the values of polarization resistance (R_p) which represents the resistance of metal to corrosion, and is defined by the slope of the polarisation curve near the corrosion potential, by the equation (1):

$$R_p = \frac{\Delta E}{\Delta i} (\Omega \text{ cm}^2) \quad (1)$$

Results of these investigations were presented on Figure 1 and in Table 2. It can be seen that CuAlMnNi alloy have higher curve slope then CuAlMn alloy i.e. higher values of R_p . As R_p value is reverse proportional to the corrosion current density (i_{corr}), higher value of R_p means lower value of i_{corr} i.e. lower corrosion.



18th INTERNATIONAL FOUNDRYMEN CONFERENCE
**Coexistence of material science and sustainable technology in
economic growth**

Sisak, May 15th-17th, 2019

<http://www.simet.hr/~foundry/>

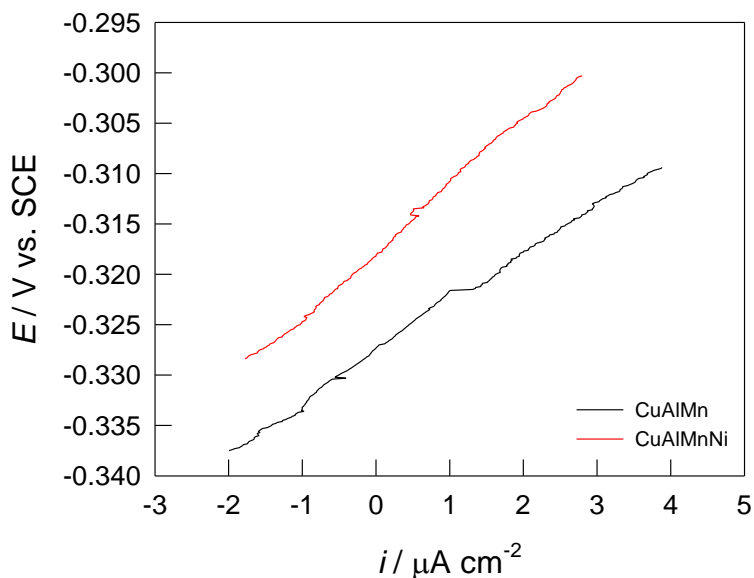


Figure 1. Linear parts of polarization curves for CuAlMn and CuAlMnNi alloys in 0.9% NaCl solution

The last applied electrochemical method was a potentiodynamic polarization method which was carried out in a wide range of potentials to gain insight into the anodic behaviour of CuAlMn and CuAlMnNi alloy in NaCl solution. Results of these investigations were presented at Figure 2 and Table 2. From the Figure 2 it can be seen different corrosion behaviour of alloys to some extent, which is manifested in anodic and cathodic parts of the curves, which is result of different alloy composition. CuAlMn alloy shows more negative corrosion potential and lower anodic current densities in higher anodic region (above 0.25 V), while in Tafel region its anodic current is slightly higher compared with CuAlMnNi alloy. After Tafel region anodic current continue to rise for both alloys and achieves its maximum after which it reduces to some extent due to formation of harder soluble corrosion compounds which act as a surface barrier and slow down the process of dissolving the alloy [18-21]. From the Figure 2 it can be seen that reduction of anodic current density for CuAlMn alloy begins earlier (on lower anodic potential) with higher reduction then CuAlMnNi alloy.



18th INTERNATIONAL FOUNDRYMEN CONFERENCE
Coexistence of material science and sustainable technology in economic growth

Sisak, May 15th-17th, 2019

<http://www.simet.hr/~foundry/>

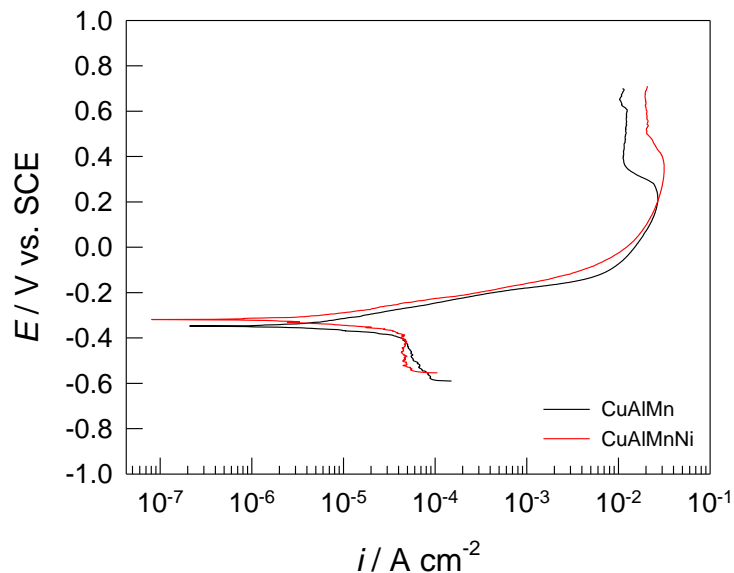


Figure 2. Potentiodynamic polarization curves for CuAlMn and CuAlMnNi alloys in 0.9% NaCl solution

Corrosion parameters for CuAlMn and CuAlMnNi alloy obtained by polarization measurements are given in Table 2.

From the Table 2 it can be seen that CuAlMnNi alloy shows lower values of corrosion current density and higher values of polarization resistance which suggest the better corrosion resistance.

Table 2. Corrosion parameters obtained from polarization measurements

Alloy	E_{corr} / V	$i_{corr} / \mu A cm^{-2}$	$R_p / k\Omega cm^2$
CuAlMn	-0.346	3.5	4.907
CuAlMnNi	-0.322	2.28	6.445

After the polarization measurements, electrode surfaces were cleaned ultrasonically in deionized water, dried in desiccator and then investigated with light microscope with magnification of 50 times. Results of these investigations are presented in Figure 3.

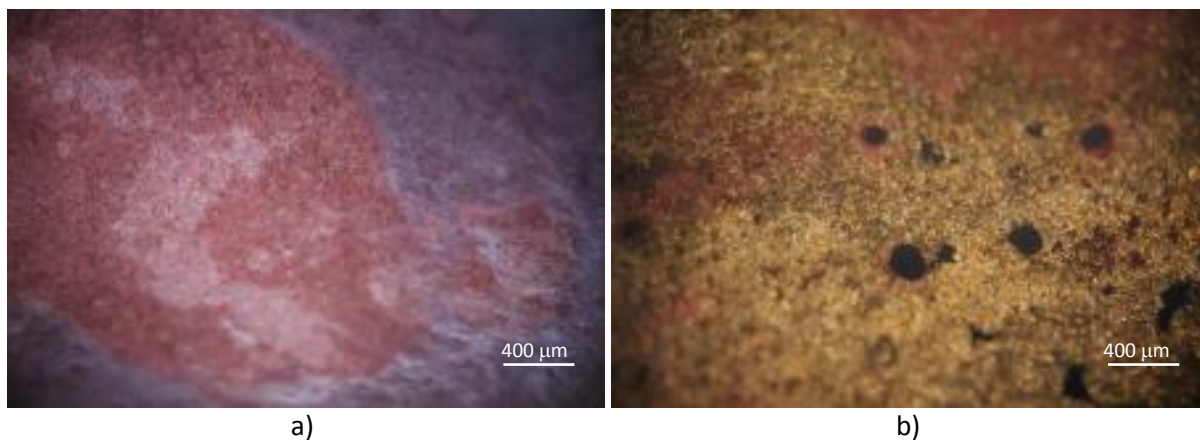


Figure 3. Optical micrographs of the corroded CuAlMn alloy surface a) and CuAlMnNi alloy surface b) in 0.9% NaCl solution

Optical images of corroded CuAlMn and CuAlMnNi surface reveal the differences in corrosion mechanism with addition of alloying element which are present in investigated alloys. On the CuAlMnNi alloy surface it can be clearly seen the existence of pitting corrosion, while the surface of CuAlMn alloy is partially covered with corrosion product without existence of pits. Earlier corrosion investigations on CuAlNi alloys have confirmed that dominant corrosion attack on the surface in chloride solution is pitting corrosion [21, 22]. Pitting corrosion is also observed on the corroded surface of the cast CuAlMnNi alloy in similar investigations in 0.9% NaCl solution but in a smaller extent compared with CuAlNi alloy [23]. It seems that the presence of Ni along with a smaller percentage of manganese and aluminium in CuAlMnNi alloy facilitates the appearance of pitting corrosion. More detail information about surface condition of corroded alloys was obtained by SEM/EDS analysis (Figure 4 and Figure 5).

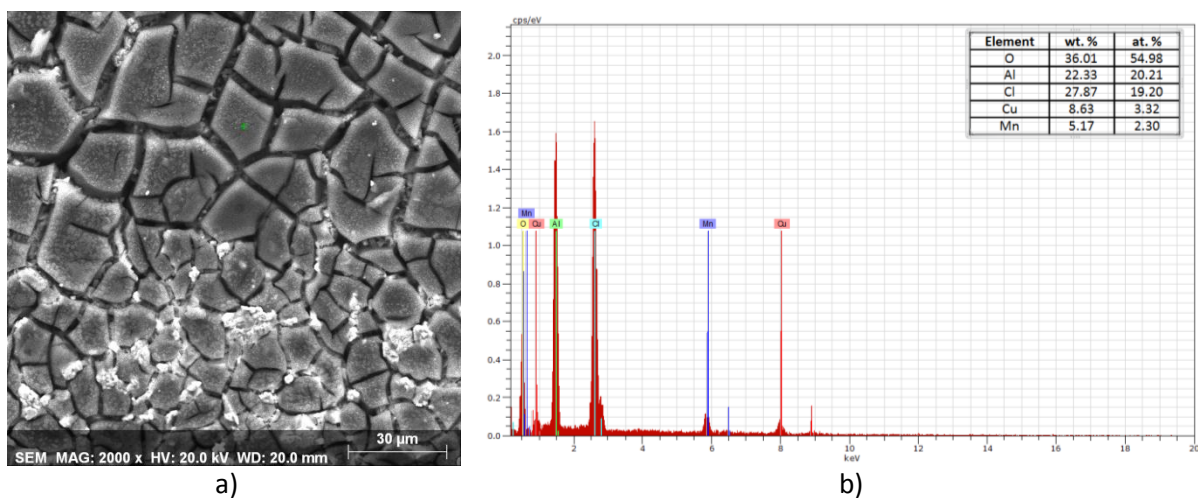


Figure 4. a) SEM images and b) EDS analysis of the CuAlMn alloy surface after polarization measurement in 0.9% NaCl solution

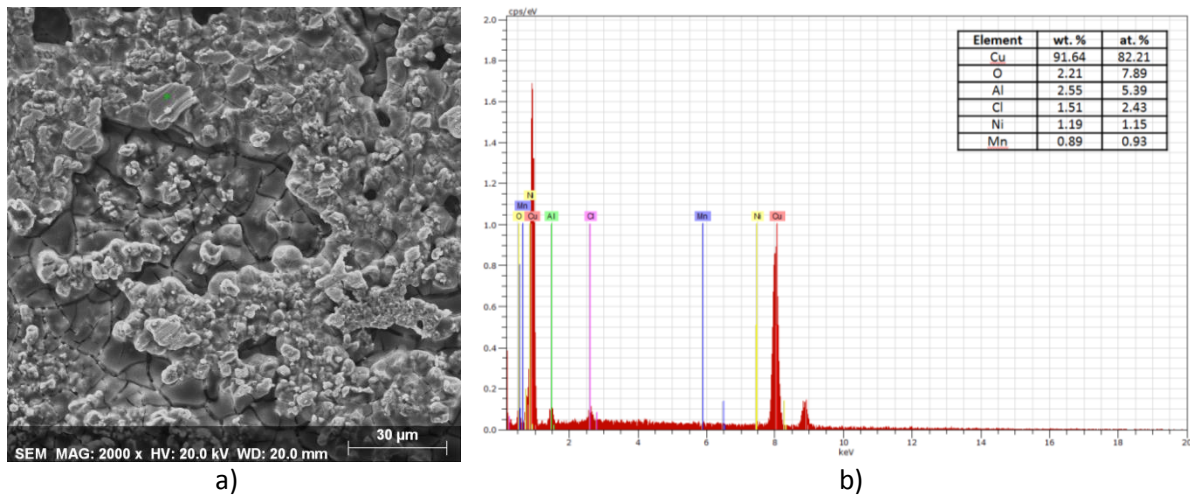


Figure 5. a) SEM images and b) EDS analysis of the CuAlMnNi alloy surface after polarization measurement in 0.9% NaCl solution

SEM/EDS analysis has shown that the cracked surface of CuAlMn alloy consist mainly of aluminum and copper oxides and chlorides, with small percentage of copper and manganese (Figure 4). A different appearance of the surface shows the CuAlMnNi alloy on which many creases and channels are formed by the corrosion process. Copper is dominant element on the surface with the small amount of oxygen, aluminum, chlorine and manganese.

CONCLUSIONS

Measurements of open circuit potential reveal the opposite trend for CuAlMn and CuAlNiMn alloy, i.e. for the CuAlMn alloy values of open circuit potential change slowly with time towards negative values while for CuAlNiMn changes of E_{OC} were observed towards more positive values. Stabilization of E_{OC} for both alloys occurs in period of 40 minutes and final E_{OC} values do not differ significantly.

Polarization measurements of CuAlMn and CuAlNiMn alloy in 0.9% NaCl solution have shown that CuAlNiMn alloy have higher values of polarization resistance and smaller values of corrosion current density. In higher anodic potentials anodic current density for CuAlMn is lower than for CuAlNiMn alloy which indicates lower dissolution of CuAlMn alloy.

On the CuAlNiMn alloy surface it can be clearly seen the existence of pitting corrosion, while the surface of CuAlMn alloy is partially covered with corrosion product without existence of pits. It seems that the presence of Ni along with a smaller percentage of manganese and aluminium in CuAlNiMn alloy facilitates the appearance of pitting corrosion.

SEM/EDS analysis has shown that the cracked surface of CuAlMn alloy consist mainly of aluminum and copper oxides and chlorides, with small percentage of copper and manganese while surface of the CuAlNiMn alloy have many creases and channels which are formed by



18th INTERNATIONAL FOUNDRYMEN CONFERENCE
**Coexistence of material science and sustainable technology in
economic growth**

Sisak, May 15th-17th, 2019

<http://www.simet.hr/~foundry/>

the corrosion process. Copper is dominant element on the CuAlMnNi surface with the small amount of oxygen, aluminum, chlorine and manganese.

Acknowledgements

This work has been fully supported by the Croatian Science Foundation under the project HRZZ-IP-2014-09-3405.

REFERENCES

- [1] I. Ivanić, M. Gojić, S. Kožuh, Slitine s prisjetljivosti oblika (I. dio): najznačajnija svojstva, *Kem. Ind.*, 63(2014)9-10, pp. 323-330.
- [2] I. Ivanić, M. Gojić, S. Kožuh, Slitine s prisjetljivosti oblika (II. dio): podjela, proizvodnja i primjena, *Kem. Ind.*, 63(2014)9-10, pp. 331-344.
- [3] S. N. Saud, E. Hamzah, T. Abubakar, H. R. Bakhsheshi-Rad, M. Zamri, M. Tanemura, Effects of Mn additions on the structure, mechanical properties and corrosion behavior of Cu-Al-Ni shape memory alloys, *JMEPEG* 23(2014)10, pp. 3620-3629.
- [4] S. Kožuh, M. Gojić, I. Ivanić, T. Holjevac Grgurić, B. Kosec, I. Anžel, The effect of heat treatment on the microstructure and mechanical properties of Cu-Al-Mn shape memory alloy, *Kem. Ind.*, 67(2018)1-2, pp. 11-17.
- [5] S. Sathish, U. S. Mallik, T. N. Raju, Microstructure and shape memory effect of Cu-Zn-Ni shape memory alloys, *JMMCE*, 2(2014), pp. 71-77.
- [6] R. Kainuma, S. Takahashi, K. Ishida, Thermoelastic martensite and shape memory effect in ductile Cu-Al-Mn alloys, *Metall. Mater. Trans. A*, 27A(1996)8, pp. 2187-2195.
- [7] R. Kainuma, N. Satoh, X. J. Liu, I. Ohnuma, K. Ishida, Phase equilibria and Heusler phase stability in Cu-Rich portion of the Cu-Al-Mn system, *J. Alloys Compd.*, 266(1998)1-2, pp. 191-200.
- [8] A. Rittapai, S. Urapepon, J. Kajornchaivakul, C. Harniratisai, Properties of experimental copper-aluminium-nickel alloys for dental post and core applications, *J. Adv. Prosthodont*, 6(2014)3, pp. 215-223.
- [9] B. Chen, C. liang, D. Fu, D. Ren, Corrosion behavior of Cu and Cu-Zn-Al shape memory alloy in simulated uterine fluid, *Contraception*, 72(2005), pp. 221-224.
- [10] R. Dasgupta, A look into Cu-based shape memory alloys: present scenario and future prospects, *J. Mater. Res.*, 29(2014)16, pp. 1681-1698.
- [11] A. K. Jain, S. Hussain, P. Kumar, A. Pandey, Effect of varying Al/Mn ratio on phase transformation in CuAlMn shape memory alloys, *Trans. Indian Inst. Met.*, 69(2016)6, pp. 1289-1295.
- [12] M. R. Rezvani, A. Shokuhfar, Synthesis and characterization of nano structured Cu-Al-Mn shape memory alloy by mechanical alloying, *Mater. Sci. Eng. A*, 532(2012), pp. 282-286.



18th INTERNATIONAL FOUNDRYMEN CONFERENCE

Coexistence of material science and sustainable technology in
economic growth

Sisak, May 15th-17th, 2019

<http://www.simet.hr/~foundry/>

- [13] U. S. Mallik, V. Sampath, Influence of quaternary alloying additions on transformation temperatures and shape memory properties of Cu-Al-Mn shape memory alloy, *J. Alloys Comp.*, 469(2009)1-2, pp. 156-163.
- [14] J. Chen, Z. Li, Y. Y. Zhao, A high-working-temperature CuAlMnZr shape memory alloy, *J. Alloys Comp.*, 480(2009)2, pp. 481-484.
- [15] S. Matsuoka, M. Hasebe, R. Oshima, F. E. Fujita, Improvement of ductility of melt spun Cu-Al-Ni shape memory alloy ribbons by addition of Ti or Zn, *Japanese Journal of Applied Physics*, 22(1983), L528-L530.
- [16] Y-W. Kim, Y-M. Yun, T-H. Nam Yun, The effect of the melt spinning processing parameters on the solidification structures in Ti-30 at.% Ni-20 at.% Cu shape memory alloys, *Mat. Sci. Eng. A*, 438-440(2006), pp. 545-548.
- [17] M. Bizjak, B. Karpe, G. Jakša, J. Kovač, Surface precipitation of chromium in rapidly solidified Cu-Cr alloys, *Apply. Surf. Sci.*, 277(2013), pp. 83-87.
- [18] A. V. Benedetti, P. T. A. Sumodjo, K. Nobe, P. L. Cabot, W. G. Proud, Electrochemical studies of copper, copper–aluminium and copper–aluminium–silver alloys: impedance results in 0.5 M NaCl, *Electrochim. Acta*, 40(1995)16, pp. 2657-2668.
- [19] M. Gojić, L. Vrsalović, S. Kožuh, A. Kneissl, I. Anžel, S. Gudić, B. Kosec, M. Kliškić, Electrochemical and microstructural study of Cu-Al-Ni shape memory alloy, *J. Alloy. Compd.*, 509(2011)41, pp. 9782-9790.
- [20] A. C. Shivasiddaramidah, U. S. Mallik, R. Mahato, C. Shashishekar, Evaluation of corrosion behavior of Cu-Al-Be-Mn quaternary shape memory alloys, *Materials Today: Proceedings*, 4(2017)10, pp. 10971-10977.
- [21] L. Vrsalović, I. Ivanić, S. Kožuh, S. Gudić, B. Kosec, M. Gojić, Effect of heat treatment on corrosion properties of CuAlNi shape memory alloy, *Trans. Nonferrous Met. Soc. China*, 28(2018)6, pp. 1149-1156.
- [22] I. Ivanić, Utjecaj toplinske obrade na mikrostrukturu i svojstva CuAlNi slitine s prisjetljivosti oblika, *Doktorski rad, Sveučilište u Zagrebu, Metalurški fakultet Sisak*, 2017.
- [23] L. Vrsalović, I. Gotovac, S. Gudić, I. Ivanić, S. Kožuh, B. Kosec, M. Bizjak, T. Holjevac Grgurić, R. Pezer, M. Gojić, Corrosion behavior of CuAlMnNi in 0.9% NaCl solution, *Proceedings of the 23th International conference of materials protection and industrial finish – KORMAT 2018*. (eds: I. Stojanović, V. Šimunović, B. Runje), Hrvatsko društvo za zaštitu materijala, 25. 4. 2018., Zagreb, Croatia, pp. 7-16.

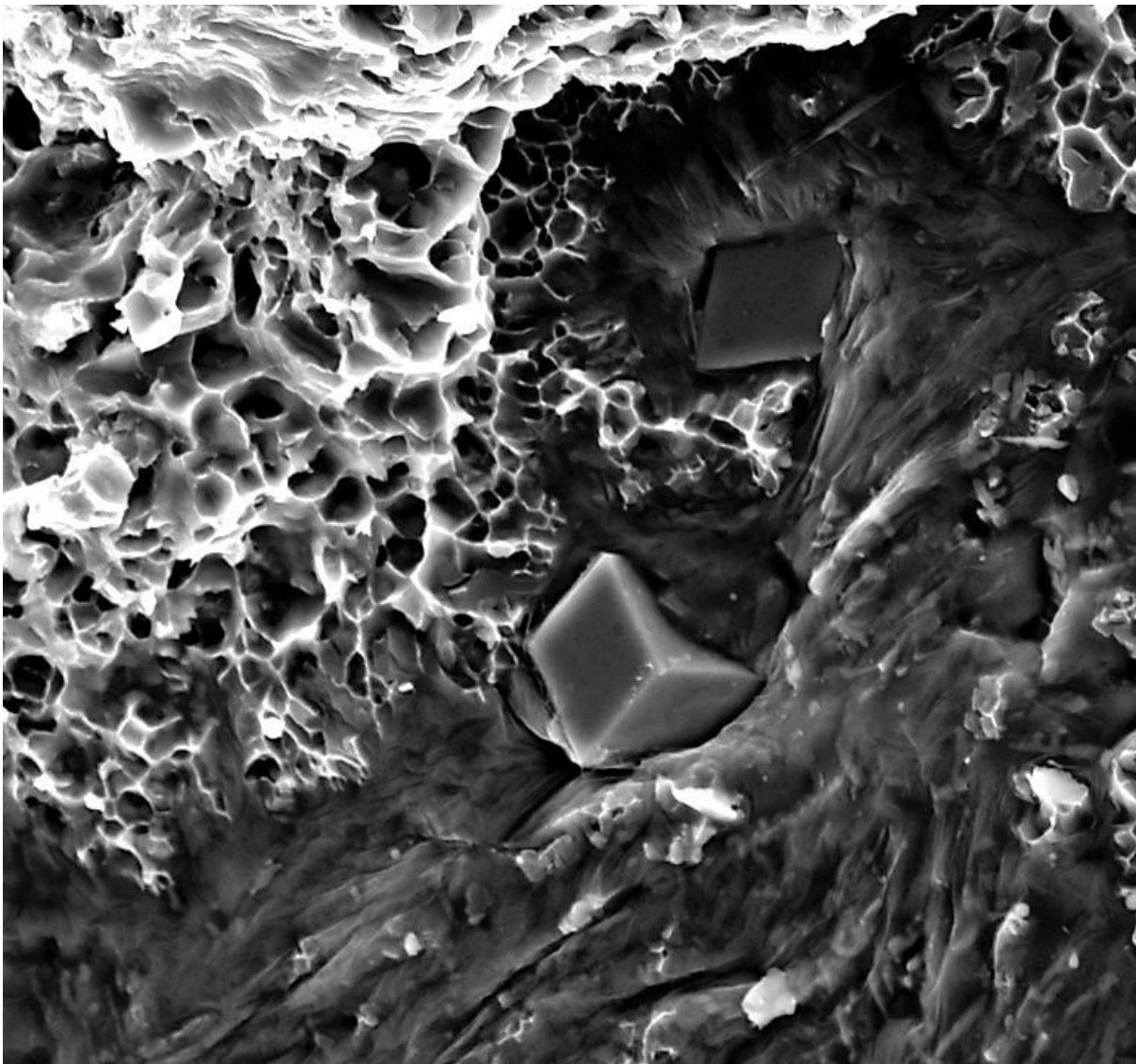


18th INTERNATIONAL FOUNDRYMEN CONFERENCE
Coexistence of material science and sustainable technology in
economic growth

Sisak, May 15th-17th, 2019

<http://www.simet.hr/~foundry/>

COMMERCIAL PAGES



F. Kozina, Z. Zovko Brodarac, The polyhedral morphology of α -Al₁₅(FeMn)₃Si₂ intermetallic phase found at the fracture surface of AlSi12 alloy



18th INTERNATIONAL FOUNDRYMEN CONFERENCE
Coexistence of material science and sustainable technology in
economic growth

Sisak, May 15th -17th, 2019

<http://www.simet.hr/~foundry/>

In alphabetical order:

SPONSORSHIP CATEGORY	COMPANY	COMPANY LOGO
CO-ORGANIZER	ELKEM ASA, Oslo (NO)	
SILVER SPONSOR	HEMOLAB Ltd, Beograd (RS)	
	LABTIM ADRIA Ltd, Sesvete (HR)	
BRONZE SPONSOR	BENTOPRODUCT Ltd, Šipovo (BA)	
	BITUS Ltd, Zagreb (HR)	
	EBERT Ltd, Ljubljana (SI)	
	FERRO-PREIS Ltd, Čakovec (HR)	
	HAGI GmbH, Pyhra (AT)	
	HEINRICH WAGNER SINTO MASCHINENFABRIK GmbH, Bad Laasphe (DE)	
	LABEKO Ltd, Zagreb (HR)	
	MECAS ESI s.r.o., Plzen (CZ) & TC LIVARSTVO Ltd, Ljubljana (SI)	
	TROKUT TEST GROUP Ltd, Zagreb (HR)	

Five steps to high quality castings



Stable and well nucleated base iron

Production of sound and cost effective iron castings begins with the selection of good quality raw materials and additives. Yet the best materials can deliver a poor quality iron unless there is sufficient nucleation carried through the process to give the graphite morphology, chill control and mechanical properties required.

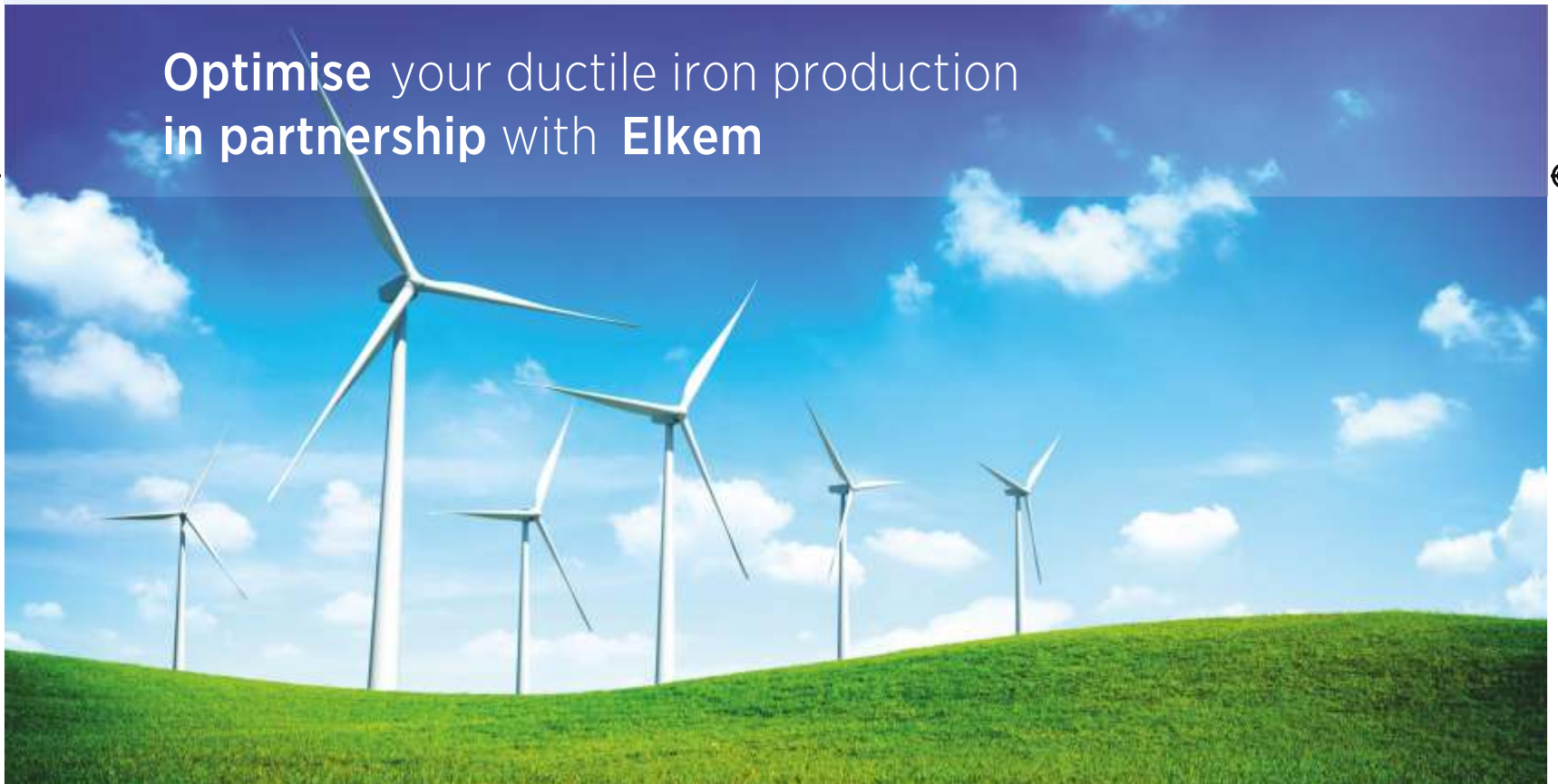
Preconditioning with a long-lasting material, such as Elkem's unique Preseed™ precondi-

tioner is the optimal way to ensure that the nuclei, once created in the melt, are stable enough to survive subsequent treatment processes prior to casting.

Essential to the process is a means of measuring the graphite activity with a melt and the thermal analysis system EPIC™ is able to quickly and accurately give an indication of whether the iron is suitable for pouring or requires correction.

www.elkem.com/foundry

Optimise your ductile iron production in partnership with Elkem



Business areas:

Silicon Materials

Silicones

Foundry Products

Carbon



Representative office:

Elkem AS

J.J. Strossmayer 176, Sisak Croatia · Tel. +385/44/659-065 · Fax +385/44/659-067 · gordana.gojsevic@elkem.com · zoran.kovacic@elkem.com

Innovative Metal Treatment Solutions



More than 100 reasons
to have a partnership

Getting the best value from nodularising alloys can be a big saving for foundries. The trend towards low Mg alloys, which have lower reactivity and hence higher recovery, continues. Elkem's extensive range of over 100 MgFeSi chemistries, coupled with Topseed® cover alloy, means that together we can optimize your total treatment alloy package. Please contact your local Elkem representative for more details or visit us at www.elkem.com/foundry.



Conventional Mg Treatment



® cover alloy

Our Partner: **Ferrosad Low Carbon Steel Shot**



**METALLTECHNIK
SCHMIDT GMBH & CO. KG**









Representative office:

Elkem AS

J.J. Strossmayer 176, Sisak Croatia · Tel. +385/44/659-065 · Fax +385/44/659-067 · gordana.gojsevic@elkem.com · zoran.kovacic@elkem.com

HEMOLAB

**Analitička hemija: instrumenti, održavanje,
metode, primena, analize voda i drugih materijala**

HEMOLAB je jedina firma koja se bavi analitičkom opremom i koja pruža
KOMPLETNU uslugu po sistemu "ključ u ruke" što znači:



Emisiona Spektrometrija

- ICP OES
- Varnični spektrometri (laboratorijski I mobilni)
- XRF Spektrometri



Termalne analize (STA, TG/DTA/DSC/



Termalna provodljivost materijala



Analizatori goriva i ulja (Benzin/Dizel/Jet fuel)



Priprema uzoraka (drobilice, mlinovi sita)

NABAVKA REZERVNIH DELOVA - POTROŠNOG MATERIJALA

- za ICP: Torch, Komore, raspršivači
- lampe za UV - VIS I AAS
- potrošni materijal za Termalne analizatore

APLIKACIJE

- izbor vrste analiza
- projekt laboratorije
- izbor metoda
- izbor odgovarajuće opreme
- nabavka opreme
- kompletna instalacija i servis
- trening i obuka za rad na instrumentima
- razvoj posebnih metoda i aplikacija

HEMOLAB • 11070 Beograd • Jurija Gagarina 14a/5
tel./fax: +381 (11) 630-4-630; 630-4-440
e-mail: office@hemolab.co.rs • www.hemolab.co.rs

OFFERING WHOLE SPECTRUM OF CUSTOMIZED SOLUTIONS

Celebrating 30 years of customer support



TA Instruments offers high technology instruments/analyzers, such as:
dilatometers, thermal conductivity meters, mechanical test instruments and dynamic mechanical analyzers for characterization of steel and metal alloys and composites.
www.tainstruments.com



ATS Creep Testing Systems offers precision lever arm testers and also furnaces, customized to user's needs.
www.atspa.com



Simultaneous ONH elemental analysis in metals and ceramics and advanced carbon and sulfur (Inductar CS) analysis for inorganic materials.
www.elementar.de



The First Name In Materials Testing
Manufacturer and supplier of static tension and/or compression testing machines, designed to measure material's strength and performance.
www.tiniusolsen.com

LJUBLJANA: Zihierlova ulica 6, 1000 Ljubljana, Slovenija, +386 1 428 36 84, info@labtim.si

ZAGREB: Jaruščica 7/A, 10020 Zagreb, Hrvatska, +385 1 662 3883, info@labtim.hr



18th INTERNATIONAL FOUNDRYMEN CONFERENCE
**Coexistence of material science and sustainable technology in
economic growth**

Sisak, May 15th-17th, 2019

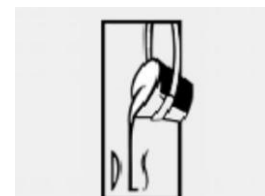
<http://www.simet.hr/~foundry/>

SUPPORTING ASSOCIATION AND COMPANIES

Croatian Foundry Association, Zagreb (HR)



Slovenian Foundry Association, Ljubljana (SI)





18th INTERNATIONAL FOUNDRYMEN CONFERENCE
**Coexistence of material science and sustainable technology in
economic growth**

Sisak, May 15th -17th, 2019

<http://www.simet.hr/~foundry/>

MEDIA COVERAGE

IRT 3000



Foundry Lexicon



Foundry Planet

